Iron-oxide geochronology to constrain the formation of soils and paleosols

Thesis by
Florian Hofmann

In Partial Fulfillment of the Requirements for the
Degree of
Doctor of Philosophy

CALIFORNIA INSTITUTE OF TECHNOLOGY
Pasadena, California

2019
Defended May 16th, 2019

Florian Hofmann
ORCID: 0000-0002-9836-2338

ACKNOWLEDGEMENTS

I wish to thank my adviser, Ken Farley, for his support and feedback over the last five years. Thank you for giving me the freedom to explore projects and ideas on my own and for entrusting your lab to someone who started out knowing next to nothing about geochronology or mass spectrometry. My heartfelt appreciation goes to the people who have supported me throughout my undergraduate studies at the University of Munich. I am extremely grateful to Anke Friedrich for inspiring me to become a scientist, providing me with many opportunities for research and teaching, and setting me on the path to go to Caltech. I want to thank Sara Carena and Hans-Peter Bunge for their helpful advice on graduate school and (academic) life in general. I very much appreciate Seth and Carol Stein's enduring friendship and great advice along the way.

In my first year at Caltech, I had the great pleasure of working with Jason and Zorka Saleeby, with whom I spent several enjoyable weeks doing field work in Croatia. I want to thank Gordon and Virginia Eaton for funding the fellowship that supported my in my first year. My fellow Pit-sters, Amber Witkosky and Sean Mullin, made the pre-qual time so much better with conversations, cake, and commiseration, as well as intra-office pranks.

I wish to thank my collaborators, who have sent me samples, shared their knowledge of regional geology, analyzed samples for me, and with whom I enjoyed many insightful discussions, namely Bettina Reichenbacher (University of Munich), Daniel Kälin (Federal Office of Topography, Berne), Michael Rummel (Naturmuseum Augsburg), Kalle Kirsimäe (University of Tartu), Roy Van Arsdale and Daniel Larsen (University of Memphis), Devin McPhillips and Katherine Kendrick (USGS Pasadena), Dylan Rood (Imperial College London), Joe Kirschvink (Caltech), and Junle Jiang (Cornell University).

I want to thank all the students who I had the fortune to TA over my years at Caltech, as well as my fellow TAs: Daniel Bowden, Voonhui Lai, and Hao Xie. Through their company, Brian Wernicke, Lydia Kivrak, Ben Cassese, and Karen Pham made field camp in the Poleta Folds (mapping many bananantic lines) an unforgettable experience. I greatly appreciate the efforts of Jenn Weaver and Olivia Wilkins at the Caltech Center for Teaching, Learning, & Outreach in helping me to improve my teaching skills during my work for the Certificate of Practice. I also wish to thank Bryan Wilbur for inviting me to guest-lecture at Pasadena City College.

I want to thank everyone in the Farley group, and those who have visited us, for helpful and inspiring discussions; in no particular order: Julia Cartwright, Ryan McKeon, Stephen Cox, Peter Martin, Frank Sousa, Jason Price, Ursula Ginster, Guillaume Avice, Forrest Horton, Andrea Balbas, Uri Ryb, Will Amidon, and Carl Swindle. I particularly like to thank Hayden Miller for sharing data and providing samples for my work in Chapter IV. Thanks also to the merry band of red-dust-encrusted adventurers on the 'Magic Bus Tour' (Paulo Vasconcelos, Davide Pistellato, Llyam White, James Sadler, Kristy Guerin, Hevelyn Monteiro, Ren Zhe) for digging enough holes to make Australia look like Swiss cheese. Special thanks go to Jonathan Treffkorn for his friendship and his great efforts in helping me with technical issues, constructing lab equipment, analyzing samples, and keeping my liquid nitrogen dewars full — especially when I was snowed in at home. I owe my deepest gratitude to Lindsey Hedges for introducing me to lab work and for her many years of friendship. I will never forget the joy you brought to my life and I miss our daily chats over a nice cup o'tea!

Many thanks also go to the people who have helped me with analytical methods. Nathan Dalleska at the Environmental Analysis Center has been extremely helpful with his practical support and sage counsel on all matters ICP-MS. I have benefited from the assistance with SEM by Ma Chi, and I greatly appreciate George Ross-

man's help with FTIR and Raman spectroscopy and for sharing his enthusiasm about new mineral acquisitions with me. I want to thank Tony Diaz for his help finding books and maps, and the staff of the Caltech Docuserve office for procuring the most obscure articles and books. Janice Grancich has been of great help with travel reports and reimbursements. I also want to acknowledge the Division of Geological and Planetary Sciences for letting me do EMR training. The work in Chapter V was supported by Grant/Cooperative Agreement Number G14AC00109 from the United States Geological Survey. I wish to thank the members of my examining committee, Paul Asimow, Brian Wernicke, and George Rossman, for contributing their time and providing thoughtful comments, which helped to improve the manuscript.

I thank all of the members of the Cahill Dungeons & Dragons group for providing regular distraction, which helped to keep me sane: Dávid 'Calenor' Guszejnov, Anna 'K' Kómár, Mike 'Chad' Grudić, Jenia 'Gruntz' Mozgunov, Denise 'Cassiopeia' Schmitz, and Clare 'Ravagella' Lahey, a.k.a. 'The Faultless Arrow'. Hæreldor will miss our epic adventures together!

I wish to thank my parents and my family for a lifetime of support and encouragement. Above all, I would like to thank my wife, Abbey Nastan, for her love, constant support, and unwavering belief in me. You have stood by me through all of the trials, travails, and triumphs of graduate school and I couldn't have done it without you!

ABSTRACT

In this thesis, I show how iron-oxide geochronology can be applied to soils and paleosols and I explore new applications of the (U-Th)/He and cosmogenic ^{3}He dating methods. In Chapters II and III, I apply the (U-Th)/He method to goethite pisoliths in paleosols and fissure fillings of the Bohnerz deposits, which are a widespread erosional lag deposit in Central Europe. I show that this deposit formed between ~55 Ma and 2 Ma and not in the late Cretaceous-early Eocene, as was previously claimed. A map compiled from published sources shows the paleo-extent of the Bohnerz deposit, which were developed on every limestone plateau in Central Europe. Concentrations of cosmogenic ^{3}He measured on pisoliths in paleosols, demonstrate that ancient cosmic-ray exposure occurred over at least 5 Ma, possibly 10-20 Ma. This shows that the Bohnerz deposits represent surfaces, which were stable for tens of millions of years before burial. Even today, these surfaces experience extremely low erosion rates of ~0.1 m/Ma, comparable to some of the Earth's most stable surfaces in arid environments. The hiatus represented by the Bohnerz unconformity lasts 125-150 Ma, yet only 30-40% of that duration is recorded in Bohnerz deposits. Pisoliths of the Bohnerz deposits are a continuous record of Central European continental climate for most of the Cenozoic.

In Chapter IV, I develop a laboratory technique to enable (U-Th)/He dating of hematite samples by the single-aliquot method. Highly retentive hematite samples have to be heated to >1000 °C to fully degas helium, but U is lost from the sample at around 980 °C. Through infrared spectroscopy and trace element analysis of heated samples, I show that U-loss correlates with a phase change from hematite to magnetite. Delaying this phase change to higher temperatures extends the usable range of temperatures to which samples can be safely heated without U-loss. This is achieved by degassing samples in a partial oxygen pressure of around 100 mbar,

which permits degassing of samples up to 1150 °C without loss of U. I demonstrate that precise and accurate (U-Th)/He ages can be obtained for hematite samples, which agree with established two-aliquot ages and I show how this method can be implemented and automated.

In Chapter V, I extend the use of ^{3}He cosmogenic dating to fine-grained iron-oxide particles, which are abundant in most types of modern soils. Diffusion modeling predicts that hematite particles down to ~10 nm should quantitatively retain helium for at least 1 Ma at Earth-surface conditions. In order to test whether pedogenic iron-oxides can be used for geochronology, I study a vertical profile of relict soil developed on a fanglomerate terrace at Whitewater Hill, California. Profiles of ^{10}Be and ^{26}Al in detrital quartz agree well with an exponential decrease in cosmogenic nuclide production and they yield an exposure age of 52.4±2.2 ka assuming no erosion. The vertical profile of ^{3}He concentrations in pedogenic iron-oxides shows a decrease with depth, but concentrations are higher than expected in the 40-100 cm depth range. This indicates vertical movement of iron-oxides in the soil, which is a well-known soil formation process. These observations are consistent with a soil age of 208±44 ka. This approach yields information on both age constraints and the formation and migration of pedogenic iron-oxides in the soil column.

PUBLISHED CONTENT AND CONTRIBUTIONS

Hofmann, F., B. Reichenbacher, and K. A. Farley (2017) "Evidence for >5 Ma paleo-exposure of an Eocene–Miocene paleosol of the Bohnerz Formation, Switzerland" in: *Earth and Planetary Science Letters* 465, pp. 168–175 DOI: 10.1016/j.epsl.2017.02.042

FH conducted the field work, collected samples, performed the analytical work, synthesized the results, and wrote the manuscript.

TABLE OF CONTENTS

Acknowledgements . . . iii
Abstract . . . vi
Published Content and Contributions . . . viii
Table of Contents . . . ix
List of Illustrations . . . xiii
List of Tables . . . xxxv
Nomenclature . . . xliv
Chapter I: Introduction . . . 1
Chapter II: Evidence for >5 Ma paleo-exposure of an Eocene–Miocene paleosol of the Bohnerz Formation, Switzerland . . . 6
2.1 Introduction . . . 7
2.2 Bohnerz Formation . . . 9
2.3 Study site . . . 11
2.4 Materials and methods . . . 12
Samples . . . 12
Analytical procedures . . . 14
2.5 Results . . . 15
Formation ages . . . 15
^{3}He concentrations of pisoliths and soil . . . 18
2.6 Discussion . . . 18
Formation of the paleosol . . . 18
Paleo-exposure history . . . 20
Long-term stability of clay soils . . . 23
2.7 Conclusions . . . 24
Appendices . . . 31
2.A ^{4}He/^{3}He experiments . . . 31
Pisoliths . . . 31
Unirradiated pisolith . . . 37
2.B Concentrations of ^{3}He . . . 38
Pisoliths . . . 38
Fine-grained iron-oxides in clay . . . 41
Exposure modeling of soil convection . . . 42
2.C Goethite (U-Th)/He ages . . . 43
2.D Step-heating of irradiated soil material . . . 50
Chapter III: Eocene-Pleistocene continental paleo-environment of Central Europe recorded by goethite pisoliths . . . 53
3.1 Introduction . . . 54
3.2 Sample Sites . . . 58
Fissure-type deposits . . . 58

Stratiform-type deposits . . . 61
Pisoliths . . . 62
3.3 Methods . . . 64
(U-Th)/He ages . . . 64
Measurements of ^{3}He concentrations . . . 66
Compilation of Bohnerz localities . . . 66
3.4 Results . . . 68
Map of Bohnerz localities . . . 68
Stratigraphic position and substrate of the Bohnerz deposits . . . 69
Goethite (U-Th)/He ages . . . 72
Cosmic-ray exposure duration of paleosols and fissure fillings . . . 75
3.5 Discussion . . . 78
Paleo-extent and temporal constraints . . . 78
Initiation of Bohnerz-type weathering in Central Europe . . . 79
Formation mechanism . . . 81
Erosion rates . . . 85
3.6 Conclusions . . . 85
Appendices . . . 92
3.A SEM images of pisoliths . . . 92
3.B Bohnerz (U-Th)/He ages . . . 100
3.C ^{3}He concentration data table . . . 110
3.D List of localities of Bohnerz deposits with references . . . 111
Fissure-type deposits . . . 112
Stratiform-type deposits . . . 122
Cave deposits . . . 127
Chapter IV: U-loss associated with laser-heating of hematite and goethite in vacuum during (U-Th)/He dating and prevention using high O_2 partial pressure . . . 142
4.1 Introduction . . . 143
4.2 Experimental setup and samples . . . 147
Samples . . . 147
^{4}He measurement . . . 148
Sample dissolution and elemental analysis . . . 150
Monitoring phase change with ATR-FTIR . . . 151
4.3 Results . . . 152
Sample inhomogeneity . . . 152
U-loss in vacuum heating . . . 155
Effect of heating time . . . 159
Phase transition during heating . . . 159
Phase transition from oxygen release . . . 162
Samples heated in oxygen . . . 164
4.4 Discussion . . . 166
Phase transition and U-loss . . . 169
Implementation of high p(O_2) method . . . 174
Replicate analyses . . . 176

Evaluating Th/U as indicator of U-loss . . . 178
He release in O_2 . . . 179
4.5 Conclusions . . . 180
Appendices . . . 186
4.A Technical Implementation of He degassing procedure in O_2 at Caltech 186
Technical challenges and implementation . . . 186
O_2 delivery . . . 186
Purification of O_2 . . . 186
Cycling of O_2 . . . 187
Interference on optical pyrometry . . . 187
Required laser power . . . 188
Heating of neighboring packets . . . 189
Packet material . . . 189
Pt packet blank . . . 190
O_2 breakthrough . . . 191
Test for interference of O_2 on He measurement . . . 192
Vacuum line configuration . . . 195
Measurement procedure . . . 195
4.B Pyrometer calibration . . . 198
Measurement procedure . . . 198
Outcome of heating experiments . . . 199
Calibration data . . . 203
4.C Ru-spike for measurement of Fe . . . 209
Importance of Fe measurement . . . 209
Measurement procedure . . . 209
Test of Ru vs. Ca-spike . . . 209
Advantages of Ru-spike . . . 214
ICP-MS data . . . 215
4.D ATR-FTIR spectroscopy of hematite and goethite phase transitions . 217
Heating and ATR-FTIR procedure . . . 217
Phase identification . . . 218
Hematite-magnetite mixtures . . . 219
Hematite samples . . . 222
Goethite samples . . . 228
U loss and magnetite percentage . . . 234
Physical parameters to test for hematite-magnetite conversion . . . 236
4.E Data of undegassed aliquots . . . 236
4.F Data of (U-Th)/He analyses . . . 245
Chapter V: The potential of fine-grained pedogenic iron-oxide for cosmogenic ^{3}He dating: a case study of a relict soil at Whitewater Hill, California . . . 270
5.1 Introduction . . . 271
5.2 Theoretical considerations . . . 272
Morphology and species of pedogenic iron-oxides . . . 273
Accumulation of helium . . . 274
Production of ^{3}He . . . 275

Retention of helium . . . 278
Change in iron-oxide concentrations with soil age . . . 280
5.3 Whitewater Hill . . . 283
Geology . . . 283
Sampling . . . 284
Expected helium retention in pedogenic iron-oxides . . . 285
Production rate of ^{3}He . . . 287
5.4 Sample processing and measurement procedures . . . 289
Soil processing . . . 289
Li measurement . . . 290
Iron-oxide concentrations in soil . . . 290
Measurement of ^{3}He concentrations . . . 291
Measuring ^{10}Be and ^{26}Al concentrations . . . 291
5.5 Results . . . 292
Concentrations of iron-oxides and trace elements . . . 292
^{10}Be and ^{26}Al concentration profiles . . . 298
^{3}He concentrations in pedogenic iron-oxides . . . 300
Step-heating of soil material . . . 301
5.6 Discussion . . . 306
Helium-retention in pedogenic iron-oxides . . . 306
Age of the Whitewater soil . . . 307
Implications for Banning Strand slip rate . . . 308
Possible uses of ^{3}He in pedogenic iron-oxides . . . 309
5.7 Conclusions . . . 310
Index . . . 317

LIST OF ILLUSTRATIONS

Number *Page*

2.1 Location of the outcrop Lohn am Randen in Central Europe. The Bohnerz Formation is a layered deposit that occurs locally in the region around the outcrop. Similar clay deposits can be found mostly as fissure fillings along the limestone plateau of the Swabian and Franconian Alb. 10

2.2 Outcrop Lohn am Randen and examples of pisoliths. (A) Northern wall of the quarry near Lohn, Switzerland. Red paleosol is overlying deeply eroded Jurassic limestone. The paleosol is covered by Miocene conglomerates. This sedimentary sequence is displaced by the Randen normal fault. Samples were taken in a depth profile along the blue line. (B) Typical appearance of a pisolith. (C) Same pisolith cracked open. (D) Polished section of a pisolith shows typical internal structure: layered cortex and fine-grained nucleus. (E) Nodule containing several pisoliths. (F) Detailed picture of the outcrop. A deep fissure filled with clay can be seen on the bottom right. (G) Stratigraphic column of the outcrop. 13

2.3 Vertical depth profiles of (U-Th)/He formation age (A) and ^{3}He concentration of (B) pisoliths as well as (C) soil samples normalized to the mass of iron-oxides in the soil from outcrop Lohn am Randen. The freshwater limestone layer occupies the 20 cm above 0 cm. A calcrete horizon is situated around 100 cm depth. One ^{3}He concentration is shown per pisolith per depth. For replicate samples of the same pisolith the average of all replicates is shown. The solid line represents the average ^{3}He concentration for each depth. Histograms show the distribution of (U-Th)/He formation ages (D) and ^{3}He concentrations of pisoliths (E) as well as soil samples (F) for all depths. (U-Th)/He ages from pisoliths collected from float, which were not part of the depth profile, were added to the formation age histogram ('other pisoliths'). Also included are the ages of the pisoliths in the nodule shown in Fig. 2.4 (ages of the matrix excluded). (U-Th)/He ages and ^{3}He concentrations are not corrected for partial retentivity (estimated to range from 92 to 98%). 16

2.4 Left: (U-Th)/He formation ages of pisoliths as well as the matrix of a nodule (BR-cut2) containing several pisoliths. The ages obtained for the pisoliths (42-17 Ma) are similar to those obtained for many other pisoliths in the depth profile (see Fig. 2.3). Matrix material, which contains more clay than the pisoliths, yields younger formation ages. This suggests that there was some minor precipitation of goethite after the deposit was covered. Center and right: Radial age profiles of two different pisoliths (L120f, L70g). L120f shows slow linear growth from 40 Ma to 20 Ma, then more rapid growth until 17 Ma. L70g has only a short growth history around 20 Ma. (U-Th)/He ages are not corrected for partial retentivity. 17

2.5 Normalized ^{4}He/^{3}He spectra of samples FH-F1 through FH-F5. Samples FH-F1 and FH-F2 were taken from the cortex of two different pisoliths. Samples FH-F3, FH-F4, and FH-F5 were taken from the 3rd and 4th layer of the cortex as well as the finer-grained nucleus of the same pisolith. The dashed line shows the 1σ uncertainty of the ^{4}He/^{3}He ratio. 36

2.6 Results of a step-heating experiment with unirradiated goethite from cortex material of pisolith L120a. The relative amounts of ^{3}He and ^{4}He are the same for every temperature step, showing that both isotopes are equally strongly bound. 37

2.7 Normalized ^{4}He/^{3}He spectra of proton irradiated samples FH-FC1-L20clay-irr and FH-FC2-L300clay-irr. Each heating step was 30 min, with temperatures ranging from 20 °C to 550 °C followed by total fusion at 1350 °C. The samples are red Bolus clays, consisting of kaolinite with about 10-15% iron-oxides. The ^{4}He/^{3}He spectra represent the combined spectra of these phases. About 20% of the total ^{3}He is released <100 °C without any measurable release of ^{4}He, suggesting no He retentivity of clay. Since the helium release in this heating schedule occurs below 150 °C for goethite and above 150 °C for hematite, the individual spectra can be isolated. This permits an estimate of the He retentivity of the individual phases, which is 60-70% for both hematite and goethite. The dashed line shows the 1σ uncertainty of the ^{4}He/^{3}He ratio. 51

3.1 The two basic types of Bohnerz deposits. Fissure-type deposits can be found as narrow fissures, funnel-shaped depressions, or pockets filled with red Bolus clay (picture from Petersbuch quarry, Germany). Stratiform-type deposits are laterally extensive deposits on the surface of a limestone, showing indications of a paleosol, but also often with signs of reworking in the upper part (picture from Lohn quarry, Switzerland). They are frequently found covered with late Eocene or younger clastic strata. Some outcrops also show fissure fillings in the subsurface, which are connected to the paleosol. 56

3.2 Photographs showing the typical appearance of pisoliths: outside of pisolith, cut concentrically layered pisolith with fine-grained core, cross-section of an unlayered pisolith, pisoliths in situ in Bolus clay, and inside of pisolith showing several episodes of goethite precipitation and dissolution. 63

3.3 East-west profile of the unconformity and map of Bohnerz deposit localities compiled from published literature of fissure-type/stratiform-type/cave deposits. Age of substratum and cover units of the Bohnerz deposits as well as range of fossils contained in the deposits are given in the diagram in absolute time. Bohnerz deposits are widespread in Central Europe. The Swabian Alb and Franconian Alb regions contain mostly fissure-type deposits, whereas stratiform-type deposits are more common in all other regions, including the Jura Mountains and the Helvetic Alps, where they are covered by Molasse units of mostly Eocene-Oligocene age. 70

3.4 Histograms of (U-Th)/He ages with 1 Ma bins for all localities with stratigraphic constraints (age of substratum, cover, fossils contained in fissure fillings). Grey bars denote fissure fillings, dark bars are stratiform-type deposits. Data for Lohn was previously published in Hofmann et al. (2017). Below: map of localities for which ages were obtained. 73

3.5 Depth profiles and distribution of ages of in adjacent fissure fillings. Ages of fissure filling P-F2 at Petersbuch quarry show no trend with depth. Ages >15 Ma are only found in pisoliths within the modern soil above the fissure. Pisoliths in fissure fillings in the Franconian Alb (Weißenburg, Rothenstein, Petersbuch) are younger than the small mammal fossils contained in them. They must have formed after deposition of material in the fissure. 75

3.6 Samples from seven adjacent pits at Cholplatz, each representing a different fissure, yield comparable age ranges (left). Age profiles of individual pisoliths (right) from Cholplatz show that ages younger than about 25 Ma (age of cover) only make up the outermost 5-15% of the radius. 76

3.7 Depth profiles of ^{3}He concentration with 1σ uncertainty measured on individual pisoliths. Malsenhof is a paleosol with a reworked upper part. Aufberg, Willmandingen, and Petersbuch are fissure fillings. Grey line denotes average concentration for Malsenhof. For Aufberg and Willmandingen, the dashed line is a representative exponential and the horizontal bar indicates the surface of limestone, with modern soil above 15 cm depth. 77

3.8 Histogram of all ages reported here with 1 Ma bins, with ages from fissures in gray and those of stratiform-type deposits in red. Ages are compared to Central European (Mosbrugger et al., 2005) and global (Hansen et al., 2013) temperature reconstructions. Also given is a histogram of ages of small mammal fossils in 1 Ma bins, constructed from individual age ranges for each locality. Initiation of Bohnerz weathering occurred around the time of the Paleocene-Eocene Thermal Maximum (PETM) and continued through the following period of stable warm climate. The youngest ages are around 2 Ma, a time which saw a global and regional drop in mean annual temperatures. The Bohnerz deposits showed great stability during regional tectonic events and a major re-organization of drainage networks. 81

3.9 SEM images of goethite pisolith W21b from Weißenburg at different magnifications. Darker zones have higher fractions of Al and Si relative to Fe, indicating higher degree of Al-substitution. The pisolith is composed of plates of goethite with thicknesses of <0.1 μm. White box indicates location of detailed view below. 93

3.10 SEM image of pisolith P62A from Peterbuch showing a layered cortex and a fine-grained nucleus with mineral inclusions. Elemental profile of the cortex (A-A') reveals a homogeneous goethite composition with Al and Si substituting for Fe. The nucleus is composed of partially ferruginized kaolinitic clay. The area around cracks in the nucleus (B-B') contains pure iron-oxide. The amount of ferruginization decreases with distance to the crack and attains a constant background value about 25-30 μm from the crack. 94

3.11 SEM image of pisolith Lohn-3m-cut1 from outcrop Lohn am Randen with elemental profile obtained by EDS. Red color indicates Fe-content, magenta shows region of high S content (sulfate or sulfide inclusion). This pisolith contains a varying fraction of clay minerals, as indicated by high Al-content, often in excess of what would be expected even for full Al-substitution for Fe in goethite. Some layers of the cortex are composed mostly of goethite. 95

3.12 SEM images of pisoliths R16d (top) from Rothenstein and L250cut1 (bottom) from Lohn am Randen. These images demonstrate the fine-grained nature of the goethite in the cortex, which is present in the form of plates of 0.1-0.5 μm diameter and <0.1 μm thickness. 96

3.13 Composite of two SEM images of a pisolith from Oberdorf highlighting the complex history represented in some pisoliths. The nucleus is formed by a broken piece of cortex from a different pisolith. The cortex shows complex layering, with multiple episodes of mechanical abrasion or chemical resorption of goethite, alternating with unconformable deposition of thin layers of goethite. A light micrograph of this pisolith can be found in Fig. 3.2. 97

3.14 Example of an unlayered pisolith, showing SEM image of pisolith R16c from Rothenstein and EDS elemental maps of Fe, Al, and Si. This pisolith has a homogeneous goethitic composition with constant amounts of substitution of Al (25%) and Si (5%) for Fe. 98

3.15 SEM image and EDS elemental profile of a pisolith from outcrop Oberbuchsiten. The structure of this pisolith is similar to that of other pisoliths described here, with a nucleus-cortex dichotomy. However, the composition is dominated by kaolinite with partial ferruginization. Samples like these have a lighter greyish color and were not used for (U-Th)/He analysis. All pisoliths from this outcrop had this appearance and they did not yield any datable material. 99

4.1 Ideal experiment outcome for sample heating. Complete He degassing occurs above the He extraction temperature. Below this temperature (U-Th)/He ages are below the 'true' age of the sample due to incomplete He extraction. U is lost at high temperatures, which leads to an increase in age as well as Th/U and Sm/U ratios. Age will tend to infinity for complete U-loss, unless Th is present. Ideally, complete He extraction will occur below the U-loss temperature. In this case, there is an age plateau between these two temperatures. . . 146

4.2 Inhomogeneity of U concentration in three samples by mass of aliquot. U concentrations were normalized by bulk concentrations measured on several milligrams of sample material. Small masses have larger variability, while larger aliquots have U concentrations close to the bulk value. 153

4.3 Concentrations of U, Th, and Sm of undegassed hematite samples measured on 25-45 aliquots of 20-800 µg, as well as Th/U and Sm/U ratios. Given are KDEs with bandwidths of the average 2σ uncertainty of individual measurements. Bars above the KDEs indicate the median value and the interquartile range. 154

4.4 Concentrations of U, Th, and Sm of undegassed goethite samples measured on 10-26 aliquots of 20-350 μg, as well as Th/U and Sm/U ratios. Given are KDEs with bandwidths of the average 2σ uncertainty of individual measurements. Bars above the KDEs indicate the median value and the interquartile range. 156

4.5 Hematite and goethite samples heated to temperature between 500 and 1300 °C in vacuum. All values were normalized by median value from undegassed aliquots (U, Th, Sm, Th/U or Sm/U) or two-aliquot bulk analyses (age, He concentration) and grey areas represent the typical range of values. U in both hematite and goethite is lost at temperatures above ~980 °C. 158

4.6 Effect of heating time on hematite sample MS with isothermal holding in vacuum at 950 °C (black). At this temperature, U-loss in vacuum is detectable for heating times >20 min. Samples heated in ~100 torr O_2 at 1000 °C (green) do not show any loss of U regardless of heating time. Black and green lines represent general trends. 160

4.7 ATR-FTIR spectra of hematite sample HM2, heated to different temperatures (given in °C) in vacuum and in 100 torr of O_2 for 10 min. U concentrations and Sm/U ratios were measured on subsamples of the same material used for ATR-FTIR. Estimated magnetite percentage (mag-%) was determined from peak ratio. Initiation of U-loss occurs at the same temperatures as detectable partial conversion of hematite to magnetite. Partial conversion of sample material to magnetite is detectable with a hand magnet. 161

4.8 Summary of all hematite ATR-FTIR experiments. Magnetite percentage (top) and U concentration (bottom) as a function of temperature for heating of samples in vacuum (left) and 100 torr of O_2 (right). U concentrations are normalized by the median value of undegassed aliquots. Massive U-loss correlates with major conversion of hematite to magnetite. Shaded region is temperature range of hematite-magnetite transition from phase diagram of Ketteler et al. (2001) based on measured and estimated oxygen partial pressures. Grey lines show general trend. 163

4.9 Pressure in the laser chamber as a function of temperature, interpreted to result from release of oxygen from hematite during transition. Measurements were normalized by the maximum observed pressure to compare samples of different mass. 165

4.10 Hematite and goethite samples heated in 30-100 torr of O_2. All values were normalized by median value from undegassed aliquots (U, Th, Sm, Th/U or Sm/U) or two-aliquot bulk analyses (age, He concentration) and grey areas represent the typical range of values. U-loss temperature for is deferred to 1180 °C for hematite and to ~1100 °C for goethite, compared to ~980 °C for heating in vacuum. . 167

4.11 Theoretical phase diagram (redrawn after Ketteler et al., 2001) with phase determinations of three different hematite samples determined by ATR-FTIR. The exact oxygen partial pressure ($p(O_2)$) of samples heated in vacuum is unknown, but lower than the maximum observed pressure of 10^{-5} mbar. Experiments in O_2 were performed at ~100 torr (133 mbar). Our observations show that partial conversion of hematite to magnetite occurs at the predicted phase transition temperature, which confirms the phase diagram, but demonstrate that full conversion of hematite to magnetite is kinetically inhibited to higher temperatures than the equilibrium phase transition temperature. . . . 170

4.12 Modeled time to extract 99.5% of total amount of He for different domain sizes using the hematite diffusion coefficients of Farley (2018). Grey areas represent 2σ uncertainty. Safe limit of vacuum degassing of hematite is around 950 °C. Degassing in 100 torr of O_2 can be done safely without U-loss up to ~1150 °C in hematite. 173

4.13 Schematic diagram of the vacuum line used for O_2 degassing. A calibrated amount of oxygen is released into the laser chamber from the O_2 tank using a pipette. The lifter mechanism can be used to release and capture O_2 on the cold finger before and after laser heating. Samples are degassed with 100 torr of O_2 present, which is completely trapped before mass spectrometric analysis. 175

4.14 (U-Th)/He ages of replicate analyses of aggregated aliquots of hematite sample MS degassed in 100 torr of O_2 at 1150 °C for 20 min, compared to the two-aliquot age of Farley and McKeon (2015). Heated aliquots show no correlation between age and effective U concentration (eU). KDE distributions of degassed samples (dark shading) overlap with those of undegassed samples (light shading). There is no indication of U-loss. 178

4.15 Results of a test for possible interference of O_2 on He measurement. Given are relative changes (normalized to average value) in ^{3}He sensitivity, ratio of one draw from internal standard tank, and amount of He detected in a draw from a different external standard tank released directly into the laser chamber. Green area and values indicate the presence of O_2 in the laser chamber during analysis. Analyses other than internal or external standards are line blanks or laser line blanks. 193

4.16 Normalized change in ^{3}He sensitivity and ^{4}He/^{3}He ratio of draws from an internal standard tank for a series of runs in vacuum (black) and with O_2 (green), with 1σ uncertainty. Every line represents a single run, each with a set of 36 individual samples or fewer being analyzed, including re-extracts, blanks, and interspersed standards. Each run spans between three and six days. 194

4.17 Schematic diagram of the vacuum line used for O_2 degassing. The lifter mechanism can be used to release and capture O_2 before and after laser heating. 195

4.18 Laser cell setup for pyrometer calibration. A Pt packet is mounted on the welded junction of a thin K-type thermocouple wire. It is heated by a laser through a sapphire window, which also permits the transmission of black-body radiation for optical pyrometry. The cell can be either turbo-pumped for vacuum experiments or filled with O_2. 198

4.19 Example of vacuum heating runs for two different Pt packets showing both prograde and retrograde heating paths. The emissivity changes between the first heating cycle and the subsequent heating cycles, leading to a difference in the calibration of 10-20 °C. 200

4.20 Heating packets under normal measurement conditions. One packet was heated in vacuum to a pyrometer set-point of 530 and a re-extract of 535, which is the regular schedule for analyzing goethite samples at Caltech. A different packet was heated in 100 torr of O_2 to a pyrometer set-point of 640, with a re-extract at the same set-point. . . 201

4.21 Data from all heating runs for Pt packets heated in vacuum and O_2 (left) and best-fit quadratic regression curves (right). The O_2 curve is about 2% higher than the one for vacuum. 201

4.22 Data from one heating run of a Nb packet heated in vacuum with best-fit quadratic regression curve and equation. 202

4.23 Fe masses of solutions with known amounts measured by isotope dilution using Ca and Ru as an elemental spike. Both methods yield linear relationships close to the 1:1 line (black). 210

4.24 Fe-based sample masses measured by ICP-MS using Ca and Ru as an elemental spike compared with weighed masses. Five aliquots each of three different hematite (left) and goethite samples (right) were analyzed. Masses derived from Ru-spike are closer to weighed masses than those from Ca-spike. 211

4.25 U and Th concentrations (ppm) derived from masses measured by means of Ca-spike (blue) and Ru-spike (red) compared to those derived from weighed masses. 212

4.26 Sm concentrations and effective uranium concentrations (ppm) derived from masses measured by means of Ca-spike (blue) and Ru-spike (red) compared to those derived from weighed masses. 213

4.27 Representative ATR-FTIR spectra of iron-oxide (left) and interfering phases (right) detected in sample spectra. Spectra for quartz, calcite, and portlandite are from the RRUFF database. Numbers are wavenumbers of peaks in cm^{-1}. 219

4.28 ATR-FTIR spectra of mixtures of synthetic hematite and magnetite powders. 221

4.29 ATR spectra of hematite sample MS, heated to different temperatures in vacuum for 10 min and in 100 torr of O_2 for 10 min and 60 min. Estimated magnetite percentage (mag-%) was determined from peak ratio. 223

4.30 ATR spectra of hematite sample HM1, heated to different temperatures for 10 min in vacuum and 100 torr of O_2. Estimated magnetite percentage (mag-%) was determined from peak ratio. 224

4.31 ATR spectra of hematite sample HM2, heated to different temperatures in vacuum for 10 min and in 100 torr of O_2 for 10 min and 60 min. Estimated magnetite percentage (mag-%) was determined from peak ratio. 225

4.32 ATR spectra of hematite samples HM2048 and GC, heated to different temperatures in vacuum for 10 min. U concentrations of HM2048 were determined, but were <0.1 ppm and below the detection limit. . 226

4.33 Summary of all hematite ATR-FTIR experiments. Magnetite percentage (top) and U concentration (bottom) as a function of temperature for both vacuum (left) and 100 torr of O_2 (right). Massive U loss correlates with major conversion of hematite to magnetite. Shaded region is temperature range of hematite-magnetite transition from phase diagram of Ketteler et al. (2001) based on measured and estimated oxygen partial pressures. 227

4.34 ATR spectra of goethite sample CIT, heated to different temperatures for 10 min in vacuum and in 100 torr of O_2. 230

4.35 ATR spectra of goethite sample RH, heated to different temperatures for 10 min in vacuum and in 100 torr of O_2. 231

4.36 ATR spectra of goethite sample YAN, heated to different temperatures in vacuum for 10 min. 232

4.37 Summary of all goethite ATR-FTIR experiments. Magnetite percentage (top) and U concentration (bottom) as a function of temperature for both vacuum (left) and 100 torr of O_2 (right). Massive U loss correlates with major conversion of hematite to magnetite. Shaded region is temperature range of hematite-magnetite transition from phase diagram of Ketteler et al. (2001) based on measured and estimated oxygen partial pressures. Grey lines show general trends. . . . 233

4.38 U concentration of four hematite samples normalized by average of undegassed aliquots plotted against estimated percent of hematite converted to magnetite. 235

4.39 U concentration of four different hematite samples normalized by average U concentration of undegassed aliquots plotted against estimated percent of hematite converted to magnetite. 235

4.40 Heating experiments of hematite sample MS in vacuum and 0.2-0.6 torr (25-80 Pa) of O_2 in Pt packets. Samples were degassed at between 6 and 90 min. Horizontal line is the median value from undegassed aliquots (U, Th, Sm, Sm/U) or two-aliquot bulk analyses (age, He concentration), grey areas represent the interquartile range of values, and red lines show general trends. Detectable U loss occurs at 960 °C in vacuum and 1100 °C in 0.2-0.6 torr of O_2. 246

4.41 Heating experiments of hematite sample MS in 30-60 torr (4-8 kPa) and 100 torr (13 kPa) of O_2 in Pt packets. Samples were degassed at between 6 and 90 min. Horizontal line is the median value from undegassed aliquots (U, Th, Sm, Sm/U) or two-aliquot bulk analyses (age, He concentration), grey areas represent the interquartile range of values, and red lines show general trends. Detectable U loss occurs at 1180 °C in 50 torr and at 1190 °C in 100 torr of O_2. 247

4.42 Heating experiments of hematite sample HM1 in vacuum using Pt and Nb packets. Samples were degassed at between 6 and 360 min. Horizontal line is the median value from undegassed aliquots (U, Th, Sm, Sm/U) or two-aliquot bulk analyses (age, He concentration), grey areas represent the interquartile range of values, and red lines show general trends. Detectable U loss occurs at ~980 °C for both Pt and Nb packets. 248

4.43 Heating experiments of hematite sample HM1 in ~0.2 torr (27 Pa) and ~100 torr (13 kPa) of O_2 in Pt packets. Samples were degassed at between 10 and 130 min. Horizontal line is the median value from undegassed aliquots (U, Th, Sm, Sm/U) or two-aliquot bulk analyses (age, He concentration), grey areas represent the interquartile range of values, and red lines show general trends. Detectable U loss occurs at ~1100 °C in 0.2 torr and at 1180 °C in 100 torr of O_2. 249

4.44 Heating experiments of hematite sample HM1 in vacuum using Pt and Nb packets. Samples were degassed at between 6 and 120 min. Horizontal line is the median value from undegassed aliquots (U, Th, Sm, Sm/U) or two-aliquot bulk analyses (age, He concentration), grey areas represent the interquartile range of values, and red lines show general trends. Detectable U loss occurs at ~980 °C for both Pt and Nb packets. 250

4.45 Heating experiments of hematite sample HM2 in ~0.2 torr (27 Pa) and ~100 torr (13 kPa) of O_2 in Pt packets. Samples were degassed at between 10 and 110 min. Horizontal line is the median value from undegassed aliquots (U, Th, Sm, Sm/U) or two-aliquot bulk analyses (age, He concentration), grey areas represent the interquartile range of values, and red lines show general trends. Detectable U loss occurs at ~1100 °C in 0.2 torr and at 1180 °C in 100 torr of O_2. 251

4.46 Heating experiments of hematite sample GC in vacuum in Pt packets. Samples were degassed for 20 min. Horizontal line is the median value from undegassed aliquots (U, Th, Sm, Sm/U) or two-aliquot bulk analyses (age, He concentration), grey areas represent the interquartile range of values, and red lines show general trends. No major U loss was observed, with minor U loss possible at ~1100 °C. Age and He concentration are only ~50% of the two-aliquot values. . 252

4.47 Heating experiments of goethite sample blade in vacuum and ~100 torr of O_2 in Pt packets. Samples were degassed between 6 and 20 min. Horizontal line is the median value from undegassed aliquots (U, Th, Sm, Sm/U), grey areas represent the interquartile range of values, and red lines show general trends. The 'true' age of the sample is unknown. U loss occurs at around 1000 °C in vacuum and no major U loss was observed in O_2. 253

4.48 Heating experiments of goethite sample CIT in vacuum and ~100 torr of O_2 in Pt packets. Samples were degassed between 6 and 20 min. Horizontal line is the median value from undegassed aliquots (U, Th, Sm, Sm/U), grey areas represent the interquartile range of values, and red lines show general trends. The age of the sample is around 10 Ma. U loss occurs at around 950 °C in vacuum and at about 1100 °C in O_2. 254

4.49 Heating experiments of goethite sample Lyp in vacuum and ~100 torr of O_2 in Pt packets. Samples were degassed between 10 and 20 min. Horizontal line is the median value from undegassed aliquots (U, Th, Sm, Sm/U), grey areas represent the interquartile range of values, and red lines show general trends. The 'true' age of the sample is the average of Vasconcelos et al. (2013). Detectable U loss occurs at 960 °C in vacuum and at about 1180 °C in O_2. 255

4.50 Heating experiments of goethite sample CIT in vacuum and ~100 torr of O_2 in Pt packets. Samples were degassed for 20 min. Horizontal line is the median value from undegassed aliquots (U, Th, Sm, Sm/U), grey areas represent the interquartile range of values and red lines are general trends. The 'true' age of the sample is the average of Vasconcelos et al. (2013). Detectable U loss occurs between 900 and 1000 °C in vacuum and at about 1100 °C in O_2. 256

5.1 Models for helium retention in pedogenic hematite particles at different effective diffusion temperatures. Crystal size is thickness of a plate with thickness:length ratio of 1:3. Four curves in each plot describe helium-retention as a function of crystal size for isothermal holding for 10 ka, 100 ka, 1 Ma, and 10 Ma. 279

5.2 The accumulation of pedogenic iron-oxides (top) and their crystallinity (bottom) compiled from data of McFadden and Hendricks (1985). Crystallinity is defined as the ratio between dithionite-extractable (highly crystalline) Fe and the total amount of dithionite- and oxalate-extractable Fe. Data shown here is from chronosequences in Southern California that contain at least one soil >100 ka: SGRNF - San Gabriel River North Fork, ESGM - Eastern San Gabriel Mountains, SGW - San Gorgonio Wash, ASC = Arroyo Seco Canyon. . . . 281

5.3 Helium recorded in pedogenic iron-oxides as a fraction of total helium that would have been present if all present iron-oxide particles had existed from the beginning of soil formation. This factor can be used to correct ^{3}He concentrations. 282

5.4 Study area on San Gorgonio Pass, California. An offset and uplifted alluvial fan surface between the Banning Strand and the Garnet Hill Strand of the San Andreas Fault shows a well-developed red soil. Samples of the relict soil on the fluvial terrace were taken at the indicated location. Aerial imagery from Google Earth, fault traces after Kendrick et al. (2015), location of apex and offset estimate from Huerta (2017). 283

5.5 Side view of the E cut of the fluvial terrace in Whitewater Canyon. The 80 m tall cut shows a well-developed relict soil at the surface as well as a paleosol in the lower part of the terrace (top is marked by dashed line). We sampled the relict soil at the indicated location. . . . 285

5.6 Trench cut for sampling at Whitewater Hill. Samples were taken at the indicated positions between the surface (0 cm) and 175 cm depth. Grey boxes indicate the thickness of samples. 286

5.7 Daily minimum (blue) and maximum (red) temperatures for the period 1981-2019 from the PRISM model. EDT is effective diffusion temperature calculated for this data set. 287

5.8 Depth profile of percentage of iron-oxides in <20 μm fraction of the soil at Whitewater Canyon measured by ICP-MS. Iron-oxide percentage was calculated assuming that they are completely composed of goethite (goe) or hematite (hem). The iron-oxide content is 7-8% near the surface and 8-10% at 60-160 cm depth. The gray envelope is the 1σ deviation from the mean. 293

5.9 Depth profiles of bulk U, Th, and Sm concentrations and Th/U and Sm/U ratios (n=120) in the relict soil at Whitewater measured by ICP-MS. Grey line is depth-averaged value with a 1σ uncertainty envelope. U is enriched relative to less soluble trace elements in the uppermost 0.5 m. 294

5.10 Depth profile of ^{10}Be and ^{26}Al concentration and ^{26}Al/^{10}Be ratios. Concentration profiles were regressed with ρ = (1.9±0.1) g cm^{-3} and Λ = 153±5 g cm^{-2}. The ^{26}Al/^{10}Be ratios are within error of the spallogenic ratio of 6.75. 299

5.11 Depth profiles of ^{3}He (top) and ^{4}He concentrations (bottom) measured in leached and bulk aliquots (left), difference between bulk and leached aliquots (middle), and difference normalized by iron-oxide content (right). Shown are age constraints of the in-situ exposure age from the ^{10}Be and ^{26}Al depth profiles (53 ka) and the burial age of the underlying paleosol of 330-510 ka. Our preferred age, determined from ^{3}He in pedogenic iron-oxides is 208±44 ka. Concentrations of ^{4}He in pedogenic iron-oxides are small and variable with several outliers. 302

5.12 Step-heating experiments of soil samples from Whitewater taken at 10-12 cm depth. A bulk aliquot and an aliquot leached in HCl to dissolve iron-oxides were heated to temperatures between 200 °C and 1400 °C for 20 min each step. Both ^{3}He and ^{4}He are extracted between 200 °C and 800 °C. Most ^{3}He is contained in the dissolved fraction, while almost all of the ^{4}He is contained in the insoluble fraction. We assume that the difference between the leached and bulk aliquots is the amount of He contained in pedogenic iron-oxides (bottom row). This data was normalized by the bulk mass and was not corrected for the fraction of iron-oxides. 306

LIST OF TABLES

Number *Page*

2.1 Results of the $^4He/^3He$ experiment of samples FH-F1-BR01-irr and FH-F2-BR04-irr from pisolith cortices. Aliquots were degassed for 30 min at each step (bdl = below detection limit). 33

2.2 Results of the $^4He/^3He$ experiment of samples FH-F3-BR03-3rdlayer-irr3 and FH-F4-BR05-4thlayer-irr4 from different layers of the same pisolith cortex. Aliquots were degassed for 30 min at each step (bdl = below detection limit). 34

2.3 Results of the $^4He/^3He$ experiment of samples FH-F5-BR05-core-irr3 from fine-grained material of the nucleus of pisolith BR05 and unirradiated cortex material of pisolith FH-L120a-diff. Aliquots were degassed for 30 min at each step (bdl = below detection limit). 35

2.4 Measured ^3He concentration of pisolith cortices (mass = mass of aliquot, d = depth below freshwater limestone layer, c = concentration of ^3He per sample mass, ul = layer of paleosol above freshwater limestone). 39

2.5 Measured ^3He concentration of pisolith cortices continued. 40

2.6 Results of ^{3}He concentration measurements of fine-grained iron-oxides in soil (d = depth below freshwater limestone layer, ul = layer of paleosol above freshwater limestone, mass = mass of the bulk soil sample for ^{3}He measurement, f_{gt} = mass fraction of stoichiometrically calculated goethite, c(^{3}He) = concentration of ^{3}He based on mass fraction of iron-oxides). Two different aliquots were used to measure ^{3}He bulk concentration and iron-oxide mass fraction. The ^{3}He concentration in fine-grained iron-oxides was calculated based on these parameters. 41

2.7 Goethite (U-Th)/He ages of pisoliths from depth profile of outcrop Lohn am Randen (d = depth below freshwater limestone layer, gt mass = mass of aliquot based on Fe, stoichiometrically calculated as goethite, ul = layer of paleosol above freshwater limestone, bdl = below detection limit). 44

2.8 Table of goethite (U-Th)/He ages continued. 45

2.9 Table of goethite (U-Th)/He ages continued. 46

2.10 Table of goethite (U-Th)/He ages continued. 47

2.11 Table of goethite (U-Th)/He ages continued. 48

2.12 Goethite (U-Th)/He ages of pisoliths from outcrop Lohn am Randen collected outside the depth profile (gt mass = mass of aliquot based on Fe, stoichiometrically calculated as goethite). Included are also formation ages of pisoliths cemented in a nodule (BR-cut2). These pisoliths show a similar age distribution to the pisoliths of the depth profile. All of the ages in this table are included in the formation age histogram (Fig. 2.3D), except for the ages of the matrix of the nodule (BR-cut2-c1, BR-cut2-h1, and BR-cut2-i1). 49

2.13 Results of the $^{4}He/^{3}He$ experiment of samples FH-FC1-L20clay-irr and FH-FC2-L300clay-irr. Aliquot was degassed for 30 min at each step. 52

3.1 (U-Th)/He ages of Bohnerz samples. goe = goethite mass, BES = Bohnerzgruben Erpfingen-Sonnenbühl 100

3.2 (U-Th)/He ages of Bohnerz samples, continued. goe = goethite mass, BES = Bohnerzgruben Erpfingen-Sonnenbühl, BH = Balsthal Holzfluh 101

3.3 (U-Th)/He ages of Bohnerz samples, continued. goe = goethite mass, BI = Balsthal Erzmatt I, BII = Balsthal Erzmatt II, C = Cholplatz . . 102

3.4 (U-Th)/He ages of Bohnerz samples, continued. goe = goethite mass, C = Cholplatz 103

3.5 (U-Th)/He ages of Bohnerz samples, continued. goe = goethite mass, C = Cholplatz 104

3.6 (U-Th)/He ages of Bohnerz samples, continued. goe = goethite mass, O = Oberdorf 105

3.7 (U-Th)/He ages of Bohnerz samples, continued. goe = goethite mass, O = Oberdorf, P = Petersbuch 106

3.8 (U-Th)/He ages of Bohnerz samples, continued. goe = goethite mass, P = Petersbuch 107

3.9 (U-Th)/He ages of Bohnerz samples, continued. goe = goethite mass, R = Rothenstein 108

3.10 (U-Th)/He ages of Bohnerz samples, continued. goe = goethite mass, W = Weißenburg 109

3.11 Measured ^{3}He concentrations of pisolith cortices (depth is measured below the modern surface, mass = mass of aliquot, 1 RA = 1.38×10^{-6}, Mat/g = millions of atoms per gram). 110

3.12 List of localities of fissure-type deposits with coordinates, location accuracy, and original references. 112
3.13 List of localities of fissure-type deposits, continued. 113
3.14 List of localities of fissure-type deposits, continued. 114
3.15 List of localities of fissure-type deposits, continued. 115
3.16 List of localities of fissure-type deposits, continued. 116
3.17 List of localities of fissure-type deposits, continued. 117
3.18 List of localities of fissure-type deposits, continued. 118
3.19 List of localities of fissure-type deposits, continued. 119
3.20 List of localities of fissure-type deposits, continued. 120
3.21 List of localities of fissure-type deposits, continued. 121
3.22 List of localities of stratiform-type deposits with coordinates, location accuracy, and original references. 122
3.23 List of localities of stratiform-type deposits, continued. 123
3.24 List of localities of stratiform-type deposits, continued. 124
3.25 List of localities of stratiform-type deposits, continued. 125
3.26 List of localities of stratiform-type deposits, continued. 126
3.27 List of localities of cave deposits with coordinates, location accuracy, and original references. 127
4.1 Hematite and goethite samples used in this study. Ages and concentrations of hematite samples are bulk values determined by the two-aliquot method on several milligrams of sample material, as reported in the original references. Values for goethite samples represent the average of several aliquots of tens to hundreds of micrograms. 149
4.2 Elemental analysis of laser-heated Pt tubes, representing the blank concentrations at 940 °C in vacuum (top) and 1150 °C in 100 torr of O_2. hem = Fe-based hematite-equivalent mass. 190

4.3 Pyrometer calibration data, P = pyrometer reading, T = thermocouple temperature. 203

4.4 Pyrometer calibration data, P = pyrometer reading, T = thermocouple temperature, pro = prograde. 204

4.5 Pyrometer calibration data, P = pyrometer reading, T = thermocouple temperature. 205

4.6 Pyrometer calibration data, P = pyrometer reading, T = thermocouple temperature. 206

4.7 Pyrometer calibration data, P = pyrometer reading, T = thermocouple temperature. 207

4.8 Conversion table for pyrometer reading (P) to actual temperature (T) and vice versa for Pt packets in vacuum and O_2 as well as for Nb packets in vacuum. 208

4.9 Masses weighed and derived from Ca-spike and Ru-spike for hematite. Given are also concentrations of U, Th, and Sm, as well as effective uranium concentration (eU) in parts per million (µg/g) derived from these masses and trace-element measurements. 215

4.10 Masses weighed and derived from Ca-spike and Ru-spike for goethite samples. Given are concentrations of U, Th, and Sm, as well as effective uranium concentration (eU) in parts per million (µg/g) derived from these masses and trace-element measurements. 216

4.11 Replicate analyses of undegassed aliquots of hematite sample HM1 (n=45). 237

4.12 Replicate analyses of undegassed aliquots of hematite sample HM2 (n=39). 238

4.13 Replicate analyses of undegassed aliquots of hematite sample MS (n=38); bdl = below detection limit. 239

4.14 Replicate analyses of undegassed aliquots of hematite sample HM2048 (n=25); bdl = below detection limit. 240

4.15 Replicate analyses of undegassed aliquots of hematite sample GC (n=25). 241

4.16 Replicate analyses of undegassed aliquots of goethite sample CIT (n=26); bdl = below detection limit. 242

4.17 Replicate analyses of undegassed aliquots of goethite sample RH (n=25); bdl = below detection limit. 243

4.18 Replicate analyses of undegassed aliquots of goethite sample Lyp (n=10). 243

4.19 Replicate analyses of undegassed aliquots of goethite sample YAN (n=26); bdl = below detection limit. 244

4.20 Replicate analyses of undegassed aliquots of goethite sample blade (n=10); bdl = below detection limit. 244

4.21 Heating experiment data for hematite sample HM1 degassed in vacuum in Pt packets. T = temperature, t = total isothermal heating time, age = calculated (U-Th)/He age, mass = Fe-based sample mass. . . . 257

4.22 Heating experiment data for hematite sample HM1 degassed in vacuum in Nb packets. T = temperature, t = total isothermal heating time, age = calculated (U-Th)/He age, mass = Fe-based sample mass. 258

4.23 Heating experiment data for hematite sample HM1 degassed in oxygen. $p(O_2)$ = oxygen partial pressure, T = temperature, t = total isothermal heating time, age = calculated (U-Th)/He age, mass = Fe-based sample mass. 259

4.24 Heating experiment data for hematite sample HM2 degassed in vacuum in Pt packets. T = temperature, t = total isothermal heating time, age = calculated (U-Th)/He age, mass = Fe-based sample mass. . . . 260

4.25 Heating experiment data for hematite sample HM2 degassed in vacuum in Nb packets. T = temperature, t = total isothermal heating time, age = calculated (U-Th)/He age, mass = Fe-based sample mass. 261

4.26 Heating experiment data for hematite sample HM2 degassed in oxygen. $p(O_2)$ = oxygen partial pressure, T = temperature, t = total isothermal heating time, age = calculated (U-Th)/He age, mass = Fe-based sample mass. 262

4.27 Heating experiment data for hematite sample MS degassed in vacuum in Pt packets. T = temperature, t = total isothermal heating time, age = calculated (U-Th)/He age, mass = Fe-based sample mass, bdl = below detection limit. 263

4.28 Heating experiment data for hematite sample MS degassed in vacuum in Pt packets at 950 °C for various lengths of time. T = temperature, t = isothermal heating time, age = calculated (U-Th)/He age, mass = Fe-based sample mass. 264

4.29 Heating experiment data for hematite sample MS degassed in oxygen in Pt packets. $p(O_2)$ = oxygen partial pressure, T = temperature, t = total isothermal heating time, age = calculated (U-Th)/He age, mass = Fe-based sample mass. 264

4.30 Heating experiment data for hematite sample MS degassed in oxygen in Pt packets (continued). $p(O_2)$ = oxygen partial pressure, T = temperature, t = total isothermal heating time, age = calculated (U-Th)/He age, mass = Fe-based sample mass. 265

4.31 Heating experiment data for hematite sample GC degassed in vacuum. T = temperature, t = total isothermal heating time, age = calculated (U-Th)/He age, mass = Fe-based sample mass. 265

4.32 Heating experiment data for goethite sample blade degassed in vacuum in Pt packets. T = temperature, t = total isothermal heating time, age = calculated (U-Th)/He age, mass = Fe-based sample mass. . . . 266

4.33 Heating experiment data for goethite sample blade degassed in oxygen in Pt packets. $p(O_2)$ = oxygen partial pressure, T = temperature, t = total isothermal heating time, age = calculated (U-Th)/He age, mass = Fe-based sample mass. 266

4.34 Heating experiment data for goethite sample CIT degassed in vacuum in Pt packets. T = temperature, t = total isothermal heating time, age = calculated (U-Th)/He age, mass = Fe-based sample mass. 266

4.35 Heating experiment data for goethite sample CIT degassed in oxygen in Pt packets. $p(O_2)$ = oxygen partial pressure, T = temperature, t = total isothermal heating time, age = calculated (U-Th)/He age, mass = Fe-based sample mass. 267

4.36 Heating experiment data for goethite sample Lyp degassed in vacuum in Pt packets. T = temperature, t = total isothermal heating time, age = calculated (U-Th)/He age, mass = Fe-based sample mass. 267

4.37 Heating experiment data for goethite sample Lyp degassed in oxygen in Pt packets. $p(O_2)$ = oxygen partial pressure, T = temperature, t = total isothermal heating time, age = calculated (U-Th)/He age, mass = Fe-based sample mass. 267

4.38 Heating experiment data for goethite sample RH degassed in vacuum in Pt packets. T = temperature, t = total isothermal heating time, age = calculated (U-Th)/He age, mass = Fe-based sample mass. 268

4.39 Heating experiment data for goethite sample RH degassed in oxygen in Pt packets. $p(O_2)$ = oxygen partial pressure, T = temperature, t = total isothermal heating time, age = calculated (U-Th)/He age, mass = Fe-based sample mass. 268

5.1 Iron-oxide concentrations in soil material. Mass/percentage is computed assuming all iron is in the form of either hematite (hem) or goethite (goe). Mass of aliquot was determined with a microbalance. 295

5.2 Bulk trace element concentrations in Whitewater soil. Amounts of trace elements were normalized by mass of aliquot measured on a microbalance. 296

5.3 Bulk trace element concentrations in Whitewater soil, continued. . . . 297

5.4 AMS measurements of ^{10}Be and ^{26}Al concentrations. Age were calculated assuming no erosion. 300

5.5 Measurements of ^{3}He and ^{4}He in bulk soil material of Whitewater Hill in the <20 μm fraction. Subscript 'bulk' denotes amounts of ^{3}He and ^{4}He normalized by bulk mass of aliquot. Samples were measured in aliquots leached in HCl to dissolve iron-oxides as well as in unleached aliquots. Concentrations of ^{3}He and ^{4}He are determined by difference and normalized by the iron-oxide concentrations of the soil material. Values of sample 17WW-02 are sums of all steps of the step-heating experiment. 303

5.6 Measurements of ^{3}He and ^{4}He from step-heating of bulk and leached aliquots of a soil sample from Whitewater Hill taken at 10-12 cm depth. Concentrations in pedogenic iron-oxides was calculated by difference. bdl = below detection limit 305

NOMENCLATURE

(U-Th)/He. A geochronologic method that uses measurements of the α-particles (^{4}He) produced by U, Th, and Sm decays to calculate ages. I routinely measure Sm and take it into account when calculating an age, but since the production of ^{4}He from Sm is mostly negligible, I use the established name '(U-Th)/He' to describe the technique.

ÄJC. Ältere Juranagelfluh conglomerate, a lithostratigraphic subunit (18.5-17.7 Ma) of the Lower Freshwater Molasse consisting mainly of Upper Jurassic clasts.

acid blank. A solution of acid and water, in the same amounts used for samples. This is used to detect possible contamination of all measured isotopes in solvents.

AMS. Accelerator Mass Spectrometry.

at. Abbreviation of 'atoms', used as a unit for number of atoms.

at g^{-1} a^{-1}. Atoms per gram per year, unit used for production rates of cosmogenic nuclides.

at/g. Unit for concentrations of atoms per gram.

ATR-FTIR. Attenuated Total Reflection Fourier-Transform Infrared spectroscopy.

bdl. Below detection limit.

blank. An analysis with no analyte. This is used to assess background concentrations of a given analyte. For helium measurements, blanks are integrated for the same amount of time as a sample, spiked with ^{3}He, and then analyzed. The resulting ^{4}He/^{3}He ratio is subtracted from all other measurements to correct for background concentrations of ^{4}He. The blank concentration also defines the detection limit.

Bohnerz. (German for 'bean ore') local name for concretions in the form of pisoliths composed mainly of goethite.

cortex. The outer, often layered, shell of a pisolith. A cortex surrounds the nucleus.

crushate. Sample material which has been crushed and sieved to a specific range of grain sizes.

cryogenic trap. A device which can be set to temperatures between ~8 and ~300 K to adsorb selected species on activated charcoal. The temperatures of complete adsorption and complete release of He from the activated charcoal are around 15 K and 34 K. Also called 'cryogenic pump' or 'cryopump'.

CTN. cosmogenic thermal neutrons.

EDS. (Energy Dispersive X-Ray Spectroscopy) An analysis technique used to detect elements and their relative proportions, commonly used with SEM.

eU. A measure of the effective uranium concentration, which combines elemental concentrations (given here in ppm) scaled by their α-productivity: eU = U + 0.235 Th + 0.00463 Sm.

formation age. The time since formation of the material. For iron-oxides, this is the time at which the material precipitated or re-crystallized to its present form.

Franconian Alb. A region in southwestern Germany, which shows cuesta morphology. It is separated from the Swabian Alb by the Ries impact crater.

goe. Abbreviation used for the mineral goethite.

goethite. Iron(III) oxide-hydroxide (α-FeOOH). A mineral found commonly in soils, produced mainly by weathering of mafic minerals. Goethite dehydroxylates to around 180-300 °C and transforms to hematite.

hem. Abbreviation used for the mineral hematite.

hematite. Iron(III) oxide (α-Fe_2O_3). A mineral found commonly in soils, produced mainly by weathering of mafic minerals. Hematite transforms to magnetite at around 1000 °C in vacuum.

IQR. (interquartile range) The middle 50% of values of a distribution.

iron-oxides. This term is used here to refer collectively to iron-oxides and iron-oxyhydroxides, mostly to goethite and hematite.

magnetite. Iron(II,III) oxide ($Fe^{2+}Fe_2^{3+}O_4$). A highly magnetic spinel-group mineral.

Mat. Millions of atoms (1 Mat = 1.6605 amol).

Mat/g. Millions of atoms per gram (1 Mat/g = 1.6605 amol/g).

ncc. ('nano cubic centimeter') A unit commonly used to measure amounts of helium, especially ^{4}He. It is the amount of helium contained in this volume at STP (1 ncc = 44.643 fmol).

nucleus. The inner part of a pisolith. It is often formed by quartz grains, clay-rich accumulations, or broken pieces of an older pisolith. A nucleus is surrounded by the cortex.

OBM. Obere Brackwassermolasse (Upper Brackish Molasse).

OSL. optically stimulated luminescence dating.

packet. A metal container enclosing a sample for (U-Th)/He dating, made by crimping the ends of a Pt or Nb tube with forceps.

paleosol. A soil which has been formed in the past and is not actively developing. Paleosols in the geologic record are often buried by younger strata.

pcc. ('pico cubic centimeter'), a unit commonly used to measure amounts of helium, especially ^{3}He. It is the amount of helium contained in this volume at STP (1 pcc = $4.4643 \cdot 10^{-17}$ mol).

ppb. parts per billion (10^{-9}), used here exclusively to denote mass fractions (e.g. ng/g).

ppm. parts per million (10^{-6}), used here exclusively to denote mass fractions (e.g. µg/g).

procedural blank. A prepared solution, which has been run through the the same processing steps as a regular sample, but has not had any analyte added to it. This is used to measure background concentrations of analytes, which can be used to correct sample concentrations.

RA. The natural atmospheric ^{3}He/^{4}He ratio, 1 RA = $1.38 \cdot 10^{-6}$, also used as a unit.

re-extract. A repeated heating of the sample to the same or slightly higher temperature as the main extraction. Re-extracts are used to ensure that helium has been fully extracted from the sample.

relict soil. A soil which formed under conditions different from those of the present and which is not in equilibrium with current conditions.

residence time. The span of time between the initial formation of a soil and its burial or erosional removal.

SEM. Scanning Electron Microscope.

SLHL. (sea level high latitude) A normalization scheme for cosmogenic production rates to make locally determined production rates globally comparable.

spike blank. A solution of acid, spike, and water, added in the same amounts as for samples. This is used to characterize background concentrations of analyte in the spike solution.

STP. (standard temperature and pressure) A temperature and pressure of 273.15 K and 101.3 kPa. At these conditions, 1 mol of any ideal gas occupies 22419 cm^3.

Swabian Alb. A region in southwestern Germany, which shows cuesta morphology. It is separated from the Franconian Alb by the Ries impact crater.

torr. A unit of pressure, 1 torr is equivalent to 133.32 Pa or 1.3332 mbar.

Chapter 1

INTRODUCTION

Iron-oxides and oxyhydroxides are ubiquitous phases in surficial sediments and soils. They are produced by weathering of iron-rich minerals and the particular species (hematite, goethite) is often used to make inferences concerning the weathering environment (e.g. Schwertmann, 1988). Determining the age of formation of these iron-oxides can help to constrain the timescales of formation of soils and paleosols. In modern soils, it can be used to make inferences about the formation, evolution, and migration of iron-oxides. In this thesis, I show how helium in iron-oxides can be used for the study of soils and paleosols, including ^{3}He produced by cosmic ray exposure and ^{4}He from radioactive decay of U, Th, and Sm. After applying the established goethite (U-Th)/He technique to a new setting, I extend the use of the method to highly-retentive hematite samples. I then present work on helium in pedogenic iron-oxides.

The use of goethite and hematite as target phases for (U-Th)/He dating was first proposed by Strutt (1909). Early experiments found that ages measured by this method were too young, most likely due to thermal resetting, and this technique was abandoned for almost a century. Renewed interest in the (U-Th)/He method was generated by the work of Wernicke and Lippolt (1993, and subsequent work), who successfully obtained geologically meaningful (U-Th)/He ages of hematites. Shuster et al. (2005) and Shuster et al. (2012) then demonstrated the use of goethite for (U-Th)/He dating and studies of cosmic-ray exposure using ^{3}He. Since then, the goethite and hematite (U-Th)/He method has been applied to a variety of environments, including vein mineralization (Wernicke and Lippolt, 1994), lateritic weathering (Pidgeon et al., 2004), fault surfaces (Ault et al., 2015), diagenetic ce-

ments (Reiners et al., 2014), and thermochronology (Farley and Flowers, 2012). In this thesis, I apply the goethite and hematite (U-Th)/He techniques to soils and paleosols and explore new phases and analytical methods to broaden their application. Chapters II and III are an exploration of the capabilities of the goethite (U-Th)/He method and its applicability to paleosols. In these chapters, I combine (U-Th)/He dating with measurements of cosmogenic ^{3}He to study when cosmic-ray exposure occurred in goethite pisoliths of the Bohnerz deposits of Central Europe. In Chapter II, I measure both (U-Th)/He ages and ^{3}He concentrations in pisoliths of a paleosol of the Bohnerz deposits to show that it formed over more than 25 Ma. Since the paleosol has been covered and shielded from cosmic rays, cosmogenic ^{3}He in goethite pisoliths represents paleo-exposure, which occurred before burial. In Chapter III, I apply this approach to outcrops of Bohnerz deposits in Germany and Switzerland. Goethite (U-Th)/He ages demonstrate that Bohnerz deposits formed from at least 55 Ma to 2 Ma, while it was previously assumed that they formed in the Late Cretaceous-early Eocene (e.g. Borger, 1990). I also map out the paleo-extent of the Bohnerz deposits to show that they represent a widespread mode of continental weathering. Since this process occurred over more than 50 Ma, the Bohnerz deposits represent a significant archive of continental climate throughout most of the Cenozoic.

In Chapter IV, I seek to extend the use of the (U-Th)/He method to hematite samples, which are often more retentive and require higher temperatures to completely degas helium than goethite. However, U-loss due to volatilization has been documented in iron-oxides at high temperatures (e.g. Vasconcelos et al., 2013). I examine the details of phase transitions, which natural hematite and goethite samples undergo in the process of laser-heating for (U-Th)/He analyses. I find that U-loss correlates to a phase change from hematite to magnetite and that U-loss can be delayed to higher temperatures by preventing this phase change. For samples with established ages,

I demonstrate that accurate and precise (U-Th)/He ages can be obtained using the oxygen degassing method and document the implementation and automation of the measurement protocol.

In the work for Chapters II and III, I noticed that ^{3}He concentrations in bulk paleosol material, when normalized to iron-oxide content, are similar to those of highly-retentive pisoliths, which was a first indication that extremely fine-grained iron-oxides might be retentive to helium. Subsequent work by Farley (2018) established absolute diffusion parameters of hematite, which permitted the calculation of retentivity of very small grain sizes. Hematite particles as small as 20 nm are predicted to quantitatively retain helium over millions of years. If helium concentrations can be measured in pedogenic iron-oxides, which are ubiquitous phases in soils and paleosols, this would eliminate the need for concretions, which are only developed in a few types of soils. Due to their diminutive size, all helium found in particles of pedogenic iron-oxides is implanted from other phases. I propose that cosmogenic ^{3}He is a more reliable system to measure in pedogenic iron-oxides, since its production is more uniform than that of radiogenic ^{4}He, which is commonly only found in high concentrations in certain accessory phases. I establish the theoretical background for the production and retention of ^{3}He in pedogenic iron-oxides. To test this hypothesis, I sample a relict soil developed on a fanglomerate terrace at Whitewater Hill, California. Depth profiles of ^{10}Be and ^{26}Al concentration agree well with a model of exponential decrease with depth and yield ages of 52.4±2.2 ka, assuming no erosion. The depth profile of ^{3}He concentration in pedogenic iron-oxides shows concentrations in excess of what would be expected for in-situ exposure at 40-100 cm depth. I interpret this as evidence for downward migration of iron-oxides in the soil column. The ^{3}He concentration profile is consistent with a true soil age of about 200 ka, which is closer to estimates based on physical soil characteristics than the in-situ ^{10}Be and ^{26}Al exposure age.

The two new techniques developed in this thesis have the potential to extend the use of iron-oxide (U-Th)/He dating and cosmogenic ^{3}He exposure dating to new environments. Highly retentive hematite can be accurately dated at spatial scales several orders of magnitude smaller than with the previous two-aliquot method. This permits the resolution of age heterogeneity in layered hematite deposits, such as pisoliths. Since pedogenic iron-oxides are present in most types of soils, they can be used to obtain cosmogenic exposure ages for soils and exposure durations for paleosols. In addition, if the exposure age of soil is known, measurements of ^{3}He can be used to study the formation and migration of iron-oxides in soils.

References

Ault, A. K., P. W. Reiners, J. P. Evans, and S. N. Thomson (2015) "Linking hematite (U–Th)/He dating with the microtextural record of seismicity in the Wasatch fault damage zone, Utah, USA" in: *Geology* 43.9, pp. 771–774.

Borger, H. (1990) "Bohnerze und Quarzsande als Indikatoren paläogeographischer Verwitterungsprozesse und der Altreliefgenese östlich von Albstadt (Schwäbische Alb)." in: *Kölner Geographische Arbeiten* 52, p. 209.

Farley, K. (2018) "Helium diffusion parameters of hematite from a single-diffusion-domain crystal" in: *Geochimica et Cosmochimica Acta* 231, pp. 117–129.

Farley, K. and R. Flowers (2012) "(U–Th)/Ne and multidomain (U–Th)/He systematics of a hydrothermal hematite from eastern Grand Canyon" in: *Earth and Planetary Science Letters* 359, pp. 131–140.

Pidgeon, R., T. Brander, and H. Lippolt (2004) "Late Miocene (U+Th)–^{4}He ages of ferruginous nodules from lateritic duricrust, Darling Range, Western Australia" in: *Australian Journal of Earth Sciences* 51.6, pp. 901–909.

Reiners, P. W., M. A. Chan, and N. S. Evenson (2014) "(U–Th)/He geochronology and chemical compositions of diagenetic cement, concretions, and fracture-filling oxide minerals in Mesozoic sandstones of the Colorado Plateau" in: *GSA Bulletin* 126.9-10, pp. 1363–1383.

Schwertmann, U. (1988) "Occurrence and formation of iron oxides in various pedoenvironments" in: *Iron in soils and clay minerals* Springer, pp. 267–308.

Shuster, D. L., K. A. Farley, P. M. Vasconcelos, G. Balco, H. S. Monteiro, K. Waltenberg, and J. O. Stone (2012) "Cosmogenic ^{3}He in hematite and goethite from Brazilian "canga" duricrust demonstrates the extreme stability of these surfaces" in: *Earth and Planetary Science Letters* 329, pp. 41–50.

Shuster, D. L., P. M. Vasconcelos, J. A. Heim, and K. A. Farley (2005) "Weathering geochronology by (U–Th)/He dating of goethite" in: *Geochimica et Cosmochimica Acta* 69.3, pp. 659–673.

Strutt, R. J. (1909) "The accumulation of helium in geological time.-II" in: *Proceedings of the Royal Society of London. Series A, Containing Papers of a Mathematical and Physical Character* 83.560, pp. 96–99.

Vasconcelos, P. M., J. A. Heim, K. A. Farley, H. Monteiro, and K. Waltenberg (2013) "^{40}Ar/^{39}Ar and (U–Th)/He–^{4}He/^{3}He geochronology of landscape evolution and channel iron deposit genesis at Lynn Peak, Western Australia" in: *Geochimica et Cosmochimica Acta* 117, pp. 283–312.

Wernicke, R. S. and H. J. Lippolt (1993) "Botryoidal hematite from the Schwarzwald (Germany): heterogeneous uranium distributions and their bearing on the helium dating method" in: *Earth and Planetary Science Letters* 114.2-3, pp. 287–300.

– (1994) "Dating of vein specularite using internal (U+Th)/^{4}He isochrons" in: *Geophysical Research Letters* 21.5, pp. 345–347.

Chapter 2

EVIDENCE FOR >5 MA PALEO-EXPOSURE OF AN EOCENE–MIOCENE PALEOSOL OF THE BOHNERZ FORMATION, SWITZERLAND

published as:

Hofmann, F., B. Reichenbacher, and K. A. Farley (2017) "Evidence for >5 Ma paleo-exposure of an Eocene–Miocene paleosol of the Bohnerz Formation, Switzerland" in: *Earth and Planetary Science Letters* 465, pp. 168–175 DOI: 10.1016/j.epsl.2017.02.042.

with Bettina Reichenbacher[1] and Kenneth A. Farley[2]

Abstract

We obtained (U-Th)/He formation ages and cosmogenic ^{3}He concentrations for pisoliths from a paleosol of the Bohnerz Formation (Siderolithic) of Central Europe. The paleosol is exposed in the Almenbühl quarry near Lohn, Canton Schaffhausen, Switzerland. The paleosol consists of red Bolus clay of 3-4 m thickness developed on deeply weathered Jurassic limestone and overlain by Early Miocene conglomerates. The (U-Th)/He formation ages of the pisoliths are between 50 Ma and 8 Ma, with most ages being older than 17 Ma. There is a sharp decline in the frequency of ages at the time of burial of the paleosol at 17 Ma. These ages are inconsistent with the previous assumption that the Bohnerz Formation formed in a Cretaceous to early Eocene laterite in a tropical climate. We propose that the Bohnerz Formation more closely resembles 'Terra Rossa' soils, which do not require a tropical climate to form.

[1]Department of Earth and Environmental Sciences and GeoBio Centre, Universität München (LMU), Richard-Wagner-Straße 10, 80333 München, Germany

[2]California Institute of Technology, 1200 E California Blvd, MC 170-25, Pasadena, CA 91125, United States

The ^{3}He concentration in the pisoliths is roughly constant with depth throughout the paleosol at 300 Mat/g. We interpret this as the result of soil convection during cosmic ray exposure. The minimum exposure duration at the surface of the paleosol is ~5 Ma. A simple model of soil convection shows that the true exposure duration of the paleosol is approximately 10-20 Ma. These results indicate that the clay soils of the Bohnerz formation were continuously exposed at the surface for millions of years. Since the paleosol was covered by conglomerate since 17 Ma, the ^{3}He measured here was produced by cosmic ray exposure before burial. Cosmogenic ^{3}He concentrations measured in peodgenic iron-oxides (<1 μm) are similar to those measured in pisoliths. This might indicate that fine-grained iron-oxides are retentive to helium and might be used for studying the formation and cosmic ray exposure of modern soils and paleosols.

2.1 Introduction

Soils are usually seen as transient deposits. Their formation, burial, and erosion have been linked to changes in tectonic and climatic conditions (e.g. Muhs and Bettis, 2003; Retallack, 2008). The residence time of soils at the surface has mostly been studied on modern soils or Quaternary paleosols. Previous studies found that the residence times of modern soils in stable environments are on the order of 10-100 ka. Paleosol sequences of long-lived soil types, such as Ultisols and Oxisols, which are highly weathered, clay and iron-oxide rich soils common in tropical and sub-tropical regions, have been found to have formed and have been buried within 10 ka to 500 ka (Retallack, 2008). The residence time of modern soils is often estimated from soil production rates or rates of chemical weathering, such as conversion of clay minerals or silica dissolution (Pavich, 1989). The age range of paleosols is generally determined by assuming that the soil development spans the entire time between the formation of the substratum and the deposition of the overlying layer

(e.g. Retallack, 2008).

Some modern soils (Pavich, 1989) as well as paleosols at major unconformities (Retallack and Mindszenty, 1994) are assumed to have been continuously exposed at the surface for millions of years. Since incremental erosion or episodes of complete stripping of the soil/saprolite might have occurred, the assumption that the paleosol represents a complete record of the time between the substratum and the overlying layer may not be valid. Determining ancient cosmic ray exposure of soils is a way to test this assumption and to quantitatively determine the period of time actually recorded in the paleosol. Since periods of erosion or non-deposition dominate the geologic record (Sadler, 1981), being able to obtain evidence of paleo-exposure would provide insight into the periods of time not represented by deposition. Since most unconformities are surfaces subject to weathering, paleosols are the prime target for such study.

Most of the tools used to date modern soils and surfaces, such as OSL and radioactive cosmogenic nuclides (e.g. ^{10}Be, ^{26}Al), are limited in use for paleo-exposure studies, because they cannot be used past a few Ma. Well-developed soils, such as those of the Ultisolic and Oxisolic order, are composed solely of clay-minerals and iron-oxides. In the absence of other datable phases, iron-oxides provide a unique opportunity to obtain information about the age range of formation and cosmic ray exposure of long-lived modern soils as well as paleosols, since they have been shown to quantitatively retain He at Earth surface conditions (Lippolt et al., 1998; Shuster et al., 2005).

Previous studies have used goethite and hematite to investigate the formation and dynamics of weathering profiles. Shuster et al. (2012) and Monteiro et al. (2014) have demonstrated the use of (U-Th)/He dating of hematite and goethite as a tool to study dissolution-reprecipitation in the lateritic canga duricrusts of Brazil. These studies also report cosmogenic ^{3}He, which suggests that these surfaces have been

exposed for millions of years. Yapp and Shuster (2011) used (U-Th)/He dating of petrified wood that was replaced by goethite to date Eocene to Pliocene paleosols. Since these studies demonstrate that helium can be quantitatively retained in iron-oxides on the million-year timescale, ^{3}He from ancient cosmogenic exposure created before burial can be preserved in iron-oxides. This study aims to measure cosmogenic and radiogenic helium in goethite pisoliths and fine-grained iron-oxides in soils. It focuses on the Bohnerz Formation in Central Europe that contains both of these features.

2.2 Bohnerz Formation

The widespread Bohnerz Formation of Central Europe has been interpreted to have been exposed at the surface from Late Cretaceous to early Eocene (Borger and Widdowson, 2001), spanning several tens of millions of years. It consists of yellowish to reddish continental clay deposits, which are called Bohnerz Formation in Germany and Siderolithic (Siderolithikum, Terrain sidérolithique) in Switzerland (Rollier, 1905). The clays themselves, as opposed to the pisoliths and quartz grains, are also locally referred to as 'Bolus'. In the Jura Mountains and the Plateau Molasse region of Switzerland there are widespread thick, layered deposits of these clays (Achenbach, 1859), which are primary paleosols or, in some cases, secondary reworked deposits. In this region, the Bohnerz Formation is assigned an Eocene age based on fossils found in this unit (e.g. Berger et al., 2005a,b). Bolus clay deposits containing ferruginous pisoliths similar to those of the Bohnerz Formation are found in karstic fissures, depressions, and caves (Ufrecht, 2008) in the Swabian Alb and Franconian Alb region of Southern Germany (Fig. 2.1). Fissure fillings generally contain an abundance of late Eocene to Pleistocene small mammal fossils (Dehm, 1961; Rummel, 1993).

Both fissure fillings and layered clay deposits contain ferruginous concretions, which

are called ‘Bohnerz’ (German for ’bean ore’). These concretions consist mostly of goethite with some kaolinite (Borger, 1990). Ferruginous concretions in the Bohnerz Fm. and other similar deposits occur mainly as pisoliths, which are spherical grains (Fig. 2.2B) with a fine-grained nucleus surrounded by a cortex of concentrically layered precipitate (Fig. 2.2CD). Ferruginous pisoliths are so abundant in some fissures and layered deposits that they were mined as iron ore in Switzerland and Germany until the early 1900s. The clays and pisoliths of the Bohnerz deposits have

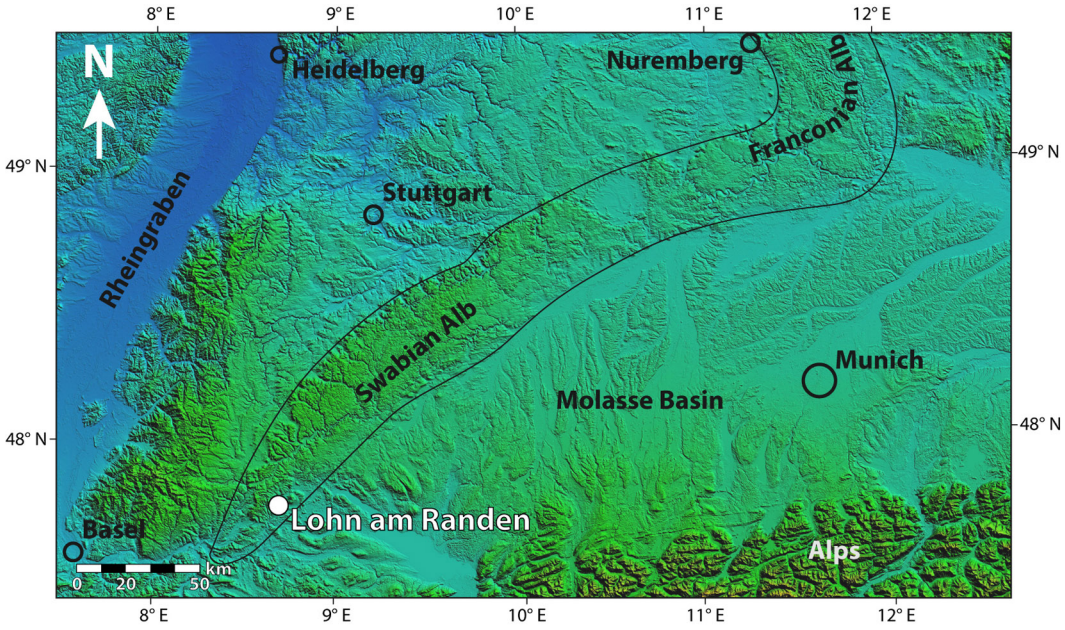

Figure 2.1: Location of the outcrop Lohn am Randen in Central Europe. The Bohnerz Formation is a layered deposit that occurs locally in the region around the outcrop. Similar clay deposits can be found mostly as fissure fillings along the limestone plateau of the Swabian and Franconian Alb.

so far been interpreted as remnants of a postulated extensive lateritic weathering surface (Borger and Widdowson, 2001; Geyer, 1957; Lang, 1914; Ufrecht, 2008). This interpretation is based on comparison of Bohnerz pisoliths with similar structures found in Indian laterites (Borger and Widdowson, 2001; Lang, 1914). Therefore, the pisoliths are assumed to have formed in a tropical weathering regime (e.g. Borger, 1990; Borger and Widdowson, 2001; Moos, 1921). The Bolus clays and ferruginous

concretions are interpreted as residual material produced by chemical dissolution of the underlying Upper Jurassic limestones based on chemical and mineralogical similarities between limestone residues and the Bohnerz deposits (Fach, 1908; Frank, 1928; Heim, 1919; Moos, 1921). A Late Cretaceous to early Eocene age was was assigned to the Bohnerz deposits based on the tropical climate in Central Europe at the time (Borger, 1990; Borger and Widdowson, 2001; Lang, 1914; Ufrecht, 2008). Borger and Widdowson (2001) argued that the development of the laterite ceased in the late Eocene. They assume that it was removed by late Eocene to Oligocene erosion and the material was subsequently deposited in fissures and depressions.

The formation age of Bohnerz pisoliths has never been determined. This study uses the poly-crystalline goethite (α-FeOOH) of Bohnerz pisoliths to measure (U-Th)/He formation ages of the Bohnerz formation. In addition, we measure cosmogenic ^{3}He in order to determine the timescales of surface exposure to cosmic radiation in the uppermost few meters of the Earth's surface. The combination of (U-Th)/He formation age and ^{3}He provides insights into the formation and stability of the paleosol.

2.3 Study site

We studied goethite pisoliths from the outcrop Lohn am Randen (47.762983° N, 8.680994° E, 544 m, WGS84, see Fig. 2.1), which is located in the Almenbühl quarry between the towns of Lohn and Bibern, Canton Schaffhausen, Switzerland (Fig. 2.2). Cenozoic deposits are preserved in the hanging wall of the NW-SE striking Randen normal fault (Müller et al., 2002). Ferruginous pisoliths occur within a dark red (Munsell 2.5YR 3/4) paleosol horizon of 2-4 m thickness on deeply weathered Tithonian (152-145 Ma) limestone of the Hangende Bankkalke Formation (Menning and Steininger, 2005). Karstic fissures filled with paleosol material are found in the limestone (Fig. 2.2F). The paleosol horizon is overlain by

Ältere Juranagelfluh conglomerate (ÄJC) and conglomerates of the Upper Brackish Molasse (OBM). The ÄJC is interbedded with Upper Marine Molasse (OMM) in this area (Schreiner, 1959). The OMM has been biostratigraphically dated at 18.5-17.7 Ma (Reichenbacher et al., 2013). Based on these stratigraphic constraints the paleosol horizon containing pisoliths must be younger than 152 Ma and older than 17.7 Ma.

The paleosol is directly overlain by a freshwater limestone layer, about 20-30 cm thick. Up to 30 cm of paleosol is found on top of the freshwater limestone layer, which might be reworked paleosol material. In some places along the outcrop the freshwater limestone layer is directly overlain by ÄJC. The paleosol material is composed mostly of kaolinite with about 10-15% pedogenic iron-oxides. About 1 m below the top of the paleosol layer is a zone of calcrete mineralization.

2.4 Materials and methods

Goethite has been shown to be rententive to helium at the Earth's surface (Lippolt et al., 1998). Polycrystalline goethite aggregates accumulate ^{4}He from U-series decay, and cosmogenic ^{3}He (Shuster et al., 2005). Therefore, they can be used for weathering geochronology and exposure studies (e.g. Monteiro et al., 2014; Shuster et al., 2012, 2005). In this study, we determined (U-Th)/He formation ages and cosmogenic ^{3}He concentrations in goethite pisoliths and fine-grained iron-oxide in soil samples.

Samples

Samples of the paleosol were taken on a vertical depth profile, indicated by the blue line in Fig. 2.2A. About 0.5 m of paleosol was removed from the surface of the quarry wall to avoid contamination with material that was slumped or washed down. About 1-2 kg of soil material was taken from the pristine paleosol from the freshwater limestone layer to the contact between the paleosol and the Jurassic

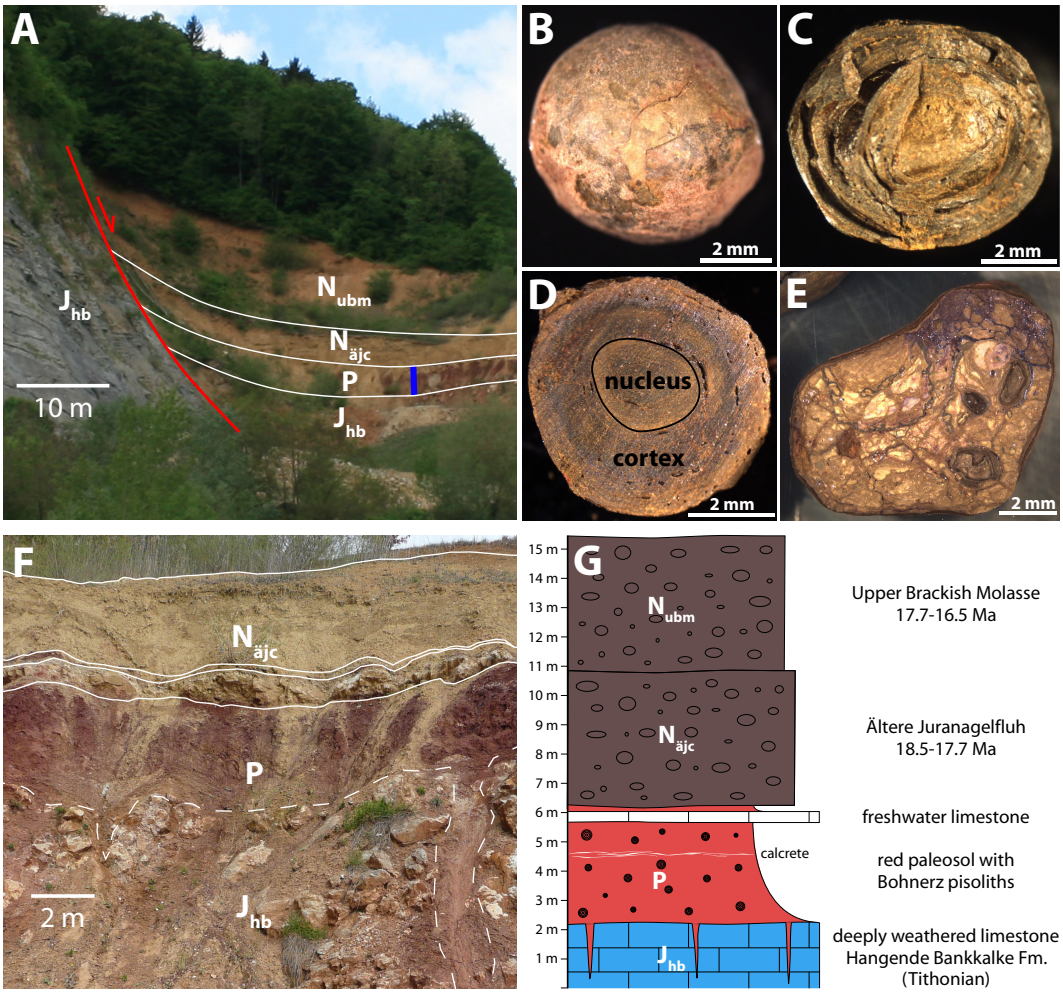

Figure 2.2: Outcrop Lohn am Randen and examples of pisoliths. (A) Northern wall of the quarry near Lohn, Switzerland. Red paleosol is overlying deeply eroded Jurassic limestone. The paleosol is covered by Miocene conglomerates. This sedimentary sequence is displaced by the Randen normal fault. Samples were taken in a depth profile along the blue line. (B) Typical appearance of a pisolith. (C) Same pisolith cracked open. (D) Polished section of a pisolith shows typical internal structure: layered cortex and fine-grained nucleus. (E) Nodule containing several pisoliths. (F) Detailed picture of the outcrop. A deep fissure filled with clay can be seen on the bottom right. (G) Stratigraphic column of the outcrop.

limestone at 3.6 m depth at intervals of 10-50 cm. We also sampled the thin, possibly reworked, paleosol layer between the freshwater limestone layer and the overlying conglomerate (upper layer = ul).

Soil samples were soaked in water for 3 days and then wet-sieved. Pisoliths were picked by hand from the fraction larger than 0.539 mm. Paleosol samples yielded 20-

100 individual pisoliths each. The average diameter of the pisoliths was consistently about 1-4 mm. The largest pisoliths were around 8 mm. The residual clay contained pisoliths smaller than 0.5 mm. A different set of pisoliths not from the depth profile were also collected from this outcrop (designated 'BR').

XRD and EDS analysis showed that pisoliths are composed mostly of goethite with up to 20% kaolinite. SEM images revealed a fine-grained texture of intergrown crystallites with a grain size of around 1 μm (see Section 3.A). Some parts of the pisoliths, especially in the nucleus, showed plates of kaolinite of 10-50 nm thickness, which were partially or fully replaced by goethite.

Most pisoliths were lightly crushed using mortar and pestle. Several larger pisoliths were cut with a saw. One half of the cut pisoliths was mounted in epoxy and polished for electron microscopy analysis. Aliquots for (U-Th)/He dating and ^{3}He analysis were picked from crushate or excavated from cut samples. Analyzed aliquots had a size of 500 μm to 5 mm for ^{3}He analysis and 200-500 μm for (U-Th)/He dating. This is larger than the grain sizes for which Protin et al. (2016) have seen significant amounts of helium adsorption.

Soil samples were crushed with tweezers. All pisoliths and quartz grains were removed from crushed material by hand to yield pure red Bolus clay samples. Aliquots of this material were taken for ^{3}He measurements as well as dissolution of the iron-oxides and subsequent elemental analysis.

Analytical procedures

The analytical procedures follow previously published protocols (Farley et al., 2006, 1999). A detailed description of the analytical procedures is provided in the Appendix 2.C. The retention of helium in samples of cortex material from pisoliths was determined using the ^{4}He/^{3}He method (see Shuster and Farley, 2003; Shuster et al. 2003). The fraction of ^{4}He retained in material from pisolith cortices is between

93% and 98%, which is consistent with previous studies of iron-oxides (Shuster et al., 2005). Any diffusive loss of ^{4}He would lead to an underestimation of the (U-Th)/He formation age. The (U-Th)/He formation age of pisoliths was determined by degassing the sample for measuring ^{4}He and subsequent dissolution of the sample for U/Th analysis by inductively coupled plasma mass spectrometry.

Concentrations of ^{3}He were determined by total fusion of separate and larger aliquots and sector-field mass spectrometry of the resulting gas. Long-term cosmogenic production rates may vary over time. However, studies have provided evidence that production rates in the past may have been within 10% of the modern value (Wieler et al., 2013). We assume that the sea level high latitude cosmogenic production rate of ^{3}He in goethite is constant over time and equivalent to 72 atoms g^{-1} a^{-1}, as derived from calibrations on a million-year time-scale (Shuster et al., 2012). This value was scaled to a latitude of 47° using the model of Lal (1991). The paleo-elevation of the paleosol horizon is unknown. The paleosol must have formed at least several tens of meters above sea level, since the area was subject to karstic weathering. The modern elevation is around 500 m above sea level. Correcting for the normal offset of the Randen fault of about 150 m (Müller et al., 2002), the elevation could have been as high as 650 m. We therefore use the elevation range between 100 m and 650 m as the uncertainty for production rate scaling.

2.5 Results

Formation ages

A total of 1-5 aliquots each of at least 5 pisoliths per depth interval were picked from crushate. Aliquots of a nodule as well as pisoliths L120f and L70g were excavated from cut samples. The 195 goethite (U-Th)/He formation ages of pisoliths collected on a vertical depth profile are between 50 Ma and 8 Ma, with analytical uncertainties of around 2% (Table 2.7). Eighty-five percent of the ages are between 50 Ma and 17

Ma (Fig. 2.3D). There is a sharp decline in frequency at ~17 Ma (dashed line in Fig. 2.3D). (U-Th)/He formation ages show no trend with depth (Fig. 2.3A). The spread of formation ages is almost the same for all depths. U and Th concentrations are 0-17 ppm (typically 2-5 ppm) and 15-230 ppm (typically 20-80 ppm), respectively. There is no systematic change of U or Th concentration or Th/U ratio with depth.

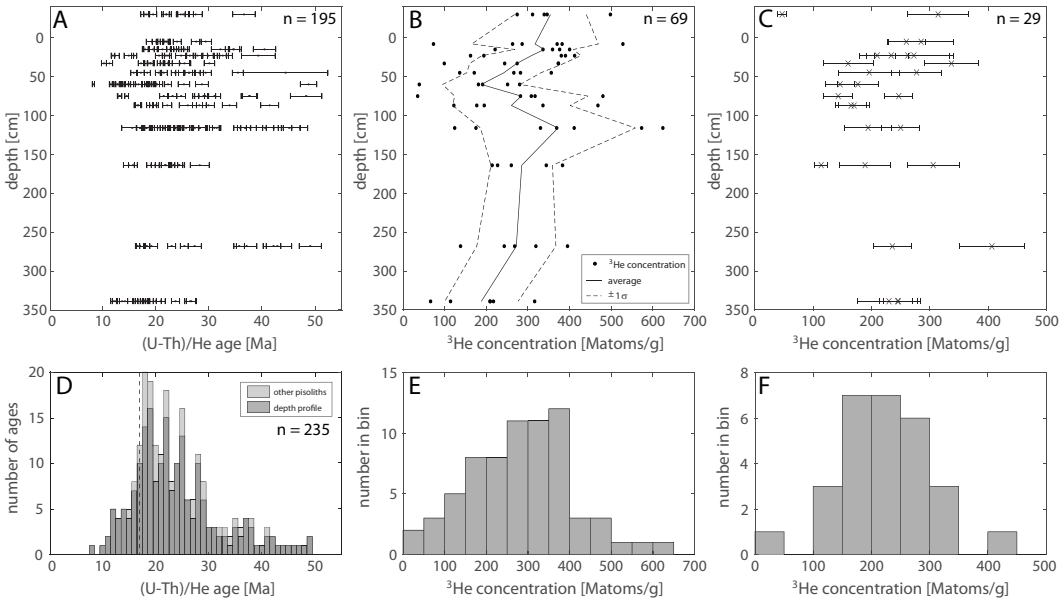

Figure 2.3: Vertical depth profiles of (U-Th)/He formation age (A) and ^{3}He concentration of (B) pisoliths as well as (C) soil samples normalized to the mass of iron-oxides in the soil from outcrop Lohn am Randen. The freshwater limestone layer occupies the 20 cm above 0 cm. A calcrete horizon is situated around 100 cm depth. One ^{3}He concentration is shown per pisolith per depth. For replicate samples of the same pisolith the average of all replicates is shown. The solid line represents the average ^{3}He concentration for each depth. Histograms show the distribution of (U-Th)/He formation ages (D) and ^{3}He concentrations of pisoliths (E) as well as soil samples (F) for all depths. (U-Th)/He ages from pisoliths collected from float, which were not part of the depth profile, were added to the formation age histogram ('other pisoliths'). Also included are the ages of the pisoliths in the nodule shown in Fig. 2.4 (ages of the matrix excluded). (U-Th)/He ages and ^{3}He concentrations are not corrected for partial retentivity (estimated to range from 92 to 98%).

From these randomly picked aliquots of crushate it seems that some pisoliths have a wide spread in ages while others have ages that are the same within uncertainty.

Two large pisoliths were studied in detail. Aliquots of every layer of the cortex as well as the nucleus were excavated and dated separately to yield radial age profiles (Fig. 2.4). Pisolith L120f has a distinct nucleus, which is not fine-grained like the nucleus of most other pisoliths, but the material of the nucleus resembles that of the cortex. The 20 ages obtained for this pisolith are between 38 Ma and 17 Ma. Aliquots of the same layer have ages that are reproducible within 5%. Age decreases with radius, showing that this pisolith grew from the inside out. Between 0 mm and 0.4 mm (38-20 Ma) the pisolith grew at a constant rate of 25 µm/Ma. The ages in the outer half of the pisolith are between 25 Ma and 17 Ma, suggesting a period of rapid growth during which 95% of the volume of this pisolith was precipitated. Ages of pisoliths L70g do not vary systematically with radial position. L70g has ages in the narrow range between 20 Ma and 15 Ma, with one aliquot at 11 Ma.

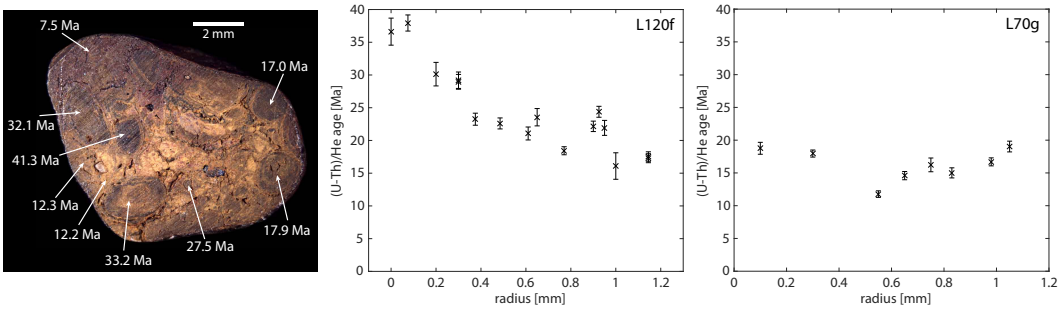

Figure 2.4: Left: (U-Th)/He formation ages of pisoliths as well as the matrix of a nodule (BR-cut2) containing several pisoliths. The ages obtained for the pisoliths (42-17 Ma) are similar to those obtained for many other pisoliths in the depth profile (see Fig. 2.3). Matrix material, which contains more clay than the pisoliths, yields younger formation ages. This suggests that there was some minor precipitation of goethite after the deposit was covered. Center and right: Radial age profiles of two different pisoliths (L120f, L70g). L120f shows slow linear growth from 40 Ma to 20 Ma, then more rapid growth until 17 Ma. L70g has only a short growth history around 20 Ma. (U-Th)/He ages are not corrected for partial retentivity.

Formation ages were also obtained for other pisoliths collected outside of the depth profile. These 40 ages range from 38 Ma to 15 Ma (Tab. 2.12). The distribution

of formation ages is similar to that of the depth profile (Fig. 2.3). A concretion in which several pisoliths are cemented (see Fig. 2.4) was also studied in detail. The pisoliths in the nodule yielded ages of 41.3 Ma to 17.0 Ma. The fine-grained matrix that cements the pisoliths yielded an age of about 12 Ma. The shiny, reddish material in the top left of the image has an age of 7 Ma. In SEM analysis this material was found to be composed of pure, metallic Fe (no oxygen) and might not be fully He-retentive.

^{3}He concentrations of pisoliths and soil

The ^{3}He concentrations measured in 89 aliquots from cortices of pisoliths are between $4.25 \cdot 10^{-17}$ mol/g and $1.04 \cdot 10^{-15}$ mol/g (26-624 Mat/g), see Tables 2.4 and 2.5. The ^{3}He concentrations of replicate aliquots are reproducible to within 10%. There is no significant trend of ^{3}He concentration with depth. The average ^{3}He concentration at a given depth is between 200 and 350 Mat/g with a standard deviation of about 100 Mat/g (Fig. 2.3E). The overall average ^{3}He concentration is (280±120) Mat/g.

Bulk ^{3}He concentrations of clay soil samples are around 20-30 Mat/g (Tab. 2.6). Since kaolinite is likely not helium-retentive, all of the ^{3}He in the soil material is contained in fine-grained iron-oxides. Therefore, the ^{3}He concentration was re-calculated based on the iron-oxide weight fraction, which was determined by ICP-MS analysis. The iron-oxide ^{3}He concentration is roughly constant with depth (Fig. 2.3C). This concentration is between 100 and 400 Mat/g and has an average of 230 Mat/g with a standard deviation of 70 Mat/g (Fig. 2.3F).

2.6 Discussion

Formation of the paleosol

The majority of pisoliths in the paleosol, for which ages were obtained from randomly picked pieces of crushed cortex material (Fig. 2.3A), show that the main

period of pisolith formation is between 50 Ma and 17 Ma, with a peak around 20 Ma. The initiation of soil development coincides with a global period that favored the production of bauxitic and lateritic soils (Beauvais et al., 2008; Retallack, 2010). The sharp drop in the number of ages below 17 Ma coincides with the deposition of the conglomerate on top of the paleosol. Since this depositional event is recorded in the precipitation of goethite, it ties the formation of the pisoliths to the development of the soil. The same age range (~40-17 Ma) can be seen in a pisolith studied in detail as well as in pisoliths cemented in a nodule (Fig. 2.4). Younger ages occur in the fine-grained cement that binds pisoliths together in the nodule. In randomly picked aliquots this might correspond to the outermost layer of the cortex. This indicates that ages younger than 17 Ma might be attributable to continued goethite precipitation after shallow burial of the paleosol. Alternatively, they might represent aliquots that have experienced open-system behavior, both in terms of loss of daughters or addition of parent nuclides.

Previous studies have suggested that the pisoliths of the Bohnerz Formation formed in a lateritic duricrust during Cretaceous-early Eocene tropical weathering (Borger and Widdowson, 2001; Ufrecht, 2008). They assume that tropical weathering, and therefore the the formation of the pisoliths, ceased in the early Eocene and that pisoliths were subsequently eroded and redeposited in the clays. Since our (U-Th)/He formation ages show that the pisoliths formed from late Eocene to Miocene, which matches the geological constraints of the paleosol, we conclude that the pisoliths formed directly in the paleosol during this time.

This paleosol is closer to a 'Terra Rossa' type (e.g. Bárdossy, 2013) Luvisol or an Ultisol than an indurated laterite. Laterites in India, which were previously taken as analogs for the formation of the Bohnerz pisoliths (Borger and Widdowson, 2001), have an entirely different morphology from the paleosol described here. 'Terra Rossa' soils are a better analog for the Bohnerz Formation. They are a widespread

type of soil development on carbonates in the Mediterranean (Boero and Schwertmann, 1989). They also have iron-oxide pisoliths and form under Mediterranean rather than tropical conditions (Boero and Schwertmann, 1989). Moreover, fissures filled with soil material are also associated with these types of soils. Fissures filled with the same material as the paleosol can be seen in the deeply weathered limestone at the base of the paleosol profile in the studied outcrop (Fig. 2.2F). This offers an explanation for the widespread occurrence of fissure fillings in the Swabian and Franconian Alb region of Southern Germany. They might have formed while covered with similar paleosols, which were subsequently eroded.

Paleo-exposure history

High ^{3}He concentrations were measured in pisoliths and in pedogenic iron-oxides. This may be due to cosmogenic , nucleogenic, muogenic, or radiogenic production. Li concentrations measured in cortex material are below 1 ppm. Using the equations and neutron production rates for clays of Lal (1987), the nucleogenic component of ^{3}He production in this paleosol over 50 Ma (oldest formation age) yields 0.3 Mat/g. The muogenic ^{3}He surface production rates are around 0.4 at g^{-1} a^{-1} and 0.8 at g^{-1} a^{-1} for high-energy μ and μ^{-} capture, respectively. This is less than the uncertainty of the cosmogenic production rate. At an average U concentration of 4 ppm in the pisoliths and the soil material, the radiogenic component of ^{3}He production from ^{238}U decay is around 4000 at/g over the same 50 Ma period (Farley et al., 2006). Since the ^{3}He concentrations measured here are on the order of 100 Mat/g, we conclude that there is no significant nucleogenic, muogenic, or radiogenic contribution to the production of ^{3}He.

Protin et al. (2016) suggested that samples crushed to small grain sizes might exhibit significant adsorption of helium from air. Crushed aliquots selected for analysis are larger than 200 µm, making this correction unnecessary. The grain size of the

crystallites that constitute the samples is significantly smaller than that. However, even the largest amounts of helium adsorption measured by Protin et al. (2016) are several orders of magnitude below the ^{3}He or ^{4}He concentrations measured in this study. A step-heating experiment of unirradiated pisolith material shows that ^{3}He and ^{4}He are being released proportionally (see Fig. 2.6) for all temperature steps. This suggests that both isotopes are equally strongly bound, which is consistent with a uniform distribution of ^{3}He and ^{4}He from cosmogenic and radiogenic processes. Helium-3 derived from air bound by adhesion would be expected to be released in a certain temperature range different from that of radiogenic and cosmogenic helium. We conclude that the ^{3}He measured in pisoliths was produced solely by spallation induced by cosmic radiation. These results are consistent with other studies of ^{3}He in iron-oxides (Shuster et al., 2012).

The cosmogenic ^{3}He measured in pisoliths and soil iron-oxides of the Bohnerz Formation is from paleo-exposure rather than modern exposure. The samples were taken in a quarry excavated in the last 100 years, prior to which they were covered by at least 10 m of Early Miocene conglomerates. This precludes cosmogenic production of ^{3}He in the paleosol after 17.7 Ma. Since the e-folding depth of the muon flux is much larger than that of neutrons, muogenic production can be significant at depths of over 5 m (Nesterenok and Yakubovich, 2016), allowing for the possibility of post-burial muogenic production of ^{3}He. The muogenic ^{3}He concentrations for 17 Ma of exposure at 10 m depth predicted by the model of Nesterenok and Yakubovich (2016) are around 2 Mat/g. This is negligible compared to the analytical uncertainty of the ^{3}He measurements. We conclude that post-burial muogenic production did not significantly add to the overall ^{3}He concentration. Therefore, cosmogenic ^{3}He must have been produced before burial of the paleosol. Stable cosmogenic nuclides from ancient exposure have so far only been reported in two studies. Libarkin et al. (2002) found ^{21}Ne in the 28 Ma old Fish Canyon Tuff in

excess of nucleogenic amounts and modern exposure. Blard et al. (2005) measured cosmogenic ^{3}He in 6-49 ka old basalt flows from Mt. Etna that were covered by other basalt flows. Other studies have used radioactive cosmogenic nuclides of sedimentary sequences to establish absolute chronology (e.g. Balco and Rovey, 2008). These studies were limited to the Quaternary because of the short half-lives of these nuclides. This study is the first to show cosmogenic paleo-exposure in pre-Quaternary paleosols.

To estimate the minimum exposure of the paleosol, we calculate the shortest amount of time that can account for the production of the highest ^{3}He concentration measured in any pisolith (624 Mat/g). Assuming that this pisolith was exposed at the surface, the minimum exposure duration is between 4.8 Ma and 7.9 Ma, depending on the paleo-elevation at the time of exposure. If this pisolith was buried for at least part of the time during which the paleosol was exposed to cosmic radiation, the true exposure duration could be far longer.

The ^{3}He concentration profile of the paleosol does not show an exponential decrease downwards (Fig. 2.3B), as would be expected for a coherent deposit exposed in situ (Lal, 1991). There is an average concentration of around 300 Mat/g throughout the paleosol. Even at depths of over 3 m there are pisoliths with ^{3}He concentrations up to 320 Mat/g, which cannot have been produced at this depth given the stratigraphic time constraints. There are also pisoliths with relatively low ^{3}He concentrations (20-100 Mat/g) at most depths. Since pisoliths are homogeneously distributed throughout the paleosol and there is no indication of fluvial reworking, we interpret this as a sign of in-situ soil and pisolith convection during exposure, e.g. due to bioturbation by plant roots and burrowing organisms. A simple model of soil convection, described in detail in 2.B, yields an equivalent cosmogenic production rate of (33.9±5.4) at g^{-1} a^{-1}. This corresponds to an equivalent exposure duration of (8.8±1.7) Ma.

Partial erosion of the paleosol before burial would lead to an underestimation of the true exposure duration. Pisoliths also grew while they were exposed to cosmic radiation. Therefore, not all layers of the cortex record the full exposure history of the paleosol. Since an aliquot of more mass than that of a single layer is required to obtain a ^{3}He measurement, ^{3}He concentrations are averaged over several layers of the pisolith. The ^{3}He concentration of pisolith L120e, which is the highest measured here, has an exposure duration of (18.3±3.5) Ma according to the soil convection model. The range of (U-Th)/He formation ages for this pisolith is 42.1-18.8 Ma. The formation of the pisolith spans about 24 Ma, which is close to the modeled exposure duration. This suggests that this pisolith recorded most of the exposure history of the paleosol.

The ^{3}He concentration profile presumed to arise from fine-grained iron-oxides in the soil closely resembles that of the pisoliths in abundance and depth distribution. This suggests that pedogenic iron-oxides might be retentive to helium. In addition, the similarities in their exposure history further ties the formation of the pisoliths to the clay soil.

Long-term stability of clay soils

Stability of modern soils and paleosols on the million-year timescale has been assumed in previous studies based on estimates of chemical weathering rates and qualitative description of soil development (Pavich, 1989; Retallack and Mindszenty, 1994). This study shows continuous iron-oxide precipitation of pisoliths in clay soils over a period of more than 30 Ma. The minimum cosmic ray exposure duration for the same material is 5 Ma. Based on modeling of the exposure history we argue that the true exposure duration of the paleosol around 10-20 Ma, which is on the timescale of iron-oxide precipitation. This is comparable to the continuous precipitation of iron-oxides in a canga duricrust for the last 50 Ma (Monteiro et al.,

2014). The same age range of laterite formation has been seen in studies using ^{39}Ar-^{40}Ar or K-Ar dating of K-Mn-oxides in laterites and bauxites (e.g. Beauvais et al., 2008; Vasconcelos et al., 1994). The deposits of the Bohnerz Fm. studied here, however, are not indurated laterites, but soils composed mostly of kaolinite with 5-15% iron-oxides. The exposure duration determined for the Bohnerz Fm. is an order of magnitude larger than the longest residence time measured for modern soils (Pavich, 1989), suggesting that clay soils may be more stable than previously thought.

Long-term stability of soils is usually associated with climatic and tectonic stasis. Yet, during the time that the Bohnerz paleosol was exposed at the surface, Central Europe was subject to climatic changes (Mosbrugger et al., 2005) and a variety of regional geologic events, such as the formation of the Alps, the opening of the Rheingraben, and a subsequent major re-organization of the main continental drainage network (Sissingh, 1998). Throughout all of these events the precipitation of goethite in the paleosol seems to have been continuous. The development of the paleosol was only concluded when it was covered by the deposition of the conglomerate. Bohnerz deposits in other locations may have continued to develop past 17 Ma.

2.7 Conclusions

The paleosol profile of the outcrop Lohn am Randen records goethite precipitation from 50 Ma to 8 Ma. The main period of goethite precipitation is between 30 Ma and 17 Ma, with a peak at around 20 Ma. The end of the main period of goethite precipitation correlates with the deposition of a conglomerate on top of the paleosol. Only minor goethite precipitation is recorded after 17 Ma. The small number of ages older than 30 Ma might be attributed to either a lower rate of goethite precipitation during this time or partial dissolution of older generations of goethite.

These formation ages are not consistent with the long-held assumption that the pisoliths of the Bohnerz Formation formed in a laterite in the Late Cretaceous-early Eocene. The goethite (U-Th)/He formation ages obtained in this study show that the pisoliths instead formed from late Eocene to Early Miocene, which is consistent with the ages of small mammal fossils found in karstic fissures in other localities. The paleosol more closely resembles a 'Terra Rossa' soil, found on limestones in Mediterranean climates rather than tropical climates.

A minimum estimate of cosmic ray paleo-exposure duration calculated from ^{3}He concentrations of the pisoliths is 5 Ma. Using a simple model of soil convection we estimate that the true exposure duration is likely closer to 10-20 Ma. This suggests that this paleosol persisted at the surface for tens of millions of years.

We have shown that a combination of goethite (U-Th)/He dating and ^{3}He paleo-exposure studies can be used to investigate the formation, dynamics, and exposure history of paleosols. This method allows the study of extremely long-lived, well-developed soils. Previously used methods to study the timescales of soil development and the residence time of soils, such as OSL and radioactive cosmogenic nuclides cannot be employed for soils and paleosols older than a few million years. Soil development tends towards a steady state and long-term soil development might be episodic rather than steady. Quantitative models of soil development need to make assumptions about these processes to predict the age of well-developed soils. The methods described here can be used to directly date the formation of soils and paleosols. They might be used to investigate these processes and calibrate models of soils development and soil conversion rates. Cosmogenic ^{3}He concentrations measured in fine-grained iron-oxide in soils are similar to the concentrations measured in pisoliths. This suggests that fine-grained iron-oxides might quantitatively retain helium over geologic periods and might be used to employ these techniques in the absence of ferruginous pisoliths.

References

Achenbach, A. (1859) "Ueber Bohnerze auf dem südwestlichen Plateau der Alp" in: *Jahreshefte des Vereins für vaterländische Naturkunde in Württemberg* 15, pp. 103–125.

Balco, G. and C. W. Rovey (2008) "An isochron method for cosmogenic-nuclide dating of buried soils and sediments" in: *American Journal of Science* 308.10, pp. 1083–1114 DOI: 10.2475/10.2008.02.

Bárdossy, G. (2013) *Karst bauxites* vol. 14 Developments in Economic Geology Elsevier, p. 441.

Beauvais, A., G. Ruffet, O. Hénocque, and F. Colin (2008) "Chemical and physical erosion rhythms of the West African Cenozoic morphogenesis: The ^{39}Ar-^{40}Ar dating of supergene K-Mn oxides" in: *Journal of Geophysical Research: Earth Surface* 113.F4.

Berger, J.-P., B. Reichenbacher, D. Becker, M. Grimm, K. Grimm, L. Picot, A. Storni, C. Pirkenseer, C. Derer, and A. Schaefer (2005a) "Paleogeography of the upper Rhine Graben (URG) and the Swiss Molasse basin (SMB) from Eocene to Pliocene" in: *International Journal of Earth Sciences* 94.4, pp. 697–710.

Berger, J.-P., B. Reichenbacher, D. Becker, M. Grimm, K. Grimm, L. Picot, A. Storni, C. Pirkenseer, and A. Schaefer (2005b) "Eocene-Pliocene time scale and stratigraphy of the Upper Rhine Graben (URG) and the Swiss Molasse Basin (SMB)" in: *International Journal of Earth Sciences* 94.4, pp. 711–731 DOI: 10.1007/s00531-005-0479-y.

Blard, P. H., J. Lavé, R. Pik, X. Quidelleur, D. Bourlès, and G. Kieffer (2005) "Fossil cosmogenic ^{3}He record from K-Ar dated basaltic flows of Mount Etna volcano (Sicily, 38°N): Evaluation of a new paleoaltimeter" in: *Earth and Planetary Science Letters* 236.3-4, pp. 613–631 DOI: 10.1016/j.epsl.2005.05.028.

Boero, V. and U. Schwertmann (1989) "Iron oxide mineralogy of Terra Rossa and its genetic implications" in: *Geoderma* 44.4, pp. 319–327.

Borger, H. (1990) "Bohnerze und Quarzsande als Indikatoren paläogeographischer Verwitterungsprozesse und der Altreliefgenese östlich von Albstadt (Schwäbische Alb)." in: *Kölner Geographische Arbeiten* 52, p. 209.

Borger, H. and M. Widdowson (June 2001) "Indian laterites, and lateritious residues of southern Germany: a petrographic, mineralogical, and geochemical comparison" in: *Zeitschrift für Geomorphologie* 45.2, pp. 177–200.

Dehm, R. (1961) "Spaltenfüllungen als Lagerstätten fossiler Landwirbeltiere" in: *Mitteilungen der Bayerischen Staatssammlung für Paläontologie und historische Geologie* 1, pp. 57–72.

Fach, B. (1908) "Chemische Untersuchungen über Roterden und Bohnerztone" PhD thesis Universität Freiburg i. B., p. 31.

Farley, K. A., R. A. Wolf, and L. T. Silver (1996) "The effects of long alpha-stopping distances on (U-Th)/He ages" in: *Geochimica et Cosmochimica Acta* 60.21, pp. 4223–4229 DOI: 10.1016/S0016-7037(96)00193-7.

Farley, K. A. (2002) "(U-Th)/He Dating: Techniques, Calibrations, and Applications" in: *Reviews in Mineralogy and Geochemistry* 47.1, pp. 819–844 DOI: 10.2138/rmg.2002.47.18.

Farley, K. A., J. Libarkin, S. Mukhopadhyay, and W. Amidon (2006) "Cosmogenic and nucleogenic ^{3}He in apatite, titanite, and zircon" in: *Earth and Planetary Science Letters* 248.1-2, pp. 436–446.

Farley, K. A. and R. McKeon (2015) "Radiometric dating and temperature history of banded iron formation-associated hematite, Gogebic iron range, Michigan, USA" in: *Geology* 43.12, pp. 1083–1086 DOI: 10.1130/G37190.1.

Farley, K. A., P. W. Reiners, and V. Nenow (1999) "An apparatus for high-precision helium diffusion measurements from minerals" in: *Analytical Chemistry* 71.10, pp. 2059–2061 DOI: 10.1021/ac9813078.

Frank, M. (1928) "Lateritische Substanzen in marinen Kalken" in: *Centralblatt für Mineralogie, Geologie und Paläontologie* Abt. B, pp. 273–291.

Geyer, O. (1957) "Über das Bohnerz in Württemberg" in: *Zeitschrift der Deutschen Geologischen Gesellschaft* 109, pp. 22–27.

Gosse, J. C. and F. M. Phillips (2001) *Terrestrial in situ cosmogenic nuclides: Theory and application* DOI: 10.1016/S0277-3791(00)00171-2.

Heim, A. (1919) "Das Tertiär des Juragebirges, 1. Die Bohnerzformation" in: *Geologie der Schweiz* 1, pp. 529–547.

Lal, D. (1987) "Production of ^{3}He in terrestrial rocks" in: *Chemical Geology: Isotope Geoscience Section* 66.1-2, pp. 89–98 DOI: 10.1016/0168-9622(87)90031-5.

– (1991) "Cosmic ray labeling of erosion surfaces: in situ nuclide production rates and erosion models" in: *Earth and Planetary Science Letters* 104.2-4, pp. 424–439 DOI: 10.1016/0012-821X(91)90220-C.

Lang, R. (1914) "Geologisch-mineralogische Beobachtungen in Indien – 3. Rezente Bohnerzbildung auf Laterit. Entstehung fossiler Bohnerze" in: *Centralblatt für Mineralogie, Geologie und Paläontologie* 21, pp. 641–653.

Libarkin, J. C., J. Quade, C. G. Chase, J. Poths, and W. McIntosh (2002) "Measurement of ancient cosmogenic ^{21}Ne in quartz from the 28 Ma Fish Canyon Tuff, Colorado" in: *Chemical Geology* 186.3-4, pp. 199–213 DOI: 10.1016/S0009-2541(01)00411-9.

Lippolt, H. J., T. Brander, and N. R. Mankopf (1998) "An attempt to determine formation ages of goethites and limonites by (U+Th)-He-4 dating" in: *Neues Jahrbuch für Mineralogie-Monatshefte* 11, pp. 505–528.

Menning, M. and F. Steininger (2005) “The ‘Stratigraphische Tabelle von Deutschland 2002 (STD 2002)’ or the Regional Stratigraphic Reference Scale and its explanations: ideas and outlook” in: *Newsletters on Stratigraphy* 41.3, pp. 1–6.

Monteiro, H. S., P. M. Vasconcelos, K. A. Farley, C. A. Spier, and C. L. Mello (2014) “(U-Th)/He geochronology of goethite and the origin and evolution of cangas” in: *Geochimica et Cosmochimica Acta* 131, pp. 267–289 DOI: 10.1016/j.gca.2014.01.036.

Moos, A. (1921) “Über die Bildung der süddeutschen Bohnerze” in: *Zeitschrift für praktische Geologie* 29, pp. 106–109.

Mosbrugger, V., T. Utescher, and D. L. Dilcher (2005) “Cenozoic continental climatic evolution of Central Europe” in: *Proceedings of the National Academy of Sciences of the United States of America* 102.42, pp. 14964–14969 DOI: 10.1073/pnas.0505267102.

Muhs, D. R. and E. A. I. Bettis (2003) “Quaternary loess-paleosol sequences as examples of climate-driven sedimentary extremes” in: *Geological Society of America Special Papers* 370.303, pp. 53–74 DOI: doi:10.1130/0-8137-2370-1.53.

Müller, W. H., H. Naef, and H. R. Graf (2002) *Geologische Entwicklung der Nordschweiz, Neotektonik und Langzeitszenarien Zürcher Weinland. Nagra Technischer Bericht NTB 99-08* tech. rep., p. 238.

Nesterenok, A. and O. Yakubovich (2016) “Production of ^{3}He in rocks by reactions induced by particles of the nuclear-active and muon components of cosmic rays: Geological and petrological implications” in: *Petrology* 24.1, pp. 21–34.

Pavich, M. J. (1989) “Regolith residence time and the concept of surface age of the Piedmont "Peneplain"” in: *Geomorphology* 2.1-3, pp. 181–196 DOI: 10.1016/0169-555X(89)90011-1.

Protin, M., P.-H. Blard, Y. Marrocchi, and F. Mathon (2016) “Irreversible adsorption of atmospheric helium on olivine: A lobster pot analogy” in: *Geochimica et Cosmochimica Acta* 179, pp. 76–88.

Reichenbacher, B., W. Krijgsman, Y. Lataster, M. Pipperr, C. G. C. Van Baak, L. Chang, D. Kälin, J. Jost, G. Doppler, D. Jung, J. Prieto, H. Abdul Aziz, M. Böhme, J. Garnish, U. Kirscher, and V. Bachtadse (2013) “A new magnetostratigraphic framework for the Lower Miocene (Burdigalian/Ottnangian, Karpatian) in the North Alpine Foreland Basin” in: *Swiss Journal of Geosciences* 2, pp. 309–334 DOI: 10.1007/s00015-013-0142-8.

Retallack, G. J. (2008) “Cool-Climate or Warm-Spike Lateritic Bauxites at High Latitudes?” In: *The Journal of Geology* 116.6, pp. 558–570 DOI: 10.1086/592387.

– (2010) “Lateritization and bauxitization events” in: *Economic Geology* 105.3, pp. 655–667.

Retallack, G. J. and A. Mindszenty (1994) "Well preserved late Precambrian paleosols from northwest Scotland" in: *Journal of Sedimentary Research A: Sedimentary Petrology & Processes* 64 A.2, pp. 264–281 DOI: 10.1306/D4267D7A-2B26-11D7-8648000102C1865D.

Rollier, L. (1905) "Die Bohnerzformation oder das Bohnerz und seine Enstehungsweise" in: *Vierteljahrsschrift der natforschenden Gesellschaft Zürich* 50.1/2, pp. 150–162.

Rummel, M. (1993) "Neue fossilführende Karstfüllungen der Schwäbisch-Fränkischen Alb" in: *Documenta naturae* 79, pp. 1–32.

Sadler, P. M. (1981) "Sediment Accumulation Rates and the Completeness of Stratigraphic Sections" in: *The Journal of Geology* 89.5, pp. 569–584 DOI: 10.1086/628623.

Schreiner, B. (1959) "Über die Juranagelfluh im Hegau" in: *Zeitschrift der Deutschen Geologischen Gesellschaft* 112, pp. 568–592.

Shuster, D. L. and K. A. Farley (2003) "^{4}He/^{3}He thermochronometry" in: *Earth and Planetary Science Letters* 217.1-2, pp. 1–17 DOI: 10.1016/S0012-821X(03)00595-8.

Shuster, D. L., K. A. Farley, J. M. Sisterson, and D. S. Burnett (2003) "Quantifying the diffusion kinetics and spatial distributions of radiogenic ^{4}He in minerals containing proton-induced ^{3}He" in: *Earth and Planetary Science Letters* 217.1-2, pp. 19–32 DOI: 10.1016/S0012-821X(03)00594-6.

Shuster, D. L., K. A. Farley, P. M. Vasconcelos, G. Balco, H. S. Monteiro, K. Waltenberg, and J. O. Stone (2012) "Cosmogenic ^{3}He in hematite and goethite from Brazilian "canga" duricrust demonstrates the extreme stability of these surfaces" in: *Earth and Planetary Science Letters* 329-330, pp. 41–50 DOI: 10.1016/j.epsl.2012.02.017.

Shuster, D. L., P. M. Vasconcelos, J. A. Heim, and K. A. Farley (2005) "Weathering geochronology by (U-Th)/He dating of goethite" in: *Geochimica et Cosmochimica Acta* 69.3, pp. 659–673 DOI: 10.1016/j.gca.2004.07.028.

Sissingh, W. (1998) "Comparative Tertiary stratigraphy of the Rhine Graben, Bresse Graben and Molasse Basin: Correlation of Alpine foreland events" in: *Tectonophysics* 300.1-4, pp. 249–284 DOI: 10.1016/S0040-1951(98)00243-1.

Ufrecht, W. (2008) "Evaluating landscape development and karstification of the Central Schwäbische Alb (Southwest Germany) by fossil record of karst fillings" in: *Zeitschrift für Geomorphologie* 52.4, pp. 417–436.

Vasconcelos, P. M., P. R. Renne, G. H. Brimhall, and T. A. Becker (1994) "Direct dating of weathering phenomena by ^{40}Ar-^{39}Ar and K-Ar analysis of supergene K-Mn oxides" in: *Geochimica et Cosmochimica Acta* 58.6, pp. 1635–1665.

Wieler, R., J. Beer, and I. Leya (2013) "The galactic cosmic ray intensity over the past 10^6-10^9 years as recorded by cosmogenic nuclides in meteorites and terrestrial samples" in: *Space Science Reviews* 176.1-4, pp. 351–363.

Yapp, C. J. and D. L. Shuster (2011) "Environmental memory and a possible seasonal bias in the stable isotope composition of (U-Th)/He-dated goethite from the Canadian Arctic" in: *Geochimica et Cosmochimica Acta* 75.15, pp. 4194–4215 DOI: 10.1016/j.gca.2011.04.029.

APPENDIX

2.A ^{4}He/^{3}He experiments

The He-retention of a phase can be determined by measuring the natural distribution of ^{4}He by step-heating of samples with a uniform, proton-induced ^{3}He concentration (Shuster et al., 2003). Sample masses between 3 mg and 40 mg were picked from crushed pisoliths. They were irradiated on January 24th, 2015, with a 228.5 MeV proton beam with a fluence of $1.05 \cdot 10^{16}$ protons/cm^2 at the Francis H. Burr Proton Therapy Center at Massachusetts General Hospital for 5.5 hours to produce a uniform concentration of ^{3}He. The procedure follows the one described in Shuster et al. (2003). After irradiation the samples were stored for several months before analysis.

Pisoliths

Several pieces with a total mass between 0.4 and 1.2 mg were picked from irradiated sample material. They were enclosed in a copper packet and mounted on a thermocouple wire inside a diffusion cell. The samples were subjected to step-wise heating with a projector lamp (Farley et al., 1999) with 5-20°C steps between 25°C and 360°C and a heating time of 30 min per step. The temperature was within 2°C of the set temperature for steps 200°C, with a maximum overshoot of 10°C at temperatures over 300°C. The resulting gas was analyzed for ^{4}He and ^{3}He according to the procedure described in section 2.B below.

The ^{4}He/^{3}He ratio of each step was normalized by the bulk ^{4}He/^{3}He ratio and plotted against the cumulative fraction of ^{3}He released. The shape of this spectrum provides information about the spatial distribution of ^{4}He (Shuster and Farley, 2003; Shuster et al., 2003). No loss would be represented by a flat spectrum at unity. Any helium loss would lead to a deficit of ^{4}He in low-temperature steps.

$^4He/^3He$ spectra were obtained for five different irradiated samples of pisolith cortices (Tab. 2.1-2.3). The $^4He/^3He$ ratio is initially zero as ^3He is released at very low temperature steps (<50°C) and ^4He is below the detection limit. The normalized $^4He/^3He$ ratio then increases in the temperature steps over 50°C and approaches unity around 100°C. Most of the gas was released between 90°C and 120°C. The shape of the $^4He/^3He$ spectra is consistent with isothermal accumulation and diffusion (Shuster and Farley, 2003; Shuster et al., 2003). The resulting retention is between 93% and 98% (Figs. 2.1-2.3).

All ages and concentrations given here are uncorrected for partial He retentivity. Since the retentivities that were obtained using the $^4He/^3He$ method are between 93% and 98%, (U-Th)/He ages as well as ^3He concentrations may be up to 7% higher than stated here.

FH-F1-BR01-irr (0.41 mg)						FH-F2-BR04-irr (0.61 mg)					
Step Number	**Temp. [°C]**	**^{3}He [pcc]**	**±1σ [pcc]**	**^{4}He [ncc]**	**±1σ [ncc]**	**Step Number**	**Temp. [°C]**	**^{3}He [pcc]**	**±1σ [pcc]**	**^{4}He [ncc]**	**±1σ [ncc]**
0	25	bdl		bdl		0	25	bdl		bdl	
1	40	0.0468	0.0004	bdl		1	50	0.2667	0.0012	bdl	
2	60	0.2927	0.0015	bdl		2	70	0.8342	0.0027	bdl	
3	80	0.1754	0.0010	bdl		3	80	0.7111	0.0021	0.1950	0.0044
4	85	0.4247	0.0017	0.0419	0.0056	4	90	2.8084	0.0064	1.7476	0.0040
5	90	0.3633	0.0014	0.1622	0.0038	5	95	3.6331	0.0088	2.3587	0.0037
6	95	0.5773	0.0017	0.3808	0.0042	6	100	1.3519	0.0040	0.9117	0.0049
7	100	1.7300	0.0036	1.3702	0.0046	7	105	0.3091	0.0016	0.1925	0.0016
8	110	6.2340	0.0096	5.4089	0.0056	8	110	1.0308	0.0036	0.6009	0.0036
9	120	1.9289	0.0060	1.8235	0.0061	9	115	4.8058	0.0084	2.9342	0.0034
10	130	0.0700	0.0007	0.0595	0.0030	10	120	1.6365	0.0036	1.0077	0.0062
11	140	0.1317	0.0012	0.1128	0.0041	11	130	0.7457	0.0022	0.4542	0.0036
12	160	0.3136	0.0011	0.2941	0.0042	12	140	0.0621	0.0007	bdl	
13	180	1.3017	0.0030	1.1682	0.0040	13	160	1.1415	0.0030	0.8077	0.0036
14	200	0.3807	0.0016	0.3421	0.0021	14	180	0.3428	0.0017	0.2335	0.0020
15	220	0.3691	0.0021	0.3458	0.0025	15	200	0.5312	0.0018	0.3360	0.0063
16	240	0.1795	0.0010	0.1624	0.0038	16	220	0.6418	0.0024	0.4235	0.0038
17	260	0.2595	0.0014	0.2232	0.0038	17	240	0.2050	0.0011	0.1214	0.0038
18	280	0.1718	0.0010	0.1650	0.0043	18	260	0.3052	0.0011	0.1961	0.0053
19	300	0.0658	0.0007	0.0657	0.0046	19	280	0.3884	0.0016	0.2808	0.0030
20	320	0.0553	0.0006	0.0439	0.0050	20	300	0.0534	0.0005	bdl	
21	340	0.0479	0.0004	0.0451	0.0042	21	320	0.0456	0.0005	bdl	
22	360	0.0339	0.0003	bdl		22	340	0.0436	0.0008	bdl	

Table 2.1: Results of the ^{4}He/^{3}He experiment of samples FH-F1-BR01-irr and FH-F2-BR04-irr from pisolith cortices. Aliquots were degassed for 30 min at each step (bdl = below detection limit).

FH-F3-BR03-3rdlayer-irr3 (0.46 mg)						FH-F4-BR05-4thlayer-irr4 (0.36 mg)					
Step Number	**Temp. [°C]**	**^{3}He [pcc]**	**±1σ [pcc]**	**^{4}He [ncc]**	**±1σ [ncc]**	**Step Number**	**Temp. [°C]**	**^{3}He [pcc]**	**±1σ [pcc]**	**^{4}He [ncc]**	**±1σ [ncc]**
0	25	bdl		bdl		0	30	bdl		bdl	
1	40	0.0199	0.0003	bdl		1	40	0.0023	0.0001	bdl	
2	60	0.2492	0.0012	bdl		2	60	0.0348	0.0004	bdl	
3	80	0.6312	0.0021	0.1134	0.0018	3	80	0.0842	0.0006	bdl	
4	90	5.8018	0.0098	4.7860	0.0048	4	90	0.1967	0.0010	0.0795	0.0029
5	100	5.3090	0.0110	4.8500	0.0050	5	100	2.0933	0.0052	1.5022	0.0050
6	110	2.4622	0.0063	2.3401	0.0052	6	110	1.7465	0.0038	1.2821	0.0015
7	120	0.0532	0.0006	bdl		7	120	1.7356	0.0086	1.2963	0.0058
8	130	0.0313	0.0002	bdl		8	130	0.1288	0.0009	0.0955	0.0055
9	140	0.1831	0.0010	0.1656	0.0049	9	140	0.6805	0.0028	0.4796	0.0042
10	150	1.1564	0.0033	1.0613	0.0032	10	150	0.2915	0.0011	0.1823	0.0042
11	160	0.6346	0.0019	0.5831	0.0051	11	160	0.0784	0.0007	0.0592	0.0051
12	170	0.1707	0.0012	0.1665	0.0045	12	170	0.1132	0.0009	0.0774	0.0057
13	180	0.2136	0.0011	0.1875	0.0021	13	180	0.0614	0.0006	0.0424	0.0039
14	200	0.3968	0.0014	0.3683	0.0046	14	200	0.3280	0.0015	0.2323	0.0058
15	220	0.1703	0.0010	0.1566	0.0036	15	220	0.1051	0.0008	0.0822	0.0034
16	240	0.1406	0.0011	0.1528	0.0033	16	240	0.0958	0.0008	0.0721	0.0030
17	260	0.0814	0.0007	0.0866	0.0025	17	260	0.2449	0.0013	0.1747	0.0043
18	280	0.0724	0.0006	0.0606	0.0039	18	280	0.0721	0.0005	0.0581	0.0022
19	300	0.0198	0.0002	0.0168	0.0039	19	300	0.0094	0.0001	bdl	
20	320	0.0149	0.0003	bdl		20	320	0.0316	0.0004	bdl	
21	340	0.0116	0.0008	bdl		21	340	0.0210	0.0002	bdl	
22	360	0.0073	0.0001	bdl		22	360	0.0148	0.0003	bdl	

Table 2.2: Results of the ^{4}He/^{3}He experiment of samples FH-F3-BR03-3rdlayer-irr3 and FH-F4-BR05-4thlayer-irr4 from different layers of the same pisolith cortex. Aliquots were degassed for 30 min at each step (bdl = below detection limit).

FH-F5-BR05-core-irr3 (0.41 mg)						FH-L120a-diff (56.44 mg)					
Step Number	**Temp. [°C]**	**^{3}He [pcc]**	**±1σ [pcc]**	**^{4}He [ncc]**	**±1σ [ncc]**	**Step Number**	**Temp. [°C]**	**^{3}He [pcc]**	**±1σ [pcc]**	**^{4}He [ncc]**	**±1σ [ncc]**
0	25	bdl		bdl		0	22	bdl		bdl	
1	40	0.0760	0.0004	bdl		1	40	0.0072	0.0002	bdl	
2	60	0.4036	0.0018	bdl		2	60	0.0013	0.0001	bdl	
3	80	1.2538	0.0057	0.2116	0.0049	3	80	0.0021	0.0001	0.0543	0.0048
4	90	0.9722	0.0040	0.4952	0.0038	4	100	0.0027	0.0002	1.0135	0.0019
5	100	3.6078	0.0086	2.1444	0.0014	5	120	0.0087	0.0002	10.3108	0.0057
6	110	5.5278	0.0096	3.4786	0.0038	6	160	0.0766	0.0008	107.3692	0.0541
7	120	6.0570	0.0198	4.0500	0.0030	7	199	0.2277	0.0020	343.3449	0.2551
8	130	0.3921	0.0020	0.2518	0.0032	8	239	0.2581	0.0018	435.7943	0.2654
9	140	0.0025	0.0001	bdl		9	274	0.0212	0.0003	42.4120	0.0125
10	150	0.0205	0.0002	bdl		10	276	0.0117	0.0004	19.7384	0.0238
11	160	1.0682	0.0039	0.7459	0.0046	11	294	0.0155	0.0002	34.9967	0.0239
12	170	0.5255	0.0018	0.3380	0.0029	12	313	0.0160	0.0004	32.6238	0.0140
13	180	0.3413	0.0016	0.2433	0.0047						
14	200	0.6308	0.0025	0.4463	0.0059						
15	220	0.1969	0.0013	0.1444	0.0015						
16	240	0.5091	0.0021	0.3538	0.0020						
17	260	0.0025	0.0002	bdl							
18	280	0.3272	0.0012	0.2354	0.0044						
19	300	0.0890	0.0007	0.0583	0.0024						
20	320	0.0744	0.0003	0.0511	0.0043						
21	340	0.0481	0.0005	bdl							
22	360	0.0423	0.0005	bdl							

Table 2.3: Results of the ^{4}He/^{3}He experiment of samples FH-F5-BR05-core-irr3 from fine-grained material of the nucleus of pisolith BR05 and unirradiated cortex material of pisolith FH-L120a-diff. Aliquots were degassed for 30 min at each step (bdl = below detection limit).

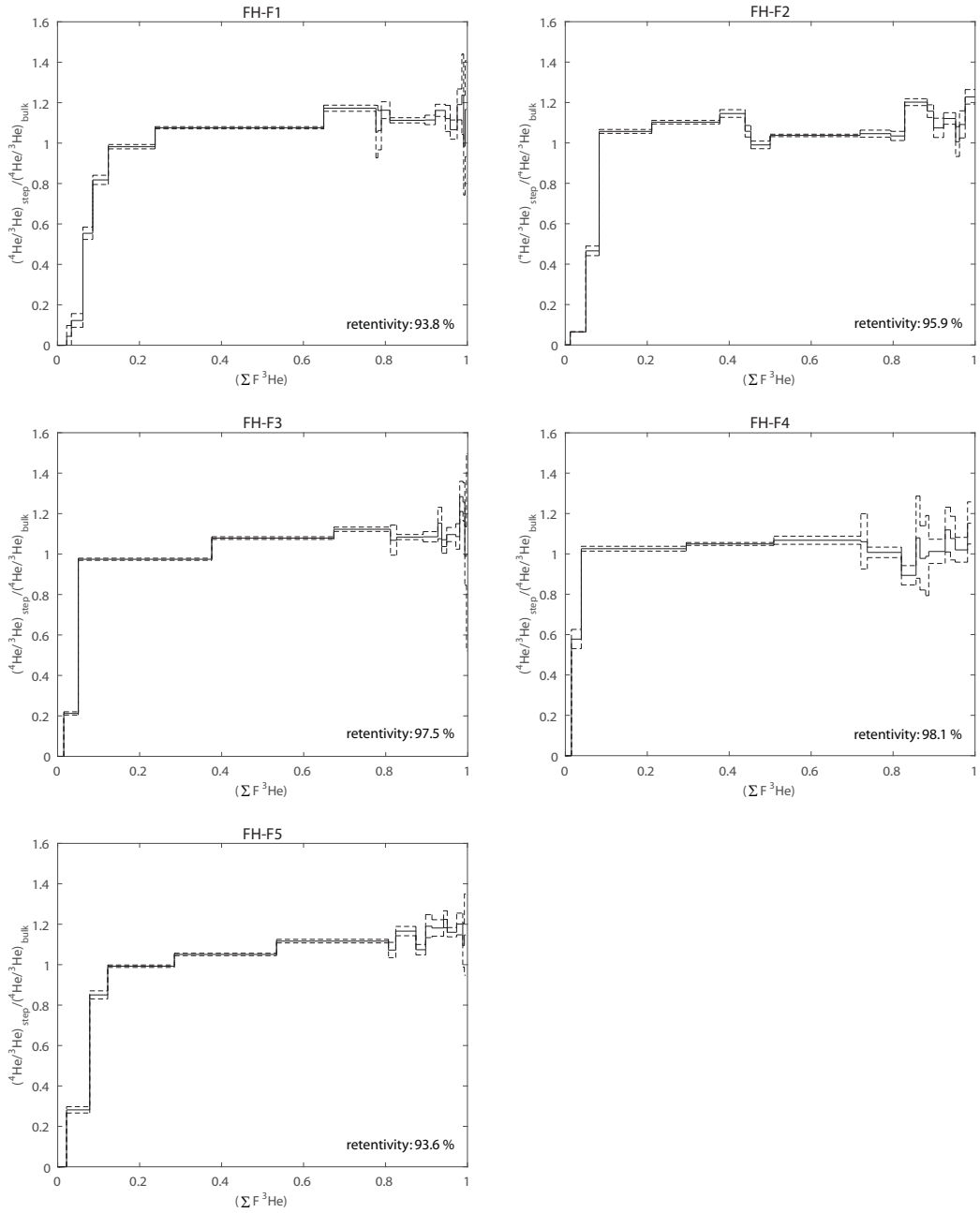

Figure 2.5: Normalized ^{4}He/^{3}He spectra of samples FH-F1 through FH-F5. Samples FH-F1 and FH-F2 were taken from the cortex of two different pisoliths. Samples FH-F3, FH-F4, and FH-F5 were taken from the 3rd and 4th layer of the cortex as well as the finer-grained nucleus of the same pisolith. The dashed line shows the 1σ uncertainty of the ^{4}He/^{3}He ratio.

Unirradiated pisolith

To investigate whether poly-crystalline goethite of Bohnerz pisoliths can trap ^{3}He from air, we performed a step-heating experiment of unirradiated cortex material (Tab. 2.3). Helium from air is more loosely bound by surface adhesion than radiogenic helium. Since air has a higher ^{3}He/^{4}He ratio than radiogenic helium, ^{3}He would disproportionately be released at lower temperatures. Pisolith L120a was selected because it had previously yielded the highest ^{3}He concentration, to ensured a ^{3}He release above blank level when degassed in temperature steps. The fraction released in every temperature step was the same for ^{3}He and ^{4}He within uncertainty (Fig. 2.6). This shows that both ^{3}He and ^{4}He are equally strongly bound. The results of this experiment do not show a higher ^{3}He/^{4}He ratio in low temperature steps. This is consistent with uniformly distributed cosmogenic ^{3}He and radiogenic ^{4}He.

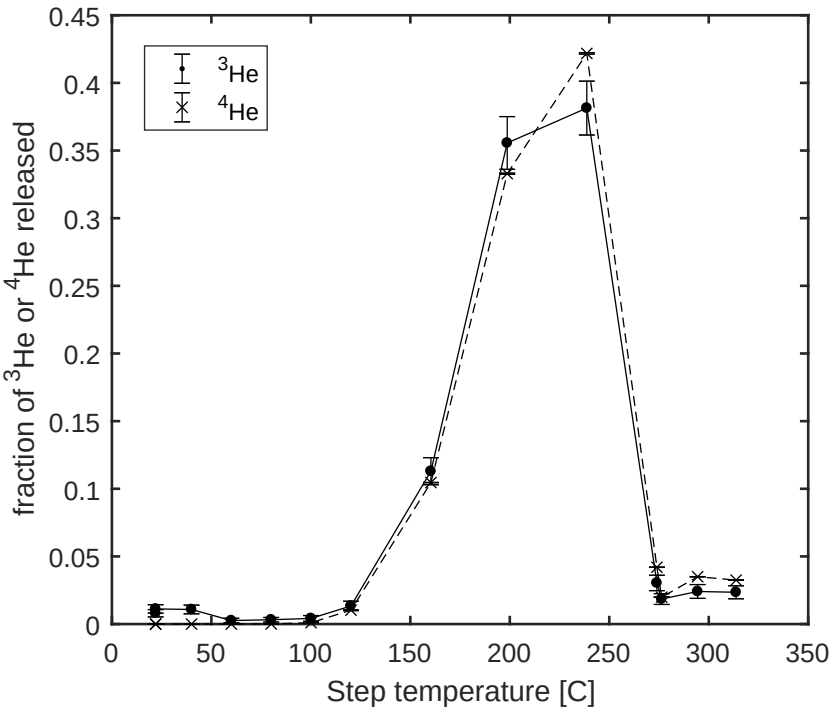

Figure 2.6: Results of a step-heating experiment with unirradiated goethite from cortex material of pisolith L120a. The relative amounts of ^{3}He and ^{4}He are the same for every temperature step, showing that both isotopes are equally strongly bound.

2.B Concentrations of ^{3}He

Pisoliths

About 10-20 mg of goethite picked from crushate was weighed and wrapped in tin foil. Samples were degassed at 1300 °C for 30 min in a double-vacuum resistance furnace. Re-extracts at 1350 °C were performed after every sample to verify complete He extraction. The extracted gas was fed through a U-trap filled with activated charcoal and submerged in liquid nitrogen and then reacted with a SAES getter. The gas was fixed on a cryogenic trap at 14 K and then released into the MAP 215-50 magnetic sector field mass spectrometer at 34 K. The abundance of ^{3}He and ^{4}He was measured on an electron multiplier and Faraday cup, respectively. The sensitivity of the mass spectrometer was determined by gas standards with a known ^{3}He/^{4}He ratio of 2.01 RA. Different amounts of standard gas are used to establish linearity within the range of measurement. Analytical detection limits of ^{3}He and ^{4}He are around $1.7 \cdot 10^{-20}$ mol and $5.0 \cdot 10^{-15}$ mol, respectively. Interspersed standards and blanks throughout each experiment were used to correct for drift in sensitivity.

Table 2.4: Measured ^{3}He concentration of pisolith cortices (mass = mass of aliquot, d = depth below freshwater limestone layer, c = concentration of ^{3}He per sample mass, ul = layer of paleosol above freshwater limestone).

Sample Name	**d [cm]**	**mass [mg]**	**^{3}He/^{4}He 10^{-7}**	**^{3}He [amol]**	**$\pm 1\sigma$ [amol]**	**c(^{3}He) [Mat/g]**	**$\pm 1\sigma$ [Mat/g]**
Lula2	ul	15.10	0.599	0.642	0.129	26	5
Lulb1	ul	12.45	12.730	10.296	0.460	498	22
Lulc2	ul	3.88	5.886	2.228	0.268	346	42
Luld1	ul	1.32	13.030	0.742	0.134	339	61
Lule1	ul	20.64	5.629	9.395	0.482	274	14
Lulf1	ul	1.36	10.430	0.703	0.107	311	47
L0a2	5	7.24	5.807	4.596	0.295	382	25
L0b1	5	10.44	7.741	9.159	0.451	528	26
L0c1	5	5.50	6.515	0.664	0.129	73	14
L0c2	5	7.04	3.661	0.860	0.161	74	14
L0d1	5	4.18	3.304	1.829	0.210	263	30
L0e1	5	7.41	5.368	3.518	0.295	286	24
L0f1	5	7.88	5.814	4.844	0.371	370	28
L10a1	15	26.68	6.529	17.733	0.598	400	14
L10b1	15	7.40	5.772	4.409	0.313	359	25
L10c1	15	10.78	6.515	5.728	0.393	320	22
L10c2	15	15.68	5.081	9.169	0.433	352	17
L10d1	15	8.61	6.206	5.383	0.371	377	26
L10e1	15	31.04	3.092	11.390	0.540	221	11
L20a1	23	28.53	3.413	17.509	0.612	370	13
L20a2	23	9.50	3.207	6.158	0.357	390	23
L20b1	23	4.75	4.286	1.972	0.219	250	28
L20c1	23	7.62	2.163	2.053	0.210	162	17
L20d2	23	6.59	3.946	4.507	0.330	412	30
L20e1	23	12.11	5.908	3.904	0.277	194	14
L30a1	33	10.70	2.917	1.759	0.188	99	11
L30b1	33	15.36	7.921	9.522	0.442	373	17
L30c1	33	6.62	5.030	3.010	0.281	274	26
L30d1	33	13.24	8.960	8.193	0.429	373	20
L30e1	33	14.93	4.034	6.055	0.379	244	15
L50a1	45	4.67	2.643	1.330	0.183	172	24
L50b1	45	25.27	4.417	11.841	0.442	282	11
L50c1	45	14.30	3.273	3.233	0.263	136	11
L50d1	45	23.00	3.825	10.145	0.438	266	12
L50e1	45	15.68	5.031	9.280	0.549	356	21
L70a2	60	14.28	0.709	0.933	0.125	39	5
L70a3	60	3.84	0.660	0.244	0.085	38	13
L70b1	60	20.51	3.509	8.532	0.455	251	13
L70c1	60	3.87	2.970	1.161	0.152	181	24
L70d1	60	12.94	3.051	4.109	0.254	191	12
L70e1	60	24.90	9.761	11.575	0.509	280	12
L80a1	75	6.50	3.481	3.676	0.290	341	27
L80a2	75	10.49	3.477	5.106	0.353	293	20

Table 2.5: Measured ^{3}He concentration of pisolith cortices continued.

Sample Name	d [cm]	mass [mg]	^{3}He/^{4}He 10^{-7}	^{3}He [amol]	$\pm 1\sigma$ [amol]	c(^{3}He) [Mat/g]	$\pm 1\sigma$ [Mat/g]
L80b1	75	14.14	0.455	0.842	0.125	36	5
L80b2	75	11.12	0.475	0.648	0.112	35	6
L80c1	75	30.15	5.054	15.422	0.656	308	13
L80d1	75	18.59	5.368	8.721	0.442	283	14
L80e1	75	6.32	7.489	5.035	0.353	480	34
L90a2	87	42.58	5.683	13.757	0.585	195	8
L90b1	87	13.53	7.117	10.521	0.424	468	19
L90c1	87	21.60	5.380	12.066	0.589	336	16
L90d2	87	6.12	4.712	1.240	0.179	122	18
L90e1	87	9.15	3.592	2.696	0.241	177	16
L120a1	116	19.99	6.432	16.796	0.527	506	16
L120a2	116	13.99	6.738	14.233	0.563	613	24
L120a3	116	7.77	6.860	7.747	0.420	600	33
L120b1	116	26.33	6.500	17.972	0.665	411	15
L120c1	116	6.13	1.578	1.279	0.179	126	18
L120c2	116	5.89	1.824	1.197	0.147	122	15
L120d2	116	4.32	3.058	2.649	0.241	369	34
L120e1	116	10.12	5.698	10.486	0.473	624	28
L120f1	116	1.39	7.533	0.779	0.134	338	58
L120f2	116	0.48	7.224	0.275	0.085	345	106
L120f3	116	0.85	6.429	0.437	0.098	309	70
L120f4	116	1.61	6.097	0.869	0.152	325	57
L120f5	116	1.24	4.785	0.697	0.134	339	65
L120f6	116	0.42	4.660	0.263	0.089	378	128
L120f7	116	1.63	4.088	0.747	0.138	276	51
L120g1	116	6.75	2.918	1.965	0.219	175	20
L170a2	164	8.60	5.654	5.469	0.326	383	23
L170b1	164	34.33	9.969	19.597	0.621	344	11
L170c1	164	5.77	4.577	2.202	0.250	230	26
L170c2	164	9.40	6.149	4.529	0.348	290	22
L170d1	164	6.46	5.128	2.291	0.254	214	24
L170e1	164	2.70	6.774	1.019	0.138	227	31
L250a1	268	12.00	5.352	6.350	0.388	319	20
L250b1	268	5.09	5.384	2.261	0.210	268	25
L250c1	268	11.48	1.555	2.632	0.228	138	12
L250d2	268	5.61	3.339	2.262	0.250	243	27
L250e1	268	25.49	7.948	16.706	0.612	395	14
L300a1	339	15.02	2.579	2.937	0.223	118	9
L300a2	339	8.14	2.557	1.503	0.183	111	14
L300b1	339	18.10	4.915	9.546	0.451	318	15
L300b2	339	14.30	4.554	7.470	0.357	315	15
L300c1	339	2.25	5.193	0.843	0.152	226	41
L300c2	339	4.09	4.659	1.411	0.170	208	25
L300d1	339	26.35	3.888	6.057	0.366	138	8
L300e1	339	12.29	0.958	1.342	0.174	66	9
L300g1	339	5.48	4.743	1.899	0.241	209	27

Fine-grained iron-oxides in clay

About 10-150 mg of red Bolus clay from the paleosol was analyzed for ^{3}He as described above. An aliquot of about 2 mg of the same crushate was used for chemical analysis. Iron-oxides in the clay were dissolved with 200 µl of concentrated HCl at 95 °C for 72 hours, leaving a kaolinite residue. The solutions were spiked and analyzed for Fe using ICP-MS as described in Appendix 2.C. The ^{3}He concentration was calculated based on the iron-oxide fraction of the clay.

Table 2.6: Results of ^{3}He concentration measurements of fine-grained iron-oxides in soil (d = depth below freshwater limestone layer, ul = layer of paleosol above freshwater limestone, mass = mass of the bulk soil sample for ^{3}He measurement, f_{gt} = mass fraction of stoichiometrically calculated goethite, c(^{3}He) = concentration of ^{3}He based on mass fraction of iron-oxides). Two different aliquots were used to measure ^{3}He bulk concentration and iron-oxide mass fraction. The ^{3}He concentration in fine-grained iron-oxides was calculated based on these parameters.

Sample Name	d [cm]	mass [mg]	^{3}He/^{4}He 10^{-7}	^{3}He [amol]	$\pm1\sigma$ [amol]	f_{gt}	c(^{3}He) Mat/g	$\pm1\sigma$ Mat/g
Lulclay1	ul	81.98	1.336	1.2188	0.1964	0.1897	47	8
Lulclay3	ul	26.33	3.400	1.3751	0.2188	0.1021	308	51
L0clay1	5	27.31	3.111	0.7813	0.1473	0.0605	285	56
L0clay3	5	59.82	2.828	1.9196	0.2277	0.0743	260	33
L20clay1	23	11.02	3.762	0.3705	0.0982	0.0774	262	71
L20clay3	23	12.86	3.060	0.5446	0.1339	0.0936	273	68
L20clay4	23	41.63	2.800	1.7232	0.2411	0.1188	210	31
L20clay5	23	53.77	9.135	2.9420	0.3348	0.1407	234	29
L30clay1	33	38.35	4.273	1.7679	0.2232	0.0824	337	46
L30clay3	33	13.39	2.652	0.5089	0.1339	0.1432	160	43
L50clay1	45	16.13	2.450	0.4598	0.1205	0.0876	196	52
L50clay3	45	40.07	1.803	1.7366	0.2545	0.0942	277	43
L70clay1	60	18.83	3.698	0.8125	0.1563	0.1468	177	35
L70clay3	60	26.87	2.772	1.0000	0.1607	0.1533	146	25
L80clay1	75	27.93	2.489	1.0670	0.1786	0.1605	143	25
L80clay3	75	87.86	3.786	4.1741	0.3527	0.1159	247	24
L90clay1	87	34.73	2.914	1.4018	0.2054	0.1469	165	26
L90clay3	87	47.29	3.076	1.6786	0.2545	0.1259	170	27
L120clay1	116	70.68	3.408	2.4509	0.2857	0.0834	250	32
L120clay3	116	23.28	2.931	0.8571	0.1696	0.1143	194	40
L170clay1	164	41.26	3.281	1.7143	0.2321	0.0819	306	44
L170clay3	164	16.84	3.197	0.5759	0.1295	0.1092	189	43
L170clay4	164	157.41	2.850	4.5625	0.3616	0.1531	114	11
L250clay1	268	23.67	3.763	1.5491	0.2009	0.0971	406	56
L250clay3	268	32.57	3.565	1.7321	0.2277	0.1355	236	33
L300clay1	339	14.53	2.005	0.5804	0.1339	0.1044	230	54
L300clay3	339	96.51	3.079	3.8750	0.3527	0.0986	245	25
L300clay4	339	43.23	2.903	1.8170	0.2188	0.1029	246	32

Exposure modeling of soil convection

To estimate the exposure duration we modeled soil convection as a continuous circular motion throughout the whole thickness of the paleosol (3.6 m). This leads to a constant concentration profile of ^{3}He in the soil for any total exposure duration that is longer than the timescale of soil convection. Since the exposure duration here is at least several Ma, we find this to be a justifiable assumption. The cosmogenic ^{3}He production rate at the surface, scaled for latitude and a range in paleo-elevation, is between 79 and 129 at g^{-1} a^{-1}. The production rate decreases exponentially with depth (Lal, 1991). We assumed an attenuation length of 160 g cm^{-2} (Gosse and Phillips, 2001) and a density of 1.6 g cm^{-3}. This yields an absorption coefficient of 0.01 cm^{-1}, which corresponds to an e-folding depth of 100 cm. At the base of the paleosol the production rate is <1% of the production rate at the surface. We numerically integrated the time any parcel spends at 3000 different depths between 0 and 360 cm on a circular trajectory. Since the resulting concentration is constant, the equivalent production rate is the same for every depth. To address uncertainties in the production rate, attenuation path length, and paleo-elevation we used a Monte-Carlo approach to propagate these uncertainties to the equivalent production rate. The equivalent production rate for this soil convection model is (33.9±5.4) at g^{-1} a^{-1}. For an average concentration of 300 Mat/g, this corresponds to an exposure duration of (8.8±1.7) Ma.

2.C Goethite (U-Th)/He ages

Several aliquots of the crushate of each pisolith were selected for age dating. Individual pieces with a cross-section of 100-500 μm and a mass of approximately 5-50 μg were loaded into platinum tubes. Samples were heated to 900 °C using a Photon Machines YAG laser and degassed under vacuum for 360 seconds. A pure ^{3}He spike for isotope dilution was added. The gas was cryogenically fixed at 14 K and released into the Pfeiffer Vacuum quadrupole mass spectrometer at 36 K. The sensitivity of the instrument was calibrated using a standard of known ^{4}He amount. Re-extracts at 950 °C were performed for every sample to ensure complete He extraction.

After degassing the Pt packets were transferred to Teflon vials. For isotope dilution, 25 μl of spike with 12.04 ng/ml of ^{235}U and 21.37 ng/ml of ^{230}Th, and ^{232}Th/^{230}Th and ^{238}U/^{235}U ratios of 0.09 and 0.007, respectively, as well as 10000 ppm of Ca was added. Each aliquot was dissolved in 100 μl of concentrated Seastar™ HCl for 12 h at 95 °C. The solution was dried down by heating to 95 °C for 1 h. The precipitate was brought into solution with 50 μl of concentrated Seastar™ HNO_3. The solution was diluted with 1000 μl of Milli-Q® water. A spiked normal solution with known amounts U, Th, and Fe was prepared. The ^{238}U, ^{232}Th, and Fe content of the solutions as well as the composition of the spike and the normal solution were determined using an Agilent 7500 inductively coupled plasma quadrupole mass spectrometer (ICP-MS) as well as an Agilent 8800 triple-quadrupole ICP-MS.

We assumed zero initial ^{4}He, no diffusive loss or gain for He, U, and Th, as well as secular equilibrium among daughter nuclides of the ^{238}U, ^{235}U, and ^{232}Th decay series. The (U-Th)/He age was calculated according to Farley (2002). Since the diameter of the pisoliths (1-50 mm) and the thickness of layers of equal age (at least 100-200 μm) is much larger than the α-stopping distance (~20 μm) of the U and Th series decays (Farley et al., 1996; Farley, 2002) no correction for α-implantation or α-ejection was applied.

Table 2.7: Goethite (U-Th)/He ages of pisoliths from depth profile of outcrop Lohn am Randen (d = depth below freshwater limestone layer, gt mass = mass of aliquot based on Fe, stoichiometrically calculated as goethite, ul = layer of paleosol above freshwater limestone, bdl = below detection limit).

sample name	d [cm]	age [Ma]	±1σ [Ma]	U [ppm]	±1σ [ppm]	Th [ppm]	±1σ [ppm]	^{4}He [nmol/g]	±1σ [nmol/g]	gt mass [µg]
FH-L-ul-a1	ul	27.45	1.22	3.93	0.15	26.39	0.59	1.521	0.008	7.39
FH-L-ul-b2	ul	17.89	0.75	1.91	0.07	28.68	0.50	0.851	0.008	13.67
FH-L-ul-c1	ul	18.25	0.54	4.46	0.12	39.79	0.53	1.372	0.017	25.39
FH-L-ul-c2	ul	21.97	0.88	2.55	0.17	35.14	0.60	1.293	0.010	13.92
FH-L-ul-c3	ul	19.44	0.69	5.12	0.16	37.97	0.63	1.487	0.010	11.44
FH-L-ul-d1	ul	36.55	2.10	0.97	0.19	22.93	0.53	1.267	0.008	10.25
FH-L-ul-d3	ul	25.42	1.61	3.95	0.19	28.68	0.80	1.480	0.006	3.97
FH-L-ul-e1	ul	24.65	0.80	2.86	0.08	17.18	0.28	0.926	0.012	26.51
FH-L-ul-e2	ul	21.90	0.56	4.04	0.07	21.04	0.25	1.071	0.032	65.89
FH-L-ul-e3	ul	25.10	0.99	3.06	0.11	16.88	0.34	0.961	0.008	14.06
FH-L-0-a1	5	20.02	0.78	2.84	0.11	58.23	0.95	1.805	0.009	8.55
FH-L-0-a2	5	19.19	1.05	3.69	0.17	50.10	1.08	1.619	0.007	4.30
FH-L-0-a3	5	21.52	0.73	1.42	0.10	39.51	0.54	1.255	0.015	24.90
FH-L-0-b1	5	21.30	1.27	3.98	0.17	32.95	0.82	1.366	0.007	4.55
FH-L-0-b2	5	29.35	1.08	3.09	0.13	75.81	1.21	3.350	0.012	7.01
FH-L-0-b3	5	22.01	0.70	3.65	0.12	69.04	0.93	2.388	0.016	13.95
FH-L-0-d1	5	27.57	0.93	4.22	0.14	46.95	0.74	2.291	0.013	11.11
FH-L-0-d3	5	23.97	0.75	3.56	0.11	48.91	0.67	1.965	0.016	17.40
FH-L-0-e1	5	21.85	0.64	2.53	0.07	29.86	0.38	1.136	0.020	37.42
FH-L-0-e2	5	20.82	0.64	2.65	0.08	28.45	0.39	1.058	0.015	29.49
FH-L-0-e3	5	21.47	1.11	2.23	0.14	45.56	0.94	1.513	5.685	5.69
FH-L-10-a1	15	19.46	0.73	2.66	0.10	44.67	0.72	1.400	0.009	11.53
FH-L-10-a3	15	23.50	0.80	3.15	0.11	60.51	0.88	2.242	0.013	11.89
FH-L-10-b1	15	34.67	1.05	3.75	0.11	66.17	0.86	3.680	0.028	16.31
FH-L-10-b2	15	24.03	1.20	bdl		73.53	1.30	2.153	0.008	6.22
FH-L-10-b3	15	25.47	0.74	3.34	0.11	43.94	0.53	1.896	0.028	32.74
FH-L-10-c1	15	18.67	0.96	3.65	0.15	34.57	0.72	1.197	0.007	6.41
FH-L-10-c3	15	40.43	2.12	0.77	0.13	18.10	0.39	1.107	0.009	15.02
FH-L-10-d1	15	32.13	1.72	3.06	0.18	48.37	1.12	2.525	0.007	3.50
FH-L-10-d2	15	24.87	1.03	2.46	0.11	40.00	0.72	1.607	0.008	8.41
FH-L-10-d3	15	34.53	1.50	bdl		39.92	0.65	1.708	0.012	14.24
FH-L-10-e1	15	21.22	0.81	4.10	0.16	64.69	1.05	2.231	0.009	7.12
FH-L-10-e2	15	17.94	0.54	4.12	0.12	73.45	0.89	2.089	0.017	17.28
FH-L-10-e3	15	22.68	0.68	3.25	0.10	61.09	0.76	2.174	21.955	21.95
FH-L-20-a1	23	24.72	1.04	3.09	0.13	57.77	1.05	2.246	0.008	6.02
FH-L-20-a2	23	26.36	0.75	3.46	0.09	75.95	0.85	3.063	0.034	24.26
FH-L-20-a3	23	32.00	1.25	3.72	0.15	49.83	0.91	2.695	0.010	6.81
FH-L-20-a4	23	21.84	0.69	4.03	0.12	58.38	0.81	2.115	0.015	14.68
FH-L-20-b1	23	12.33	0.71	3.08	0.12	36.43	0.71	0.790	0.006	7.59

Table 2.8: Table of goethite (U-Th)/He ages continued.

sample name	d [cm]	age [Ma]	±1σ [Ma]	U [ppm]	±1σ [ppm]	Th [ppm]	±1σ [ppm]	^{4}He [nmol/g]	±1σ [nmol/g]	gt mass [µg]
FH-L-20-b2	23	22.23	0.63	3.55	0.09	63.44	0.72	2.240	0.028	27.47
FH-L-20-b3	23	20.56	0.68	3.30	0.11	60.06	0.85	1.954	0.013	13.38
FH-L-20-c1	23	33.15	1.23	bdl		60.70	0.86	2.577	0.017	14.17
FH-L-20-c2	23	28.57	1.11	0.56	0.14	50.35	0.77	1.929	0.013	13.82
FH-L-20-c3	23	39.26	3.17	bdl		47.40	1.07	1.703	0.007	5.29
FH-L-20-d1	23	32.56	1.05	3.76	0.13	68.32	0.96	3.515	0.019	11.28
FH-L-20-d2	23	29.88	1.04	3.03	0.11	45.21	0.71	2.222	0.013	11.51
FH-L-20-d3	23	27.80	0.83	3.93	0.11	37.03	0.51	1.913	0.020	22.57
FH-L-20-e1	23	11.88	0.35	2.83	0.07	42.54	0.50	0.829	0.014	33.78
FH-L-20-e2	23	14.84	0.88	3.31	0.15	43.61	0.89	1.096	0.006	5.40
FH-L-20-e3	23	15.87	0.50	2.97	0.09	34.87	0.47	0.965	0.013	25.52
FH-L-30-a1	33	10.18	0.46	4.21	0.14	41.50	0.69	0.774	0.007	11.06
FH-L-30-a2	33	11.23	0.58	2.82	0.11	37.25	0.67	0.708	0.007	9.76
FH-L-30-b1	33	17.17	0.54	4.06	0.12	63.52	0.85	1.795	0.014	15.46
FH-L-30-b2	33	18.66	0.77	3.27	0.12	38.70	0.69	1.261	0.008	9.57
FH-L-30-b3	33	25.36	0.98	1.48	0.15	45.42	0.71	1.679	0.012	14.04
FH-L-30-c2	33	30.04	1.00	2.04	0.12	46.04	0.64	2.105	0.020	20.20
FH-L-30-d1	33	24.54	2.00	2.67	0.15	22.66	0.72	1.069	0.006	3.90
FH-L-30-d2	33	19.01	0.57	3.16	0.09	32.57	0.43	1.119	0.016	28.61
FH-L-30-d3	33	20.94	0.73	2.80	0.12	48.89	0.72	1.630	0.012	14.19
FH-L-30-e1	33	21.53	0.78	3.47	0.13	43.62	0.71	1.608	12.136	12.14
FH-L-30-e2	33	22.17	0.85	2.94	0.11	40.78	0.68	1.511	0.009	10.28
FH-L-30-e3	33	18.98	0.66	2.95	0.10	44.08	0.65	1.375	0.011	14.55
FH-L-50-a1	45	21.43	0.66	5.47	0.16	85.24	1.12	3.013	0.018	12.23
FH-L-50-a2	45	26.16	0.72	6.49	0.14	52.85	0.65	2.707	0.030	20.02
FH-L-50-b1	45	23.55	0.68	5.40	0.13	64.03	0.79	2.633	0.024	20.07
FH-L-50-b2	45	17.13	0.63	3.82	0.13	43.28	0.70	1.312	0.009	11.62
FH-L-50-b3	45	35.42	1.05	4.20	0.11	28.05	0.42	2.089	0.023	23.63
FH-L-50-c1	45	15.78	0.52	3.45	0.13	35.35	0.51	1.010	0.012	23.43
FH-L-50-c2	45	44.40	7.98	bdl		29.18	1.21	1.182	0.006	2.96
FH-L-50-c3	45	25.48	1.76	bdl		30.63	0.71	0.993	0.007	7.79
FH-L-50-d1	45	18.34	0.57	3.08	0.10	81.20	1.00	2.214	0.016	15.10
FH-L-50-d2	45	26.26	1.00	3.01	0.13	51.73	0.86	2.169	0.010	8.21
FH-L-50-d3	45	29.34	1.06	1.05	0.13	49.89	0.72	2.043	0.016	16.29
FH-L-50-e1	45	20.46	0.59	3.67	0.10	58.33	0.69	1.935	26.729	26.73
FH-L-50-e3	45	28.12	0.78	2.89	0.07	51.08	0.56	2.280	0.036	35.02
FH-L-70-a1	60	8.18	0.21	9.15	0.20	229.27	2.04	2.811	0.021	16.20
FH-L-70-a2	60	12.74	0.30	16.89	0.22	214.80	1.67	4.683	0.052	24.59
FH-L-70-a3	60	11.46	0.27	15.72	0.21	208.04	1.64	4.032	0.045	24.49

Table 2.9: Table of goethite (U-Th)/He ages continued.

sample name	d [cm]	age [Ma]	±1σ [Ma]	U [ppm]	±1σ [ppm]	Th [ppm]	±1σ [ppm]	^{4}He [nmol/g]	±1σ [nmol/g]	gt mass [µg]
FH-L-70-b1	60	12.75	0.68	4.88	0.20	69.14	1.29	1.474	0.007	4.62
FH-L-70-b2	60	20.22	1.05	2.69	0.12	40.38	0.83	1.343	0.007	5.91
FH-L-70-b3	60	19.41	0.57	3.60	0.09	35.82	0.46	1.277	0.018	30.55
FH-L-70-c1	60	28.64	1.21	0.19	0.24	80.67	1.30	2.988	0.011	7.32
FH-L-70-c2	60	22.25	0.64	3.50	0.13	75.22	0.83	2.567	0.030	25.29
FH-L-70-c3	60	48.73	1.55	0.45	0.18	152.26	1.81	9.625	0.044	10.03
FH-L-70-d1	60	17.97	0.62	2.95	0.16	51.64	0.73	1.476	0.013	16.76
FH-L-70-d2	60	17.88	0.53	3.65	0.11	67.08	0.80	1.890	0.018	19.93
FH-L-70-d3	60	25.24	1.09	1.32	0.19	45.64	0.79	1.657	0.010	10.62
FH-L-70-e1	60	13.66	0.39	4.77	0.11	44.52	0.55	1.133	0.015	27.32
FH-L-70-e2	60	14.26	0.56	6.13	0.17	20.80	0.41	0.855	0.008	12.76
FH-L-70-e3	60	20.05	0.59	5.77	0.13	18.74	0.30	1.111	0.014	25.27
FH-L-70-g1	60	19.03	0.82	3.06	0.17	87.34	1.50	2.445	5.076	5.08
FH-L-70-g2	60	14.59	0.63	2.98	0.16	103.02	1.66	2.160	5.282	5.28
FH-L-70-g3	60	15.01	0.77	2.90	0.19	95.08	1.73	2.063	3.860	3.86
FH-L-70-g4	60	16.23	1.05	2.82	0.20	70.33	1.51	1.710	3.257	3.26
FH-L-70-g5	60	16.69	0.61	3.13	0.14	103.25	1.50	2.489	7.457	7.46
FH-L-70-g6	60	11.77	0.50	13.48	0.42	79.24	1.44	2.055	4.698	4.70
FH-L-70-g7	60	17.96	0.54	3.16	0.10	65.87	0.80	1.823	21.705	21.70
FH-L-70-g8	60	18.76	0.91	2.92	0.17	67.59	1.28	1.921	4.842	4.84
FH-L-80-a1	75	23.11	0.76	4.07	0.14	88.69	1.24	3.139	0.015	9.56
FH-L-80-a2	75	21.45	0.77	3.77	0.14	85.27	1.29	2.785	0.011	7.52
FH-L-80-b1	75	13.17	0.35	5.20	0.13	84.58	0.82	1.798	0.028	33.68
FH-L-80-b2	75	13.11	0.41	6.69	0.17	73.61	0.97	1.716	0.013	14.21
FH-L-80-b3	75	14.47	0.34	13.50	0.16	156.00	1.21	3.953	0.061	34.38
FH-L-80-c1	75	37.64	1.35	4.30	0.20	63.75	1.05	3.955	0.015	7.70
FH-L-80-c2	75	48.28	2.97	bdl		33.59	0.71	1.824	0.009	8.66
FH-L-80-c3	75	28.03	1.11	3.29	0.15	31.65	0.59	1.637	0.010	10.39
FH-L-80-d1	75	24.73	0.81	3.58	0.12	53.42	0.76	2.173	0.014	13.55
FH-L-80-d2	75	28.92	0.85	2.64	0.08	27.13	0.35	1.420	0.027	42.06
FH-L-80-e1	75	31.03	1.13	2.35	0.09	23.89	0.42	1.347	0.011	15.35
FH-L-80-e2	75	37.56	1.56	bdl		42.89	0.68	2.025	0.014	14.33
FH-L-80-e3	75	29.25	1.98	2.31	0.19	42.38	1.15	1.954	3.130	3.13
FH-L-90-b1	87	41.41	1.68	3.60	0.16	54.50	1.05	3.708	0.011	5.29
FH-L-90-b2	87	19.44	0.65	3.09	0.11	71.70	0.99	2.115	0.013	12.27
FH-L-90-c1	87	33.84	1.35	1.45	0.13	30.70	0.52	1.597	0.013	16.50
FH-L-90-c2	87	28.15	1.28	3.04	0.18	38.28	0.78	1.845	0.008	6.78
FH-L-90-c3	87	29.87	1.12	1.75	0.13	35.25	0.56	1.632	0.014	17.31
FH-L-90-d1	87	16.47	0.63	2.82	0.11	39.96	0.64	1.095	13.548	13.55

Table 2.10: Table of goethite (U-Th)/He ages continued.

sample name	d [cm]	age [Ma]	±1σ [Ma]	U [ppm]	±1σ [ppm]	Th [ppm]	±1σ [ppm]	^{4}He [nmol/g]	±1σ [nmol/g]	gt mass [µg]
FH-L-90-d2	87	18.85	0.62	3.93	0.13	40.60	0.60	1.383	0.012	17.35
FH-L-90-d3	87	25.98	1.62		bdl	29.66	0.63	0.959	0.007	9.63
FH-L-90-e1	87	19.86	0.54	2.54	0.07	70.92	0.71	2.077	0.032	33.86
FH-L-90-e2	87	22.11	0.86	3.27	0.14	68.32	1.11	2.328	0.009	6.76
FH-L-90-e3	87	16.67	0.61	3.41	0.13	78.63	1.15	1.988	0.010	8.56
FH-L-120-a1	116	31.42	0.80	4.54	0.08	46.26	0.47	2.645	0.064	54.12
FH-L-120-a2	116	45.07	2.07	0.81	0.14	27.83	0.53	1.806	0.012	13.54
FH-L-120-b1	116	47.08	1.49	3.32	0.11	64.23	0.89	4.740	0.029	13.50
FH-L-120-b2	116	24.14	0.85	3.01	0.12	64.20	0.96	2.380	0.012	9.66
FH-L-120-b3	116	45.53	1.59	3.03	0.12	57.56	0.92	4.119	0.018	9.18
FH-L-120-c1	116	25.65	1.12		bdl	70.51	1.10	2.142	0.011	9.09
FH-L-120-c2	116	37.71	2.39		bdl	66.84	1.30	2.462	0.008	5.28
FH-L-120-c3	116	23.62	0.88	3.03	0.13	76.77	1.20	2.711	0.010	6.99
FH-L-120-d1	116	24.61	0.64	3.17	0.07	70.64	0.65	2.650	0.051	42.91
FH-L-120-d2	116	30.96	0.90	1.65	0.09	74.11	0.80	3.217	0.041	28.15
FH-L-120-d3	116	27.35	0.72	4.24	0.09	61.34	0.62	2.779	0.047	37.35
FH-L-120-e1	116	36.91	0.93	5.82	0.09	21.88	0.28	2.204	0.056	56.75
FH-L-120-e2	116	42.16	1.43	5.77	0.17	14.92	0.34	2.133	0.013	12.05
FH-L-120-e3	116	18.80	0.92	8.50	0.31	42.99	0.97	1.904	0.007	4.19
FH-L-120-f1	116	17.05	0.69	3.03	0.13	59.36	0.97	1.576	0.008	8.46
FH-L-120-f2	116	17.68	1.35	3.23	0.20	52.37	1.32	1.496	0.006	2.93
FH-L-120-f3	116	16.96	0.70	2.71	0.12	58.50	0.97	1.520	0.008	8.16
FH-L-120-f4	116	15.51	1.96	2.54	0.26	63.89	1.98	1.482	0.006	1.59
FH-L-120-f5	116	18.23	0.96	2.91	0.16	59.30	1.18	1.672	0.007	4.68
FH-L-120-f7	116	21.39	1.13	2.23	0.12	44.33	0.92	1.473	0.007	5.50
FH-L-120-f8	116	23.46	0.81	2.20	0.09	52.36	0.77	1.854	0.013	13.86
FH-L-120-f9	116	21.54	0.79	2.20	0.09	40.00	0.63	1.361	0.011	14.32
FH-L-120-f10	116	18.12	0.61	2.23	0.08	44.36	0.62	1.249	0.012	18.97
FH-L-120-f11	116	23.56	1.35	2.67	0.14	36.44	0.86	1.441	0.007	4.94
FH-L-120-f12	116	20.32	0.96	2.37	0.11	38.88	0.76	1.273	0.007	7.59
FH-L-120-f13	116	21.60	0.81	2.25	0.09	37.38	0.61	1.298	0.010	13.53
FH-L-120-f14	116	22.61	0.91	2.32	0.10	37.20	0.65	1.362	0.009	10.87
FH-L-120-f16	116	28.02	1.68	1.65	0.15	64.46	1.50	2.564	0.007	2.88
FH-L-120-f17	116	28.25	1.34	1.83	0.11	54.91	1.08	2.268	0.008	5.16
FH-L-120-f18	116	28.19	1.12	2.76	0.13	54.93	0.96	2.406	0.010	7.35
FH-L-120-f20	116	28.21	1.23	1.86	0.11	53.79	0.99	2.228	0.009	6.34
FH-L-120-f21	116	40.54	1.65	1.13	0.06	24.27	0.45	1.509	0.011	13.86
FH-L-120-f22	116	35.83	1.18	1.08	0.04	23.84	0.34	1.305	0.021	34.21
FH-L-120-f23	116	36.76	2.14	1.43	0.09	24.76	0.64	1.452	0.007	5.85

Table 2.11: Table of goethite (U-Th)/He ages continued.

Sample Name	d [cm]	age [Ma]	±1σ [Ma]	U [ppm]	±1σ [ppm]	Th [ppm]	±1σ [ppm]	^{4}He [nmol/g]	±1σ [nmol/g]	Gt Mass [µg]
FH-L-170-a1	164	23.27	0.78	2.12	0.07	43.36	0.62	1.567	0.014	17.98
FH-L-170-a2	164	24.42	0.95	1.73	0.07	37.52	0.63	1.432	0.010	12.13
FH-L-170-a3	164	23.39	0.67	2.21	0.06	60.97	0.68	2.141	0.030	30.60
FH-L-170-b2	164	19.82	0.74	1.48	0.05	24.14	0.39	0.778	0.009	21.32
FH-L-170-b3	164	24.30	0.75	1.77	0.05	32.86	0.43	1.259	0.020	33.50
FH-L-170-c2	164	28.22	1.78	bdl		37.99	0.74	1.107	0.007	9.21
FH-L-170-d1	164	21.67	0.69	1.50	0.05	25.32	0.34	0.880	0.015	34.00
FH-L-170-d2	164	21.81	1.14	1.23	0.10	25.67	0.53	0.862	0.007	10.04
FH-L-170-d3	164	19.05	0.78	1.71	0.08	35.54	0.59	1.044	0.008	12.34
FH-L-170-e2	164	14.87	1.02	2.99	0.16	52.27	1.12	1.236	0.006	3.91
FH-L-170-e3	164	15.63	0.82	3.06	0.13	34.68	0.68	0.953	0.007	7.53
FH-L-250-a1	268	22.93	0.75	3.83	0.13	69.10	0.98	2.515	0.014	11.63
FH-L-250-a2	268	16.99	0.76	2.71	0.13	75.91	1.30	1.903	0.008	5.54
FH-L-250-b1	268	18.27	0.57	5.45	0.16	77.05	1.03	2.349	0.015	12.68
FH-L-250-b2	268	27.27	1.25	3.55	0.16	48.74	1.00	2.233	0.008	5.01
FH-L-250-b3	268	19.13	1.15	2.79	0.14	48.86	1.07	1.490	0.007	4.20
FH-L-250-c1	268	16.52	0.41	4.36	0.08	80.77	0.67	2.099	0.052	54.81
FH-L-250-c2	268	42.85	2.70	bdl		87.26	1.71	3.661	0.009	3.98
FH-L-250-c3	268	37.06	1.93	bdl		91.75	1.61	3.635	0.010	5.05
FH-L-250-d1	268	35.66	0.98	3.59	0.08	38.25	0.45	2.445	0.042	38.08
FH-L-250-d2	268	49.05	2.09	1.30	0.16	32.43	0.59	2.386	0.015	12.97
FH-L-250-d3	268	42.13	1.39	2.68	0.13	35.06	0.52	2.508	0.025	21.93
FH-L-250-e2	268	25.33	0.76	2.19	0.07	46.81	0.57	1.820	0.022	26.27
FH-L-300-a1	339	19.90	1.06	2.08	0.12	58.57	1.16	1.726	0.007	4.55
FH-L-300-a2	339	20.86	0.84	1.76	0.08	57.68	0.94	1.742	0.009	8.53
FH-L-300-a3	339	18.73	0.71	2.04	0.08	56.19	0.86	1.558	0.009	10.68
FH-L-300-b1	339	23.66	0.76	3.78	0.13	110.89	1.45	3.855	0.018	9.54
FH-L-300-b2	339	17.14	0.56	2.83	0.10	90.28	1.16	2.272	0.014	12.41
FH-L-300-b4	339	26.63	0.98	2.47	0.10	46.12	0.75	1.935	0.011	10.88
FH-L-300-b5	339	12.43	0.67	3.59	0.17	95.45	1.70	1.766	0.007	3.86
FH-L-300-b6	339	13.61	1.05	2.92	0.18	79.28	1.73	1.603	0.006	2.59
FH-L-300-c2	339	26.42	1.07	3.18	0.14	58.41	1.02	2.432	0.009	6.24
FH-L-300-c3	339	14.12	1.44	1.96	0.13	39.49	1.02	0.865	0.006	3.39
FH-L-300-d1	339	17.80	0.70	5.03	0.19	33.28	0.61	1.245	0.008	10.36
FH-L-300-d2	339	16.18	0.41	5.19	0.09	32.72	0.36	1.134	0.027	52.73
FH-L-300-d3	339	16.52	0.48	4.45	0.10	28.40	0.39	1.000	32.529	32.53
FH-L-300-e1	339	18.11	0.53	6.50	0.16	61.65	0.79	2.070	0.017	17.07
FH-L-300-e2	339	17.91	0.44	6.12	0.10	65.77	0.60	2.104	0.046	48.81
FH-L-300-e3	339	12.06	0.59	6.16	0.25	89.37	1.54	1.784	0.007	4.31

Table 2.12: Goethite (U-Th)/He ages of pisoliths from outcrop Lohn am Randen collected outside the depth profile (gt mass = mass of aliquot based on Fe, stoichiometrically calculated as goethite). Included are also formation ages of pisoliths cemented in a nodule (BR-cut2). These pisoliths show a similar age distribution to the pisoliths of the depth profile. All of the ages in this table are included in the formation age histogram (Fig. 2.3D), except for the ages of the matrix of the nodule (BR-cut2-c1, BR-cut2-h1, and BR-cut2-i1).

Sample Name	age [Ma]	±1σ [Ma]	U [ppm]	±1σ [ppm]	Th [ppm]	±1σ [ppm]	^{4}He [nmol/g]	±1σ [nmol/g]	gt mass [µg]
BR-01-1	15.04	0.72	3.22	0.20	80.26	1.83	1.811	0.002	2.20
BR-01-2	37.78	1.50	3.87	0.17	42.60	0.91	2.862	0.006	4.85
BR-01-4	24.84	1.00	3.66	0.18	79.60	1.55	3.034	0.005	3.35
BR-01-5	17.77	0.68	4.82	0.22	112.91	2.01	3.040	0.004	3.11
BR-01-6	17.87	0.66	5.35	0.23	111.88	1.93	3.086	0.005	3.47
BR-04-1	17.79	0.51	6.83	0.19	134.83	1.56	3.735	0.019	11.57
BR-04-2	18.36	0.62	5.69	0.21	96.06	1.51	2.830	0.007	5.54
BR-04-3	19.51	0.58	6.16	0.17	68.78	0.95	2.375	0.013	11.94
BR-04-4	19.09	0.56	5.96	0.16	66.36	0.88	2.243	0.014	14.19
BR-04-5	19.62	0.64	5.69	0.19	80.12	1.23	2.624	0.008	7.12
BR-04-6	19.26	0.57	4.20	0.13	117.71	1.39	3.346	0.018	12.25
BR-05-2	19.50	0.60	8.26	0.24	66.63	1.04	2.544	0.010	8.69
BR-05-3	18.23	0.67	7.95	0.30	64.19	1.29	2.290	0.004	3.98
BR-06-2	21.79	0.68	8.80	0.27	116.05	1.66	4.283	0.013	6.64
BR-06-3	15.57	0.50	10.00	0.30	79.16	1.30	2.425	0.007	6.08
BR-07-2	35.97	1.39	4.58	0.18	38.27	0.83	2.667	0.007	5.42
BR-07-3	27.05	0.86	4.48	0.15	70.98	1.03	3.124	0.014	10.25
BR-08-1	33.66	1.03	4.01	0.11	27.36	0.44	1.924	0.016	18.82
BR-08-2	28.56	0.94	6.52	0.21	43.03	0.78	2.599	0.009	8.06
BR-08-3	24.68	0.74	5.04	0.15	72.44	0.97	2.972	0.018	13.64
BR-09-1	22.40	0.67	3.99	0.13	125.86	1.52	4.103	0.021	11.27
BR-09-2	19.25	0.52	3.61	0.09	70.11	0.74	2.109	0.030	32.07
BR-09-3	21.11	0.64	4.13	0.13	97.36	1.23	3.110	0.017	12.15
BR-10-1	22.54	0.78	6.71	0.24	74.86	1.32	2.986	0.007	5.12
BR-10-2	21.59	0.65	6.46	0.18	71.83	1.02	2.747	0.014	11.19
BR-10-3	19.84	0.64	7.33	0.22	38.55	0.70	1.772	0.007	8.90
BR-cut2-a1	33.16	1.13	5.00	0.17	50.65	0.88	3.059	0.011	7.92
BR-cut2-b1	27.51	0.89	10.69	0.33	73.87	1.29	4.208	0.010	5.36
BR-cut2-c1	12.27	0.44	4.45	0.16	50.23	0.90	1.087	0.004	7.18
BR-cut2-d1	32.10	1.13	5.77	0.20	41.78	0.82	2.731	0.008	6.57
BR-cut2-e1	41.25	2.09	1.00	0.07	27.01	0.68	1.656	0.004	5.39
BR-cut2-f1	17.91	0.55	12.08	0.34	79.71	1.30	3.006	0.008	6.11
BR-cut2-g1	16.98	0.51	10.67	0.29	81.64	1.24	2.763	0.010	7.61
BR-cut2-h1	7.54	0.25	5.18	0.17	83.73	1.23	1.021	0.004	8.41
BR-cut2-i1	12.20	0.36	6.97	0.18	49.87	0.74	1.242	0.008	13.93
BR-cut2-i2	17.39	0.52	6.46	0.17	45.03	0.68	1.615	0.010	14.02
BR-cut3-a1	27.05	0.81	6.82	0.19	98.01	1.29	4.403	0.021	10.48
BR-cut3-a2	28.75	0.90	4.85	0.16	101.56	1.38	4.499	0.019	9.21
BR-cut3-b1	24.86	0.83	5.91	0.21	104.43	1.60	4.128	0.011	5.83
BR-cut3-b2	35.26	1.02	5.63	0.15	82.19	1.03	4.796	0.032	15.00

2.D Step-heating of irradiated soil material

Proton-irradiated clay samples were analyzed according to the procedure described in 2.A. The samples are composed mostly of kaolinite with about 10% iron-oxides (mostly hematite, some goethite). These samples released helium up to 480 °C, which is the highest temperature step available with the projector lamp setup. They were additionally subjected to heating to 1300 °C with re-extracts at 1350 °C in a double-walled vacuum furnace to release the remaining helium.

The resulting normalized ^{4}He/^{3}He ratio plots are complex (Fig. 2.7), because they show the release of helium of three different phases with different diffusion coefficients and retentivities. About 20% of the total ^{3}He is released without any release of ^{4}He in low temperature steps (<90 °C). Since the proton-irradiation took place several months before the experiment, spallation-induced ^{3}He is still present, but radiogenic ^{4}He is not retained in kaolinite over geologic timescales. Between 20% and 60% of the total ^{3}He release fraction the spectrum reaches a plateau. This corresponds to the temperature steps between 90 °C and 150 °C, which is the typical temperature range for helium release in goethite (see Section 2.A). The remaining 40% of ^{3}He is released at temperatures above 150 °C. Hematite has been shown to release most of its helium well above 150 °C, with a major release of helium between 300 °C and 800 °C at a similar heating schedule (Farley and McKeon, 2015). Based on these similarities we interpret the second peak in the ^{4}He/^{3}He spectra to be from hematite. Since the release temperatures are different between hematite and goethite, the spectra can be separated. The individual spectra of hematite and goethite suggest He-retentivities of around 60-70% for both phases.

We argue that the ^{4}He/^{3}He spectra of red Bolus clay represent the combined ^{4}He/^{3}He spectra of kaolinite, goethite, and hematite. Kaolinite does not retain any radiogenic ^{4}He over geologic time, whereas the fine-grained particles of goethite and hematite show at least partial retention of helium.

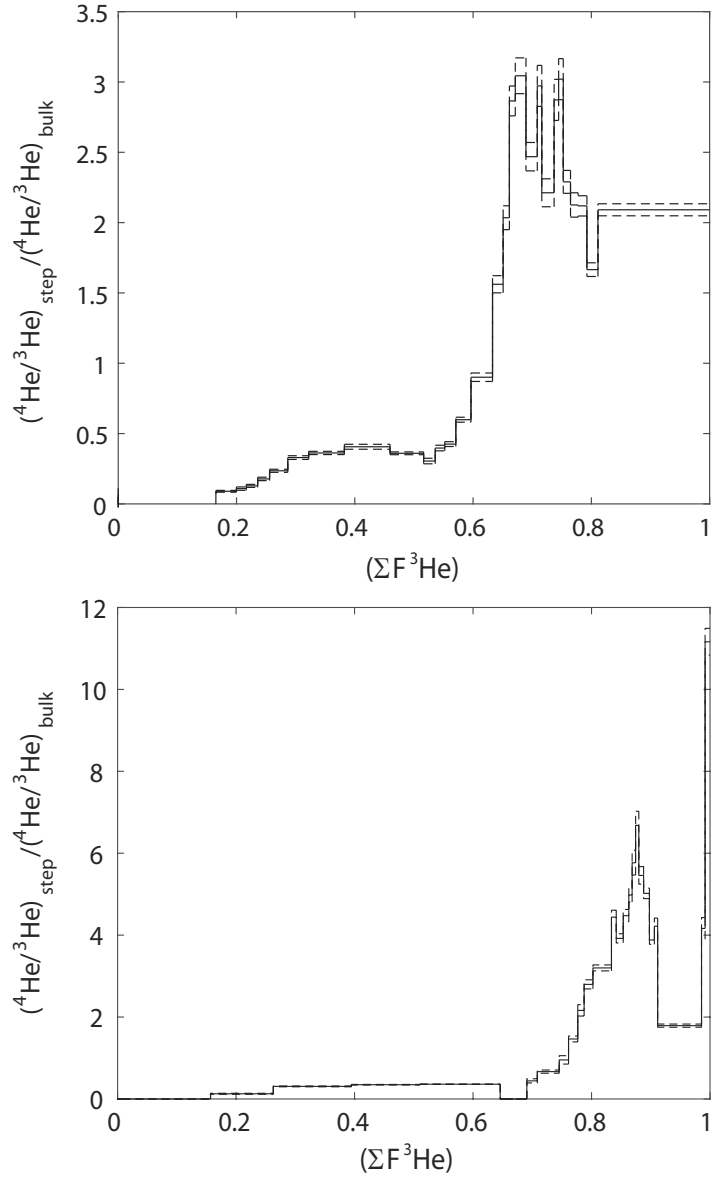

Figure 2.7: Normalized $^4He/^3He$ spectra of proton irradiated samples FH-FC1-L20clay-irr and FH-FC2-L300clay-irr. Each heating step was 30 min, with temperatures ranging from 20 °C to 550 °C followed by total fusion at 1350 °C. The samples are red Bolus clays, consisting of kaolinite with about 10-15% iron-oxides. The $^4He/^3He$ spectra represent the combined spectra of these phases. About 20% of the total ^3He is released <100 °C without any measurable release of ^4He, suggesting no He retentivity of clay. Since the helium release in this heating schedule occurs below 150 °C for goethite and above 150 °C for hematite, the individual spectra can be isolated. This permits an estimate of the He retentivity of the individual phases, which is 60-70% for both hematite and goethite. The dashed line shows the 1σ uncertainty of the $^4He/^3He$ ratio.

Table 2.13: Results of the $^4He/^3He$ experiment of samples FH-FC1-L20clay-irr and FH-FC2-L300clay-irr. Aliquot was degassed for 30 min at each step.

FH-FC1-L20clay-irr						**FH-FC2-L300clay-irr**					
Step Number	**Temp. [°C]**	**^3He [pcc]**	**$\pm1\sigma$ [pcc]**	**^4He [ncc]**	**$\pm1\sigma$ [ncc]**	**Step Number**	**Temp. [°C]**	**^3He [pcc]**	**$\pm1\sigma$ [pcc]**	**^4He [ncc]**	**$\pm1\sigma$ [ncc]**
0	20	bdl	bdl	bdl	bdl	0	20	bdl	bdl	bdl	bdl
1	40	0.3277	0.0017	bdl	bdl	1	40	0.3437	0.0014	bdl	bdl
2	60	4.4616	0.0155	bdl	bdl	2	60	6.6071	0.0166	bdl	bdl
3	80	7.5909	0.0185	bdl	bdl	3	80	4.6980	0.0123	0.0973	0.0047
4	90	2.6396	0.0059	bdl	bdl	4	90	5.8387	0.0143	0.2933	0.0043
5	95	1.2847	0.0059	bdl	bdl	5	95	5.1356	0.0140	0.2924	0.0023
6	100	1.4543	0.0048	bdl	bdl	6	100	5.9981	0.0163	0.3538	0.0031
7	105	1.5003	0.0062	bdl	bdl	7	105	0.1400	0.0007	bdl	bdl
8	110	2.3483	0.0097	0.0532	0.0014	8	110	0.2134	0.0011	bdl	bdl
9	115	2.7412	0.0091	0.0630	0.0020	9	115	bdl	bdl	bdl	bdl
10	120	4.6647	0.0136	0.1543	0.0046	10	120	0.8251	0.0024	bdl	bdl
11	130	6.0191	0.0181	0.2298	0.0046	11	125	0.3761	0.0019	bdl	bdl
12	140	4.2250	0.0124	0.1421	0.0042	12	130	0.1389	0.0009	bdl	bdl
13	150	1.4574	0.0072	0.0465	0.0033	13	140	0.2977	0.0015	bdl	bdl
14	160	1.2406	0.0034	0.0333	0.0036	14	160	0.7839	0.0034	0.0567	0.0030
15	180	1.4003	0.0048	0.0650	0.0027	15	180	1.6392	0.0039	0.1791	0.0048
16	200	1.9604	0.0057	0.1072	0.0034	16	200	0.6960	0.0029	0.1086	0.0054
17	220	2.7415	0.0090	0.2588	0.0034	17	220	0.6913	0.0028	0.1660	0.0034
18	240	1.3449	0.0053	0.2076	0.0039	18	240	0.4742	0.0023	0.1677	0.0046
19	260	0.8107	0.0030	0.1650	0.0034	19	260	0.6600	0.0027	0.3020	0.0048
20	280	0.7554	0.0028	0.1944	0.0053	20	280	1.3864	0.0040	0.7255	0.0062
21	290	1.4593	0.0055	0.3526	0.0046	21	300	0.3575	0.0017	0.2596	0.0036
22	300	0.6052	0.0027	0.1693	0.0040	22	320	0.5230	0.0025	0.3354	0.0032
23	320	1.5704	0.0070	0.3509	0.0023	23	340	0.4167	0.0024	0.3050	0.0034
24	340	0.5721	0.0027	0.1555	0.0058	24	360	0.2477	0.0014	0.2018	0.0024
25	360	0.5673	0.0030	0.1625	0.0027	25	380	0.2606	0.0014	0.2458	0.0051
26	380	0.9339	0.0032	0.2074	0.0048	26	400	0.2394	0.0016	0.2616	0.0049
27	396	1.0059	0.0036	0.1940	0.0033	27	414	0.3599	0.0015	0.3213	0.0050
28	417	1.1755	0.0024	0.2257	0.0048	28	432	0.4337	0.0024	0.3560	0.0026
29	433	1.4298	0.0042	0.2370	0.0031	29	434	0.3714	0.0020	0.2358	0.0020
30	1350	20.9360	0.0832	4.8220	0.0074	30	437	0.2445	0.0014	0.1687	0.0030
						32	561	0.2677	0.0015	0.1823	0.0048
						33	1350	0.3683	0.0012	0.6724	0.0077

Chapter 3

EOCENE-PLEISTOCENE CONTINENTAL PALEO-ENVIRONMENT OF CENTRAL EUROPE RECORDED BY GOETHITE PISOLITHS

with Kenneth A. Farley[1]

Abstract

Discontinuous near-surface sediment can record physical processes during periods of erosion, which would otherwise be missing from the geologic record. We study the Bohnerz deposits, a widespread erosional lag deposit in Central Europe, which consists of reddish to yellowish clays and contains abundant ferruginous pisoliths. They are present on mostly Mesozoic carbonates in karstic fissures and depressions as well as in the form of stratiform deposits, some of which are intact paleosols. We measure (U-Th)/He formation ages as well as cosmogenic ^{3}He in goethite pisoliths from paleosols and fissure fillings in Switzerland and southern Germany to investigate the time recorded by the weathering processes representing this unconformity. (U-Th)/He geochronology undertaken on over 100 goethite pisoliths of the Bohnerz deposits indicate the onset of pisolith growth at about the beginning of the Eocene, with a peak in the Oligocene, and continuing in the Pleistocene, with no observable gaps in the age distribution. While some individual pisoliths grew quickly (<a few Ma), the concentric zones of others grew over several tens of Ma. Cosmogenic ^{3}He measurements of 27 pisoliths indicate extremely low surface denudation rates of around 0.1 m/Ma. This demonstrates the long-lived nature of Bohnerz-type weathering and an extremely slowly eroding landscape conducive to the development of ferruginous soils on a deeply weathered substratum. In fissure fillings with well-

[1]California Institute of Technology, 1200 E California Blvd, MC 170-25, Pasadena, CA 91125, United States

constrained fossil ages, pisolith formation ages are consistently younger than the biostratigraphic ages, showing that these pisoliths grew in the fissure filling after it was deposited. We map the paleo-extent of the Bohnerz deposits in Central Europe based on published studies and field observation to show that Fe-rich kaolinitic soils covered all of the Central European limestone plateaux. We conclude that the Bohnerz deposits represent an extensive mode of continental-scale weathering in Central Europe and that Bohnerz pisoliths are a continuous record of Eocene to Pleistocene continental climatic conditions.

3.1 Introduction

Unconformities represent times of erosion or non-deposition. In the geologic record more time is represented by periods of non-deposition than by sedimentation (Sadler, 1981). Long-lived, discontinuous near-surface sediment, which is evolving during erosional periods, can help to elucidate the physical processes of developing unconformities as well as timescales of their formation. Iron-oxides are ubiquitous products of continental weathering (Schwertmann, 1988). They are quantitatively retentive to helium (Shuster et al., 2005), and therefore they accumulate radiogenic ^{4}He, which can be used to determine formation ages through the (U-Th)/He method, as well as cosmogenic ^{3}He, which indicates the timescales of near-surface exposure. Combining these methods can give an insight into the timescale and processes of sub-surface iron-oxide precipitation, which are products related to surface weathering (Hofmann et al., 2017; Monteiro et al., 2014; Monteiro et al., 2018).

The Bohnerz ('bean ore') deposits in Central Europe are widespread reddish to yellowish clays, often containing ferruginous pisoliths (Achenbach, 1859; Rollier, 1905). Iron-rich clays, locally referred to as 'Bolus', are frequently found as fissure fillings with abundant small mammal fossils (e.g. Rummel, 1993) in the Franconian Alb and Swabian Alb regions of southern Germany. Fissure fillings take the form of

narrow channels, wide funnels, or pockets filled with red Bolus clay (Fig. 3.1) and can extend up to 100 m into the substratum (Menkveld-Gfeller et al., 2016; Rollier, 1905). The Swiss and French equivalent of the Bohnerz Fm. are the Siderolithic deposits ('Siderolithikum', 'Sidérolithique'), which are often found as stratiform deposits of reddish clay (Pirkenseer et al., 2018). Some stratiform deposits (see Fig. 3.1) show characteristics of an in-situ paleosol (Hofmann et al., 2017), often with signs of reworking in the upper part of the deposit (Pirkenseer et al., 2018). The definition of the Siderolithic is broader than that of the Bohnerz Fm., also including freshwater limestones and conglomerates, as well as iron-cemented sandstones (Pirkenseer et al., 2018). Some of the Bohnerz deposits have been translocated into limestone caves (Ufrecht, 2008), especially in the Swabian Alb. Since the Bohnerz deposits show only a laterally discontinuous extent, they have not been deemed to merit formation status (Pirkenseer et al., 2018). We use the term 'Bohnerz deposits' here to refer to Bolus clays with ferruginous pisoliths, regardless of the local name. Bolus clays and iron-oxides of the Bohnerz deposits have been interpreted as residua from karstic weathering of the limestones, which generally form their substratum or host fissures (Fach, 1908). The weathering regime has been described as tropical to sub-tropical, based on comparing the morphology of Bohnerz pisoliths with that of ferruginous pisoliths of Indian laterites (Borger and Widdowson, 2001; Lang, 1914). Since Central Europe last experienced tropical to sub-tropical conditions in the Late Cretaceous/early Eocene, the formation of the pisoliths, and therefore of the Bohnerz deposits as a whole, has been assumed to be Late Cretaceous (Borger, 1990; Borger and Widdowson, 2001; Ufrecht, 2008). In this interpretation, the formation of the Bohnerz deposits ceased in the late Eocene and since then they have been reworked and deposited in caves and fissures (Borger and Widdowson, 2001; Ufrecht, 2008).

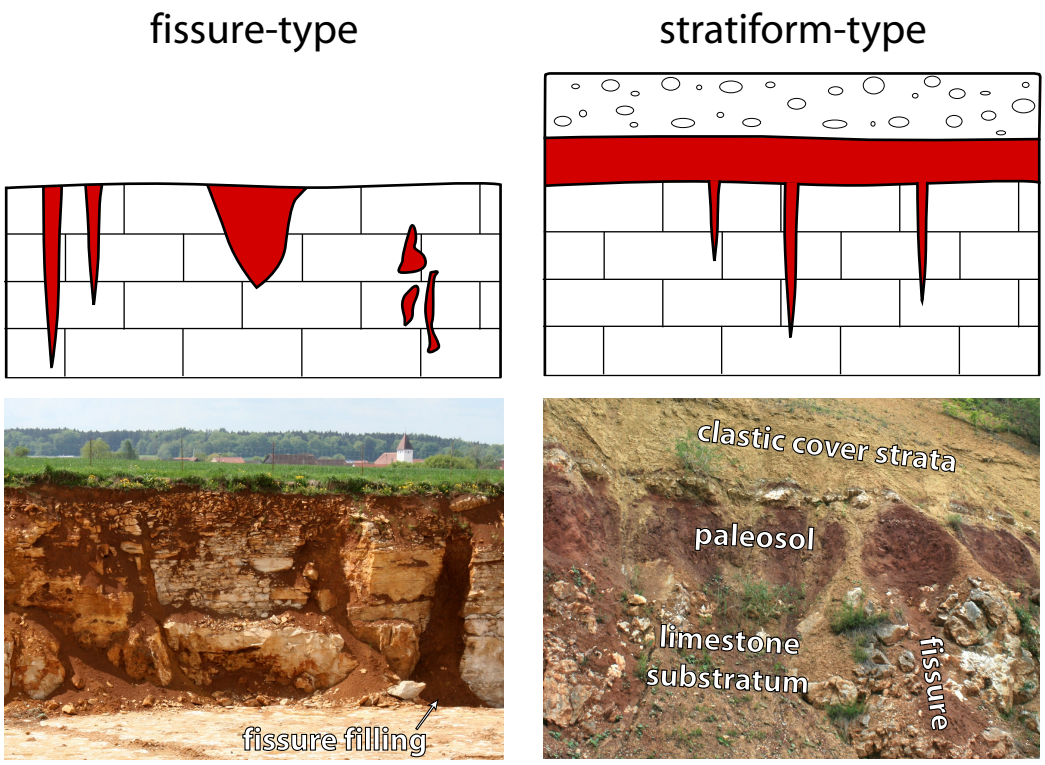

Figure 3.1: The two basic types of Bohnerz deposits. Fissure-type deposits can be found as narrow fissures, funnel-shaped depressions, or pockets filled with red Bolus clay (picture from Petersbuch quarry, Germany). Stratiform-type deposits are laterally extensive deposits on the surface of a limestone, showing indications of a paleosol, but also often with signs of reworking in the upper part (picture from Lohn quarry, Switzerland). They are frequently found covered with late Eocene or younger clastic strata. Some outcrops also show fissure fillings in the subsurface, which are connected to the paleosol.

Clays of the Bohnerz deposits are frequently associated with well-rounded quartz sands, called 'Huppersand' (Rollier, 1905). In some outcrops, quartz sand has been described as underlying Siderolithic deposits (Rollier, 1905), but it is also frequently present in the Bolus clays, often randomly distributed throughout the deposit. There is no quartz in the limestones, therefore it had to be derived from regions outside of the limestone plateau (Ufrecht, 2008), possibly the southern slopes of the Massif Central (Aubert and Le Ribault, 1974). The close association between quartz sand and Bolus clays has led to the hypothesis that the whole deposit is allochthonous (Borger and Widdowson, 2001).

Nearly all Bohnerz deposits contain ferruginous pisoliths, which range from millimeters to centimeters in diameter. Most pisoliths are composed of poly-crystalline goethite, which quantitatively retains helium at earth-surface conditions and can be dated using the (U-Th)/He method (Lippolt et al., 1998; Shuster et al., 2005). Recently, (U-Th)/He formation ages from a single paleosol of the Bohnerz deposits were reported by Hofmann et al. (2017). They found ages between 50 Ma and 8 Ma, with few ages younger than the age of the 17 Ma cover rocks, which showed that Bohnerz deposits are not be of Late Cretaceous-early Eocene age, but mid-Eocene and younger.

Ferruginous precipitates in lateritic weathering environments can record a protracted history of iron-oxide precipitation (Monteiro et al., 2014). They represent a nearly continuous record of dissolution-precipitation reactions (Monteiro et al., 2018), which are controlled by weathering as well as paleo-climate. The Bohnerz deposits contain pisoliths, many of which grow concentrically from the center outward. Profiles of individual pisoliths have revealed a record of tens of millions of years of iron-oxide precipitation (Hofmann et al., 2017).

To construct a more complete geologic history of the Bohnerz deposits and expore implications for Central European paleoenvironment, we characterize the post-Jurassic erosional unconformity in Central Europe by compiling stratigraphic information on the substratum and cover, as well as ages of fossils contained in fissure fillings. We obtain (U-Th)/He formation ages of goethite pisoliths of the Bohnerz deposits to directly date the precipitation of iron-oxides during periods of weathering. We also measure concentrations of cosmogenic ^{3}He to constrain paleo-exposure of paleosols at the surface and post-depositional near-surface exposure of fissure fillings.

3.2 Sample Sites

We sampled 13 outcrops of Bohnerz deposits, including 5 paleosol locations and 8 fissure locations. Every single sample consists of 0.5-1 kg of clay, which was later soaked in water and sieved to extract pisoliths.

Fissure-type deposits

We sampled pisoliths from fissure fillings in the Swabian and Franconian Alb regions of Germany as well as in the Jura Mountains in Switzerland. In many localities in which fossils in fissure fillings have been described, individual fissures are numbered in sequence of discovery (Rummel, 1993). Ages of fossils contained in fissure fillings are described according to the European Mammal Neogene (MN) and Mammal Paleogene (MP) biostratigraphic systems (Agustı et al., 2001; Mein, 1975; Schmidt-Kittler et al., 1987).

Petersbuch, Weißenburg, Rothenstein These three sample sites are located in the Franconian Alb and represent some of the north-easternmost occurrences of fissure fillings. Samples were taken from fissure fillings exposed in limestone quarries. Samples from fissures Petersbuch 62A, 100, 115, 125, Weißenburg 21N, and Rothenstein 16 are from the collection of the Naturmuseum Augsburg and were provided to the authors by Michael Rummel. The fissures in these localities are developed in limestones of the upper Kimmeridgian Treuchtlingen Formation (Rummel, 1993).

Petersbuch 62A is a large, bifurcated fissure system filled with dark brown to reddish clays that contains fossils of MN 3 (Rosina and Rummel, 2012). Pisoliths were recovered together with fossils at a depth of about 11-16 m below the modern surface. Fissure filling Petersbuch 100 consists of reddish brown clays, which shows horizontal layering in the lower part and has calcrete in the upper part. Petersbuch 115 also consists of reddish brown clay with occasional calcrete structures. Fossils

in these two fissure fillings are MN 7/8 (Michael Rummel, pers. comm.).

Weißenburg 21 is a karst system several hundred meters in length. The clay matrix contained variable amounts of calcrete, limestone fragments, and quartz sand. Bohnerz pisoliths occur as concentrated layers. Fossils in this fissure filling are MP 19. Fissure filling Rothenstein 16 consists of mostly light brown clay with calcrete that contains clasts of Jurassic and Cretaceous strata. Bohnerz pisoliths are concentrated in areas that contained large fossils.

Additional samples were collected by FH at Petersbuch quarry. A yet undescribed fissure, referred to here as P-F2, is exposed in the quarry wall at UTM 32U, 660834m E, 5428655m N. It is overlain by modern soil, which was present before the quarry was established, which was used for agriculture. The uppermost 20 cm are a dark O horizon with active vegetation and root development. The following 3.5 m of the soil are mostly comprised of disaggregated limestone slabs about 5 cm thick and 10-20 cm in width, with clay in the interstitial space. The limestone below about 4 m is not affected by soil development. The fissure developed in the limestone is filled with reddish brown clay, with pisoliths randomly distributed throughout. No fossils have been documented from this fissure, but it is in close proximity (<10 m) to fossiliferous fissure fillings. The fissure was sampled on a depth profile from the topsoil down to 3.5 m.

Erpfingen This locality about 1 km WNW of Erpfingen contains 2-3 m deep elongate Bohnerz pits that follow individual fissures, which are developed in limestone of the upper Kimmeridgian Unterer Massenkalk Formation. Fossils from fissure fillings in this locality have been reported as late Pliocene to early Pleistocene (Rummel, 1993). Samples of red Bolus clay with pisoliths were taken from the sides of one pit (UTM 32U, 513341 m E, 5355775 m N).

Willmandingen Fossils from fissure fillings about 1 km north of the town of Willmandingen have been described as spanning between Lower Oligocene and Lower Pliocene (Dehm, 1935; Jäger, 1835; Rummel, 1993). Samples were collected on a depth profile from the surface to 1.6 m depth in a fissure filling just north of the quarry (UTM 32U, 511230 m E, 5359994 m N).

Aufberg This locality is located 1.5 km southeast of Salmendingen. Upper Miocene to Lower Pliocene fossils have been described from fissures exposed in Bohnerz pits (Borger, 1990; Ufrecht, 2008; Weiger, 1908). One pit at UTM 32U, 509736 m E, 5354760 m N was sampled on a depth profile from the surface to 90 cm depth.

Cholplatz A plateau between Jestetten, Wilchingen, Guntmadingen, and Neuhausen am Rheinfall has a dense accumulation of fissures filled with red Bolus clay and abundant Bohnerz pisoliths (Achenbach, 1859; Baumberger, 1923; Birchmeier, 1986). Thousands of pits following individual fissure fillings were dug to extract pisoliths as iron ore. We sampled seven different pits within a radius of 100 m at the locality 'Cholplatz'. Since most pits had standing water, samples were collected around the edges of the pits.

Balsthal Holzfluh The contact between deeply weathered Upper Jurassic limestone and the overlying Molasse alsacienne, which contains fossils of MP27, is exposed in a former quarry (UTM 32T 401927 m E, 5241690 m N). The Molasse deposits are offset against the Jurassic limestones along the contact, as shown by down-dip striations and a 5-10 cm thick fault breccia. However, the basic stratigraphic order is still preserved. Both the Jurassic limestone and the Molasse deposits are part of a limb of an anticline and are dipping about 70-80 ° to the south. No laterally extensive Siderolithic deposits are present in this location. We collected

several pisoliths from fissure fillings just below the contact to the Molasse.

Stratiform-type deposits

Stratiform deposits are laterally extensive accumulations of Bohnerz clays on the surface of the limestone (Fig. 3.1). Deposits were classified as paleosols if showed at least 50 cm of laterally extensive surface accumulation, with little or no signs of reworking.

Balsthal Erzmatt Siderolithic deposits in this locality with abundant pisoliths are laterally extensive, but are not well-exposed. They are overlain by Lower Freshwater Molasse with fossils of MP26-27. We collected samples at a tailings heap at UTM 32T, 402013 m E, 5240573 m N (Balsthal Erzmatt I). A second sample was taken close to the base of Siderolithic deposits in-situ at UTM 32T, 402179 m E, 5240418 m N (Balsthal Erzmatt II).

Malsenhof One of the most well-exposed outcrops of the Siderolithic is found about 2 km west of Welschenrohr at UTM 32T, 386502 m E, 5237465 m N., near the hamlet of Malsenhof (Baumberger, 1923). About 10-15 m of red Bolus clay with Bohnerz pisoliths rest conformably on weathered limestones of the Kimmeridgian Reuchenette Formation, which has fissures filled with the same Bolus clay. The Siderolithic deposits are overlain by Molasse of approximately MP24-26. The lower 4-5 m of the Siderolithic consists of homogeneous dark red Bolus clay with Bohnerz pisoliths distributed randomly throughout. The next 4 m are reworked deposits of red, sandy clay, separated sharply from the homogeneous red Bolus clay below by an unconformity. The reworked deposits exhibit several layered and graded horizons, which contain centimeter-thick layers of sand as well as of pure Bohnerz pisoliths. The uppermost 3-5 m and the contact to the Molasse are covered by scree. However, since the Molasse deposits form a topographic ridge, which

projects above the Siderolithic deposits, the stratigraphic thickness of the covered section can be estimated to within 1-2 m. The Siderolithic was sampled on a depth profile from just above the contact to the limestone to about 3-5 m below the contact to the Molasse.

Mervelier On the northern limb of an anticline, about 500 m south of the town of Mervelier (UTM 32T, 386530 m E, 5243823 m N), the steeply dipping limestones of the Kimmeridgian Reuchenette Formation are covered by several meters of laterally extensive Siderolithic deposits. The contact to the overlying Molasse deposits of the Delsberg Formation (MP29) is covered. We took one sample of the basal part of the Siderolithic.

Oberdorf Samples at Oberdorf were taken in a layer of Siderolithic between two freshwater limestones of MP 20/21 and MP 22. This overlies about 20-30 m of Siderolithic on limestones of the Reuchenette Fm. This sequence was studied in detail during the construction of a tunnel (Rollier, 1910), which also uncovered several fissures in the limestone, which are filled with red and green clay containing iron-oxide pisoliths.

Lohn am Randen This locality was described in detail by Hofmann et al. (2017), also see Chapter II. (U-Th)/He age data from this locality was included in the compilation of the age distribution of the Bohnerz deposits.

Pisoliths

Ferruginous concretions collected at every outcrop take the form of pisoliths, which are concretions 2-50 mm in diameter. They are composed of goethite, as confirmed through x-ray diffraction and infrared spectroscopy. Some parts of pisoliths can also contain a minor amount of kaolinite, which is the main constituent of the red

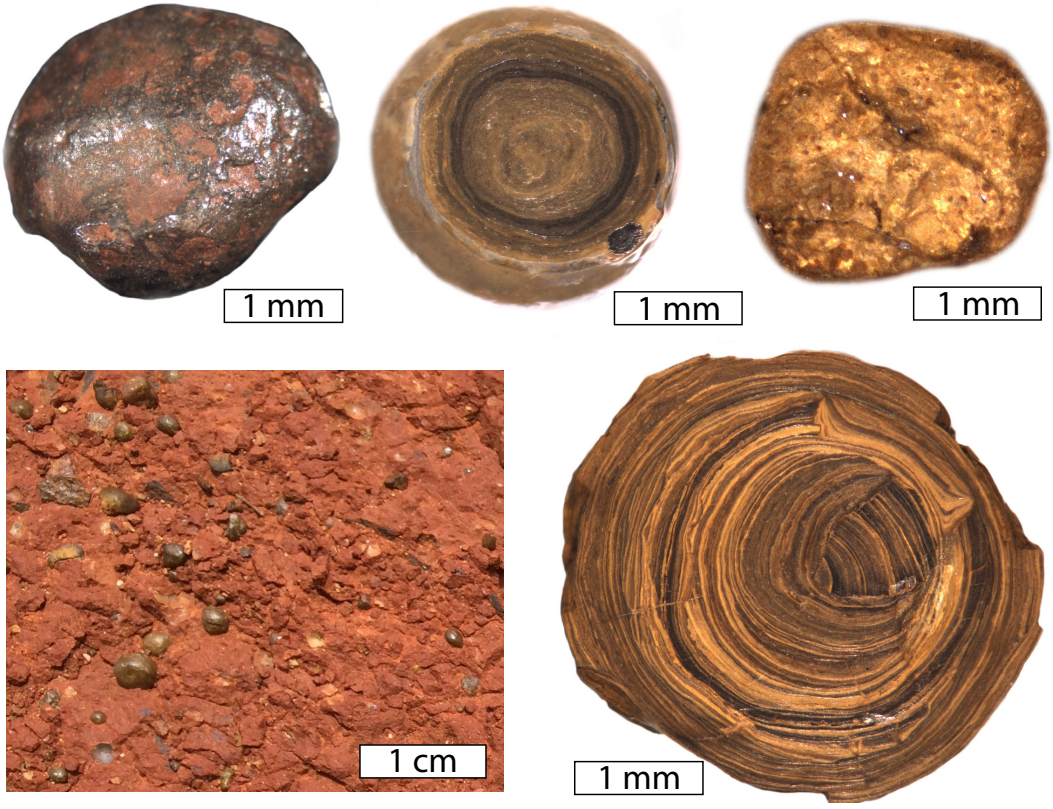

Figure 3.2: Photographs showing the typical appearance of pisoliths: outside of pisolith, cut concentrically layered pisolith with fine-grained core, cross-section of an unlayered pisolith, pisoliths in situ in Bolus clay, and inside of pisolith showing several episodes of goethite precipitation and dissolution.

Bolus clay in which they are embedded. Pisoliths commonly show one of two different morphologies (Fig. 3.2). Layered pisoliths display an outer shell (cortex) of thin concentric layers surrounding a core (nucleus), which is mostly made of fine-grained goethite and kaolinite, but can also be a piece of a different pisolith. Unlayered pisoliths do not display the nucleus-cortex structure and are generally more homogeneous. Some pisoliths show evidence of partial dissolution of older layers, with some of them terminating against a new generation of concentric layers.

3.3 Methods

(U-Th)/He ages

Pisoliths were either lightly crushed or 'peeled' under a light microscope to isolate a single concentric layer. Individual layers were then sampled by breaking off pieces using tweezers and dental tools. Aliquots of 5-100 µg were loaded into platinum tubes, which were pinched at the ends to produce flat packets. These packets were loaded into pits on a copper planchet with a steel radiation shield to prevent accidental heating of neighboring samples. Packets were heated with a Photon Machines diode laser to about 930 °C for 6 minutes to extract helium. The resulting gas was exposed to a U-trap with charcoal cooled by liquid nitrogen and then spiked with pure ^{3}He. The He was sorbed on charcoal in a cryostat at 14 K and then released into the Pfeiffer quadrupole mass spectrometer at 34 K. Absolute amounts of helium were determined relative to regularly interspersed standards with known amounts of ^{4}He, also spiked with ^{3}He. Complete helium extraction was confirmed by performing another heating to about 940 °C for 6 minutes and analyzing the He in the same manner.

Packets were then unloaded from the planchet and transferred to teflon vials. A consistent amount of spike solution enriched in ^{230}Th and ^{235}U, as well as containing Ru of natural isotopic abundance as an elemental spike to trace Fe and other minor metals, was added to each teflon vial, along with 100 µl of concentrated Seastar hydrochloric acid. Teflon vials were kept in an oven at 100 °C for at least 12 hours. The vials were then opened and dried on a hotplate at 95 °C. The resulting salts were brought back into solution with 50 µl of concentrated Seastar nitric acid. Then 1 ml of MilliQ water was added to the solution and it was decanted into a 1.5 ml vial. A isotopically natural standard solution ('normal') containing 1 ng of U and Th, 0.1 ng Sm, 10 µg Fe, 1 µg Al and Si, and 0.1 µg Mn was prepared and spiked. Analysis for U, Th, and Sm as well as for Fe, Mn, Si, and Al was performed on an

Agilent 8800 inductively coupled plasma mass spectrometer using isotope dilution. The measured isotope ratios were $^{238}U/^{235}U$, $^{232}Th/^{230}Th$, $^{147}Sm/^{235}U$, $^{27}Al/^{101}Ru$, $^{28}Si/^{101}Ru$, $^{55}Mn/^{101}Ru$, and $^{58}Fe/^{101}Ru$. Absolute amounts of each isotope or element were determined relative to the spiked standard and blank-corrected using a spiked solution of nitric acid and MilliQ H_2O. Amounts of Fe, Al, Si, and Mn were determined, and the mass of the dissolved aliquot was calculated assuming perfect goethite stoichiometry. Concentrations of U, Th, and Sm were calculated relative to the Fe-based sample mass. Assuming that all dissolved Si, Al, and Mn was contained in the goethite sample and was substituting for Fe, we calculate the molar percentage of these elements in the Fe site. We use this for checking correct phase identification and to track patterns in non-Fe constituents. Possible polyatomic interference of $^{195}Pt^{40}Ar$ on ^{235}U was reduced to negligible level by colliding ions with H gas in a reaction cell. Since no measurable amount of ^{234}U is expected in, mass 234 ($^{194}Pt^{40}Ar$) was used to check for possible presence of PtAr. No signal over 10 cps was detected on mass 234, and therefore absolute amounts of U were not corrected for PtAr inference.

(U-Th-Sm)/He ages were calculated from absolute amounts of U, Th, Sm, and He, according to Farley (2002). Ages were determined on a single aliquot, so uncertainty in sample mass does not propagate to ages. Quantitative retention of helium in Bohnerz pisoliths was demonstrated through $^4He/^3He$ diffusion experiments of irradiated samples by Hofmann et al. (2017). Therefore, we assume no diffusive loss of helium at earth-surface conditions. A Monte-Carlo error propagation was performed to calculate a 1σ uncertainty for every age.

Individual dated aliquots were rejected from further consideration if they met any of the following criteria: (a) the Fe-based mass was under 1 µg, which indicates that the aliquot was lost from the tube before dissolution, (b) the fraction of Fe among all determined structural elements (Fe, Mn, Al, Si) is less than 60% of the measured

mass, which indicates a phase other than goethite, (c) the absolute amount of He was below two times the blank level (0.001 ncc), (d) all measured amounts of U, Th, and Sm are below two times the procedural blank level (0.004 ng), or (e) the sample has an uncharacteristically high He concentration with U, Th, and Sm concentrations that are above blank level, which might indicate that He is derived from a detrital phase, such as zircon, either contained in the aliquot or implanted helium from a nearby high eU phase, (f) aliquots that were accidentally heated to more than 960 °C, which might lead to U loss (Vasconcelos et al., 2013).

Measurements of ^{3}He concentrations

Aliquots of several milligrams of goethite, which represent a large part of the cortex of an individual pisolith, were wrapped in tin foil and were heated to about 1100 °C in a double-vacuum resistance furnace. The resulting gas was purified by means of a charcoal trap cooled with liquid nitrogen and several SAES getters. Helium was cryogenically concentrated and released into an SFT sector-field mass spectrometer. Complete helium outgassing was confirmed by re-extracts. Absolute amounts of ^{3}He were determined relative to regularly interspersed standards with known amounts of ^{3}He. Typical blank levels of ^{3}He are around 1-2·10^{-20} mol. Concentration was calculated by dividing blank-corrected absolute amounts of ^{3}He by the weighed mass of the aliquot.

Compilation of Bohnerz localities

To put our sampling locations into a broader context, we compiled a list of locations that contain clays of the Bohnerz deposits from published literature, including those of the fissure-type and the stratiform-type as well as cave deposits. Because of the discontinuous nature of the deposit and the focus on fossils and mining, it has mostly been described at discrete localities in the literature. Only locations that are described as ferruginous pisolith-bearing red/yellow clays were recorded for this

study. The Rossemaison Fm. (‘terre jaune’, ‘Gelberde’) of the Delemont basin is recognized as a separate deposit (Pirkenseer et al., 2018) and has not been included. Pisoliths from the Bohnerz deposits have been mined as iron ore since antiquity (Borger, 1990; Borger and Widdowson, 2001). Since they used to be of economic importance, the vast literature describing the Bohnerz deposits spans over three centuries. There are five distinct sources for the localities compiled here: (1) documents about mining, containing mostly technical information on productive localities and few details about the deposits themselves, (2) literature describing the Bohnerz Fm./Siderolithic as a deposit, such as works about regional geology, (3) local and regional geologic maps, which do not offer a comprehensive account of deposits in any given area due to the small scale and the distributed nature of the deposits, (4) paleontological literature focusing chiefly on fossils found in individual fissure fillings, and (5) borehole logs for localities in the North Alpine Foreland Basin buried under several kilometers of Molasse sediments. The information compiled from these sources were as follows: name, coordinates, type of deposit (fissure-type, stratiform-type, cave deposit), substratum unit, age of fossils, and age of units covering the deposit. Most sources did not contain all of this information. In many cases, information on substratum and cover units was determined from official geologic maps of Germany, Switzerland, France, and Luxembourg.

Most of the literature used to compile the map describes a single fissure or locality. The paleontological literature has a naming scheme, in which fissures in a defined area are named after the closest town/locality. Individual fissures are then numbered in order of discovery. For localities other than those described in the paleontological literature we used the name given in the publication and employed the same naming scheme for as yet unnamed localities. About three quarters of all localities were described in enough detail, through maps, descriptions of the outcrop, or map coordinates, to locate them within 100 m on a map. These localities were marked

'exact'. Other localities are only identified by the name of the closest town. In these cases, coordinates of the town are given and the locality is marked 'approx'.

While this compilation maps out the extent and stratigraphic position of the Bohnerz deposits, it is not meant to be a comprehensive account of all occurrences of Bohnerz deposits. Since the focus is not on the paleontology of fossils found in the Bohnerz deposits, no extensive review of fossil ages has been undertaken. Fossil ages compiled here only represent a fraction of the available data.

3.4 Results

Map of Bohnerz localities

We compiled 517 locations of the Bohnerz deposits from 189 sources of published literature spanning the years 1707-2018. The list of localities including attributes and sources used to compile the map can be found in Appendix 3.D. The compilation includes 316 localities of fissure-type deposits, 187 of the stratiform-type, and 14 cave deposits. Some of the stratiform-deposits might represent paleosols in situ, as in the example described by Hofmann et al. (2017), but many laterally extensive deposits show evidence of (partial) reworking (e.g. Pirkenseer et al., 2018), such as sorting or grading of components. Bohnerz pisoliths have been found in most localities mentioned here, but some have been described as pure clays without pisoliths and are annotated as such.

The locations were plotted on a map, with type being indicated (see Fig. 3.3). The widely recognized extent of the Bohnerz Fm. is on the Franconian Alb and Swabian Alb, where numerous fissure fillings have been described (e.g. Dehm, 1935; Rummel, 1993). Stratiform-type deposits in this region are only present in a few localities, mostly preserved due to local cover by Paleogene or Neogene strata (e.g. Gall, 1971). Bohnerz deposits are found in most boreholes in the North Alpine Foreland Basin (e.g. Bloos, 1967; Volz, 1957). In the Swiss Jura mountains,

Siderolithic deposits, often of the stratiform-type, have been reported for at least 300 years (Baumberger, 1923; Rollier, 1905; Scheuchzer, 1707). Fissure fillings are also present in areas that predominantly show stratiform-type deposits, either in the substratum of the stratiform deposits (Pirkenseer et al., 2018) or as individual fissure-type deposits (Becker et al., 2013).

Outside of this 'classical' region of Bohnerz deposits, similar deposits have been reported from the Kraichgau region of southern Germany (Schmidt, 1941) and flanking the Rheingraben (Rutte, 1953). Siderolithic deposits occur as both the fissure-type and the stratiform-type on Cretaceous limestones in the Helvetic nappes of the Alps (Epprecht, 1957) where they are weakly metamorphic (Wieland, 1979). In the Rheinhessen area of Germany, Bohnerz deposits are found mainly as the stratiform-type (Bartz, 1940). Bohnerz deposits are also found in southern Luxembourg (Gassmann and Schäfer, 2018).

Stratigraphic position and substrate of the Bohnerz deposits

The Bohnerz deposits are developed on a substrate ranging from Middle Triassic to Lower Cretaceous, but most commonly on Upper Jurassic. In the Swabian Alb and Franconian Alb regions of southern Germany (see Fig. 3.3) they are mostly developed on Tithonian strata. In the transition between the Swabian Alb and the Jura as well as in the eastern Jura the substratum of the Bohnerz deposits is composed of Oxfordian and Kimmeridgian strata. In the southwestern Jura the youngest substrata are the Hauterivian-Barremian (Early Cretaceous) Vallorbe Fm. Bohnerz deposits are found on the whole range of Helvetic units of the Alps, the substratum is formed by Cretaceous strata from the Berriasian Öhrli Fm. to the Cenomanian-Santonian (Late Cretaceous

) Seewen Fm. (Wieland, 1979). In other regions, the substratum can locally be formed by older limestones, such as the Bajocian-Bathonian (Middle Jurassic)

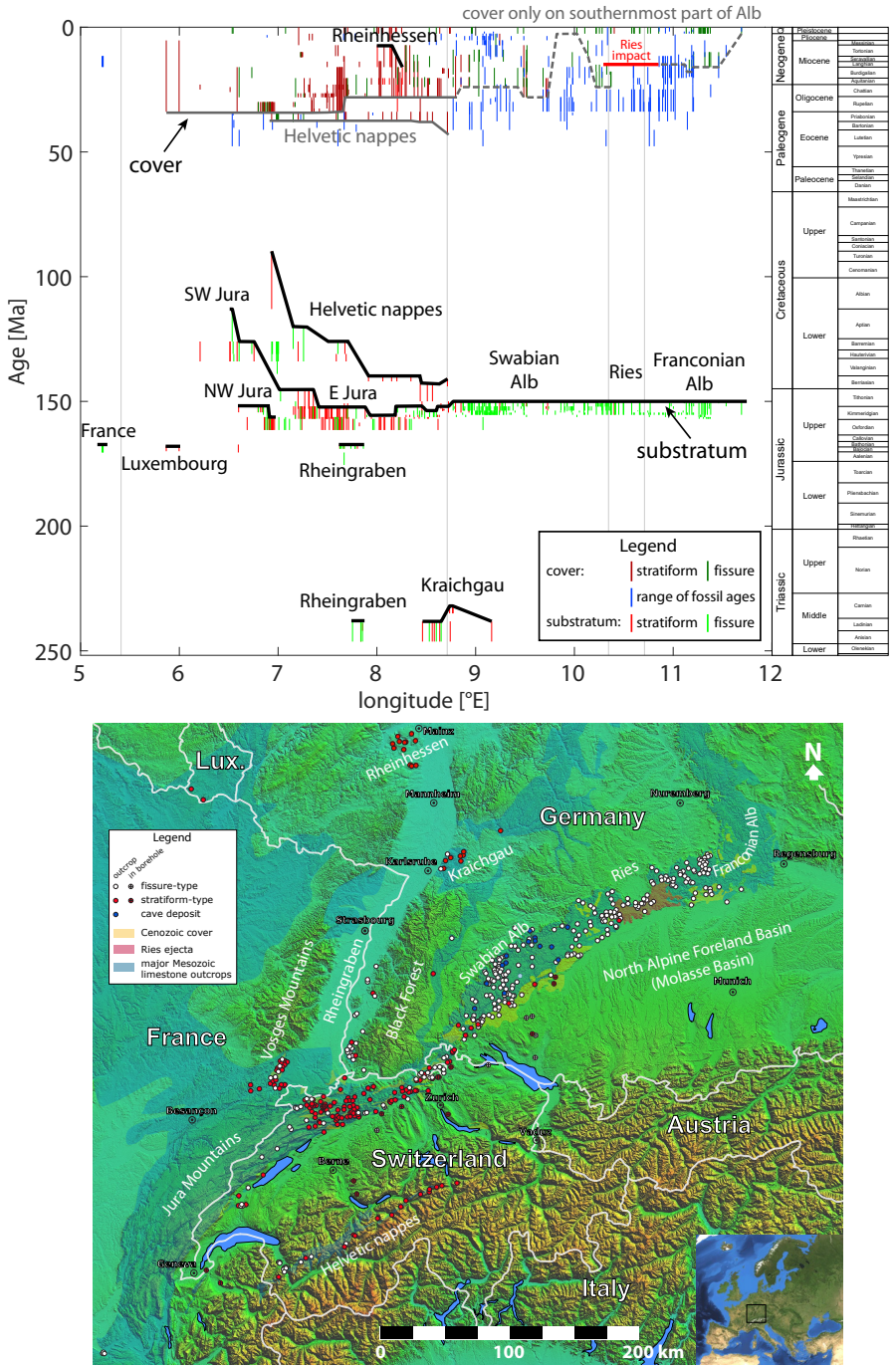

Figure 3.3: East-west profile of the unconformity and map of Bohnerz deposit localities compiled from published literature of fissure-type/stratiform-type/cave deposits. Age of substratum and cover units of the Bohnerz deposits as well as range of fossils contained in the deposits are given in the diagram in absolute time. Bohnerz deposits are widespread in Central Europe. The Swabian Alb and Franconian Alb regions contain mostly fissure-type deposits, whereas stratiform-type deposits are more common in all other regions, including the Jura Mountains and the Helvetic Alps, where they are covered by Molasse units of mostly Eocene-Oligocene age.

Hauptrogenstein Fm. in the Rheingraben area (Rutte, 1953) and the Middle Triassic Muschelkalk units in the Rheingraben and Kraichgau regions (Schmidt, 1941). The Rheinhessen region shows unusually young substrata of Chattian-Burdigalian (Miocene) age Cerithium beds and Rüssingen Fm. The Bohnerz deposits in this area might be allochthonous (Bartz, 1940), and might therefore have developed on a different substratum.

The oldest cover units reported in the literature are the Niederhorn Fm. and the Sanetsch Fm. of Priabonian (Eocene) age in the Helvetic nappes of the Alps (Menkveld-Gfeller et al., 2016). Oligocene and Miocene Molasse units have only transgressed onto the southernmost part of the Franconian Alb and Swabian Alb, leaving major areas exposed, which is the area in which most fissure fillings are found today.

Ages of cover units increase from east to west. The Bohnerz deposits in the Swiss and French Jura have been covered by mostly early Oligocene Molasse. In the Delemont basin, the early Oligocene (MP21-20) Rossemaison Fm. directly covers Bohnerz deposits and contains reworked pisoliths (Pirkenseer et al., 2018). In other regions, Bohnerz deposits are either not covered or are covered by Pleistocene loess. Most fissure fillings contain fossils of a single age, only few have mixed ages (Bolliger and Rummel, 1994). Mixed ages might represent reworking of older fissure fillings due to slow surface-lowering. The oldest fossils reported in Bohnerz deposits are molluscs of possible Lutetian (Eocene) age (Tavel, 1936) as well as a rodent tooth of Bartonian (Eocene) age (Weidmann, 1984), both from fissure fillings developed on Cretaceous limestones of the Helvetic nappes. Fossils of similar age have been found in fissure fillings in southern Germany (Dehm, 1935; Heissig, 1978; Rummel, 1993). Most fossil ages reported in the literature are Oligocene and Miocene, with the youngest ages being Pleistocene (e.g. Dehm, 1935; Rummel, 1993).

Goethite (U-Th)/He ages

We obtained 508 (U-Th)/He ages for 113 goethite pisoliths from 12 different localities (for data see Appendix 3.B). In the following discussion, we also included an additional 235 previously published ages from pisoliths of the Lohn am Randen paleosol (Hofmann et al., 2017). Newly reported ages range from 53.9 Ma to 1.2 Ma (Fig. 3.8), with aliquots having 0.1-20 ppm U, 0.5-200 ppm Th, and 1.5-200 ppm Sm. Ratios of Th/U are generally 2-30, with Th being the dominating part of effective uranium concentration (eU), which indicates weathering-related fractionation of U and Th due to the higher solubility of U. There was no systematic difference in Th/U ratios between samples from fissure-type and stratiform-type deposits. Al-substitution for Fe was between 10 and 35 mol-%, which is a typical range for supergene goethite (Schwertmann, 1988). We observed no correlation between the amount of Al-substitution and age.

We rejected 32 out of 508 aliquots based on the criteria outlined in the methods section. Most aliquots were rejected for having very low Fe-based mass, indicating either loss of sample from the packet between the degassing and dissolution steps or a phase other than iron-oxides and not of other metals analyzed here. Several aliquots were also rejected for having uncharacteristically high helium concentrations without correspondingly high U or Th amounts. These ages were higher than the depositional age of the substratum and are likely due to the presence of a detrital high-eU phase, such as zircon, which cannot be dissolved in HCl. Pisolith formation ages are generally below 15 Ma in the Franconian Alb (Fig. 3.4), with only two older ages reported for the Petersbuch location. There is no trend of age with depth in a fissure, which was sampled at Petersbuch from the surface to 3.5 m depth (Fig. 3.5). Ages over 15 Ma only occur in pisoliths found in the soil that overlies the fissure. For individual fissure fillings with known age ranges of small mammal fossils from Weißenburg, Rothenstein, and Petersbuch quarries, the pisoliths are younger than

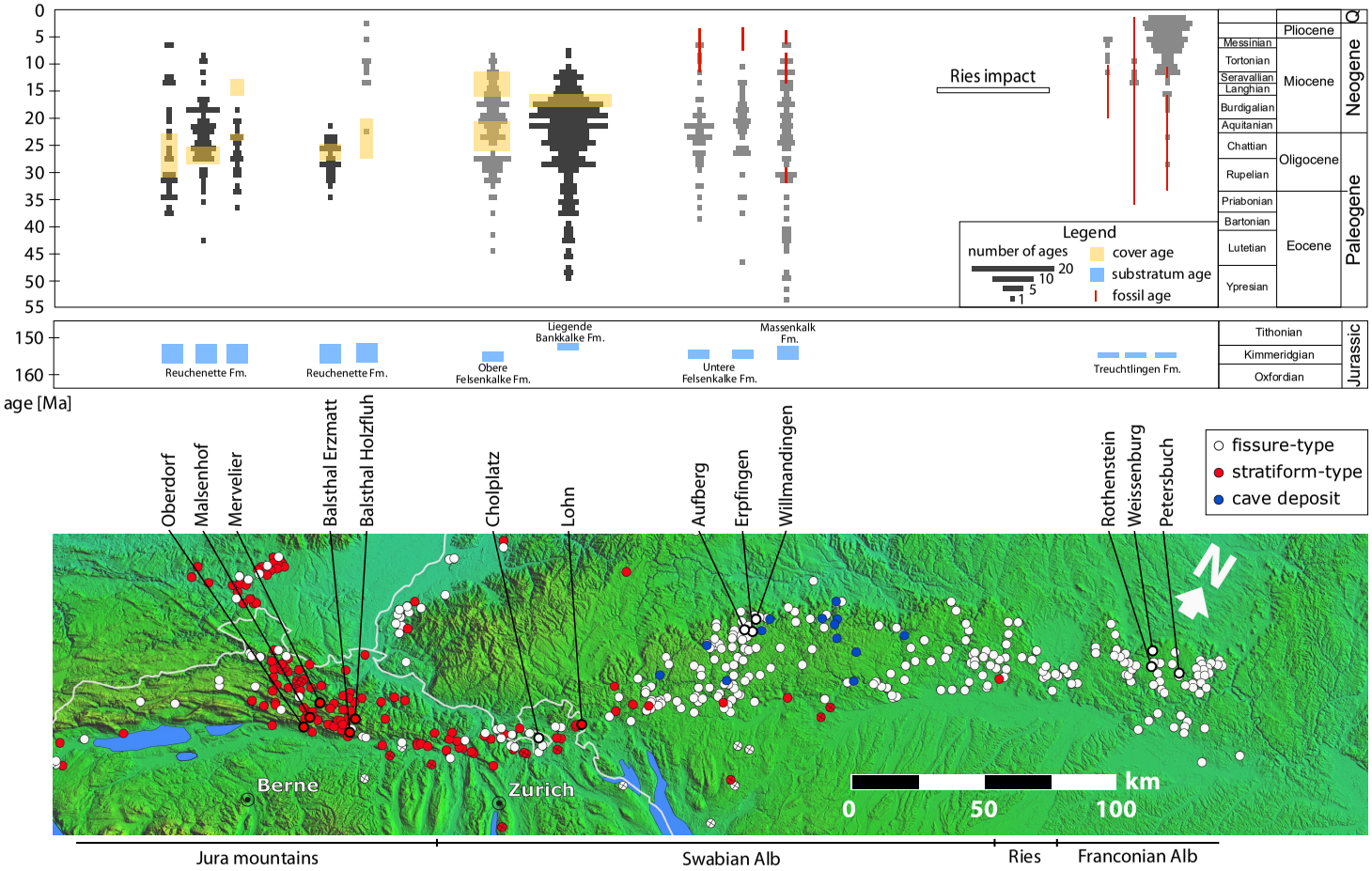

Figure 3.4: Histograms of (U-Th)/He ages with 1 Ma bins for all localities with stratigraphic constraints (age of substratum, cover, fossils contained in fissure fillings). Grey bars denote fissure fillings, dark bars are stratiform-type deposits. Data for Lohn was previously published in Hofmann et al. (2017). Below: map of localities for which ages were obtained.

the fossil age (Fig. 3.5). They must have formed after the deposition of the fossils and Bolus clay in the fissure.

Fissure fillings in the Swabian Alb region (Aufberg, Erpfingen, Willmandingen) have overlapping pisolith age ranges (Fig. 3.4), from 55 Ma to about 5 Ma. No fossils have been described for the particular fissures sampled here. Reported fossil ages for the localities as a whole are concentrated toward the end of goethite precipitation. Based on our age distrubtion, these pisoliths likely formed before the Bolus clay and fossils were translocated into the fissure.

In the Jura mountains, fissures and stratiform-type deposits show preferentially older ages than those further east (Fig. 3.4). Stratiform deposits (Oberdorf, Malsenhof, Mervelier, Balsthal Erzmatt, Lohn) have ages that are older than the cover. Around the time of deposition of the cover, the number of goethite formation ages declines. All of these localities have evidence of at least some renewed goethite precipitation after deposition of the cover strata (Fig. 3.4).

The same trend can be seen in the fissure fillings of Cholplatz. Age profiles of individual pisoliths (Fig. 3.6) show the oldest ages in the core of the pisolith, with outer layers becoming progressively younger. Ages younger than the cover only occur in the outermost 20% of the pisolith. The cores, which make up the bulk of the material, are mostly older than the age of deposition of the strata covering the fissures. The fissure fillings of Cholplatz, which are within 50 m of each other, show the same approximate range of goethite precipitation ages (Fig. 3.6). In the Jura Mountains, no ages younger than 6 Ma have been measured, other than one sample in Balsthal Holzfluh, which has ages that are significantly younger than the cover. The pisoliths analyzed from this locality are within 1 m of a normal fault. Ages might have been reset by partial alteration due to fluid flow along the fault surface.

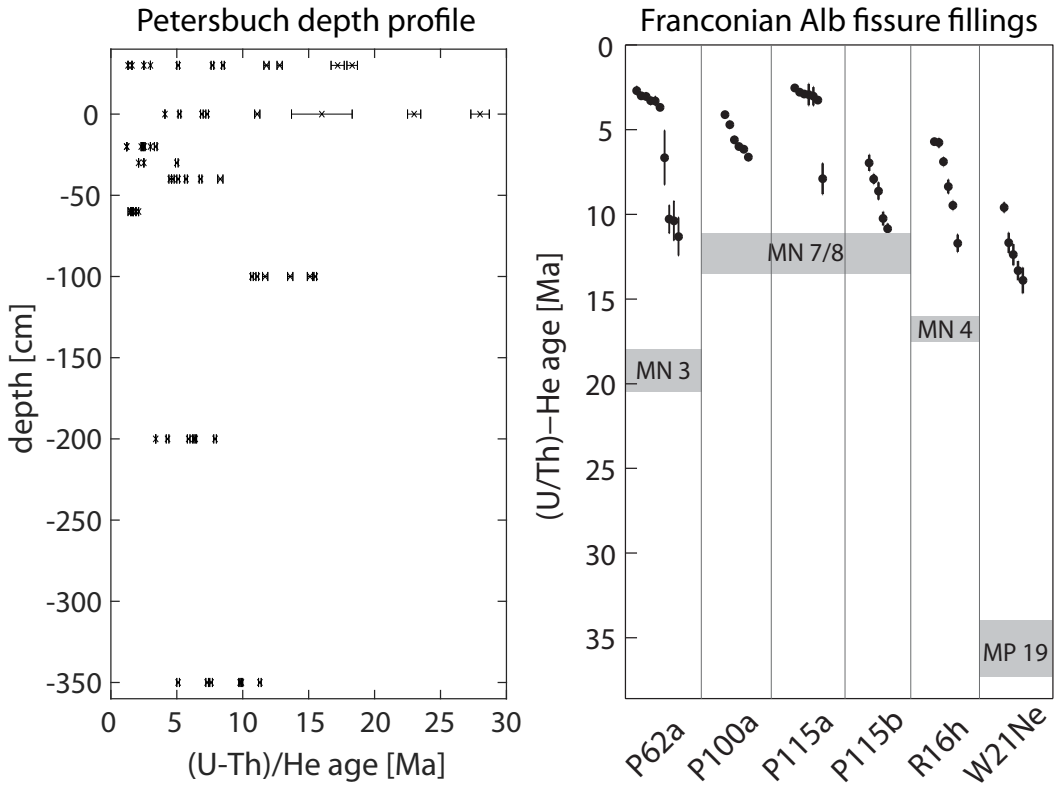

Figure 3.5: Depth profiles and distribution of ages of in adjacent fissure fillings. Ages of fissure filling P-F2 at Petersbuch quarry show no trend with depth. Ages >15 Ma are only found in pisoliths within the modern soil above the fissure. Pisoliths in fissure fillings in the Franconian Alb (Weißenburg, Rothenstein, Petersbuch) are younger than the small mammal fossils contained in them. They must have formed after deposition of material in the fissure.

Cosmic-ray exposure duration of paleosols and fissure fillings

We obtained 27 measurements of ^{3}He concentrations of goethite from individual pisoliths (see Appendix 3.C). Depth-profiles were constructed for the Malsenhof, Aufberg, Willmandingen, and Petersbuch localities (Fig. 3.7). We used the high-latitude sea-level production rate of Shuster et al. (2012) and scaled it for latitude and elevation using the model of Lal (1991). In the absence of other constraints, we assume no erosion, thereby calculating minimum exposure durations. Cosmic-ray exposure that occurred before burial is termed paleo-exposure. Malsenhof is a paleosol with a total thickness of about 14 m, which is covered by Chattian molasse. The uppermost 5-6 meters of the deposit show evidence of reworking, such as sandy

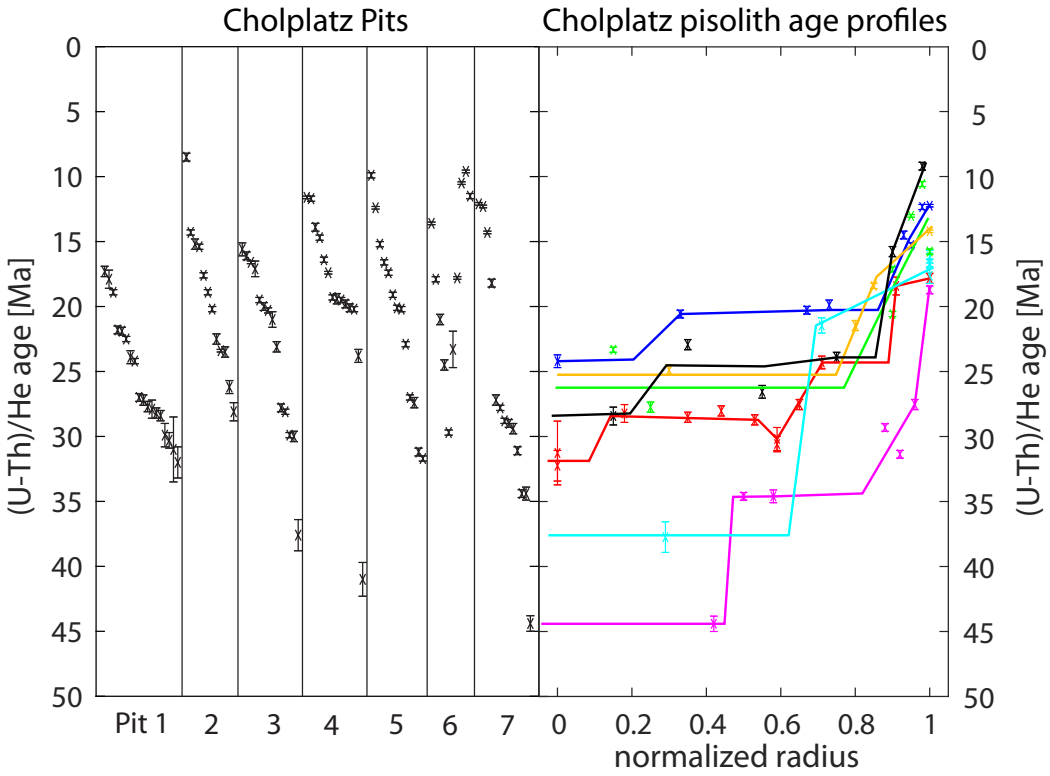

Figure 3.6: Samples from seven adjacent pits at Cholplatz, each representing a different fissure, yield comparable age ranges (left). Age profiles of individual pisoliths (right) from Cholplatz show that ages younger than about 25 Ma (age of cover) only make up the outermost 5-15% of the radius.

layers and sorting of components. The ^{3}He concentration is roughly constant with depth, with an average of 300 Mat/g. A similar observation was made by Hofmann et al. (2017) for the Lohn am Randen paleosol, which was interpreted as in-situ paleo-exposure with soil-convection. The ^{3}He concentrations measured here are also comparable to those measured at Lohn am Randen. Using the soil convection model of Hofmann et al. (2017), the minimum cosmic-ray exposure duration for Malsenhof is 8.8±1.7 Ma. The ^{3}He concentrations in the reworked upper part of the deposit are the same as in the in-situ part, indicating that the timescale of reworking is small compared to the exposure duration of the paleosol. Two pisoliths from a paleosol at Balsthal Erzmatt have concentrations of 200-500 Mat/g, indicating similar paleo-exposure durations as the other paleosols.

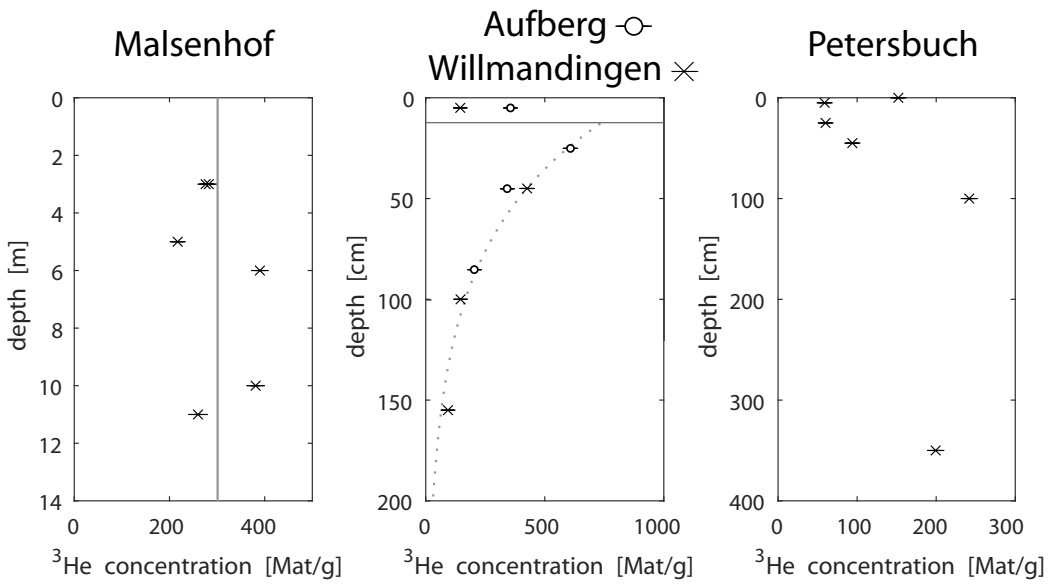

Figure 3.7: Depth profiles of ^{3}He concentration with 1σ uncertainty measured on individual pisoliths. Malsenhof is a paleosol with a reworked upper part. Aufberg, Willmandingen, and Petersbuch are fissure fillings. Grey line denotes average concentration for Malsenhof. For Aufberg and Willmandingen, the dashed line is a representative exponential and the horizontal bar indicates the surface of limestone, with modern soil above 15 cm depth.

Aufberg and Willmandingen are fissure fillings, which were sampled in the uppermost 2 m below the modern surface. The two outcrops are within 5 km of each other and have a similar substratum, thus sharing a common geologic and, presumably, cosmic-ray exposure history. They both show an exponential decrease in ^{3}He concentration (Fig. 3.7). Projecting the exponential trend to the surface of the limestone yields a surface concentration of about 750±80 Mat/g, corresponding to a minimum exposure duration of 7.2±1.4 Ma. We interpret this as in-situ exposure without major vertical movement of pisoliths for the duration of cosmic-ray exposure. This is likely due to recent exposure by slow surface-lowering, after the deposition of the material in the fissure. Both localities have a measurement in the upper 10 cm of the deposit, which is lower than would be expected based on the exponential fit to the rest of the data points. This is likely due to detrital pisoliths being incorporated into the modern soil. Both localities have been used for agriculture within the last

100 years. They are both surrounded by areas of higher elevation, which also have fissure fillings.

A fissure filling at Petersbuch was sampled from the surface to about 3.5 m depth. Measured ^{3}He concentrations are between 50 and 250 Mat/g and show no clear trend with depth. We interpret this as evidence of paleo-exposure of pisoliths in a paleosol before deposition into the fissure. Assuming soil-convection similar to that of the Lohn am Randen outcrop, this yields 3.9±0.8 Ma of minimum paleo-exposure. An addition of recent cosmogenic production of ^{3}He is possible for samples within several meters of the surface, which would lead to an overestimation of the paleo-exposure duration.

We also analyzed several other pisoliths from fissure fillings of Weißenburg and Rothenstein, which precipitated after the formation of the fissure filling. Since they were taken for paleontological purposes, the exact depth below the modern surface was not recorded, but is within several meters of the modern surface. The ^{3}He concentrations recorded for these pisoliths are much lower than those of other localities, at several tens of Mat/g. A combination of cosmogenic and muogenic production of ^{3}He at depths of 4 m and below for 10 Ma or longer could lead to an accumulation on that order of magnitude, depending on the exact depth. We therefore interpret these minor accumulations of ^{3}He as post-depositional.

3.5 Discussion

Paleo-extent and temporal constraints

Bohnerz deposits have been reported for almost all major outcrops of Triassic-Cretaceous limestones in Central Europe (Fig. 3.3). In a compilation of localities from published literature, Bohnerz deposits have been shown to exist in southern Germany, the Jura mountains of Switzerland and France, the Helvetic nappes of the Swiss Alps, the Rheingraben and Kraichgau regions of southern Germany, Rhein-

hessen, and Luxembourg. Two regions of extensive limestone outcrops in Central Europe do not have Bohnerz deposits: northern Franconian Alb and large parts of the French Jura Mountains.

In the Helvetic nappes of the Alps, Siderolithic deposits are only found where the substratum was covered by Priabonian transgression of the Niederhorn Fm. and Sanetsch Fm. (Menkveld-Gfeller et al., 2016), indicating that pre-Priabonian erosion has removed enough limestone to obliterate any trace of any previous weathering episode, without establishment of a new weathering surface before burial. Similarly, partial stripping from the northern Franconian Alb has left no fissures or stratiform deposits. This is evidenced by the occurrence of ferruginous pisoliths in conglomerates together with limestone clasts at the base of the limestone plateau (Berger, 1971). While local factors might have led to the erosion of the Bohnerz weathering surface, fissures and stratiform deposits survive to this day where covered by sediments or where they were able to slowly evolve without experiencing major erosion.

Initiation of Bohnerz-type weathering in Central Europe

The oldest ages in both fissure-type and stratiform-type deposits are around 54-45 Ma, suggesting that many of the deposits started forming within or before the early Eocene time. Dissolution of older generations of goethite could lead to preservational bias, in which material representing the oldest ages is no longer present or only constitutes a minute part of the surviving material. This diminution of the number of older ages has been documented in laterites of Brazil (Monteiro et al., 2014; Monteiro et al., 2018). Therefore, many aliquots have to be analyzed to constrain the full range of iron-oxide precipitation. An indicator of preservational bias is that the oldest ages determined here are from localities with the greatest number of measured ages (Cholplatz, Lohn, Willmandingen). The oldest ages can be found

in the nuclei of pisoliths, which frequently have older ages than cortices (Fig. 3.6). The oldest formation ages of Bohnerz pisoliths coincide with the global Paleocene-Eocene Thermal Maximum (PETM) at around 55.5 Ma (Hansen et al., 2013) during the Eocene Climatic Optimum (see Fig. 3.8). During the early Eocene, lateritic and bauxitic weathering was initiated globally due to favorable climatic conditions (Beauvais et al., 2008; Retallack, 2010) and many of these systems have continued to evolve through dissolution-precipitation of iron-oxides to this day (e.g. Monteiro et al., 2014; Monteiro et al., 2018). High mean annual temperatures and precipitation have also been documented for the oldest part of the record in continental Europe in the mid-Eocene, reaching almost tropical conditions (Mosbrugger et al., 2005). This is an indication that the oldest ages here actually attest the initiation of Bohnerz-type weathering in Central Europe.

The oldest fossils contained in Bohnerz deposits have been reported as Lutetian/Bartonian (Tavel, 1936; Weidmann, 1984), which is about 10 Ma younger than the oldest pisolith formation ages. Weathering profiles and ferruginous clay deposits similar to the Bohnerz deposits have been reported from the Massif Central in France (Ricordel-Prognon et al., 2010). They have been assigned an Early Cretaceous age based on paleomagnetic measurements. There is evidence for paleo-weathering of Jurassic limestones in the Early Cretaceous in Switzerland and Germany (Dehm, 1935; Menkveld-Gfeller et al., 2016). However, no Bohnerz deposits have been reported to be covered by Cretaceous-age units. Fissure fillings and stratiform-type Bohnerz deposits are developed on a substratum of Early Cretaceous rocks in the western Jura and the Helvetic units of the Alps. Weathering in the early Cretaceous might have occurred with the formation of structures similar to the Bohnerz deposits, in which case they were completely eroded before the deposition of Cretaceous strata or initiation of the Bohnerz weathering in the early Eocene. In the Helvetic Alps, Bohnerz deposit are frequently associated with basal conglomerates

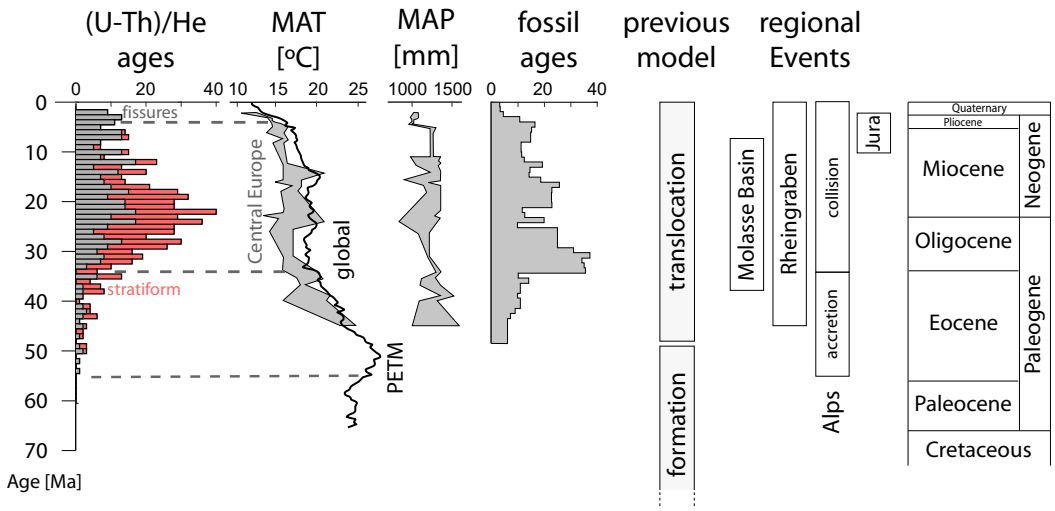

Figure 3.8: Histogram of all ages reported here with 1 Ma bins, with ages from fissures in gray and those of stratiform-type deposits in red. Ages are compared to Central European (Mosbrugger et al., 2005) and global (Hansen et al., 2013) temperature reconstructions. Also given is a histogram of ages of small mammal fossils in 1 Ma bins, constructed from individual age ranges for each locality. Initiation of Bohnerz weathering occurred around the time of the Paleocene-Eocene Thermal Maximum (PETM) and continued through the following period of stable warm climate. The youngest ages are around 2 Ma, a time which saw a global and regional drop in mean annual temperatures. The Bohnerz deposits showed great stability during regional tectonic events and a major re-organization of drainage networks.

(Menkveld-Gfeller et al., 2016), indicating a period of fluvial erosion before inception of weathering. This hints to a pre-Eocene removal event, possibly related to the formation of the forebulge unconformity, before establishment of Bohnerz weathering and relative stasis of the deposit as a paleosol, with associated formation of fissures in the substratum. In the Franconian Alb, Cretaceous sandstones, which once covered the area, can be found in some fissure fillings (Dehm, 1935; Rummel, 1993), further suggesting a post-Cretaceous formation of fissure fillings.

Formation mechanism

Bohnerz pisoliths have previously been interpreted as having formed in a laterite, similar to those in India, in the Cretaceous-early Eocene. (e.g. Borger and Wid-

dowson, 2001; Ufrecht, 2008). According to this model, pisoliths and clays created in the Cretaceous were eroded in the early Eocene and subsequently deposited in fissure and caves, during which fossils were admixed. Pisolith formation ages measured here are much younger than the Cretaceous, ranging between 55 and 2 Ma. We also found that goethite precipitation ages in fissure fillings of the Franconian Alb are consistently younger than the small mammal fossils found in them. This suggests that the pisoliths formed after the Bolus clay was deposited in the fissure. In other localities, like those in the Swabian Alb, we have found that pisoliths precipitated before the formation of the fissure filling. Therefore, Bohnerz pisoliths can form both close to the surface and up to tens of meters below the surface of the limestone. In lateritic duricrusts, iron-oxide precipitation far below the surface has been demonstrated. Monteiro et al. (2018) found ages as young as 0.8 Ma at around 100 m depth.

Iron-oxides in fissure fillings evolve at depth even after the karstified surface has been covered by younger strata, as shown for the samples of Cholplatz (Figs. 3.4, 3.6). Fissures might act as a conduit for groundwater, which can facilitate a continuation of iron-oxide dissolution-precipitation. In the case of Cholplatz, marine sedimentation on the surface led to a sharp decrease in the number of ages. At a later time of terrestrial sedimentation, this process was re-started and led to the precipitation of iron-oxide in the outer layers of pisoliths. Although most deposits seemed to experience goethite dissolution-precipitation even after burial by tens of meters of sandstones and conglomerates, no ages younger than 6 Ma have been found in the Jura Mountains, suggesting that the folding in the Jura and associated uplift terminated the precipitation of goethite in the subsurface.

Stratiform deposits show some evidence of having been paleosols, such as homogeneous distribution of pisoliths and absence of re-working, which is best documented for the Lohn am Randen outcrop (Hofmann et al., 2017). Most deposits show signs

of reworking in the upper part, which occurred prior to the deposition of cover strata. All localities have a significant number of ages that are younger than that of the cover strata. This might represent continued dissolution-precipitation in the subsurface. Most deposits were covered by tens of meters of Molasse deposits. These cover rocks are composed mainly of sandstones and conglomerates, which are permeable enough to allow exchange with groundwater. This might help to sustain dissolution-precipitation reactions.

Age distributions can be skewed towards younger ages by sampling bias from the selection of material for (U-Th)/He dating. Many pisoliths have older cores, which contain detrital minerals, such as quartz, or are composed partly of clay minerals. Outer concentric layers, which are thinner but generally composed of more pure goethite, were preferentially sampled because of the greater suitability of the material. Age profiles from Cholplatz showed that the bulk of the pisoliths is made of old material, which was precipitated before the fissures were covered by Molasse. Younger ages only composed the outermost 10-20% of the radius of the pisolith. The occurrence of a large number of ages younger than the age of the cover strata can partially be explained by preferential selection of the youngest layers of the pisolith. The material from which the Bolus clays and pisoliths are made has been interpreted as residual material from dissolution of the limestone substratum. This has been shown by a number of studies based on chemical and mineralogical similarities between limestone residues and the material of the Bohnerz deposits (Borger and Widdowson, 2001; Fach, 1908; Weiger, 1908). Since major constituent elements that make up the Bohnerz deposits, such as Fe and Al, are only present as traces in the limestone, the equivalent of many times the volume of the Bohnerz deposits has to be dissolved (Borger, 1990). Dissolution of about 100 m of limestone could have produced the several meters of Bolus clays which are observed today. Quartz grains found in many deposits of Bolus clay are detrital and derived from elsewhere,

because there are no quartz grains in the limestone (Borger, 1990).

We present evidence of tens of millions of years of continuous goethite precipitation in paleosols and fissure fillings since the Eocene. Paleosols of the Bohnerz deposits have evolved for a duration up to 30 Ma on the surface before being buried. Minimum cosmic-ray exposure durations for these paleosols are on the same timescale, around 8-10 Ma (Fig. 3.7). Fissure fillings consist of material precipitated over a span of up to 50 Ma (Fig. 3.4). This material might have been precipitated in a paleosol overlying the fissure or it might have precipitated inside of a fissure filling, possibly being translocated downward by successive deepening of the fissure. Most aliquots of goethite analyzed here have a high degree of Al substitution, which is a sign of great soil age (Fritsch et al., 2005).

This evidence demonstrates the long-lived nature of the Bohnerz deposits. Since they are closely associated with limestone substrates, we argue that they form from dissolution residua of the limestone and evolve in-situ as paleosols and fissure fillings. This is in contrast to Borger and Widdowson (2001), who argued that the Bohnerz deposits as a whole are allochthonous and the material is derived from a source other than the limestones.

After initiation of major chemical weathering in the early Eocene, mean annual temperatures dropped in the late Eocene. Central European mean annual temperature and mean annual precipitation were stable throughout latest Eocene-Pliocene times (Fig. 3.8). The sparsity of Eocene ages demonstrates vigorous dissolution-precipitation, during which iron was continuously cycled and older generations of goethite were dissolved. The preservation of many ages in the Oligocene indicates a decline in dissolution rate as a result of less favorable climatic conditions. A decline in paleosol ages in the Miocene can be explained by sampling bias, since most paleosols are covered by this time and some deposits are being tectonically deformed. Fissures provide a more constant record of goethite precipitation, which

continues steadily until about 2 Ma.

Erosion rates

Dissolution of at least tens of meters of limestone to form the Bohnerz deposits occurred over tens of millions of years. If assumed to be constant in time, this would equal erosion rates of 2-10 m/Ma. Dehm (1935) reports about 40 m of erosion since the late Eocene, based on the fossil ages of fissure fillings on different surfaces, attesting similarly low erosion rates. Cosmic-ray exposure of pisoliths in paleosols demonstrates that Bohnerz deposits remained at the surface for similar amounts of time. Formation of the Bohnerz deposits was shown to be more active in the Eocene, with a slow-down associated with a decline in temperatures. Post-Eocene erosion rates might therefore have been even lower. Fissures with fossil ages ranging from Eocene to Pliocene, such as those of Weißenburg (Rummel, 1993), have been found in close proximity (tens of meters), with each fissure having only fossils of a short age range. This further supports low amounts of surface lowering during this time.

Apparent exposure duration derived from ^{3}He concentrations of pisoliths in fissure fillings (Fig. 3.7) is at least 7 Ma. The ages of fossils in those fissure fillings constrain the time since the deposition of the material in the fissure to about 10-15 Ma. This constrains surface lowering to less than 1 m, with resultant erosion rates of around 0.1 m/Ma. Comparable erosion rates have been reported for thick lateritic duricrusts in Brazil (e.g. Monteiro et al., 2014; Monteiro et al., 2018). Limestone plateaux of Central Europe seem to be able to sustain similarly low erosion rates throughout their Cenozoic history.

3.6 Conclusions

Karstic weathering with accumulation of erosional lags from dissolution of the limestone substratum represents a widespread, continental-scale Cenozoic weathering

phenomenon in Central Europe. Bohnerz-type weathering was initiated around the Paleocene-Eocene Thermal Maximum, as shown by the oldest goethite (U-Th)/He ages reported here. This age is about 10 Ma older than the oldest fossil ages reported in published literature. Bohnerz pisoliths, as we find them today, are not remnants of Late Cretaceous-early Eocene weathering conditions, as was suggested by previous workers (e.g. Borger and Widdowson, 2001; Ufrecht, 2008), but formed between 55 Ma and 2 Ma. The youngest substratum of the Bohnerz deposits is upper Cretaceous. Any previous pre-Eocene weathering surface must have been eroded before the initiation of Bohnerz weathering.

During formation of Bohnerz deposits, red, clay-rich paleosols formed from weathering residue of limestones. Iron is fixed locally as goethite and the deposits of iron-rich clay mantle the limestone, increasing its erosional resistance. These landscapes are stable for tens of millions of years, as evidenced by the large span in ages represented in paleosols and fissure fillings as well as minimum exposure durations determined from measurements of ^{3}He concentrations. We found evidence of at least 7 Ma of cosmic-ray exposure for fissures fillings in the Swabian Alb, demonstrating extremely low post-depositional erosion rates.

The hiatus represented by the unconformity between deposition of the limestone substratum and the cover strata is 50-240 Ma, but mostly 100-150 Ma. For localities in this study, of the 125-150 Ma hiatus, only about 50 Ma are recorded in iron-oxide precipitation, which represents 30-40% of the total duration. However, the Bohnerz deposits provide a record of a significant part of Paleogene and Neogene history, which would otherwise be lost. Despite their scattered and discontinuous nature, the Bohnerz deposits as a whole provide a unique, continuous record of Central European continental weathering from the early Eocene to Quaternary. They are a potential target for goethite stable isotope studies to assess long-term continental climate trends in Central Europe.

References

Achenbach, A. (1859) "Ueber Bohnerze auf dem südwestlichen Plateau der Alp" in: *Jahreshefte des Vereins für vaterländische Naturkunde in Württemberg* 15, pp. 103–125.

Agustı, J., L. Cabrera, M. Garcés, W. Krijgsman, O. Oms, and J. Parés (2001) "A calibrated mammal scale for the Neogene of Western Europe. State of the art" in: *Earth-Science Reviews* 52.4, pp. 247–260 DOI: 10.1016/S0012-8252(00)00025-8.

Aubert, D. and L. Le Ribault (1974) "Quartz du pied du Jura" in: *Bulletin de la Société vaudoise des sciences naturelles* 72, pp. 231–240.

Bartz, J. (1940) "Die Bohnerzablagerungen in Rheinhessen und ihre Entstehung" in: *Archiv für Lagerstättenforschung der Preußischen Geologischen Landesanstalt* 72, pp. 1–57.

Baumberger, E. (1923) "Die Eisen-und Manganerze der Schweiz. 1. Teil: Bohnerz" in: *Beiträge zur geologischen Karte der Schweiz, geotechnische Serie* 13, pp. 1–150.

Beauvais, A., G. Ruffet, O. Hénocque, and F. Colin (2008) "Chemical and physical erosion rhythms of the West African Cenozoic morphogenesis: The ^{39}Ar-^{40}Ar dating of supergene K-Mn oxides" in: *Journal of Geophysical Research: Earth Surface* 113.F4.

Becker, D., G. Rauber, and L. Scherler (2013) "New small mammal fauna of late Middle Eocene age from a fissure filling at La Verrerie de Roches (Jura, NW Switzerland)" in: *Revue de Paléobiologie* 32.2, pp. 433–446.

Berger, K. (1971) *Erläuterungen zur geologischen Karte von Bayern 1:25000, Blatt Nr. 6831 Spalt* Bayerisches Geologisches Landesamt, München, p. 212.

Birchmeier, C. (1986) *Bohnerzbergbau im Südranden, Neujahrsblatt der Naturforschenden Gesellschaft Schaffhausen 38* 1st ed. Thayngen-Schaffhausen: Naturforschende Gesellschaft Schaffhausen, p. 80.

Bloos, G. (1967) "Über Jura und Tertiär im Gebiet von Ehingen/Donau (Baden-Württemberg)" in: *Jahresberichte und Mitteilungen des Oberrheinischen Geologischen Vereins* 49, pp. 75–115.

Bolliger, T. and M. Rummel (1994) "Säugetierfunde aus Karstspalten–Die komplexe Genese am Beispiel eines Steinbruches bei Petersbuch, Südliche Frankenalb (Bayern)" in: *Mitteilungen der Bayerischen Staatssammlung für Paläontologie und historische Geologie* 34, pp. 239–264.

Borger, H. (1990) "Bohnerze und Quarzsande als Indikatoren paläogeographischer Verwitterungsprozesse und der Altreliefgenese östlich von Albstadt (Schwäbische Alb)." in: *Kölner Geographische Arbeiten* 52, p. 209.

Borger, H. and M. Widdowson (June 2001) "Indian laterites, and lateritious residues of southern Germany: a petrographic, mineralogical, and geochemical comparison" in: *Zeitschrift für Geomorphologie* 45.2, pp. 177–200.

Dehm, R. (1935) "Über tertiäre Spaltenfüllungen im Fränkischen und Schwäbischen Jura" in: *Abhandlungen der Bayerischen Akademie der Wissenschaften Mathematisch-naturwissenschaftliche Abteilung Neue Folge* 29, pp. 1–91.

Epprecht, W. (1957) "Unbekannte schweizerische Eisenerzgruben sowie Inventar und Karte aller Eisen- und Manganerz-Vorkommen der Schweiz" in: *Schweizerische mineralogische und petrographische Mitteilungen* 37, pp. 217–246.

Fach, B. (1908) "Chemische Untersuchungen über Roterden und Bohnerztone" PhD thesis Universität Freiburg i. B., p. 31.

Farley, K. A. (2002) "(U-Th)/He Dating: Techniques, Calibrations, and Applications" in: *Reviews in Mineralogy and Geochemistry* 47.1, pp. 819–844 DOI: 10.2138/rmg.2002.47.18.

Fritsch, E., G. Morin, A. Bedidi, D. Bonnin, E. Balan, S. Caquineau, and G. Calas (2005) "Transformation of haematite and Al-poor goethite to Al-rich goethite and associated yellowing in a ferralitic clay soil profile of the middle Amazon basin (Manaus, Brazil)" in: *European Journal of Soil Science* 56.5, pp. 575–588 DOI: 10.1111/j.1365-2389.2005.00693.x.

Gall, H. (1971) "Geologische Karte von Bayern 1:25000, Erläuterungen zum Blatt 7328 Wittislingen" in: *Bayerisches Geologisches Landesamt*, p. 186.

Gassmann, G. and A. Schäfer (2018) *Luxemburger Eisen: Montanarchäologische Untersuchungen zur frühen Eisenproduktion im Umland des Titelbergs in Südwestluxemburg* vol. 6 University of Bamberg Press, p. 108.

Hansen, J., M. Sato, G. Russell, and P. Kharecha (2013) "Climate sensitivity, sea level and atmospheric carbon dioxide" in: *Philosophical Transactions of the Royal Society A: Mathematical, Physical and Engineering Sciences* 371, pp. 1–31 DOI: 10.1098/rsta.2012.0294.

Heissig, K. (1978) "Fossilführende Spaltenfüllungen Süddeutschlands und die Ökologie ihrer oligozänen Huftiere" in: *Mitteilungen der Bayerischen Staatssammlung für Paläontologie und Historische Geologie* 18, pp. 237–288.

Hofmann, F., B. Reichenbacher, and K. A. Farley (2017) "Evidence for >5 Ma paleoexposure of an Eocene–Miocene paleosol of the Bohnerz Formation, Switzerland" in: *Earth and Planetary Science Letters* 465, pp. 168–175.

Jäger, G. (1835) *Über die fossilen Säugetiere welche in Würtemberg in verschiedenen Formationen aufgefunden worden sind, nebst geognostischen Bemerkungen über diese Formationen* C. Erhard Verlag, Stuttgart, 212 pp., p. 212.

Lal, D. (1991) "Cosmic ray labeling of erosion surfaces: in situ nuclide production rates and erosion models" in: *Earth and Planetary Science Letters* 104.2-4, pp. 424–439 DOI: 10.1016/0012-821X(91)90220-C.

Lang, R. (1914) "Geologisch-mineralogische Beobachtungen in Indien – 3. Rezente Bohnerzbildung auf Laterit. Entstehung fossiler Bohnerze" in: *Centralblatt für Mineralogie, Geologie und Paläontologie* 21, pp. 641–653.

Lippolt, H. J., T. Brander, and N. R. Mankopf (1998) "An attempt to determine formation ages of goethites and limonites by (U+Th)-He-4 dating" in: *Neues Jahrbuch für Mineralogie-Monatshefte* 11, pp. 505–528.

Mein, P. (1975) "Resultats du groupe de travail des vertebres: biozonation du Neogene mediterraneen partir des mammiferes" in: *Report on Activity of the RCMNS Working Groups (1971-1975)* ed. by J. Senes Bratislava, pp. 78–81.

Menkveld-Gfeller, U., O. Kempf, and H. Funk (2016) "Lithostratigraphic units of the Helvetic Palaeogene: review, new definition, new classification" in: *Swiss Journal of Geosciences* 109.2, pp. 171–199 DOI: 10.1007/s00015-016-0217-4.

Monteiro, H. S., P. M. Vasconcelos, K. A. Farley, C. A. Spier, and C. L. Mello (2014) "(U–Th)/He geochronology of goethite and the origin and evolution of cangas" in: *Geochimica et Cosmochimica Acta* 131, pp. 267–289 DOI: 10.1016/j.gca.2014.01.036.

Monteiro, H., P. Vasconcelos, K. Farley, and C. Lopes (2018) "Age and evolution of diachronous erosion surfaces in the Amazon: Combining (U-Th)/He and cosmogenic ^{3}He records" in: *Geochimica et Cosmochimica Acta* 229, pp. 162–183 DOI: 10.1016/j.gca.2018.02.045.

Mosbrugger, V., T. Utescher, and D. L. Dilcher (2005) "Cenozoic continental climatic evolution of Central Europe" in: *Proceedings of the National Academy of Sciences of the United States of America* 102.42, pp. 14964–14969 DOI: 10.1073/pnas.0505267102.

Pirkenseer, C., G. Rauber, and S. Rousse (2018) "A revised Palaeogene lithostratigraphic framework for the Northern Swiss Jura and the Southern Upper Rhine Graben and its relationship to the North Alpine Foreland Basin" in: *Rivista Italiana di Paleontologia e Stratigrafia* 124.1.

Retallack, G. J. (2010) "Lateritization and bauxitization events" in: *Economic Geology* 105.3, pp. 655–667.

Ricordel-Prognon, C., F. Lagroix, M.-G. Moreau, and M. Thiry (2010) "Lateritic paleoweathering profiles in French Massif Central: paleomagnetic datings" in: *Journal of Geophysical Research: Solid Earth* 115.B10104, pp. 1–19 DOI: 10.1029/2010JB007419.

Rollier, L. (1905) "Die Bohnerzformation oder das Bohnerz und seine Entstehungsweise" in: *Vierteljahrsschrift der natforschenden Gesellschaft Zürich* 50, p. 151.

– (1910) "Nouvelles observations sur le Sidérolithique et la Molasse oligocène du Jura central et septentrional" in: *Beitrage zur geologischen Karte der Schweiz* 25, pp. 1–230.

Rosina, V. V. and M. Rummel (2012) “The bats (Chiroptera, Mammalia) from the Early Miocene of Petersbuch (Bavaria, Southern Germany)” in: *Geobios* 45.5, pp. 463–478.

Rummel, M. (1993) “Neue fossilführende Karstfüllungen der Schwäbisch-Fränkischen Alb” in: *Documenta naturae* 79, pp. 1–32.

Rutte, E. (1953) “Der fossile Karst der südbadischen Vorbergzone” in: *Jahresberichte und Mitteilungen des Oberrheinischen Geologischen Vereins* Neue Folge 33, pp. 1–43.

Sadler, P. M. (1981) “Sediment Accumulation Rates and the Completeness of Stratigraphic Sections” in: *The Journal of Geology* 89.5, pp. 569–584 DOI: 10.1086/628623.

Scheuchzer, J. J. (1707) *Beschreibung der Natur-Geschichten des Schweizerlands Erster-Dritter Theil* Michael Schaufelberger und Christoff Hardmeier, p. 188.

Schmidt-Kittler, N., M. Brunet, M. Godinot, J. Franzen, J. Hooker, S. Legendre, et al. (1987) “European reference levels and correlation tables” in: *Münchner Geowissenschaftliche Abhandlungen A* 10, pp. 15–31.

Schmidt, K. (1941) “Über bohnerzführendes Tertiär und Diluvium im Kraichgau” in: *Jahresberichte und Mitteilungen des Oberrheinischen Geologischen Vereins* 30, pp. 48–91.

Schwertmann, U. (1988) “Occurrence and formation of iron oxides in various pedoenvironments” in: *Iron in soils and clay minerals* Springer, pp. 267–308.

Shuster, D. L., K. A. Farley, P. M. Vasconcelos, G. Balco, H. S. Monteiro, K. Waltenberg, and J. O. Stone (2012) “Cosmogenic ^{3}He in hematite and goethite from Brazilian "canga" duricrust demonstrates the extreme stability of these surfaces” in: *Earth and Planetary Science Letters* 329-330, pp. 41–50 DOI: 10.1016/j.epsl.2012.02.017.

Shuster, D. L., P. M. Vasconcelos, J. A. Heim, and K. A. Farley (2005) “Weathering geochronology by (U–Th)/He dating of goethite” in: *Geochimica et Cosmochimica Acta* 69.3, pp. 659–673.

Tavel, H. von (1936) “Stratigraphie der Balmhorngruppe: mit Einschluss des Gemmipasses (Berner Oberland)” in: *Mitteilungen der naturforschenden Gesellschaft Bern* 1936, pp. 43–120.

Ufrecht, W. (2008) “Evaluating landscape development and karstification of the Central Schwäbische Alb (Southwest Germany) by fossil record of karst fillings” in: *Zeitschrift für Geomorphologie* 52.4, pp. 417–436.

Vasconcelos, P. M., J. A. Heim, K. A. Farley, H. Monteiro, and K. Waltenberg (2013) “^{40}Ar/^{39}Ar and (U–Th)/He–^{4}He/^{3}He geochronology of landscape evolution and channel iron deposit genesis at Lynn Peak, Western Australia” in: *Geochimica et Cosmochimica Acta* 117, pp. 283–312.

Volz, E. (1957) "Geologische Ergebnisse neuerer Erdölbohrungen in Oberschwaben" PhD thesis Technische Hochschule Stuttgart, p. 73.

Weidmann, M. (1984) "Paléokarst éocène dans l'autochtone chablaisien (VS et VD)" in: *Bulletin de la Murithienne* 102, pp. 119–128.

Weiger, K. (1908) "Beiträge zur Kenntnis der Spaltenausfüllungen im weissen Jura auf der Tübinger, Uracher und Kirchheimer Alb" in: *Jahreshefte des Vereins für vaterländische Naturkunde in Württemberg* 64, pp. 187–248.

Wieland, B. (1979) "Zur Diagenese und schwachen Metamorphose eozäner siderolithischer Gesteine des Helvetikums" in: *Schweizerische Mineralogische und Petrographische Mitteilungen* 59, pp. 41–60.

APPENDIX

3.A SEM images of pisoliths

We obtained images of cut and polished pisoliths using a Scanning Electron Microscope (SEM). We also used Energy Dispersive X-Ray Spectroscopy (EDS) to collect data on elemental compositions of samples on points, linear profiles, and maps. We found that pisoliths are mostly of segregated into a fine-grained, clay-rich nucleus and a cortex of mostly pure goethite (e.g. Fig. 3.9). The nucleus is often composed of ferruginized clay minerals and has mineral inclusions. Some nuclei contain cracks, which have pure goethite at the crack interface, with progressively smaller amounts of ferruginization with distance from the crack (Fig. 3.10). The cortex often shows tens of layers of 10-50 μm thickness (Fig. 3.10). The structure of some pisoliths records a complex history of removal and addition of material (see Fig. 3.13).

Goethite is present in the form of plates with thicknesses generally below 1 μm and often <0.1 μm (see Figs. 3.9, 3.12). Some pisoliths are unlayered and appear homogeneous in their elemental composition (Fig. 3.14). A small number of pisoliths appears fully formed in their nucleus-cortex structure, but are mostly composed of kaolinitic clays with varying amounts of ferruginization (Fig. 3.15). Their color is much lighter and more greyish than goethite pisoliths. These pisoliths were not used for (U-Th)/He measurements.

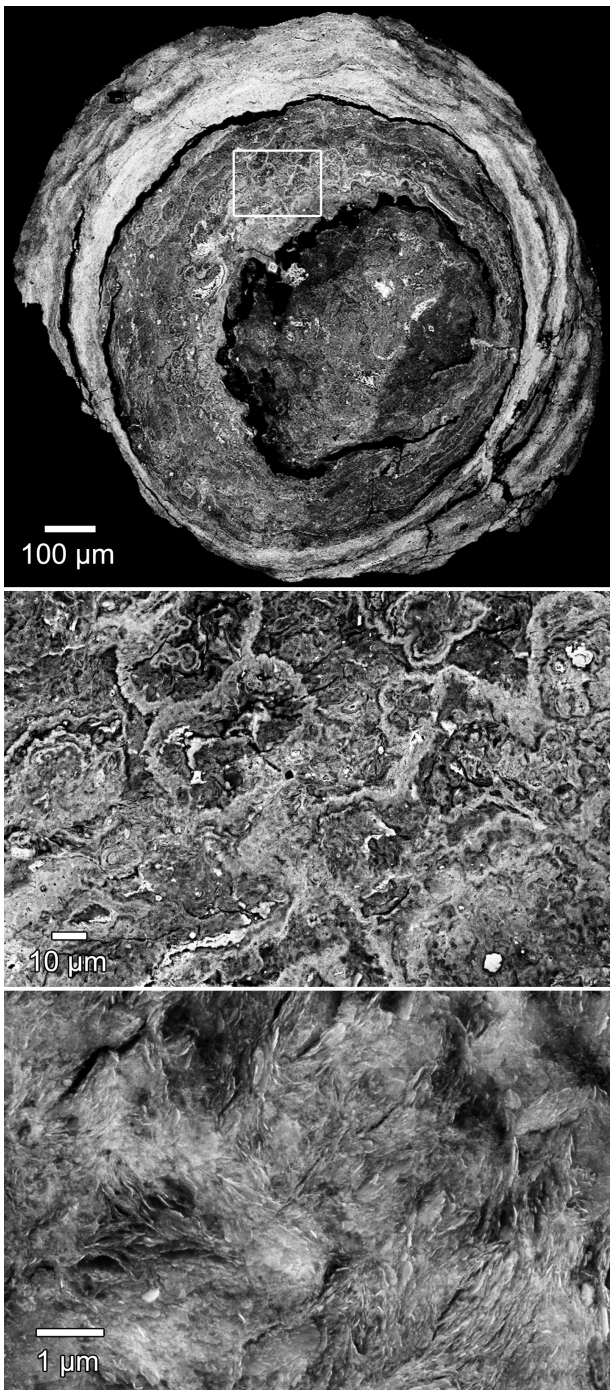

Figure 3.9: SEM images of goethite pisolith W21b from Weißenburg at different magnifications. Darker zones have higher fractions of Al and Si relative to Fe, indicating higher degree of Al-substitution. The pisolith is composed of plates of goethite with thicknesses of <0.1 µm. White box indicates location of detailed view below.

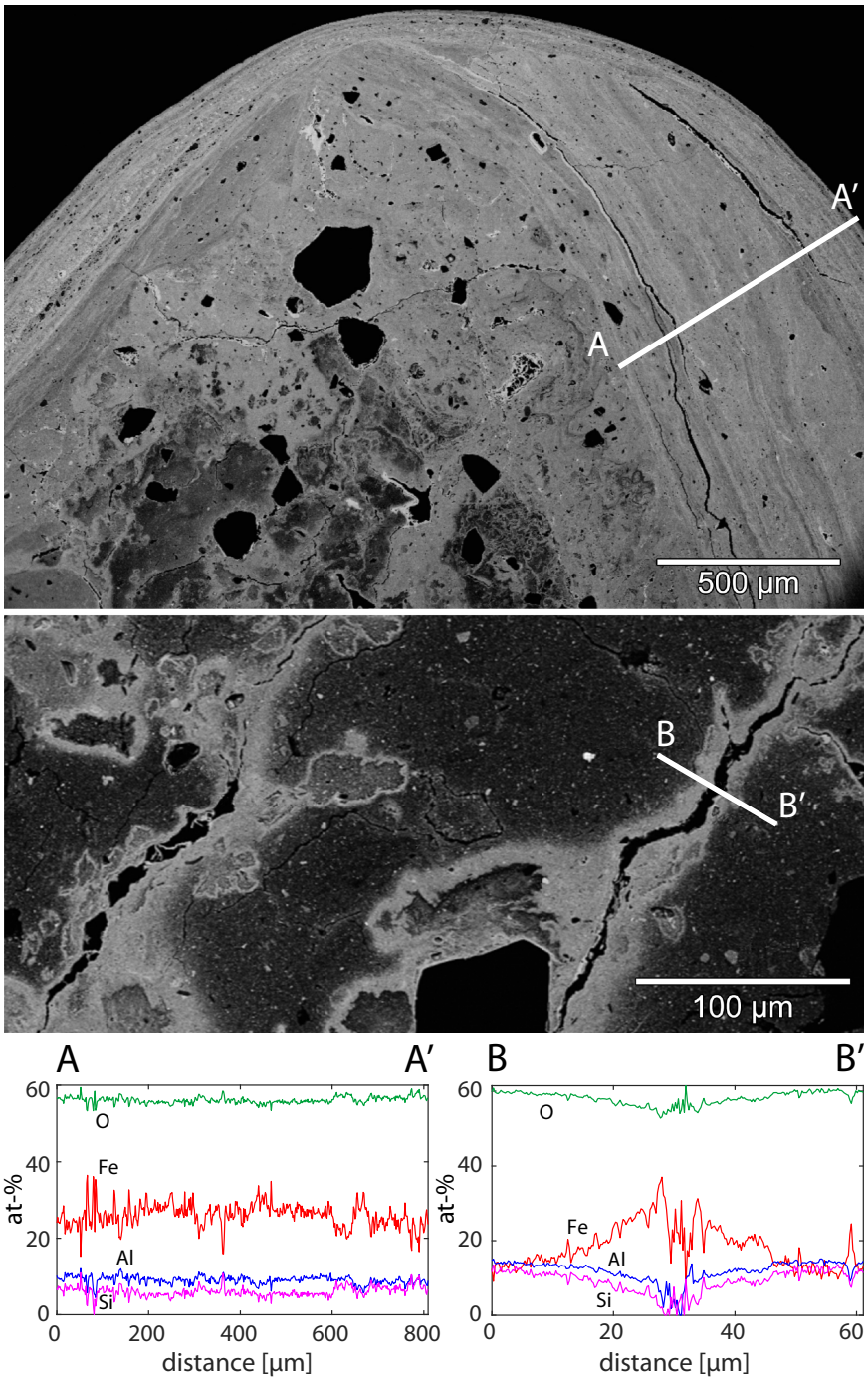

Figure 3.10: SEM image of pisolith P62A from Peterbuch showing a layered cortex and a fine-grained nucleus with mineral inclusions. Elemental profile of the cortex (A-A') reveals a homogeneous goethite composition with Al and Si substituting for Fe. The nucleus is composed of partially ferruginized kaolinitic clay. The area around cracks in the nucleus (B-B') contains pure iron-oxide. The amount of ferruginization decreases with distance to the crack and attains a constant background value about 25-30 µm from the crack.

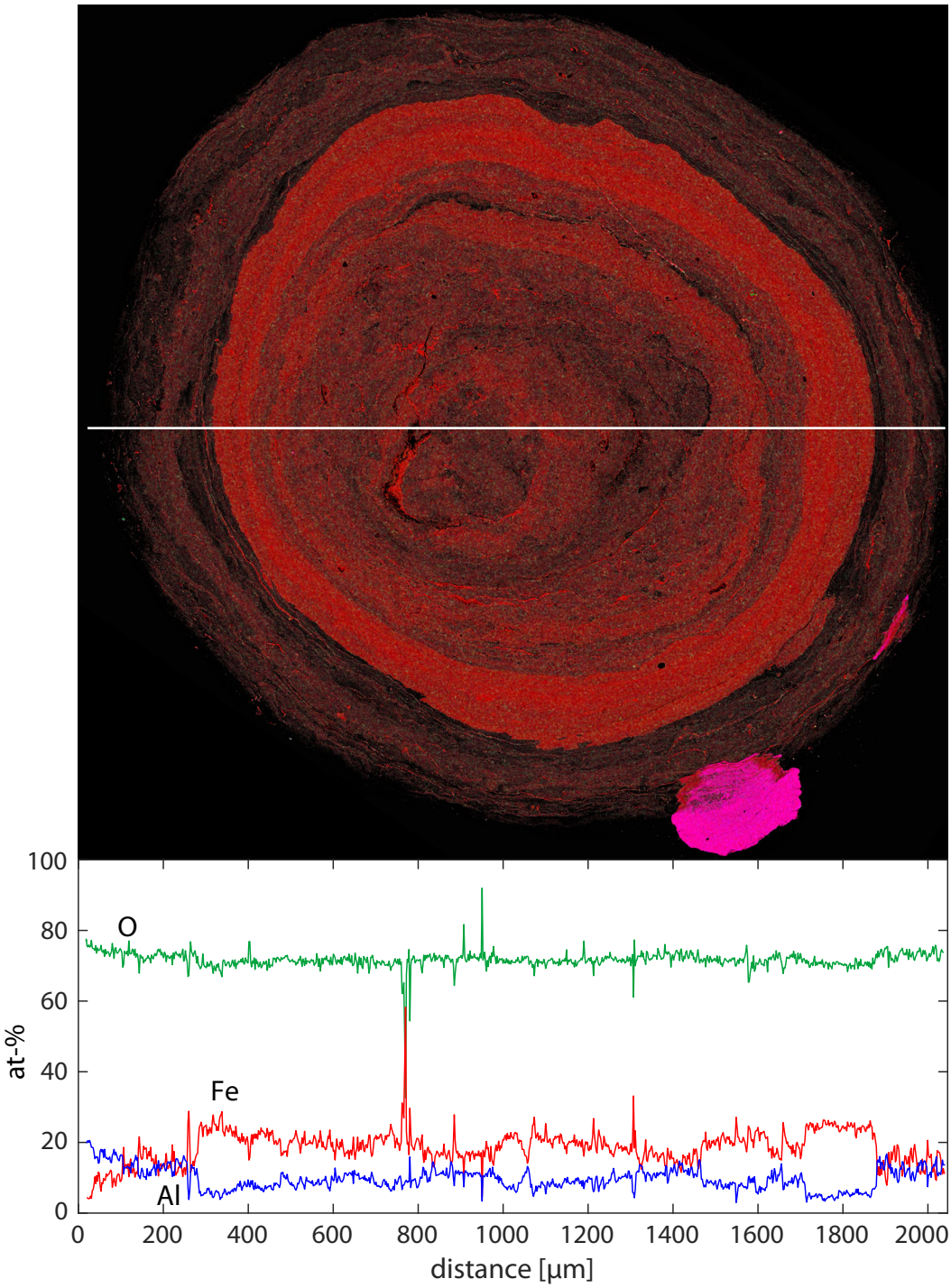

Figure 3.11: SEM image of pisolith Lohn-3m-cut1 from outcrop Lohn am Randen with elemental profile obtained by EDS. Red color indicates Fe-content, magenta shows region of high S content (sulfate or sulfide inclusion). This pisolith contains a varying fraction of clay minerals, as indicated by high Al-content, often in excess of what would be expected even for full Al-substitution for Fe in goethite. Some layers of the cortex are composed mostly of goethite.

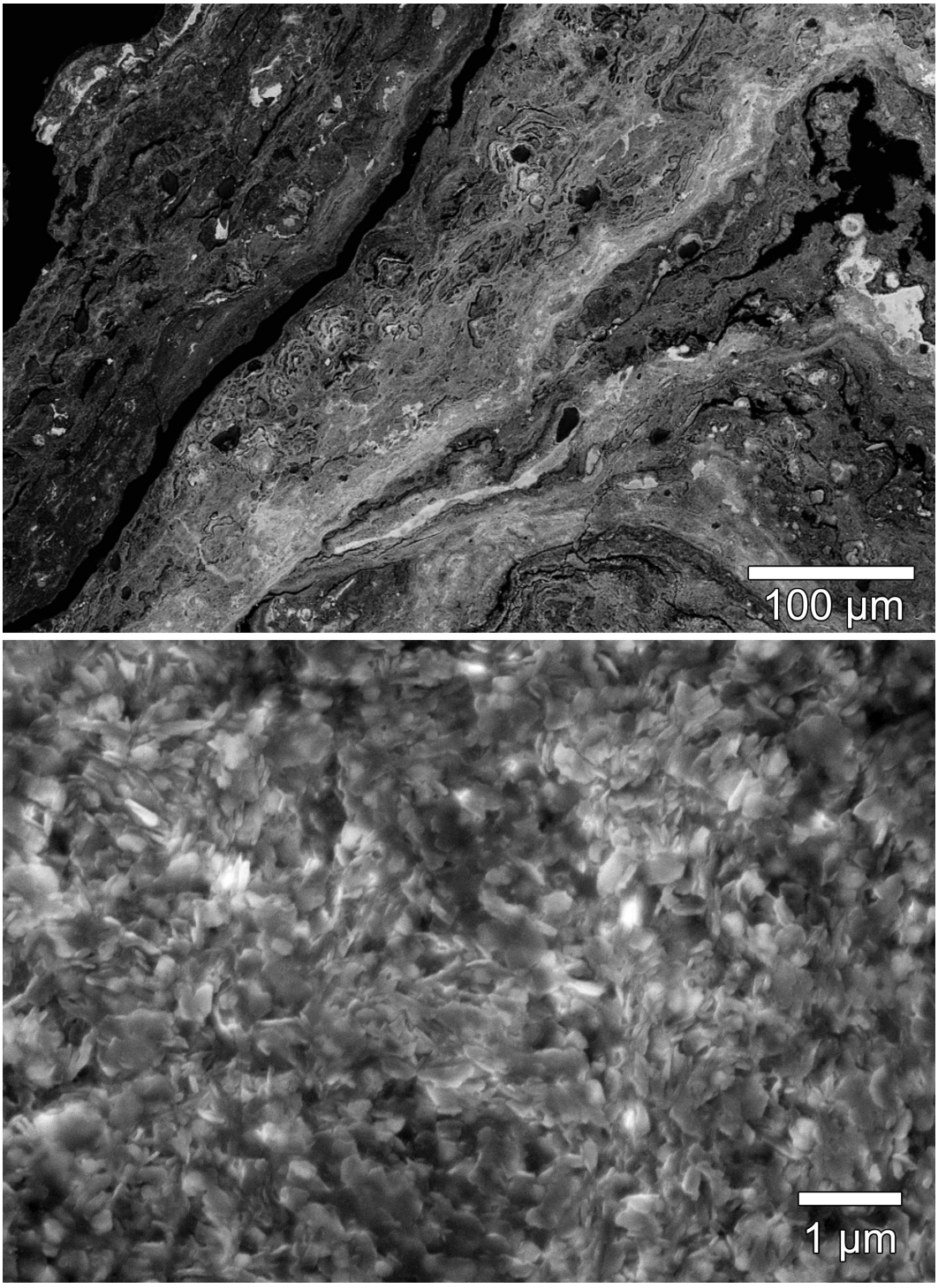

Figure 3.12: SEM images of pisoliths R16d (top) from Rothenstein and L250cut1 (bottom) from Lohn am Randen. These images demonstrate the fine-grained nature of the goethite in the cortex, which is present in the form of plates of 0.1-0.5 µm diameter and <0.1 µm thickness.

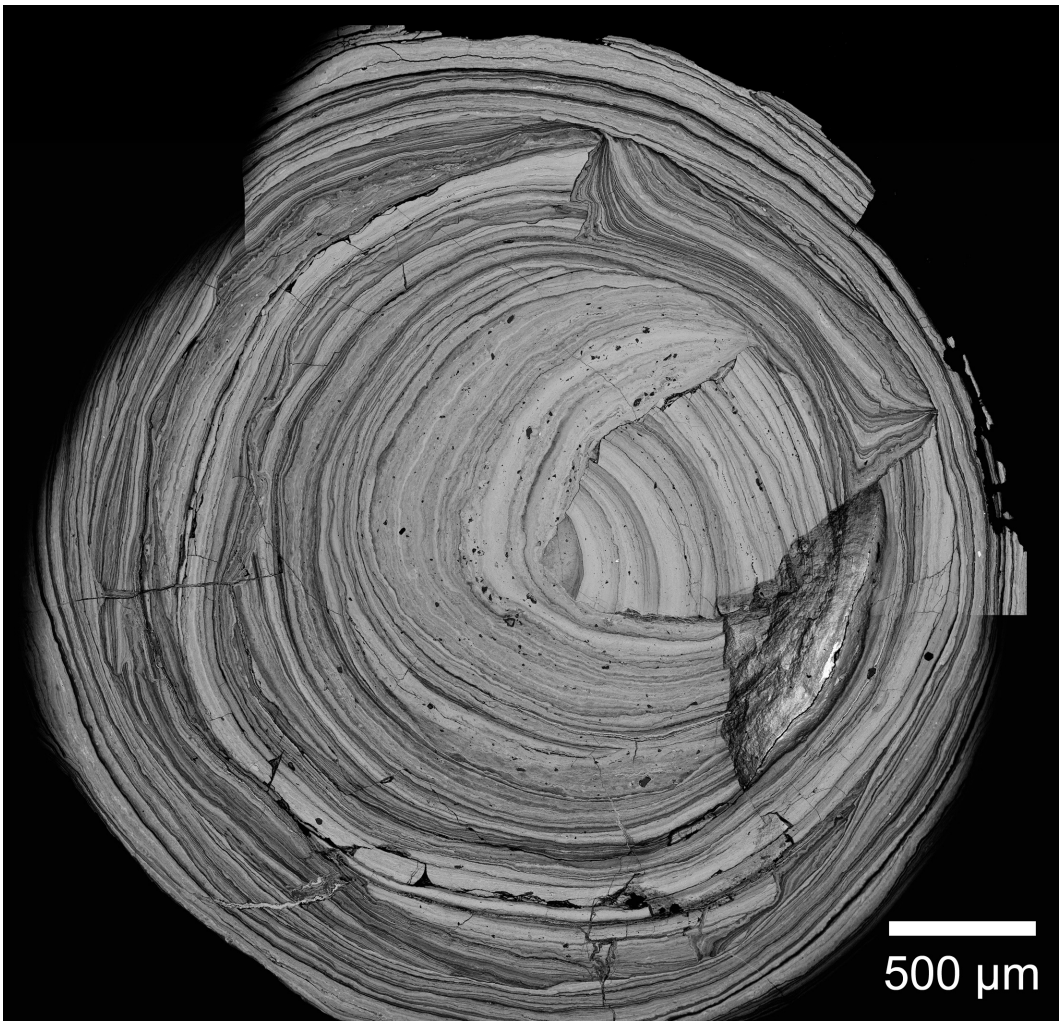

Figure 3.13: Composite of two SEM images of a pisolith from Oberdorf highlighting the complex history represented in some pisoliths. The nucleus is formed by a broken piece of cortex from a different pisolith. The cortex shows complex layering, with multiple episodes of mechanical abrasion or chemical resorption of goethite, alternating with unconformable deposition of thin layers of goethite. A light micrograph of this pisolith can be found in Fig. 3.2.

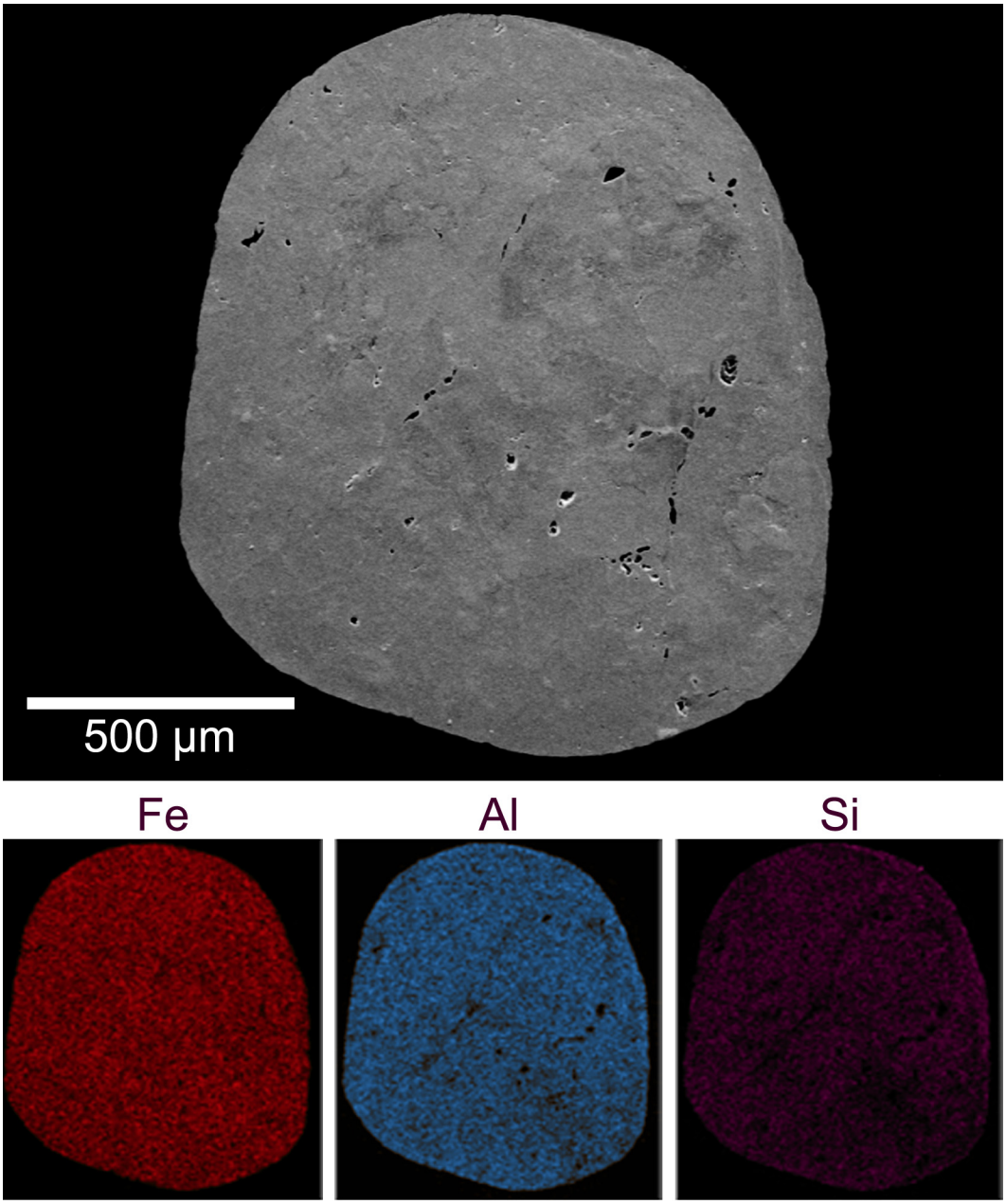

Figure 3.14: Example of an unlayered pisolith, showing SEM image of pisolith R16c from Rothenstein and EDS elemental maps of Fe, Al, and Si. This pisolith has a homogeneous goethitic composition with constant amounts of substitution of Al (25%) and Si (5%) for Fe.

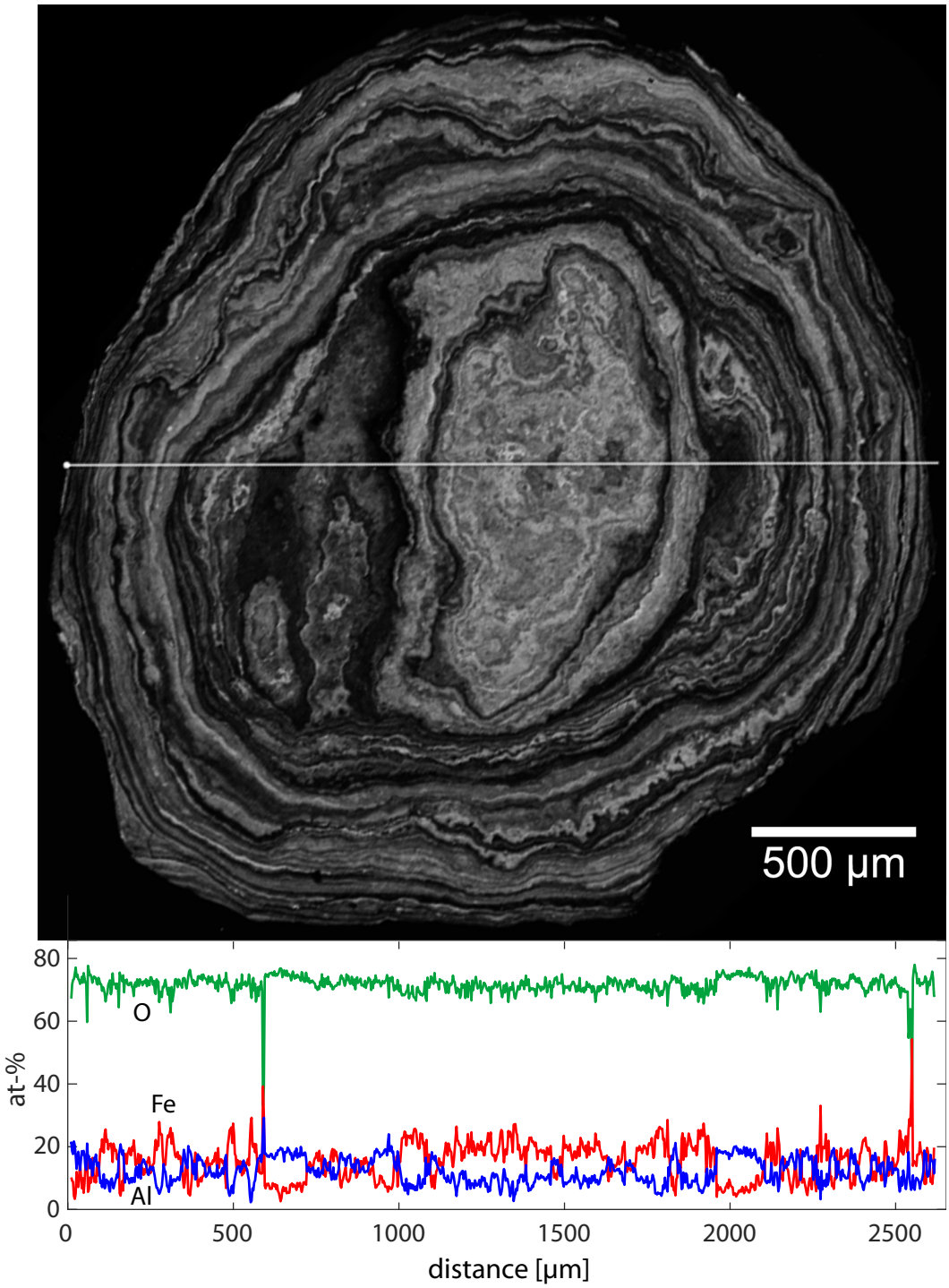

Figure 3.15: SEM image and EDS elemental profile of a pisolith from outcrop Oberbuchsiten. The structure of this pisolith is similar to that of other pisoliths described here, with a nucleus-cortex dichotomy. However, the composition is dominated by kaolinite with partial ferruginization. Samples like these have a lighter greyish color and were not used for (U-Th)/He analysis. All pisoliths from this outcrop had this appearance and they did not yield any datable material.

3.B Bohnerz (U-Th)/He ages

Given here is the essential data for all (U-Th)/He ages of pisoliths from outcrops Aufberg, Bohnerzgruben Erpfingen-Sonnenbühl (BES), Balsthal Erzmatt I (BI) and II (BII), Cholplatz (C), Malsenhof, Mervelier, Oberdorf (O), Petersbuch (P), Rothenstein (R), Willmandingen, and Weißenburg (W).

Table 3.1: (U-Th)/He ages of Bohnerz samples. goe = goethite mass, BES = Bohnerzgruben Erpfingen-Sonnenbühl

Aufberg												
Sample name	(U-Th-Sm)/He [Ma]		goe [ug]	1σ	U [ppm]	1σ	Th [ppm]	1σ	Sm [ppm]	1σ	He [nmol/g]	1σ
Aufberg-0-1b	36.5	0.5	10.05	0.05	2.87	0.03	58.60	0.57	26.00	1.12	3.31	0.69
Aufberg-0-1c	21.7	0.3	9.70	0.05	4.51	0.05	100.98	0.86	45.75	1.97	3.34	0.48
Aufberg-0-1d	38.3	0.4	23.10	0.11	2.96	0.02	48.69	0.40	54.10	2.33	3.00	0.34
Aufberg-0-1e	21.9	0.2	8.18	0.04	4.16	0.04	135.46	1.05	73.30	3.15	4.30	0.70
Aufberg-0-1f	24.5	0.3	10.66	0.05	3.10	0.04	96.15	0.82	97.95	4.21	3.42	0.58
Aufberg-0-1i	18.1	0.2	7.27	0.04	4.97	0.04	158.33	1.43	113.99	4.90	4.16	0.60
Aufberg-0-1j	23.9	0.3	23.25	0.12	5.32	0.04	196.13	1.72	74.67	3.21	6.69	0.57
Aufberg-0-2a	24.8	1.4	23.69	0.26	4.36	0.07	106.18	3.66	82.36	2.68	3.97	0.26
Aufberg-0-2b	22.0	0.2	13.99	0.13	4.37	0.08	195.08	2.02	87.05	3.86	6.04	0.59
Aufberg-0-2c	28.2	1.6	14.25	0.19	3.19	0.06	113.24	4.02	87.36	2.98	4.59	0.31
Aufberg-0-2d	34.1	0.3	12.69	0.10	3.61	0.08	154.19	1.50	95.97	4.29	7.42	0.66
Aufberg-20-1a	19.6	0.2	19.32	0.10	7.41	0.05	264.71	2.09	139.81	6.01	7.43	0.68
Aufberg-20-1b	21.3	0.2	18.20	0.09	5.97	0.04	247.72	1.96	129.81	5.58	7.44	0.88
Aufberg-20-1c	19.6	0.3	7.14	0.05	3.40	0.05	131.36	1.30	69.25	2.98	3.66	0.51
Aufberg-20-1d	21.4	0.3	8.65	0.04	4.40	0.05	116.41	1.09	42.22	1.82	3.71	0.53
Aufberg-20-2a	32.7	0.4	26.24	0.47	1.66	0.04	16.79	0.32	29.26	1.82	1.00	0.06
Aufberg-20-2b	28.3	0.2	48.76	0.63	1.88	0.03	22.92	0.31	36.54	2.29	1.12	0.08
Aufberg-20-2c	20.8	0.3	44.89	0.76	2.03	0.04	32.89	0.61	34.81	2.21	1.11	0.05
Aufberg-30-1a	8.6	0.1	9.45	0.07	3.32	0.05	120.42	1.14	84.33	3.42	1.48	0.27
Aufberg-30-1b	6.5	0.4	8.97	0.11	5.21	0.09	110.35	4.64	112.87	3.97	1.10	0.15
Aufberg-30-1c	6.6	0.5	9.25	0.10	2.49	0.07	100.53	4.17	94.00	3.79	0.94	0.12
Aufberg-30-2a	9.4	0.1	17.58	0.12	6.45	0.07	33.21	0.34	30.58	1.75	0.73	0.12
Aufberg-30-2b	16.4	1.0	7.59	0.08	3.61	0.07	30.06	1.32	39.65	1.71	0.96	0.18
Aufberg-30-2c	26.0	0.3	20.29	0.16	3.03	0.04	38.00	0.41	41.03	1.66	1.70	0.20
Aufberg-30-2d	21.2	1.2	5.62	0.08	4.17	0.10	98.37	3.48	74.51	3.11	3.16	0.25
Aufberg-30-2e	23.0	0.2	8.30	0.07	9.15	0.10	135.83	1.34	202.04	7.59	5.16	0.58
Aufberg-30-2f	23.0	0.2	16.65	0.26	8.70	0.15	226.70	3.81	187.74	8.62	7.79	0.29
Aufberg-40-1a	22.4	1.3	207.80	4.07	0.18	0.00	2.74	0.11	2.11	0.10	0.10	0.01
Aufberg-40-1b	23.1	0.2	21.84	0.17	3.50	0.05	109.90	1.06	69.64	2.65	3.70	0.48
Aufberg-40-1c	16.1	0.3	3.20	0.03	8.50	0.21	119.21	1.57	54.55	2.50	3.20	0.56
Aufberg-40-1d	23.5	1.6	4.44	0.06	3.14	0.09	75.13	3.18	75.68	3.29	2.67	0.27
Aufberg-40-1e	21.6	0.3	15.49	0.16	5.21	0.08	47.27	0.57	48.82	2.17	1.93	0.19
Aufberg-40-2a	13.9	0.6	28.47	0.34	8.70	0.12	58.78	1.97	93.19	3.30	1.71	0.13
Aufberg-40-2b	11.4	0.1	22.96	0.16	7.17	0.07	78.99	0.82	56.59	2.92	1.60	0.16
Aufberg-40-2c	24.1	1.3	3.22	0.04	7.71	0.16	57.32	2.53	82.69	3.83	2.79	0.33
Aufberg-80-1a	29.3	0.3	38.22	0.35	6.29	0.07	34.96	0.40	49.64	1.94	2.32	0.19
Aufberg-80-1b	26.0	0.3	33.50	0.26	7.25	0.08	75.44	0.79	96.73	4.71	3.55	0.28
Aufberg-80-1c	19.0	0.3	15.85	0.14	5.28	0.09	68.23	0.81	71.60	3.07	2.22	0.20
Aufberg-80-1d	32.1	0.3	61.19	0.51	5.64	0.07	36.54	0.34	61.15	2.31	2.50	0.27
Aufberg-80-2a	21.5	1.5	18.75	0.19	3.54	0.06	74.46	3.07	57.31	1.87	2.47	0.18
Aufberg-80-2b	26.0	2.1	34.96	0.41	6.45	0.09	129.32	6.23	101.07	3.23	5.23	0.26
Aufberg-80-2c	27.7	1.5	30.41	0.33	4.87	0.07	78.41	2.70	58.14	1.84	3.52	0.29
Aufberg-80-2d	27.0	1.4	20.81	0.23	3.22	0.04	58.71	2.03	51.29	2.17	2.51	0.20
Aufberg-80-2e	23.1	1.2	6.95	0.09	3.90	0.07	47.03	1.67	40.92	1.76	1.89	0.21

Table 3.2: (U-Th)/He ages of Bohnerz samples, continued. goe = goethite mass, BES = Bohnerzgruben Erpfingen-Sonnenbühl, BH = Balsthal Holzfluh

Bohnerzgruben Erpfingen-Sonnenbühl (BES)												
Sample name	(U-Th-Sm)/He [Ma]		goe [ug]	1σ	U [ppm]	1σ	Th [ppm]	1σ	Sm [ppm]	1σ	He [nmol/g]	1σ
BES-1a	25.8	0.4	23.46	0.12	4.00	0.04	117.46	1.18	not measured		4.43	0.46
BES-1d	26.3	0.3	16.80	0.09	7.63	0.05	173.55	1.37	not measured		6.95	0.69
BES-2a	26.8	9.8	14.33	4.75	2.94	0.98	60.65	37.85	55.31	31.68	2.52	0.01
BES-2b	21.4	0.6	7.98	0.24	2.81	0.11	70.59	2.37	54.61	3.67	2.27	0.08
BES-2c	19.9	0.5	8.82	0.40	3.41	0.21	91.29	4.31	55.39	5.55	2.70	0.08
BES-2d	20.6	0.5	13.55	1.13	3.03	0.26	92.91	7.85	46.27	5.93	2.80	0.04
BES-2e	20.3	0.5	10.23	0.55	3.97	0.22	95.99	5.32	57.12	7.80	2.94	0.05
BES-2f	13.7	0.7	3.32	0.32	2.49	0.29	66.11	6.73	67.93	8.43	1.35	0.04
BES-2g	25.9	0.5	38.75	1.16	3.23	0.11	71.47	2.32	44.27	2.56	2.83	0.06
BES-2h	22.3	0.5	24.70	1.22	3.38	0.17	73.44	3.75	46.17	3.47	2.51	0.03
BES-2i	17.5	0.5	3.44	0.44	4.76	0.62	82.36	10.57	81.07	11.78	2.30	0.04
BES-2k	14.1	0.5	8.66	0.57	5.93	0.40	185.03	12.70	116.32	10.83	3.81	0.04
BES-2l	21.7	0.7	3.28	0.38	5.20	0.63	151.29	17.92	97.01	14.12	4.82	0.06
BES-2m	23.5	0.5	6.07	0.29	4.34	0.24	118.13	5.84	69.27	6.05	4.12	0.08
BES-3a	37.2	0.4	34.98	0.34	4.16	0.06	30.40	0.35	72.47	4.80	2.31	0.20
BES-3b	20.5	0.2	31.25	1.14	4.05	0.15	30.00	1.12	72.21	5.48	1.25	0.03
BES-3c	17.4	0.3	7.38	0.08	5.06	0.09	47.61	0.66	60.12	3.94	1.54	0.19
BES-3d	34.6	0.5	22.19	0.23	2.54	0.06	22.97	0.27	46.96	2.33	1.51	0.23
BES-3e	13.3	0.2	15.87	0.14	3.15	0.06	48.43	0.54	40.18	2.82	1.05	0.13
BES-4a	46.1	0.5	22.45	0.16	8.89	0.10	174.91	1.70	138.82	6.31	12.60	1.48
BES-4b	18.1	0.1	24.27	0.25	11.33	0.13	217.31	2.41	204.18	13.39	6.17	0.35
BES-4c	16.5	0.3	5.93	0.06	4.83	0.11	110.70	1.44	77.80	4.29	2.78	0.44
BES-4d	18.7	0.2	11.29	0.11	6.39	0.09	129.83	1.50	85.19	5.67	3.76	0.32
BES-4e	21.6	0.2	9.16	0.06	5.47	0.09	109.00	0.88	92.22	6.02	3.67	0.64
BES-4f	18.5	0.2	5.62	0.04	5.32	0.10	123.12	1.12	98.20	7.03	3.46	0.52
BES-4g	19.2	0.3	9.29	0.07	5.71	0.07	128.77	1.40	102.36	6.88	3.77	0.54
BES-4h	22.3	0.3	15.38	0.12	7.48	0.08	133.40	1.37	124.58	8.13	4.73	0.59
BES-4i	20.2	0.3	29.77	0.30	8.70	0.12	199.25	2.71	162.47	10.65	6.12	0.60
BES-4j	15.9	0.2	3.04	0.04	6.97	0.19	126.35	1.71	99.77	7.15	3.19	0.49
BES-5a	34.8	0.4	23.05	0.21	3.83	0.04	19.67	0.26	50.18	3.38	1.61	0.20
BES-5b	25.4	0.2	23.56	0.21	8.65	0.09	57.47	0.56	101.67	6.97	3.08	0.21
BES-5c	26.7	0.4	20.81	0.22	4.49	0.07	31.03	0.40	50.93	3.36	1.72	0.17
BES-5d	26.6	0.3	18.68	0.14	4.99	0.06	37.98	0.37	58.26	3.76	2.02	0.31
BES-5e	30.9	0.4	16.16	0.12	5.83	0.09	26.58	0.24	71.81	4.65	2.05	0.25
Balsthal Holzfluh (BH)												
Sample name	(U-Th-Sm)/He [Ma]		goe [ug]	1σ	U [ppm]	1σ	Th [ppm]	1σ	Sm [ppm]	1σ	He [nmol/g]	1σ
BH-1a	9.3	0.1	6.74	0.05	103.20	1.04	349.09	3.82	176.69	2.97	9.39	0.98
BH-1b	10.4	0.1	8.87	0.14	121.78	1.99	262.01	4.64	142.24	3.84	10.35	0.41
BH-1c	22.2	0.2	5.75	0.05	76.36	0.87	175.68	2.12	42.18	1.83	14.23	1.14
BH-2a	13.9	0.1	9.07	0.14	47.00	0.84	170.00	2.77	222.66	11.15	6.57	0.25
BH-2b	13.7	0.1	9.71	0.14	39.42	0.61	120.02	1.81	199.10	9.31	5.07	0.32
BH-2c	5.8	0.1	8.98	0.14	75.04	1.22	1290.17	22.96	620.64	32.08	11.90	0.52
BH-3a	11.0	0.1	17.25	0.28	29.48	0.52	109.41	1.95	45.13	2.19	3.31	0.17
BH-3b	9.6	0.1	20.37	0.38	30.23	0.59	167.80	3.29	51.33	2.73	3.64	0.12
BH-3c	2.3	0.0	14.82	0.25	161.01	2.89	1180.18	21.14	1038.09	54.26	5.54	0.30

Table 3.3: (U-Th)/He ages of Bohnerz samples, continued. goe = goethite mass, BI = Balsthal Erzmatt I, BII = Balsthal Erzmatt II, C = Cholplatz

Balsthal Erzmatt I (BI)												
Sample name	(U-Th-Sm)/He [Ma]		goe [ug]	1σ	U [ppm]	1σ	Th [ppm]	1σ	Sm [ppm]	1σ	He [nmol/g]	1σ
BI-1a	28.1	0.3	37.35	0.64	3.05	0.06	130.08	2.37	34.56	0.73	5.16	0.19
BI-1b	22.7	0.4	9.09	0.12	2.58	0.07	48.30	0.78	14.94	0.61	1.73	0.21
BI-1c	30.4	0.5	19.32	0.29	1.25	0.03	33.12	0.57	17.80	0.55	1.50	0.10
BI-1d	29.5	0.4	32.16	0.71	1.67	0.04	66.45	1.54	23.88	0.78	2.78	0.08
BI-1e	28.1	0.4	15.48	0.18	8.92	0.11	88.16	1.28	20.84	0.63	4.53	0.31
BI-2a	23.0	0.2	18.12	0.21	3.69	0.07	122.31	1.57	36.16	2.19	4.06	0.24
BI-2b	28.7	0.3	31.84	0.48	2.00	0.03	141.48	2.26	29.48	1.40	5.51	0.18
BI-2c	32.5	0.5	19.77	0.37	2.45	0.05	45.80	0.93	10.06	0.52	2.34	0.09
BI-2d	25.6	0.3	22.19	0.35	3.07	0.06	85.76	1.47	15.94	0.82	3.24	0.14
BI-3a	28.6	0.4	19.34	0.37	2.90	0.06	73.79	1.53	24.86	1.10	3.16	0.13
BI-3b	34.0	0.5	15.88	0.25	2.04	0.04	57.94	1.04	20.43	1.05	2.90	0.15
BI-3c	23.5	0.3	17.17	0.24	3.91	0.06	112.57	1.77	26.28	1.62	3.88	0.18
BI-4a	21.6	0.3	18.95	0.28	2.48	0.05	97.87	1.59	15.92	0.89	3.00	0.13
BI-4b	30.2	0.4	8.51	0.14	2.87	0.08	57.08	1.00	11.52	0.63	2.68	0.20
BI-4c	27.6	0.3	27.00	0.35	3.39	0.06	121.42	1.75	35.20	2.19	4.80	0.26
Balsthal Erzmatt II (BII)												
Sample name	(U-Th-Sm)/He [Ma]		goe [ug]	1σ	U [ppm]	1σ	Th [ppm]	1σ	Sm [ppm]	1σ	He [nmol/g]	1σ
BII-1a	26.6	0.4	10.27	0.13	0.87	0.04	47.89	0.73	36.12	0.77	1.76	0.19
BII-1b	22.3	0.3	38.10	0.37	2.89	0.04	83.38	1.01	62.48	2.31	2.74	0.19
BII-1c	23.7	0.3	15.92	0.15	2.34	0.05	45.77	0.57	42.31	1.05	1.69	0.20
BII-1d	24.3	6.0	22.47	2.52	2.13	0.37	65.63	11.69	37.42	6.17	2.33	0.02
BII-1e	27.7	0.4	31.80	0.51	1.44	0.03	37.30	0.67	20.05	0.76	1.54	0.07
BII-1f	25.3	0.3	22.09	0.17	2.69	0.03	52.32	0.55	38.86	0.66	2.07	0.30
BII-1g	31.6	6.7	15.41	1.49	1.02	0.15	36.25	5.43	21.89	3.30	1.65	0.02
BII-1h	31.0	0.4	36.40	0.42	3.16	0.05	56.51	0.79	11.48	0.40	2.78	0.15
BII-1j	25.7	0.3	22.97	0.19	3.45	0.05	91.24	0.99	67.11	1.20	3.50	0.31
BII-1k	28.4	0.4	11.23	0.18	1.33	0.04	33.77	0.59	9.58	0.36	1.43	0.10
BII-2a	25.6	0.2	9.99	0.18	3.99	0.08	65.57	1.22	31.58	1.83	2.71	0.16
BII-2b	25.1	0.3	24.70	0.43	6.32	0.12	180.85	3.30	146.03	5.69	6.69	0.26
BII-2c	22.9	0.3	10.71	0.20	3.66	0.07	90.92	1.85	50.58	3.03	3.13	0.15
BII-3a	22.1	0.2	12.06	0.13	3.25	0.05	66.41	0.79	31.34	2.04	2.27	0.18
BII-3b	24.5	0.3	18.77	0.43	3.85	0.09	72.91	1.78	46.14	2.11	2.81	0.10
BII-3c	29.5	0.3	13.77	0.25	2.84	0.07	51.47	0.95	23.91	1.54	2.41	0.12
BII-4a	22.3	0.3	33.27	0.62	3.56	0.07	54.84	1.10	29.20	1.45	2.00	0.07
BII-4b	24.2	0.2	22.30	0.21	4.73	0.06	92.63	0.96	73.59	4.68	3.50	0.28
BII-4c	22.7	0.3	24.84	0.41	5.60	0.11	90.18	1.63	55.05	2.18	3.32	0.09
Cholplatz (C)												
Sample name	(U-Th-Sm)/He [Ma]		goe [ug]	1σ	U [ppm]	1σ	Th [ppm]	1σ	Sm [ppm]	1σ	He [nmol/g]	1σ
C-Pit1-1a	17.3	0.4	7.06	0.26	6.96	0.30	72.94	2.89	32.96	3.57	2.27	0.09
C-Pit1-1b	17.9	0.7	11.76	0.36	3.79	0.16	34.93	1.32	21.15	1.85	1.17	0.06
C-Pit1-1c	29.9	0.9	6.75	0.33	3.96	0.22	31.63	1.65	11.73	1.52	1.86	0.06
C-Pit1-1d	30.3	0.6	22.24	0.95	2.89	0.13	20.21	0.90	12.01	1.07	1.26	0.03
C-Pit1-1e	27.2	0.4	37.19	0.91	3.24	0.09	25.73	0.66	10.70	0.99	1.38	0.04
C-Pit1-1f	23.9	0.5	58.57	2.84	6.03	0.30	65.34	3.28	19.59	2.64	2.78	0.03
C-Pit1-1g	28.4	0.4	32.15	1.53	6.72	0.33	61.17	2.97	40.40	3.87	3.27	0.05
C-Pit1-1h	27.7	0.4	28.68	1.11	6.80	0.27	59.07	2.36	45.32	3.45	3.13	0.04
C-Pit1-1i	28.2	0.4	25.28	0.95	6.77	0.26	68.81	2.66	41.98	4.10	3.53	0.05
C-Pit1-1j	27.9	0.7	15.00	0.53	3.16	0.13	30.25	1.18	15.91	1.43	1.56	0.06
C-Pit1-1k	32.0	1.2	15.84	1.06	6.86	0.47	80.45	5.73	42.55	4.31	4.50	0.05
C-Pit1-1l	31.0	2.5	10.72	1.28	7.94	0.98	92.29	12.10	42.61	5.83	5.01	0.03
C-Pit1-2a	18.9	0.2	8.03	0.07	8.51	0.14	98.34	1.06	33.16	1.71	3.25	0.46
C-Pit1-2b	21.8	0.3	10.47	0.08	13.20	0.16	58.63	0.72	40.51	2.87	3.20	0.48
C-Pit1-2c	21.9	0.3	10.44	0.10	14.54	0.19	60.28	0.68	47.76	3.25	3.43	0.37
C-Pit1-3a	22.5	0.2	34.18	0.35	5.18	0.07	58.48	0.76	33.61	2.02	1.97	0.11
C-Pit1-3b	27.0	0.3	38.46	0.41	7.67	0.11	126.37	1.60	23.61	1.38	3.38	0.15
C-Pit1-3c	24.2	0.2	26.01	0.18	7.98	0.10	149.97	1.73	38.68	2.37	2.47	0.13

Table 3.4: (U-Th)/He ages of Bohnerz samples, continued. goe = goethite mass, C = Cholplatz

Cholplatz (C)												
Sample name	(U-Th-Sm)/He [Ma]		goe [ug]	1σ	U [ppm]	1σ	Th [ppm]	1σ	Sm [ppm]	1σ	He [nmol/g]	1σ
C-Pit2-1b	15.2	0.4	7.55	0.39	5.72	0.33	51.04	2.74	8.61	1.13	1.47	0.05
C-Pit2-1c	23.5	0.4	20.09	0.48	11.47	0.28	57.26	1.63	45.77	3.15	3.19	0.08
C-Pit2-1d	26.2	0.5	29.24	0.85	5.51	0.17	30.63	0.99	34.57	2.44	1.82	0.06
C-Pit2-1e	22.5	0.4	10.59	0.33	11.08	0.36	39.90	1.31	34.67	2.93	2.51	0.10
C-Pit2-1f	28.1	0.7	15.68	1.12	7.95	0.59	25.99	1.90	29.75	3.30	2.15	0.02
C-Pit2-2a	17.6	0.2	20.50	0.13	18.95	0.18	99.41	1.03	96.00	6.44	4.06	0.51
C-Pit2-2b	14.3	0.2	13.91	0.16	14.66	0.20	89.19	1.26	69.99	4.80	2.78	0.21
C-Pit2-2c	15.4	0.2	9.58	0.09	10.38	0.13	55.25	0.69	48.11	3.16	1.97	0.21
C-Pit2-3a	20.2	0.2	26.00	0.28	9.88	0.14	108.51	1.58	37.95	1.57	3.71	0.17
C-Pit2-3b	18.9	0.2	26.02	0.32	10.88	0.09	38.75	0.31	82.53	3.35	3.25	0.22
C-Pit2-3c	23.4	0.1	36.30	0.43	6.64	0.09	109.39	1.26	31.16	1.97	1.70	0.08
C-Pit3-1a	15.6	0.5	7.97	0.37	4.69	0.24	39.77	2.03	25.51	2.25	1.20	0.04
C-Pit3-1b	21.0	0.6	11.34	0.47	3.96	0.18	9.86	0.51	18.42	1.64	0.72	0.04
C-Pit3-1c	37.6	1.2	5.98	0.31	4.58	0.28	58.57	3.26	51.47	5.93	3.78	0.09
C-Pit3-1d	16.1	0.3	34.59	1.21	3.83	0.14	27.13	1.01	9.89	0.75	0.89	0.03
C-Pit3-1e	17.1	0.6	14.11	0.81	3.74	0.22	31.17	1.94	9.15	0.97	1.03	0.03
C-Pit3-2a	20.3	0.2	14.04	0.11	5.57	0.08	57.05	0.54	43.04	2.90	2.10	0.37
C-Pit3-2b	30.0	0.4	16.01	0.12	5.16	0.06	42.84	0.52	69.85	4.58	2.50	0.40
C-Pit3-2c	23.1	0.4	6.89	0.07	7.09	0.15	37.65	0.51	37.51	2.61	2.01	0.24
C-Pit3-2d	27.8	0.3	44.39	0.28	7.82	0.07	40.12	0.37	80.35	5.26	2.62	0.31
C-Pit3-2e	20.0	0.3	32.01	0.23	15.09	0.17	22.97	0.28	37.73	2.49	2.24	0.47
C-Pit3-2f	19.5	0.2	6.19	0.05	7.93	0.08	11.30	0.15	23.28	1.71	1.13	0.28
C-Pit3-3a	29.9	0.2	19.84	0.20	5.94	0.08	36.86	0.45	46.18	2.69	2.30	0.08
C-Pit3-3b	16.6	0.1	26.20	0.31	7.35	0.10	64.10	0.81	23.51	1.38	3.30	0.14
C-Pit3-3c	28.1	0.2	24.63	0.27	11.59	0.16	125.24	1.50	10.50	0.69	2.75	0.14
C-Pit4-1a	11.6	0.1	9.70	0.08	6.48	0.13	90.39	0.88	57.11	3.82	1.75	0.37
C-Pit4-1b	11.7	0.2	5.08	0.05	6.30	0.14	66.61	0.82	36.73	2.93	1.40	0.26
C-Pit4-1c	14.7	0.2	15.16	0.13	5.72	0.07	77.28	0.81	40.50	1.93	1.91	0.25
C-Pit4-1d	13.9	0.3	5.74	0.05	6.51	0.12	78.15	1.10	71.33	3.79	1.88	0.29
C-Pit4-1e	19.4	0.4	13.63	0.10	8.60	0.09	140.52	1.98	86.13	3.30	4.41	0.44
C-Pit4-1f	19.8	0.3	10.78	0.10	0.17	0.02	201.10	2.55	146.41	9.62	5.13	0.52
C-Pit4-1g	20.1	0.3	5.56	0.05	14.44	0.21	59.95	0.65	41.16	2.52	3.12	0.36
C-Pit4-1h	23.8	0.5	6.67	0.05	10.57	0.16	70.30	1.00	58.48	2.58	3.52	0.53
C-Pit4-2a	16.4	0.2	13.99	0.11	7.18	0.11	73.85	0.81	47.03	2.46	2.19	0.40
C-Pit4-2b	19.5	0.2	15.23	0.13	8.69	0.10	121.10	1.26	78.26	5.47	3.95	0.32
C-Pit4-2c	41.0	1.3	5.12	0.04	5.40	0.14	24.09	0.44	51.54	3.60	2.48	0.45
C-Pit4-3a	19.3	0.2	28.27	0.37	6.69	0.10	0.62	0.02	19.71	1.20	0.01	0.00
C-Pit4-3b	17.4	0.1	39.63	0.40	7.10	0.10	133.21	1.56	58.88	3.42	2.17	0.11
C-Pit4-3c	20.2	0.2	28.52	0.30	4.81	0.05	36.62	0.43	51.01	2.98	5.31	0.16
C-Pit5-1a	15.2	0.2	8.97	0.13	8.62	0.17	79.13	1.39	39.48	3.00	2.25	0.14
C-Pit5-1b	12.4	0.1	6.39	0.04	15.95	0.18	165.45	1.57	66.85	4.62	3.70	0.60
C-Pit5-1c	20.1	0.2	13.21	0.11	10.35	0.15	98.32	0.93	43.53	2.42	3.66	0.39
C-Pit5-1d	16.6	0.2	11.77	0.08	11.59	0.11	125.95	1.28	53.09	2.07	3.74	0.43
C-Pit5-1e	27.4	0.4	13.84	0.10	7.90	0.09	32.86	0.40	21.46	1.00	2.34	0.34
C-Pit5-1f	22.9	0.2	20.93	0.18	8.92	0.09	43.03	0.46	27.24	1.84	2.38	0.18
C-Pit5-1g	9.9	0.2	6.30	0.06	4.68	0.10	33.07	0.49	13.85	0.76	0.67	0.33
C-Pit5-2a	19.1	0.2	42.93	0.52	6.32	0.09	0.50	0.02	35.34	1.85	0.01	0.00
C-Pit5-2b	17.4	0.2	43.73	0.31	7.11	0.08	0.35	0.02	29.91	1.73	0.02	0.01
C-Pit5-2c	20.2	0.2	23.92	0.22	11.60	0.17	101.23	1.45	55.22	3.27	3.44	0.11
C-Pit5-3a	31.2	0.3	76.33	0.71	14.39	0.15	4.40	0.06	102.41	3.93	0.13	0.03
C-Pit5-3b	31.7	0.2	85.74	1.00	5.20	0.07	155.04	2.13	42.88	1.82	2.62	0.17
C-Pit5-3c	27.0	0.2	58.80	0.65	7.10	0.10	133.21	1.56	58.88	3.42	5.66	0.16
C-Pit6-1a	13.6	0.1	13.36	0.10	9.15	0.09	72.79	0.65	34.26	1.93	1.95	0.28
C-Pit6-1b	17.9	0.2	25.65	0.17	0.26	0.02	136.78	1.33	90.45	4.20	3.17	0.37
C-Pit6-1c	21.0	0.4	6.42	0.05	5.71	0.13	64.85	0.91	51.38	2.61	2.40	0.42
C-Pit6-1d	24.5	0.4	6.21	0.06	3.66	0.05	82.24	1.13	56.64	4.16	3.08	0.29
C-Pit6-2a	29.7	0.2	38.45	0.26	6.81	0.10	172.69	2.17	9.68	0.60	3.13	0.15
C-Pit6-2b	23.3	1.4	22.17	1.24	15.19	0.21	114.75	1.66	40.95	2.55	4.35	0.17
C-Pit6-2c	17.8	0.1	47.89	0.64	11.32	0.15	88.35	0.97	44.46	2.38	5.24	0.30
C-Pit6-3a	10.5	0.1	49.58	0.54	8.79	0.09	109.22	1.18	98.43	3.80	3.28	0.22
C-Pit6-3b	9.6	0.1	49.68	0.54	17.01	0.23	165.08	1.93	56.69	3.44	8.54	0.38

Table 3.5: (U-Th)/He ages of Bohnerz samples, continued. goe = goethite mass, C = Cholplatz

Cholplatz (C)												
Sample name	(U-Th-Sm)/He [Ma]		goe [ug]	1σ	U [ppm]	1σ	Th [ppm]	1σ	Sm [ppm]	1σ	He [nmol/g]	1σ
C-Pit6-3c	11.5	0.2	22.42	0.21	8.82	0.11	76.13	0.88	24.63	1.47	3.27	0.20
C-Pit7-1a	18.2	0.3	9.49	0.11	5.09	0.12	85.34	1.14	40.08	2.91	2.49	0.21
C-Pit7-1b	27.2	0.4	39.19	0.30	9.60	0.08	93.20	1.19	139.25	8.98	4.69	0.28
C-Pit7-1c	31.1	0.3	37.17	0.34	7.23	0.07	66.72	0.79	41.89	1.87	3.89	0.25
C-Pit7-1d	44.4	0.6	25.19	0.21	3.26	0.05	30.66	0.34	18.52	1.28	2.54	0.24
C-Pit7-1e	34.4	0.3	31.84	0.30	5.60	0.06	38.84	0.41	56.43	3.72	2.77	0.17
C-Pit7-1f	34.4	0.5	23.67	0.17	5.20	0.06	34.96	0.44	58.52	2.28	2.53	0.24
C-Pit7-1g	29.0	0.3	20.94	0.13	8.40	0.07	21.50	0.28	79.38	3.70	2.14	0.29
C-Pit7-2a	14.3	0.1	27.81	0.30	8.31	0.09	84.62	0.92	59.65	3.06	4.80	0.21
C-Pit7-2b	12.1	0.1	28.04	0.34	4.21	0.06	0.45	0.02	13.48	0.79	0.01	0.00
C-Pit7-2c	12.3	0.1	24.84	0.29	24.65	1.69	55.39	3.68	71.38	8.34	4.78	0.06
C-Pit7-3a	28.8	0.2	122.10	1.45	17.95	0.16	63.83	0.64	26.97	1.18	4.33	0.28
C-Pit7-3b	27.8	0.2	62.64	0.63	4.81	0.05	36.62	0.43	51.01	2.98	2.04	0.11
C-Pit7-3c	29.4	0.4	49.76	0.53	20.61	0.26	118.57	1.38	145.54	7.48	5.35	0.29
Malsenhof												
Sample name	(U-Th-Sm)/He [Ma]		goe [ug]	1σ	U [ppm]	1σ	Th [ppm]	1σ	Sm [ppm]	1σ	He [nmol/g]	1σ
Malsenhof-B-1a	42.4	0.9	56.23	0.62	4.83	0.09	12.76	0.17	48.51	2.16	1.82	0.11
Malsenhof-B-1b	27.0	0.4	42.87	0.49	6.84	0.14	60.49	0.78	60.81	2.38	3.10	0.15
Malsenhof-B-1c	25.9	0.4	30.06	0.37	4.78	0.11	45.49	0.66	43.57	1.32	2.19	0.13
Malsenhof-B-2a	33.9	0.4	22.17	0.41	6.27	0.13	44.94	0.89	37.11	2.84	3.12	0.12
Malsenhof-B-2b	30.7	0.3	43.41	0.64	9.54	0.16	131.19	2.10	128.70	9.54	6.78	0.20
Malsenhof-B-2c	29.5	0.4	25.35	0.36	8.31	0.13	55.65	0.92	55.87	2.58	3.44	0.15
Malsenhof-C-1a	18.3	1.1	5.15	0.09	4.99	0.64	68.91	1.33	40.34	2.36	2.12	0.24
Malsenhof-C-1b	22.6	0.4	23.95	0.21	8.39	0.20	105.76	1.16	79.36	3.61	4.11	0.32
Malsenhof-C-1c	20.0	0.3	18.93	0.21	5.92	0.17	92.89	1.22	56.33	2.56	3.04	0.35
Malsenhof-C-1d	24.0	0.5	20.58	0.21	4.79	0.23	85.98	1.14	54.05	2.33	3.28	0.23
Malsenhof-C-1e	30.2	0.7	20.41	0.28	6.49	0.19	40.52	0.63	22.97	0.71	2.63	0.54
Malsenhof-C-1f	24.6	0.5	23.79	0.26	6.74	0.16	52.97	0.72	33.54	1.57	2.58	0.19
Malsenhof-C-1g	27.0	0.4	41.70	0.72	8.42	0.18	49.43	0.92	40.05	1.30	2.95	0.10
Malsenhof-C-1h	24.1	0.5	21.24	0.28	6.19	0.16	39.73	0.62	26.05	1.19	2.04	0.13
Malsenhof-D-1a	20.7	0.3	19.23	0.24	12.97	0.28	102.22	1.44	12.97	0.65	4.17	0.26
Malsenhof-D-1b	23.6	0.2	30.20	0.32	14.80	0.20	128.73	1.62	18.87	0.89	5.79	0.29
Malsenhof-D-2	18.1	0.3	6.04	0.10	6.80	0.15	68.50	1.31	92.61	6.75	2.27	0.20
Malsenhof-F-2a	8.0	0.1	15.99	0.14	14.07	0.16	74.69	0.94	20.09	0.89	1.38	0.21
Malsenhof-F-2b	9.0	0.1	11.70	0.20	16.00	0.31	96.94	1.80	26.86	2.30	1.90	0.12
Malsenhof-G-1a	19.3	0.5	10.22	0.19	6.25	0.31	79.44	1.57	44.80	2.38	2.62	0.14
Malsenhof-G-1b	17.2	0.3	22.44	0.21	17.54	0.31	169.23	2.11	128.31	5.78	5.39	0.38
Malsenhof-G-1c	18.7	0.5	11.31	0.11	12.66	0.38	87.94	1.20	90.52	4.32	3.40	0.30
Malsenhof-G-1d	18.1	0.5	9.04	0.19	7.95	0.33	65.09	1.47	67.85	2.34	2.30	0.14
Malsenhof-G-1e	27.4	0.4	39.24	0.31	10.12	0.12	83.20	0.98	68.12	3.01	4.44	0.24
Malsenhof-G-2a	23.0	0.3	28.63	0.31	8.42	0.20	111.21	1.44	47.81	2.28	4.33	0.20
Malsenhof-G-2b	21.9	0.5	15.00	0.20	5.84	0.23	65.62	1.03	39.41	1.40	2.54	0.16
Malsenhof-G-2c	25.4	0.3	34.91	0.44	10.32	0.17	101.76	1.43	70.50	3.01	4.74	0.21
Malsenhof-G-2e	21.5	0.3	21.50	0.30	7.60	0.18	105.43	1.58	46.67	1.44	3.79	0.17
Malsenhof-G-2f	25.2	0.5	25.66	0.29	7.18	0.21	56.78	0.80	45.41	1.98	2.83	0.19
Malsenhof-G-2g	26.3	0.7	21.21	0.25	4.26	0.14	31.61	0.44	26.07	1.18	1.68	0.12
Malsenhof-G-2h	26.9	0.7	21.82	0.21	4.77	0.17	38.63	0.46	25.08	1.14	2.03	0.24
Malsenhof-G-2i	29.4	0.5	46.05	0.56	4.59	0.12	35.53	0.49	28.80	1.25	2.08	0.11
Malsenhof-G-2j	21.2	0.5	21.05	0.27	7.24	0.21	52.26	0.81	20.67	0.66	2.26	0.15
Malsenhof-G-2k	25.9	0.3	36.10	0.46	10.06	0.16	50.68	0.70	72.82	2.33	3.11	0.14
Malsenhof-G-2l	26.3	0.4	34.95	0.32	8.46	0.15	47.47	0.60	72.81	3.39	2.82	0.19
Malsenhof-G-3a	13.2	0.1	21.52	0.38	11.76	0.23	63.22	1.19	30.44	2.33	1.91	0.10
Malsenhof-G-3b	9.2	0.1	13.51	0.12	18.37	0.20	103.74	1.33	34.30	1.84	2.14	0.30
Malsenhof-G-3c	11.4	0.1	25.14	0.48	15.93	0.33	83.34	1.69	33.33	2.64	2.21	0.08
Malsenhof-G-4a	18.2	0.2	16.04	0.30	18.46	0.37	321.03	6.30	142.17	10.58	9.30	0.25
Malsenhof-G-4b	26.5	0.3	30.87	0.29	10.35	0.13	130.89	1.55	54.21	2.01	5.94	0.33
Malsenhof-G-4c	24.7	0.3	20.69	0.32	10.76	0.19	111.41	1.85	58.58	4.27	4.97	0.24
Malsenhof-G-5a	21.9	0.2	47.24	1.12	8.39	0.21	104.24	2.55	137.22	10.54	3.95	0.08
Malsenhof-G-5b	20.1	0.2	36.31	0.61	14.08	0.27	109.92	2.00	48.02	3.51	4.38	0.15

Table 3.6: (U-Th)/He ages of Bohnerz samples, continued. goe = goethite mass, O = Oberdorf

Malsenhof												
Sample name	(U-Th-Sm)/He [Ma]		goe [ug]	1σ	U [ppm]	1σ	Th [ppm]	1σ	Sm [ppm]	1σ	He [nmol/g]	1σ
Malsenhof-G-5c	25.9	0.3	40.57	0.72	8.57	0.16	74.11	1.44	28.68	2.10	3.67	0.10
Malsenhof-G-6a	21.1	0.2	27.79	0.35	9.77	0.16	87.86	1.25	69.14	2.77	3.51	0.22
Malsenhof-G-6b	17.8	0.2	19.08	0.17	20.24	0.23	203.03	2.42	254.60	10.14	6.61	0.56
Malsenhof-G-6c	21.1	0.3	22.19	0.23	12.40	0.20	142.53	1.95	138.27	5.37	5.29	0.31
Malsenhof-H-1a	23.3	0.3	48.43	0.53	11.19	0.17	75.99	0.95	26.29	1.20	3.69	0.20
Malsenhof-H-1b	22.7	0.3	46.78	1.06	10.66	0.27	65.47	1.58	24.11	0.84	3.22	0.06
Malsenhof-H-1d	18.9	1.0	8.06	0.12	8.65	0.50	47.29	0.82	24.42	1.13	2.03	0.22
Malsenhof-H-2a	16.7	0.2	18.91	0.31	18.62	0.32	162.58	2.89	139.83	10.06	5.19	0.22
Malsenhof-H-2b	16.5	0.2	12.52	0.18	21.61	0.35	270.00	4.34	183.45	13.03	7.66	0.31
Malsenhof-H-2c	18.2	0.2	15.86	0.19	21.35	0.30	199.45	2.76	201.76	8.92	6.78	0.36
Malsenhof-I-1a	18.8	0.3	26.71	0.35	15.13	0.26	51.48	0.76	38.93	1.74	2.79	0.15
Malsenhof-I-1b	16.0	0.3	21.29	0.26	13.09	0.25	43.11	0.65	34.24	1.16	2.02	0.16
Malsenhof-I-2a	22.1	0.2	25.88	0.41	20.20	0.38	205.12	3.46	197.81	14.06	8.24	0.23
Malsenhof-I-2b	25.7	0.3	18.03	0.26	13.26	0.22	119.05	1.84	87.24	6.34	5.78	0.25
Malsenhof-I-2c	35.0	0.5	47.00	0.56	12.03	0.17	129.49	1.98	78.30	3.00	8.11	0.33
Malsenhof-J-1a	22.8	0.2	22.07	0.33	9.93	0.17	202.93	3.31	152.36	10.81	7.18	0.28
Malsenhof-J-1b	22.6	0.3	22.73	0.23	9.61	0.12	101.60	1.31	50.20	2.35	4.13	0.27
Malsenhof-J-1c	27.8	0.3	67.04	1.34	7.49	0.16	69.56	1.47	25.09	1.24	3.61	0.09
Malsenhof-J-2a	32.3	0.3	25.95	0.44	2.58	0.06	41.46	0.74	74.17	5.37	2.19	0.08
Malsenhof-J-2b	27.8	0.4	18.75	0.22	10.55	0.15	60.82	0.94	103.15	4.11	3.78	0.28
Malsenhof-J-2c	31.8	0.3	36.72	0.46	10.52	0.14	47.63	0.72	101.14	4.31	3.78	0.17
Mervelier												
Sample name	(U-Th-Sm)/He [Ma]		goe [ug]	1σ	U [ppm]	1σ	Th [ppm]	1σ	Sm [ppm]	1σ	He [nmol/g]	1σ
Mervelier-1a	18.4	0.3	12.92	0.17	3.99	0.08	53.45	0.82	70.10	2.42	1.66	0.17
Mervelier-1b	33.3	0.4	47.06	0.56	5.55	0.08	26.50	0.38	44.80	1.23	2.14	0.13
Mervelier-1c	32.5	0.4	39.92	0.33	6.43	0.07	32.62	0.37	43.60	0.78	2.50	0.22
Mervelier-1d	27.9	5.0	21.81	2.17	12.91	1.94	27.65	4.29	20.21	3.09	2.95	0.04
Mervelier-1e	23.5	0.4	10.76	0.12	7.97	0.12	12.73	0.23	14.21	0.45	1.41	0.15
Mervelier-2a	22.5	0.3	30.48	0.26	3.77	0.06	69.14	0.77	159.14	2.39	2.47	0.28
Mervelier-2b	24.1	5.3	37.10	0.30	8.10	0.08	147.81	19.66	147.66	2.14	5.64	0.44
Mervelier-2c	26.7	0.3	12.85	0.24	2.60	0.07	54.12	1.07	87.28	2.15	2.24	0.14
Mervelier-2d	33.5	0.4	22.36	0.28	5.31	0.07	83.70	1.19	151.42	5.00	4.59	0.26
Mervelier-2e	29.2	6.7	13.64	1.51	2.37	0.40	47.40	8.28	93.99	15.37	2.16	0.02
Mervelier-2g	26.0	0.4	9.59	0.13	3.61	0.08	34.66	0.56	50.38	1.93	1.67	0.15
Mervelier-2h	23.3	0.3	30.06	0.26	5.17	0.07	48.35	0.55	61.47	1.55	2.11	0.33
Mervelier-2i	27.3	5.4	18.47	1.91	3.26	0.51	37.88	6.11	138.41	21.63	1.83	0.02
Mervelier-2k	25.7	0.3	26.09	0.65	4.76	0.13	28.85	0.77	62.23	2.09	1.62	0.06
Mervelier-a1	21.5	0.3	10.39	0.05	4.69	0.05	41.93	0.39	not measured		1.70	0.50
Mervelier-a2	23.2	0.3	16.32	0.08	4.79	0.04	40.69	0.40	not measured		1.81	0.38
Mervelier-a3	20.3	0.3	11.96	0.05	4.45	0.04	31.46	0.34	not measured		1.31	0.35
Mervelier-a5	30.0	0.3	33.31	0.16	5.59	0.04	41.98	0.35	not measured		2.53	0.30
Mervelier-a7	36.8	2.0	3.42	0.03	1.16	0.05	17.77	0.60	not measured		1.07	0.29
Mervelier-a8	28.9	0.2	31.34	0.16	5.75	0.03	33.09	0.26	not measured		2.13	0.22
Mervelier-a9	24.8	0.3	13.30	0.06	6.49	0.05	33.61	0.33	not measured		1.94	0.46
Mervelier-b2	20.2	0.3	18.05	0.09	4.81	0.04	11.75	0.16	not measured		0.83	0.19
Mervelier-b3	27.2	0.3	27.37	0.11	4.49	0.04	16.63	0.18	not measured		1.24	0.25
Mervelier-b4	29.4	0.4	12.89	0.07	3.81	0.05	22.79	0.24	not measured		1.47	0.28
Mervelier-b5	30.7	0.4	17.13	0.10	3.96	0.04	22.64	0.23	not measured		1.55	0.28
Oberdorf (O)												
Sample name	(U-Th-Sm)/He [Ma]		goe [ug]	1σ	U [ppm]	1σ	Th [ppm]	1σ	Sm [ppm]	1σ	He [nmol/g]	1σ
O-a1	31.9	1.1	10.03	0.15	4.88	0.16	31.68	0.59	54.07	2.27	2.15	0.01
O-a2	31.9	0.8	41.01	0.63	7.12	0.11	31.37	0.39	107.89	4.53	2.54	0.05
O-a3	30.8	1.4	4.58	0.07	6.73	0.25	35.40	0.84	59.59	2.50	2.54	0.01
O-a4	31.0	1.1	7.13	0.11	7.65	0.24	41.86	0.79	50.04	2.10	2.97	0.01
O-a5	30.8	1.3	5.56	0.09	6.59	0.23	32.63	0.74	50.31	2.11	2.40	0.01
O-a6	34.3	1.5	4.31	0.07	6.27	0.24	38.33	0.90	46.44	1.95	2.86	0.01
O-a7	34.6	1.1	12.01	0.19	6.54	0.18	38.38	0.63	70.62	2.97	2.95	0.02

Table 3.7: (U-Th)/He ages of Bohnerz samples, continued. goe = goethite mass, O = Oberdorf, P = Petersbuch

Oberdorf (O)												
Sample name	(U-Th-Sm)/He [Ma]		goe [ug]	1σ	U [ppm]	1σ	Th [ppm]	1σ	Sm [ppm]	1σ	He [nmol/g]	1σ
O-c1	13.6	0.8	9.98	0.15	2.74	0.11	20.45	0.44	11.35	0.48	0.56	0.01
O-c2	13.2	2.0	5.25	0.08	2.28	0.12	10.73	0.45	11.11	0.47	0.35	0.01
O-c3	18.9	1.5	8.97	0.14	1.76	0.08	11.92	0.34	12.06	0.51	0.47	0.01
O-c4	12.9	0.5	17.53	0.27	3.31	0.10	22.66	0.39	15.06	0.63	0.61	0.01
O-c5	19.2	1.4	9.85	0.15	1.78	0.08	10.83	0.31	11.64	0.49	0.45	0.01
O-d1	30.9	1.1	6.59	0.10	10.40	0.30	35.09	0.72	35.12	1.48	3.15	0.01
O-d2	31.6	1.6	3.56	0.05	3.93	0.19	52.29	1.17	17.82	0.75	2.80	0.01
O-d3	32.0	1.0	12.24	0.19	7.94	0.20	48.26	0.74	30.61	1.29	3.37	0.02
O-d4	26.4	0.8	15.30	0.24	3.78	0.11	85.76	1.05	30.37	1.28	3.45	0.02
O-d5	34.2	1.0	10.99	0.17	11.23	0.26	35.34	0.61	26.45	1.11	3.65	0.02
O-e1	33.2	1.6	20.66	0.32	1.27	0.05	5.93	0.16	9.99	0.42	0.48	0.01
O-e2	37.2	1.2	19.70	0.30	3.39	0.10	18.15	0.32	34.96	1.47	1.56	0.01
O-e3	36.7	1.3	15.30	0.24	3.41	0.11	16.37	0.33	33.16	1.39	1.46	0.01
O-e4	34.2	2.0	5.89	0.09	2.79	0.13	16.88	0.51	24.77	1.04	1.27	0.01
O-e5	37.1	1.1	27.00	0.42	3.55	0.09	23.10	0.35	39.70	1.67	1.82	0.02
O-f1	20.7	1.6	3.35	0.05	2.75	0.16	35.62	0.97	42.38	1.78	1.26	0.01
O-f2	27.1	1.2	7.69	0.12	2.17	0.10	40.68	0.76	51.39	2.16	1.74	0.01
O-f3	22.8	1.5	3.86	0.06	3.23	0.16	32.89	0.87	50.06	2.10	1.37	0.01
O-f4	23.1	0.9	8.23	0.13	2.37	0.10	52.26	0.88	64.74	2.72	1.85	0.01
O-f5	25.4	1.6	3.57	0.05	2.96	0.16	38.20	0.98	56.01	2.35	1.66	0.01
O-7	27.7	0.4	17.29	0.24	2.78	0.05	33.45	0.55	47.07	2.33	1.61	0.10
O-8a	6.6	0.1	12.91	0.21	3.34	0.07	80.32	1.40	9.83	0.62	0.80	0.06
O-8b	6.4	0.1	19.69	0.31	4.54	0.09	112.43	1.88	12.52	0.67	1.08	0.07
O-9a	13.4	0.2	32.67	0.46	3.45	0.06	43.67	0.67	28.96	1.80	1.00	0.07
O-9b	12.7	0.2	26.43	0.46	2.76	0.05	36.50	0.69	23.27	1.09	0.79	0.06
Petersbuch (P)												
Sample name	(U-Th-Sm)/He [Ma]		goe [ug]	1σ	U [ppm]	1σ	Th [ppm]	1σ	Sm [ppm]	1σ	He [nmol/g]	1σ
P100A1	5.59	0.20	11.78	0.18	6.82	0.20	29.88	0.59	14.94	0.93	0.31	0.00
P100A2	4.10	0.16	8.72	0.13	4.95	0.17	20.52	0.47	9.29	0.58	0.25	0.00
P100A3	4.70	0.21	8.30	0.13	6.02	0.13	25.75	0.39	14.70	0.91	0.39	0.00
P100A4	5.99	0.17	23.91	0.37	6.14	0.14	25.13	0.40	15.03	0.93	0.40	0.00
P100A5	6.14	0.18	19.34	0.30	5.57	0.13	22.34	0.36	15.43	0.96	0.39	0.00
P100A6	6.63	0.19	22.08	0.34	5.63	0.20	26.01	0.61	10.67	0.66	0.16	0.00
P115Ab1	2.54	0.17	6.22	0.10	4.90	0.26	23.46	1.09	8.00	0.50	0.17	0.00
P115Ab2	3.02	0.54	2.01	0.03	4.60	0.27	24.97	1.25	7.82	0.49	0.17	0.00
P115Ab3	2.92	0.63	1.70	0.03	2.47	0.96	17.50	7.81	0.00	0.00	0.01	0.00
P115Ac3	7.90	0.91	2.10	0.03	6.58	0.19	31.91	0.59	11.07	0.69	0.25	0.00
P115Ad1	3.24	0.13	9.59	0.15	7.17	0.19	33.83	0.58	11.97	0.74	0.24	0.00
P115Ad2	2.89	0.11	11.62	0.18	6.44	0.19	32.00	0.60	13.52	0.84	0.21	0.00
P115Ad3	2.78	0.12	9.08	0.14	7.86	0.70	43.48	4.17	5.21	0.32	0.65	0.00
P115b-1	10.85	0.31	13.80	0.21	4.16	0.17	43.05	0.86	9.30	0.58	0.80	0.00
P115b-2	7.91	0.30	5.37	0.08	5.11	0.24	28.56	0.92	25.86	1.60	0.56	0.00
P115b-3	8.62	0.51	3.00	0.05	1.69	0.09	13.03	0.41	3.94	0.24	0.18	0.00
P115b-5	6.96	0.48	6.79	0.10	9.07	0.21	43.05	0.65	26.23	1.63	1.13	0.01
P115b-6	10.25	0.41	5.75	0.09	4.16	0.17	43.05	0.86	9.30	0.58	0.80	0.00
P125S1-1a	9.3	0.2	2.10	0.03	9.03	0.18	94.45	1.67	78.65	4.99	1.58	0.86
P125S1-1b	5.1	0.1	2.31	0.05	15.56	0.44	214.42	5.02	163.16	10.51	1.83	0.25
P125S1-1c	4.0	0.1	3.93	0.06	6.32	0.13	59.81	1.20	53.93	3.21	0.45	0.14
P62Aa1	6.65	1.60	0.43	0.01	2.85	1.11	14.41	9.00	0.00	0.00	0.02	0.00
P62Aa3	10.29	0.82	1.07	0.02	8.56	0.53	42.54	2.53	17.69	1.10	1.14	0.00
P62Aa4	11.31	1.12	0.79	0.01	9.88	0.60	37.77	2.68	14.83	0.92	1.06	0.00
P62Aa5	10.37	1.16	0.71	0.01	6.16	0.17	51.35	0.78	13.37	0.83	0.37	0.00
P62Ab1	3.69	0.12	11.69	0.18	7.14	0.29	35.61	1.00	6.35	0.39	0.28	0.00
P62Ab2	3.30	0.26	3.09	0.05	8.29	0.30	32.84	0.87	6.56	0.41	0.26	0.00
P62Ab3	3.03	0.21	3.83	0.06	8.42	0.28	39.17	0.84	7.88	0.49	0.29	0.00
P62Ab4	3.00	0.16	5.17	0.08	10.17	0.39	41.05	1.20	7.94	0.49	0.29	0.00
P62Ab5	2.69	0.24	2.48	0.04	7.73	0.29	33.17	0.88	5.61	0.35	0.28	0.00
P62Ab6	3.29	0.22	3.76	0.06	7.14	0.34	55.71	1.57	12.75	0.79	1.29	0.00

Table 3.8: (U-Th)/He ages of Bohnerz samples, continued. goe = goethite mass, P = Petersbuch

Petersbuch (P)												
Sample name	(U-Th-Sm)/He [Ma]		goe [ug]	1σ	U [ppm]	1σ	Th [ppm]	1σ	Sm [ppm]	1σ	He [nmol/g]	1σ
P-F2field-a1	7.7	0.1	12.86	0.16	5.91	0.09	49.67	0.79	33.99	1.52	0.73	0.11
P-F2field-a2	8.5	0.1	15.10	0.19	4.86	0.09	39.10	0.60	26.17	1.36	0.65	0.10
P-F2field-a3	11.8	0.2	13.23	0.14	3.22	0.07	23.20	0.33	68.76	2.23	0.56	0.10
P-F2field-a4	18.3	0.4	20.42	0.16	2.83	0.04	1.09	0.09	1.67	0.09	0.31	0.08
P-F2field-a5	17.2	0.5	9.33	0.11	2.38	0.05	4.89	0.18	45.64	2.21	0.33	0.10
P-F2field-a6	12.8	0.2	32.98	0.37	2.25	0.03	6.39	0.10	39.56	2.11	0.26	0.04
P-F2field-b1	2.5	0.0	87.31	0.82	5.65	0.08	44.51	0.56	19.12	0.94	0.22	0.03
P-F2field-b2	1.6	0.0	16.42	0.20	8.99	0.13	80.02	1.23	44.01	2.14	0.25	0.04
P-F2field-b3	5.1	0.1	5.48	0.08	7.88	0.15	45.20	0.74	21.89	1.18	0.52	0.11
P-F2field-b4	3.0	0.0	66.10	0.56	8.48	0.09	89.75	0.97	36.67	1.16	0.48	0.04
P-F2field-b5	1.3	0.0	18.02	0.19	7.90	0.12	118.42	1.62	28.72	1.43	0.25	0.06
P-F2-0-a1	23.0	0.5	28.55	0.21	1.45	0.02	1.45	0.04	20.11	0.72	0.23	0.06
P-F2-0-a2	16.0	2.3	15.66	0.24	2.35	0.21	3.14	0.10	21.55	1.30	0.27	0.05
P-F2-0-a3	28.0	0.7	33.22	0.28	0.36	0.01	9.16	0.15	17.76	0.77	0.39	0.06
P-F2-0-a4	11.1	0.2	24.53	0.26	1.79	0.03	23.12	0.35	17.87	1.01	0.44	0.06
P-F2-0-a5	7.3	0.1	10.15	0.10	3.31	0.09	96.85	1.14	30.82	1.40	1.04	0.19
P-f2-0-2a	5.2	0.1	42.48	0.48	3.53	0.06	36.45	0.43	35.77	2.10	0.34	0.04
P-f2-0-2b	6.9	0.1	55.06	0.70	3.76	0.06	36.56	0.51	49.02	2.11	0.46	0.03
P-f2-0-2c	4.1	0.0	32.09	0.28	5.36	0.06	67.87	0.70	93.56	4.01	0.48	0.05
P-F2-20-a1	1.2	0.0	32.74	0.16	7.40	0.05	212.77	1.65	not measured		0.38	0.12
P-F2-20-a2	2.3	0.0	17.58	0.08	9.72	0.08	16.86	0.16	not measured		0.17	0.11
P-F2-20-a3	1.2	0.0	10.10	0.05	11.40	0.08	155.05	1.32	not measured		0.32	0.15
P-F2-20-a4	2.5	0.1	4.80	0.03	8.04	0.07	13.25	0.45	not measured		0.15	0.10
P-f2-20-2a	2.5	0.0	26.73	0.30	2.04	0.03	30.85	0.39	14.87	0.99	0.13	0.06
P-f2-20-2b	3.4	0.1	20.09	0.29	3.02	0.06	16.99	0.27	19.06	0.87	0.13	0.11
P-f2-20-2c	3.0	0.0	27.75	0.33	3.53	0.05	34.74	0.48	27.02	1.41	0.19	0.02
P-F2-30-1a	2.5	0.0	7.05	0.04	23.30	0.23	218.81	1.56	1067.24	46.67	1.05	0.37
P-F2-30-1b	2.1	0.0	2.49	0.03	13.41	0.30	123.08	1.81	587.71	39.15	0.49	0.19
P-F2-30-1c	5.0	0.1	7.62	0.08	13.52	0.23	131.27	1.51	591.87	29.89	1.21	0.16
P-f2-40-1a	5.1	0.1	2.11	0.04	5.25	0.22	88.30	1.80	251.43	10.63	0.73	0.16
P-f2-40-1b	4.7	0.1	9.72	0.08	5.41	0.09	58.69	0.63	90.90	3.74	0.49	0.14
P-f2-40-1c	6.8	0.1	22.20	0.26	6.61	0.09	70.48	0.96	85.87	5.06	0.86	0.08
P-f2-40-2a	4.5	0.1	9.78	0.10	6.44	0.09	40.22	0.57	385.80	15.78	0.40	0.09
P-f2-40-2b	5.7	0.1	10.92	0.11	7.90	0.10	68.23	0.87	868.77	35.38	0.78	0.12
P-f2-40-2c	8.3	0.2	13.38	0.13	3.61	0.08	16.84	0.24	236.77	11.93	0.36	0.08
P-f2-60-1a	1.7	0.0	46.56	0.51	7.34	0.09	28.68	0.33	54.08	3.22	0.13	0.03
P-f2-60-1b	1.9	0.0	59.77	0.47	7.72	0.08	25.96	0.25	73.83	2.92	0.14	0.03
P-f2-60-1c	2.1	0.0	41.93	0.42	5.48	0.08	15.03	0.17	44.21	2.57	0.10	0.02
P-f2-60-2a	1.5	0.2	67.55	0.76	6.57	0.08	107.57	8.36	37.67	2.19	0.25	0.02
P-f2-60-2b	1.6	0.0	46.23	0.50	7.12	0.10	171.10	2.10	59.98	3.16	0.40	0.05
P-f2-60-2c	1.5	0.0	56.07	0.70	7.48	0.10	181.12	2.49	59.06	3.04	0.40	0.04
P-f2-100-1a	11.1	0.1	32.14	0.35	5.20	0.09	115.86	1.43	24.75	1.47	1.96	0.15
P-f2-100-1b	15.1	0.2	35.96	0.39	6.06	0.08	133.17	1.71	49.52	1.95	3.08	0.22
P-f2-100-1c	15.5	0.1	67.73	0.73	7.75	0.12	133.34	1.53	32.73	1.90	3.29	0.17
P-f2-100-2a	10.7	0.1	52.84	0.54	4.50	0.05	34.31	0.44	73.32	3.12	0.74	0.06
P-f2-100-2b	13.6	0.2	63.65	0.58	2.28	0.03	23.02	0.28	44.76	1.85	0.57	0.06
P-f2-100-2c	11.7	0.2	22.59	0.32	2.69	0.05	37.05	0.61	32.21	1.44	0.73	0.07
P-f2-200-1a	3.4	0.0	36.40	0.38	7.61	0.10	26.09	0.29	37.66	2.17	0.26	0.04
P-f2-200-1b	6.4	0.1	31.13	0.28	6.48	0.08	53.22	0.65	53.51	2.24	0.67	0.09
P-f2-200-1c	7.9	0.1	16.14	0.26	4.27	0.09	21.65	0.37	39.74	2.16	0.40	0.05
P-f2-200-2a	4.3	0.1	10.18	0.10	5.68	0.09	53.18	0.62	166.60	6.91	0.43	0.09
P-f2-200-2b	6.3	0.1	11.91	0.13	3.15	0.07	24.23	0.30	75.69	4.53	0.31	0.06
P-f2-200-2c	5.9	0.1	8.54	0.08	4.22	0.12	38.76	0.47	129.80	5.42	0.43	0.17
P-f2-350-1a	9.9	0.1	22.82	0.22	9.13	0.11	50.24	0.61	22.59	1.09	1.13	0.11
P-f2-350-1b	11.3	0.1	30.21	0.37	8.09	0.11	47.16	0.62	14.38	0.93	1.18	0.09
P-f2-350-1c	9.8	0.1	23.43	0.42	9.30	0.18	50.82	1.03	20.61	0.90	1.13	0.06
P-f2-350-2a	7.3	0.1	19.15	0.23	6.67	0.10	82.45	1.06	45.78	2.84	1.04	0.10
P-f2-350-2b	5.1	0.1	21.65	0.24	8.40	0.14	98.73	1.25	64.53	3.40	0.88	0.09
P-f2-350-2c	7.6	0.1	23.16	0.26	7.26	0.10	55.68	0.70	82.46	4.80	0.84	0.08

Table 3.9: (U-Th)/He ages of Bohnerz samples, continued. goe = goethite mass, R = Rothenstein

Rothenstein (R)												
Sample name	(U-Th-Sm)/He [Ma]		goe [ug]	1σ	U [ppm]	1σ	Th [ppm]	1σ	Sm [ppm]	1σ	He [nmol/g]	1σ
R16h-1	6.89	0.26	5.07	0.08	4.30	0.20	41.05	0.99	14.31	0.60	0.64	0.00
R16h-2	9.47	0.27	18.82	0.29	5.51	0.21	27.60	0.68	12.50	0.53	0.38	0.00
R16h-3	5.77	0.28	5.22	0.08	5.04	0.15	85.92	1.11	24.71	1.04	0.78	0.00
R16h-4	5.70	0.17	12.38	0.19	2.98	0.13	23.74	0.56	15.56	0.65	0.55	0.00
R16h-5	11.70	0.51	6.72	0.10	5.64	0.21	72.73	1.27	19.74	0.83	0.85	0.00
R16h-6	8.36	0.41	3.75	0.06	5.89	0.22	50.98	0.98	9.42	0.40	0.77	0.00
Willmandingen												
Sample name	(U-Th-Sm)/He [Ma]		goe [ug]	1σ	U [ppm]	1σ	Th [ppm]	1σ	Sm [ppm]	1σ	He [nmol/g]	1σ
Willmandingen-0-1a	9.0	0.3	12.97	0.39	3.96	0.14	58.29	2.05	49.96	3.69	0.87	0.05
Willmandingen-0-1b	11.3	0.2	17.81	0.41	4.09	0.13	55.91	1.40	47.88	3.89	1.06	0.07
Willmandingen-0-1c	9.2	0.3	17.48	1.50	5.45	0.48	70.65	6.25	36.21	5.07	1.11	0.02
Willmandingen-0-1d	11.9	0.3	22.71	0.36	3.82	0.08	45.21	1.02	43.07	3.54	0.94	0.08
Willmandingen-0-2b	16.0	0.4	2.69	0.39	4.30	0.66	90.58	13.08	57.24	9.98	2.24	0.05
Willmandingen-0-2c	18.9	0.8	3.25	0.19	2.74	0.27	66.96	4.01	56.58	5.55	1.90	0.13
Willmandingen-0-2d	19.9	0.8	11.41	0.53	2.96	0.16	88.08	4.59	64.07	5.65	2.57	0.04
Willmandingen-0-2e	21.9	0.9	7.12	0.34	2.51	0.16	24.34	1.28	70.63	5.51	0.99	0.06
Willmandingen-0-2f	20.2	0.4	25.96	1.51	2.47	0.15	41.06	2.43	74.85	7.03	1.34	0.03
Willmandingen-0-2g	21.2	0.6	52.38	1.93	2.20	0.09	42.64	1.71	76.71	6.23	1.42	0.04
Willmandingen-0-2h	30.7	0.7	34.79	0.85	1.36	0.05	10.51	0.28	46.87	3.66	0.65	0.04
Willmandingen-0-3a	24.5	1.1	18.57	0.23	5.83	0.10	55.95	1.96	97.30	3.54	2.55	0.18
Willmandingen-0-3b	16.9	1.1	20.22	0.21	6.56	0.09	110.63	4.57	125.94	4.08	3.01	0.23
Willmandingen-0-3c	20.5	1.0	16.17	0.18	4.18	0.06	54.59	1.89	73.05	2.49	1.90	0.12
Willmandingen-0-3d	31.1	0.7	8.96	0.19	1.95	0.05	12.20	0.32	24.54	1.26	0.82	0.08
Willmandingen-0-3e	19.3	0.5	6.82	0.07	3.57	0.09	30.92	0.54	32.07	1.63	1.14	0.20
Willmandingen-0-3f	15.6	0.2	11.28	0.21	4.10	0.10	42.27	0.83	38.19	1.93	1.19	0.07
Willmandingen-20-1a	51.4	1.8	33.47	1.44	1.21	0.06	6.59	0.31	20.13	1.81	0.78	0.03
Willmandingen-20-1b	42.2	1.8	5.82	0.23	1.79	0.12	27.15	1.24	28.44	3.99	1.89	0.09
Willmandingen-20-1c	44.1	1.5	26.96	0.72	1.53	0.07	8.98	0.28	20.75	2.22	0.88	0.04
Willmandingen-20-1d	38.7	3.6	33.77	17.22	1.76	0.98	34.93	17.84	26.41	15.20	2.11	0.00
Willmandingen-20-2c	28.5	0.6	56.14	1.62	2.02	0.06	37.66	1.19	39.92	4.94	1.69	0.07
Willmandingen-20-2d	41.5	1.0	9.28	0.59	4.12	0.28	21.24	1.39	38.14	3.24	2.07	0.04
Willmandingen-20-2e	24.6	2.0	2.93	0.19	2.37	0.20	27.96	2.33	54.15	5.17	1.20	0.06
Willmandingen-20-2f	27.6	0.5	10.90	0.33	7.16	0.25	72.19	2.30	52.16	5.80	3.63	0.10
Willmandingen-20-2h	17.3	0.8	2.93	0.17	4.31	0.36	54.79	3.40	41.57	6.61	1.62	0.13
Willmandingen-20-2i	21.6	0.6	12.18	0.63	5.68	0.30	88.65	4.76	74.82	7.71	3.13	0.08
Willmandingen-20-2j	31.5	0.7	39.23	1.78	2.17	0.10	31.82	1.52	41.02	4.07	1.66	0.03
Willmandingen-20-2k	30.1	0.6	15.46	1.06	4.89	0.35	43.47	3.02	52.52	5.98	2.49	0.05
Willmandingen-20-2l	40.5	1.3	7.10	0.54	4.08	0.32	36.48	2.89	22.66	2.90	2.80	0.04
Willmandingen-40-1a	30.7	0.7	16.43	0.67	9.04	0.39	35.33	1.58	43.42	4.28	2.91	0.10
Willmandingen-40-1b	43.9	0.7	28.01	0.86	9.05	0.29	17.72	0.64	19.82	1.67	3.17	0.09
Willmandingen-40-1d	34.6	0.7	17.28	0.35	7.94	0.20	25.64	0.63	27.29	2.10	2.64	0.16
Willmandingen-40-1f	42.6	0.7	24.59	0.88	6.63	0.25	13.59	0.53	17.29	1.53	2.28	0.07
Willmandingen-40-2a	24.9	1.3	33.05	0.37	3.92	0.05	49.78	1.74	86.93	2.81	2.13	0.10
Willmandingen-40-2b	6.1	0.5	14.21	1.10	27.96	2.78	109.45	10.26	63.87	8.95	1.77	0.03
Willmandingen-40-2c	23.9	0.3	31.82	0.24	4.00	0.04	81.29	0.79	126.59	5.22	3.02	0.28
Willmandingen-40-2d	17.8	1.0	25.27	0.31	2.74	0.05	74.45	2.62	79.72	2.55	1.97	0.14
Willmandingen-40-2e	9.8	0.3	8.37	0.26	51.16	1.83	156.23	6.42	257.89	14.82	4.70	0.13
Willmandingen-40-2f	17.4	0.2	8.46	0.06	5.34	0.07	38.87	0.41	58.45	2.30	1.38	0.25
Willmandingen-40-2g	23.9	0.4	11.18	0.18	4.32	0.11	32.28	0.58	53.40	2.58	1.56	0.11
Willmandingen-60-1a	22.7	1.2	32.15	0.52	4.80	0.09	64.20	2.41	65.70	2.63	2.47	0.10
Willmandingen-60-1b	23.5	1.7	28.64	0.30	4.60	0.07	134.32	5.55	103.67	3.71	4.64	0.25
Willmandingen-60-1c	22.3	0.3	25.67	0.21	8.86	0.10	104.47	1.22	125.36	5.08	4.08	0.32
Willmandingen-60-2a	14.5	0.1	15.66	0.11	19.54	0.21	76.37	0.70	131.62	5.61	2.97	0.35
Willmandingen-60-2b	24.9	0.7	13.84	0.10	2.11	0.07	48.80	0.80	47.31	2.08	1.85	0.29
Willmandingen-60-2c	13.2	0.2	11.79	0.10	13.61	0.17	60.96	0.81	112.42	4.57	2.02	0.19

Table 3.10: (U-Th)/He ages of Bohnerz samples, continued. goe = goethite mass, W = Weißenburg

Willmandingen												
Sample name	(U-Th-Sm)/He [Ma]		goe [ug]	1σ	U [ppm]	1σ	Th [ppm]	1σ	Sm [ppm]	1σ	He [nmol/g]	1σ
Willmandingen-100-1a	36.7	0.4	30.89	0.54	2.09	0.04	27.99	0.52	36.31	1.74	1.74	0.06
Willmandingen-100-1b	25.3	0.4	23.85	0.18	2.92	0.05	46.49	0.54	42.12	1.43	1.91	0.22
Willmandingen-100-1c	25.5	0.5	18.06	0.12	2.35	0.03	28.77	0.41	29.31	1.31	1.27	0.20
Willmandingen-100-1d	31.1	0.4	44.62	0.33	1.89	0.03	32.37	0.36	42.07	1.70	1.62	0.16
Willmandingen-100-2a	19.8	0.3	6.15	0.06	2.89	0.06	121.97	1.52	77.59	4.38	3.41	0.39
Willmandingen-100-2c	27.9	1.6	25.84	0.42	6.50	0.12	170.55	6.24	130.08	4.62	7.11	0.30
Willmandingen-100-2e	30.2	0.4	16.63	0.11	3.76	0.04	124.16	1.22	62.81	2.50	5.43	0.72
Willmandingen-150-1a	11.9	0.1	29.04	0.48	10.73	0.19	74.08	1.30	73.47	3.53	1.82	0.11
Willmandingen-150-1b	14.2	0.6	13.37	0.16	3.42	0.07	18.00	0.69	33.06	1.08	0.59	0.08
Willmandingen-150-1c	13.5	0.2	14.49	0.11	4.05	0.05	36.12	0.44	35.45	1.20	0.93	0.13
Willmandingen-150-1d	17.8	0.9	17.95	0.27	2.85	0.06	21.20	0.90	32.35	1.17	0.76	0.06
Willmandingen-150-1e	6.0	0.5	9.92	0.10	10.46	0.19	22.87	2.52	46.34	2.30	0.52	0.09
Willmandingen-150-1f	14.1	0.2	10.62	0.18	4.01	0.08	27.39	0.59	54.35	2.56	0.81	0.08
Willmandingen-150-1g	11.9	0.2	12.81	0.11	4.36	0.09	26.48	0.29	56.26	2.59	0.69	0.13
Willmandingen-150-2a	48.9	0.4	25.37	0.21	12.66	0.12	30.19	0.35	38.72	1.73	5.27	0.51
Willmandingen-150-2b	49.3	0.5	27.35	0.50	14.82	0.29	48.69	0.96	50.89	2.42	7.07	0.21
Willmandingen-150-2c	53.9	2.7	8.51	0.17	5.19	0.12	39.86	1.73	50.67	1.91	4.30	0.17
Willmandingen-150-2d	49.9	2.3	26.07	0.26	20.38	0.23	118.27	4.87	111.42	3.72	13.13	0.78
Willmandingen-150-2e	41.8	1.8	23.44	0.23	12.87	0.16	62.70	2.59	81.61	2.78	6.31	0.41
Willmandingen-150-2f	30.4	0.4	17.96	0.13	12.04	0.11	82.49	1.05	60.34	2.96	5.21	0.41
Willmandingen-150-2g	40.2	0.5	17.57	0.31	8.21	0.17	39.53	0.75	34.72	1.99	3.84	0.15
Weißenburg (W)												
Sample name	(U-Th-Sm)/He [Ma]		goe [ug]	1σ	U [ppm]	1σ	Th [ppm]	1σ	Sm [ppm]	1σ	He [nmol/g]	1σ
W21Ne-1	11.68	0.60	1.97	0.03	7.03	0.32	42.64	1.28	13.41	0.56	1.15	0.00
W21Ne-2	12.38	0.63	2.28	0.04	0.95	0.24	6.15	1.74	not measured		1.33	0.00
W21Ne-4	9.59	0.30	17.98	0.28	6.58	0.30	88.66	1.90	17.82	0.75	1.99	0.00
W21Ne-5	13.32	0.57	2.31	0.04	4.62	0.28	70.38	1.93	12.13	0.51	1.60	0.00
W21Ne-6	13.90	0.77	1.64	0.03	7.31	0.16	29.64	0.46	17.84	0.75	0.74	0.01

3.C ^{3}He concentration data table

Table 3.11: Measured ^{3}He concentrations of pisolith cortices (depth is measured below the modern surface, mass = mass of aliquot, 1 RA = 1.38×10^{-6}, Mat/g = millions of atoms per gram).

Locality	Sample	depth [cm]	mass [mg]	^{3}He/^{4}He [RA]	1σ	^{3}He [amol]	1σ	^{3}He conc. [Mat/g]	1σ
Aufberg	A-0-1	5	9.2	0.228	0.001	5.38	0.03	352	2
	A-20-2	25	10.46	1.450	0.006	10.51	0.05	605	3
	A-40-1	45	9.61	0.309	0.002	5.41	0.03	339	2
	A-80-1	85	9.97	0.253	0.002	3.33	0.03	201	2
Balsthal Erzmatt I	BI-1	unknown	12.04	0.393	0.003	4.84	0.03	242	2
Balsthal Erzmatt II	BII-1	unknown	9.26	0.470	0.002	7.56	0.04	492	3
Malsenhof	M-B-a	1000	4.13	0.410	0.004	2.61	0.03	381	5
	M-C-1	1100	1.95	0.339	0.006	0.84	0.01	260	6
	M-G-2	600	5.47	0.527	0.004	3.54	0.03	390	4
	M-I-2	500	7.09	0.156	0.001	2.56	0.02	217	2
	M-J-1	300	5.87	0.202	0.002	2.75	0.02	283	3
	M-J-2	300	8.61	0.189	0.001	3.94	0.03	276	2
Petersbuch	P-F2-field-b	0	10.43	1.022	0.009	2.64	0.02	152	1
	P-F2-0-a	5	7.43	0.276	0.005	0.73	0.01	59	1
	P-F2-20-2	25	7.77	0.885	0.016	0.77	0.01	60	1
	P-F2-40-1	45	8.59	0.493	0.006	1.34	0.02	94	1
	P-F2-100-2	100	8.54	0.739	0.006	3.43	0.03	242	2
	P-F2-350-1	350	7.41	0.565	0.006	2.45	0.02	199	2
Rothenstein	FH-R16-01	unknown	9.90	0.230	0.025	0.51	0.05	31	3
	FH-R16-02	unknown	2.96	0.111	0.035	0.18	0.06	37	12
Weißenburg	FH-W21N-02	unknown	1.76	0.020	0.009	0.11	0.05	39	17
	FH-W21N-01	unknown	4.69	0.454	0.084	0.33	0.06	43	8
	W21Ne	unknown	3.04	0.102	0.021	0.26	0.05	52	11
Willmandingen	W-0-2	0	7.88	0.156	0.002	1.90	0.02	145	2
	W-40-2	45	6.41	0.555	0.004	4.53	0.03	426	4
	W-100-1	100	8.17	0.467	0.005	1.98	0.02	146	2
	W-150-2	155	5.18	0.049	0.001	0.80	0.01	93	2

3.D List of localities of Bohnerz deposits with references

Given here is are tables listing localities of Bohnerz deposits compiled from published literature, containing deposits separated by fissure-type and stratiform-type, as well as cave deposits. Coordinates for each locality are given in latitude and longitude. Most localities were located to within 100 m, from coordinates given or localities indicated on maps in the reference, from precise descriptions of the location of the outcrops, from local names on topographic maps, or from the position of a mappable deposit on official geologic maps. The accuracy of these localities is marked as 'exact'. For other deposits, only the name of the nearest town is mentioned and they could not be located further. They are marked as 'approx'.

Names of localities were listed under the name given in the earliest reference. Fossiliferous fissure fillings have a naming convention (Dehm and Fahlbusch, 1970), in which they are named after the closest town and then given a number in order of discovery. We only recorded localities, not individual fissures. Locality names followed by numbers represent boreholes, according to their naming convention. Some localities were defined here and were named after the closest town/locality name on official topographic maps.

This database was used to construct a map, which is Fig. 3 in the main body of the paper. More details on the localities listed below can be found in an accompanying spreadsheet (Appendix 3.D). It contains additional information on substratum, cover, and fossils found in fissure fillings, and thickness of stratiform deposits, as well as comments on locations and the nature of the deposit.

Fissure-type deposits

Location of fissure-type Bohnerz deposits were compiled primarily from references that focused on a single fissure filling or a set of fissures. Regional compilations of fossiliferous fissure fillings can be found in Borger (1990), Dehm (1935, 1961), Heissig (1970), and Rummel (1993).

Table 3.12: List of localities of fissure-type deposits with coordinates, location accuracy, and original references.

Locality	latitude [°]	longitude [°]	accuracy	references
Aalberg bei Nattheim	48.70780	10.27153	exact	Kranz (1952)
Adelschlag	48.83225	11.20669	approx	Andres (1951) and Dehm (1961)
Albabstiegtunnel	48.41126	9.97854	exact	Wunderle and Abele (2018)
Albführen	47.64126	8.48481	approx	Metz (1989)
Albstadt	48.22293	9.03596	exact	Borger (1990) and Borger and Widdowson (2001)
Albuchpyramide	48.80447	10.49482	approx	Dehm (1935), Nathan (1925), and Rummel (1993)
Altdorf	48.98142	11.28808	exact	Birzer (1939)
Altebürg	48.66989	10.41758	exact	Kranz (1952)
Alten Hau	48.28186	9.20647	exact	Borger (1990)
Altenstadt	48.62088	9.80686	approx	Jäger (1835)
Altenstall	48.32582	9.17139	exact	Achenbach (1859) and Borger (1990)
Altheim	48.58623	10.05094	exact	Dehm (1978) and Lutzeier (1922)
Appertshofen bei Ingolstadt	48.87024	11.46031	approx	Dehm (1961) and Rummel (1993)
Arnegg	48.41745	9.86095	exact	Berger (1986), Dehm (1935, 1961, 1978), Miller (1907), Nathan (1925), and Rummel (1993)
Asang, Oberriffingen	48.83835	10.28980	exact	Kranz (1952)
Attenfeld bei Neuburg a. d. D.	48.79385	11.18793	approx	Dehm (1935), Rummel (1993), and Schlosser (1916)
Audincourt	47.48022	6.85213	approx	Kuntz (1973), Pharisat (1982), and Rosenthal (1990)
Aufberg, Salmendingen	48.34543	9.13243	exact	Achenbach (1859), Borger (1990), Pickford (2012), Rummel (1993), Ufrecht (2008), and Weiger (1908)
Auggen, Breisgau	47.78204	7.60367	exact	Achenbach (1859) and Weiger (1908)
Bachhagel O Giengen a. d. Brenz	48.63749	10.32095	approx	Dehm (1935, 1961), Hennig (1923), Miller (1907), Moos (1924), Nathan (1925), and Rummel (1993)
Badenweiler	47.80358	7.66923	approx	Rutte (1953)
Balsthal Holzfluh	47.32137	7.70240	exact	Baumberger (1923), this study
Bärental	48.10086	8.89976	exact	Weiger (1908)
Bassays	46.20788	6.99060	exact	Weidmann (1984b)
Bechtersbohl	47.60385	8.34872	approx	Metz (1989)
Beimerstetten-Hörvelsingen	48.48418	9.98303	approx	Dehm (1935), Engel (1908), and Rummel (1993)
Bellelay	47.26252	7.17776	exact	Aufranc et al. (2016)
Bennenberg	48.76944	10.34227	exact	Kranz (1952)

Table 3.13: List of localities of fissure-type deposits, continued.

Locality	latitude [°]	longitude [°]	accuracy	references
Beringen	47.70866	8.58054	exact	Schreiner (1992)
Berlingen-1	47.66147	9.03202	exact	Büchi et al. (1965)
Bernloch (Münsingen)	48.35237	9.34565	exact	Berger (1959), Dehm (1961), Hrubesch (1957), and Rummel (1993)
Bethoncourt	47.55051	6.80175	exact	Rosenthal (1990)
Bingen	48.11125	9.27389	approx	Achenbach (1859) and Borger (1990)
Bissingen	48.60031	9.49215	approx	Rummel (1993) and Schalk (1957)
Bitz	48.24234	9.08914	exact	Dehm and Fahlbusch (1970), Dehm (1961), Heller (1943), Jäger (1835), Kiderlen (1931), Rummel (1993), and Weiger (1908)
Bloc Studer	46.27338	6.93699	exact	Weidmann (1984b)
Boécourt (Moulin de Séprais)	47.37167	7.22945	exact	Mojon et al. (2018)
Böhmfeld	48.85994	11.36385	exact	Andres (1951)
Bolberg	48.40014	9.14363	exact	Weiger (1908)
Böllen	48.23950	9.04879	exact	Borger (1990)
Bönisch-Berg	48.30577	9.15602	exact	Borger (1990)
Bötzen bei Staufen	47.88449	7.73758	approx	Rutte (1953)
Brand	47.98111	8.87231	exact	Borger (1990)
Bruchsal	49.12248	8.60246	approx	Berger (1959)
Brunegg	47.42078	8.21060	exact	Epprecht (1958)
Buchheim	47.99983	8.98558	exact	Schöttle (2005)
Burghalden	48.35233	9.12146	exact	Borger (1990), Ufrecht (2008), and Weiger (1908)
Burgholz, Liptingen	47.93536	8.93300	exact	Achenbach (1859), Borger (1990), Heissig (1970, 1978), Pickford (2012), Ufrecht (2008), and Weiger (1908)
Burgmagerbein	48.73736	10.59841	exact	Berger (1986), Dehm (1961, 1978), Rummel (1993), and Schalk (1957)
Burladingen	48.29221	9.10948	approx	Achenbach (1859)
Burren bei Gauselfingen	48.28770	9.21426	approx	Achenbach (1859)
Carrière Carco	46.27290	6.94126	exact	Weidmann (1984b)
Carrière de Sous-Vent	46.23466	7.00453	exact	Murat (1956) and Weidmann (1984b)
Chamblon	46.78369	6.60656	approx	Jordi (1994) and Stehlin (1901, 1910)
Chambovey	46.23477	6.98963	exact	Weidmann (1984b)
Châtenois-les-Forges	47.55767	6.84906	approx	Rosenthal (1990)
Chemin Les Cases-Bassays	46.20906	6.99177	exact	Weidmann (1984b)
Cholplatz, Wangental (Jestetten)	47.64595	8.53385	exact	Achenbach (1859), Baumberger (1923), Birchmeier (1986), and Metz (1989)
Collombey	46.26880	6.94341	exact	Weidmann (1984b)
Cornol	47.40857	7.17359	exact	Diebold et al. (1963)
Côte de Develier-Dessus	47.36909	7.26122	exact	Keller and Liniger (2017)
Court	47.24579	7.35519	exact	Baumberger (1923), Epprecht (1958), and Schmidt (1920)
Dachsberg	48.23593	9.32879	exact	Borger (1990)
Dangstetten	47.59404	8.33050	approx	Metz (1989)
Daubenhubet-Lämmernplatten	46.41160	7.60611	exact	Tavel (1937) and Wieland (1979)
Degerfeld	48.25191	9.06753	exact	Borger (1990)
Deggingen (Möttingen)	48.59747	9.72239	approx	Dehm (1935), Kiderlen (1931), Nathan (1925), Rummel (1993), and Schlosser (1902)
Dinkelberg	47.61835	7.75419	approx	Metz (1989)

Table 3.14: List of localities of fissure-type deposits, continued.

Locality	latitude [°]	longitude [°]	accuracy	references
Dischingen	48.71203	10.35107	exact	Kranz (1952)
Dorfmerkingen	48.80478	10.32492	exact	Kranz (1952)
Ebingen (Balingen)	48.22824	9.01685	approx	Dehm (1935), Jäger (1835), Kiderlen (1931), Rummel (1993), and Schlosser (1902)
Eclépens-Gare	46.65823	6.55263	exact	Schmidt-Kittler et al. (1987)
Egelfingen	48.14039	9.29034	exact	Borger (1990)
Egelswang bei Veringen	48.15834	9.23917	exact	Achenbach (1859) and Borger (1990)
Egelwies	48.04355	9.13246	approx	Achenbach (1859)
Egenhäuser Kapf / Egenhausen	48.53853	8.65135	approx	Dehm (1961) and Rummel (1993)
Egerkingen	47.32405	7.79164	approx	Jordi et al. (2003), Moesch (1867), and Schmidt-Kittler et al. (1987)
Ehingen a.D.	48.28248	9.68326	exact	Berger (1986), Dehm (1939), Dehm and Fahlbusch (1970), Dehm (1935, 1961, 1978), and Rummel (1993)
Ehrenstein (Mähringen bei Ulm, Oberer Eselsberg)	48.42644	9.92499	exact	Berger (1986), Dehm (1935, 1978), Dietrich (1922), Kiderlen (1931), Rummel (1993), Schmidt-Kittler (1969), and Ziegler and Heizmann (1991)
Eigeltingen	47.86541	8.89072	exact	Schöttle (2005) and Schreiner (1974)
Eisenloch (Ringingen)	48.31234	9.10371	exact	Achenbach (1859), Borger (1990), Dehm (1935), Jäger (1835), Kiderlen (1931), Ufrecht (2008), and Weiger (1908)
Eitensheim	48.81922	11.32039	approx	Andres (1951) and Dehm (1961)
Enkering	48.99274	11.36189	approx	Birzer (1939)
Erkertshofen	48.97861	11.20595	exact	Berger (1986), Dehm (1978), Fahlbusch (1966, 1970), Heissig (1973, 1978), Koenigswald (1970), Müller (1967), and Rummel (1993)
Erpfingen	48.35497	9.18008	exact	Borger (1990), Dehm (1935), and Rummel (1993)
Eselsberg bei Ulm	48.41420	9.97212	approx	Dietrich (1930), Hennig (1923), Miller (1907), and Schlosser (1902)
Esselberg	49.03792	11.27470	exact	Birzer (1939)
Ettenkirch I	47.71159	9.51538	exact	Volz (1957)
Farrenberg (Mössingen)	48.38667	9.07472	exact	Dehm (1935), Jäger (1835), Kiderlen (1931), and Rummel (1993)
Fleinheim	48.71503	10.31346	exact	Kranz (1952)
Forheim	48.75841	10.44916	approx	Dehm (1978), Müller (1967), and Rummel (1993)
Fronhofen 1	47.86609	9.51972	exact	Volz (1957)
Gaimersheim westlich Ingolstadt	48.81976	11.37964	exact	Andres (1951), Berger (1959), Dehm and Fahlbusch (1970), Dehm (1935, 1937, 1961), Fahlbusch (1970), and Rummel (1993)
Gammertingen (Sigmaringen)	48.24745	9.21545	approx	Achenbach (1859), Dehm (1935), Kiderlen (1931), and Rummel (1993)
Geissenloch	48.26563	9.13336	exact	Borger (1990)
Genkingen (Reutlingen)	48.41545	9.20404	exact	Dehm (1935), Rathgeber (2002), Rummel (1993), and Schlosser (1902)
Gennenbach	47.76787	7.62760	approx	Rutte (1953)
Gockeler, Onstmettingen	48.29646	9.00856	exact	Achenbach (1859) and Borger (1990)
Gösgen SB2	47.36314	7.97368	exact	Beauheim (2013)

Table 3.15: List of localities of fissure-type deposits, continued.

Locality	latitude [°]	longitude [°]	accuracy	references
Götzelshard	48.96312	11.26071	exact	Birzer (1939)
Grabenstetten	48.53438	9.46027	exact	Weiger (1908)
Grafenberg	49.01554	11.28873	exact	Birzer (1939)
Grafenmühle (Pappenheim)	48.93177	10.94361	exact	Berger (1986), Dehm and Fahlbusch (1970), Dehm (1935, 1961, 1978), Heissig (1970, 1973), Müller (1967), and Schlosser (1902)
Grandes Roches	47.40655	7.22876	exact	Diebold et al. (1963)
Greding (Kraftsbucher Str)	49.04089	11.33464	exact	Birzer (1939)
Griessen im Klettgau	47.60689	8.41157	exact	Kuhn and Meigen (1924)
Grobschwart	48.98509	11.08491	exact	Heissig (1978) and Rummel (1993)
Gross-Höbing	49.07507	11.31604	exact	Birzer (1939)
Grossmehring bei Ingolstadt	48.76454	11.53615	approx	Dehm (1935, 1937), Rummel (1993), and Schlosser (1916)
Guldesmühle (S Dischingen)	48.68095	10.36292	approx	Dehm (1978), Gall (1971), Gall (1969), and Rummel (1993)
Gunzenheim	48.77940	10.76700	exact	Dehm (1931) and Dehm (1935, 1978)
Gussenstadt (Geislingen)	48.63540	9.96540	exact	Dehm (1935) and Rummel (1993)
Haag	48.93538	10.89332	exact	Berger (1986), Dehm (1978), Heissig (1973, 1978), and Rummel (1993)
Hagau O Wemding	48.91958	10.75310	exact	Dehm (1935, 1961), Rummel (1993), and Weber (1951)
Hammerstein	47.69044	7.64714	approx	Rutte (1953)
Härdtle bei Frohnstetten	48.14319	9.05516	exact	Achenbach (1859), Alberti (1853), Dehm (1935), Fraas (1859), Hennig (1923), Kiderlen (1931), Rummel (1993), Schlosser (1902), and Weiger (1908)
Hart	47.97331	8.87641	exact	Borger (1990)
Harthausen (Veringendorf)	48.19617	9.15791	approx	Achenbach (1859)
Hassenberg bei Stetten unter Höhlstein	48.33200	9.15013	exact	Achenbach (1859)
Hattingen (Hattinger Tunnel)	47.91242	8.77287	exact	Dehm (1935, 1961), Kiderlen (1931), and Rummel (1993)
Haunsheim	48.60708	10.37156	exact	Gall (1971)
Hausen	49.05460	11.31275	exact	Birzer (1939)
Heidenheim am Hahnenkamm	49.01624	10.75879	exact	Dehm (1935, 1961), Gümbel (1891), Maack (1865), Rummel (1993), and Schlosser (1902)
Heldenfingen	48.62136	10.10517	exact	Lutzeier (1922)
Hengen/Böhringen	48.49193	9.48566	approx	Weiger (1908)
Herbolzheim	48.23032	7.78148	approx	Rutte (1953)
Herdern	47.57476	8.45672	approx	Metz (1989)
Hermaringen a. d. Brenz	48.59285	10.27856	exact	Dehm (1935) and Rummel (1993)
Herrenwald	48.31724	9.11763	exact	Ufrecht (2008)
Herrlingen	48.42089	9.89973	exact	Berger (1986), Dehm and Fahlbusch (1970), Dehm (1978), Palmowski and Wachendorf (1966), Rummel (1993), Ziegler (1998), and Ziegler and Heizmann (1991)
Herrnsberg	49.08735	11.37567	exact	Birzer (1939)

Table 3.16: List of localities of fissure-type deposits, continued.

Locality	latitude [°]	longitude [°]	accuracy	references
Hettingen	48.21826	9.19007	approx	Achenbach (1859) and Borger (1990)
Heuberg von Frohnstetten	48.14242	9.01400	approx	Dehm (1935, 1961) and Fraas (1859)
Heuberg, Laucherthal	48.08778	9.27226	exact	Borger (1990), Dehm (1935), Jäger (1835), Kiderlen (1931), Leonhard (1838), and Schlosser (1902)
Heudorf und Altstatt bei Messkirch i. Bad.	47.99480	9.07319	approx	Dehm (1935), Kiderlen (1931), Rummel (1993), Schill (1858), and Schlosser (1902)
Hexerwiesen	47.97956	8.96041	exact	Borger (1990)
Hirnstetten	48.96954	11.30049	exact	Birzer (1939)
Hochberg bei Jungnau	48.14969	9.25277	exact	Borger (1990), Dehm (1931), Kiderlen (1931), Rummel (1993), and Schlosser (1902)
Hofstetten O Eichstaett	48.86637	11.31969	exact	Andres (1951), Dehm (1935), and Rummel (1993)
Hohentengen	47.57114	8.43290	approx	Metz (1989)
Hoher Stich	48.65127	10.23686	exact	Kranz (1952)
Hölschloch (Ringingen)	48.32086	9.09631	exact	Achenbach (1859), Borger (1990), Dehm (1935), Jäger (1835), Kiderlen (1931), Ufrecht (2008), and Weiger (1908)
Homburg SE Liptingen	47.92327	8.92940	exact	Borger (1990)
Huisheim	48.82519	10.70409	approx	Rummel (1993)
Hülbe-Wald	48.21289	9.28491	exact	Borger (1990)
Hundersingen	48.34288	9.48828	approx	Dehm (1961) and Rummel (1993)
Hundszell	49.06464	11.26074	exact	Birzer (1939)
Hürth	48.92568	10.92172	exact	Berger (1986), Dehm (1978), Heissig (1973, 1978), and Rummel (1993)
Igelswies	48.00574	9.14362	approx	Achenbach (1859)
Iggenhausen	48.73033	10.37418	exact	Kranz (1952)
Inneringen	48.18981	9.28055	approx	Achenbach (1859)
Jungnau	48.14329	9.19932	exact	Achenbach (1859)
Kaisheim	48.76854	10.74338	exact	Dehm (1961) and Rummel (1993)
Käpfle-Gruben	48.34311	9.13853	exact	Ufrecht (2008)
Karlshof südlich Nördlingen	48.76917	10.49950	approx	Dehm (1935, 1961), Nathan (1925), and Rummel (1993)
Katzenfels bei Egesheim	48.11647	8.86925	exact	Weiger (1908)
Katzenstein	48.79985	10.66392	approx	Dehm (1978), Müller (1967), Müller (1972), and Rummel (1993)
Köbele bei Salmendingen	48.35504	9.11604	exact	Borger (1990) and Weiger (1908)
Kohlhau	48.28616	9.18790	exact	Borger (1990)
Kolbingen (Tuttlingen)	48.05240	8.88940	approx	Achenbach (1859), Jäger (1835), and Rummel (1993)
Kraftsbuch	49.03959	11.30567	exact	Birzer (1939)
Kugelberg, Ulm	48.416479	9.976874	exact	Tetzel and Franz (2019)
La Cernie Dessous	47.35680	7.11624	exact	Diebold et al. (1963)
La Corde	46.27885	7.15381	exact	Linder (2005)
La Grive-Saint-Alban (Lechartier)	45.60247	5.22639	exact	López-Antoñanzas and Mein (2011) and Mein and Ginsburg (2002)
La Grive-Saint-Alban (Milliat)	45.59805	5.21856	exact	López-Antoñanzas and Mein (2011) and Mein and Ginsburg (2002)
La Grive-Saint-Alban (Peyre et Beau)	45.59558	5.22999	exact	López-Antoñanzas and Mein (2011) and Mein and Ginsburg (2002)
La Motte	47.34655	7.06565	exact	Diebold et al. (1963)

Table 3.17: List of localities of fissure-type deposits, continued.

Locality	latitude [°]	longitude [°]	accuracy	references
La Verrerie de Roches	47.31625	7.39339	exact	Baumberger (1923), Becker et al. (2013), Epprecht (1958), and Schmidt (1920)
Lahr-Dinglingen	48.33722	7.86416	approx	Rutte (1953)
Laisacker	48.74953	11.16224	exact	Heissig (1973, 1978) and Rummel (1993)
Langenaltheim	48.89242	10.96211	exact	Berger (1986), Dehm and Fahlbusch (1970), and Rummel (1993)
Langenenslingen	48.14756	9.37849	approx	Achenbach (1859), Dehm (1935), Kiderlen (1931), and Rummel (1993)
Langenhart	48.04630	9.10372	approx	Achenbach (1859)
Laubenthal	48.97733	11.05695	exact	Berger (1986) and Rummel (1993)
Lauchertgraben	48.15113	9.21919	exact	Borger (1990)
Lauffohr	47.50015	8.22481	approx	Moesch (1867)
Lautern	48.79680	9.98159	approx	Rummel (1993) and Ziegler and Heizmann (1991)
Le Moulin	46.22801	6.98438	exact	Weidmann (1984b)
Leimberg bei Merdingen	48.00592	7.67219	exact	Illies (1956) and Schöttle (2005)
Leimen	48.24741	9.03903	exact	Borger (1990)
Leitenhof	48.74775	10.60794	approx	Dehm (1978), Müller (1967), Müller (1972), and Rummel (1993)
Les Breuleux	47.21128	7.00862	approx	Aubert (1975) and Suter (1936)
Les Envers	47.19738	7.02583	exact	Aufranc and Burkhalter (2016)
Les Mûriers	46.23931	7.00335	exact	Gagnebin et al. (1934) and Weidmann (1984b)
Les Ponts-de-Martel	47.00064	6.73516	exact	Pasquier and Burkhard (2018)
Leupe	47.59529	6.87663	approx	Rosenthal (1990)
Liel	47.73928	7.60454	approx	Rutte (1953)
Lienheim	47.57362	8.37497	approx	Metz (1989)
Linden	49.02525	11.32059	exact	Birzer (1939)
Lippertshofen	48.83878	11.36550	exact	Andres (1951)
Liptingen	47.93650	8.93876	exact	Borger (1990), Borger and Widdowson (2001), Geyer et al. (2011), Scherzinger (2005), Schöttle (2005), and Schreiner (1974)
Lobsing	48.84791	11.69162	exact	Dehm and Fahlbusch (1970) and Rummel (1993)
Lottstetten	47.62937	8.57335	approx	Metz (1989)
Macksen-Schlucht	48.30767	8.99884	exact	Borger (1990)
Mähringen	48.42753	9.92737	exact	Dehm (1935), Dietrich (1922, 1929, 1936), Kiderlen (1931), and Roll (1934)
Margarethe bei Nattheim	48.68055	10.21927	exact	Fluhr (1908) and Kranz (1952)
Mauren	48.76807	10.65900	exact	Dehm (1978), Heissig (1973, 1978), and Rummel (1993)
Melchingen	48.35941	9.14669	exact	Achenbach (1859), Dehm (1935), Jäger (1835), Kiderlen (1931), Rummel (1993), and Schlosser (1902)
Mettenberg	48.30440	9.10381	exact	Borger (1990)
Möhren	48.92821	10.85766	exact	Berger (1986), Dehm and Fahlbusch (1970), Dehm (1961, 1978), Heissig (1970, 1973, 1978), Rummel (1993), and Schmidt-Kaler (1962)
Mönchsdeggingen (Deggingen am Ries)	48.77577	10.57951	approx	Dehm (1935, 1961, 1978), Nathan (1925), and Rummel (1993)

Table 3.18: List of localities of fissure-type deposits, continued.

Locality	latitude [°]	longitude [°]	accuracy	references
Monk, Salmendingen	48.36028	9.10669	exact	Achenbach (1859), Borger (1990), Ufrecht (2008), and Weiger (1908)
Montpalais	47.34584	7.07643	exact	Diebold et al. (1963)
Mormont-Eclépens	46.65538	6.53633	approx	Custer and Aubert (1935) and Stehlin (1910)
Mormont-Entreroches	46.66276	6.54568	approx	Custer and Aubert (1935), Harpe (1870), Schmidt-Kittler et al. (1987), and Stehlin (1910)
Mörnsheim (Maxbruch/Maxberg/Neue Welt)	48.88100	11.00231	exact	Dehm (1935), Rummel (1993), and Schlosser (1916)
Morsbach	49.03192	11.26318	exact	Birzer (1939)
Münsingen	48.40513	9.49022	approx	Weiger (1908)
Nack	47.60430	8.57518	approx	Metz (1989)
Nattheim	48.68756	10.22358	exact	Bleich et al. (1987), Dehm (1961), Kranz (1952), Leonhard (1838), and Rummel (1993)
Nendingen bei Tuttlingen	48.00133	8.88615	approx	Jäger (1835) and Weiger (1908)
Nennslingen	49.04410	11.12678	approx	Rummel (1993)
Neufra	48.24880	9.18288	approx	Achenbach (1859)
Neuhausen, Engen	47.83801	8.78338	exact	Fraas (1859), Jäger (1835), Schöttle (2005), and Schreiner (1974)
Niederrimsingen	47.99669	7.65365	approx	Rutte (1953)
Niefang	48.99775	11.32596	exact	Birzer (1939)
Nollhof (Sigmaringen)	48.10802	9.20497	exact	Borger (1990)
Oberbechingen	48.60951	9.31049	exact	Berger (1986) and Rummel (1993)
Oberbuchsiten	47.31962	7.77377	exact	Baumberger (1923) and Moesch (1867)
Obergösgen	47.37683	7.95939	exact	Moesch (1867) and Schmidt-Kittler et al. (1987)
Oberheumödern	48.95041	10.85361	exact	Rummel (1993)
Oberkochen (Aalen)	48.75932	10.10597	exact	Dehm (1935), Kranz (1952), Rummel (1993), and Schlosser (1922)
Oberschmeien (Sigmaringen)	48.10603	9.14227	approx	Achenbach (1859), Dehm (1935, 1961), Jäger (1853), Kiderlen (1931), and Rummel (1993)
Oberstotzingen	48.53787	10.22237	approx	Dehm (1935) and Rummel (1993)
Ochsenberg	48.74303	10.13730	exact	Kranz (1952)
Oppertshofen	48.71352	10.67201	exact	Berger (1986), Dehm (1978), Heissig (1970), and Rummel (1993)
Örlinger Tal (Ulm)	48.41725	9.99276	approx	Dehm (1935), Dietrich (1929), Miller (1907), Rummel (1993), and Schlosser (1902)
Österberg	49.09667	11.34984	exact	Birzer (1939)
Pappenheim (Weinberg)	48.93667	10.98209	exact	Dietrich (1930), Rummel (1993), and Schlosser (1902, 1916)
Pérouse	47.63397	6.89528	approx	Rosenthal (1990)
Petersbuch	48.98971	11.19874	exact	Dehm (1978), Fahlbusch (1966), Heissig (1978), Rosina and Rummel (2012), Rummel (1993), and Rummel (2001)
Pfaffnau Süd-1	47.20326	7.90003	exact	Büchi et al. (1965) and Wieland (1979)
Pfahldorf	48.96326	11.34603	exact	Birzer (1939)
Pfronstetten (Münsing)	48.27709	9.36005	approx	Dehm (1961) and Rummel (1993)
Raitenbuch	49.00304	11.14373	exact	Dehm (1935), Gümbel (1891), Rummel (1993), and Schlosser (1902)

Table 3.19: List of localities of fissure-type deposits, continued.

Locality	latitude [°]	longitude [°]	accuracy	references
Rammingen (Ulm)	48.51743	10.17276	approx	Dehm (1935), Miller (1907), and Rummel (1993)
Rehberg	47.74259	7.58829	approx	Achenbach (1859)
Reistingen	48.69591	10.40907	exact	Gall (1971)
Reuth	49.01924	8.53166	exact	Berger (1959)
Riedlingen	47.71565	7.63624	approx	Rutte (1953)
Ringsheim	48.24619	7.78010	approx	Rutte (1953)
Röckenhofen	49.08007	11.35372	exact	Birzer (1939)
Rohrach	48.99110	10.80757	exact	Heissig (1978) and Rummel (1993)
Ronheim	48.79226	10.69810	exact	Berger (1986), Heissig (1973, 1978), Rummel (1993), and Trischler and Winkler (1968)
Roppe	47.66967	6.91982	approx	Rosenthal (1990)
Rötenberg	48.66188	10.24253	exact	Kranz (1952)
Rothenstein 1	48.96318	11.05529	exact	Dehm (1978), Heissig (1978), and Rummel (1993)
Rothenstein 2	48.95158	11.10070	exact	Dehm (1978) and Heissig (1978)
Rupertsbuch	48.93033	11.13193	exact	Berger (1986), Heissig (1978), and Rummel (1993)
Russberghof bei Tuttlingen	48.00228	8.80492	exact	Dehm (1935, 1961), Jäger (1835), Kiderlen (1931), Rummel (1993), and Schlosser (1902)
Sankt Johann	48.48502	9.31213	exact	Weiger (1908)
Saulgau 1	47.99701	9.48539	exact	Volz (1957)
Saulgau 3	47.98753	9.42608	exact	Volz (1957)
Schaffhausen (Harburg)	48.76874	10.64176	exact	Dehm (1978), Heissig (1973), and Rummel (1993)
Schalmenäcker	47.96166	8.92521	exact	Borger (1990)
Scheer	48.07307	9.29998	approx	Achenbach (1859)
Schelklingen	48.37251	9.73906	exact	Dehm and Fahlbusch (1970), Dehm (1978), Heissig (1970), Mayr and Schindlmayr (1967), and Rummel (1993)
Schernfeld	48.90869	11.11209	exact	Dehm (1961, 1978)
Schindergrube	47.95575	8.93026	exact	Borger (1990)
Schliengen	47.75680	7.57729	approx	Rutte (1953) and Weiger (1908)
Schnaitheim bei Heidenheim an der Brenz	48.70891	10.15042	exact	Berger (1959), Dehm (1939), Dehm (1935, 1961), Herre and Lunau (1950), Hrubesch (1957), and Rummel (1993)
Schratenhof	48.65399	10.25339	exact	Kranz (1952)
Schutzendorf	49.05467	11.27855	exact	Birzer (1939)
Schwandorfer Wald, Neuhausen ob Eck	47.95890	8.96216	exact	Dehm (1935), Kiderlen (1931), Schlosser (1902), Schöttle (2005), and Schreiner (1979)
Sigmaringen	48.09435	9.20438	exact	Achenbach (1859), Borger (1990), and Borger and Widdowson (2001)
Sigmaringendorf	48.07279	9.26373	approx	Achenbach (1859)
Solnhofen	48.89176	10.97887	exact	Ameghino (1905, 1908), Dehm (1935, 1937, 1961), Fahlbusch (1970), Rummel (1993), Schlosser (1904), and Schlosser (1916)
Sommerwies	47.71723	8.60320	exact	Schreiner (1992)
Sontheim an der Brenz	48.55945	10.28081	approx	Rummel (1993)

Table 3.20: List of localities of fissure-type deposits, continued.

Locality	latitude [°]	longitude [°]	accuracy	references
Steinbuck (Karlshof)	48.75627	10.57978	exact	Dehm (1935), Nathan (1925), and Rummel (1993)
Stetten am kalten Markt	48.12561	9.07411	approx	Dehm (1935), Kiderlen (1931), and Schlosser (1902)
Straßberg	48.19740	9.08639	exact	Scherzinger (2005)
Stubersheim SO Geislingen	48.58819	9.92621	approx	Dehm and Fahlbusch (1970), Dehm (1935, 1961), Lutzeier (1922), and Rummel (1993)
Sur le Scé	46.22501	6.98501	exact	Weidmann (1984b)
Tailfingen	48.25909	9.03334	exact	Borger (1990)
Tannenkirch	47.71065	7.60704	approx	Rutte (1953)
Tanningen	47.97223	8.96747	exact	Borger (1990)
Tauchenweiler	48.78054	10.02582	exact	Bleich et al. (1987)
Teck bei Kirchheim	48.58846	9.47027	approx	Jäger (1835)
Tegerfelden	47.55617	8.29543	exact	Epprecht (1958) and Scheuchzer (1707)
Teningen	48.15216	7.83857	exact	Brüderlin (1969), Rutte (1953), and Schöttle (2005)
Thalheim	48.00643	9.03775	approx	Achenbach (1859)
Thiergarten westlich Sigmaringen	48.08709	9.09405	exact	Dehm (1935, 1961), Jäger (1853), Kiderlen (1931), and Rummel (1993)
Tomerdingen	48.47616	9.90399	exact	Dehm and Fahlbusch (1970), Dehm (1935, 1961), Fraas (1859), Palmowski and Wachendorf (1966), Rummel (1993), and Seemann and Berckhemer (1930)
Treuchtlingen	48.95193	10.90409	exact	Berger (1986), Dehm and Fahlbusch (1970), Dehm (1978), and Fahlbusch (1970)
Trochtelfingen	48.30835	9.23980	approx	Achenbach (1859), Dehm (1935), Jäger (1835), Kiderlen (1931), Rummel (1993), and Schlosser (1902)
Tsanfleuron	46.31863	7.25862	exact	Epprecht (1958)
Übermatzhofen	48.91873	10.97795	exact	Berger (1986), Dehm (1961), and Rummel (1993)
Undingen	48.48641	9.27137	approx	Dehm (1935), Rummel (1993), and Schlosser (1902)
Unterbechingen	48.61525	10.36753	exact	Gall (1971)
Unterringer Spitalwald	48.13924	9.28451	exact	Borger (1990)
Urach	48.49295	9.39919	approx	Jäger (1835)
Veringendorf	48.15850	9.20043	approx	Achenbach (1859), Kiderlen (1931), Rummel (1993), and Schlosser (1902)
Veringenstadt	48.18761	9.21662	exact	Berger (1986), Borger (1990), Borger and Widdowson (2001), Dehm (1935), Kiderlen (1931), Rummel (1993), and Schlosser (1902)
Vilsingen (Inzigkofen)	48.06093	9.14276	approx	Achenbach (1859)
Vohbühl Bopfingen	48.85557	10.33531	exact	Dehm (1939), Dehm (1961), and Rummel (1993)
Vue-des-Alpes	47.06102	6.88906	exact	Bolliger (1997) and Bolliger et al. (1993)
Wahlberg bei Nattheim	48.69034	10.27389	exact	Kranz (1952)
Waldberg	47.93785	8.94277	exact	Scherzinger (2005)

Table 3.21: List of localities of fissure-type deposits, continued.

Locality	latitude [°]	longitude [°]	accuracy	references
Weidenstetten (Ulm)	48.55767	9.98081	exact	Dehm (1935) and Rummel (1993)
Weidenstock	47.95637	8.92534	exact	Borger (1990)
Weißenburg	49.01138	11.01963	exact	Berger (1986), Dehm (1939), Dehm and Fahlbusch (1970), Dehm (1935, 1937, 1961, 1978), Fahlbusch (1968), Fahlbusch and Schmidt (1969), Heissig (1973, 1978), Müller (1967), Rummel (1993), and Schmidt-Kittler (1971)
Wellesberg	48.64748	10.09691	exact	this study
Wenningen	47.97427	8.95760	exact	Borger (1990)
Westerstetten	48.52687	9.94893	exact	Dehm (1935), Dietrich (1925), and Rummel (1993)
Willmandingen (Reutlingen)	48.39299	9.15172	exact	Borger (1990), Borger and Widdowson (2001), Dehm (1935), Jäger (1835), Kiderlen (1931), Rummel (1993), Schlosser (1902), and Weiger (1908)
Wintershof-Ost	48.90366	11.18444	exact	Dehm (1939), Dehm (1935, 1937, 1961), and Rummel (1993)
Wintershof-West	48.90882	11.16313	exact	Berger (1959), Dehm (1939, 1950a,b), Dehm and Fahlbusch (1970), Dehm (1935, 1937, 1961), and Rummel (1993)
Winzloch	48.40523	9.17043	exact	Weiger (1908)
Wippingen	48.42734	9.86362	approx	Dehm (1935, 1961), Kiderlen (1931), and Rummel (1993)
Wolferstadt O Wemding	48.90212	10.77013	exact	Dehm (1935, 1961), Rummel (1993), and Weber (1958)
Wöpplinsberg	48.13494	7.85499	approx	Rutte (1953) and Steinmann and Graeff (1897)
Würtingen	48.45578	9.34375	approx	Dehm (1935), Jäger (1835), Rummel (1993), and Weiger (1908)
Zitterberg	48.71526	10.27084	exact	Kranz (1952)
Zöschingen	48.68040	10.32710	exact	Dehm (1978), Kranz (1952), Rummel (1993), and Weiger (1908)

Stratiform-type deposits

Many references for stratiform-type deposits focused on mining. Mappable quantities of Bohnerz deposits (mainly of the stratiform type) on the official geologic map of Switzerland are also noted here and the respective map sheet is given as a source. Regional compilations of mostly stratiform-type deposits can be found in Bartz (1940), Baumberger (1923), Birchmeier (1986), Epprecht (1958), and Wieland (1979).

Table 3.22: List of localities of stratiform-type deposits with coordinates, location accuracy, and original references.

Locality	latitude [°]	longitude [°]	accuracy	references
Aareschlucht-Willigen	46.71738	8.20337	exact	Epprecht (1958)
Aedermannsdorf (Hammer)	47.29410	7.60394	exact	Baumberger (1923), Borger (1990), and Borger and Widdowson (2001)
Allschwil	47.56001	7.55997	exact	Schmidt et al. (1924)
Andelnans	47.60418	6.86113	approx	Rosenthal (1990)
Bachtalen	47.32340	7.64822	exact	Baumberger (1923)
Badevel	47.50078	6.93895	approx	Rosenthal (1990)
Bärenmatt-Wengi (Matzendorf)	47.32313	7.63364	exact	Baumberger (1923) and Baumberger (1907)
Bartlibrunnen (Herzimatt)	47.31696	7.62627	exact	Baumberger (1923)
Bauerbach	49.07363	8.74311	exact	Schmidt (1941)
Benken	47.64485	8.64949	exact	Birkhäuser et al. (2001), Marchant et al. (2005), and Nagra (2001)
Berlincourt	47.32407	7.22957	exact	Aufranc et al. (2016), Baumberger (1923), and Epprecht (1958)
Bessoncourt	47.64443	6.94220	approx	Rosenthal (1990)
Biesendorf (Engen)	47.86409	8.79720	exact	Achenbach (1859)
Birnbaumgewann	49.95419	8.20847	exact	Bartz (1940)
Bleichkopf	49.90002	8.07862	exact	Bartz (1940)
Böbikon	47.55321	8.33383	exact	Matousek et al. (2000)
Boecourt	47.34983	7.20909	exact	Diebold et al. (1963)
Bogenthal	47.37229	7.65236	exact	Koch et al. (1939)
Boppelsen	47.48091	8.41672	exact	Haldimann et al. (2017) and Scheuchzer (1707)
Bornfeld	47.33200	7.88249	exact	Baumberger (1923)
Bourrignon	47.40511	7.24079	exact	Diebold et al. (1963) and Keller and Liniger (2017)
Bözberg	47.50009	8.14836	exact	Epprecht (1958) and Scheuchzer (1707)
Breitruetti	47.29540	7.61452	exact	Baumberger (1923)
Brugg	47.48175	8.19509	exact	Moesch (1867)
Buchebene	47.40269	8.02447	exact	Baumberger (1923) and Wullschleger (2005)
Buus	47.50533	7.85613	exact	Amsler (1935) and Epprecht (1958)

Table 3.23: List of localities of stratiform-type deposits, continued.

Locality	latitude [°]	longitude [°]	accuracy	references
Cerneux	47.36453	7.23487	exact	Baumberger (1923) and Diebold et al. (1963)
Champoz	47.25335	7.31008	exact	Pfirter et al. (1996)
Chèvremont	47.62882	6.92104	approx	Rosenthal (1990)
Corcelles	47.28869	7.47788	exact	Baumberger (1923)
Cornol	47.40276	7.15768	exact	Diebold et al. (1963)
Courcelon	47.36485	7.41855	exact	Pfirter et al. (1996)
Courrendlin	47.33487	7.37869	exact	Pfirter et al. (1996)
Courroux	47.37567	7.36553	exact	Pfirter et al. (1996)
Crémines	47.29269	7.44204	exact	Baumberger (1923)
Dampierre-les-Bois	47.50628	6.91258	approx	Rosenthal (1990)
Danjoutin	47.61840	6.86724	approx	Rosenthal (1990)
Dasle	47.47789	6.89525	approx	Rosenthal (1990)
Dattenhausen	48.65593	10.40319	exact	Gall (1971)
Delemont Communance Forage 5	47.35117	7.34426	exact	Pirkenseer et al. (2018)
Denney	47.65541	6.90952	approx	Rosenthal (1990)
Dents du Midi	46.17354	6.93582	exact	Chaix (1923), Epprecht (1958), and Gagnebin et al. (1934)
Dettenwies (Lohn)	47.75363	8.66745	exact	Baumberger (1923) and Zschokke (1907)
Develier-dessus	47.36623	7.27048	exact	Baumberger (1923), Epprecht (1958), and Keller and Liniger (2017)
Diableret	46.30676	7.20350	exact	Badoux et al. (1990), Epprecht (1958), and Schmidt (1920)
Diegten	47.41484	7.82374	exact	Amsler (1935) and Epprecht (1958)
Eglisau I	47.57563	8.52318	exact	Epprecht et al. (1963)
Eglisau II	47.57437	8.51318	exact	Cadisch (1959) and Epprecht et al. (1963)
Eguenigue	47.67139	6.93441	approx	Rosenthal (1990)
Ehingen 1	48.26849	9.72907	exact	Bloos (1967)
Ehingen CF 1002	48.22344	9.71363	exact	Bloos (1967)
Einsiedelei Baden	47.47892	8.29732	exact	Moesch (1867)
Elay (le Bechlet)	47.29672	7.49250	exact	Baumberger (1923)
Endingen	47.54932	8.29600	exact	Epprecht (1958), Moesch (1867), and Scheuchzer (1707)
Engelberg (Blakenalp-Fürrenalp-Stierenbach)	46.81393	8.51150	exact	Epprecht (1958) and Labhart et al. (2015)
Engi	47.40445	7.60784	exact	Koch et al. (1939)
Erzmatt (Balsthal)	47.30846	7.70400	exact	Baumberger (1923); this study
Eselschinder	49.11560	8.76746	exact	Berger (1959)
Exincourt	47.50112	6.83925	exact	Rosenthal (1990)
Faimbe	47.49637	6.59842	exact	Rosenthal (1990)
Faucigny	46.11840	6.35858	approx	Wieland (1979)
Féche-l'Église	47.50459	6.95068	approx	Rosenthal (1990)
Fisistöcke	46.46941	7.68960	exact	Epprecht (1958) and Wieland (1979)
Fleckwiesli	47.75044	8.66879	exact	Baumberger (1923)
Fluorn	48.29153	8.46246	approx	Bräuhäuser (1916)
Flurlingen	47.68452	8.63250	approx	Epprecht (1958), Hofmann (1989), and Schmidt (1920)
Fronhofen 2	47.87504	9.48799	exact	Volz (1957)
Füegenhof	47.27336	7.48870	exact	Baumberger (1923)

Table 3.24: List of localities of stratiform-type deposits, continued.

Locality	latitude [°]	longitude [°]	accuracy	references
Gallmoos (Galmis)	47.23842	7.54730	exact	Baumberger (1923)
Gau-Heppenheim	49.73972	8.19548	exact	Bartz (1940)
Gebensdorf	47.47421	8.23585	exact	Moesch (1867)
Gemmipass (Lämmernalp, Varneralp)	46.39119	7.58989	exact	Epprecht (1958) and Furrer et al. (1956)
Gental (Scharmadbänder, Arnialp)	46.76177	8.34533	exact	Epprecht (1958) and Wieland (1979)
Gheld	47.41434	8.08172	exact	Widmer (2015) and Wullschleger (2005)
Girlang	47.36208	7.56124	exact	Amsler (1935) and Epprecht (1958)
Gochsheim	49.10879	8.73708	exact	Berger (1959)
Goleten	47.30159	7.66853	exact	Baumberger (1923)
Goumoens-le-Jux	46.66705	6.58610	exact	Schardt (1883)
Grand-Charmont	47.52827	6.82333	approx	Rosenthal (1990)
Grindelwald (Eiger-N-Fuss)	46.61702	8.06112	exact	Epprecht (1958) and Günzler-Seiffert (1938)
Grübli (Lohn)	47.75542	8.66753	exact	Baumberger (1923)
Gundelsheim	49.28411	9.16249	approx	Berger (1959)
Harxheim	49.90615	8.25132	approx	Bartz (1940) and Grooss (1867)
Hattingen (Immendingen)	47.93641	8.72560	approx	Achenbach (1859)
Haulen	47.32027	7.68789	exact	Baumberger (1923)
Heidelsheim	49.09773	8.63718	exact	Berger (1959)
Herbetswil	47.29196	7.59703	exact	Baumberger (1923) and Borger (1990)
Himmelried	47.42201	7.59957	exact	Koch et al. (1939)
Hoh Faulen (Uri)	46.84011	8.71487	exact	Brückner and Zbinden (1987) and Epprecht (1958)
Hohfad	46.79738	8.43965	exact	Labhart et al. (2015)
Hungerberg	47.39667	8.03304	exact	Baumberger (1923), Metz (1989), Moesch (1867), and Wullschleger (2005)
Hungerbol	47.94233	8.93287	exact	Borger (1990)
Im Hohl (Faichlen)	47.32430	7.64374	exact	Baumberger (1923)
Jegertosse	46.47355	7.67723	exact	Epprecht (1958)
Jöhlingen	49.02328	8.56143	exact	Schmidt (1941)
Kalkofen	47.29653	7.62457	exact	Baumberger (1923)
Kandern	47.71919	7.66443	approx	Achenbach (1859) and Rutte (1953)
Kappelerhöfe (Baden)	47.48045	8.28736	exact	Epprecht (1958)
Klettgauer Berg	47.63874	8.42851	approx	Baumberger (1923) and Epprecht (1958)
Kloppberg-Höllenberg	49.73262	8.21599	exact	Bartz (1940)
Kohlholz s. Lausen	47.45608	7.75851	exact	Rollier (1903)
Küsnacht I (Limberg)	47.31819	8.61975	exact	Epprecht et al. (1963)
Küssnach (Metz)	47.59342	8.37872	exact	Metz (1989) and Schöttle (2005)
Küttigen	47.40787	8.04226	exact	Jordan et al. (2011) and Wullschleger (2005)
La Sarraz	46.65729	6.51377	approx	Baumberger (1923), Custer and Aubert (1935), Epprecht (1958), and Harpe (1870)
La Scheulte	47.34117	7.55878	exact	Koch et al. (1939)

Table 3.25: List of localities of stratiform-type deposits, continued.

Locality	latitude [°]	longitude [°]	accuracy	references
Lacollonge	47.66261	6.96486	approx	Rosenthal (1990)
Lämmlismatt	47.40318	7.58284	exact	Koch et al. (1939)
Le Perceux	47.28238	7.26509	exact	Pasquier and Burkhard (2018)
Lengnau	47.18305	7.35739	exact	Antenen et al. (2004), Baumberger (1923), Epprecht (1958), and Scheuchzer (1707)
L'Essert Dessus	47.32172	7.32224	exact	Pfirter et al. (1996)
Lieu Galet	47.37038	7.24880	exact	Baumberger (1923) and Pfirter et al. (1996)
Linden-1	46.84788	7.67112	exact	Maurer et al. (1978)
Lindhof	47.46815	8.21994	exact	Graf et al. (2006) and Moesch (1867)
Liptingen (Emmingen)	47.91687	8.85199	exact	Achenbach (1859) and Eichler (1961)
Lohn am Randen	47.76300	8.68099	exact	Hofmann et al. (2017), Hofmann (1956, 1960), Wieland (1979), and Zschokke (1907)
Lougres	47.47118	6.68822	approx	Rosenthal (1990)
Löwenberg	49.73506	8.25848	exact	Bartz (1940)
Lützel-Röschenz-Laufen-Liesberg	47.39111	7.45853	exact	Baumberger (1923), Epprecht (1958), and Pfirter et al. (1996)
Malleray	47.22441	7.27077	exact	Aufranc and Burkhalter (2016), Epprecht (1958), and Kündig and Quervain (1953)
Malsenhof	47.28087	7.49913	exact	Baumberger (1923),this study
Malsly-Mühlebach ob Welschenrohr	47.28556	7.51451	exact	Baumberger (1923)
Médière	47.45672	6.60141	approx	Rosenthal (1990)
Menoncourt	47.67041	6.94488	approx	Rosenthal (1990)
Menzingen	49.13796	8.77234	approx	Berger (1959)
Mervelier	47.33802	7.49795	exact	this study
Mettembert	47.39456	7.31661	exact	Baumberger (1923), Epprecht (1958), and Keller and Liniger (2017)
Mont Girod	47.25019	7.31494	exact	Pfirter et al. (1996)
Montavon	47.37585	7.23167	exact	Diebold et al. (1963)
Montbéliard	47.51036	6.79847	approx	Rosenthal (1990)
Mühlheim	47.80987	7.62494	exact	Achenbach (1859)
Mümliswil	47.35773	7.69259	exact	Baumberger (1923) and Koch et al. (1939)
Neuberg	49.89767	8.14742	approx	Bartz (1940)
Neuhüsli	47.36399	7.61658	exact	Koch et al. (1939)
Neuwies	47.74741	8.66635	exact	Baumberger (1923)
Niederkorn	49.53110	5.86904	exact	Gassmann and Schäfer (2018)
Nommay	47.53970	6.85231	approx	Rosenthal (1990)
Nusshof	47.49366	7.80365	exact	Pfirter et al. (2017)
Oberdorf	47.23745	7.49482	exact	Baumberger (1923), Mojon et al. (2018), and Rollier (1910)
Oberfeld	47.40616	7.64526	exact	Koch et al. (1939)
Obergrombach	49.07720	8.58207	approx	Schmidt (1941)
Oensingen	47.29283	7.71352	exact	Baumberger (1923)
Oftringen	47.31759	7.94567	exact	Beauheim (2013)
Orbe	46.72571	6.51504	exact	Aubert and Dreyfuss (1963), Baumberger (1923), Epprecht (1958), and Weidmann (1984a)

Table 3.26: List of localities of stratiform-type deposits, continued.

Locality	latitude [°]	longitude [°]	accuracy	references
Pertuisat	47.32958	7.37439	exact	Pfirter et al. (1996)
Pfadberg	49.89479	8.13371	exact	Bartz (1940)
Phaffans	47.65964	6.93631	approx	Rosenthal (1990)
Puits Blancherie (Delemont)	47.35893	7.33963	exact	Baumberger (1923)
Puits L'Avenir	47.36205	7.24461	approx	Baumberger (1923)
Puits Rondez (Delemont)	47.36222	7.36205	approx	Baumberger (1923)
Ramiswil	47.34359	7.66430	exact	Baumberger (1923) and Koch et al. (1939)
Roggenburg	47.42801	7.34774	exact	Baumberger (1923), Epprecht (1958), and Pfirter et al. (1996)
Rumelange	49.46229	5.99895	exact	Gassmann and Schäfer (2018)
Schadenboden	47.32261	7.65070	exact	Baumberger (1923)
Schafisheim	47.36932	8.14850	exact	Matter et al. (1988b)
Scherzberg	47.43754	8.17398	exact	Epprecht (1958)
Schiltwald (Lauterbrunnen)	46.59201	7.91597	exact	Epprecht (1958) and Günzler-Seiffert (1938)
Schloss Laufen am Rheinfall	47.67672	8.61446	exact	Moesch (1867), Hofmann (1989)
Seewen	47.43077	7.66528	exact	Amsler (1935) and Epprecht (1958)
Seprais	47.36795	7.23143	exact	Diebold et al. (1963)
Sevay	47.36688	7.17744	exact	Diebold et al. (1963)
Sigmaringen	48.08780	9.24382	exact	Achenbach (1859)
St. Joseph	47.26432	7.47723	exact	Baumberger (1923)
Steinberg	49.88304	8.00553	exact	Bartz (1936, 1940)
Steinenberg	47.32078	7.69891	exact	Baumberger (1923)
Stockrüti	47.75045	8.66540	exact	Baumberger (1923)
Tavannes	47.21405	7.20323	approx	Aufranc and Burkhalter (2016), Epprecht (1958), and Kündig and Quervain (1953)
Teningen	48.15216	7.83857	approx	Schöttle (2005)
Thônex-1	46.20183	6.21137	exact	Jenny et al. (1995)
Thun-1	46.75799	7.70516	exact	Micholet (1992)
Titlisgipfel	46.77762	8.43498	exact	Epprecht (1958) and Labhart et al. (2015)
Umiken	47.48291	8.19058	exact	Moesch (1867)
Undervelier-Soulce-Rebeuvelier	47.30808	7.26627	exact	Baumberger (1923), Epprecht (1958), and Pfirter et al. (1996)
Vaumarcus	46.87515	6.75748	exact	Rigassi et al. (2006)
Vétrigne	47.66946	6.89387	approx	Rosenthal (1990)
Vézelois	47.60747	6.91746	approx	Rosenthal (1990)
Villnachern	47.47552	8.15419	exact	Epprecht (1958)
Waldnacht-Surenenpass-Surenen	46.82199	8.56334	exact	Wieland (1979)
Weiach	47.56272	8.45727	exact	Matter et al. (1988a)
Welligrat-Rosenlaui	46.67389	8.14983	exact	Epprecht (1958), Günzler-Seiffert (1938), and Wieland (1979)
Welschenrohr	47.28390	7.53676	exact	Baumberger (1923)
Westerberg	49.93405	8.06134	exact	Bartz (1940)
Wissberg	49.85220	8.01978	exact	Bartz (1940)
Witterswil	47.48113	7.52024	exact	Schmidt et al. (1924)
Wörrstadt	49.84371	8.12801	exact	Bartz (1940)
Zeihen	47.46599	8.07349	exact	Amsler (1935), Epprecht (1958), and Metz (1989)
Zwiefaltendorf	48.21880	9.51418	approx	Kiderlen (1931)

Cave deposits

Deposits of Bolus clay containing Bohnerz pisoliths have been found in some caves. They have most likely been washed into the cave from fissures in the roof of the cave.

Table 3.27: List of localities of cave deposits with coordinates, location accuracy, and original references.

Locality	latitude [°]	longitude [°]	accuracy	references
Bären- und Karlshöhle	48.37084	9.21528	exact	Abel et al. (2006)
Falkensteiner Höhle	48.51405	9.45266	exact	Griesinger (1991), Jäger (1835), Leonhard (1829), and Weiger (1908)
Heldensteinhöhle	48.22453	9.01936	exact	Borger (1990)
Heppenloch bei Gutenberg	48.54226	9.51968	exact	Dehm (1935), Engel (1908), Hedinger (1891, 1892), Hennig (1923), Rummel (1993), and Weiger (1908)
Kolbingen	48.05240	8.88940	approx	Achenbach (1859) and Jäger (1835)
Laichinger Tiefenhöhle	48.47830	9.69336	exact	Glöckler and Ufrecht (1983)
Laierhöhle	48.61488	9.86115	exact	Strasser (2011)
Mondmilchhöhle	48.52145	9.52076	exact	Weiger (1908)
Nebelhöhle Genkingen	48.41741	9.22076	exact	Borger (1990)
Rossberghöhle	48.35475	9.17897	exact	Jäger (1835) and Ufrecht (2008)
Sirgensteinhöhle	48.38699	9.76114	exact	Weiger (1908)
Sybillenloch (Teck)	48.58905	9.46983	exact	Weiger (1908)
Veringendorf	48.15850	9.20043	approx	Achenbach (1859)
Zaininger Höhle	48.48328	9.56800	exact	López Correa and Rosendahl (2002)

References

Abel, T., C. Harlacher, and W. Ufrecht (2006) "Zur Verkarstungsgeschichte der Bären-und Karlshöhle bei Erpfingen (Schwäbische Alb) im Plio-Pleistozän unter Berücksichtigung von Sinterchronologie und Paläontologie" in: *Jahresberichte und Mitteilungen des Oberrheinischen Geologischen Vereins Neue Folge* 88, pp. 9–51.

Achenbach, A. (1859) "Ueber Bohnerze auf dem südwestlichen Plateau der Alp" in: *Jahreshefte des Vereins für vaterländische Naturkunde in Württemberg* 15, pp. 103–125.

Alberti, von (1853) "Die Bohnerze des Jura ihre Beziehung zur Molasse und zu den Gypsen von Paris, Aix und Hohenhoewen" in: *Jahreshefte des Vereins für vaterländische Naturkunde in Württemberg* 9, pp. 76–111.

Ameghino, F. (1905) "Les édentés de France et de l'Allemagne" in: *Anales Museo Nacional de Historia Natural de Buenos Aires* 13.

– (1908) "Encore quelques mots sur les Tatous fossiles de France et de L'Allemagne" in: *Anales Museo Nacional de Historia Natural de Buenos Aires* 17.

Amsler, A. (1935) "Die alten Eisenindustrien des Fricktales, bei Erlinsbach und in benachbarten Gebieten des östlichen Juras im Licht der Flurnamen" in: *Beiträge zur Geologie der Schweiz, Geotechnische Serie, Kleinere Mitteilungen* 6.

Andres, G. (1951) *Die Landschaftsentwicklung der südlichen Frankenalb im Gebiet Hofstetten-Gaimersheim-Wettstetten nördlich von Ingolstadt* Geologica Bavarica, Bayerisches Geologisches Landesamt, p. 68.

Antenen, M., P. Kellerhals, and B. Tröhler (2004) *Geological Atlas of Switzerland 1:25,000 109 Büren a. A. (LK 1126)* Federal Office of Topography swisstopo.

Aubert, D. and M. Dreyfuss (1963) *Geological Atlas of Switzerland 1:25,000 42 Orbe (CN 1202)* Federal Office of Topography swisstopo.

Aubert, D. (1975) "L'évolution du relief jurassien" in: *Eclogae Geologica Helvetiae* 68.1, pp. 1–64.

Aufranc, J. and R. Burkhalter (2016) *Geological Atlas of Switzerland 1:25,000 155 Chasseral (CN 1125)* Federal Office of Topography swisstopo.

Aufranc, J., H. P. Laubscher, M. Suter, and R. Burkhalter (2016) *Geological Atlas of Switzerland 1:25,000 147 Bellelay-Saignelégier (CN 1105/1104)* Federal Office of Topography swisstopo.

Badoux, H., J. H. Gabus, and C. H. (1990) *Geological Atlas of Switzerland 1:25,000 88 Les Diablerets (CN 1285)* Federal Office of Topography swisstopo.

Bartz, J. (1936) "Das Unterpliocän in Rheinhessen" in: *Jahresberichte und Mitteilungen des Oberrheinischen Geologischen Vereins Neue Folge* 25, pp. 121–228.

Bartz, J. (1940) “Die Bohnerzablagerungen in Rheinhessen und ihre Entstehung” in: *Archiv für Lagerstättenforschung der Preußischen Geologischen Landesanstalt* 72, pp. 1–57.

Baumberger, E. (1923) “Die Eisen-und Manganerze der Schweiz. 1. Teil: Bohnerz” in: *Beiträge zur geologischen Karte der Schweiz, geotechnische Serie* 13, pp. 1–150.

Baumberger, E. (1907) “Die Eisenerze im Schweizer Jura” in: *Mitteilungen der Naturforschenden Gesellschaft Bern* 1907, pp. 58–67.

Beauheim, R. (2013) “Hydraulic conductivity and head distributions in the host rock formations of the proposed siting regions” in: *Nagra Arbeitsbericht NAB 13-13. Nagra, Wettingen*, pp. 1–106.

Becker, D., G. Rauber, and L. Scherler (2013) “New small mammal fauna of late Middle Eocene age from a fissure filling at La Verrerie de Roches (Jura, NW Switzerland)” in: *Revue de Paléobiologie* 32.2, pp. 433–446.

Berger, F.-E. (1959) “Untersuchungen an Schädel-und Gebißresten von Cainotheriidae besonders aus den oberoligocaenen Spaltenfüllungen von Gaimersheim bei Ingolstadt” in: *Palaeontographica Abteilung A*, pp. 1–58.

Berger, G. (1986) “Neu entdeckte tertiäre fossilführende Karstfüllungen auf der Alb” in: *Mitteilungen der Bayerischen Staatssammlung für Paläontologie und Historische Geologie* 26, pp. 163–188.

Birchmeier, C. (1986) “Bohnerzbergbau am Südranden” in: *Neujahrsblatt der Naturforschenden Gesellschaft Schaffhausen* 38, pp. 1–79.

Birkhäuser, P., P. Roth, B. Meier, and H. Naef (2001) *3D-Seismik: Räumliche Erkundung der mesozoischen Sedimentschichten im Zürcher Weinland, Technischer Bericht 00-03* Nationale Genossenschaft für die Lagerung radioaktiver Abfälle.

Birzer, F. (1939) “Verwitterung und Landschaftsentwicklung in der südlichen Frankenalb” in: *Zeitschrift der Deutschen Geologischen Gesellschaft* 91, pp. 1–57.

Bleich, K., K. Papenfuß, R. van der Ploeg, and E. Schlichting (1987) “Exkursionsführer zur Jahrestagung 1987 in Stuttgart-Hohenheim” in: *Mitteilungen Deutsche Bodenkundliche Gesellschaft* 54, pp. 1–246.

Bloos, G. (1967) “Über Jura und Tertiär im Gebiet von Ehingen/Donau (Baden-Württemberg)” in: *Jahresberichte und Mitteilungen des Oberrheinischen Geologischen Vereins Neue Folge* 49, pp. 75–115.

Bolliger, T. (1997) “Small mammal faunas from karstic fissure fillings” in: *Proceedings of the 12th International Congress of Speleology, Symposium 2 Archaeology and Paleontology in Caves* 3, pp. 141–144.

Bolliger, T., B. Engesser, and M. Weidmann (1993) “Première découverte de mammifères pliocènes dans le Jura neuchâtelois” in: *Eclogae Geologicae Helvetiae* 86.3, pp. 1031–1068.

Borger, H. (1990) “Bohnerze und Quarzsande als Indikatoren paläogeographischer Verwitterungsprozesse und der Altreliefgenese östlich von Albstadt (Schwäbische Alb).” in: *Kölner Geographische Arbeiten* 52, p. 209.

Borger, H. and M. Widdowson (June 2001) “Indian laterites, and lateritious residues of southern Germany: a petrographic, mineralogical, and geochemical comparison” in: *Zeitschrift für Geomorphologie* 45.2, pp. 177–200.

Bräuhäuser, M. (1916) “Die Bohnerzbildung im Muschelkalkgebiet am Oberen Neckar: Ein Beitra zur Kenntnis alter Landflächen im Schwäbischen Stufenland” in: *Verein für Vaterl. Naturkunde in Württemberg* 72, pp. 210–271.

Brückner, W. and P. Zbinden (1987) *Geological Atlas of Switzerland 1:25,000 83 Schächental (LK 1192)* Federal Office of Topography swisstopo.

Brüderlin, M. (1969) “Beiträge zur Lithostratigraphie und Sedimentpetrographie des Oberen Muschelkalks im südwestlichen Baden-Württemberg” in: *Jahresberichte und Mitteilungen des Oberrheinischen Geologischen Vereins* 51, pp. 125–158.

Büchi, U., K. Lemcke, G. Wiener, and J. Zimdars (1965) “Geologische Ergebnisse der Erdölexploration auf das Mesozoikum im Untergrund des schweizerischen Molassebeckens” in: *Bulletin der Schweizerischen Vereinigung von Petroleum-Geologen und -Ingenieuren* 15, pp. 7–38.

Cadisch, J. (1959) “Geologische Ergebnisse der Mineralquellenbohrung Eglisau II” in: *Bulletin der Schweizerischen Vereinigung von Petroleum-Geologen und -Ingenieuren* 28, pp. 5–8.

Chaix, A. (1923) “Gisements sidérolithiques des Dents-du-Midi” in: *Beiträge zur Geologie der Schweiz, Geotechnische Serie* 13.1, pp. 141–150.

Custer, W. and D. Aubert (1935) *Geological Atlas of Switzerland 1:25,000 5 Mont la Ville-La Sarraz-Montricher-Cossonay (CN 1222)* Federal Office of Topography swisstopo.

Dehm, R. (1931) “Geologische Untersuchungen im Ries. Das Gebiet des Blattes Monheim.” in: *Neues Jahrbuch Mineralogie usw. Beilagenband* 67, pp. 139–256.

– (1939) “Über neue tertiäre Spaltenüllungen im Fränkischen und Schwäbischen Jura” in: *Zentralblatt für Minerlogie Abt. B* 1939, pp. 113–124.

– (1950a) “Die Nagetiere aus dem Mittel-Miozän (Burdigalium) von Winterhof-West bei Eichstätt in Bayern” in: *Neues Jahrbuch der Mineralogie Abhandlungen* 91, pp. 321–428.

– (1950b) “Die Raubtiere aus dem Mittel-Miozän (Burdigalium) von Winterhof-West bei Eichstätt in Bayern” in: *Abhandlungen der Bayerischen Akademie der Wissenschaften Mathematische-naturwissenschaftliche Klasse Neue Folge* 58, pp. 1–141.

Dehm, R. and V. Fahlbusch (1970) "Zur Bezeichnung fossilführender Spaltenfüllungen" in: *Mitteilungen der Bayerischen Staatssammlung für Paläontologie und historische Geologie* 10, pp. 351–364.

Dehm, R. (1935) "Über tertiäre Spaltenfüllungen im Fränkischen und Schwäbischen Jura" in: *Abhandlungen der Bayerischen Akademie der Wissenschaften Mathematisch-naturwissenschaftliche Abteilung Neue Folge* 29, pp. 1–91.

– (1937) "Neue tertiäre Spaltenfüllungen im südlichen Fränkischen Jura" in: *Zentralblatt für Mineralogie, Geologie und Paläontologie, Abteilung B* 9, pp. 349–369.

– (1961) "Über neue tertiäre Spaltenfüllungen im des süddeutschen Jura- und Muschelkalk-Gebietes" in: *Mitteilungen der Bayerischen Staatssammlung für Paläontologie und historische Geologie* 1, pp. 27–56.

– (1978) "Neue tertiäre Spaltenfüllungen im süddeutschen Jura" in: *Mitteilungen der Bayerischen Staatssammlung für Paläontologie und Historische Geologie* 18, pp. 289–313.

Diebold, P., H. P. Laubscher, A. Schneider, and R. Tschopp (1963) *Geological Atlas of Switzerland 1:25,000 40 St-Ursanne (CN 1085)* Federal Office of Topography swisstopo.

Dietrich, W. (1922) "Beitrag zur Kenntnis der säugetierführenden Bohnerzformation in Schwaben. 1. Ein vergessenes, neu erschlossenes Höhlenvorkommen terrestrischen Eozäns auf der Ulmer Alb" in: *Zentralblatt für Mineralogie, Geologie und Paläontologie* 1922, pp. 209–224.

– (1925) "Über ein neues Vorkommen burdigalischer Molasse auf der Ulmer Alb" in: *Jahresbericht und Mitteilungen des Oberrheinischen Geologischen Vereins* 1925.

– (1929) "Bericht über die obereozänen Säugetiere der Ulmer Alb" in: *Palaeontologische Zeitschrift* 11.3, pp. 258–261.

– (1930) "Beitrag zur Kenntnis der Bohnerzformation in Schwaben 3. Raubtiere aus den Bohnerzablagerungen der Ulmer und der Eichstätter Alb" in: *Neues Jahrbuch für Mineralogie Beilagen* 63, pp. 451–474.

– (1936) "Die Huftiere aus dem Obereozän von Mähringen auf der Ulmer Alb" in: *Palaeontographica Abteilung A*, pp. 163–209.

Eichler, J. (1961) "Mineralogische und geologische Untersuchungen von Bohnerzen in Baden-Württemberg, besonders der Vorkommen bei Liptingen, Kreis Stockach" in: *Neues Jahrbuch für Mineralogie - Abhandlungen* 97, pp. 51–111.

Engel, T. (1908) *Geognostischer Wegweiser durch Württemberg. 3rd Ed.*

Epprecht, W., U. Büchi, F. Hofmann, and T. Hügi (1963) "Die Bohnerz-Funde in den Tiefbohrungen von Limberg (Küsnacht, Kt. Zürich) und Eglisau II" in: *Schweizerische mineralogische und petrographische Mitteilungen* 43, pp. 313–338.

Epprecht, W. (1958) "Unbekannte schweizerische Eisenerzgruben sowie Inventar und Karte aller Eisen- und Manganerz-Vorkommen der Schweiz" in: *Beiträge zur Geologie der Schweiz, Geotechnische Serie, Kleinere Mitteilungen* 19.

Fahlbusch, V. (1968) "Neue Eomyidae (Rodentia, Mamm.) aus einer aquitanen Spaltenfüllung von Weißenburg in Bayern" in: *Mitteilungen der Bayerischen Staatssammlung für Paläontologie und Historische Geologie* 8, pp. 219–245.

Fahlbusch, V. (1966) "Cricetidae (Rodentia, Mamm.) aus der mittelmiozänen Spaltenfüllung Erkertshofen bei Eichstätt" in: *Mitteilungen der Bayerischen Staatssammlung für Paläontologie und historische Geologie* 6, pp. 109–131.

– (1970) "Populationsverschiebungen bei tertiären Nagetieren, eine Studie an oligozänen und miozänen Eomyidae Europas" in: *Abhandlungen der Bayerischen Akademie der Wissenschaften Mathematisch–naturwissenschaftliche Abteilung Neue Folge* 145, pp. 1–136.

Fahlbusch, V. and N. Schmidt (1969) "Über eine weitere unteroligozäne Spaltenfüllung von Weissenburg in Bayern" in: *Mitteilungen der Bayerischen Staatssammlung für Paläontologie und Historische Geologie* 9, pp. 209–211.

Fluhr, R. (1908) "Die Eisenerzlagerstätten Württembergs und ihre volkswirtschaftliche Bedeutung" in: *Zeitschrift für praktische Geologie* 1908, pp. 1–23.

Fraas, O. (1859) "Ueber Bohnerz" in: *Jahreshefte des Vereins für vaterländische Naturkunde in Württemberg* 15, pp. 38–42.

Furrer, H., H. Badoux, K. Huber, and H. von Tavel (1956) *Geological Atlas of Switzerland 1:25,000 32 Gemmi (LK 1267)* Federal Office of Topography swisstopo.

Gagnebin, E., F. de Loys, M. Reinhard, M. Lugeon, N. Oulianoff, W. Hotz, E. Poldini, and F. Kaenel (1934) *Geological Atlas of Switzerland 1:25,000 8 St-Maurice (CN 1304)* Federal Office of Topography swisstopo.

Gall, H. (1971) "Geologische Karte von Bayern 1:25000, Erläuterungen zum Blatt 7328 Wittislingen" in: *Bayerisches Geologisches Landesamt*, p. 186.

Gall, H. (1969) "Geologische Untersuchungen im südwestlichen Vorries: das Gebiet des Blattes Wittislingen" PhD thesis Ludwig-Maximilians Universität München, p. 156.

Gassmann, G. and A. Schäfer (2018) *Luxemburger Eisen: Montanarchäologische Untersuchungen zur frühen Eisenproduktion im Umland des Titelbergs in Südwestluxemburg* vol. 6 University of Bamberg Press, p. 108.

Geyer, O. F., M. P. Gwinner, M. Geyer, E. Nitsch, and T. Simon (2011) *Geologie von Baden-Württemberg* Schweizerbart'sche Verlagsbuchhandlung.

Glöckler, K. and W. Ufrecht (1983) "Die Entstehung der Laichinger Tiefenhöhle (Mittlere Schwäbische Alb)" in: *Jahresberichte und Mitteilungen des Oberrheinischen Geologischen Vereins* Neue Folge 65, pp. 223–242.

Graf, H., P. Bitterli-Dreher, H. Burger, T. Bitterli, and P. D. und H. Naef (2006) *Geological Atlas of Switzerland 1:25,000 120 Baden (LK 1070)* Federal Office of Topography swisstopo.

Griesinger, H. (1991) "Veränderungen in Gangverlauf und Profilen der Falkensteiner Höhle durch menschliche Tätigkeit" in: *Berichte zum Symposium "Die Grabenstetter Großhöhle"* 1989, pp. 126–135.

Grooss, A. (1867) *Erläuterungen der Spezialkarte der Section Mainz* Darmstadt.

Gümbel, C. (1891) "Geognostische Beschreibung der Fränkischen Alb (Frankenjura) mit dem anstossenden Fränkischen Keupergebiete" in: *Geognostische Beschreibung des Königreichs Bayern* 4, pp. 1–763.

Günzler-Seiffert, H. (1938) *Geological Atlas of Switzerland 1:25,000 13 Grindelwald–Meiringen (LK 1229)* Federal Office of Topography swisstopo.

Haldimann, P., H. Graf, and J. Jost (2017) *Geological Atlas of Switzerland 1:25,000 151 Bülach (LK 1071)* Federal Office of Topography swisstopo.

Harpe, P. de la (1870) "La faune de terrain sidérolithique dans le canton de Vaud" in: *Bulletin de la Société Vaudoise des Sciences Naturelles* 10, pp. 457–467.

Hedinger, A. (1891) "Die Höhlenfunde aus dem Heppenloch" in: *Jahreshefte des Vereins für vaterländische Naturkunde in Württemberg* 41, pp. 1–5.

– (1892) "Über fossile Affen" in: *Jahreshefte des Vereins für vaterländische Naturkunde in Württemberg*.

Heissig, K. (1970) "Neue Fundstellen oligozäner Spaltenfaunen im schwäbisch-fränkischen Jura" in: *Mitteilungen der Bayerischen Staatssammlung für Paläontologie und historische Geologie* 10, pp. 331–350.

– (1973) "Oligozäne Vertebraten aus der Spaltenfüllung "Möhren" 13 bei Treuchtlingen" in: *Mitteilungen der Bayerischen Staatssammlung für Paläontologie und historische Geologie* 13, pp. 177–182.

– (1978) "Fossilführende Spaltenfüllungen Süddeutschlands und die Ökologie ihrer oligozänen Huftiere" in: *Mitteilungen der Bayerischen Staatssammlung für Paläontologie und Historische Geologie* 18, pp. 237–288.

Heller, F. (1943) "Die Wirbeltierkleinfauna der Felsspalte von Bitz bei Ebingen (Wttg.)" in: *Zeitschrift für Karst- und Höhlenkunde* 1-4.

Hennig, E. (1923) *Geologie von Württemberg nebst Hohenzollern* Gebrüder Borntraeger, Berlin, p. 383.

Herre, W. and H. Lunau (1950) "Neue fossile Schwanzlurche aus dem Burdigalium" in: *Neues Jahrbuch der Geologie und Paläontologie Monatshefte* 1950, pp. 247–259.

Hofmann, F., B. Reichenbacher, and K. A. Farley (2017) "Evidence for >5 Ma paleo-exposure of an Eocene–Miocene paleosol of the Bohnerz Formation, Switzerland" in: *Earth and Planetary Science Letters* 465, pp. 168–175.

Hofmann, F. (1956) "Die Obere Süsswasseroase in der Ostschweiz und im Hegau" in: *Bulletin der Schweizerischen Vereinigung von Petroleum-Geologen und -Ingenieuren* 23, pp. 23–34.

– (1960) "Sedimente einer ariden Klimaperiode zwsichen Siderolithikum und Molasse in Lohn, Kanton Schaffhausen, und am Rheinfall" in: *Eclogae Geologicae Helvetiae* 53.1, pp. 27–32.

– (1989) "Geologie des Rheinfalls (Exkursion B, Teil 1, am 28. März 1989)" in: *Jahresberichte und Mitteilungen des Oberrheinischen Geologischen Vereins Neue Folge* 71, pp. 27–34.

Hrubesch, K. (1957) *Zahnstudien an tertiären Rodentia als Beitrag zu deren Stammesgeschichte: über die Evolution der Melissiodontidae, eine Revision der Gattung Melissiodon* Verlag der Bayerischen Akademie der Wissenschaften.

Illies, H. (1956) "Der mittlere Dogger im badischen Oberrheingebiet" in: *Berichte der Naturforschenden Gesellschaft zu Freiburg im Breisgau* 46, pp. 5–52.

Jäger, G. (1853) "Überreste von Säugetieren aus einigen Bohnerzgruben der Schwäbischen Alb" in: *Württembergisches Jahresheft* 1853.

Jäger, G. (1835) *Ueber die fossilen Säugethiere welche in Würtemberg aufgefunden worden sind* C. Erhard Verlag, Stuttgart, p. 266.

Jenny, J., J.-P. Burri, R. Muralt, A. Pugin, R. Schegg, P. Ungemach, F.-D. Vuataz, and R. Wernli (1995) "Le forage géothermique de Thônex (Canton de Genève): Aspects stratigraphiques, tectoniques, diagénétiques, géophysiques et hydrogéologiques" in: *Eclogae Geologicae Helvetiae* 88.2, pp. 365–396.

Jordan, P., M. Eberhard, H. R. Graf, P. Diebold, J. Jost, and R. Schurch (2011) *Geological Atlas of Switzerland 1:25,000 135 Aarau (LK 1089)* Federal Office of Topography swisstopo.

Jordi, H. A. (1994) *Geological Atlas of Switzerland 1:25,000 94 Yverdon-les-Bains (CN 1203)* Federal Office of Topography swisstopo.

Jordi, H. A., T. Bitterli, and M. Gerber (2003) *Geological Atlas of Switzerland 1:25,000 113 Murgenthal (LK 1108)* Federal Office of Topography swisstopo.

Keller, W. T. and H. Liniger (2017) *Geological Atlas of Switzerland 1:25,000 1 Movelier-Soyhières-Delémont-Courrendlin (CN 1086)* Federal Office of Topography swisstopo.

Kiderlen, H. (1931) "Beiträge zur Stratigraphie und Paläogeographie des süddeutschen Tertiärs" PhD thesis Universität Tübingen.

Koch, R., E. Lehner, A. Waibel, and M. Mühlberg (1939) *Geological Atlas of Switzerland 1:25,000 3 Laufen-Bretzwi-Erschwil-Mümliswil (LK 1087)* Federal Office of Topography swisstopo.

Koenigswald, W. von (1970) "Peratherium (Marsupialia) im Ober-Oligozän und Miozän von Europa" in: *Abhandlungen der Bayerischen Akademie der Wissenschaften Mathematisch–naturwissenschaftliche Abteilung Neue Folge* 144, pp. 1–79.

Kranz, W. (1952) "Die Bohnerze im westlichen und südwestlichen Vorries (Härtsfeld usw.)" in: *Zeitschrift der Deutschen Geologischen Gesellschaft*, pp. 41–52.

Kuhn, W. and W. Meigen (1924) "Bohnerz und Bohnerzton im Klettgau" in: *Jahresbericht des Oberrheinischen geologischen Vereins*, pp. 46–55.

Kündig, E. and F. de Quervain (1953) *Fundstellen mineralischer Rohstoffe in der Schweiz* Kümmerly & Frey, p. 214.

Kuntz Georges; Contini, D. (1973) *Carte géologique de la France (1/50000), Montbéliard* Bureau de Recherches Géologiques et Minières.

Labhart, T., B. Schwizer, C. Gisler, and F. Renner (2015) *Geological Atlas of Switzerland 1:25,000 146 Meiental-Engelberg (LK 1211/1191)* Federal Office of Topography swisstopo.

Leonhard, C. C. von (1829) *Taschenbuch für die gesammte Mineralogie mit Hinsicht auf die neuesten Entdeckungen. Drei und zwanzigster Jahrgang. II. Band* Akademische Buchhandlung von J.C.B. Mohr, p. 960.

Leonhard, K. (1838) *Agenda Geognostica. Hülfsbuch für reisende Gebirgsforscher und Leitfaden zu Vorträgen über angewandte Geognosie. Zweite, vermehrte und verbesserte Ausgabe* Mohr, Heidelberg, p. 384.

Linder, P. (2005) "An Eocene paleodoline in the Morcles Nappe of Anzeindaz (Canton of Vaud, Switzerland)" in: *Eclogae Geologicae Helvetiae* 98.1, pp. 51–61.

López Correa, M. and W. Rosendahl (2002) "Über eine neue Höhle auf der mittleren Schwäbischen Alb–zur Geologie, Paläontologie und Speläologie der Zaininger Höhle" in: *Jahresberichte und Mitteilungen des Oberrheinischen Geologischen Vereins* Neue Folge 84, pp. 333–353.

López-Antoñanzas, R. and P. Mein (2011) "First detailed description of Hispanomys decedens (Rodentia) from the Middle Miocene of La Grive-Saint Alban (France)" in: *Swiss Journal of Geosciences* 104.2, p. 345.

Lutzeier, H. (1922) "Beiträge zur Kenntnis der Meeresmolasse in der Ulmer Gegend" in: *Neues Jahrbuch der Mineralogie und Petrographie*, pp. 117–181.

Maack, G. A. (1865) *Palaeontologische Untersuchungen über noch unbekannte Lophiodonfossilien von Heidenheim am Hahnenkamme in Mittelfranken: Nebst einer kritischen Betrachtung sämmtlicher bis jetzt bekannten Species des Genus Lophiodon* Wilhelm Engelmann, p. 76.

Marchant, R., Y. Ringgenberg, G. Stampfli, P. Birkhäuser, P. Roth, and B. Meier (2005) "Paleotectonic evolution of the Zürcher Weinland (northern Switzerland), based on 2D and 3D seismic data" in: *Eclogae Geologicae Helvetiae* 98.3, pp. 345–362.

Matousek, F., M. Wanner, A. Baumann, H. R. Graf, R. Nüesch, and T. Bitterli (2000) *Geological Atlas of Switzerland 1:25,000 102 Zurzach (LK 1050)* Federal Office of Topography swisstopo.

Matter, A., T. Peters, H. Bläsi, J. Meyer, H. Ischi, and C. Meyer (1988a) *Sondierbohrung Weiach, Textband, Technischer Bericht 86-01* Nationale Genossenschaft für die Lagerung radioaktiver Abfälle, p. 470.

Matter, A., T. Peters, H. Bläsi, F. Schenker, and H. Weiss (1988b) *Sondierbohrung Schafisheim. Geologie, Textband, Technischer Bericht 86-03* vol. 8 Nationale Genossenschaft für die Lagerung radioaktiver Abfälle, p. 321.

Maurer, H., H. Funk, and W. Nabholz (1978) *Sedimentpetrographische Untersuchungen an Molasse-Abfolgen der Bohrung Linden 1 und ihrer Umgebung (Kt. Bern)* vol. 71.

Mayr, H. and W.-E. Schindlmayr (1967) "Über eine neue Spaltenfüllung bei Schelklingen im Schwäbischen Jura" in: *Mitteilungen der Bayerischen Staatssammlung für Paläontologie und Historische Geologie* 7, pp. 327–329.

Mein, P. and L. Ginsburg (2002) "Sur l'âge relatif des différents dépôts karstiques miocènes de La Grive-Saint-Alban (Isère)" in: *Publications du musée des Confluences* 5.2, pp. 7–47.

Metz, R. (1989) "Westlicher Hotzenwald, Geologie und Lagerstätten (Exkursion D am 30. März 1989)" in: *Jahresberichte und Mitteilungen des Oberrheinischen Geologischen Vereins*, pp. 51–84.

Micholet, J. (1992) "Le puits de Thoune: forage d'exploration pétrolière en Suisse, consortium pétrolier fribourgeois et bernois" in: *Bulletin der Schweizerischen Vereinigung von Petroleum-Geologen und -Ingenieuren* 58.133, pp. 23–32.

Miller, K. (1907) "Alttertiäre Land-und Süßwasserschnecken der Ulmer Gegend" in: *Jahreshefte des Vereins für vaterländische Naturkunde in Württemberg* 63, pp. 448–457.

Moesch, C. (1867) *Geologische Beschreibung der Umgebungen von Brugg* In Commission bei S. Höhr, Zürich, p. 88.

Mojon, P.-O., E. De Kaenel, D. Kälin, D. Becker, C. M. Pirkenseer, G. Rauber, K. Ramseyer, B. Hostettler, and M. Weidmann (2018) "New data on the biostratigraphy (charophytes, nannofossils, mammals) and lithostratigraphy of the Late Eocene to Early Late Miocene deposits in the Swiss Molasse Basin and Jura Mountains" in: *Swiss Journal of Palaeontology* 137, pp. 1–48.

Moos, A. (1924) "Beiträge zur Geologie des Tertiärs im Gebiet zwischen Ulm a. D. und Donauwörth" in: *Geognostische Jahreshefte* 37, pp. 167–252.

Müller, A. (1967) "Die Geschichte der Familie Dimylidae (Insectivora, Hamm.) auf Grund der Funde aus tertiären Spaltenfüllungen Süddeutschlands" in: *Abhandlungen der Bayerischen Akademie der Wissenschaften Mathematisch–naturwissenschaftliche Abteilung Neue Folge* 129, pp. 1–93.

Müller, E.-D. (1972) "Die Oligozän-Ablagerungen im Gebiet des Nördlinger Rieses" PhD thesis Ludwig-Maximilians Universität München.

Murat, R. (1956) "Existence et signification des filons élastiques dans le Barrémien inférieur de l'Autochtone de St-Maurice (VS)" in: *Arch. Sciences Genève* 9.4, pp. 478–487.

Nagra (2001) *Sondierbohrung Benken Untersuchungsbericht, Technischer Bericht 00-01* Nationale Genossenschaft für die Lagerung radioaktiver Abfälle.

Nathan, H. (1925) "Geologische Untersuchungen im Ries. Das Gebiet des Blattes Möttingen." in: *Neues Jahrbuch für Mineralogie, Geologie und Paläontologie. Abt. B: Referate* 53.1925, pp. 31–97.

Palmowski, J. and H. Wachendorf (1966) "Eine unteroligozäne Wirbeltierfauna aus einer Spaltenfüllung in Herrlingen/Blau (Württ.)" in: *Mitteilungen der Bayerischen Staatssammlung für Paläontologie und Historische Geologie* 6, pp. 229–245.

Pasquier, F. and M. Burkhard (2018) *Geological Atlas of Switzerland 1:25,000 162 Travers (CN 1163)* Federal Office of Topography swisstopo.

Pfirter, U., M. Antenen, W. Heckendorn, R. M. Burkhalter, B. Gürler, and D. Krebs (1996) *Geological Atlas of Switzerland 1:25,000 96 Moutier (CN 1106)* Federal Office of Topography swisstopo.

Pfirter, U., A. Isler, F. Pasquier, and M. Huber (2017) *Geological Atlas of Switzerland 1:25,000 1068 Sissach (LK 1068)* Federal Office of Topography swisstopo.

Pharisat, A. (1982) "La faune de mammiferes de l'Eocene superieur de la poche karstique de la carriere de la Baume a Audincourt (Doubs)" in: *Bulletin de la Société d'Histoire Naturelle du Pays de Montbéliard*, pp. 65–75.

Pickford, M. (2012) "Hominoids from Neuhausen and other Bohnerz localities, Swabian Alb, Germany: evidence for a high diversity of apes in the Late Miocene of Germany" in: *Estudios geologicos* 68.1, pp. 113–147.

Pirkenseer, C., G. Rauber, and S. Rousse (2018) “A revised Palaeogene lithostratigraphic framework for the Northern Swiss Jura and the Southern Upper Rhine Graben and its relationship to the North Alpine Foreland Basin” in: *Rivista Italiana di Paleontologia e Stratigrafia* 124.1.

Rathgeber, T. (2002) “Fossilführende KarstSpalten bei Sonnenbühl–Genkingen/-Fossil–bearing karst fissures near Sonnenbühl–Genkingen” in: *Cave Bear Researches Höhlen–Bären–Forschungen. Abhandlung zur Karst- und Höhlenkunde,* 34, pp. 83–85.

Rigassi, D., H. A. Jordi, and R. Arn (2006) *Geological Atlas of Switzerland 1:25,000 114 Grandson (CN 1183)* Federal Office of Topography swisstopo.

Roll, A. (1934) “Versuch einer Paläomorphologie und tektonischen Entwicklungsgeschichte des Lauchertgebietes (Schw. Alb)” in: *Jahrbuch der Preussischen Geologischen Landesanstalt* 55.

Rollier, L. (1910) “Nouvelles observations sur le Sidérolithique et la Molasse oligocène du Jura central et septentrional” in: *Beitrage zur geologischen Karte der Schweiz* 25, pp. 1–230.

Rollier, L. (1903) “Beweis, dass die Nattheim–Wettinger–Schichten (weiss–Jura ϵ = Ober–Kimeridge) auch auf der Basler Tafellandschaft etc. ursprünglich vorhanden waren” in: *Vierteljahrschrift der naturforschenden Gesellschaft Zürich* 48, p. 458.

Rosenthal, P. (1990) “Les minerais de fer Franche-Comte” in: *Bulletin de la Société d’Histoire Naturelle du Doubs* 1990-91, pp. 25–62.

Rosina, V. V. and M. Rummel (2012) “The bats (Chiroptera, Mammalia) from the Early Miocene of Petersbuch (Bavaria, Southern Germany)” in: *Geobios* 45.5, pp. 463–478.

Rummel, M. (1993) “Neue fossilführende Karstfüllungen der Schwäbisch-Fränkischen Alb” in: *Documenta naturae* 79, pp. 1–32.

Rummel, M. (2001) “Ein neuer Cricetodon aus dem Miozän von Petersbuch bei Eichstätt” in: *Stuttgarter Beiträge zur Naturkunde Serie B (Geologie und Paläontologie)* 311, pp. 1–8.

Rutte, E. (1953) “Der fossile Karst der südbadischen Vorbergzone” in: *Jahresberichte und Mitteilungen des Oberrheinischen Geologischen Vereins* Neue Folge 33, pp. 1–43.

Schalk, K. (1957) *Geologische Untersuchungen im Ries: das Gebiet des Blattes Bissingen* Geologica Bavarica, Bayerisches Geologisches Landesamt, p. 107.

Schardt, H. (1883) “Notice géologique sur la mollasse rouge et le terrain sidérolitique du pied du Jura” in: *Bulletin de la Société Vaudoise des Sciences Naturelles* 16.83, pp. 609–640.

Scherzinger, A. (2005) “Neue Spaltenfüllungen aus dem nördlichen Hegau und der Umgebung von Sigmaringen (westliche Schwäbische Alb)” in: *Stuttgarter Beiträge zur Naturkunde. Serie B, Geologie und Paläontologie* 345, pp. 1–45.

Scheuchzer, J. J. (1707) *Beschreibung der Natur-Geschichten des Schweizerlands Erster-Dritter Theil* Michael Schaufelberger und Christoff Hardmeier, p. 188.

Schill, J. (1858) *Die Tertiär- und Quartärbildungen des Landes am nördl: Bodensee und im Höhgau* Ebner & Seubert, p. 78.

Schlosser, M. (1904) “Notizen über einige Säugetierfaunen aus dem Miocän von Württemberg und Bayern” in: *Neues Jahrbuch für Mineralogie Beilagenband* 19.

– (1922) “Untermiocäne Wirbeltierreste aus einer Spalte im Jurakalk von Oberkochen in Württemberg” in: *Zentralblatt für Mineralogie, Geologie und Paläontologie* 1922, pp. 57–60.

Schlosser, M. (1902) “Beiträge zur Kenntnis der Säugethierreste aus den süddeutschen Bohnerzen” in: *Geologische und Palaeontologische Abhandlungen* Neue Folge V.3, pp. 117–258.

– (1916) *Neue Funde fossiler Säugetiere in der Eichstätter Gegend* Verlag der Königlich Bayerischen Akademie der Wissenschaften.

Schmidt-Kaler, H. (1962) “Stratigraphische und tektonische Untersuchungen im Malm des nordöstlichen Ries–Rahmens: nebst Parallelisierung des Malm Alpha bis Delta der sudlichen Frankenalb über das Riesgebiet mit der schwäbischen Ostalb” in: *Erlanger Geologische Abhandlungen* 44, pp. 1–51.

Schmidt-Kittler, N. (1969) “Eine alttertiäre Spaltenfüllung von Ehrenstein westlich Ulm” in: *Mitteilungen der Bayerischen Staatssammlung für Paläontologie und historische Geologie* 9, pp. 201–208.

– (1971) “Odontologische Untersuchungen an Pseudosciuriden (Rodentia, Mammalia) des Alttertiärs” in: *Abhandlungen der Bayerischen Akademie der Wissenschaften Mathematische-naturwissenschaftliche Klasse Neue Folge* 150, pp. 1–133.

Schmidt-Kittler, N., M. Brunet, M. Godinot, J. Franzen, J. Hooker, S. Legendre, et al. (1987) “European reference levels and correlation tables” in: *Münchner Geowissenschaftliche Abhandlungen A* 10, pp. 15–31.

Schmidt, C. (1920) *Texte explicatif de la Carte des Gisements des matières premières minérales de la Suisse 1: 500000* E. Birkhaeuser & Cie.

Schmidt, C., L. Braun, G. Paltzer, M. Mühlberg, P. Christ, and F. Jacob (1924) *Die Bohrungen von Buix bei Pruntrut und Allschwil bei Basel* Kümmerly und Frey, p. 74.

Schmidt, K. (1941) “Über bohnerzführendes Tertiär und Diluvium im Kraichgau” in: *Jahresberichte und Mitteilungen des Oberrheinischen Geologischen Vereins* 30, pp. 48–91.

Schöttle, M. (2005) *Geotope im Regierungsbezirk Freiburg* Landesanstalt für Umweltschutz Baden–Württemberg, Karlsruhe, Germany, p. 393.

Schreiner, A. (1979) *Geologische Karte von Baden-Württemberg 1:25000, Erläuterungen zu Blatt 8019 Neuhausen ob Eck* Geologisches Landesamt Baden-Württemberg, Stuttgart.

– (1992) *Erläuterungen zu Blatt Hegau und westlicher Bodensee, Geologische Karte 1:50000* Geologisches Landesamt Baden-Württemberg.

Schreiner, A. (1974) *Erläuterungen zur geologischen Karte des Landkreises Konstanz mit Umgebung, 1:50000. 2. berichtigte Auflage* Geologisches Landesamt Baden-Württemberg.

Seemann, R. and F. Berckhemer (1930) "Eine Spaltenfüllung mit reicher aquitaner Wirbeltierfauna im Massenkalk des Weissen Jura bei Tomerdingen (Ulmer Alb)" in: *Palaeontologische Zeitschrift* 12.1, pp. 14–25.

Stehlin, H. (1901) "Ueber die Säugetierfauna aus dem Bohnerz bei Chamblon bei Yverdon" in: *Eclogae Geologicae Helvetiae* 7.4, pp. 365–366.

– (1910) "Ueber die Säugetiere der schweizerischen Bohnerzformation" in: *Verhandlungen der Schweizerischen Naturforschenden Gesellschaft* 93, pp. 138–167.

Steinmann, G. and F. Graeff (1897) *Erläuterungen zum Blatt Hartheim-Ehrenstetten der Geologischen Spezialkarte des Großherzogtums Baden* Heidelberg, p. 83.

Strasser, M. (2011) "Höhlen der Schwäbischen Alb als Pegelschreiber für Flussgeschichte und Tektonik in Südwestdeutschland seit dem Miozän" PhD thesis Universität Stuttgart, p. 109.

Suter, H. (1936) *Geologische Beschreibung der Kartengebiete Les Bois und St-Imier im Berner Jura* Matériaux pour la Carte Géologique de la Suisse 72.

Tavel, H. von (1937) "Stratigraphie der Balmhorngruppe: mit Einschluss des Gemmipasses (Berner Oberland)" in: *Mitteilungen der Naturforschenden Gesellschaft Bern* 1936, pp. 43–120.

Tetzel, C. and M. Franz (2019) "3D-palaeorelief model of the Jurassic/Tertiary disconformity in the region north of Ulm (Swabian Alb, S Germany)" in: *Neues Jahrbuch für Geologie und Paläontologie-Abhandlungen* 292.1, pp. 113–120.

Trischler, J. and H. Winkler (1968) "Eine neue unteroligozäne Spaltenfüllung" in: *Mitteilungen der Bayerischen Staatssammlung für Paläontologie und Historische Geologie* 8, pp. 323–326.

Ufrecht, W. (2008) "Evaluating landscape development and karstification of the Central Schwäbische Alb (Southwest Germany) by fossil record of karst fillings" in: *Zeitschrift für Geomorphologie* 52.4, pp. 417–436.

Volz, E. (1957) "Geologische Ergebnisse neuerer Erdölbohrungen in Oberschwaben" PhD thesis Technische Hochschule Stuttgart, p. 73.

Weber, E. (1958) "Über ein neues fossilführendes Vorkommen der alttertiären Bohnerzlehmüberdeckung von Wolferstadt (Nördlinger Ries)" in: *Neues Jahrbuch der Geologie und Paläontologie Monatshefte* 8-9, pp. 398–406.

Weber, E. (1951) "Eine neue Lattorfium-Spaltenfüllung von Hagau bei Wemding/Ries" in: *Neues Jahrbuch für Geologie und Paläontologie Monatshefte* 1951, pp. 119–124.

Weidmann, M. (1984a) "Le Sidérolithique et la Molasse basale d'Orbe (VD)" in: *Bulletin de la Société vaudoise des Sciences naturelles* 77.2, pp. 135–141.

– (1984b) "Paléokarst éocène dans l'autochtone chablaisien (VS et VD)" in: *Bulletin de la Murithienne* 102, pp. 119–128.

Weiger, K. (1908) "Beiträge zur Kenntnis der Spaltenausfüllungen im weissen Jura auf der Tübinger, Uracher und Kirchheimer Alb" in: *Jahreshefte des Vereins für vaterländische Naturkunde in Württemberg* 64, pp. 187–248.

Widmer, R. (2015) *Der Bergbau am Südranden. Exkursion 18. April 2015* Schweizerische Geotechnische Kommission. ETH Zürich. NO F 35.

Wieland, B. (1979) "Zur Diagenese und schwachen Metamorphose eozäner siderolithischer Gesteine des Helvetikums" in: *Schweizerische Mineralogische und Petrographische Mitteilungen* 59, pp. 41–60.

Wullschleger, E. (2005) "Das Bohnerz von Küttigen - Entstehung, Fossilien- und Mineraliengehalt" in: *Aargauer Naturforschende Gesellschaft Mitteilungen* 36, pp. 27–60.

Wunderle, M. and M. Abele (2018) "Geotechnical challenges during the construction of the Albabstieg Tunnel in prediction and construction: Geotechnische Herausforderungen beim Bau des Tunnel Albabstieg in Prognose und Ausführung" in: *Geomechanics and Tunnelling* 11.6, pp. 647–658.

Ziegler, R. (1998) "Marsupialia und Insectivora (Mammalia) aus den oberoligozänen Spaltenfüllungen Herrlingen 8 und Herrlingen 9 bei Ulm (Baden-Württemberg)" in: *Senckenbergiana lethaea* 77.1-2, pp. 101–143.

Ziegler, R. and E. P. Heizmann (1991) "Oligozäne Säugetierfaunen aus den Spaltenfüllungen von Lautern, Herrlingen und Ehrenstein bei Ulm (Baden–Württemberg)" in: *Stuttgarter Beiträge zur Naturkunde Serie B* 171, pp. 1–26.

Zschokke, B. (1907) "Resultate der technologischen Untersuchung der schweizerischen Tone" in: *Mitteilungen der Eidgenössischen Materialprüfungsanstalt in Zürich* 11, pp. 1–170.

Chapter 4

U-LOSS ASSOCIATED WITH LASER-HEATING OF HEMATITE AND GOETHITE IN VACUUM DURING (U-TH)/HE DATING AND PREVENTION USING HIGH O_2 PARTIAL PRESSURE

with Kenneth A. Farley[1] and Jonathan Treffkorn[1]

Abstract

Single-aliquot (U-Th)/He dating of hematite has been used to study iron-oxide precipitation in various environments. Highly retentive hematite samples require temperatures of >1000 °C to be completely degassed, but the temperature for major U-loss is ~980 °C. We characterize the natural variability of U, Th, and Sm concentrations of five hematite and five goethite samples and detect U-loss by comparing U concentrations, Th/U, and Sm/U of heated aliquots to these values. We demonstrate that prolonged heating at temperatures of 950 °C can also lead to U-loss. Through the use of infrared spectroscopy, we show that loss of U in goethite and hematite samples is associated with phase change from hematite to magnetite. The onset of this phase transition can be changed from about 800-900 °C in vacuum to approximately 1250 °C in an oxygen partial pressure of 100 mbar. We show that samples can be outgassed at 1150 °C while simultaneously preventing U-loss in an oxygen-rich atmosphere during heating and we describe our implementation and automation of the procedure. An average age calculated from replicate samples (n=12), which were analyzed using this procedure, has a relative uncertainty of 2% (1σ), and is within the uncertainty of the previously measured two-aliquot age. We suggest this oxygen degassing procedure as a way to precisely and reproducibly determine single-aliquot hematite (U-Th)/He ages.

[1]California Institute of Technology, 1200 E California Blvd, Pasadena, CA 91125, United States

4.1 Introduction

(U-Th)/He geochronology and thermochronology of hematite has been used in the past to quantify the time-scales of lateritic weathering (Cooper et al., 2016; Danišík et al., 2013; Pidgeon et al., 2004; Wells et al., 2019), fault activity (Adams et al., 2013; Ault et al., 2016, 2015; Calzolari et al., 2018; Evenson et al., 2014; Garcia et al., 2018; McDermott et al., 2017; Moser et al., 2017), episodes of hydrothermal mineralization (Bähr et al., 1994; Farley and Flowers, 2012; Farley and McKeon, 2015; Jensen et al., 2018; Kerkhof et al., 2018; Lippolt et al., 1995; Wernicke and Lippolt, 1993, 1994a,b, 1997; Wu et al., 2019), and diagenetic cementation (Reiners et al., 2014). Highly retentive hematite samples must be heated to >1000 °C to completely degas He. In goethite, which transforms to hematite around 180-300 °C (Prasad et al., 2006; Ruan et al., 2001), a substantial loss of U has been documented (Vasconcelos et al., 2013). Loss of U due to sample heating leads to erroneously high (U-Th)/He ages.

In order to circumvent the problem of U-loss, some studies have employed the two-aliquot approach (Bähr et al., 1994; Pidgeon et al., 2004; Strutt, 1909; Wernicke and Lippolt, 1993, 1994a,b), by which analyses of parent and daughter isotopes are performed on separate aliquots. A large amount of material (tens of mg to g quantities) is crushed and homogenized. An aliquot of this material is weighed and heated to 1200-1400 °C (Bähr et al., 1994; Farley and Flowers, 2012; Farley and McKeon, 2015; Wernicke and Lippolt, 1994b) to achieve complete degassing of helium, which is measured using a noble gas mass spectrometer. A different aliquot is analyzed for parent isotope concentrations (e.g. Farley and Flowers, 2012; Farley and McKeon, 2015; Wu et al., 2019), usually by isotope dilution inductively-coupled plasma mass spectrometry (ICP-MS). Separately measured He, U, Th, and Sm concentrations are then used to compute a single (U-Th-Sm)/He age.

However, a large amount of sample is required to perform separate measurements

because of the need for homogeneous material. Homogenization of sample material obliterates any inhomogeneity in parent or daughter isotopes, which might be of interest. A span of time represented in the sample is reduced to an average age, which might not be geologically meaningful.

Single-aliquot (U-Th)/He dating, in which He and parent isotopes are measured on the same aliquot, is the preferred approach for geochronology and thermochronology of apatite (Wolf et al., 1996), zircon (Reiners et al., 2002), titanite (Reiners and Farley, 1999), goethite (Shuster et al., 2005), and other phases. Aliquots of typically 10-100 μg are loaded into Pt or Nb tubes and pinched at the ends to form packets. These packets are laser-heated in the wells of a copper planchet. After degassing and He measurement, the sample inside the packet is dissolved. Parent isotopes are measured by isotope dilution, along with determination of the mass of the sample, using ICP-MS. Since both parent and daughter isotopes are measured on the same aliquot, a (U-Th)/He age is calculated from absolute amounts of U, Th, Sm, and He in the sample.

Single-aliquot dating has several advantages over the two-aliquot method. Since there is no need for homogenization, the required sample masses are several orders of magnitude lower than those for the two-aliquot method. Inhomogeneity in parent and daughter isotopes is taken into account in calculating (U-Th)/He ages, since they are measured on the same material. This permits age determination with high spatial resolution. Layered iron-oxide deposits, such as pisoliths, can be formed slowly over tens of millions of years (Hofmann et al., 2017). Significant age inhomogeneity in such deposits might be present on length-scales of tens of micrometers. These samples might not yield enough sample material for the application of the two-aliquot method, leaving the single-aliquot method as the only feasible way to determine meaningful (U-Th)/He ages.

If any U or Th, or even sample material, was lost before the dissolution step, the

absolute amounts of parent isotopes would be deficient relative to the amount of extracted He and ages would appear anomalously high. Extraction temperatures for (U-Th)/He dating are chosen based on the phase – 940 °C for goethite, 1050 °C for apatite, 1200 °C for zircon, and 1280 °C for titanite. Potential volatilization of parent isotopes has been a concern since the initial development of the (U-Th)/He method. For apatite, Wolf et al. (1996) showed no measurable loss of U or Th at 1100 °C. Zircon has been shown to retain U at temperatures of 1300 °C (Reiners et al., 2005). Major loss of U as a result of laser-heating has been documented in titanite (Reiners and Farley, 1999).

Extraction time and temperature required to completely degas helium from hematite are dependent on the He-retentivity of the material. In goethite, U is lost, while Th is retained, at high temperatures (Vasconcelos et al., 2013), which might be due to reduction of Fe^{3+}. This process can be investigated by heating aliquots of the same sample, which should yield the same ages, to different temperatures and expressing the outcome as an apparent age. More He is extracted with increasing temperature, leading to an increase in apparent age (Fig. 4.1). As U-loss occurs at high temperatures, the resulting age of aliquots increases rapidly. In samples in which effective uranium concentration (eU) is dominated by U, the apparent age will tend to infinity for complete U-loss. With Th or Sm present, the age will increase to a value higher than the age of the sample. Ideally, U-loss will occur at temperatures well above the temperature for complete He extraction, which will define a plateau accurately corresponding to the 'true' (U-Th)/He age of the sample (Vasconcelos et al., 2013). If U-loss occurs at temperatures below those required for complete He extraction, there is no plateau and, consequently, no 'safe' temperature range for sample degassing.

Vasconcelos et al. (2013) performed this experiment on one goethite sample, which fully degassed when heated to around 925 °C for 6 min. Apparent ages increased

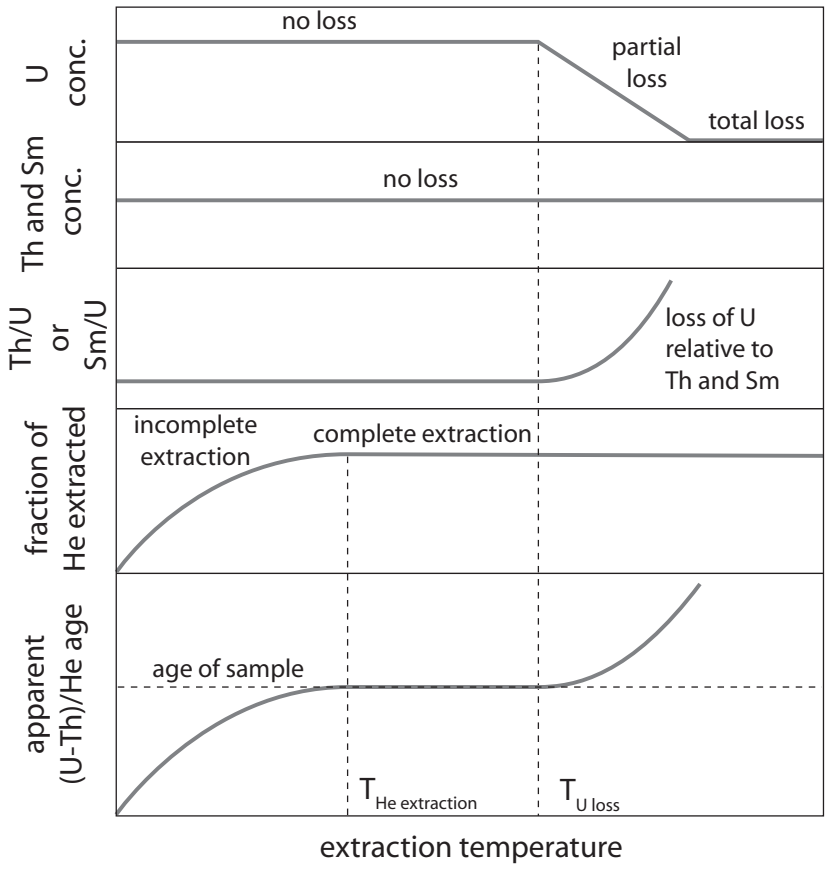

Figure 4.1: Ideal experiment outcome for sample heating. Complete He degassing occurs above the He extraction temperature. Below this temperature (U-Th)/He ages are below the 'true' age of the sample due to incomplete He extraction. U is lost at high temperatures, which leads to an increase in age as well as Th/U and Sm/U ratios. Age will tend to infinity for complete U-loss, unless Th is present. Ideally, complete He extraction will occur below the U-loss temperature. In this case, there is an age plateau between these two temperatures.

above the bulk age of the sample between 1050 °C and 1100 °C, along with a significant increase in the Th/U ratio. In the case of goethite, degassing temperature seems to be significantly lower than the U-loss temperature. Goethite samples can therefore be degassed at an intermediate temperature, ensuring complete He extraction and preventing volatilization of U. The same pattern of U-loss in goethite and hematite at high temperatures has been observed in subsequent studies (e.g. Garcia et al., 2018; Kerkhof et al., 2018; Reiners et al., 2014).

In this study, we perform the same type of heating experiment on small aliquots (5-

200 µg) of hematite to find optimal extraction parameters while preventing U-loss, thus enabling a single-aliquot methodology similar to that for goethite. We show a correlation between phase transition from hematite to magnetite and U-loss and demonstrate that samples can be degassed in an atmosphere of pure O_2 to prevent U-loss. We describe how this method can be implemented and automated for routine single-aliquot dating of hematite and goethite samples.

4.2 Experimental setup and samples

We performed experiments with two basic setups to degas samples (a) in vacuum while exposed to a charcoal trap cooled with liquid nitrogen (LN_2), and (b) in a pure O_2 atmosphere of about 100 torr. Laser heating, helium measurement, sample dissolution, and elemental analysis followed the standard procedures for iron-oxides at Caltech described by Hofmann et al. (2017).

Samples

We performed heating experiments on hematite samples with well-established two-aliquot (U-Th)/He ages and (U-Th)/Ne ages (Tab. 4.1). They represent a wide range of ages (130-1760 Ma), as well as U and Th concentrations (0.2-15 ppm). These values were determined by previous studies on bulk samples of at least several milligrams using the two-aliquot method. We adopted abbreviations for samples used in previous studies. HM1 (13-N64 'Black Rock') and HM2 (03QK-90 'Beeshoek') are massive iron ore samples from boreholes (Miller, 2019), MS (CIT-10443, MI-43) is botryoidal hematite from the Pabst Mine in the Gogebic Range, Michigan (Farley and McKeon, 2015), GC (CP06-1 P300) is a hydrothermal hematite sample from the Redwall Limestone of the Grand Canyon (Farley and Flowers, 2012), and HM2048 (CIT-2048) is sample material derived from crushing a single-crystal hematite from Minas Gerais, Brazil (Farley, 2018).

Additional samples were used to probe the effect of laser-heating and O_2 degassing

on goethite (Tab. 4.1), which transforms to hematite at 180-300 °C (Prasad et al., 2006; Ruan et al., 2001) and are therefore present as hematite at iron-oxide degassing temperatures (800-1200 °C). The following goethite samples were analyzed in this study: blade (DMNH-10029) is from a sample with radiating blades of goethite on massive quartz (Miller, 2019), Lyp (LynP02-09-A2) and RH (Roy-02-02-C3) are from a banded vein and a massive block of goethite from a channel iron deposit (Vasconcelos et al., 2013), YAN (YAN-02-01-A) is vitreous goethite cement from a channel iron deposit (Heim et al., 2006), and sample CIT (CIT-16406) is a banded goethite sample collected at Igarape Bahia Mine, Carajas, Brazil from the Caltech collection.

These samples were used for heating experiments, to investigate phase changes using ATR-FTIR, and to obtain single-aliquot ages. Additionally, we dissolved between 10 and 45 aliquots of undegassed hematite and goethite samples to establish median values and natural variability of U, Th, and Sm concentrations as well as Th/U and Sm/U ratios. Aliquots were of the same size as those used for heating experiments (tens to hundreds of micrograms).

^{4}He measurement

Samples were loaded into Pt tubes with a diameter of 1 mm and the ends were pinched shut to produce flat packets. These packets were then heated with a diode laser in vacuum while exposed to a charcoal trap submerged in liquid nitrogen (LN_2). Temperatures during heating were monitored using a one-wavelength pyrometer. Pyrometric readings were calibrated by laser-heating a Pt packet enclosing a K-type thermocouple under both vacuum and O_2 conditions (for details see Appendix 4.B). This empirical calibration was used to determine temperatures by optical pyrometry to within 2-3% (5-20 °C). The stated uncertainty takes into account slight differences in emissivity between different packets and changes in emissivity

Table 4.1: Hematite and goethite samples used in this study. Ages and concentrations of hematite samples are bulk values determined by the two-aliquot method on several milligrams of sample material, as reported in the original references. Values for goethite samples represent the average of several aliquots of tens to hundreds of micrograms.

Hematite Samples											
Sample	Sample Name	Reference	(U-Th)/He [Ma]	(U-Th)/Ne [Ma]	^{4}He [nmol/g]	U [ppm]	Th [ppm]	Sm [ppm]	eU [ppm]	Th/U	Sm/U
HM1	Black Rock	Miller (2019)	1523±61	1706±141	3.54±0.15	0.26±0.01	0.50±0.01	0.63±0.02	0.38±0.02	1.9231	2.4231
HM2	Beeshoek	Miller (2019)	1761±39	1776±97	14.42±0.02	1.03±0.02	1.08±0.01	0.26±0.01	1.28±0.02	1.0485	0.2524
MS	CIT-10443	Farley and McKeon (2015)	571±18	756±18	22.80±0.60	7.00±0.11	0.01±0.01	0.88	7.00±0.11	0.0014	0.1257
GC	CP06-1 P300	Farley and Flowers (2012)	130±1.7	217±5	14.10±0.20	15.70±0.20	14.90±0.10		19.20±0.22	0.9490	
MG	CIT-2048	Farley (2018)	not reported								
Goethite Samples											
Sample	Sample Name	Reference	(U-Th)/He [Ma]	(U-Th)/Ne [Ma]	^{4}He [nmol/g]	U [ppm]	Th [ppm]	Sm [ppm]	eU [ppm]	Th/U	Sm/U
blade	DMNH-10029	Miller (2019)	not measured								
Lyp	LynPP02-09-A2	Vasconcelos et al. (2013)	30.7±1.6		9.7	36.8				2.49	
RH	Roy-02-02-C3	Vasconcelos et al. (2013)	63.9±6.4								
YAN	YAN02-01-A	Heim et al. (2006)	10±0.3						1.08		
CIT	CIT-16406	this study									

as a result of repeated heating cycles.

We heated individual aliquots to a temperature between 600 °C and 1450 °C, Most aliquots were heated for 10-20 min, but some up to 4 h. The extracted ^{4}He was spiked with pure ^{3}He and helium was cryogenically concentrated before introduction into the mass spectrometer. The ^{4}He/^{3}He ratio was measured using a Pfeiffer quadrupole mass spectrometer. Absolute amounts of ^{4}He were determined relative to a standard with a known amount of ^{4}He. Standards and procedural blanks were interspersed every 3-6 sample measurements to track instrumental drift.

We amended this setup for degassing of samples in ~100 torr of O_2. Implementation of this method is discussed below and further details can be found in Appendix 4.A.

Sample dissolution and elemental analysis

Samples in Pt packets were transferred to a Teflon vial and 100 µl of concentrated HCl as well as a spike solution containing ^{235}U, ^{230}Th, and Ru was added. The Teflon vials were capped and refluxed on a hot plate at 150 °C for at least 12 hours. We did not observe any insoluble residue in undegassed aliquots, showing that samples were completely dissolved by this procedure. Solutions were dried on a hot plate at 95 °C, dissolved in 50 µl of concentrated nitric acid, and diluted with 1 ml of MilliQ water. Elemental analysis of U, Th, Sm, Fe, Mn, Al, and Si was performed by isotope dilution and elemental spiking on an Agilent 8800 ICP-MS.

The mass of iron-oxide aliquots is routinely determined by measuring Fe by ICP-MS and calculating hematite or goethite mass by assuming perfect stoichiometry. The precise and accurate determination of Fe-based sample mass is vital for detecting absolute U-loss, because U concentrations are calculated using Fe-based mass. We improved the precision and accuracy of the Fe-based sample mass measurement by using Ru as an elemental spike for ICP-MS. We weighed aliquots of 50-650 µg on a microbalance and analyzed them using the procedure outlined above. The root mean

square deviation of the Fe-based mass measurement from weighed mass is ~3% for the Ru-spike. This shows that the external uncertainty of our U concentration measurements, including the effect of analytical and dissolution issues, is around 3% (1σ). Complete data and additional discussion can be found in Appendix 4.C.

Monitoring phase change with ATR-FTIR

We studied phase transitions in natural hematite and goethite samples due to laser-heating. Aliquots of several milligram of crushed material (tens to hundreds of individual grains) were loaded into Pt packets of about 5 mm diameter. These packets were heated with the same laser heating system as described above. We prepared several aliquots of a sample and heated each packet to a temperature between 550 °C and 1450 °C. We performed experiments in both vacuum and ~100 torr of O_2. Samples degassed in vacuum were heated while being turbo-pumped, to ensure that O_2 released by the sample due to phase change does not create conditions different from those of vacuum heating.

After heating, the packets were tested for being magnetic with a hand magnet. Pt packets were opened under a light microscope using tweezers. Two individual grains were picked for dissolution and ICP-MS analysis. The rest of the heated material was powdered using mortar and pestle. The powder was investigated with Attenuated Total Reflection Fourier-Transform Infrared Spectroscopy (ATR-FTIR). A spectrum from 400 to 4000 cm^{-1} was recorded with ten passes of 10 s integration time each. Phase was determined by comparing the spectra to those of synthetic hematite and magnetite powders as well as those of unheated samples. We also determined the height of peaks representative of hematite and magnetite and calculated a peak ratio. We use this ratio to estimate the amount of hematite converted to magnetite based on calibration with mixtures of synthetic hematite and magnetite (see Appendix 4.D). Since the FTIR method can only detect a fraction of at least 5-10% magnetite in

hematite, we also performed another set of experiments to constrain the onset of the hematite-magnetite phase change. We measured the release of O_2 resulting from the conversion of hematite into magnetite. Samples were laser-heated with progressively higher power, and the temperature and pressure were recorded. These experiments used a capacitance manometer, which was degassed and pumped for 24 h before the beginning of measurements. Since the laser chamber was not actively pumped during the experiment, we characterized the background rise rate several times and subtracted the background pressure from the sample measurements. After the highest temperatures were reached, the gas was exposed to an LN_2 trap to confirm the species as O_2, which is condensable gas.

4.3 Results

Sample inhomogeneity

Undegassed hematite samples with masses of 20-800 μg show large natural variability of U, Th, and Sm concentrations as well as Th/U and Sm/U ratios (Fig. 4.3). We constructed kernel density estimates (KDEs) with bandwidths equal to the average 2σ-uncertainty of 10-45 replicate analyses. We determined the median value of the distribution, which we use as a reference for judging U-loss. KDEs of measured parameters often have a single peak, although many distributions are asymmetric and skewed toward higher values. The same sample can have parameters which have a broad and asymmetric distribution, while the KDEs of other parameters are more defined. The edges of the interquartile range (IQR) of the distributions of U, Th, and Sm concentrations are between 5% of 150% from the median. U concentrations are most well-defined at around 10-20% variability , with Th and Sm concentrations both showing a variability of 20-50%. Th/U and Sm/U ratios vary about 20-40% in the IQR. Some samples have Th concentrations that are below the detection limit (MS, HM2048). These samples had Sm concentrations well above procedural blank

levels and we utilized the Sm/U ratio instead of the Th/U ratio to detect U-loss.

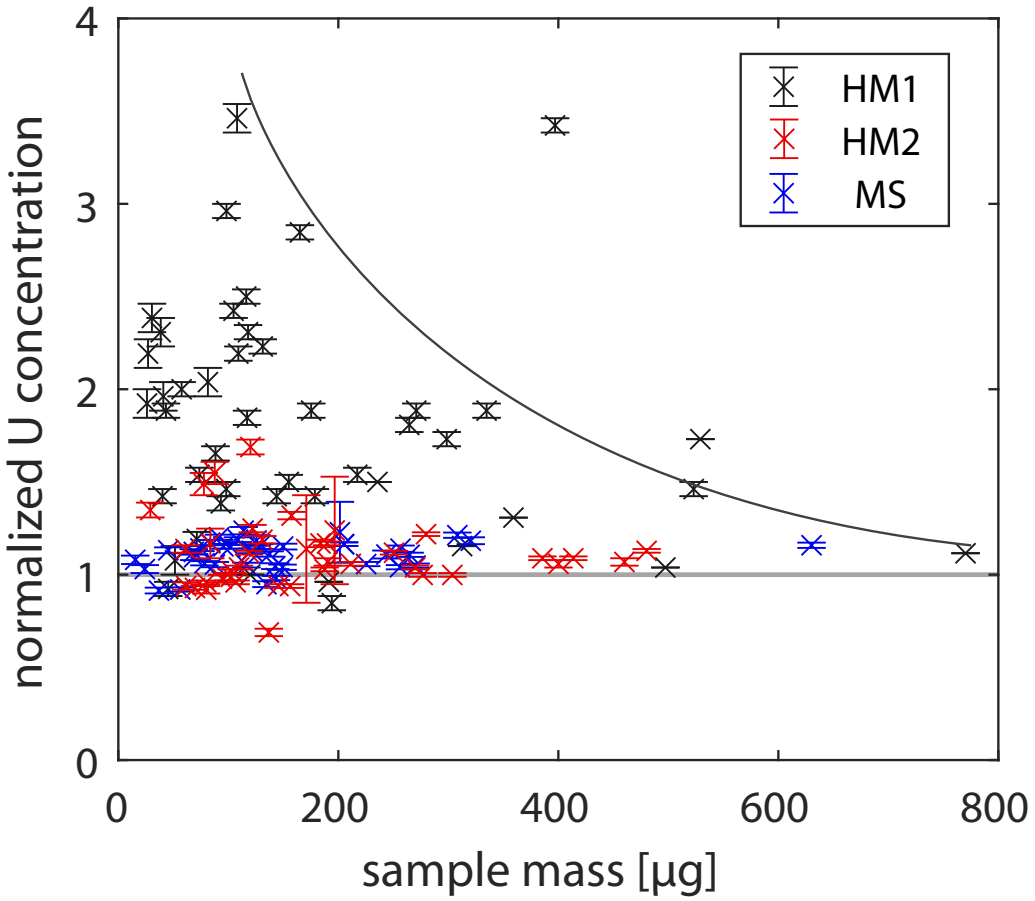

Figure 4.2: Inhomogeneity of U concentration in three samples by mass of aliquot. U concentrations were normalized by bulk concentrations measured on several milligrams of sample material. Small masses have larger variability, while larger aliquots have U concentrations close to the bulk value.

Each set of replicates contains several outliers, almost exclusively of higher than average U, Th, or Sm concentrations (Fig. 4.3). Inhomogeneity in U, Th, and Sm concentrations increases with smaller sample mass (Fig. 4.2), and concentrations of aliquots >500 µg are close to the bulk values. This suggests that there are volumes of <100 µm in diameter in the crystal, in which any or all of these elements are present at several times the bulk concentration. Inhomogeneity at this scale could cause potential issues of α-ejection from these areas and α-implantation into neighboring areas, leading to a dispersion of ages if material is sampled at this scale. The

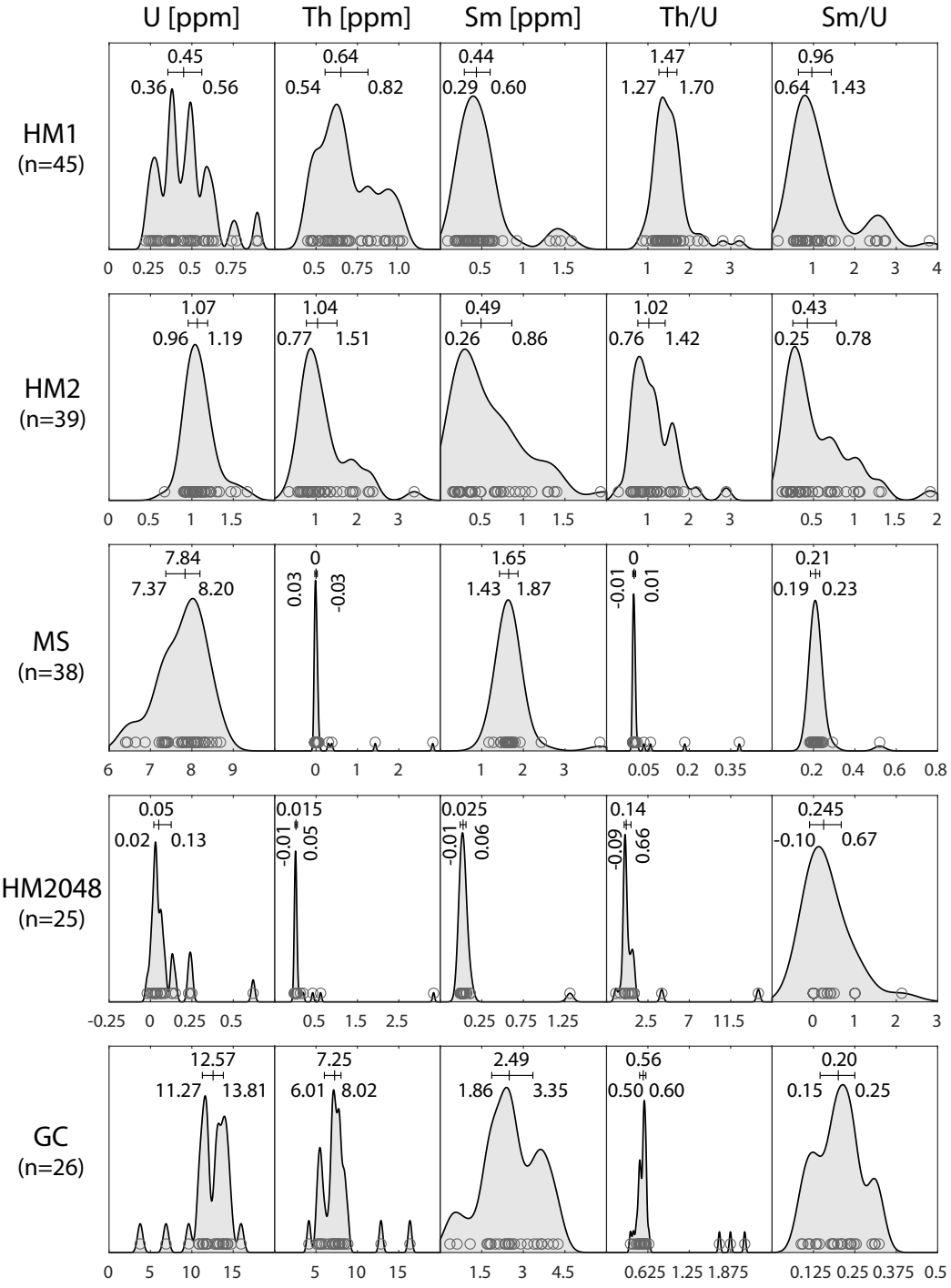

Figure 4.3: Concentrations of U, Th, and Sm of undegassed hematite samples measured on 25-45 aliquots of 20-800 µg, as well as Th/U and Sm/U ratios. Given are KDEs with bandwidths of the average 2σ uncertainty of individual measurements. Bars above the KDEs indicate the median value and the interquartile range.

inhomogeneity in U, Th, and Sm concentrations at small scales varies between sample (Fig. 4.2).

Goethite samples have a larger natural variability in U, Th, and Sm concentrations (Fig. 4.4). Samples CIT and RH have defined peaks of U and Th concentration, similar to most of hematite samples. Samples YAN, blade, and Lyp did not show a defined peak of U or Th concentrations, but a broad distribution of values with multiple peaks. Due to their great natural variability, samples blade and YAN were not used for heating experiments, but they were analyzed for phase changes using ATR-FTIR.

U-loss in vacuum heating

We heated aliquots of four hematite (n=197) and four goethite samples (n=41) to temperatures between 500 °C and 1400 °C under vacuum. Measured values of U, Th, and Sm concentrations as well Th/U and Sm/U ratios were normalized by the median value of undegassed aliquots or the average values measured by two-aliquot bulk analyses to show a summary of the results (see Fig. 4.5). Plots and data for each individual hematite and goethite sample, separated by vacuum and O_2 experiments as well as by whether Pt or Nb tubes were used, can be found in Appendix 4.E.

Aliquots of the same sample heated to different temperatures showed the first signs of U-loss at ~980 °C for both hematite and goethite (Fig. 4.5). There is considerable scatter of all measured parameters due to natural variability of the samples. However, clear trends emerge with a large number of aliquots of the same sample. U-loss manifests as a decrease in U concentration with a concurrent increase in Th/U or Sm/U ratio. The amount of U-loss at any specific temperature varies between 5% and >95% and is not reproducible. We observed no systematic loss of either Th or Sm at high temperatures. Some samples had Th concentrations that were below the detection limit. For these samples, we utilized the Sm/U ratio, which showed

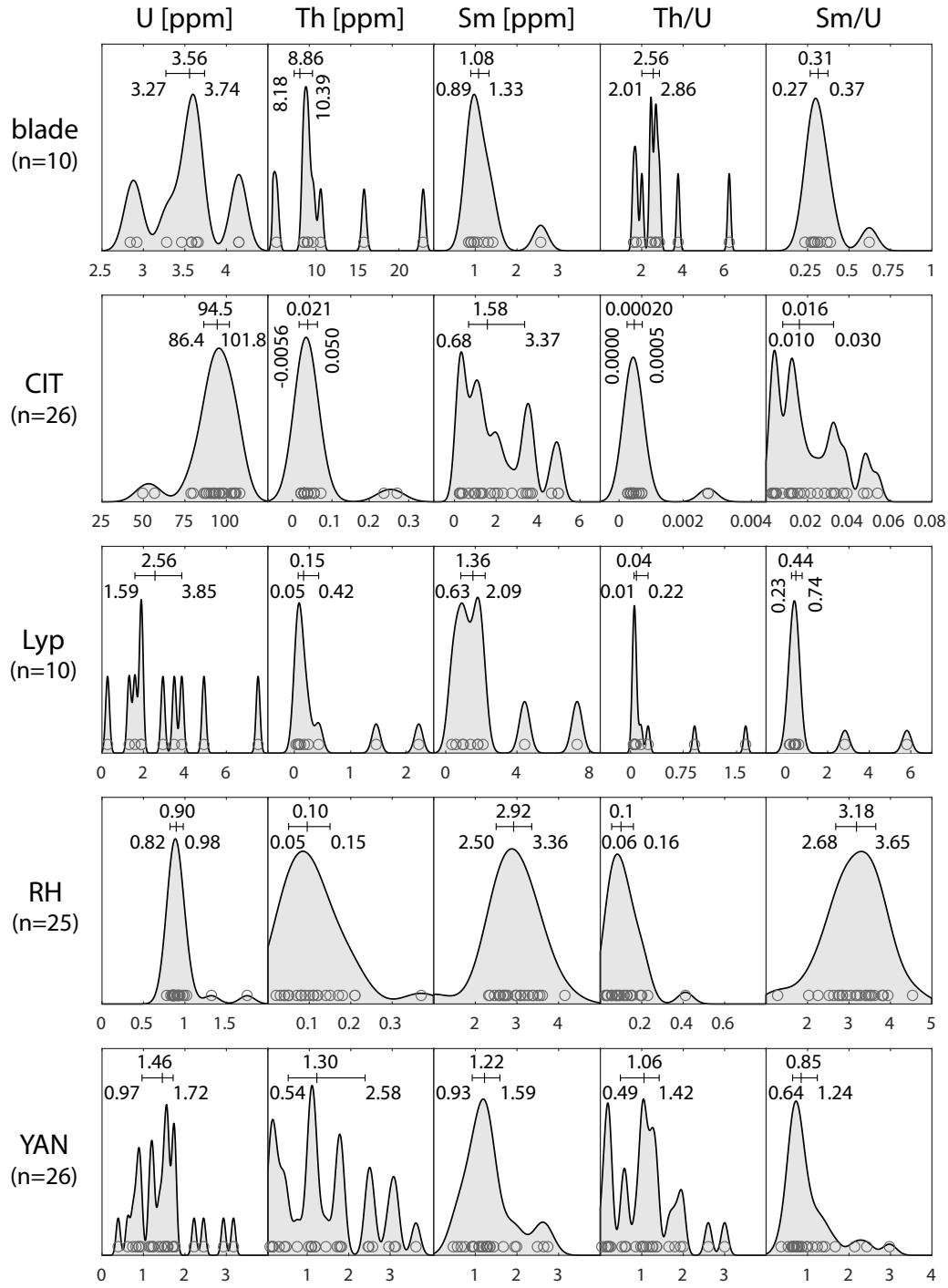

Figure 4.4: Concentrations of U, Th, and Sm of undegassed goethite samples measured on 10-26 aliquots of 20-350 µg, as well as Th/U and Sm/U ratios. Given are KDEs with bandwidths of the average 2σ uncertainty of individual measurements. Bars above the KDEs indicate the median value and the interquartile range.

the same increase due to U-loss as the Th/U ratio. The Th/U or Sm/U ratios are indicative of major U-loss. The natural variability of these parameters is 20-50% of the median value, therefore U-loss in individual samples was only apparent when it deviates by at least this amount. The Th/U or Sm/U ratio rapidly increases within a narrow temperature range of 50-100 °C from the point of initial U-loss (Fig. 4.5). We found no difference in the U-loss temperature or amount of U-loss between Pt packets and Nb packets (for data see Appendix 4.F).

The amount of He extracted from the sample is a function of both temperature and heating time. For the same temperature, aliquots which have been heated for longer show a larger fraction of total He extracted than those heated for shorter periods of time. Helium is extracted at a different rate for each sample, reflecting differences in retentivity. Some samples have He concentration higher than those measured on bulk material, most likely due to U and Th concentrations in the aliquot, which are higher than the bulk values.

The apparent age is below the two-aliquot bulk age (the 'true' age) of the sample at low temperatures. Hematite sample MS as well as goethite samples are fully outgassed at around 800 °C. In hematite samples HM1 and HM2, which are highly retentive, helium is fully extracted at ~1150 °C for HM1 and at ~1250 °C for HM2. Therefore, in these samples, He is not fully extracted below the temperature of U-loss. Apparent ages are below the bulk age up to the U-loss temperature, then they increase rapidly as U is lost and more He is extracted. The apparent ages at high temperatures are higher than the bulk age, quickly rising to several billions of years. This shows that some hematite samples have high-retentivity domains that do not permit the complete extraction of He without the loss of U. For these samples, there is no age plateau and standard approaches cannot be used to accurately date the sample. An increase of several hundred degrees without U-loss is required to make these samples datable by the single-aliquot (U-Th)/He method.

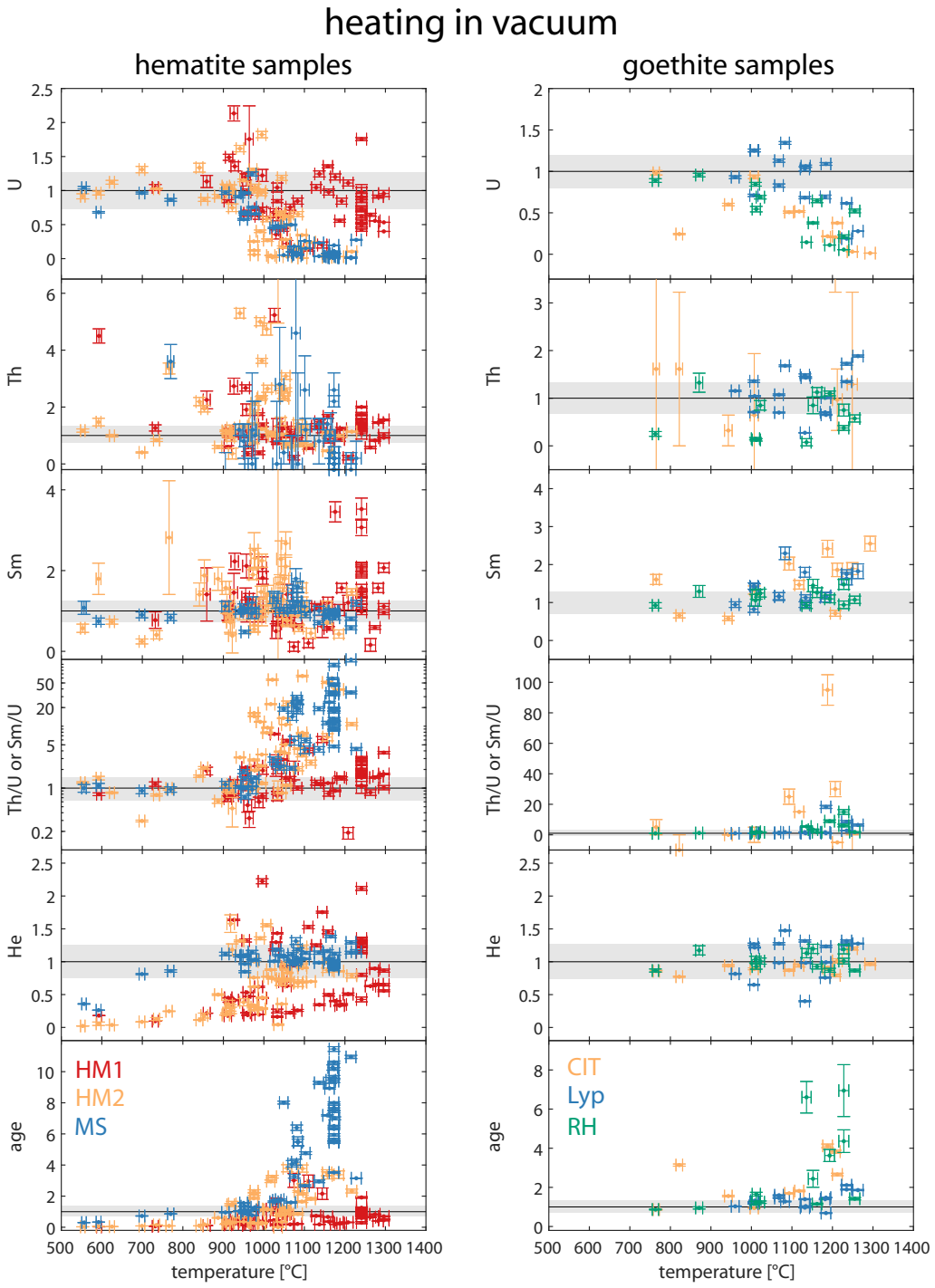

Figure 4.5: Hematite and goethite samples heated to temperature between 500 and 1300 °C in vacuum. All values were normalized by median value from undegassed aliquots (U, Th, Sm, Th/U or Sm/U) or two-aliquot bulk analyses (age, He concentration) and grey areas represent the typical range of values. U in both hematite and goethite is lost at temperatures above ~980 °C.

Effect of heating time

Since the extraction of He occurs by diffusion, prolonged heating time at a lower temperature can be substituted for high temperatures to extract all the helium. To test whether U-loss occurs at lower, 'safe' degassing temperatures, we performed experiments in which samples were heated to 950 °C for various lengths of time between 5 min and 4 h. U-loss was detectable at isothermal holding times over 20 min (Fig. 4.6). U-loss increased with holding time, with almost complete U-loss occurring at around 4 h. The same trend can be seen in an increase of both the Sm/U ratio and the apparent age. Partial U-loss therefore occurs at temperatures below those of massive U-loss, but only becomes apparent at long holding times. Therefore, longer holding times at lower temperatures are not a solution to the problem of U-loss in hematite and goethite.

Phase transition during heating

We acquired ATR-FTIR spectra of samples heated to temperatures between 500 °C and 1350 °C to investigate phase change due to laser-heating in vacuum and O_2. The dominant phase was interpreted by comparing spectra of samples to those of synthetic goethite, hematite, and magnetite powders of 0.15-0.35 μm grain-size. An example of a series of ATR-FTIR analyses is shown for sample HM2 (Fig. 4.7). We performed similar analyses on a total of five hematite samples and three goethite samples, the full results of which can be found in Appendix 4.D.

We observed partial conversion of hematite to magnetite in vacuum starting at around 950-990 °C. Minor U-loss, measured on the same material was detected in the same temperature range (Fig. 4.8). Complete conversion of hematite to magnetite occurred between 1050 °C and 1200 °C, associated with major loss of U. This pattern of U-loss is similar to that found in vacuum heating experiments described above. The samples that contained detectable amounts of magnetite were

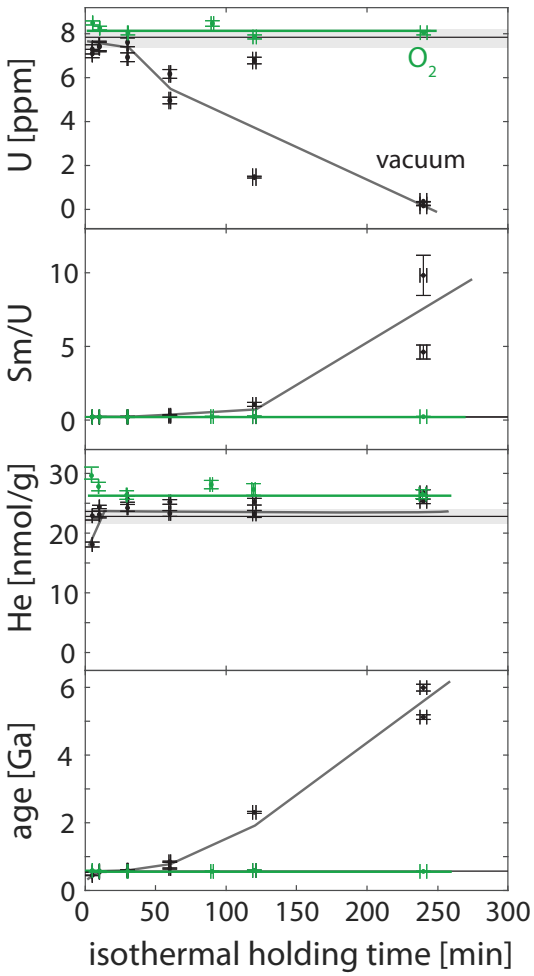

Figure 4.6: Effect of heating time on hematite sample MS with isothermal holding in vacuum at 950 °C (black). At this temperature, U-loss in vacuum is detectable for heating times >20 min. Samples heated in ~100 torr O_2 at 1000 °C (green) do not show any loss of U regardless of heating time. Black and green lines represent general trends.

found to respond to a weak hand magnet while still in their Pt packets. The streak of the sample, when powdered, showed progressive darkening as a result of the increasing amounts of magnetite relative to hematite at high temperatures.

Samples heated at a p(O_2) of ~100 torr for 10 min or 60 min showed a delayed conversion of hematite to magnetite (Fig. 4.7), as predicted by the phase diagram of Ketteler et al. (2001) (Fig. 4.11). Partial conversion of hematite to magnetite was observed between 1250 °C and 1350 °C. Conversion of about 40% of the

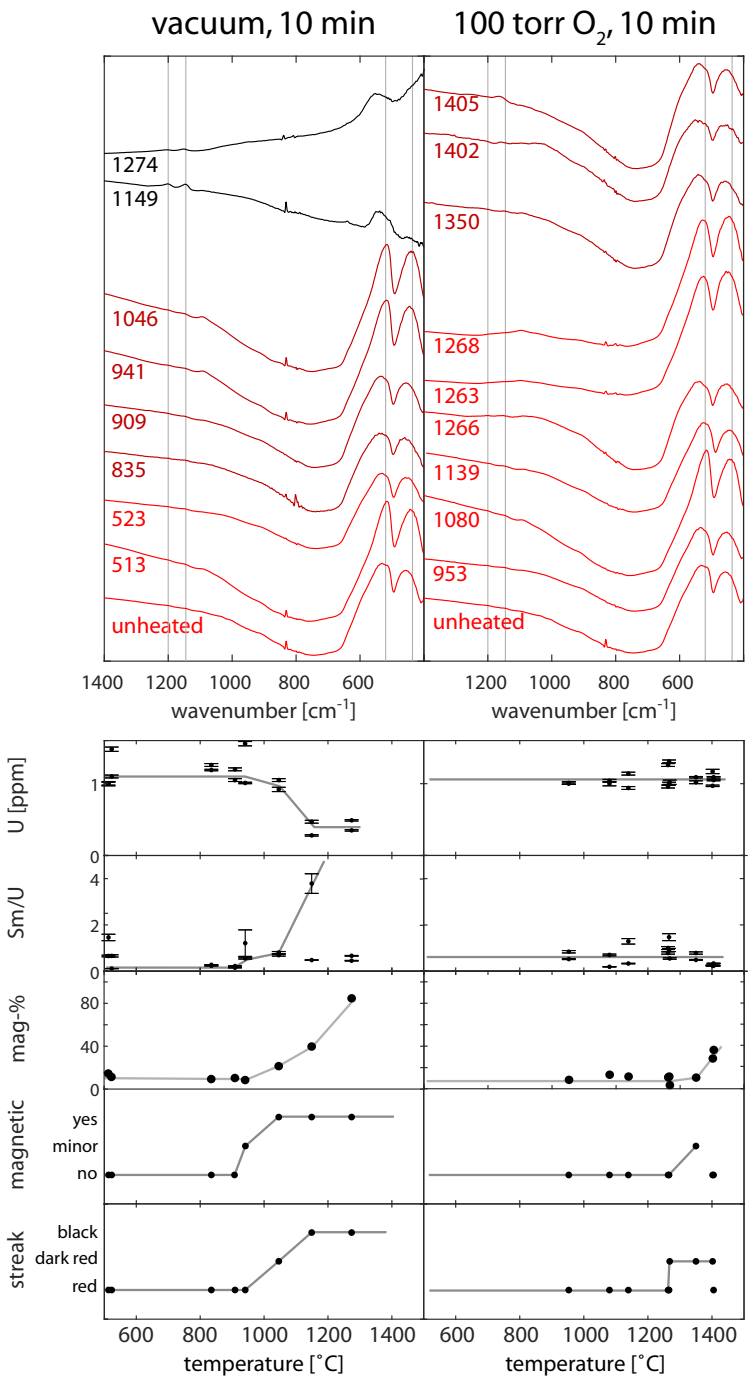

Figure 4.7: ATR-FTIR spectra of hematite sample HM2, heated to different temperatures (given in °C) in vacuum and in 100 torr of O_2 for 10 min. U concentrations and Sm/U ratios were measured on subsamples of the same material used for ATR-FTIR. Estimated magnetite percentage (mag-%) was determined from peak ratio. Initiation of U-loss occurs at the same temperatures as detectable partial conversion of hematite to magnetite. Partial conversion of sample material to magnetite is detectable with a hand magnet.

sample to magnetite was observed at the highest temperatures studied here (~1400 °C). This demonstrates that the phase transition starts when the temperatures cross the predicted phase boundary. However, due to kinetic effects, the samples are only partially converted from hematite to magnetite and much higher temperatures are required to fully convert samples to magnetite within the time-frame of the experiments.

Similar patterns were found for goethite, although conversion to magnetite and U concentration differ more between samples. Goethite samples heated in vacuum were present as hematite at the lowest temperatures studied here (~550 °C), with no evidence of remnant OH-groups. The first conversion of hematite to magnetite in goethite samples was observed at around 950 °C. Massive U-loss occurs around 1000-1050 °C, associated with a rapid increase in the magnetite fraction. Hematite is fully converted to magnetite at 1300 °C. Over 1300 °C, all goethite samples showed ATR-FTIR spectra that were almost flat, which we interpret as decomposition of magnetite to elemental iron. This was not observed in any hematite samples heated to similar temperatures.

Goethite samples heated in oxygen at the lowest observed temperatures (~900 °C) are mainly hematite, but there is evidence of remnant OH-groups up to 1400 °C. The first conversion of hematite to magnetite in goethite samples was observed at around 1050 °C, implying that hematite derived from dehydroxylation of samples originally present as goethite is thermodynamically and kinetically different from hematite samples. Major U-loss in goethite samples coincides with a rapid increase in magnetite fraction at around 1200 °C.

Phase transition from oxygen release

With ATR-FTIR, identification of hematite-magnetite phase transition was only possible for more than 5% conversion. In order to identify whether there is conversion

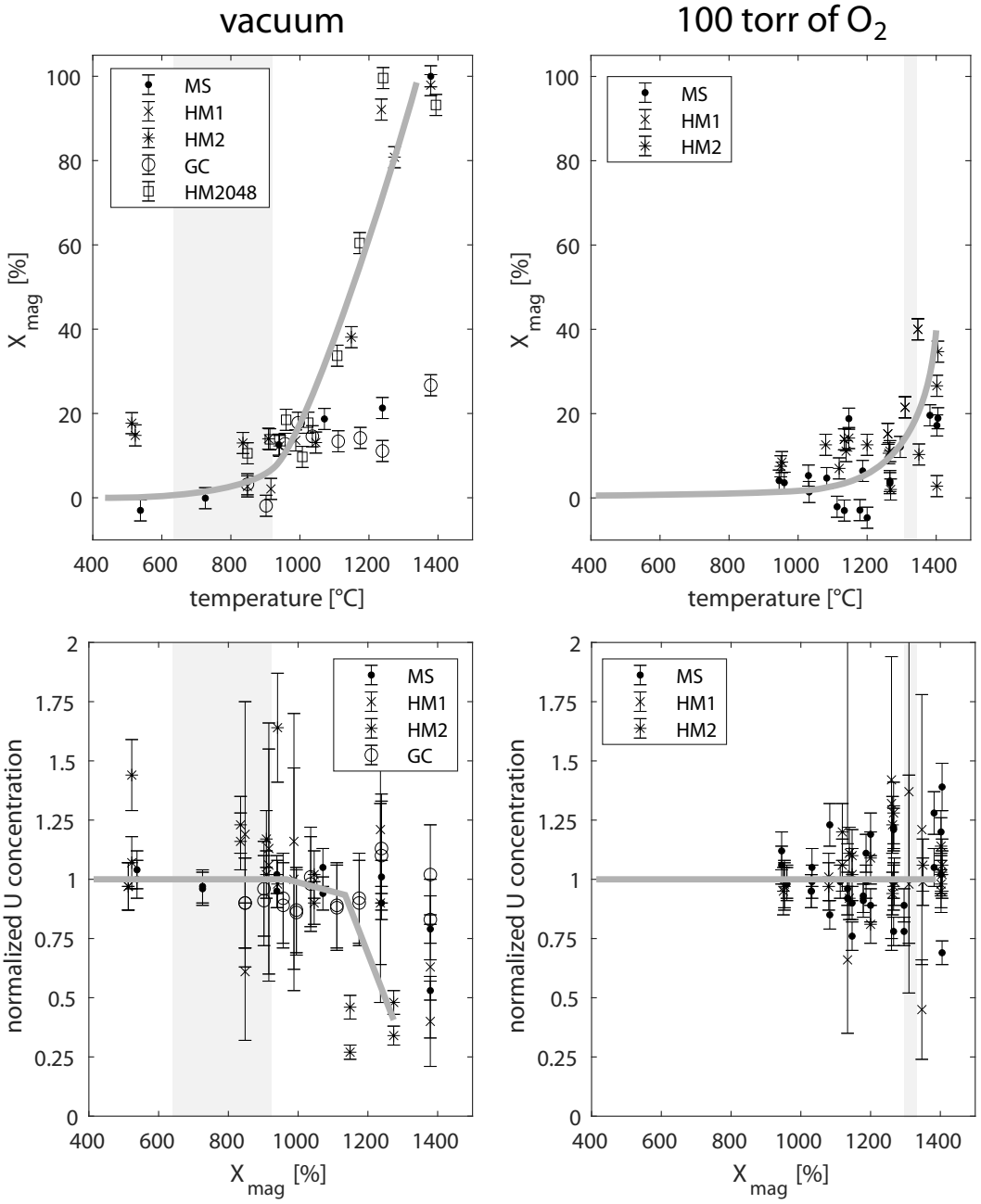

Figure 4.8: Summary of all hematite ATR-FTIR experiments. Magnetite percentage (top) and U concentration (bottom) as a function of temperature for heating of samples in vacuum (left) and 100 torr of O_2 (right). U concentrations are normalized by the median value of undegassed aliquots. Massive U-loss correlates with major conversion of hematite to magnetite. Shaded region is temperature range of hematite-magnetite transition from phase diagram of Ketteler et al. (2001) based on measured and estimated oxygen partial pressures. Grey lines show general trend.

of hematite to magnetite at temperatures below ~980 °C in vacuum, we laser-heated samples and monitored pressure build-up due to release of O_2 from the sample with a capacitance manometer. The lower limit of the pyrometer is about 550 °C, and therefore samples were heated to this temperature or above on the first heating step. We observed a minor pressure increase of 1-3% of the final pressure at temperatures below 550 °C (Fig. 4.9), which stays constant up to about 800-900 °C. This is presumably due to outgassing of volatiles, such as CO_2, N_2, or H_2O contained in the sample. A significant amount of gas evolved at temperatures >800 °C, suggesting the first release of O_2 due to phase change from hematite to magnetite. Pressure increased rapidly between 1000 °C and 1300 °C, with the largest increase around 1150 °C. Above ~1300 °C there is only minor change in pressure, which suggests that most of the hematite has transformed to magnetite. The final pressure was about 10^{-2} torr, which is consistent with the amount of oxygen (10^{-7} mol from ~20 µg of hematite sample) released into the volume of the laser chamber and tubing (~$5 \cdot 10^{-4}$ m^3) due to complete conversion of hematite to magnetite (release of 0.5 mol of O_2 per mole of hematite). After the experiment, we exposed the gas to a charcoal trap cooled with liquid nitrogen, which led to a reduction of 95-99% of the total pressure. This indicates that most of the gas is oxygen, while only a small fraction is composed of other gases, which are only incompletely trapped, such as hydrogen.

Samples heated in oxygen

Since we have shown that U-loss correlates with phase change from hematite to magnetite, we used an increased $p(O_2)$ to raise the phase transition temperature (Ketteler et al., 2001) to test whether this will prevent U-loss at high temperatures. In early experiments, we heated CuO packets to liberate oxygen. This produced oxygen partial pressures <1 torr. This was enough to delay U-loss to temperatures

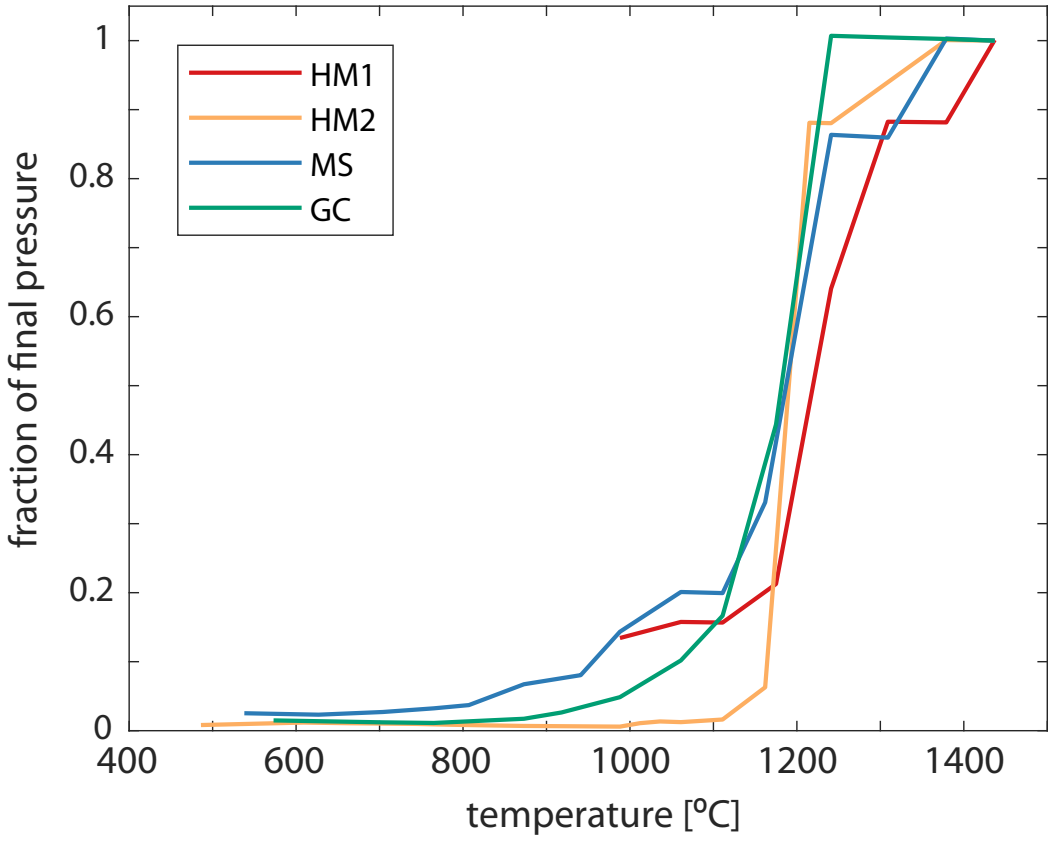

Figure 4.9: Pressure in the laser chamber as a function of temperature, interpreted to result from release of oxygen from hematite during transition. Measurements were normalized by the maximum observed pressure to compare samples of different mass.

of around 1100 °C (for details see data and plots in Appendix 4.F).

To increase the U-loss temperature even further and to automate the extraction process, we connected an oxygen tank with a pipette to the existing vacuum-degassing system to deliver oxygen partial pressures between 30 and 150 torr. We performed heating experiments of both hematite and goethite samples with this setup.

In hematite, the inception of U-loss occurred at 1180-1200 °C in the presence of oxygen, with massive U-loss of up to 99% between 1200 °C and ~1400 °C (Fig. 4.10). U-loss increases with both temperature and heating time. U-loss is apparent in both U concentrations and Th/U or Sm/U ratios. As in vacuum, we observed no systematic loss of either Th or Sm at high temperatures.

Extraction of He was dependent on the retentivity. Helium in sample MS was extracted at ~1000 °C. Samples HM1 and HM2 were completely outgassed at 1250 °C and 1350 °C. Longer holding times increased the fraction of extracted helium. Apparent age is close to the two-aliquot age of the sample for samples MS and HM2 and increases exponentially for temperatures >1300 °C. In sample HM1, apparent age remains below the two-aliquot bulk age at temperatures above which massive U-loss occurred, and He could not be fully extracted even at heating times of several hours. Some aliquots show clear U-loss of 20-50%, yet the apparent ages are still below two-aliquot age since less than 50% of the total helium was extracted.

In goethite, the initiation of U-loss is deferred to ~1100 °C (Fig. 4.10). Progressive U-loss occurs between 1100 °C and 1300 °C, as indicated by decrease in U concentration and concurrent increase in Th/U or Sm/U ratio.

4.4 Discussion

U-loss as a result of heating is a concern in single-aliquot (U-Th)/He geochronology and thermochrology of hematite and goethite, because it can lead to incorrect ages. The aim of this study was to find ideal extraction conditions, at which single-aliquot dating of hematite is possible. U-loss has been studied in goethite by Vasconcelos et al. (2013), who found a plateau of 'safe' degassing temperatures between the points of complete extraction of He and U-loss. They reported that U was volatilized from the sample at high temperatures. Reiners et al., 2014 reports decomposition of sample material and flowage out of the enclosing tube at temperatures >850 °C. Garcia et al., 2018 even report volatilization of Fe and Mn in iron- and manganese-oxides at high temperatures. We have also observed volatilization of Fe in the form of a 'spray' out of Pt packets which were open at the sides. This suggests that this oxidation of hematite to magnetite can be a quite violent reaction.

Several studies have lowered extraction temperatures for both goethite and hematite

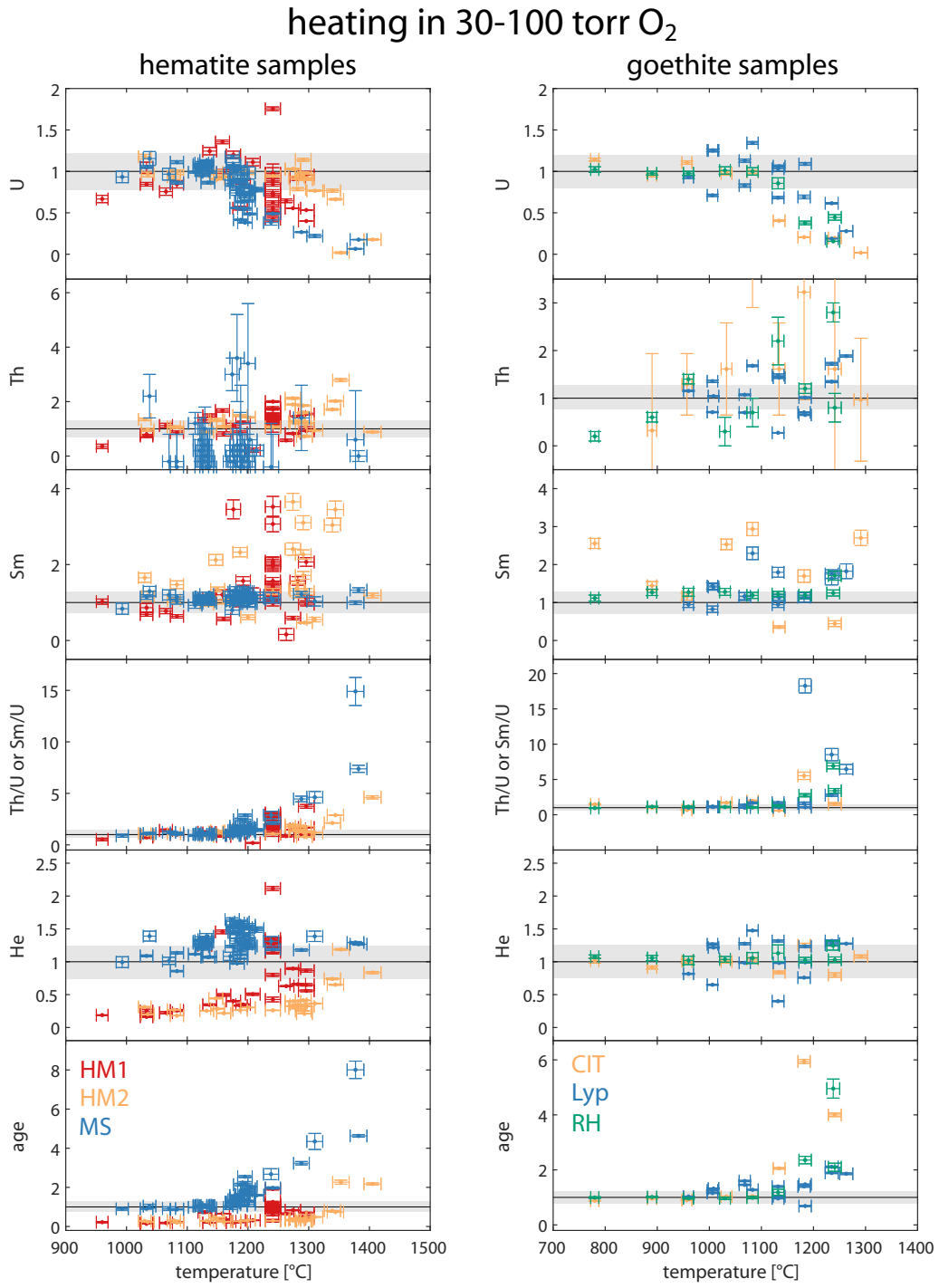

Figure 4.10: Hematite and goethite samples heated in 30-100 torr of O_2. All values were normalized by median value from undegassed aliquots (U, Th, Sm, Th/U or Sm/U) or two-aliquot bulk analyses (age, He concentration) and grey areas represent the typical range of values. U-loss temperature for is deferred to 1180 °C for hematite and to ~1100 °C for goethite, compared to ~980 °C for heating in vacuum.

to 500-850 °C because U volatilization was observed at temperatures above 1000 °C (Danišík et al., 2013; Garcia et al., 2018; Reiners et al., 2014; Wells et al., 2019). For very fine-grained hematite samples, these temperatures might be sufficient to completely extract helium. Re-extracts are one approach to test for complete helium extraction. In some samples, there might be highly retentive domains which require much higher temperatures to extract significant amounts of helium, which we observed in sample HM1. Complete helium extraction in such samples can only be assured by degassing a previously heated sample to temperatures close to fusion, which leads to loss of the sample. This is a way to test complete helium extraction if there is a large amount of homogeneous sample material, but might not be feasible if the sample material is severely limited or displays large inhomogeneity in parent isotopes.

Kerkhof et al. (2018) suggested the use of an 'evaporation correction' to correct U concentrations in samples that were heated to temperatures at which they experience U-loss. This is essentially a two-aliquot approach. However, we have shown that U concentrations in undegassed samples can be highly variable, especially at the scale of tens to hundreds of micrograms, which is typical size of single-aliquot samples. In addition, the amount of absolute U-loss is not reproducible between aliquots. This suggests that any 'evaporation correction' would carry an uncertainty of at least 20-50% and is therefore not a feasible way of obtaining precise and reproducible (U-Th)/He ages. Partial U-loss of homogeneous material produces age-eU correlations, in which low U concentrations are associated with high age, and vice versa.

Another possibility for completely extracting helium from a sample is to hold them for longer periods of time at lower temperatures. Due to the logarithmic nature of thermally activated Fickian diffusion of helium through the crystal, isothermal holding times increase manyfold from even a slight reduction in temperature (Fig.

4.12). Conversely, any small temperature increase without U-loss would lead to a considerable reduction in the required heating time. We found that heating samples at a temperature ~950 °C, which was previously assumed to be 'safe' for iron-oxide outgassing (Vasconcelos et al., 2013) resulted in massive U-loss at heating times over 20 min (Fig. 4.6). In order to completely extract helium from a highly retentive sample at temperatures below 950 °C, would require much longer heating times.

Phase transition and U-loss

In experiments in which we heated aliquots of hematite and goethite samples to different temperature in vacuum, we found that U-loss first occurs at 980-1000 °C (Fig. 4.5), as evidenced by a decrease in U concentrations and increased Th/U and Sm/U ratios. This is the same temperature range as was observed for goethite and hematite in previous studies (Danišík et al., 2013; Reiners et al., 2014; Vasconcelos et al., 2013). Hematite samples showed a more consistent U-loss temperature than goethite samples. This difference could be due to the nature of samples, or it might be a because of the larger natural variability of U, Th, and Sm concentrations in goethite, which make U-loss harder to detect.

The phase diagram of Ketteler et al. (2001) predicts the phase transition from hematite to magnetite at equilibrium conditions to occur at 850 °C and 710 °C at a $p(O_2)$ of 10^{-5} mbar and 10^{-8} mbar, respectively (Fig. 4.11). Pressure in the laser chamber before degassing is about 10^{-8} mbar. The highest pressures observed during degassing are around 10^{-5} mbar. This can be taken as an upper bound for the possible O_2 partial pressure. The fraction of O_2 in the total gas released from the sample is likely to be small. The O_2 partial pressure is probably several orders of magnitude lower than 10^{-5} mbar. Since oxygen is being released by the sample as hematite transforms to magnetite, the $p(O_2)$ in the laser chamber might increase and lead to a higher hematite-magnetite transition temperature. This negative feedback

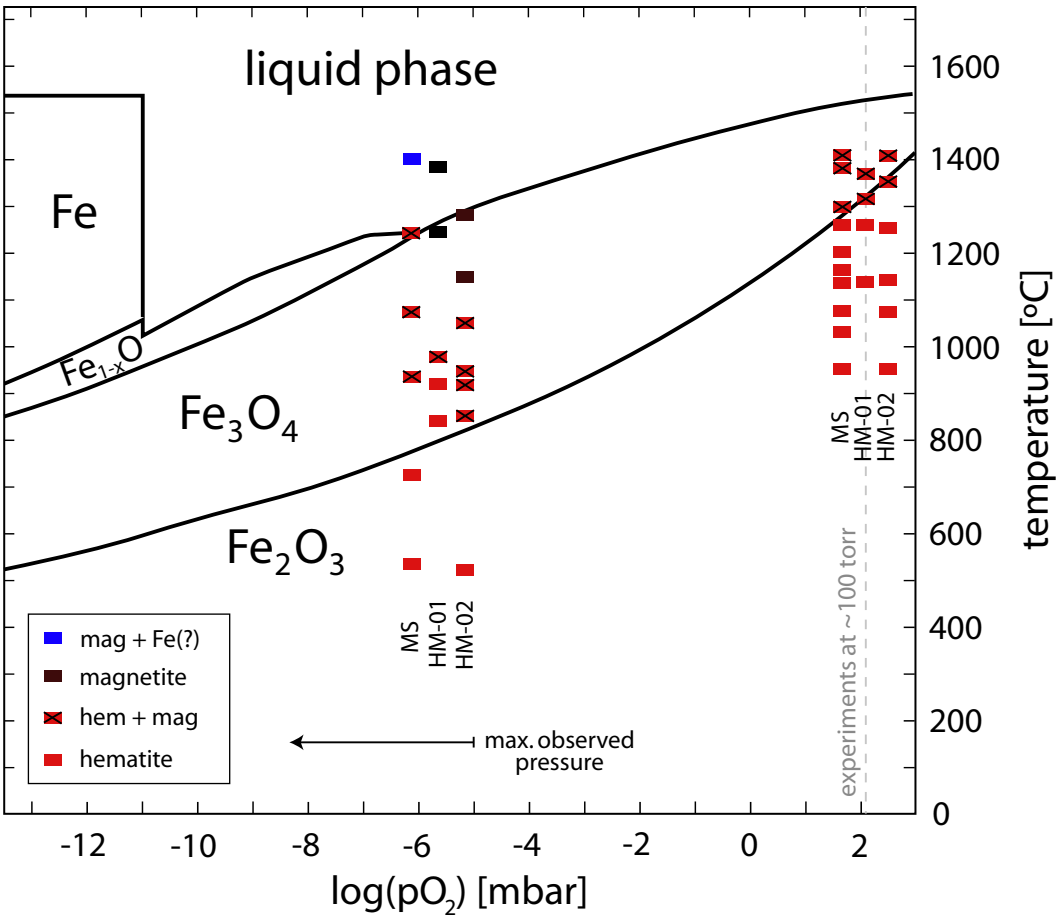

Figure 4.11: Theoretical phase diagram (redrawn after Ketteler et al., 2001) with phase determinations of three different hematite samples determined by ATR-FTIR. The exact oxygen partial pressure ($p(O_2)$) of samples heated in vacuum is unknown, but lower than the maximum observed pressure of 10^{-5} mbar. Experiments in O_2 were performed at ~100 torr (133 mbar). Our observations show that partial conversion of hematite to magnetite occurs at the predicted phase transition temperature, which confirms the phase diagram, but demonstrate that full conversion of hematite to magnetite is kinetically inhibited to higher temperatures than the equilibrium phase transition temperature.

process can cause an increase in the actual phase transition temperature compared to that at vacuum. At Caltech, samples are usually degassed while exposed to a charcoal trap cooled with liquid nitrogen. Most gases released during heating, including O_2, will be immediately adsorbed onto the charcoal, keeping the pressure low. A pressure increase while heating will most likely be due to species that can only be incompletely trapped, such as hydrogen. Since oxygen can be effectively

trapped on charcoal, a major increase in oxygen partial pressure is therefore unlikely to occur during degassing. However, there might be a minor increase in $p(O_2)$ due to dynamic effects of trapping released gas on charcoal. We observed a lag time of about 2 min between the release of oxygen and complete capture on the charcoal trap.

We investigated the phase change from hematite to magnetite in samples initially present as hematite and goethite using ATR-FTIR. The first detectable conversion of hematite to magnetite was observed at temperatures of 950-990 °C, which coincides with the inception of U-loss measured on aliquots of the same material used for ATR-FTIR analyses. There was more scatter of U concentrations of aliquots which had experienced U-loss in ATR-FTIR experiments than was observed in heating experiments. Each packet heated for ATR-FTIR samples contained tens of milligrams of sample material aggregated from tens to hundreds of individual grains, whereas the much smaller packets for single-aliquot analyses contained only a single fragment of sample with masses of 10-100 μg. U volatilized from the outside of any individual grain might condense onto the neighboring grain with a large amount of sample material present, and consequently the aliquot might appear to have experienced a smaller amount of U-loss. With only a single grain present in a small packet, U volatilized from the sample might be absorbed by the packet or escape through the ends of the tube and is not quantitatively recoverable.

Goethite samples were observed to convert more readily from hematite to magnetite. We also observed decomposition of magnetite to elemental iron in these samples, which is predicted by a published phase diagram (Fig. 4.11), but was not observed in any hematite samples heated to comparable temperatures. Since goethite samples used in this study are more fine-grained than hematite samples, this might be evidence of grain-size dependent kinetics of the phase transition. The dehydroxylation reaction that transforms goethite to hematite at 180-300 °C

(Prasad et al., 2006; Ruan et al., 2001) can also lead to major re-crystallization of the sample, with a possible further reduction of grain-size. This might influence the kinetics of the hematite-magnetite transition at higher temperatures, which could contribute to cause the phase transition and U-loss to happen at temperatures lower than those for hematite. The goethite-hematite transformation temperature is affected by the amount of Al-substitution for Fe (Cornell and Schwertmann, 2003). We are not aware of any published works on the effect of Al-substitution on the hematite-magnetite transition. None of the samples studied here had any significant amounts of Al-substitution, so we cannot exclude effects on the hematite-magnetite transition temperature and associated U-loss.

We interpret the correlation between phase transition temperature and U-loss as evidence that these processes are connected. The phase transition of hematite to magnetite causes a major re-organization of the crystal structure as Fe^{3+} is oxidized to Fe^{2+}. The coordination of Fe changes from octahedral coordination to a spinel structure and oxygen is released from the crystal. This seems to lead to a major fractionation of U, with Th and Sm being quantitatively retained, while almost none of the U is being incorporated into the magnetite. U incorporated in hematite likely substitutes for Fe in octahedral configuration (Ilton et al., 2012) and might be reduced if it cannot attain this configuration for steric reasons (Skomurski et al., 2011). Unlike Th and Sm, U is redox-sensitive and incorporation of U into iron-oxides also depends on the Fe^{2+} density (Skomurski et al., 2011). The fractionation of U relative to Th and Sm during the hematite-magnetite transition is therefore likely a result of change in oxidation state of Fe and the re-organization of the crystal structure. If U is not incorporated into magnetite crystal structure during re-crystallization, it might be brought to the surface the crystallite, where it could evaporate and be ejected from the packet.

We observed no major loss of U as a result of the goethite-hematite transition. This

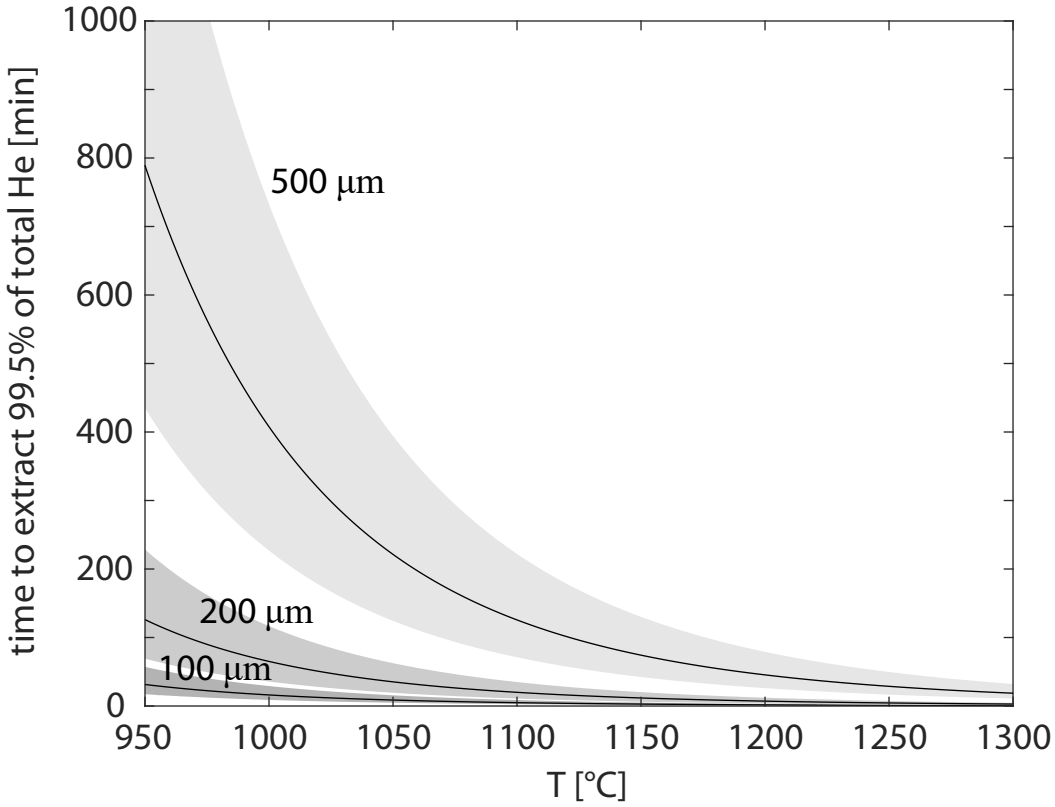

Figure 4.12: Modeled time to extract 99.5% of total amount of He for different domain sizes using the hematite diffusion coefficients of Farley (2018). Grey areas represent 2σ uncertainty. Safe limit of vacuum degassing of hematite is around 950 °C. Degassing in 100 torr of O_2 can be done safely without U-loss up to ~1150 °C in hematite.

transition involves only dehydroxylation of inter-layer -OH groups and the oxidation state of Fe does not change. Fractionation due on differences in redox-sensitivity is therefore not expected for this reaction. However, due to the natural variability of undegassed samples, we cannot exclude minor amounts of U-loss associated with this process. However, some goethite samples have previously given very reproducible ages when degassed at 900-950 °C (e.g. Vasconcelos et al., 2013), so we do not expect any U-loss due to goethite-hematite transition of samples during laser-heating. Since our results indicated that U-loss in iron-oxides might be caused by the phase transition from hematite to magnetite, we investigated ways to delay this phase transition to higher temperatures. The phase diagram of (Ketteler et al.,

2001) predicts that the phase transition temperature is higher for increased $p(O_2)$ — about 1120 °C at 1 mbar and 1320 °C at 100 mbar. In ATR-FTIR experiments, we observed that the phase transition of hematite samples was delayed to about 1250 °C at ~100 torr (130 mbar) of O_2 (Fig. 4.8).

We observed no U-loss in samples heated in O_2 for ATR-FTIR analyses. Laser-heating experiments of aliquots in comparable oxygen pressures similarly showed that U-loss was initiated at around 1180 °C in hematite samples and 1100 °C in goethite samples. This demonstrates that delaying the hematite-magnetite transition to higher temperatures has affected the temperature at which U-loss occurs. It provides further evidence that U-loss is caused by the phase transition from hematite to magnetite. This information can be used to raise the phase transition temperature, and therefore the U-loss temperature, as required by the sample. According to the phase diagram of Ketteler et al. (2001), oxygen partial pressures of 1 mbar, 10 mbar, and 100 mbar can raise the hematite-magnetite transition to about 1120 °C, 1210 °C, and 1310 °C. We have found minor amounts of magnetite up to 100 °C below these temperatures, suggesting that modeled T-$p(O_2)$ conditions are slightly different in natural samples.

Implementation of high $p(O_2)$ method

The normal setup for (U-Th)/He laser heating was amended for heating samples in a pure O_2 atmosphere. A manifold with an oxygen tank, a cold finger, and a manometer was connected between the laser chamber and the line (Fig. 4.13). We filled the tank with O_2 to a pressure of 22 psi (152 kPa). After pumping the laser chamber to $<10^{-8}$ torr, oxygen was released into the laser chamber with a pipette that delivers about 100 torr (130 mbar) per draw. Oxygen pressure was measured using a manometer. The oxygen was then fixed on a cold finger cooled with LN_2, and this was turbo-pumped for 1 h to remove any helium impurities in the oxygen.

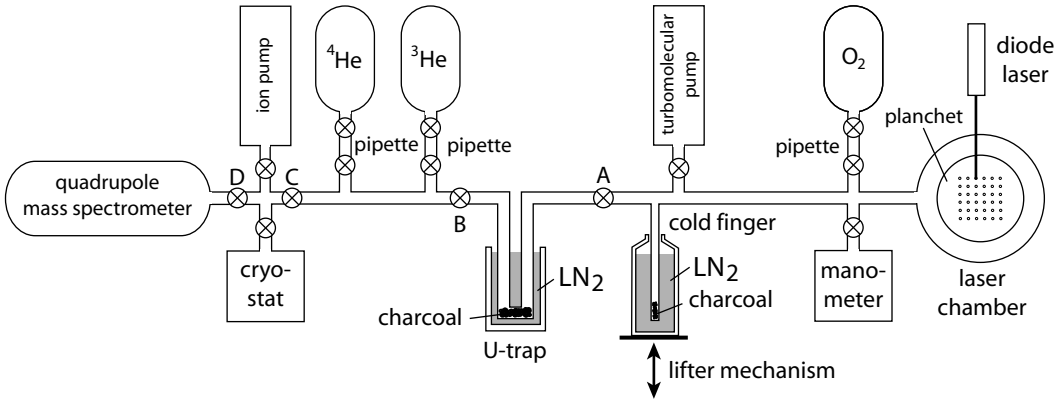

Figure 4.13: Schematic diagram of the vacuum line used for O_2 degassing. A calibrated amount of oxygen is released into the laser chamber from the O_2 tank using a pipette. The lifter mechanism can be used to release and capture O_2 on the cold finger before and after laser heating. Samples are degassed with 100 torr of O_2 present, which is completely trapped before mass spectrometric analysis.

Before a measurement, the laser chamber is ion-pumped for 20 min. The laser chamber was closed to the U-trap at valve A (Fig. 4.13) and oxygen was released into the laser chamber by removing the LN_2 dewar from the cold finger with an automated lifter mechanism. The aliquot was then heated using a diode laser controlled by a PID system with feedback from an optical pyrometer. The required laser output power for heating samples in O_2 was a factor of five to ten larger than for samples heated to the same temperatures in vacuum, due to the higher attenuation of the laser beam in O_2 as well as increased conductive and convective loss of heat from the packet.

We did not heat samples to setpoints within less than 50 °C below the actual phase transition temperatures to allow for minor temperature overshoots and inhomogeneity within the Pt packet as well as sample-dependent differences in transition temperature. We have observed minor U-loss for long holding times at around 1200 °C, therefore this should be taken as the maximum allowable temperature for degassing of hematites in 100 torr of oxygen partial pressure.

After degassing, the LN_2 dewar is moved back onto the cold finger and the oxygen

is again captured on the activated charcoal. A controlled amount of ^{3}He spike is released and degassed He is adsorbed onto activated charcoal on a cryogenic pump at 14 K. The gas passes through a U-trap filled with activated charcoal and cooled by LN_2, which helps to capture any remaining oxygen in the line and prevents it from reaching the cryogenic pump or the mass spectrometer. He is released into the mass spectrometer at 36 K.

We initially performed some experiments using Nb packets, which have been used for many past studies (e.g. Calzolari et al., 2018; Evenson et al., 2014; Garcia et al., 2018; McDermott et al., 2017). We found that Nb turned dark within seconds of heating in an oxygen-rich atmosphere, associated also with a drop in oxygen pressure in the laser chamber. This suggests that Nb packets oxidize at temperatures required to fully extract He from iron-oxides in an oxygen-rich environment. Therefore, we recommend using Pt packets instead of Nb packets for heating in O_2.

Technical implementation of the O_2 degassing procedure as an automated system is described in Appendix 4.A, along with a discussion of technical challenges, proposed solution, and long-term performance of the degassing setup. We show that the presence of O_2 during degassing does not interfere with cryogenic capture, ionization efficiency, or mass spectrometric measurement of He.

Replicate analyses

Due to the natural variability of U, Th, and Sm concentrations of tens to hundreds of micrograms observed in some samples (see Fig. 4.2), some aliquots have U and Th concentrations that are several times that of the bulk of the sample. This can lead to α-ejection from high-eU areas and α-implantation into low-eU areas (Farley et al., 1996). In initial tests, we observed that ages of replicate analyses of individual had average ages that are close to the two-aliquot age, but showed more scatter and a slight age-eU correlation with higher ages for lower eU and vice versa, even when

degassed at temperatures significantly below those for which loss of U was observed. We interpret this as an indication that the age scatter was due to natural variability of parent isotopes and associated α-redistribution rather than a result of U-loss.

To demonstrate the capabilities of the oxygen degassing technique, we reduced the inter-aliquot variability of parent and daughter isotope concentrations by producing 12 replicate aliquots of sample MS, which were aggregated from about 10 individual grains each. These aliquots were loaded into the same small Pt tubes used for individual grains and heated to 1150 °C for 20 min. The results are given in Fig. 4.14. The average U concentration is slightly higher than the median value of undegassed aliquots. Sm concentrations are correspondingly higher as well, leading to Sm/U ratios that exactly match that of undegassed aliquots. We observed larger scatter and higher average U concentrations at smaller aliquot masses in undegassed aliquots. Since the samples were aggregated from grains of 10-20 μg each, the U concentrations in these samples might not exactly match the median value of all undegassed aliquots. The average of n=12 ages is 579±11 Ma, which matches, within uncertainty, the age of 571±18 measured by Farley and McKeon (2015) using the two-aliquot method (Fig. 4.14). This set of 12 replicate analyses shows no age-eU correlation and has Sm/U ratios that match those of undegassed aliquots. We therefore conclude that no U-loss occurred in this hematite sample during laser-heating in 100 torr of O_2 at 1150 °C, which is more than 170 °C above the U-loss temperature in vacuum.

We also obtained ages of 1732±35 Ma and 1725±39 Ma for the highly retentive sample HM2 by holding them at 1150 °C for 4 h. This is within uncertainty of the two-aliquot age of 1761±39 Ma. These results demonstrate that the oxygen degassing method can be used to obtain precise and accurate single-aliquot (U-Th)/He ages of hematite. Sample HM1 could not be fully extracted even through holding at 1150 °C for 4 h, but also did not show any U-loss. Full helium extraction might be

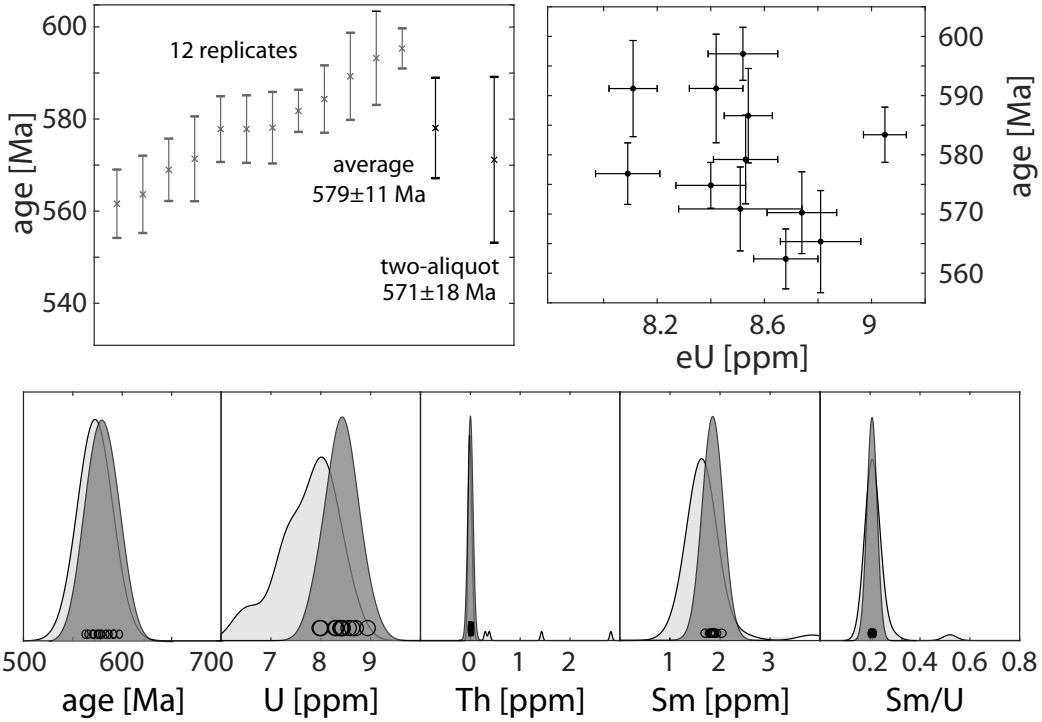

Figure 4.14: (U-Th)/He ages of replicate analyses of aggregated aliquots of hematite sample MS degassed in 100 torr of O_2 at 1150 °C for 20 min, compared to the two-aliquot age of Farley and McKeon (2015). Heated aliquots show no correlation between age and effective U concentration (eU). KDE distributions of degassed samples (dark shading) overlap with those of undegassed samples (light shading). There is no indication of U-loss.

possible at even longer holding times. The increase in degassing temperature compared to vacuum degassing and the ability to hold samples at these temperatures for several hours without U-loss allows for the analysis of much more highly retentive hematite samples than previously possible.

Evaluating Th/U as indicator of U-loss

The Th/U ratio is frequently used as a criterion to assess possible U-loss in iron-oxides (e.g. Ault et al., 2015; Calzolari et al., 2018; Danišík et al., 2013; Evenson et al., 2014; Garcia et al., 2018; Vasconcelos et al., 2013). However, as we show in this study, the natural variability in U and Th concentrations might obscure small amounts (<20%) of U-loss. An increase in the Th/U ratio can indicate major U-loss,

provided that the normal range and distribution of U and Th concentrations have been characterized on a statistically significant number of aliquots, both degassed and undegassed.

Some samples have very low Th concentrations (<0.1 ppm). Even for aliquots of hundreds of micrograms, the absolute amount of Th in these samples is close to blank level in ICP-MS analyses. The samples analyzed in this study that had insufficient Th concentrations showed Sm concentrations that were significantly higher. None of the samples studied here showed any systematic loss of Sm with temperature. We therefore utilized the Sm/U ratio, which showed the same pattern of rapid increase with U-loss as the Th/U ratio. Since Sm contributes to He production, albeit only to a minor extent, it is routinely measured in (U-Th)/He dating of iron-oxides. In the samples analyzed in this study, Sm concentrations and Sm/U ratios in undegassed aliquots were found to show a natural variability comparable to that of Th. The Sm/U ratio is therefore an indicator that can be used in conjunction with or in place of the Th/U ratio to detect major loss of U, if the natural variability of undegassed aliquots has been sufficiently characterized. However, the use of the Sm/U ratio is subject to the same restrictions as that of the Th/U ratio, due to the large variability in natural samples.

He release in O_2

The delayed hematite-magnetite transition for heating in O_2 relative to vacuum might affect He extraction. The diffusion parameters of helium in magnetite are likely different than those of hematite. Preventing the phase from changing to magnetite means that He diffusion will occur according to hematite parameters at higher temperatures. Additionally, the phase transition from hematite to magnetite leads to re-crystallization of the sample material, along with a change in specific density and volume as well as loss of oxygen. This might open fractures and lead

to a reduction of effective diffusion domain size. A resulting change in diffusivity might alter the time and temperature required to completely release helium from the sample, which could be responsible for an increase in helium release around the phase transition.

4.5 Conclusions

We have shown that U-loss in iron-oxides correlates with the phase transition from hematite to magnetite. In vacuum, measurable U-loss initiates at around 980 °C in both hematite and goethite samples, although U-loss occurs at lower temperatures when samples are heated for longer periods of time. The hematite-magnetite transition temperature can be raised to ~1250 °C with 100 torr (130 mbar) of oxygen partial pressure in the laser chamber during heating. U-loss is consequently delayed to about 1200 °C, enabling the safe degassing of samples up to ~1150 °C.

Samples can be held at those temperatures for several hours without any detectable U-loss, which can be used to extract helium from highly retentive hematite samples. The phase diagram of Ketteler et al., 2001 (Fig. 4.11) can be used to predict the onset of the phase transition from hematite to magnetite, although we observed it up to 100 °C below the modeled temperatures. The O_2 partial pressure can then be adjusted based on the required He extraction temperature. About 1 torr of O_2 is enough to raise the U-loss temperature to about 1100 °C. Time and temperature for degassing can be estimated based on the maximum domain size in the sample using the diffusion parameters of Farley (2018).

Our experiments demonstrate that temperatures during iron-oxide degassing should be tightly controlled. We have shown that temperature can be measured to within 2% accuracy using a one-wavelength pyrometer, taking into account changes in emissivity of the Pt packet. Exceeding the temperature above which hematite readily converts to magnetite can lead to partial or total U-loss. This temperature threshold

might be several tens of degrees higher than predicted based on the phase diagram, due to the influence of kinetics. This is especially important for samples with large domain sizes that require high temperatures to completely extract helium.

Due to natural variability in U and Th concentration, U-loss of 20-50% in individual samples might not be detectable as an increased Th/U ratio. We have also demonstrated the use of Sm/U ratio as an indicator for U-loss. It might be used instead of Th/U in samples which have only minor Th concentrations, or it could be used together with the Th/U ratio to diagnose U-loss. Th/U or Sm/U ratios can only be used as an indicator U-loss if the natural variability of a samples has been sufficiently characterized.

Overheated samples, which had partially transformed to magnetite were identified by testing whether sample, still in the Pt packet, responded to weak hand magnet. This magnetic analysis can be used to screen goethite and hematite samples which have possibly experienced loss of U as a result of to partial transformation of hematite to magnetite.

We have demonstrated that we can obtain reproducible single-aliquot (U-Th)/He ages of hematite samples through laser-heating to 1150°C in a pure oxygen atmosphere. The average of a set of single-aliquot ages is within uncertainty of the previously established two-aliquot age of the sample. The single-aliquot approach has several advantages over the two-aliquot method. It requires much less sample material (tens of micrograms instead of several milligrams), enabling age determination when sample material is limited. Smaller sample size also allows for the resolution of age inhomogeneity at a finer scale, which would be obscured by the homogenization necessary for the two-aliquot method.

References

Adams, B., K. Hodges, M. Van Soest, and K. Whipple (2013) "Evidence for Pliocene–Quaternary normal faulting in the hinterland of the Bhutan Himalaya" in: *Lithosphere* 5.4, pp. 438–449.

Ault, A. K., M. Frenzel, P. W. Reiners, N. H. Woodcock, and S. N. Thomson (2016) "Record of paleofluid circulation in faults revealed by hematite (U–Th)/He and apatite fission-track dating: An example from Gower Peninsula fault fissures, Wales" in: *Lithosphere* 8.4, pp. 379–385.

Ault, A. K., P. W. Reiners, J. P. Evans, and S. N. Thomson (2015) "Linking hematite (U–Th)/He dating with the microtextural record of seismicity in the Wasatch fault damage zone, Utah, USA" in: *Geology* 43.9, pp. 771–774.

Bähr, R., H. J. Lippolt, and R. S. Wernicke (1994) "Temperature-induced ^{4}He degassing of specularite and botryoidal hematite: A 4He retentivity study" in: *Journal of Geophysical Research: Solid Earth* 99.B9, pp. 17695–17707.

Calzolari, G., F. Rossetti, A. K. Ault, F. Lucci, V. Olivetti, and R. Nozaem (2018) "Hematite (U–Th)/He thermochronometry constrains intraplate strike-slip faulting on the Kuh-e-Faghan Fault, central Iran" in: *Tectonophysics* 728, pp. 41–54.

Cooper, F., B. Adams, J. Blundy, K. Farley, R. McKeon, and A. Ruggiero (2016) "Aridity-induced Miocene canyon incision in the Central Andes" in: *Geology* 44.8, pp. 675–678.

Cornell, R. M. and U. Schwertmann (2003) *The iron oxides: structure, properties, reactions, occurrences and uses* John Wiley & Sons.

Danišík, M., N. J. Evans, E. R. Ramanaidou, B. J. McDonald, C. Mayers, and B. I. McInnes (2013) "(U–Th)/He chronology of the Robe River channel iron deposits, Hamersley Province, Western Australia" in: *Chemical Geology* 354, pp. 150–162.

Evenson, N. S., P. W. Reiners, J. E. Spencer, and D. L. Shuster (2014) "Hematite and Mn oxide (U–Th)/He dates from the Buckskin-Rawhide detachment system, western Arizona: Gaining insights into hematite (U–Th)/He systematics" in: *American Journal of Science* 314.10, pp. 1373–1435.

Farley, K. (2018) "Helium diffusion parameters of hematite from a single-diffusion-domain crystal" in: *Geochimica et Cosmochimica Acta* 231, pp. 117–129.

Farley, K. and R. Flowers (2012) "(U–Th)/Ne and multidomain (U–Th)/He systematics of a hydrothermal hematite from eastern Grand Canyon" in: *Earth and Planetary Science Letters* 359, pp. 131–140.

Farley, K. and R. McKeon (2015) "Radiometric dating and temperature history of banded iron formation–associated hematite, Gogebic iron range, Michigan, USA" in: *Geology* 43.12, pp. 1083–1086.

Farley, K., R. Wolf, and L. Silver (1996) "The effects of long alpha-stopping distances on (U–Th)/He ages" in: *Geochimica et cosmochimica acta* 60.21, pp. 4223–4229.

Garcia, V. H., P. W. Reiners, D. L. Shuster, B. Idleman, and P. K. Zeitler (2018) "Thermochronology of sandstone-hosted secondary Fe-and Mn-oxides near Moab, Utah: Record of paleo-fluid flow along a fault" in: *GSA Bulletin* 130.1-2, pp. 93–113.

Heim, J. A., P. M. Vasconcelos, D. L. Shuster, K. A. Farley, and G. Broadbent (2006) "Dating paleochannel iron ore by (U–Th)/He analysis of supergene goethite, Hamersley province, Australia" in: *Geology* 34.3, pp. 173–176.

Hofmann, F., B. Reichenbacher, and K. A. Farley (2017) "Evidence for >5 Ma paleoexposure of an Eocene–Miocene paleosol of the Bohnerz Formation, Switzerland" in: *Earth and Planetary Science Letters* 465, pp. 168–175.

Ilton, E. S., J. S. L. Pacheco, J. R. Bargar, Z. Shi, J. Liu, L. Kovarik, M. H. Engelhard, and A. R. Felmy (2012) "Reduction of U(VI) incorporated in the structure of hematite" in: *Environmental science & technology* 46.17, pp. 9428–9436.

Jensen, J. L., C. S. Siddoway, P. W. Reiners, A. K. Ault, S. N. Thomson, and M. Steele-MacInnis (2018) "Single-crystal hematite (U–Th)/He dates and fluid inclusions document widespread Cryogenian sand injection in crystalline basement" in: *Earth and Planetary Science Letters* 500, pp. 145–155.

Kerkhof, A. M. van den, G. M. Sosa, T. Oberthür, F. Melcher, T. Fusswinkel, A. Kronz, K. Simon, and I. Dunkl (2018) "The hydrothermal Waterberg platinum deposit, Mookgophong (Naboomspruit), South Africa. Part II: Quartz chemistry, fluid inclusions and geochronology" in: *Mineralogical Magazine* 82.3, pp. 751–778.

Ketteler, G., W. Weiss, W. Ranke, and R. Schlögl (2001) "Bulk and surface phases of iron oxides in an oxygen and water atmosphere at low pressure" in: *Physical Chemistry Chemical Physics* 3.6, pp. 1114–1122.

Lippolt, H. J., R. S. Wernicke, R. Ba, et al. (1995) "Paragenetic specularite and adularia (Elba, Italy): concordant (U+Th)-He and K-Ar ages" in: *Earth and Planetary Science Letters* 132.1-4, pp. 43–51.

McDermott, R. G., A. K. Ault, J. P. Evans, and P. W. Reiners (2017) "Thermochronometric and textural evidence for seismicity via asperity flash heating on exhumed hematite fault mirrors, Wasatch fault zone, UT, USA" in: *Earth and Planetary Science Letters* 471, pp. 85–93.

Miller, H. B. D. (2019) "Stable and Radiogenic Isotope Studies of Iron-oxides as Paleoenvironmental and Tectonic Archives" PhD thesis California Institute of Technology.

Moser, A. C., J. P. Evans, A. K. Ault, S. U. Janecke, and K. K. Bradbury (2017) "(U–Th)/He thermochronometry reveals Pleistocene punctuated deformation and synkinematic hematite mineralization in the Mecca Hills, southernmost San Andreas Fault zone" in: *Earth and Planetary Science Letters* 476, pp. 87–99.

Pidgeon, R., T. Brander, and H. Lippolt (2004) "Late Miocene (U+Th)–^{4}He ages of ferruginous nodules from lateritic duricrust, Darling Range, Western Australia" in: *Australian Journal of Earth Sciences* 51.6, pp. 901–909.

Prasad, P., K. S. Prasad, V. K. Chaitanya, E. Babu, B. Sreedhar, and S. R. Murthy (2006) "In situ FTIR study on the dehydration of natural goethite" in: *Journal of Asian Earth Sciences* 27.4, pp. 503–511.

Reiners, P. W., I. Campbell, S. Nicolescu, C. M. Allen, J. Hourigan, J. Garver, J. Mattinson, and D. Cowan (2005) "(U–Th)/(He–Pb) double dating of detrital zircons" in: *American Journal of Science* 305.4, pp. 259–311.

Reiners, P. W., M. A. Chan, and N. S. Evenson (2014) "(U–Th)/He geochronology and chemical compositions of diagenetic cement, concretions, and fracture-filling oxide minerals in Mesozoic sandstones of the Colorado Plateau" in: *GSA Bulletin* 126.9-10, pp. 1363–1383.

Reiners, P. W. and K. A. Farley (1999) "Helium diffusion and (U–Th)/He thermochronometry of titanite" in: *Geochimica et Cosmochimica Acta* 63.22, pp. 3845–3859.

Reiners, P. W., K. A. Farley, and H. J. Hickes (2002) "He diffusion and (U–Th)/He thermochronometry of zircon: initial results from Fish Canyon Tuff and Gold Butte" in: *Tectonophysics* 349.1-4, pp. 297–308.

Ruan, H., R. Frost, and J. Kloprogge (2001) "The behavior of hydroxyl units of synthetic goethite and its dehydroxylated product hematite" in: *Spectrochimica Acta Part A: Molecular and Biomolecular Spectroscopy* 57.13, pp. 2575–2586.

Shuster, D. L., P. M. Vasconcelos, J. A. Heim, and K. A. Farley (2005) "Weathering geochronology by (U–Th)/He dating of goethite" in: *Geochimica et Cosmochimica Acta* 69.3, pp. 659–673.

Skomurski, F. N., E. S. Ilton, M. H. Engelhard, B. W. Arey, and K. M. Rosso (2011) "Heterogeneous reduction of U^{6+} by structural Fe^{2+} from theory and experiment" in: *Geochimica et Cosmochimica Acta* 75.22, pp. 7277–7290.

Strutt, R. J. (1909) "The accumulation of helium in geological time.-II" in: *Proceedings of the Royal Society of London. Series A, Containing Papers of a Mathematical and Physical Character* 83.560, pp. 96–99.

Vasconcelos, P. M., J. A. Heim, K. A. Farley, H. Monteiro, and K. Waltenberg (2013) "^{40}Ar/^{39}Ar and (U–Th)/He–^{4}He/^{3}He geochronology of landscape evolution and channel iron deposit genesis at Lynn Peak, Western Australia" in: *Geochimica et Cosmochimica Acta* 117, pp. 283–312.

Wells, M., M. Danišík, B. McInnes, and P. Morris (2019) "(U-Th)/He-dating of ferruginous duricrust: Insight into laterite formation at Boddington, WA" in: *Chemical Geology, accepted manuscript in print*.

Wernicke, R. S. and H. J. Lippolt (1993) "Botryoidal hematite from the Schwarzwald (Germany): heterogeneous uranium distributions and their bearing on the helium dating method" in: *Earth and Planetary Science Letters* 114.2-3, pp. 287–300.

– (1994a) "^{4}He age discordance and release behavior of a double shell botryoidal hematite from the Schwarzwald, Germany" in: *Geochimica et Cosmochimica Acta* 58.1, pp. 421–429.

– (1994b) "Dating of vein specularite using internal (U+Th)/^{4}He isochrons" in: *Geophysical Research Letters* 21.5, pp. 345–347.

– (1997) "(U+Th)–He evidence of Jurassic continuous hydrothermal activity in the Schwarzwald basement, Germany" in: *Chemical Geology* 138.3-4, pp. 273–285.

Wolf, R., K. Farley, and L. Silver (1996) "Helium diffusion and low-temperature thermochronometry of apatite" in: *Geochimica et Cosmochimica Acta* 60.21, pp. 4231–4240.

Wu, L.-Y., F. M. Stuart, L. Di Nicola, M. Heizler, M. Benvenuti, and R.-Z. Hu (2019) "Multi-aliquot method for determining (U+Th)/He ages of hydrothermal hematite: Returning to Elba" in: *Chemical Geology* 504, pp. 151–157.

APPENDIX

4.A Technical Implementation of He degassing procedure in O_2 at Caltech

Technical challenges and implementation

The introduction of oxygen into the degassing procedure provided several technical challenges. The following is a brief account of our experiences with and considerations about potential issues and our proposed solutions.

O_2 delivery

A pressure of ~100 torr of O_2 is needed to raise the hematite-magnetite phase transition temperature for from ~700 in vacuum to ~1300 °C (Ketteler et al., 2001). In our early experiments, we used CuO pellets in a Pt packet to release and partially re-capture O_2. This produced O_2 without significantly increasing the He blank. However, the pressures produced by even several tens of milligrams of CuO were <0.2 torr. Re-capturing of O_2 by slow retrograde heating of CuO over 30 min was inefficient and lead to a decrease in pressure in subsequent re-heating of the CuO packet. This required the use of a new CuO packet per analysis.

In order to ensure a consistent delivery, achieve higher O_2 pressures, and simplify the extraction process, we switched to using an O_2 tank with a pipette. The tank was filled directly from a commercially available oxygen bottle by pressure equilibration at 22 psi (152 kPa). Draws from this tank produced a pressure of 120 torr in the laser chamber, with subsequent draws showing a predictable rate of decline.

Purification of O_2

Every draw of O_2 from the tank contains a certain amount of helium, which might come directly from impurities of the O_2 tank or could be derived from air leaking into the line during filling of the tank. Most of this He blank was removed before

analysis. The oxygen was adsorbed onto a cold finger filled with charcoal cooled by LN_2. The cold finger was then turbo-pumped for at least 1 h. This removed most of the He blank, leaving only about 0.01 ncc of He. The rest of the He blank is removed by running a blank measurement of the laser chamber, during which the remaining He is adsorbed onto the cryostat.

Cycling of O_2

In early experiments, we delivered one draw of O_2 per degassing and pumped it away after each analysis. With this procedure, we had to purify every draw of O_2 or calibrate the amount of He in each draw. Since the amount of O_2 withdrawal from a tank with a fixed pipette was predictable, this was possible, but complicated the analysis. It required the determination of the amount of He in draws from the O_2 tank before and after a batch of samples, which were then interpolated to yield a He blank value for each sample.

We moved from this system one in which one draw of O_2 is released and then adsorbed onto a charcoal trap. We then turbo-pumped for 1 h to remove He and other impurities in O_2. The O_2 was then released from the activated charcoal in a cold finger by moving a dewar with LN_2 down and exposing the cold finger. All of the O_2 was released after 10 min. The sample was then heated with a diode laser for a set amount of time. After the heating step, the dewar was lifted up and the cold finger was completely submerged in the LN_2. Depletion of LN_2 due to repeated release-capture cycles was observed to be low. More than 50 cycles over four days were run on a single dewar, initially filled to the top with LN_2.

Interference on optical pyrometry

Oxygen in the laser chamber instead of vacuum leads to attenuation of the emission of the packet reaching the pyrometer of about 2 %. This leads to a slightly different

calibration curve for the single-wavelength pyrometer. Otherwise, optical pyrometry is unaffected and retains the same accuracy and precision as is vacuum. This is discussed in detail in Appendix 4.B.

Required laser power

Heating a packet in O_2 requires a higher laser power than in vacuum, because of increased heat diffusion from the packet and reduced transmission of the laser beam in the presence of a gas phase. PID parameters of the laser heating system had to be adjusted to account for the increased laser power requirements. A blue glow can be observed around around the laser beam, demonstrating loss of laser efficiency due to ionization of O_2. This reduced the maximum temperature that can be reached using the laser heating system. Some samples could not be heated to high set-points in excess of 1250 °C. Part of the reason for not reaching the set-point is the diffusion of heat into the copper planchet and the gas in the chamber, which is noticeable for samples heated to 1300 °C and above in both vacuum and O_2. An increase in temperature from room temperature (~19 °C) to 50 °C and 25 °C of the planchet and the O_2 in the laser chamber, respectively, was observed. Some samples reached the set-point initially, but the laser power required to keep the sample at the set-point increased steadily. Once 100% laser output power was reached, temperature declined an converged on an equilibrium temperature below the set-point.

The exact laser power required to keep the sample at the set-point depends on O_2 pressure, the position of the laser relative to the packet, and the shape and position of the packet in the well. We noticed that the required laser power can be reduced by 20-30% if the packet is elevated above the surface of the planchet by a piece of coiled-up Pt wire. This can be used to reach higher temperatures at the same laser power.

Heating of neighboring packets

Due to increased heat diffusion and heating of the gas, samples other than the one being lased might be heated enough to release part of their He content. Samples are arrayed in a 6x6 grid of wells about 1 mm deep on a copper planchet. A 5 mm thick steel radiation shield containing an array of holes identical to the wells of the planchet is centered of the planchet. To test for possible degassing of neighboring packets, we laser-heated an empty Pt packet surrounded by nine other Pt packets with a hematite sample with high He concentration. The neighboring packets had a total estimated He content of >50 ncc. The empty packet was heated to 1400 °C in 100 torr of O_2 for 20 min, which represents a typical degassing time and pressure for O_2 analyses, but temperatures in excess of the typical set-point. The blank-corrected amount of helium measured was <0.0005 ncc, showing that neighboring packet are not heated enough to release any significant amount of helium under normal O_2 heating conditions.

Packet material

We used Pt and Nb tubes to produce packets by crimping the ends with forceps. These packets are used to wrap hematite samples for O_2 degassing experiments. For Pt packets, there was no difference between heating in vacuum and in 100 torr of O_2, except for a slight pyrometer interference (see Appendix 4.B). There was no change in appearance of Pt packets laser-heated in vacuum or in O_2. Heating of Nb packets in O_2 lead to an immediate drop in O_2 pressure due to oxidation of the packet material, changing the appearance of the packet from metallic to black. We therefore do not recommend the use of Nb tubes for O_2 degassing.

Pt packet blank

Pre-heated Pt tubes have in the past yielded better U and Th blanks than unheated tubes. We were concerned that heating Pt packets to temperatures higher than those used for routine (U-Th)/He dating could lead to an increased trace element blank. All Pt tubes used in this study were cleaned by treating them with concentrated HCl at 100 °C for 5 hours. They were rinsed with MilliQ water several times and dried in an oven at 100 °C. To test for procedural blanks of measured elements, we laser-heated two sets of clean Pt tubes to 940 °C in vacuum and to 1150 °in 100 torr of O_2 for 10 min. The detected blank amounts of both sets of tubes are indistinguishable at 4±2 pg U, 18±4 pc Th, and 3±2 pg Sm (Tab. 4.2), with procedural spike blanks for all of these elements being <1 pg. This shows that heating in O_2 does not increase the trace-element blank of Pt tubes. Amounts of U, Th, and Sm measured in samples were blank-corrected using these values.

Table 4.2: Elemental analysis of laser-heated Pt tubes, representing the blank concentrations at 940 °C in vacuum (top) and 1150 °C in 100 torr of O_2. hem = Fe-based hematite-equivalent mass.

heated to 940 °C in vacuum for 10 min														
Pt tube	hem	1σ	Al	1σ	Si	1σ	Mn	1σ	U	1σ	Th	1σ	Sm	1σ
	[µg]	[µg]	[µg]	[µg]	[µg]	[µg]	[µg]	[µg]	[pg]	[pg]	[pg]	[pg]	[pg]	[pg]
v1	0.01	0.01	0.00	0.00	0.00	0.00	0.00	0.00	8.7	0.2	23.0	1.6	4.3	0.5
v2	-0.01	0.01	0.00	0.00	0.00	0.00	0.00	0.00	3.7	0.3	18.8	1.5	2.5	0.9
v3	0.00	0.01	0.00	0.00	0.00	0.00	0.00	0.00	2.2	0.2	18.2	1.3	2.5	0.5
v4	-0.01	0.01	0.00	0.00	0.00	0.00	0.00	0.00	6.6	0.2	19.8	1.6	3.0	0.6
v5	0.01	0.01	0.00	0.00	0.00	0.00	0.00	0.00	4.3	0.3	25.3	1.6	8.9	1.2
v6	-0.01	0.01	0.02	0.00	0.00	0.00	0.00	0.00	1.4	0.3	15.4	1.7	2.0	1.0
average	0.00	0.01	0.00	0.01	0.00	0.00	0.00	0.00	4.5	2.7	20.1	3.5	3.9	2.6
heated to 1150 °C in 100 torr of O_2 for 10 min														
Pt tube	hem	std	Al	std	Si	std	Mn	std	U	std	Th	std	Sm	std
	[ug]	[ug]	[ug]	[ug]	[ug]	[ug]	[ug]	[ug]	[pg]	[pg]	[pg]	[pg]	[pg]	[pg]
o1	-0.01	0.01	0.00	0.00	0.00	0.00	0.00	0.00	3.7	0.3	13.3	1.2	2.0	0.7
o2	-0.01	0.01	0.01	0.00	0.00	0.00	0.00	0.00	4.7	0.2	13.3	1.6	1.8	0.9
o3	0.00	0.01	0.01	0.00	0.00	0.00	0.00	0.00	4.2	0.3	13.4	1.4	2.7	0.8
o4	-0.01	0.01	0.00	0.00	0.00	0.00	0.00	0.00	1.3	0.2	19.1	1.4	3.0	0.7
o5	0.00	0.01	0.02	0.00	0.00	0.00	0.00	0.00	7.4	0.3	19.1	1.4	3.3	0.8
o6	-0.01	0.01	0.08	0.00	0.00	0.00	0.00	0.00	2.2	0.3	22.0	1.5	3.2	1.0
average	-0.01	0.01	0.02	0.03	0.00	0.00	0.00	0.00	3.9	2.1	16.7	3.8	2.7	0.6

O_2 breakthrough

The activated charcoal in the cold finger cooled by LN_2 traps most of the O_2 before the transfer of the helium into the mass spectrometer. However, a small fraction remains in the laser chamber due to vapor pressure. We attached a cold finger close to the laser chamber, with an additional flow-through U-trap between the O_2 side and the rest of the vacuum line (see Fig. 4.13). The U-trap is filled with activated charcoal and permanently cooled by LN_2. During a normal analysis, the gas in the laser chamber is exposed to this U-trap for several minutes to adsorb most of the remaining O_2. This is also a fail-safe mechanism designed to protect the sensitive instruments in the rest of the line. Should the O_2 not be captured on the cold finger, because of failure of the lifter mechanism or insufficient amount of LN_2 in the dewar, most of the O_2 would be adsorbed onto the charcoal of the U-trap. This prevents the exposure of the cryostat and the mass spectrometer to oxygen. Even with these precautions, a minor amount of O_2 was observed to adsorb on the cryostat. This O_2 was released from the cryostat >80 K. It was completely removed after He was released into the mass spectrometer by heating the cryostat to 100 K and ion-pumping the resulting gas.

We observed an incremental transfer of O_2 from the cold finger to the U-trap. Over many sample analyses, during which the two traps are open to each other, as much as 30% of the O_2 was transferred. Increasing the amount activated charcoal in the cold finger of led to a reduction in the amount of O_2 transferred to the U-trap. Removing the dewar from the U-trap and heating the charcoal while the cold finger was submerged in LN_2 led to a transfer of the O_2 back to the cold finger. We repeated this about every 24 individual analyses (12 samples with re-extracts). This could be automated by adding a lifter mechanism to the dewar on the U-trap.

Test for interference of O_2 on He measurement

We identified three potential concerns about how the introduction of O_2 into the degassing process might affect the He measurement: (a) incomplete capture of He outgassed from the sample on the cryostat due to breakthrough of a small fraction of O_2 to the cryostat, (b) decline in ionization efficiency of He due partial release of O_2 into the mass spectrometer, and (c) oxidation of the filament leading to degradation of sensitivity. In order to test for the possible interference of the two former conditions, we connected an standard tank to the laser chamber (external standard). We released a known amount of He into the laser chamber in vacuum as well as with O_2, which was released and captured before cryo-pumping and measurement of the He (Fig. 4.15). Additionally, we bracket these analyses with analyses of draws from an internal standard tank, which is used to determine the ^{4}He sensitivity of the instrument. All ^{4}He amounts of sample analyses are determined relative to this internal standard, by isotope dilution with ^{3}He. The sensitivity of the ^{3}He measurement declined for unknown reasons in the initial vacuum sequence (Fig. 4.15). It then returned to the previous values during subsequent standard and blank measurements. There was no change in ^{3}He sensitivity due to the introduction of O_2, with values remaining steady through the change back to vacuum analyses. Internal standard ^{4}He/^{3}He ratios were all within 1% over the course of this test run. The ~1% drift in the standard ratio is typical for a 24 h period over which these analyses were performed. Analyses of draws from the external tank, which were delivered into the laser chamber, show a drift of equal magnitude. The last draw was expanded over a larger volume and might contain a slightly larger amount of helium. These analyses show that the introduction of O_2 in the laser chamber does not have a significant immediate impact on the ^{4}He measurement of samples. He can be completely captured on the cryostat even in the presence of O_2. No decline in ^{3}He sensitivity due decreased ionization efficiency was observed. The reproducibility

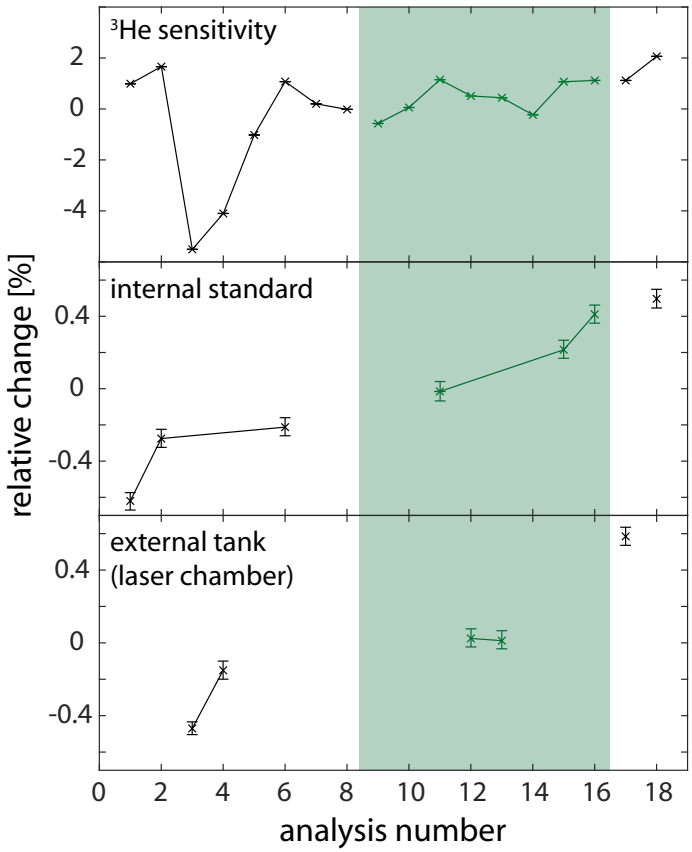

Figure 4.15: Results of a test for possible interference of O_2 on He measurement. Given are relative changes (normalized to average value) in ^{3}He sensitivity, ratio of one draw from internal standard tank, and amount of He detected in a draw from a different external standard tank released directly into the laser chamber. Green area and values indicate the presence of O_2 in the laser chamber during analysis. Analyses other than internal or external standards are line blanks or laser line blanks.

of measurements of known amounts of He released into the laser chamber was <1% over a 24 h period.

We also analyzed long-term changes of ^{3}He sensitivity and internal standard over the course of full sequences of 36 sample analyses, including re-extracts, blanks, and standards (Fig. 4.16). Since individual analyses with O_2 require at least 1.5x the amount of time of a vacuum analysis and degassing times are often longer than in vacuum, the time represented by O_2 runs is significantly longer and more instrument drift is expected for these runs. A vacuum run of 36 samples typically takes 2.5-3 days, whereas an O_2 run takes 3.5-6 days.

Both ^{3}He sensitivity and internal standards ratios show drift over the course of a run, with sensitivity showing drift of several percent of the average value, and standard ratio showing a drift of 1-3%. The absolute amount of drift from beginning to end of the run as well as the rate of drift are similar for vacuum and O_2 analyses. The change between two successive standards (usually bracketing 3-6 samples) is typically significantly less than 1%, which is around the value of the uncertainty of every individual He measurement. These observations demonstrate that no significant long-term degradation of precision or accuracy of the He measurement over the course of a run or beyond is expected due to the introduction of O_2.

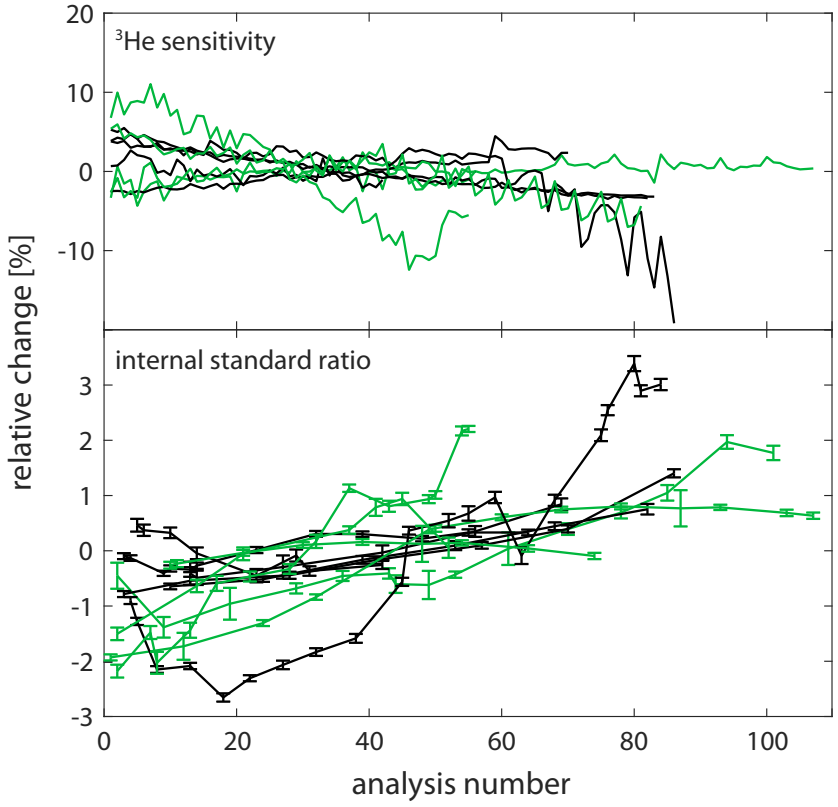

Figure 4.16: Normalized change in ^{3}He sensitivity and ^{4}He/^{3}He ratio of draws from an internal standard tank for a series of runs in vacuum (black) and with O_2 (green), with 1σ uncertainty. Every line represents a single run, each with a set of 36 individual samples or fewer being analyzed, including re-extracts, blanks, and interspersed standards. Each run spans between three and six days.

Vacuum line configuration

Based on the experience described above, the final configuration of the vacuum line for O_2 degassing was assembled as shown in Fig. 4.17. This setup permits the release and capture of O_2 before and after each heating. The flow-through U-trap helps to reduce O_2 to the rest of the line and acts as a fail-safe in case of failure of the lifter mechanism. The O_2 pressure is measured with the manometer and can be adjusted for each set of samples by using double-draws or partially pumping one draw. Analysis of a set of 36 aliquots includes re-extracts, standards, and laser line blanks, and can be run in approximately four days with this setup. The ^{4}He measurement is made by isotope dilution, with a known amount of pure ^{3}He spike being released before cryo-pumping. The amount of ^{4}He for every analysis is calculated relative to a draw from an internal standard tank with a known amount of pure ^{4}He, which is also spiked with ^{3}He. The blank amount of ^{4}He in the laser chamber for a 20 min integration time is 0.002 ncc (0.09 fmol).

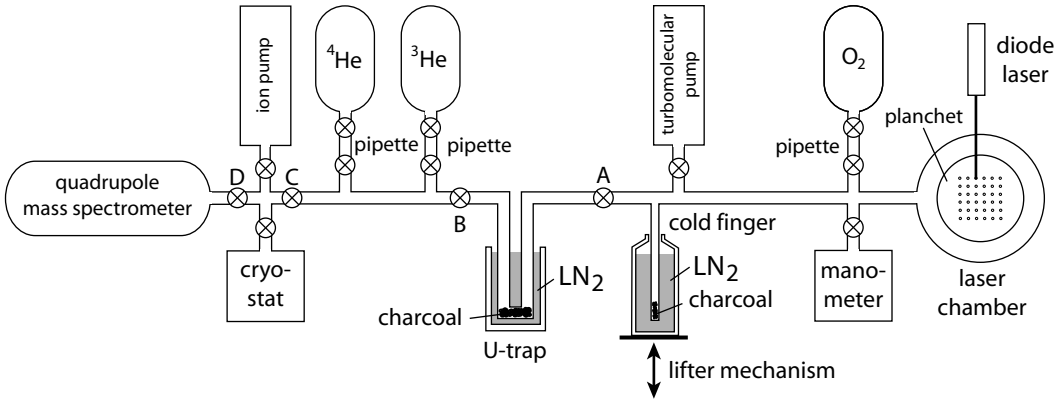

Figure 4.17: Schematic diagram of the vacuum line used for O_2 degassing. The lifter mechanism can be used to release and capture O_2 before and after laser heating.

Measurement procedure

We arrived at the optimal measurement procedure as a result of the experiences outlined above. The following describes the procedure implemented for O_2 degassing at Caltech. The preparation of the line for degassing is as follows (see Fig. 4.13 for

line configuration):

1. Load samples in Pt packets into planchet
2. Seal laser chamber
3. Pump laser chamber with turbo-molecular pump for at least 2 h
4. Close valve A
5. Release one draw of O_2 into line
6. Measure pressure with manometer
7. Fill dewar on cold finger with LN_2, move lifter up
8. Close manometer valve
9. Pump with turbo-molecular pump for at least 1 h
10. Close valve to turbo-molecular pump

After this initial sequence, a series of two laser line blanks is run, one to remove any remaining He impurity from the O_2 and the second one to characterize the blank level of He for the subsequent analyses. Both laser line blanks measurements use the same integration time as that of a regular sample analysis. The following describes the measurement procedure for a single analysis (one heating):

1. Close valve A
2. Move lifter down
3. Wait 10 min to completely release O_2
4. Heat sample with laser for 20 min
5. Move lifter up
6. Wait 2 min to completely trap O_2
7. Open valve A
8. Wait for 2 min to trap any remaining O_2 (this also acts as fail-safe to protect the rest of the line in case the lifter mechanism fails or the LN_2 level in the

dewar is too low)

9. Close valve C
10. Open valve B
11. Release a draw of ^{3}He into line
12. Set cryostat to 14 K
13. Open valve C and wait 2 min to adsorb all He onto cryostat
14. Close Valve C
15. Set cryostat to 34 K
16. Open valve D to inlet gas into quadrupole mass spectrometer
17. Measure $^{4}He/^{3}He$ ratio for 6 min
18. Close valve D
19. Set cryostat to 100 K to remove any O_2
20. Ion-pump for 5 min
21. Close valve to cryostat
22. Open valves C, B, and A
23. Ion-pump line for 10 min
24. The line is then ready for the next analysis

The same procedure is used for first extractions, re-extracts, and laser line blanks. Standards are expanded up to valve B only. A typical sequence for the degassing of a set of 36 samples in O_2 will include standards and laser line blanks interspersed every three to six samples as well as re-extracts at a slightly higher set-point for every sample.

4.B Pyrometer calibration

Measurement procedure

We calibrated the one-wavelength pyrometer used for single-aliquot laser heating at Caltech in order to allow accurate temperature control and to investigate the effects of high oxygen partial pressures on pyrometry. The laser heating system is a Teledyne Photon Machines Fusions Diode with a 75 W variable power output 970 nm diode laser and a LumaSense IMPAC IGA-140-TV pyrometer (1.45 to 1.8 μm). A Pt (or Nb) tube was mounted on a K-type thermocouple wire and pinched at the ends to produce a packet of the same size and shape as those used to contain samples (Fig. 4.18).

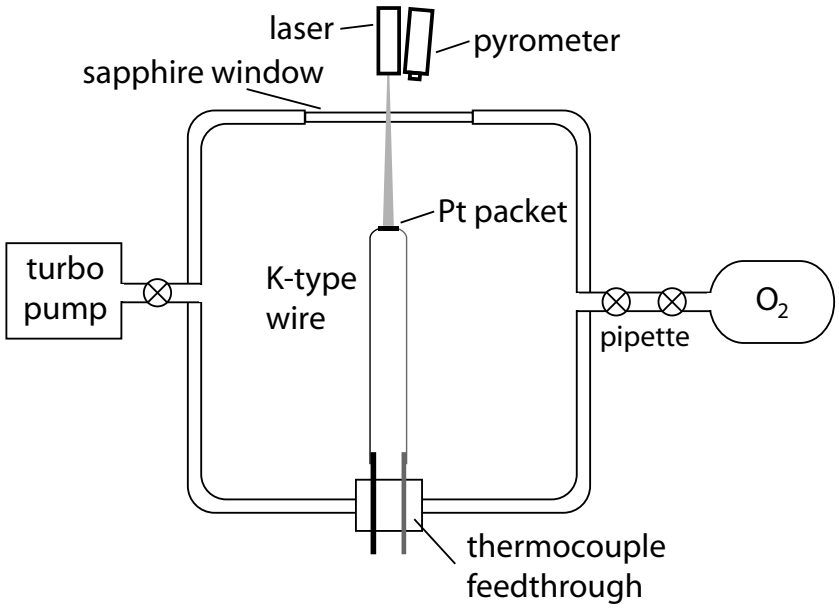

Figure 4.18: Laser cell setup for pyrometer calibration. A Pt packet is mounted on the welded junction of a thin K-type thermocouple wire. It is heated by a laser through a sapphire window, which also permits the transmission of black-body radiation for optical pyrometry. The cell can be either turbo-pumped for vacuum experiments or filled with O_2.

The Pt packet was positioned over the welded junction of the thermocouple wires, which were a sample would be located during degassing. The ends of the thermocouple wires were welded onto the contacts of a thermocouple feed-through. This

assembly was mounted into a laser diffusion cell with a sapphire window, which allows the transmission of both the laser and the infrared emission used for optical pyrometry. We also connected an oxygen tank with a pipette and a manometer to deliver a known amount of O_2 pressure.

The cell was evacuated to pressures comparable to those of normal measurement conditions. For vacuum experiments, the cell was exposed to a charcoal trap cooled with liquid nitrogen. For oxygen experiments, the cell was closed off to the U-trap and a draw of O_2 of about 100 torr was expanded into the laser chamber. Temperature measured through the thermocouple and pyrometer readings were recorded as a function of time. Thermocouple readings were taken every 2 seconds and pyrometer readings were taken about every 4 seconds. Laser power was increased gradually until the pyrometer returned a valid reading (>299). It was then ramped up in steps of about 20 °C, leaving enough time for both the pyrometer and the thermocouple reading to stabilize. This prograde heating was continued up to a pyrometer reading of 600 or 700. In most heating runs, temperature was then decreased step-wise until the pyrometer reading was 300. Most heating experiments featured several prograde-retrograde cycles using the same packet.

The temperature curves for the pyrometer and thermocouple recordings were synchronized after they were recorded. Plateaux of stable temperature were detected in both data sets and the average value for each heating step was calculated and recorded. Thermocouple temperature was then plotted against pyrometer reading to determine the pyrometer calibration curves for both vacuum and O_2. The same process was also applied to a Nb packet heated in vacuum.

Outcome of heating experiments

A total of nine heating experiments with different packets were performed: three Pt packets heated in vacuum, three Pt packets heating in 100 torr of O_2, and one Nb

packet heated in vacuum. Different packets showed similar shapes of thermocouple-pyrometer curves (Fig. 4.19), which can be described by quadratic functions. The thermocouple-pyrometer curve for each prograde or retrograde path could be modeled with a quadratic function with a high of goodness-of-fit. Both the pyrometer reading and the thermocouple temperature of individual heating plateaux were stable within 1 or 1 °C, respectively, even when held for tens of minutes (Fig. 4.20), indicating that the precision of the pyrometer measurement is <2 °C.

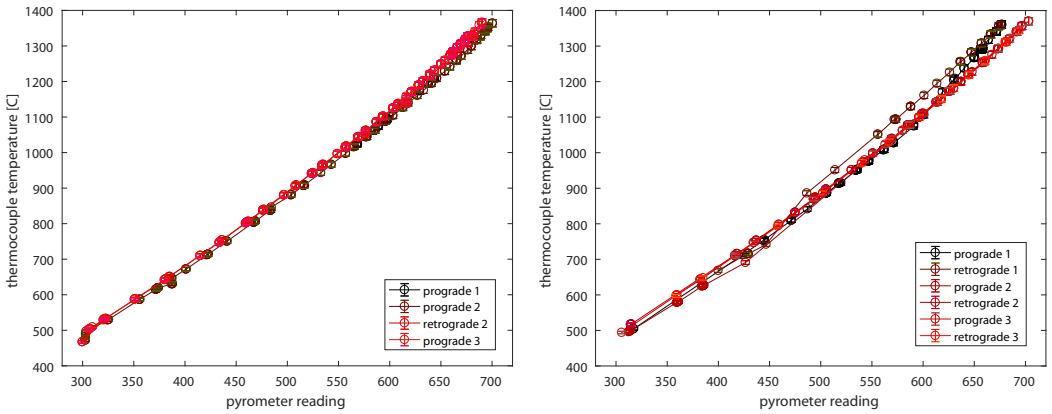

Figure 4.19: Example of vacuum heating runs for two different Pt packets showing both prograde and retrograde heating paths. The emissivity changes between the first heating cycle and the subsequent heating cycles, leading to a difference in the calibration of 10-20 °C.

Re-heating of the same packet causes the curve to shift by 5-20 °C. Shifts were observed both to higher and lower thermocouple temperatures for the same pyrometer reading. Subsequent re-heating cycles are the same as the first re-heating cycle. Individual heating cycles showed greater divergence above a pyrometer reading of 650. The calibration is most robust between a pyrometer reading of 450 and 650, which is the relevant range for iron-oxide degassing.

The data for all heating experiments was grouped by vacuum and O_2 (Fig. 4.21). Best-fit quadratic regressions with were calculated for both sets of data. The 2σ range for the spread of data points from the respective curve was about 15-20 °C for both data sets. The curves are nearly identical, except for an offset of +5-20 °C of

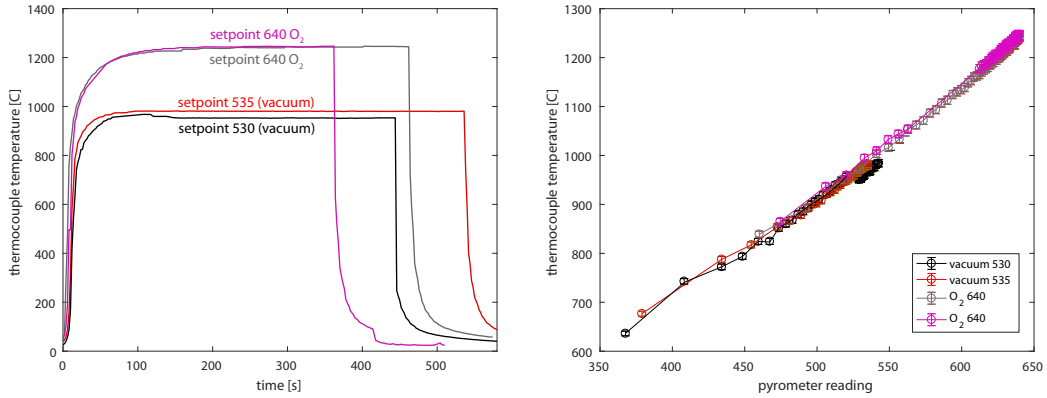

Figure 4.20: Heating packets under normal measurement conditions. One packet was heated in vacuum to a pyrometer set-point of 530 and a re-extract of 535, which is the regular schedule for analyzing goethite samples at Caltech. A different packet was heated in 100 torr of O_2 to a pyrometer set-point of 640, with a re-extract at the same set-point.

the O_2 curve relative to the vacuum curve. The relative offset is nearly constant at 1.9-2.2% (9 to 32 °C). This offset can be explained by the attenuation of black-body radiation due to the passage through an O_2 atmosphere relative to vacuum.

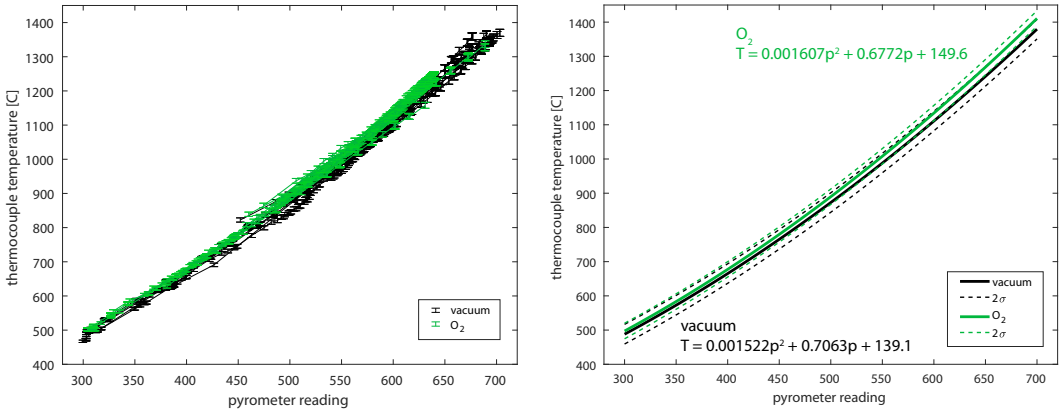

Figure 4.21: Data from all heating runs for Pt packets heated in vacuum and O_2 (left) and best-fit quadratic regression curves (right). The O_2 curve is about 2% higher than the one for vacuum.

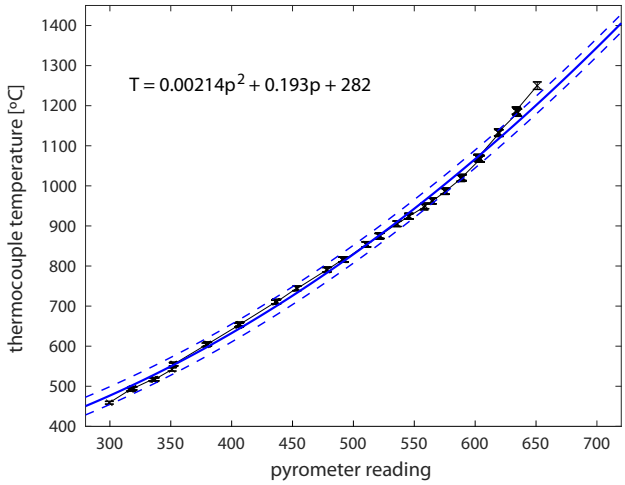

Figure 4.22: Data from one heating run of a Nb packet heated in vacuum with best-fit quadratic regression curve and equation.

The calibration equations used to convert between pyrometer reading and actual temperature (and vice versa) are given below.

Conversion from pyrometer reading (P) to actual temperature (T [°C]):

For Pt packet in vacuum: $T_{Pt,vac} = 0.0015223 \cdot P^2 + 0.70627 \cdot P + 139.09$

For Pt packet in ~100 torr of O_2: $T_{Pt,O_2} = 0.0016065 \cdot P^2 + 0.67715 \cdot P + 149.56$

For Nb packet in vacuum: $T_{Nb,vac} = 0.0021474 \cdot P^2 + 0.19307 \cdot P + 282.36$

Conversion from temperature (T [°C]) to pyrometer reading (P):

For Pt packet in vacuum: $P_{Pt,vac} = -231.97 + \sqrt{656.9 \cdot T - 37556}$

For Pt packet in ~100 torr of O_2: $P_{Pt,O_2} = -210.75 + \sqrt{622.47 \cdot T - 48680}$

For Nb packet in vacuum: $P_{Nb,vac} = -4.4954 + \sqrt{465.68 \cdot T - 131460}$

Calibration data

The data used for the pyrometer calibration for Pt packets in vacuum and O_2 as well as for an Nb packet in vacuum is given in Tables 4.3-4.7 below. Table 4.8 is a conversion table compiled using the calibrations equations above.

Table 4.3: Pyrometer calibration data, P = pyrometer reading, T = thermocouple temperature.

Pt packet 1, vacuum							
cycle 1 (prograde)				cycle 2 (prograde)			
P	T [°C]	P	T [°C]	P	T [°C]	P	T [°C]
353.0	571.8	543.0	952.4	452.0	822.3	580.0	1065.8
355.0	572.2	542.0	949.3	486.0	875.6	581.0	1068.5
350.0	562.9	540.0	945.4	499.0	897.2	583.0	1074.1
349.0	562.2	539.0	950.1	506.0	905.8	585.0	1079.1
364.0	601.3	545.0	958.9	511.0	919.3	587.0	1084.4
380.0	620.9	546.0	959.3	515.0	924.9	588.0	1084.4
391.0	639.4	547.0	962.5	518.0	930.4	589.0	1087.7
395.0	650.9	549.0	965.8	521.0	936.6	590.0	1089.6
399.0	654.7	550.0	965.7	525.0	944.0	592.0	1097.5
400.0	655.5	551.0	970.9	528.0	950.9	593.0	1097.6
407.0	676.7	552.0	971.4	529.0	953.7	594.0	1102.4
422.0	706.1	554.0	977.6	530.0	954.8	595.0	1102.4
434.0	724.8	555.0	982.5	531.0	957.3	596.0	1106.8
440.0	731.4	556.0	983.9	533.0	963.4	597.0	1110.7
446.0	740.6	557.0	989.0	534.0	964.2	598.0	1111.4
447.0	743.8	558.0	994.2	537.0	970.8	599.0	1114.4
448.0	744.8	563.0	1006.5	539.0	974.9	600.0	1115.1
449.0	745.3	561.0	1000.3	540.0	976.4	601.0	1121.8
463.0	776.9	560.0	999.5	543.0	983.4	602.0	1122.0
475.0	799.5	566.0	1016.1	545.0	989.0		
482.0	815.9	568.0	1019.6	547.0	995.5		
488.0	820.6	569.0	1023.2	548.0	995.5		
492.0	830.1	570.0	1026.5	549.0	996.1		
494.0	832.0	572.0	1030.5	550.0	1000.3		
495.0	837.9	574.0	1036.5	551.0	1005.4		
499.0	842.5	576.0	1041.3	552.0	1005.8		
500.0	843.7	575.0	1040.6	554.0	1010.6		
501.0	846.2	577.0	1045.7	555.0	1012.6		
504.0	854.2	581.0	1057.6	557.0	1018.0		
506.0	855.6	580.0	1056.8	558.0	1017.9		
508.0	861.8	583.0	1061.9	559.0	1022.4		
509.0	863.8	584.0	1066.4	560.0	1020.4		
510.0	863.5	585.0	1066.8	561.0	1024.5		
513.0	874.2	586.0	1070.9	562.0	1029.3		
514.0	875.0	587.0	1076.1	564.0	1029.6		
517.0	881.7	601.0	1099.3	566.0	1036.3		
516.0	883.4	599.0	1094.3	567.0	1036.3		
518.0	888.9	598.0	1093.0	569.0	1041.9		
519.0	889.5	595.0	1087.4	570.0	1042.6		
515.0	881.4	594.0	1084.5	571.0	1048.9		
520.0	901.2	592.0	1080.5	574.0	1052.2		
523.0	908.8	591.0	1079.8	576.0	1057.9		
526.0	917.4	590.0	1078.9	577.0	1060.8		
528.0	925.6	589.0	1077.4	579.0	1063.5		
529.0	926.1			578.0	1063.5		

Table 4.4: Pyrometer calibration data, P = pyrometer reading, T = thermocouple temperature, pro = prograde.

Pt packet 2, vacuum															
cycle 1 (pro)		cycle 2 (prograde)						(retrograde)		cycle 3 (prograde)					
P	T [°C]	P	T [°C]	P	T [°C]	P	T [°C]	P	T [°C]	P	T [°C]	P	T [°C]	P	T [°C]
568.7	1024.5	302.8	472.2	503.5	880.3	646.0	1209.2	677.3	1309.4	299.7	467.3	534.2	964.6	639.8	1220.1
568.8	1024.5	303.0	478.1	503.8	881.4	653.7	1228.4	677.1	1308.8	320.1	528.8	534.5	964.7	639.5	1220.1
568.5	1024.5	303.0	490.6	504.0	881.5	654.0	1228.9	665.9	1280.5	320.7	530.3	534.9	964.9	639.2	1220.0
568.2	1024.3	303.2	491.0	515.5	906.8	658.9	1241.7	665.7	1280.1	321.0	531.3	535.0	965.0	639.0	1219.8
568.0	1024.1	303.5	497.3	516.0	907.5	659.0	1241.8	665.0	1279.8	321.4	531.9	535.2	965.5	643.9	1231.2
568.0	1024.2	325.6	530.2	516.5	907.7	665.5	1258.2	621.0	1168.9	322.1	532.3	548.7	996.3	644.0	1231.5
576.8	1043.8	325.0	529.4	516.8	907.9	665.6	1260.0	593.4	1101.6	322.7	532.6	549.0	996.8	643.9	1231.0
577.0	1044.2	324.5	528.7	517.0	908.3	665.5	1260.0	593.1	1100.8	323.0	532.9	556.4	1013.6	643.5	1231.1
588.7	1073.7	355.5	586.5	516.8	908.3	665.2	1260.1	593.0	1100.4	322.6	532.8	556.8	1016.0	650.5	1249.4
589.0	1073.5	355.8	586.5	516.5	908.2	665.0	1260.2	576.8	1062.4	307.3	504.6	557.0	1016.4	650.2	1249.4
589.0	1073.6	356.0	586.6	516.3	908.1	665.0	1260.4	576.2	1061.8	306.5	503.1	557.2	1016.7	650.0	1249.2
596.4	1092.0	356.0	586.9	516.5	908.2	665.4	1260.5	557.4	1017.7	306.2	502.2	557.5	1017.0	650.0	1249.0
596.9	1092.0	371.3	614.5	532.8	943.2	669.6	1271.9	557.1	1016.6	306.0	502.0	557.8	1017.4	650.5	1248.8
597.0	1091.9	371.9	615.6	542.9	966.2	670.0	1272.2	535.0	966.8	350.5	586.7	558.0	1017.7	653.8	1257.9
597.1	1094.1	372.4	616.2	543.0	966.5	675.8	1288.8	534.5	966.2	351.0	587.6	558.0	1017.8	654.0	1259.8
597.4	1094.6	372.8	616.7	556.8	997.1	679.8	1299.1	508.8	909.0	351.2	588.0	568.8	1043.1	659.6	1272.6
597.7	1095.1	373.0	616.9	557.0	997.6	679.9	1299.5	477.0	840.3	351.5	588.7	569.0	1044.0	660.0	1275.6
597.9	1095.4	372.9	616.7	564.7	1015.8	679.6	1299.6	476.3	838.3	379.8	641.9	569.1	1044.3	659.9	1275.4
598.0	1095.4	372.6	616.3	565.1	1016.4	685.3	1316.5	476.0	837.7	380.5	642.9	576.2	1050.2	659.6	1275.1
615.0	1136.7	372.5	616.6	565.4	1016.7	685.3	1316.6	436.3	754.3	380.8	643.4	576.7	1056.1	659.3	1274.8
615.6	1138.4	372.9	617.4	565.7	1017.0	685.1	1316.8	436.0	753.5	381.0	643.8	577.0	1062.0	659.1	1274.5
629.0	1173.3	373.5	618.4	566.0	1017.1	685.5	1318.8	385.0	651.5	381.0	643.8	586.7	1086.2	662.7	1283.1
629.3	1173.9	373.9	619.2	565.9	1016.8	688.8	1326.7	384.8	650.5	414.6	709.5	587.0	1086.7	662.9	1284.4
637.1	1195.0	374.0	619.6	565.6	1016.4	689.0	1327.0	384.5	649.4	415.0	710.4	587.3	1086.3	662.6	1284.4
637.7	1195.1	373.9	619.4	577.4	1044.0	689.5	1331.2	309.6	509.2	415.0	710.7	593.2	1101.7	662.3	1284.3
638.0	1194.9	373.6	619.0	577.9	1044.9	693.4	1341.2	299.7	467.3	433.3	746.6	593.7	1101.9	662.1	1284.0
637.8	1194.6	373.8	618.8	584.0	1061.7	693.4	1341.1			433.8	747.4	593.9	1101.9	662.0	1283.7
637.5	1194.7	386.8	630.7	584.8	1062.2	693.4	1342.9			434.0	747.7	594.0	1102.0	661.9	1283.4
637.4	1195.0	387.0	635.6	585.3	1062.4	693.9	1346.1			434.0	748.0	603.0	1124.6	661.7	1283.2
637.6	1195.4	387.1	645.9	585.6	1062.6	694.7	1349.2			459.2	801.3	603.1	1124.8	661.3	1282.9
643.5	1209.9	387.4	646.1	585.6	1062.8	695.4	1350.2			459.7	802.2	603.3	1124.9	661.1	1282.4
643.9	1210.4	400.8	671.8	585.3	1062.9	695.9	1350.0			459.9	802.8	603.6	1125.3	661.4	1281.3
644.0	1210.5	401.1	672.1	585.1	1062.7	696.5	1353.9			460.1	803.3	607.5	1132.8	665.6	1295.2
643.8	1210.5	401.3	672.3	585.0	1062.5	700.3	1363.7			460.4	803.6	608.0	1136.7	666.0	1296.7
643.5	1210.5	421.3	711.8	585.1	1062.1	700.6	1363.6			460.7	804.0	608.5	1138.0	666.2	1295.9
643.2	1210.5	421.8	712.7	585.7	1062.5					460.9	804.5	616.1	1144.7	669.0	1302.2
643.0	1210.5	422.1	712.9	585.9	1062.8					461.1	805.1	616.0	1151.3	669.6	1305.7
		422.3	713.3	585.9	1063.1					461.4	805.6	616.2	1157.9	669.6	1306.0
		422.7	713.7	585.7	1062.9					461.7	806.1	621.6	1171.4	669.4	1305.9
		422.9	714.0	595.7	1087.1					461.9	806.6	621.6	1171.7	669.1	1305.6
		440.6	750.4	595.9	1087.4					476.4	837.1	621.4	1171.4	669.0	1305.3
		441.1	750.5	596.0	1087.6					476.9	837.9	621.1	1171.1	669.3	1304.8
		441.3	750.6	596.5	1089.6					477.0	838.3	621.0	1170.9	673.5	1312.1
		467.0	804.0	603.0	1103.4					496.4	880.0	621.3	1170.2	674.0	1317.1
		467.1	803.6	603.4	1104.5					496.8	881.1	629.0	1190.2	673.9	1318.7
		467.3	803.8	612.6	1126.5					497.0	881.2	628.8	1190.0	673.7	1318.6
		467.6	804.3	613.0	1126.6					507.6	906.1	628.5	1189.7	673.6	1318.4
		467.9	804.7	613.2	1128.0					508.0	906.4	628.1	1189.3	676.5	1326.7
		468.0	805.0	618.0	1139.5					523.5	941.0	628.0	1189.1	677.0	1327.4
		468.0	806.4	618.2	1139.6					524.1	941.3	628.0	1188.9	676.8	1327.4
		468.6	806.5	627.0	1160.6					524.3	941.4	633.0	1201.9	676.4	1327.3
		468.6	806.3	627.1	1161.5					524.6	941.8	632.8	1201.3	682.7	1333.7
		469.0	807.2	633.1	1175.3					524.9	942.0	632.5	1201.1	683.2	1340.1
		483.0	837.2	640.5	1194.4					525.0	942.2	632.3	1200.8	687.6	1358.5
		483.0	837.3	640.9	1195.0					525.3	943.3	639.5	1216.0	690.2	1364.0
		483.2	837.6	641.0	1195.0					533.6	962.0	639.8	1219.8	690.5	1366.2
		483.6	837.8	641.0	1195.2					533.9	964.3	640.0	1220.4	690.1	1365.8
		484.4	846.4	646.0	1208.8					534.0	964.5	640.0	1220.2	690.0	1365.3

Table 4.5: Pyrometer calibration data, P = pyrometer reading, T = thermocouple temperature.

Pt packet 3, vacuum												
cycle 1 (prograde)		(retrograde)		cycle 2 (prograde)		(retrograde)		cycle 3 (prograde)		(retrograde)	
P	T [°C]	P	T [°C]	P	T [°C]	P	T [°C]	P	T [°C]	P	T [°C]	P	T [°C]
317.2	504.0	640.1	1237.8	676.0	1358.9	312.2	496.1	696.1	1355.6	305.6	494.1	694.0	1344.8
317.5	505.0	650.6	1267.6	674.2	1356.3	313.0	496.9	673.0	1292.6	382.1	643.6	681.6	1311.5
423.7	712.6	650.3	1267.6	674.0	1356.2	313.6	497.6	658.0	1255.3	382.6	643.8	681.6	1311.6
444.0	753.1	650.1	1267.5	674.0	1356.1	314.1	498.6	644.1	1219.3	382.9	644.1	681.4	1311.6
444.7	754.1	650.0	1267.5	666.0	1333.2	359.2	578.4	644.0	1219.4	416.5	711.6	681.0	1311.4
445.0	755.0	649.9	1266.9	666.1	1332.9	360.1	579.4	625.7	1172.9	416.4	711.4	680.3	1311.2
471.0	809.1	649.7	1266.8	666.5	1333.1	360.7	580.1	625.4	1173.0	416.1	710.6	661.0	1258.7
471.2	810.2	658.9	1293.1	666.5	1333.0	361.2	580.6	625.4	1173.0	416.0	709.9	645.0	1218.6
471.5	810.5	658.7	1292.6	657.2	1308.0	383.9	624.4	624.8	1172.8	416.7	709.8	630.2	1181.2
487.0	841.7	658.3	1292.2	657.0	1308.0	384.5	625.0	613.0	1142.4	434.3	746.8	630.0	1181.1
506.0	886.6	658.1	1291.7	647.1	1282.8	384.8	625.6	612.6	1142.1	434.5	747.1	618.1	1150.6
505.9	886.5	657.9	1291.5	647.1	1282.7	385.0	626.1	599.0	1109.6	434.7	747.1	618.0	1150.5
505.6	886.3	657.7	1291.2	647.4	1282.9	385.2	626.5	599.0	1109.6	459.0	798.1	596.1	1098.9
505.4	886.1	657.3	1290.9	637.0	1255.9	385.5	626.8	599.2	1109.9	459.2	798.2	596.0	1099.0
505.5	886.2	657.1	1290.5	636.8	1255.8	385.8	627.0	599.5	1110.1	493.0	869.6	567.0	1030.5
505.8	886.5	657.0	1290.4	636.2	1255.9	386.0	627.1	585.0	1077.2	493.0	869.8	540.3	971.3
506.0	886.8	656.9	1290.6	626.0	1226.1	426.5	691.0	585.0	1077.4	493.2	869.9	540.1	971.1
517.4	912.9	656.7	1290.7	613.6	1194.9	617.0	1149.7	585.2	1077.6	493.8	869.9	540.0	970.9
517.7	913.8	656.4	1290.8	601.0	1161.2	636.9	1200.1	585.5	1077.8	543.0	979.4	502.1	886.7
518.0	914.3	656.0	1290.9	588.1	1130.0	637.0	1200.1	585.5	1078.0	551.0	997.3	502.1	886.5
518.1	914.7	656.3	1291.3	588.0	1129.8	637.2	1199.6	569.2	1039.6	563.0	1023.5	458.0	793.2
518.4	914.8	663.7	1317.4	587.8	1130.0	648.0	1227.5	569.0	1039.4	570.0	1039.9	385.0	647.7
519.0	915.1	664.0	1317.4	573.4	1093.5	658.0	1252.6	551.0	998.6	579.9	1062.6	359.1	598.9
519.8	915.4	672.0	1341.6	573.4	1093.4	667.5	1275.9	551.0	998.9	580.0	1062.7	359.0	598.3
534.1	950.1	672.0	1341.3	573.6	1093.6	684.0	1319.8	530.0	951.7	586.7	1077.8	359.2	598.7
534.4	950.4	671.7	1341.1	573.4	1093.5	691.0	1339.9	530.0	951.6	586.9	1078.0	359.5	599.2
534.7	950.5	671.4	1341.1	572.8	1093.3	697.0	1356.8	505.1	897.1	587.0	1078.1	359.6	599.5
534.9	950.8	677.0	1360.6	571.9	1093.3			505.1	897.1	587.6	1078.5		
535.1	951.3	677.0	1360.1	556.0	1051.2			505.4	897.3	595.9	1099.5		
535.4	952.0	676.8	1360.0	555.8	1052.0			505.4	897.5	596.0	1099.5		
535.7	952.6	676.5	1359.8	514.0	951.4			495.0	874.4	596.2	1099.7		
535.9	952.9	676.1	1359.6	486.5	886.4			494.9	874.4	600.0	1110.2		
546.2	975.0	676.0	1359.4	446.7	742.2			494.6	874.2	600.5	1110.4		
546.7	975.6			429.6	715.7			494.3	873.7	614.0	1142.2		
546.9	975.9			429.2	716.1			494.1	873.4	614.3	1141.8		
547.0	976.1			429.0	716.6			494.0	873.1	626.5	1173.3		
547.1	977.7			429.0	717.0			475.2	832.5	626.5	1173.4		
547.3	977.7			399.8	668.5			474.9	831.9	626.1	1173.2		
561.2	1007.5							474.7	831.7	626.0	1173.0		
561.6	1008.1							437.2	753.9	626.2	1172.9		
561.9	1008.4							437.0	753.0	626.7	1173.1		
562.0	1009.0							436.9	752.7	626.5	1173.1		
561.9	1008.9							418.4	715.9	645.0	1220.7		
561.7	1008.6							418.1	715.7	659.8	1256.4		
570.3	1031.1							418.0	715.5	660.0	1256.5		
570.6	1030.6							315.0	517.9	674.0	1293.2		
570.9	1030.1							315.0	517.3	673.9	1292.7		
571.0	1027.5							314.8	517.2	673.6	1292.4		
571.4	1027.2							314.5	516.9	673.2	1292.3		
591.0	1074.7							314.3	516.7	673.0	1292.1		
591.1	1080.1							314.5	516.8	685.0	1321.4		
601.0	1106.2							314.7	516.9	691.9	1340.4		
619.0	1171.0							314.3	516.6	692.0	1340.4		
631.0	1208.7									691.8	1340.3		
630.0	1203.9									703.0	1370.1		
640.3	1237.8									703.4	1369.7		

Table 4.6: Pyrometer calibration data, P = pyrometer reading, T = thermocouple temperature.

Pt packet 4, O_2								Pt packet 5, O_2				Pt packet 6, O_2			
cycle 1 (prograde)						cycle 2 (pro)		cycle 1 (prograde)				cycle 1 (prograde)			
P	T [°C]	P	T [°C]	P	T [°C]	P	T [°C]	P	T [°C]	P	T [°C]	P	T [°C]	P	T [°C]
329.0	555.4	504.0	903.9	568.0	1050.6	381.0	627.7	309.7	507.5	536.3	956.1	304.0	501.8	463.0	808.8
345.0	586.8	505.0	906.3	569.0	1054.3	434.0	749.9	309.5	507.7	548.0	982.2	304.2	502.1	492.0	870.6
359.0	603.1	506.0	906.6	570.0	1054.4	468.0	829.3	309.3	507.7	548.0	983.0	304.5	502.3	508.0	905.0
368.0	624.3	507.0	908.6	574.0	1068.8	493.0	888.2	317.0	520.9	548.2	983.1	304.7	502.5	517.6	926.6
376.0	633.4	508.0	911.5	575.0	1068.9	511.0	937.6	326.9	539.8	548.5	983.3	304.5	502.6	517.6	926.6
381.0	645.4	509.0	915.4	576.0	1070.6	527.0	972.8	327.0	539.9	548.9	983.6	304.3	502.6	517.3	926.7
385.0	653.2	510.0	916.6	577.0	1073.5	538.0	992.1	334.9	554.5	549.0	983.8	304.5	502.4	517.1	926.8
389.0	658.3	511.0	921.3	578.0	1075.9	549.0	1015.9	362.7	607.1	549.3	984.5	304.7	502.2	517.0	926.8
392.0	661.8	513.0	923.6	579.0	1079.3	557.0	1035.3	363.1	607.5	565.0	1020.8	304.5	502.1	517.7	926.5
394.0	666.1	514.0	926.4	580.0	1081.4	564.0	1047.0	363.4	607.8	565.2	1020.9	305.1	502.1	530.0	956.0
396.0	669.9	515.0	928.5	581.0	1084.8	570.0	1063.4	363.8	608.1	565.5	1021.0	310.3	502.1	530.1	956.4
398.0	673.4	516.0	931.3	583.0	1090.3	575.0	1067.9	370.2	620.6	565.8	1021.2	310.9	502.1	530.3	956.5
399.0	675.4	517.0	933.6	584.0	1092.5	576.0	1069.8	370.8	621.1	566.0	1021.3	311.4	502.1	530.6	956.5
400.0	676.5	518.0	934.0	585.0	1095.5	577.0	1073.4	371.0	621.4	566.1	1021.8	311.4	502.1	530.9	956.5
403.0	686.6	519.0	936.8	586.0	1097.4	578.0	1075.6	371.1	621.5	578.8	1049.4	310.7	502.1	531.8	956.5
406.0	693.0	520.0	938.9	587.0	1098.9	579.0	1077.4	379.8	639.0	579.0	1049.4	309.9	513.3	545.0	989.3
409.0	697.7	521.0	943.9	588.0	1101.9	580.0	1079.5	380.0	639.1	579.0	1049.4	309.6	513.0	545.4	989.5
411.0	702.8	523.0	945.9	589.0	1105.4	582.0	1088.4	386.7	650.9	579.2	1049.4	326.6	546.1	562.0	1028.7
413.0	706.5	524.0	948.7	591.0	1111.0	584.0	1092.3	387.0	651.0	579.5	1049.4	326.4	545.9	562.0	1028.8
415.0	709.5	525.0	951.0	592.0	1115.0	586.0	1097.4	395.5	667.9	579.8	1049.4	326.4	545.7	562.2	1028.7
416.0	710.1	526.0	953.0	593.0	1120.3	587.0	1101.0	396.0	668.1	580.0	1049.4	326.7	545.6	562.9	1028.4
417.0	713.5	527.0	955.1	594.0	1120.5	589.0	1103.9	396.7	668.1	590.0	1073.0	326.9	545.5	580.0	1071.4
418.0	714.6	528.0	957.6	595.0	1122.3	590.0	1107.6	410.4	695.9	600.9	1096.9	327.0	545.4	580.0	1071.1
419.0	715.3	529.0	960.1	596.0	1124.5	592.0	1109.7	410.6	696.1	601.0	1097.0	326.9	545.5	600.2	1121.1
420.0	717.1	530.0	961.0	597.0	1127.7	593.0	1113.8	410.6	695.8	601.2	1096.9	326.6	545.6	600.5	1120.9
421.0	728.5	531.0	967.0	598.0	1130.2	594.0	1115.5	427.4	731.2	601.5	1096.8	343.0	577.6	600.8	1121.1
427.0	735.9	532.0	969.3	599.0	1133.0	595.0	1117.8	428.1	731.3	601.8	1096.8	343.1	577.5	601.0	1121.2
431.0	744.9	534.0	971.5	600.0	1136.4	596.0	1121.2	428.4	731.6	602.0	1096.6	343.4	577.5	600.8	1121.3
435.0	752.2	535.0	973.6	601.0	1142.0	597.0	1123.0	428.7	731.9	602.0	1096.6	343.6	577.8	600.5	1121.3
438.0	756.4	536.0	975.6	602.0	1144.3	598.0	1124.2	428.9	732.1	615.0	1126.0	343.6	578.1	600.2	1121.4
440.0	759.7	537.0	978.0	603.0	1148.4	599.0	1127.7	429.0	732.2	615.1	1125.3	343.3	578.4	600.0	1121.4
443.0	764.8	538.0	980.4	604.0	1150.4	600.0	1129.0	440.9	757.7	615.5	1125.2	343.1	578.4	600.0	1121.4
444.0	767.7	539.0	982.6	605.0	1151.9	601.0	1132.8	441.0	757.9	615.8	1124.9	390.0	660.0	622.0	1175.5
445.0	770.8	541.0	987.3	606.0	1154.9	602.0	1135.4	441.6	758.1	616.0	1124.8	390.1	660.0	642.0	1224.9
446.0	773.3	542.0	991.4	607.0	1157.6	603.0	1137.1	454.4	785.8	631.0	1157.9	390.3	660.0	641.9	1224.5
447.0	775.3	543.0	993.6	608.0	1160.7	604.0	1140.8	455.0	786.2	646.0	1188.4	390.6	660.0	641.6	1224.5
448.0	776.1	544.0	995.5	609.0	1164.9	605.0	1143.6	455.1	786.5	646.1	1185.3	390.6	660.0	641.3	1224.5
449.0	779.0	545.0	997.6	610.0	1166.5	606.0	1145.3	470.0	817.8	646.4	1185.0	391.4	660.0	641.1	1224.3
450.0	779.5	546.0	999.3			607.0	1146.1	485.9	849.9	646.8	1184.7	405.4	689.2	641.0	1224.1
458.0	808.7	547.0	1001.6			608.0	1150.2	486.1	850.1	647.0	1184.5	405.1	689.3	656.0	1260.6
465.0	818.7	548.0	1004.0			609.0	1152.1	486.3	850.4	661.7	1214.7	405.0	689.3	655.9	1259.0
471.0	832.5	549.0	1005.9			610.0	1155.6	486.6	850.6	662.0	1214.1	419.6	717.9	655.7	1258.8
476.0	839.5	550.0	1007.6					486.9	850.8	662.0	1213.6	419.4	717.9	655.3	1258.5
480.0	850.2	551.0	1012.9					487.0	851.0	662.3	1213.3	419.1	717.8	655.1	1258.3
483.0	858.2	553.0	1016.7					486.9	851.1	673.0	1229.0	419.0	717.6	655.0	1258.0
486.0	862.4	554.0	1020.2					486.7	851.2	690.0	1254.7	419.0	717.9	655.5	1257.6
489.0	868.0	555.0	1020.6					487.2	851.1	690.9	1246.4	419.3	718.0	673.0	1301.4
491.0	873.4	556.0	1021.9					511.0	903.1	709.7	1267.0	419.3	718.3	672.9	1300.8
492.0	876.2	557.0	1025.3					535.0	954.4	731.2	1296.1	425.9	730.6	672.7	1300.1
494.0	878.3	558.0	1027.7					535.0	955.1	731.6	1295.2	426.0	730.7	672.4	1299.4
495.0	880.9	559.0	1029.5					535.3	955.4			426.2	731.4	672.1	1298.6
496.0	883.7	560.0	1031.5					535.5	955.5			446.0	772.4	672.0	1298.0
497.0	885.4	561.0	1037.9					535.6	955.5			446.0	772.6	672.8	1296.2
498.0	886.7	563.0	1039.7					535.5	955.6			446.2	772.9	689.0	1336.9
499.0	891.1	564.0	1042.8					535.4	955.5			446.5	773.0	688.8	1328.3
500.0	891.4	565.0	1045.1					535.6	955.5			446.8	773.2	688.7	1327.1
502.0	898.4	566.0	1047.0					535.9	955.5			447.0	773.4		
503.0	901.5	567.0	1050.7					536.0	955.6			447.0	773.7		

Table 4.7: Pyrometer calibration data, P = pyrometer reading, T = thermocouple temperature.

Nb packet 1, vacuum cycle 1 (prograde)			
P	T [°C]	P	T [°C]
299.5	458.9	521.5	875.0
316.8	491.8	521.2	874.8
317.7	493.1	521.0	874.7
318.4	494.0	535.6	905.3
318.8	494.4	536.0	905.4
319.0	494.6	545.6	924.3
335.2	517.5	545.9	924.3
351.1	542.0	545.6	924.2
352.2	554.6	545.4	924.0
352.6	555.3	545.4	923.9
352.6	555.0	558.0	947.1
352.3	554.9	558.7	950.2
352.0	555.0	564.5	962.1
378.9	603.3	565.0	962.4
379.8	604.9	575.7	986.5
380.1	605.3	575.4	986.4
380.4	605.5	575.1	986.3
405.7	652.1	575.0	986.2
405.9	652.6	575.4	986.3
406.0	652.5	589.6	1020.8
406.1	652.6	589.6	1020.9
406.3	653.2	589.4	1020.4
406.6	653.8	589.1	1020.0
406.6	653.9	589.0	1019.6
406.4	654.0	589.0	1019.3
406.4	654.1	588.7	1019.2
406.7	654.4	588.4	1019.0
406.9	654.8	588.1	1018.8
436.6	711.0	588.3	1018.6
436.9	711.1	604.3	1067.1
436.9	710.9	604.4	1067.5
436.7	710.8	604.1	1067.8
436.4	710.7	604.0	1067.9
436.1	710.5	603.8	1068.0
436.0	710.3	603.4	1068.2
436.1	710.3	603.1	1068.4
436.3	710.6	603.0	1068.6
437.2	711.1	602.8	1068.9
453.2	744.2	602.4	1069.2
454.0	744.3	602.1	1069.5
478.0	790.1	602.0	1069.6
478.0	790.7	602.4	1071.0
478.2	791.0	619.8	1131.6
478.7	791.2	619.5	1131.8
491.0	815.9	619.2	1132.3
491.0	815.7	619.0	1133.7
510.4	853.3	635.0	1182.4
511.0	853.9	634.9	1183.4
510.8	854.1	634.5	1184.5
510.3	854.2	634.2	1185.2
510.5	854.1	634.0	1186.5
510.8	854.3	634.0	1187.7
521.3	875.3	633.6	1187.7
522.0	875.2	651.0	1250.0
521.9	875.0		

Table 4.8: Conversion table for pyrometer reading (P) to actual temperature (T) and vice versa for Pt packets in vacuum and O_2 as well as for Nb packets in vacuum.

Pyrometer to temperature conversion				Temperature to pyrometer conversion							
P	T [°C]	T [°C]	T [°C]	T [°C]	P	P	P	T [°C]	P	P	P
	Pt, vacuum	Pt, O_2	Nb, vacuum		Pt, vacuum	Pt, O_2	Nb, vacuum		Pt, vacuum	Pt, O_2	Nb, vacuum
300	488.0	497.3	481.4	500	307.4	301.7	313.9	960	538.1	530.1	557.3
310	504.3	513.9	494.7	510	313.4	307.7	321.1	970	542.4	534.3	561.4
320	521.0	530.8	508.4	520	319.4	313.7	328.2	980	546.6	538.5	565.5
330	537.9	548.0	522.6	530	325.3	319.6	335.1	990	550.8	542.6	569.6
340	555.2	565.5	537.2	540	331.2	325.4	341.9	1000	555.0	546.7	573.6
350	572.8	583.4	552.2	550	337.0	331.2	348.6	1010	559.2	550.8	577.6
360	590.6	601.5	567.6	560	342.8	336.9	355.1	1020	563.3	554.9	581.6
370	608.8	620.0	583.5	570	348.4	342.5	361.5	1030	567.4	559.0	585.6
380	627.3	638.9	599.8	580	354.1	348.1	367.8	1040	571.5	563.0	589.5
390	646.1	658.0	616.5	590	359.7	353.7	374.0	1050	575.6	567.0	593.4
400	665.2	677.5	633.7	600	365.2	359.2	380.1	1060	579.7	571.0	597.3
410	684.6	697.2	651.3	610	370.7	364.6	386.2	1070	583.7	575.0	601.2
420	704.3	717.3	669.3	620	376.1	370.0	392.1	1080	587.7	578.9	605.0
430	724.3	737.8	687.7	630	381.5	375.3	397.9	1090	591.7	582.9	608.8
440	744.6	758.5	706.6	640	386.8	380.6	403.6	1100	595.7	586.8	612.6
450	765.2	779.6	725.9	650	392.1	385.8	409.3	1110	599.7	590.7	616.3
460	786.1	801.0	745.6	660	397.3	391.0	414.9	1120	603.6	594.5	620.1
470	807.3	822.7	765.8	670	402.5	396.2	420.4	1130	607.5	598.4	623.8
480	828.8	844.7	786.4	680	407.7	401.3	425.9	1140	611.4	602.2	627.5
490	850.7	867.1	807.4	690	412.8	406.4	431.2	1150	615.3	606.0	631.2
500	872.8	889.8	828.9	700	417.9	411.4	436.5	1160	619.2	609.9	634.8
510	895.2	912.8	850.7	710	422.9	416.4	441.8	1170	623.0	613.6	638.5
520	918.0	936.1	873.1	720	427.9	421.3	447.0	1180	626.9	617.4	642.1
530	941.0	959.7	895.8	730	432.8	426.2	452.1	1190	630.7	621.2	645.7
540	964.4	983.7	919.0	740	437.8	431.1	457.2	1200	634.5	624.9	649.2
550	988.0	1008.0	942.6	750	442.7	435.9	462.2	1210	638.3	628.6	652.8
560	1012.0	1032.6	966.6	760	447.5	440.7	467.2	1220	642.0	632.3	656.3
570	1036.3	1057.5	991.1	770	452.3	445.5	472.1	1230	645.8	636.0	659.8
580	1060.8	1082.7	1015.9	780	457.1	450.2	476.9	1240	649.5	639.7	663.3
590	1085.7	1108.3	1041.3	790	461.9	454.9	481.7	1250	653.2	643.3	666.8
600	1110.9	1134.2	1067.0	800	466.6	459.5	486.5	1260	656.9	646.9	670.3
610	1136.4	1160.4	1093.2	810	471.3	464.2	491.2	1270	660.6	650.6	673.7
620	1162.1	1186.9	1119.8	820	475.9	468.8	495.9	1280	664.3	654.2	677.1
630	1188.2	1213.8	1146.8	830	480.5	473.3	500.5	1290	667.9	657.8	680.5
640	1214.6	1241.0	1174.3	840	485.1	477.9	505.1	1300	671.6	661.3	683.9
650	1241.3	1268.5	1202.2	850	489.7	482.4	509.7	1310	675.2	664.9	687.3
660	1268.3	1296.3	1230.5	860	494.2	486.8	514.2	1320	678.8	668.4	690.7
670	1295.7	1324.4	1259.3	870	498.7	491.3	518.7	1330	682.4	672.0	694.0
680	1323.3	1352.9	1288.4	880	503.2	495.7	523.1	1340	686.0	675.5	697.3
690	1351.2	1381.6	1318.1	890	507.7	500.1	527.5	1350	689.6	679.0	700.6
700	1379.4	1410.8	1348.1	900	512.1	504.5	531.8	1360	693.1	682.5	703.9
				910	516.5	508.8	536.2	1370	696.7	686.0	707.2
				920	520.9	513.1	540.5	1380	700.2	689.4	710.5
				930	525.2	517.4	544.7	1390	703.7	692.9	713.7
				940	529.6	521.7	548.9	1400	707.2	696.3	717.0
				950	533.9	525.9	553.1				

4.C Ru-spike for measurement of Fe

Importance of Fe measurement

In routine iron-oxide single-aliquot (U-Th)/He dating, the mass of the sample is determined by measuring the amount of dissolved Fe and assuming perfect stoichiometry of either goethite or hematite. The measurement of the Fe-based mass does not influence the age, since the same aliquot is used to measure the absolute amounts of ^{4}He, U, Th, and Sm. However, to detect even small amounts of U loss requires a precise and accurate determination of sample mass. This also allows the quantification of the natural variability of U, Th, and Sm concentrations in unheated samples, which is used as a baseline to test for loss of these volatiles.

Measurement procedure

Samples are dissolved with 100 µl of concentrated HCl and 100 µl of a spike solution, which is enriched in ^{235}U and synthetic ^{230}Th for the measurement of U, Th, and Sm. We test the performance of using Ru as an elemental spike for Fe and other low masses (Al, Si, Mn), compared to the previously used Ca. The Ru-spike contained 0.8 µg of Ru and the Ca-spike contained 50 µg per draw. Mass ratios were measured on an Agilent 8800 triple-quadrupole inductively coupled plasma mass spectrometer (ICP-MS) using an Elemental Scientific PFA MicroFlow nebulizer with self-aspirating tubing with a fixed flow rate of 50 µl/min. Eight sets of 500 measurements of the ^{58}Fe/^{48}Ca and ^{58}Fe/^{101}Ru ratios were acquired over a total time of 6 minutes.

Test of Ru vs. Ca-spike

In a first test of the feasibility of using Ru as an elemental spike to measure Fe, we prepared solutions with known amounts of Fe between 10 and 70 µg. These solutions were spiked with both Ru and Ca. They were analyzed by ICP-MS as described above. The data was reduced to yield absolute amounts of Fe. Both the

Ca and Ru-spike method yielded Fe masses that are within 2% (1σ) of the actual value (Fig. 4.23), showing no obvious difference between the different spikes.

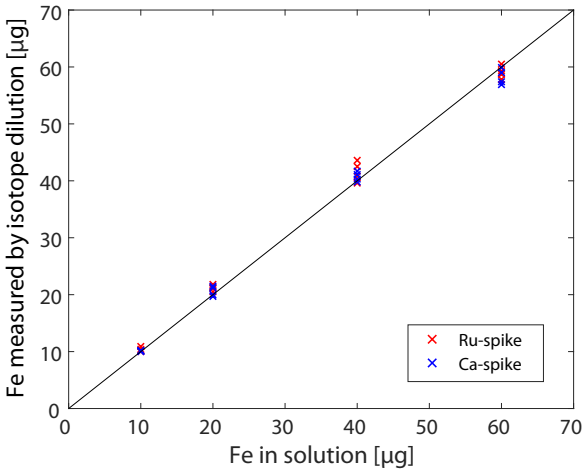

Figure 4.23: Fe masses of solutions with known amounts measured by isotope dilution using Ca and Ru as an elemental spike. Both methods yield linear relationships close to the 1:1 line (black).

For a second test, five aliquots of several different hematite and goethite samples with masses of 50-650 µg were weighed on a microbalance. Most aliquots were weighed more than once to ensure precision and accuracy. Uncertainties of repeated microbalance measurements are around 2-10 µg (1σ). Aliquots were spiked, dissolved, and measured as described above. The data was reduced using the same procedure as for regular iron-oxide (U-Th)/He samples to yield absolute amounts of Fe as well as U, Th, and Sm concentrations. Fe-based masses are calculated by assuming perfect hematite or goethite stoichiometry. The absolute amount of Fe is multiplied by the ratio of the molar mass of hematite or goethite to Fe, which is 1.43 and 1.59, respectively, which yields an estimate of the actual mass of the aliquot. Contributions from Al, Si, and Mn in addition to Fe were taken into account in calculating total sample mass, but were minor. Fe-based masses and concentrations were compared to weighed masses and U, Th, and Sm concentrations calculated by normalizing amounts of U, Th, and Sm by weighed mass. This tests both the

efficiency of the dissolution process and the effectiveness of the Ru and Ca-spikes. The results of the ICP-MS measurements are given in Fig. 4.24 and Tabs. 4.9 and 4.10. For hematite (n=15), sample masses derived from Ru-spike agreed with weighed massed to within 3% (30-700 µg). For Ca-spike, this was 9% (<150 µg) and 22% (150-700 µg). Goethite masses (n=15) show the same trend, with masses determined based on Ru-spike being closer to the weighed mass than those using Ca-spike. However, masses derived from Ru-spike are systematically low by about 5-10%. This could be due deviation from ideal stoichiometry, such as a higher degree of hydration of goethite, or substitution for Fe of elements other than the ones determined here. For both hematite and goethite, the Ru-spike yielded more precise and accurate results than the Ca-spike. The external 1σ-uncertainty of the Fe-based mass determination is about 3%. Concentrations of U, Th, and Sm, as well as effective uranium concentrations (eU) of samples calculated from Fe-based sample masses also show greater accuracy and precision of Ru-spike compared to Ca-spike (Figs. 4.25, 4.26).

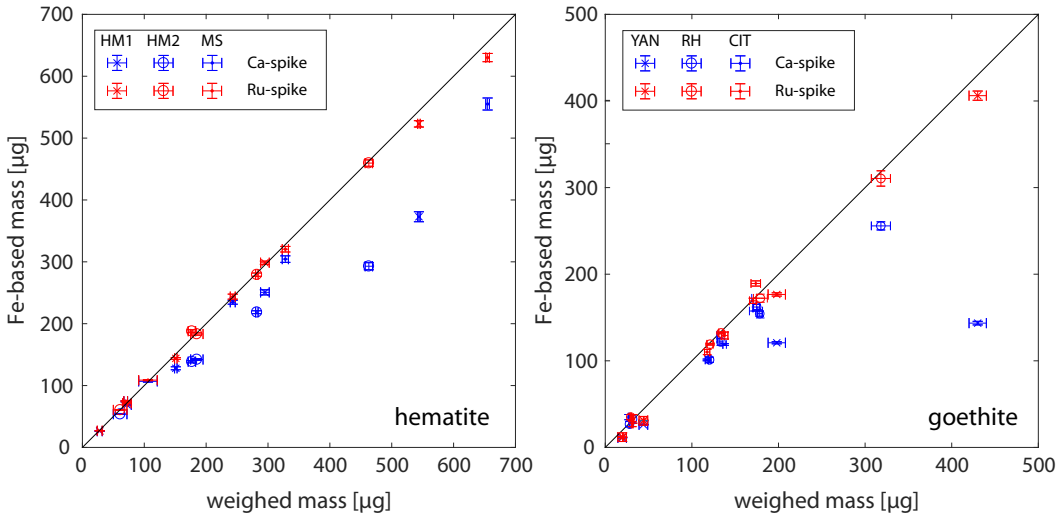

Figure 4.24: Fe-based sample masses measured by ICP-MS using Ca and Ru as an elemental spike compared with weighed masses. Five aliquots each of three different hematite (left) and goethite samples (right) were analyzed. Masses derived from Ru-spike are closer to weighed masses than those from Ca-spike.

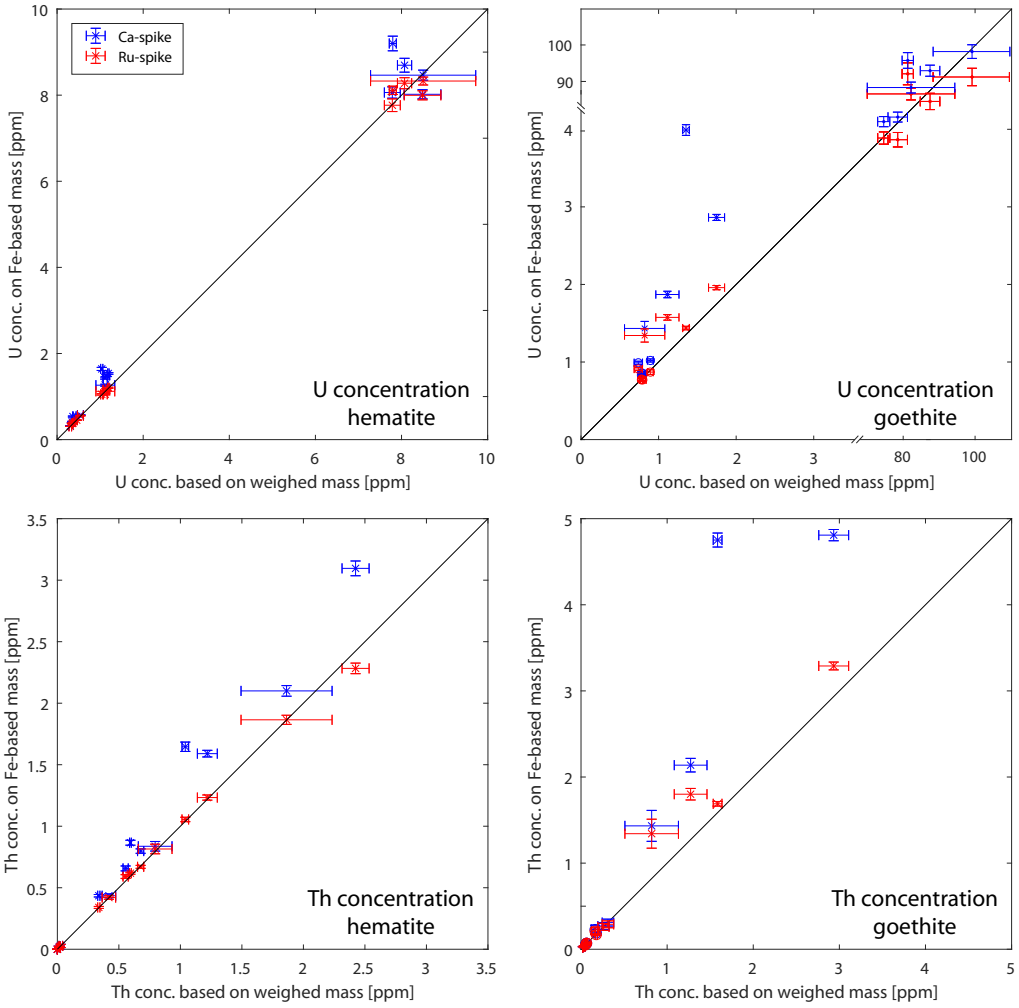

Figure 4.25: U and Th concentrations (ppm) derived from masses measured by means of Ca-spike (blue) and Ru-spike (red) compared to those derived from weighed masses.

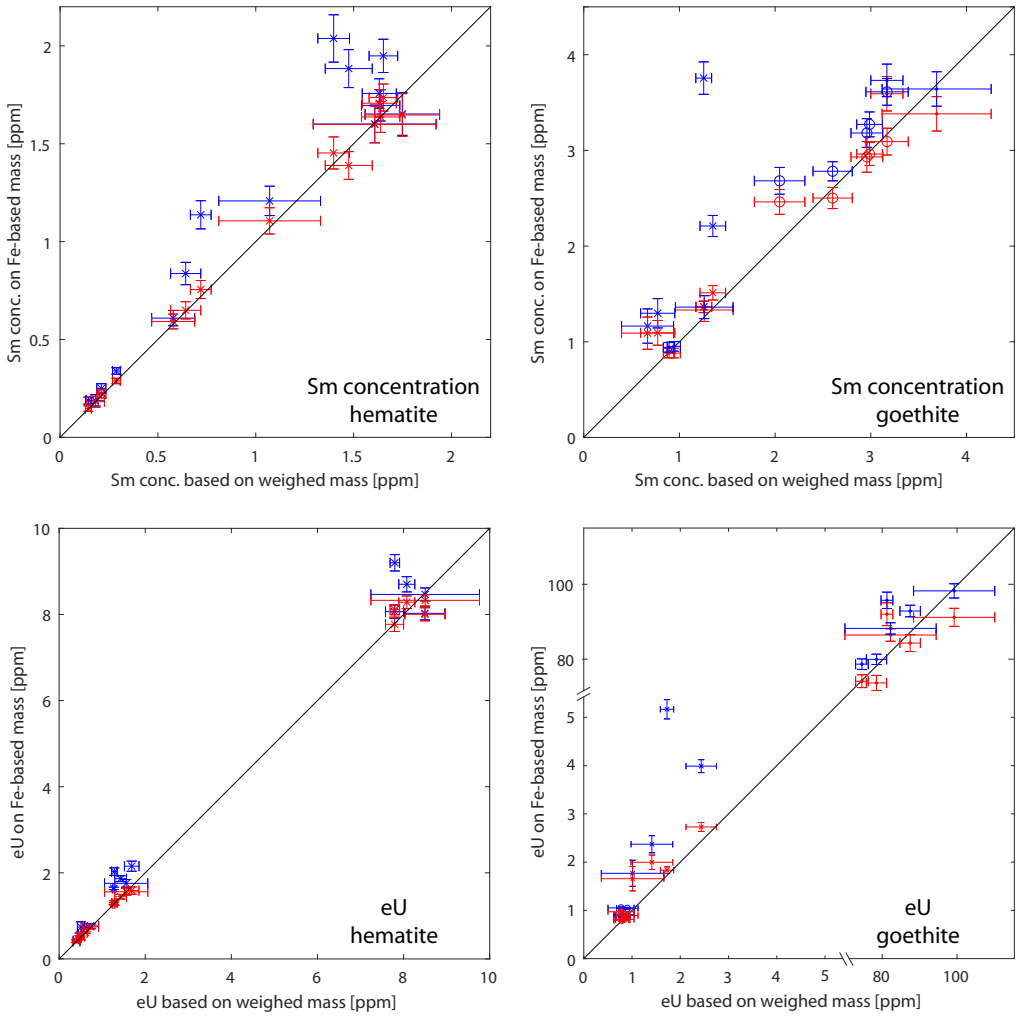

Figure 4.26: Sm concentrations and effective uranium concentrations (ppm) derived from masses measured by means of Ca-spike (blue) and Ru-spike (red) compared to those derived from weighed masses.

Advantages of Ru-spike

There are several aspects that make Ru a better choice than Ca as an elemental spike to measure Fe and to derive Fe-based sample masses. Ru is one of the least abundant elements and therefore background concentrations are diminutive in iron-oxide samples. Although Ca is rare in iron-oxides, it is a common constituent of other rock-forming mineral and might be present in mineral inclusions in iron-oxides. The previously measured Ca isotope ^{48}Ca has a natural abundance of 0.19%, whereas ^{101}Ru has a natural abundance of 17% (May and Wiedmeyer, 1998), requiring a much smaller amount of spike to be added to the sample to obtain the same number of instrumental counts in ICP-MS. Since the chemical behavior of Fe and Ru is similar and they have very similar first ionization efficiencies (Houk, 1986), instrumental fractionation of Ru relative to Fe is expected to be small.

There are no elemental isobaric interferences of stable nuclides on mass 101. The ^{48}Ca measurement has a possible isobaric interference from ^{48}Ti. Since ^{48}Ti has a natural abundance of 73.7%, a small amount of Ti in a sample could lead to a major interference of the Ca measurement. While using Ca-spike, we have measured ^{49}Ti to correct for this interference. $^{101}Ru^{+}$ has possible polyatomic interferences of $^{40}Ar^{61}Ni^{+}$ and $^{64}Ni^{37}Cl^{+}$ (May and Wiedmeyer, 1998). The measurement protocol at Caltech routinely measures ^{61}Ni, because of the possible isobaric interference of ^{58}Ni (68% natural abundance) on the ^{58}Fe measurement. In the analysis of several thousand iron-oxide aliquots of samples from various environments over the last five years, we have not detected Ni concentrations high enough to interfere with either the ^{58}Fe or ^{101}Ru measurement.

ICP-MS data

Table 4.9: Masses weighed and derived from Ca-spike and Ru-spike for hematite. Given are also concentrations of U, Th, and Sm, as well as effective uranium concentration (eU) in parts per million (µg/g) derived from these masses and trace-element measurements.

Masses and concentrations derived from weighed mass										
Sample name	mass	1σ	U	1σ	Th	1σ	Sm	1σ	eU	1σ
	[µg]	[µg]	[ppm]	[ppm]	[ppm]	[ppm]	[ppm]	[ppm]	[ppm]	[ppm]
HM1-A	151	2	0.350	0.011	0.555	0.021	0.211	0.023	0.480	0.033
HM1-B	544	2	0.368	0.005	0.594	0.007	1.398	0.081	0.507	0.082
HM1-C	28	4	0.542	0.069	0.795	0.137	0.578	0.110	0.728	0.188
HM1-D	295	7	0.457	0.017	0.677	0.025	0.288	0.020	0.616	0.036
HM1-E	72	7	0.307	0.030	0.419	0.055	0.181	0.046	0.405	0.078
HM2-A	463	6	1.038	0.025	1.040	0.027	0.719	0.053	1.282	0.065
HM2-B	177	6	1.119	0.046	2.424	0.110	1.475	0.120	1.686	0.169
HM2-C	61	11	1.121	0.219	1.863	0.370	1.071	0.260	1.557	0.502
HM2-D	185	10	1.144	0.077	1.219	0.081	0.642	0.077	1.429	0.136
HM2-E	282	2	1.191	0.016	0.337	0.009	0.145	0.015	1.270	0.024
MS-A	243	4	7.786	0.185	0.016	0.004	1.638	0.098	7.790	0.210
MS-B	70	3	8.488	0.426	0.028	0.015	1.749	0.190	8.495	0.466
MS-C	328	5	8.070	0.165	0.021	0.003	1.631	0.087	8.075	0.186
MS-D	655	3	7.797	0.082	0.000	0.000	1.652	0.073	7.797	0.110
MS-E	106	15	8.502	1.221	0.000	0.000	1.608	0.314	8.502	1.261
Masses and concentrations derived from Ca-spike										
Sample name	mass	1σ	U	1σ	Th	1σ	Sm	1σ	eU	1σ
	[µg]	[µg]	[ppm]	[ppm]	[ppm]	[ppm]	[ppm]	[ppm]	[ppm]	[ppm]
HM1-A	127.94	2.40	0.414	0.011	0.657	0.020	0.250	0.024	0.568	0.033
HM1-B	372.87	8.06	0.536	0.013	0.866	0.020	2.038	0.121	0.739	0.123
HM1-C	26.27	0.31	0.571	0.007	0.837	0.039	0.609	0.039	0.767	0.056
HM1-D	250.66	4.16	0.539	0.012	0.798	0.018	0.339	0.017	0.725	0.027
HM1-E	68.90	0.85	0.319	0.004	0.435	0.015	0.189	0.029	0.421	0.033
HM2-A	292.88	5.72	1.642	0.036	1.646	0.038	1.137	0.072	2.028	0.089
HM2-B	138.56	1.89	1.429	0.024	3.096	0.060	1.884	0.097	2.154	0.117
HM2-C	53.81	0.57	1.264	0.023	2.100	0.043	1.208	0.075	1.755	0.090
HM2-D	142.13	1.46	1.492	0.026	1.590	0.027	0.837	0.057	1.864	0.068
HM2-E	218.55	2.32	1.537	0.019	0.435	0.010	0.188	0.018	1.639	0.028
MS-A	234.70	3.18	8.061	0.131	0.017	0.004	1.696	0.080	8.066	0.154
MS-B	74.44	0.85	8.020	0.106	0.027	0.013	1.652	0.109	8.026	0.153
MS-C	304.42	5.27	8.695	0.161	0.023	0.003	1.757	0.075	8.701	0.177
MS-D	555.12	9.73	9.200	0.170	0.000	0.000	1.949	0.085	9.200	0.190
MS-E	106.80	1.29	8.464	0.117	0.000	0.000	1.601	0.096	8.465	0.151
Masses and concentrations derived from Ru-spike										
Sample name	mass	1σ	U	1σ	Th	1σ	Sm	1σ	eU	1σ
	[µg]	[µg]	[ppm]	[ppm]	[ppm]	[ppm]	[ppm]	[ppm]	[ppm]	[ppm]
HM1-A	143.91	1.41	0.375	0.008	0.591	0.015	0.222	0.021	0.513	0.027
HM1-B	523.03	5.12	0.382	0.005	0.618	0.008	1.453	0.082	0.527	0.082
HM1-C	27.01	0.36	0.555	0.007	0.815	0.039	0.592	0.038	0.746	0.055
HM1-D	298.54	2.64	0.452	0.008	0.670	0.012	0.288	0.014	0.609	0.020
HM1-E	71.39	0.63	0.308	0.003	0.420	0.014	0.182	0.028	0.407	0.032
HM2-A	459.61	5.11	1.051	0.016	1.055	0.018	0.755	0.046	1.298	0.052
HM2-B	187.90	2.40	1.054	0.017	2.283	0.043	1.389	0.071	1.588	0.085
HM2-C	60.58	0.54	1.122	0.019	1.865	0.037	1.106	0.067	1.559	0.079
HM2-D	183.35	2.02	1.156	0.021	1.233	0.021	0.649	0.044	1.445	0.053
HM2-E	279.27	2.67	1.203	0.014	0.340	0.008	0.147	0.014	1.283	0.021
MS-A	243.74	4.06	7.766	0.147	0.016	0.004	1.637	0.079	7.771	0.167
MS-B	74.66	0.84	7.996	0.105	0.027	0.013	1.647	0.109	8.003	0.152
MS-C	320.40	4.51	8.277	0.128	0.022	0.003	1.707	0.070	8.283	0.146
MS-D	630.18	6.67	8.112	0.097	0.000	0.000	1.736	0.069	8.112	0.119
MS-E	108.79	0.96	8.328	0.092	0.000	0.000	1.599	0.093	8.328	0.131

Table 4.10: Masses weighed and derived from Ca-spike and Ru-spike for goethite samples. Given are concentrations of U, Th, and Sm, as well as effective uranium concentration (eU) in parts per million (µg/g) derived from these masses and trace-element measurements.

Masses and concentrations derived from weighed mass										
Sample name	mass	1σ	U	1σ	Th	1σ	Sm	1σ	eU	1σ
	[µg]	[µg]	[ppm]	[ppm]	[ppm]	[ppm]	[ppm]	[ppm]	[ppm]	[ppm]
YAN-A	19.5	4.9	0.82	0.26	0.82	0.31	0.67	0.27	1.01	0.49
YAN-B	44.0	5.0	1.11	0.15	1.27	0.19	0.77	0.18	1.41	0.30
YAN-D	430.0	10.0	1.35	0.04	1.59	0.05	1.25	0.08	1.72	0.11
YAN-E	198.0	10.0	1.75	0.10	2.93	0.17	1.35	0.13	2.43	0.24
CIT-A	189.2	2.8	81.27	1.57	0.04	0.01	3.17	0.17	81.28	1.58
CIT-B	33.4	4.8	82.19	12.18	0.24	0.06	1.26	0.30	82.24	12.18
CIT-C	168.8	3.3	74.59	1.69	0.01	0.01	0.89	0.06	74.59	1.69
CIT-D	128.8	4.1	78.49	2.71	0.02	0.01	0.94	0.07	78.49	2.71
CIT-E	27.4	2.9	99.16	10.83	0.29	0.07	3.69	0.57	99.23	10.84
CIT-F	109.6	3.1	87.47	2.72	0.00	0.00	4.71	0.29	87.47	2.73
RH-A	310.0	10.9	0.89	0.04	0.03	0.00	3.17	0.22	0.90	0.22
RH-B	35.2	2.6	0.74	0.05	0.14	0.04	2.05	0.26	0.77	0.27
RH-C	132.0	1.2	0.78	0.01	0.05	0.01	2.98	0.13	0.79	0.13
RH-D	172.0	7.8	0.80	0.04	0.16	0.01	2.60	0.21	0.83	0.21
RH-E	119.4	1.3	0.78	0.02	0.04	0.01	2.96	0.17	0.79	0.17
Masses and concentrations derived from Ca-spike										
Sample name	mass	1σ	U	1σ	Th	1σ	Sm	1σ	eU	1σ
	[µg]	[µg]	[ppm]	[ppm]	[ppm]	[ppm]	[ppm]	[ppm]	[ppm]	[ppm]
YAN-A	11.9	0.1	1.43	0.09	1.43	0.18	1.16	0.18	1.77	0.27
YAN-B	30.8	0.3	1.87	0.04	2.14	0.08	1.30	0.15	2.37	0.18
YAN-D	401.2	5.3	4.06	0.07	4.75	0.08	3.76	0.17	5.17	0.20
YAN-E	173.5	1.9	2.86	0.04	4.81	0.07	2.21	0.11	3.99	0.13
CIT-A	166.6	3.6	95.69	2.18	0.04	0.01	3.73	0.17	95.72	2.18
CIT-B	31.2	0.5	88.16	1.51	0.25	0.04	1.36	0.12	88.22	1.51
CIT-C	160.2	2.8	78.67	1.41	0.01	0.01	0.94	0.05	78.67	1.41
CIT-D	126.6	2.2	79.94	1.38	0.01	0.01	0.95	0.05	79.95	1.38
CIT-E	28.7	0.5	98.16	1.90	0.29	0.04	3.64	0.18	98.24	1.90
CIT-F	106.4	1.7	92.84	1.54	0.00	0.01	4.99	0.18	92.86	1.54
RH-A	273.3	4.7	1.02	0.02	0.04	0.01	3.61	0.14	1.04	0.02
RH-B	26.8	0.5	0.99	0.02	0.21	0.05	2.68	0.14	1.05	0.02
RH-C	121.0	2.0	0.86	0.02	0.05	0.01	3.27	0.13	0.89	0.02
RH-D	161.4	2.7	0.85	0.02	0.17	0.01	2.78	0.10	0.91	0.02
RH-E	111.4	2.0	0.83	0.02	0.05	0.01	3.18	0.15	0.86	0.02
Masses and concentrations derived from Ru-spike										
Sample name	mass	1σ	U	1σ	Th	1σ	Sm	1σ	eU	1σ
	[µg]	[µg]	[ppm]	[ppm]	[ppm]	[ppm]	[ppm]	[ppm]	[ppm]	[ppm]
YAN-A	11.1	0.1	1.34	0.08	1.34	0.17	1.09	0.17	1.66	0.25
YAN-B	25.9	0.2	1.58	0.04	1.80	0.07	1.09	0.13	2.00	0.15
YAN-D	141.8	2.1	1.44	0.02	1.69	0.03	1.36	0.06	1.83	0.07
YAN-E	118.7	1.3	1.96	0.03	3.29	0.05	1.51	0.08	2.73	0.09
CIT-A	173.4	5.5	91.98	3.05	0.04	0.01	3.59	0.18	92.01	3.05
CIT-B	31.8	0.6	86.38	1.66	0.24	0.04	1.33	0.12	86.45	1.66
CIT-C	170.1	3.9	74.11	1.71	0.01	0.01	0.88	0.05	74.12	1.71
CIT-D	137.5	3.7	73.64	2.01	0.01	0.01	0.88	0.05	73.65	2.01
CIT-E	30.9	0.8	91.09	2.41	0.27	0.04	3.38	0.18	91.17	2.41
CIT-F	117.2	3.0	84.29	2.26	0.00	0.01	4.53	0.19	84.31	2.26
RH-A	319.1	8.9	0.87	0.03	0.03	0.00	3.09	0.14	0.89	0.03
RH-B	29.3	0.7	0.91	0.02	0.19	0.04	2.46	0.13	0.97	0.03
RH-C	133.9	2.6	0.78	0.02	0.05	0.01	2.96	0.12	0.80	0.02
RH-D	179.5	4.7	0.77	0.02	0.15	0.01	2.50	0.11	0.81	0.02
RH-E	121.2	3.5	0.77	0.02	0.05	0.01	2.93	0.16	0.79	0.02

4.D ATR-FTIR spectroscopy of hematite and goethite phase transitions

Heating and ATR-FTIR procedure

We determined the phase of samples heated to different temperatures using Attenuated Total Reflection Fourier-Transform Infrared (ATR-FTIR) spectroscopy. Heating conditions were similar to those of samples analyzed for (U-Th)/He ages, with samples being heated with the same laser system and pyrometer in a copper planchet. Due to ATR-FTIR sample requirements, we heated milligram-quantities of sample material in a Pt packet larger than those used for (U-Th)/He dating. Samples were heated in vacuum as well as in about 100 torr of O_2 for either 10 min or 60 min.

After heating, we tested if the Pt packet moved under the influence of a weak hand magnet held at about 1 cm distance through 5 mm of glass. This might be used as a possible test for phase change to magnetite. The packet was then opened using forceps under a light microscope. The contents of the packet were transferred to a glass petri dish. The sample was then tested again with the magnet. Two or three aliquots of 30-100 μg were randomly picked from the sample material and transferred to Teflon vials for dissolution and ICP-MS measurement of U, Th, and Sm concentrations as well as Fe-based mass according to the standard protocol for iron-oxides described here.

The remaining sample material was ground to a fine powder using a quartz mortar and pestle. The color of the powder (streak color) was recorded. The powder was transferred onto the crystal of a SensIR DuraScope. The absorption spectrum from 400 cm^{-1} to 4000 cm^{-1} was measured using a Thermo-Nicolet iS50 FTIR with a KBr beam splitter.

Phase identification

The phase of a sample was identified from the ATR-FTIR spectrum by comparing it to reference spectra of synthetic goethite, hematite, and magnetite pigment powders with grain diameters of 0.15-0.25 μm. Representative spectra for those phases are given in Fig. 4.27. Synthetic powders have a narrower grain-size distribution than ground samples, and therefore have more well-defined spectra. In the following, spectra for goethite, hematite and magnetite are color-coded as yellow, red, and black, with dark red being used for samples of mainly hematite with a noticeable amount of magnetite.

Characteristic peaks for goethite are at 795 cm^{-1}, 899 cm^{-1}, 1662 cm^{-1}, 1793 cm^{-1}, as well as a broad peak with a center at 3090-3110 cm^{-1}. Hematite is characterized by a doublet with peaks at 430-450 cm^{-1} and 510-520 cm^{-1}. Magnetite has a single peak at 520-540 cm^{-1}, as well as a doublet with peaks at 1145 cm^{-1} and 1200 cm^{-1}. In addition to iron-oxide phases, other minerals were present in some of the spectra (Fig. 4.27), which were identified based on the RRUFF database (Lafuente et al., 2016). A minor amount of quartz, most likely derived from the quartz mortar and pestle used to grind the samples into a powder, was present in some samples, showing broad peaks at 1079 cm^{-1} and 453 cm^{-1}, as well as a defined close doublet at 783 cm^{-1}. Calcite (peaks at 1394 cm^{-1}, 872 cm^{-1}, 712 cm^{-1}) and portlandite (sharp peak at 3641 cm^{-1}) were present in one sample (GC). Peaks of these minerals can be found superimposed on iron-oxide spectra. Both calcite and quartz have peaks that interfere with the magnetite doublet at 1145 cm^{-1} and 1200 cm^{-1}. However, the interfering peaks are much broader than the defined magnetite doublet, which can be clearly distinguished.

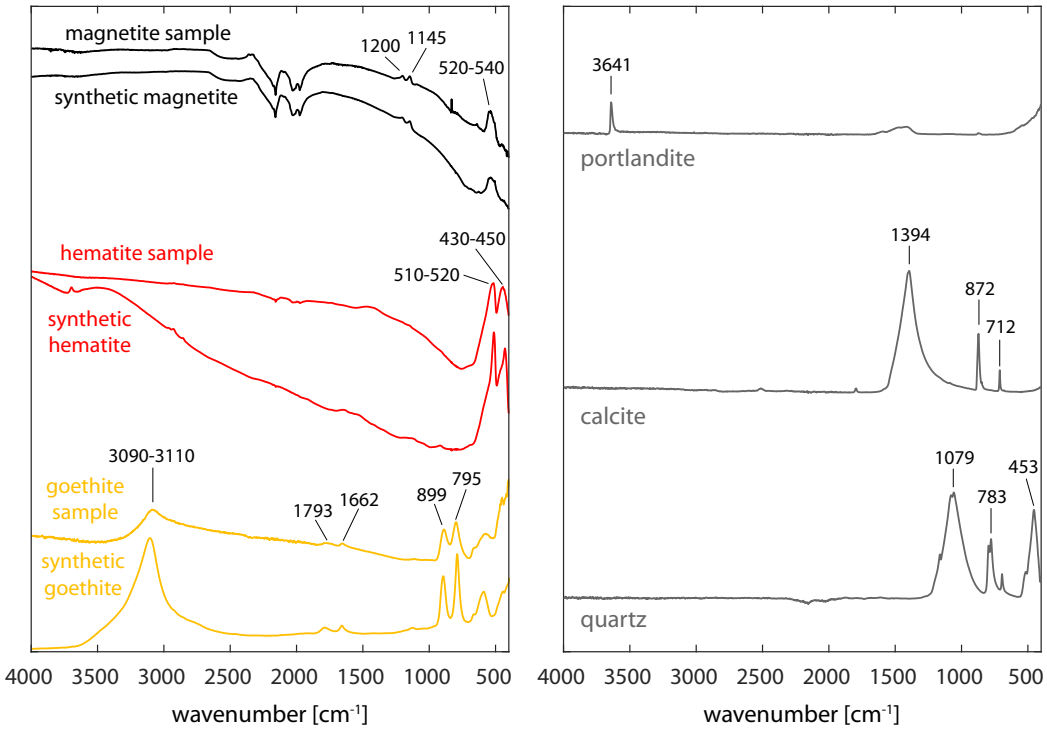

Figure 4.27: Representative ATR-FTIR spectra of iron-oxide (left) and interfering phases (right) detected in sample spectra. Spectra for quartz, calcite, and portlandite are from the RRUFF database. Numbers are wavenumbers of peaks in cm^{-1}.

Hematite-magnetite mixtures

Since the object of ATR-FTIR phase identification is to track the conversion of hematite to magnetite, we analyzed a series mixtures with varying amounts of hematite and magnetite. The fraction of magnetite as a part of the whole sample (X_{mag}) was determined by weighing amounts of magnetite and hematite before grinding them to produce a homogeneous mixture. Spectra for these mixtures were recorded in the same way as those of natural samples.

ATR-FTIR spectra show a progressive change from the pure hematite spectrum to that of pure magnetite (Fig. 4.29) for intermediate mixtures. The peaks characteristic for hematite at 430-450 cm^{-1} and 510-520 cm^{-1} diminish with increasing magnetite fraction. The peak at 430-450 cm^{-1} is non-existent in the pure magnetite spectrum, whereas the peak at 510-520 cm^{-1} gradually becomes the magnetite peak at 520-540

cm^{-1}. The magnetite doublet with peaks at 1145 cm^{-1} and 1200 cm^{-1} emerges from the spectrum above the background of the hematite spectrum. It becomes clearly distinguishable above 10-15% magnetite.

We quantified this change by introducing the peak ratio (pr) measure, which is calculated as:

$$pr = \frac{p_{1145} + p_{1200}}{p_{520}} \tag{4.1}$$

where p are peak heights above background at approximately 520 cm^{-1}, 1145 cm^{-1}, and 1200 cm^{-1}.

Peak ratio is <0.01 for pure hematite and increases to a ratio of about 0.8 for pure magnetite (Fig. 4.28). The relationship between peak ratio and magnetite fraction can be approximated with the cubic function:

$$pr = 6.401 \cdot 10^{-7} \cdot X_{mag}^3 + 7.055 \cdot 10^{-6} \cdot X_{mag}^2 + 0.0008252 \cdot X_{mag} + 0.007686 \tag{4.2}$$

The inverse relationship is approximated by:

$$X_{mag} = 153 \cdot pr^{\frac{1}{3}} - 16.17 \cdot pr - 29.33 \tag{4.3}$$

where pr is the peak ratio and X_{mag} [%] is the magnetite percentage. This permits the estimation of the percentage of hematite converted to magnetite in natural samples.

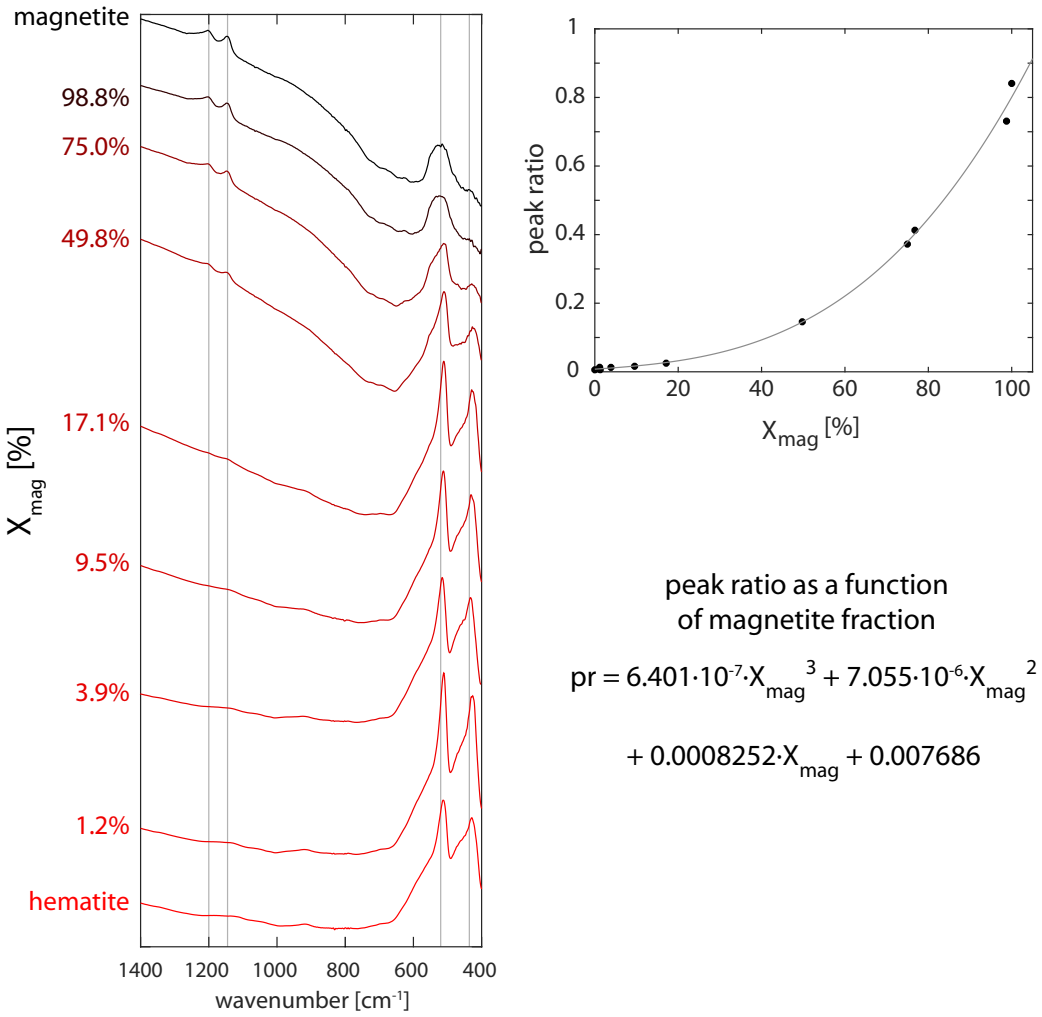

Figure 4.28: ATR-FTIR spectra of mixtures of synthetic hematite and magnetite powders.

Hematite samples

We tested five different hematite samples for phase change and U loss (Figs. 4.29, 4.30, 4.31, and 4.32). Since the most characteristic peaks for the detection of magnetite and hematite are between 400 cm^{-1} and 1500 cm^{-1}, ATR-FTIR spectra for hematite samples are only shown in this range. Samples show a gradual conversion from hematite to magnetite between 800 and 1200 °C in vacuum. This conversion is delayed to 1250-1300 °C in 100 torr of O_2.

Phase transition temperatures from the phase diagram of Ketteler et al. (2001) based on oxygen partial pressures of 10^{-10}-10^{-3} mbar in vacuum and 130 mbar of O_2 are 620-930 °C and 1320 °C, respectively. The initiation of conversion of hematite to magnetite was observed at these temperatures, but major conversion occurred at much higher temperatures, with full conversion to magnetite at around 1350 °C. This is an indication that thermodynamic phase equilibrium is not attained and that kinetics are an important factor controlling the conversion of hematite to magnetite on timescales of minutes to hours.

In vacuum, the inception of U loss coincides with the first detectable conversion of hematite to magnetite at 900-1000 °C (Fig. 4.33). Major conversion of hematite to magnetite (20-100%) occurs between 1050 °C and 1300 °C and is associated with massive U loss of up to 50-75% of the initial concentration. Most hematite samples show the same trend, except for the sample GC, which exhibited neither major conversion of hematite to magnetite nor massive U loss. This might be due to interactions of the hematite with associated calcite and portlandite in the sample. The presence of these phases in the ATR-FTIR spectra (Fig. 4.32) might have also interfered with phase interpretation, U measurement, and the determination of the peak ratio and magnetite percentage. Sample HM2048 had U, Th, and Sm concentrations <0.1 ppm. Trace elements were measured for this sample, but they are below the detection limit and the results are not reported.

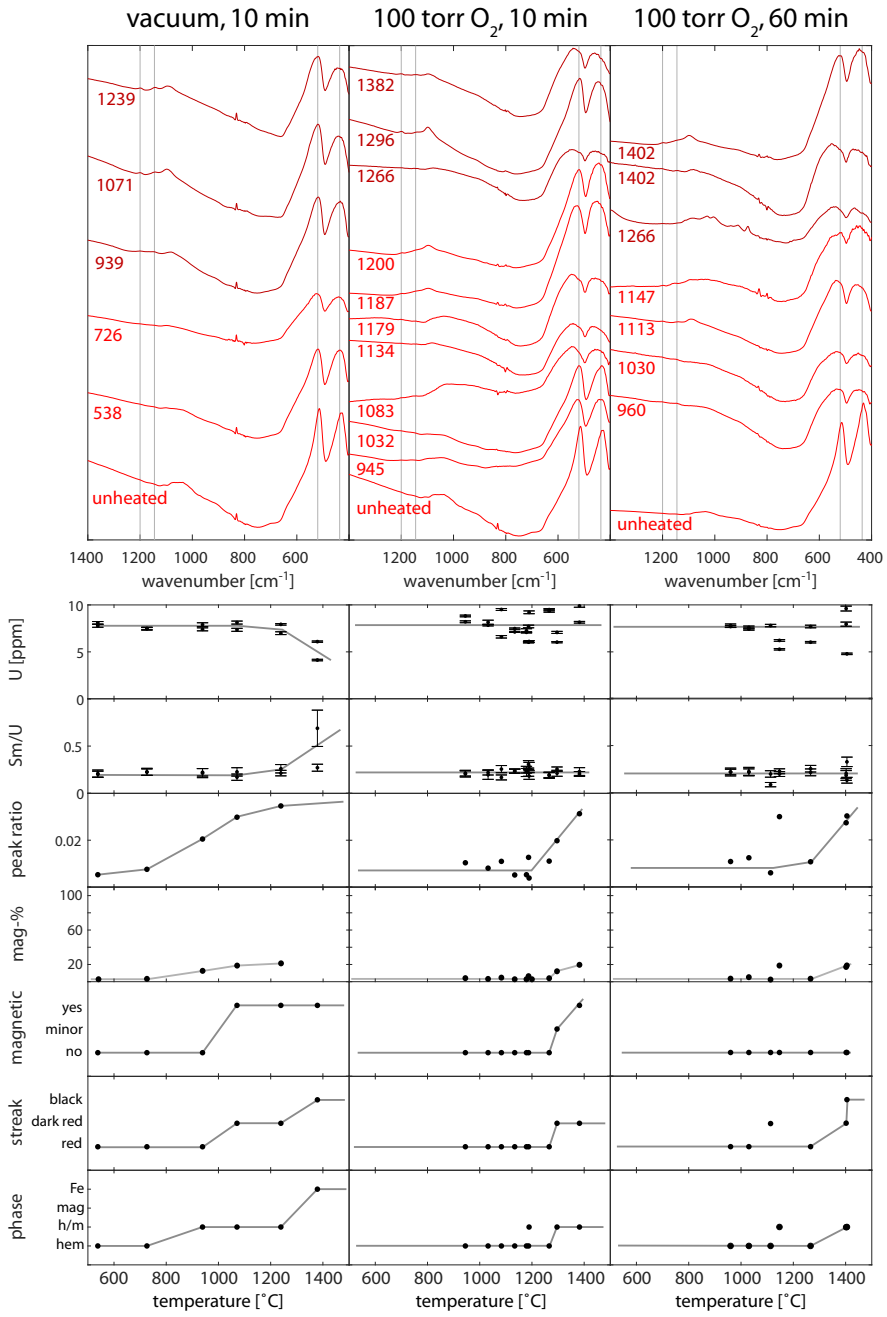

Figure 4.29: ATR spectra of hematite sample MS, heated to different temperatures in vacuum for 10 min and in 100 torr of O_2 for 10 min and 60 min. Estimated magnetite percentage (mag-%) was determined from peak ratio.

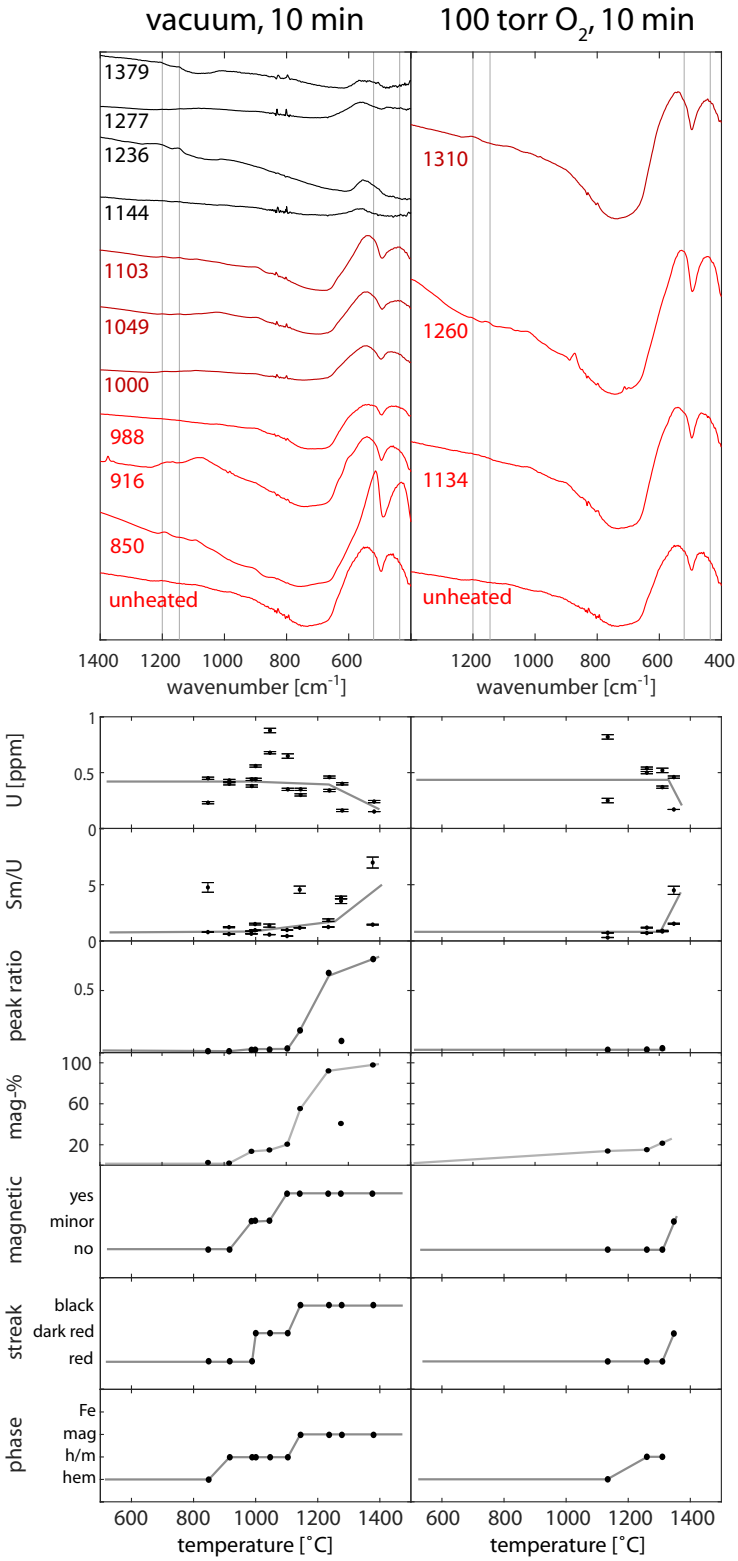

Figure 4.30: ATR spectra of hematite sample HM1, heated to different temperatures for 10 min in vacuum and 100 torr of O_2. Estimated magnetite percentage (mag-%) was determined from peak ratio.

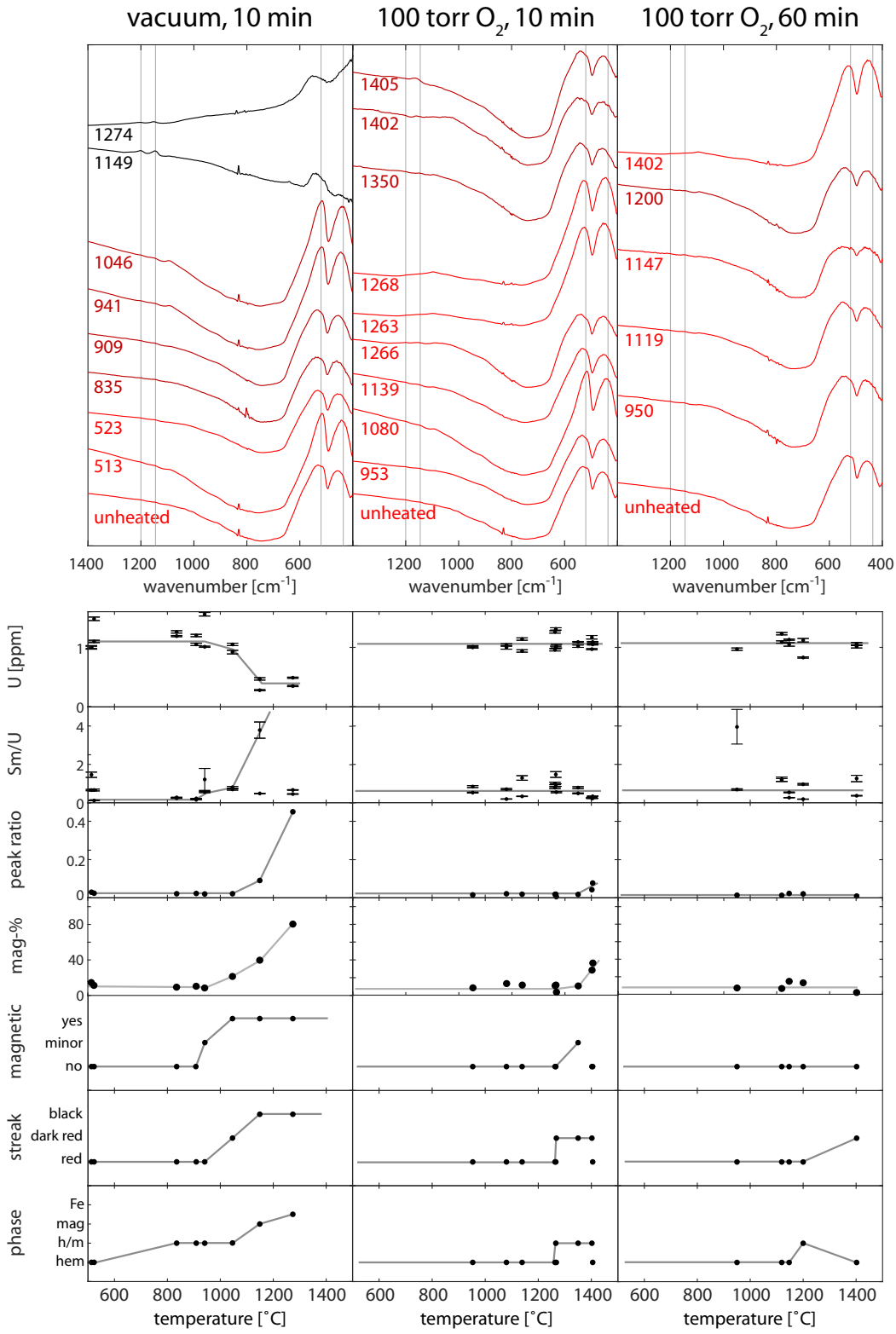

Figure 4.31: ATR spectra of hematite sample HM2, heated to different temperatures in vacuum for 10 min and in 100 torr of O_2 for 10 min and 60 min. Estimated magnetite percentage (mag-%) was determined from peak ratio.

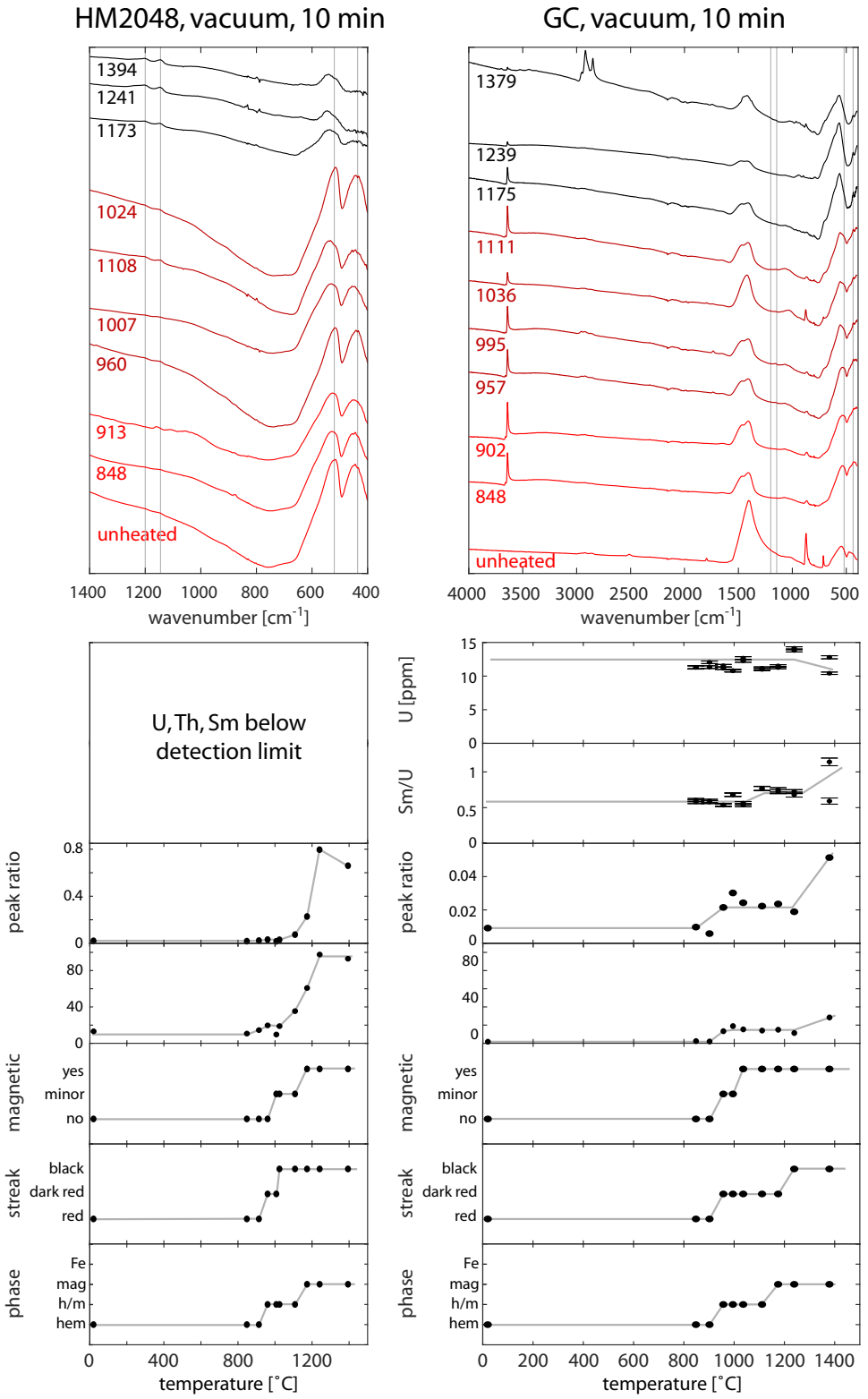

Figure 4.32: ATR spectra of hematite samples HM2048 and GC, heated to different temperatures in vacuum for 10 min. U concentrations of HM2048 were determined, but were <0.1 ppm and below the detection limit.

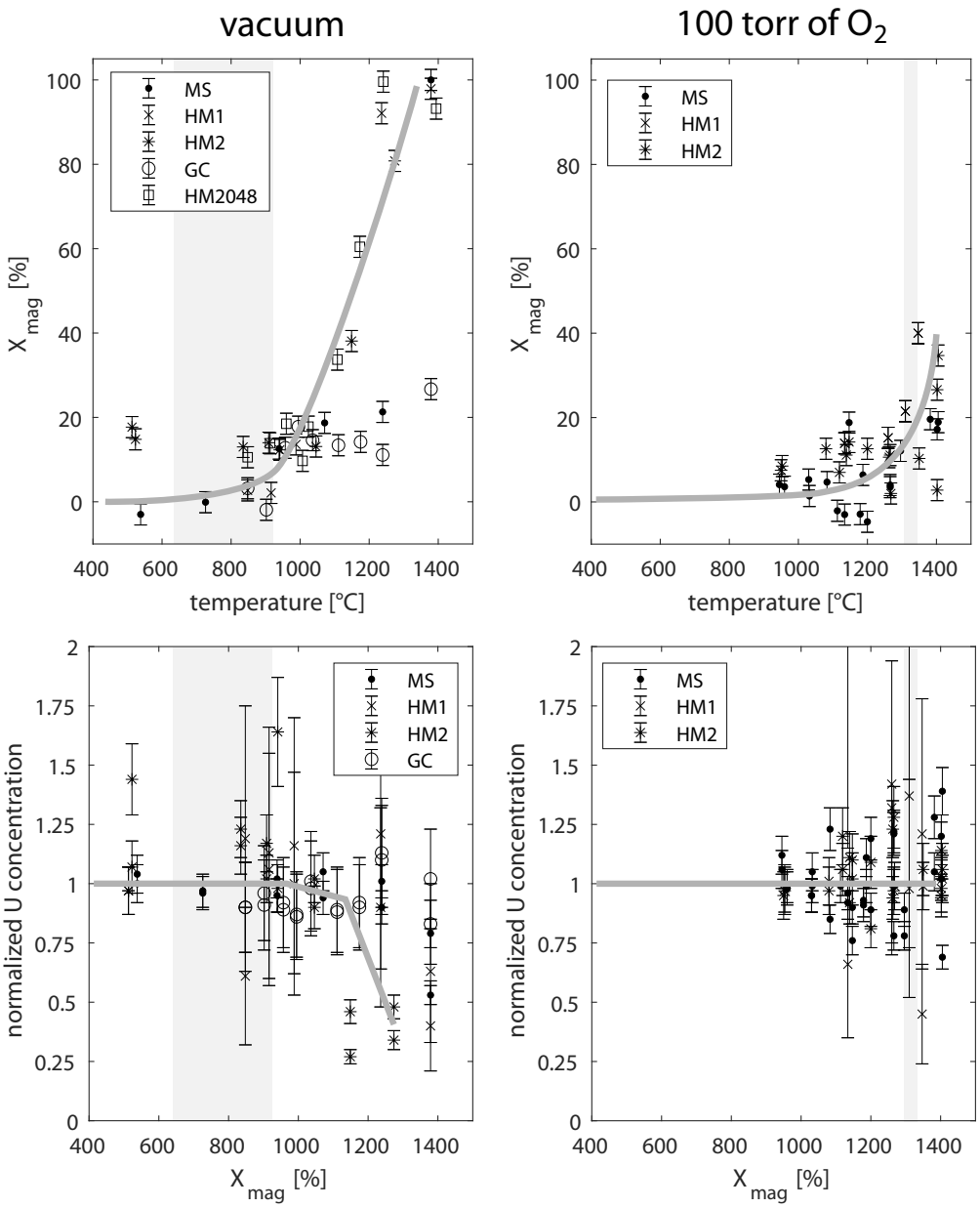

Figure 4.33: Summary of all hematite ATR-FTIR experiments. Magnetite percentage (top) and U concentration (bottom) as a function of temperature for both vacuum (left) and 100 torr of O_2 (right). Massive U loss correlates with major conversion of hematite to magnetite. Shaded region is temperature range of hematite-magnetite transition from phase diagram of Ketteler et al. (2001) based on measured and estimated oxygen partial pressures.

Goethite samples

Unheated goethite samples show a clear goethite signature in ATR-FTIR spectra (Figs. 4.34, 4.35, 4.36). Dehydroxylation of goethite occurs at 180-300 °C (Prasad et al., 2006; Ruan et al., 2001), leading to a conversion of the sample to hematite. There is a proposed, partially dehydrated intermediate phase between goethite and hematite termed 'proto-hematite' or 'hydrohematite' (Wolska, 1981), which has been reported in some studies (e.g. Gualtieri and Venturelli, 1999). Other studies have reported direct transition from goethite to hematite (e.g. Ruan et al., 2001). The kinetics of the goethite-hematite transition might be grain-size dependent (Prasad et al., 2006) and the exact mechanism of conversion remains a highly debated problem. However, goethite is fully converted to hematite at 800-1050 °C (Prasad et al., 2006), which is the relevant range of degassing temperatures for (U-Th)/He dating.

Goethite samples heated to above 500 °C were observed to be mainly composed of hematite (Figs. 4.34, 4.35), but many show small peaks at 795 cm^{-1} and 899 cm^{-1}, which indicate the presence of hydroxyl groups Ruan et al., 2001. Remnant hydroxyl bands are more apparent in spectra of samples heated in oxygen than in those heated in vacuum, suggesting that the transition from goethite to hematite is also retarded by high pO_2.

In vacuum, the conversion of hematite to magnetite of samples that were initially goethite occurs between 900 °C and 1200 °C. U loss also occurs in this temperature range (Fig. 4.37), with many aliquots experiencing 50-100% U loss at temperatures >1150 C. In ~100 torr pO_2, major conversion from hematite to magnetite was observed at >1200 °C, with coincides with massive U loss. The phase transition occured at temperatures below those predicted by the phase diagram of Ketteler et al. (2001).

In goethite samples, the peaks characteristic of the magnetite spectrum diminished at temperatures between 1200 °C and 1350 °C (Figs. 4.34, 4.35, and 4.36). We

interpret this as evidence of conversion of the sample to elemental iron. Based on the phase diagram of Ketteler et al., 2001, this is expected at around 1080-1350 °C in vacuum (depending on the exact pO_2), and 1520 °C at 100 torr. Since the preceding hematite-magnetite conversion has lead to the release of O_2, build-up of oxygen partial pressures up to 0.01-0.1 mbar are possible, which would delay the magnetite-Fe transition to higher temperatures.

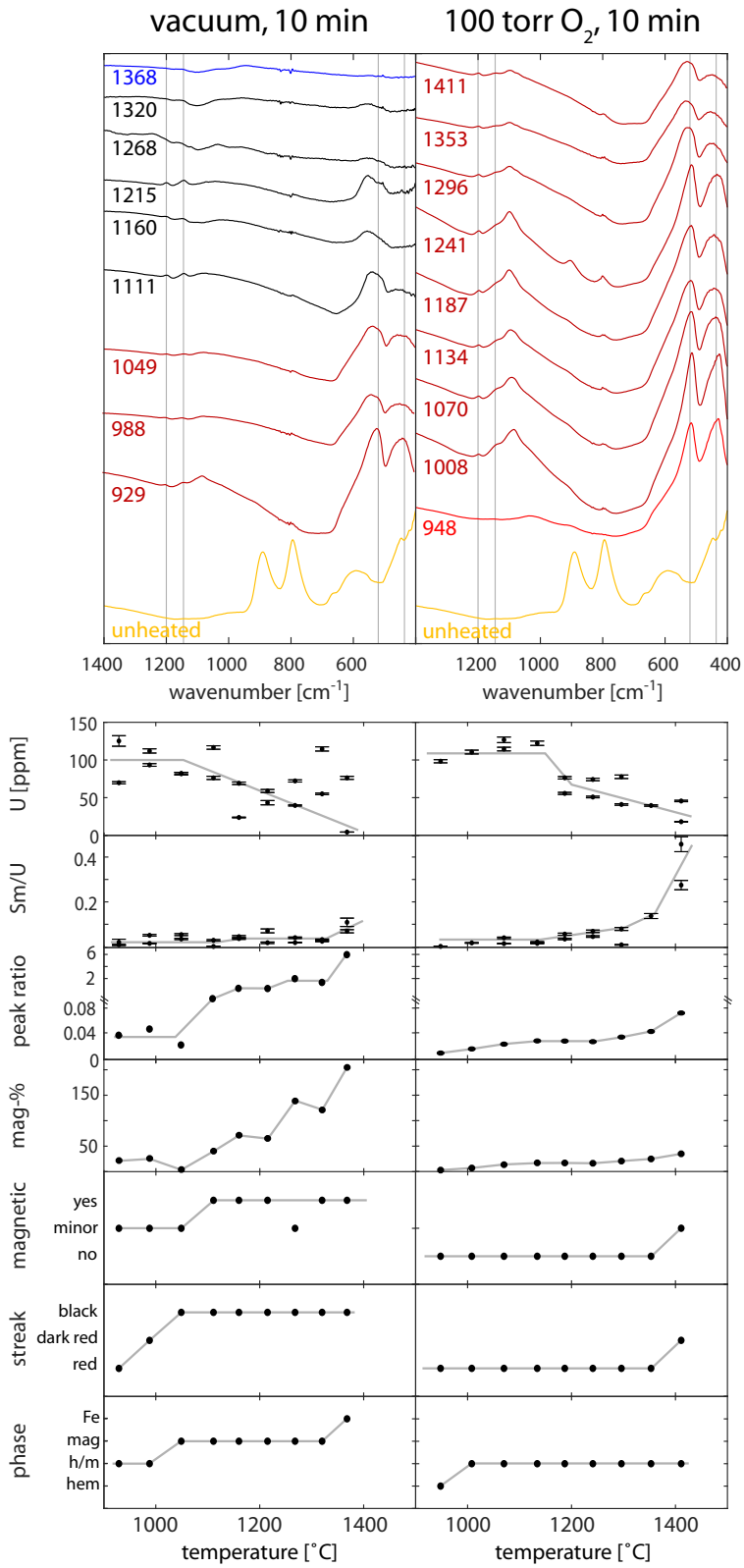

Figure 4.34: ATR spectra of goethite sample CIT, heated to different temperatures for 10 min in vacuum and in 100 torr of O_2.

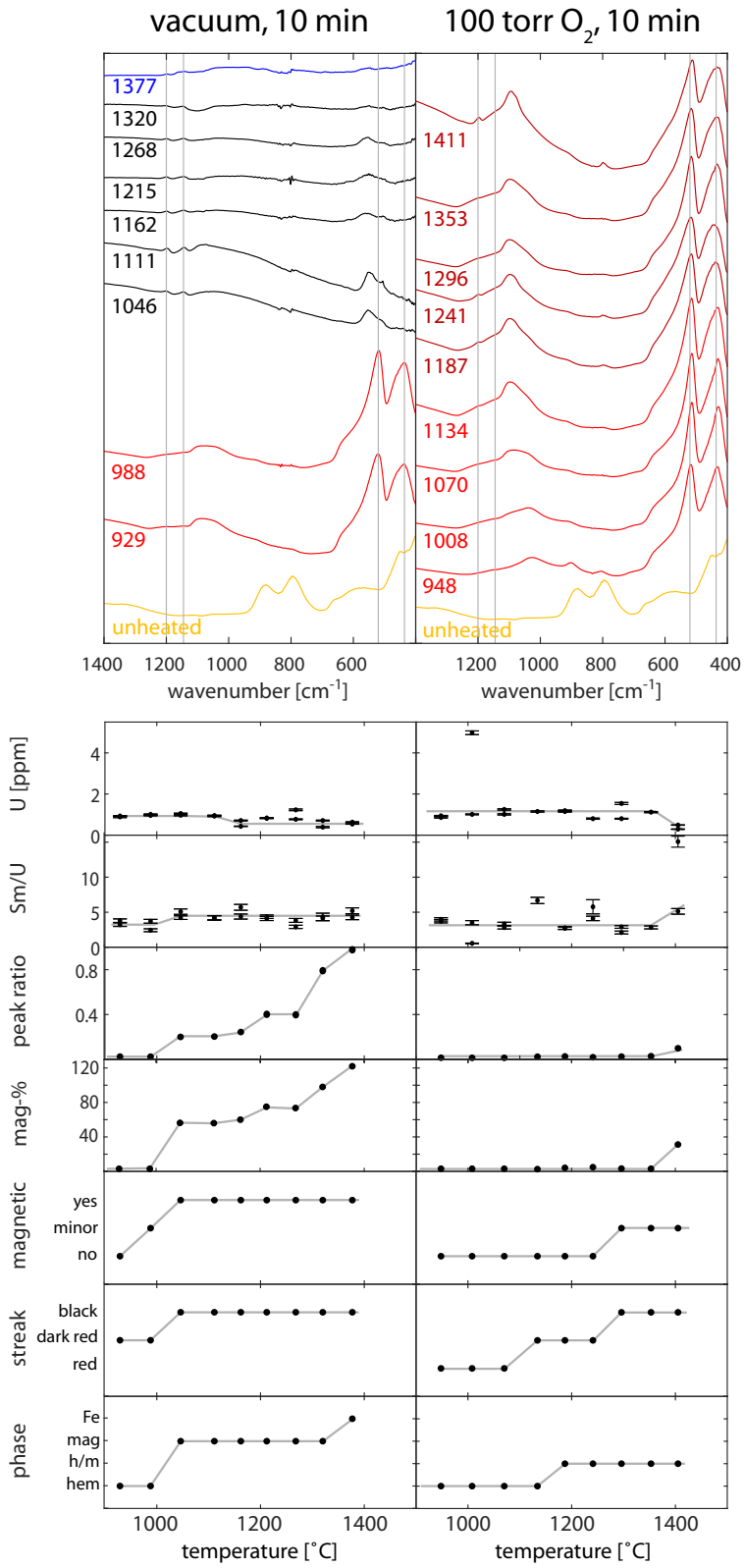

Figure 4.35: ATR spectra of goethite sample RH, heated to different temperatures for 10 min in vacuum and in 100 torr of O_2.

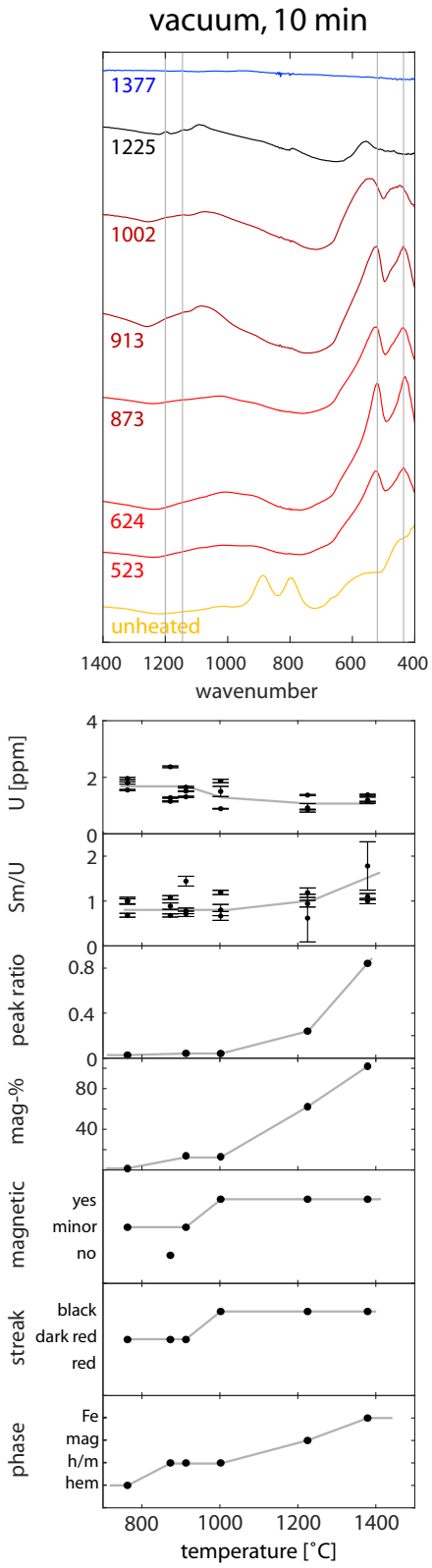

Figure 4.36: ATR spectra of goethite sample YAN, heated to different temperatures in vacuum for 10 min.

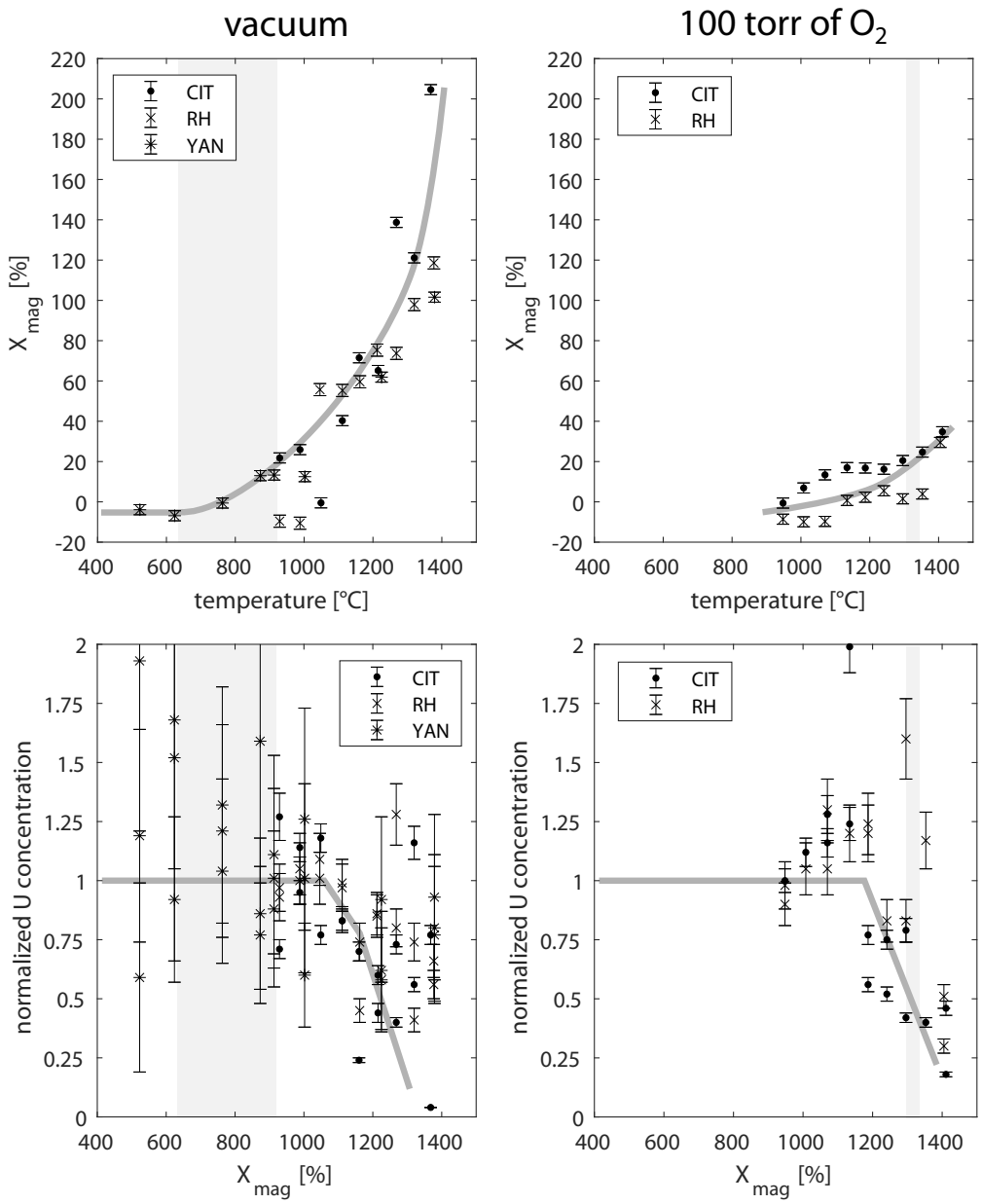

Figure 4.37: Summary of all goethite ATR-FTIR experiments. Magnetite percentage (top) and U concentration (bottom) as a function of temperature for both vacuum (left) and 100 torr of O_2 (right). Massive U loss correlates with major conversion of hematite to magnetite. Shaded region is temperature range of hematite-magnetite transition from phase diagram of Ketteler et al. (2001) based on measured and estimated oxygen partial pressures. Grey lines show general trends.

U loss and magnetite percentage

To investigate generals trends of U loss with increasing conversion of hematite to magnetite, we normalized U concentrations from aliquots of bulk heating experiments by the U concentration of the sample, which was determined from at least 20 undegassed aliquots. The natural variability of U concentration in samples was taken into account in the calculation of the uncertainty of normalized U concentration. Large uncertainties in normalized U concentrations are mostly due to high variability of U concentration in undegassed samples.

Four different hematite samples degassed in vacuum and three in 100 torr of O_2 show no detectable U loss up to a magnetite percentage of ~20% (Fig. 4.38). Only two samples showed major conversion to magnetite and associated massive U loss. From this data, U loss of 50-75% occurs between 30% and 40% magnetite and remains constant at higher magnetite percentage. Conversion of hematite to magnetite is retarded in O_2 relative to vacuum and there is no associated massive U loss up to 40%. Only one sample heated in O_2 shows conversion to magnetite and contains the only aliquot with detectable U loss.

Goethite U concentrations are generally more variable than those of hematite, but the data shows the same trends (Fig. 4.39), with U loss in vacuum occurring between 20% and 40% conversion of hematite to magnetite. Heating goethite samples in O_2 lead to massive U loss at 15-40%, initiating at lower magnetite conversion percentages than in hematite. Massive U loss in both goethite and hematite occurs between 20% and 40%. This is similar for heating in vacuum and O_2. Smaller amounts of U might be lost at lower magnetite percentages, but cannot be detected due to the natural variability of U concentration in hematite and goethite samples. The temperature at which the conversion from hematite to magnetite takes place varies slightly between individual samples. Goethites go through this transition at lower temperatures than hematites. This might be due to the fine-grained nature

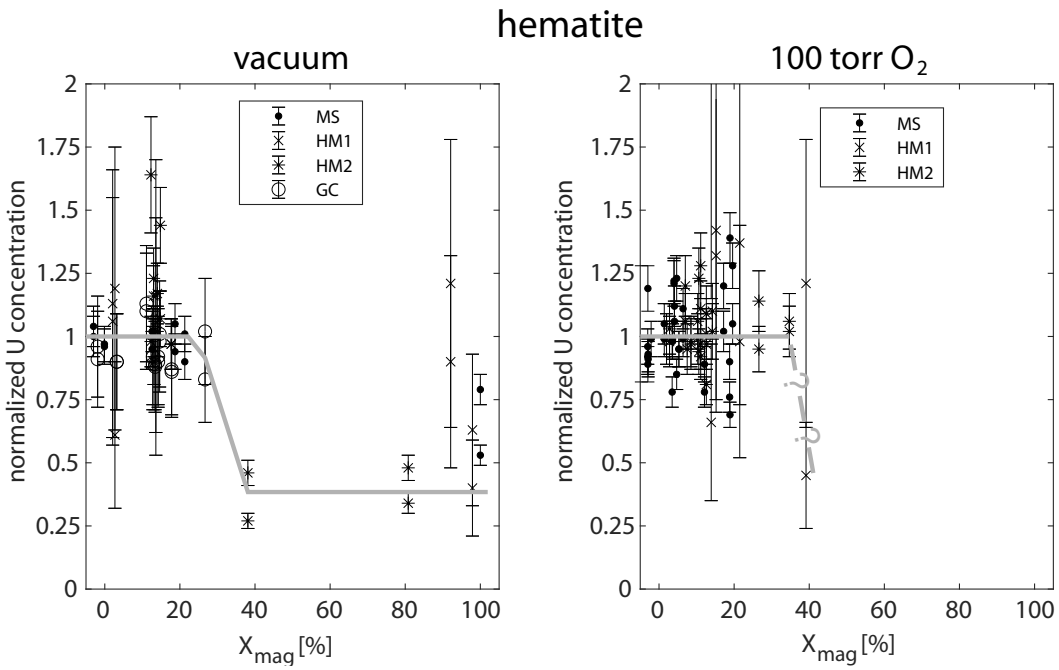

Figure 4.38: U concentration of four hematite samples normalized by average of undegassed aliquots plotted against estimated percent of hematite converted to magnetite.

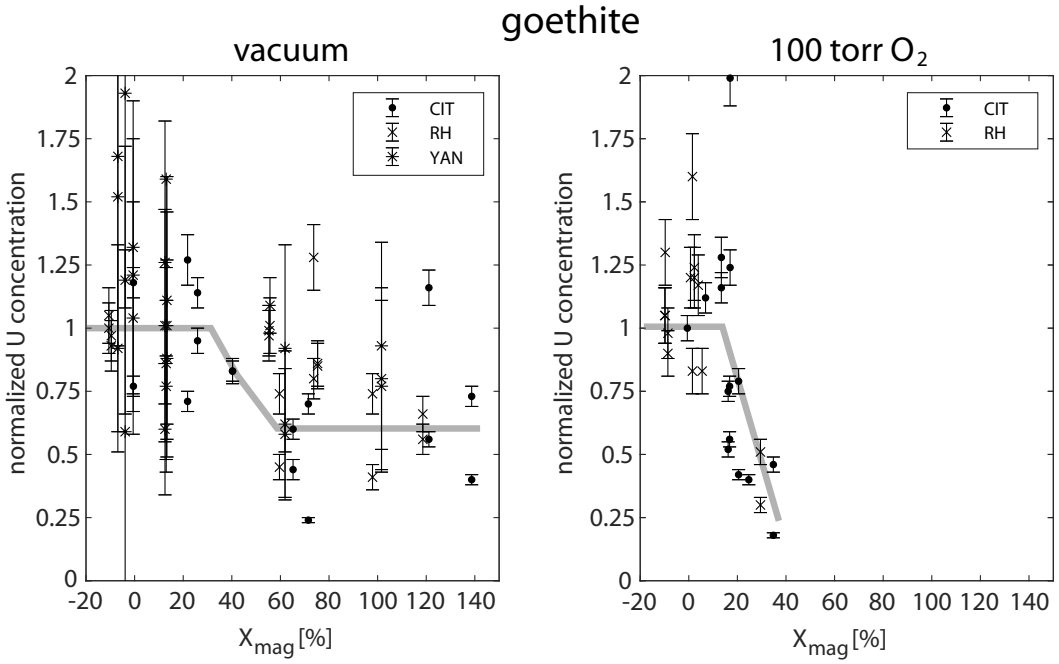

Figure 4.39: U concentration of four different hematite samples normalized by average U concentration of undegassed aliquots plotted against estimated percent of hematite converted to magnetite.

of supergene goethite samples. Another contributing factor might be preceding phase change from goethite to hematite, which might influence the kinetics of the hematite-magnetite transition.

Physical parameters to test for hematite-magnetite conversion

Every sample packet was checked for being magnetic before opening. A subjective measure of the response of the packet to a weak hand magnet through the bottom of a glass Petri dish was recorded. We distinguished between no response ('no'), weak response ('minor'), and strong response ('yes'). In both hematite and goethite samples, a switch from no response to minor or strong response was observed at around 20% magnetite conversion. This also corresponds to the magnetite fraction above which major U loss was observed. Testing the response of packets to a weak magnet could be used as a non-destructive screening tool to detect major conversion of hematite to magnetite in (U-Th)/He samples after degassing.

A change in streak color of the sample from red to dark red or black also indicates phase change. This destructive test can be used to test for phase change without the need for spectroscopic phase determination before actual sample analysis.

4.E Data of undegassed aliquots

Given here are replicate analyses of 10-45 undegassed aliquots each of five hematite samples (Tabs. 4.11-4.15) and three goethite samples (Tabs. 4.16-4.19) used in this study. Hematite/goethite mass have been determined stoichiometrically from the amount of Fe. Some aliquots had trace element concentrations below the detection limit (bdl).

Table 4.11: Replicate analyses of undegassed aliquots of hematite sample HM1 (n=45).

mass	1σ	U	1σ	Th	1σ	Sm	1σ	U	1σ	Th	1σ	Sm	1σ	Th/U	1σ	Sm/U	1σ
[µg]		[ng]		[ng]		[ng]		[ppm]		[ppm]		[ppm]					
26.05	0.50	0.013	0.000	0.022	0.001	0.024	0.002	0.50	0.02	0.84	0.06	0.92	0.09	1.69	0.08	1.85	0.15
30.55	0.61	0.019	0.000	0.027	0.001	0.014	0.002	0.62	0.02	0.88	0.05	0.46	0.06	1.42	0.05	0.74	0.11
38.55	0.92	0.023	0.001	0.030	0.001	0.019	0.003	0.60	0.02	0.78	0.04	0.49	0.08	1.30	0.07	0.83	0.14
40.89	0.82	0.021	0.000	0.028	0.001	0.057	0.005	0.51	0.02	0.68	0.04	1.39	0.13	1.33	0.05	2.71	0.24
40.14	0.59	0.015	0.000	0.033	0.001	0.008	0.001	0.37	0.01	0.82	0.03	0.20	0.03	2.20	0.07	0.53	0.07
43.29	0.67	0.021	0.000	0.020	0.001	0.017	0.002	0.49	0.01	0.46	0.02	0.39	0.04	0.95	0.05	0.81	0.10
45.33	0.73	0.011	0.000	0.022	0.001	0.009	0.002	0.24	0.01	0.49	0.02	0.20	0.04	2.00	0.09	0.82	0.18
57.55	0.90	0.030	0.000	0.033	0.001	0.076	0.004	0.52	0.01	0.57	0.02	1.32	0.08	1.10	0.03	2.53	0.13
98.31	0.99	0.076	0.001	0.091	0.003	0.047	0.004	0.77	0.01	0.93	0.03	0.48	0.04	1.20	0.04	0.62	0.05
109.09	0.94	0.062	0.001	0.103	0.002	0.057	0.005	0.57	0.01	0.94	0.02	0.52	0.05	1.66	0.04	0.92	0.08
104.74	1.02	0.066	0.001	0.110	0.002	0.165	0.012	0.63	0.01	1.05	0.03	1.58	0.12	1.67	0.04	2.50	0.19
116.26	0.97	0.075	0.001	0.108	0.002	0.039	0.006	0.65	0.01	0.93	0.02	0.34	0.05	1.44	0.03	0.52	0.08
107.91	1.64	0.097	0.002	0.083	0.003	0.010	0.006	0.90	0.02	0.77	0.03	0.09	0.05	0.86	0.04	0.10	0.06
131.31	1.06	0.076	0.001	0.135	0.002	0.085	0.008	0.58	0.01	1.03	0.02	0.65	0.06	1.78	0.04	1.12	0.11
497.28	3.03	0.132	0.001	0.223	0.002	0.200	0.014	0.27	0.00	0.45	0.01	0.40	0.03	1.69	0.02	1.52	0.11
165.07	1.59	0.123	0.001	0.168	0.002	0.073	0.005	0.74	0.01	1.02	0.02	0.44	0.03	1.37	0.02	0.59	0.04
178.69	2.50	0.066	0.001	0.103	0.001	0.073	0.006	0.37	0.01	0.58	0.01	0.41	0.03	1.56	0.03	1.11	0.09
117.90	1.70	0.071	0.001	0.114	0.002	0.052	0.004	0.60	0.01	0.96	0.02	0.44	0.03	1.61	0.04	0.73	0.06
397.01	1.96	0.355	0.002	0.393	0.001	0.205	0.007	0.89	0.01	0.99	0.01	0.52	0.02	1.11	0.01	0.58	0.02
312.56	3.76	0.092	0.001	0.171	0.002	0.234	0.016	0.30	0.00	0.55	0.01	0.75	0.05	1.86	0.03	2.54	0.18
270.82	2.19	0.134	0.002	0.168	0.002	0.112	0.007	0.49	0.01	0.62	0.01	0.41	0.03	1.25	0.02	0.84	0.05
529.08	3.67	0.238	0.002	0.329	0.003	0.244	0.016	0.45	0.00	0.62	0.01	0.46	0.03	1.38	0.02	1.03	0.07
73.65	0.85	0.029	0.001	0.040	0.001	0.040	0.004	0.40	0.01	0.54	0.02	0.55	0.05	1.38	0.06	1.38	0.15
191.40	2.14	0.047	0.000	0.132	0.002	0.067	0.006	0.25	0.00	0.69	0.01	0.35	0.03	2.81	0.04	1.43	0.13
194.08	4.36	0.042	0.001	0.135	0.040	0.115	0.081	0.22	0.01	0.70	0.21	0.59	0.42	3.21	0.96	2.74	1.93
770.19	8.97	0.226	0.002	0.347	0.003	0.235	0.011	0.29	0.00	0.45	0.01	0.31	0.05	1.54	0.02	1.04	0.05
117.02	0.98	0.056	0.001	0.066	0.002	0.067	0.005	0.48	0.01	0.56	0.01	0.57	0.04	1.18	0.04	1.20	0.09
264.46	3.84	0.125	0.001	0.152	0.002	0.065	0.005	0.47	0.01	0.58	0.01	0.25	0.02	1.22	0.02	0.52	0.04
359.20	3.51	0.121	0.001	0.160	0.002	0.132	0.008	0.34	0.00	0.45	0.01	0.37	0.02	1.32	0.02	1.09	0.07
93.19	1.43	0.033	0.001	0.059	0.001	0.029	0.003	0.36	0.01	0.63	0.02	0.32	0.08	1.79	0.06	0.88	0.09
334.79	3.27	0.163	0.002	0.216	0.003	0.193	0.012	0.49	0.01	0.65	0.01	0.58	0.03	1.33	0.02	1.18	0.08
175.30	1.32	0.086	0.001	0.144	0.001	0.058	0.007	0.49	0.01	0.82	0.01	0.33	0.04	1.67	0.02	0.67	0.08
81.44	0.60	0.043	0.001	0.056	0.001	0.051	0.003	0.53	0.02	0.69	0.01	0.62	0.04	1.30	0.04	1.19	0.08
98.10	0.57	0.037	0.000	0.044	0.001	0.051	0.003	0.38	0.01	0.45	0.01	0.51	0.03	1.19	0.03	1.38	0.08
235.53	1.93	0.091	0.001	0.154	0.002	0.076	0.005	0.39	0.00	0.65	0.01	0.32	0.02	1.69	0.03	0.84	0.06
217.20	2.21	0.088	0.001	0.134	0.002	0.074	0.006	0.40	0.01	0.62	0.01	0.34	0.01	1.52	0.03	0.84	0.07
51.48	0.54	0.014	0.001	0.023	0.003	0.033	0.003	0.28	0.02	0.44	0.07	0.63	0.04	1.64	0.24	2.36	0.27
119.75	0.93	0.031	0.000	0.073	0.002	0.021	0.003	0.26	0.00	0.61	0.01	0.18	0.02	2.35	0.06	0.68	0.10
154.96	2.35	0.061	0.001	0.077	0.002	0.042	0.003	0.39	0.01	0.50	0.01	0.27	0.10	1.26	0.04	0.69	0.05
88.31	0.68	0.038	0.001	0.047	0.001	0.020	0.003	0.43	0.01	0.53	0.01	0.22	0.03	1.24	0.04	0.53	0.08
143.91	1.41	0.054	0.001	0.085	0.002	0.032	0.003	0.37	0.01	0.59	0.02	0.23	0.02	1.57	0.05	0.59	0.06
523.03	5.12	0.200	0.002	0.323	0.003	0.760	0.042	0.38	0.01	0.62	0.01	1.45	0.08	1.62	0.02	3.80	0.21
27.01	0.36	0.015	0.000	0.022	0.001	0.016	0.001	0.57	0.02	0.82	0.05	0.60	0.05	1.47	0.07	1.07	0.07
298.54	2.64	0.135	0.002	0.200	0.003	0.086	0.004	0.45	0.01	0.67	0.01	0.29	0.02	1.48	0.03	0.64	0.03
71.39	0.63	0.022	0.000	0.030	0.001	0.013	0.002	0.31	0.01	0.42	0.02	0.18	0.03	1.36	0.05	0.59	0.09

Table 4.12: Replicate analyses of undegassed aliquots of hematite sample HM2 (n=39).

mass	1σ	U	1σ	Th	1σ	Sm	1σ	U	1σ	Th	1σ	Sm	1σ	Th/U	1σ	Sm/U	1σ
[μg]		[ng]		[ng]		[ng]		[ppm]		[ppm]		[ppm]					
28.61	0.4	0.038	0.001	0.043	0.001	0.040	0.003	1.33	0.04	1.50	0.05	1.40	0.10	1.13	0.04	1.05	0.08
121.62	0.7	0.149	0.002	0.231	0.002	0.158	0.007	1.23	0.02	1.90	0.02	1.30	0.05	1.55	0.02	1.06	0.05
189.3	1.77	0.218	0.002	0.153	0.002	0.070	0.004	1.15	0.01	0.81	0.01	0.37	0.02	0.70	0.01	0.32	0.02
118.31	0.76	0.130	0.001	0.109	0.001	0.030	0.003	1.10	0.01	0.92	0.01	0.25	0.03	0.84	0.01	0.23	0.02
136.34	2.71	0.092	0.003	0.266	0.007	0.176	0.008	0.67	0.02	1.95	0.07	1.29	0.06	2.89	0.12	1.91	0.11
87.20	2.97	0.133	0.002	0.207	0.009	0.171	0.009	1.53	0.06	2.37	0.13	1.97	0.12	1.56	0.07	1.29	0.07
119.65	1.89	0.200	0.003	0.129	0.008	0.079	0.006	1.67	0.04	1.08	0.07	0.66	0.05	0.65	0.04	0.40	0.03
77.32	1.82	0.114	0.004	0.067	0.007	0.038	0.005	1.47	0.06	0.87	0.10	0.49	0.07	0.59	0.06	0.33	0.05
250.18	2.36	0.276	0.003	0.192	0.002	0.086	0.004	1.10	0.01	0.77	0.01	0.34	0.16	0.70	0.01	0.31	0.01
303.15	2.33	0.296	0.002	0.551	0.004	0.308	0.015	0.98	0.01	1.82	0.02	1.02	0.04	1.86	0.02	1.04	0.05
413.15	3.69	0.444	0.004	0.676	0.005	0.397	0.020	1.07	0.01	1.64	0.02	0.96	0.05	1.52	0.02	0.89	0.05
69.19	0.57	0.063	0.001	0.047	0.001	0.024	0.003	0.91	0.01	0.68	0.02	0.34	0.04	0.75	0.02	0.38	0.05
106.16	0.86	0.100	0.001	0.060	0.002	0.018	0.003	0.94	0.01	0.56	0.02	0.17	0.76	0.60	0.02	0.18	0.03
196.22	7.44	0.239	0.057	0.215	0.006	0.132	0.016	1.22	0.29	1.10	0.05	0.67	0.06	0.90	0.22	0.55	0.15
101.92	0.87	0.099	0.001	0.111	0.002	0.075	0.005	0.97	0.02	1.08	0.02	0.73	0.05	1.12	0.02	0.76	0.05
79.41	0.94	0.075	0.001	0.072	0.002	0.019	0.002	0.94	0.01	0.91	0.03	0.24	0.04	0.96	0.03	0.25	0.03
187.12	1.25	0.189	0.002	0.429	0.424	0.065	0.039	1.01	0.01	2.29	2.26	0.35	0.21	2.27	2.24	0.34	0.21
61.22	0.62	0.056	0.001	0.206	0.002	0.014	0.002	0.92	0.02	3.37	0.04	0.22	0.03	3.68	0.07	0.25	0.04
157.05	1.57	0.204	0.001	0.211	0.002	0.142	0.008	1.30	0.02	1.34	0.02	0.90	0.03	1.03	0.01	0.70	0.04
385.06	3.19	0.411	0.003	0.236	0.003	0.090	0.006	1.07	0.01	0.61	0.01	0.23	0.63	0.57	0.01	0.22	0.01
155.74	1.20	0.143	0.001	0.186	0.001	0.113	0.005	0.92	0.01	1.19	0.01	0.73	0.03	1.30	0.01	0.79	0.04
210.93	1.46	0.219	0.002	0.172	0.002	0.036	0.002	1.04	0.01	0.82	0.01	0.17	0.03	0.79	0.01	0.16	0.01
93.84	1.15	0.090	0.001	0.077	0.001	0.040	0.004	0.96	0.02	0.82	0.02	0.42	0.02	0.86	0.01	0.44	0.04
83.21	0.52	0.096	0.007	0.081	0.024	0.017	0.002	1.15	0.08	0.98	0.29	0.21	0.03	0.84	0.26	0.18	0.02
109.27	1.19	0.112	0.001	0.147	0.001	0.075	0.006	1.02	0.01	1.35	0.02	0.69	0.06	1.31	0.01	0.67	0.05
130.51	1.78	0.153	0.002	0.159	0.002	0.108	0.008	1.17	0.02	1.21	0.02	0.83	0.03	1.04	0.02	0.71	0.05
145.00	1.24	0.134	0.002	0.118	0.001	0.055	0.004	0.92	0.01	0.81	0.01	0.38	0.02	0.88	0.02	0.41	0.03
170.45	17.40	0.190	0.148	0.122	0.011	0.062	0.016	1.12	0.88	0.72	0.10	0.36	0.04	0.64	0.50	0.33	0.27
479.78	4.18	0.531	0.003	0.446	0.004	0.182	0.010	1.11	0.01	0.93	0.01	0.38	0.02	0.84	0.01	0.34	0.02
399.66	4.26	0.416	0.004	0.245	0.003	0.070	0.005	1.04	0.02	0.61	0.01	0.17	0.05	0.59	0.01	0.17	0.01
276.20	1.84	0.271	0.002	0.289	0.003	0.132	0.009	0.98	0.01	1.05	0.01	0.48	0.05	1.07	0.01	0.49	0.03
269.41	1.99	0.274	0.003	0.176	0.001	0.065	0.005	1.02	0.01	0.65	0.01	0.24	0.04	0.64	0.01	0.24	0.02
79.44	0.80	0.071	0.001	0.065	0.001	0.018	0.002	0.90	0.02	0.81	0.02	0.23	0.03	0.92	0.02	0.25	0.03
102.52	0.48	0.103	0.000	0.082	0.001	0.019	0.001	1.00	0.01	0.80	0.01	0.18	0.01	0.80	0.01	0.18	0.01
459.61	5.11	0.483	0.005	0.485	0.006	0.347	0.021	1.05	0.02	1.06	0.02	0.76	0.05	1.00	0.02	0.72	0.04
189.88	2.40	0.198	0.002	0.429	0.006	0.261	0.013	1.05	0.02	2.26	0.04	1.37	0.07	2.17	0.04	1.32	0.07
60.58	0.54	0.068	0.001	0.113	0.002	0.067	0.004	1.12	0.02	1.87	0.03	1.10	0.07	1.66	0.04	0.99	0.06
183.35	2.02	0.212	0.003	0.226	0.003	0.119	0.008	1.15	0.02	1.23	0.02	0.65	0.05	1.07	0.02	0.56	0.04
279.27	2.67	0.336	0.002	0.095	0.002	0.041	0.004	1.20	0.01	0.34	0.01	0.15	0.01	0.28	0.01	0.12	0.01

Table 4.13: Replicate analyses of undegassed aliquots of hematite sample MS (n=38); bdl = below detection limit.

mass	1σ	U	1σ	Th	1σ	Sm	1σ	U	1σ	Th	1σ	Sm	1σ	Th/U	1σ	Sm/U	1σ
[µg]		[ng]		[ng]		[ng]		[ppm]		[ppm]		[ppm]					
15.34	0.21	0.120	0.002	bdl		0.026	0.003	7.56	0.16	bdl		1.69	0.17	<0.001		0.217	0.025
113.92	1.62	0.990	0.008	0.004	0.001	0.218	0.013	8.66	0.14	0.04	0.01	1.92	0.11	0.004	0.001	0.220	0.013
125.64	3.00	1.045	0.006	0.012	0.001	0.305	0.010	8.29	0.20	0.10	0.01	2.43	0.10	0.011	0.001	0.292	0.010
24.08	0.46	0.174	0.002	bdl		0.035	0.003	7.21	0.15	bdl		1.45	0.11	<0.001		0.201	0.017
36.93	0.59	0.236	0.001	0.014	0.001	0.054	0.004	6.40	0.11	0.38	0.03	1.46	0.12	0.059	0.004	0.229	0.017
56.33	0.52	0.363	0.003	bdl		0.066	0.005	6.44	0.08	bdl		1.17	0.10	<0.001		0.182	0.014
134.65	2.06	0.895	0.005	0.005	0.001	0.172	0.009	6.64	0.11	0.04	0.01	1.28	0.07	0.006	0.001	0.192	0.010
116.49	0.86	0.857	0.008	bdl		0.202	0.011	7.36	0.09	bdl		1.74	0.05	<0.001		0.236	0.013
149.82	1.97	1.208	0.006	bdl		0.233	0.015	8.06	0.11	bdl		1.56	0.39	<0.001		0.193	0.012
205.20	1.34	1.672	0.010	bdl		0.342	0.020	8.15	0.07	bdl		1.67	0.01	<0.001		0.205	0.012
45.44	0.47	0.360	0.003	bdl		0.073	0.005	7.92	0.11	bdl		1.61	0.04	<0.001		0.203	0.014
205.20	1.34	1.672	0.010	bdl		0.342	0.020	8.15	0.07	bdl		1.67	0.10	<0.001		0.205	0.012
256.55	3.50	2.047	0.012	0.002	0.001	0.423	0.029	7.98	0.12	0.01	0.00	1.65	0.03	0.001	0.000	0.207	0.014
68.59	0.74	0.539	0.004	bdl		0.108	0.008	7.86	0.10	bdl		1.57	0.02	<0.001		0.200	0.015
149.28	1.86	1.087	0.007	bdl		0.240	0.017	7.28	0.10	bdl		1.61	0.02	<0.001		0.221	0.016
68.95	0.91	0.528	0.003	bdl		0.113	0.009	7.66	0.11	bdl		1.64	1.79	<0.001		0.214	0.017
264.78	2.08	2.053	0.016	bdl		0.454	0.020	7.75	0.08	bdl		1.71	0.09	<0.001		0.221	0.010
308.17	3.05	2.617	0.016	0.008	0.001	0.492	0.024	8.49	0.10	0.03	0.00	1.60	0.07	0.003	0.000	0.188	0.009
225.30	1.58	1.667	0.013	bdl		0.369	0.019	7.40	0.08	bdl		1.64	0.10	<0.001		0.221	0.012
256.06	2.30	1.863	0.012	bdl		0.449	0.018	7.28	0.08	bdl		1.75	0.07	<0.001		0.241	0.010
78.26	0.77	0.582	0.003	bdl		0.123	0.010	7.43	0.08	bdl		1.57	0.13	<0.001		0.211	0.017
83.51	0.75	0.686	0.005	bdl		0.138	0.008	8.21	0.10	bdl		1.66	0.10	<0.001		0.201	0.012
91.50	1.03	0.769	0.004	0.003	0.000	0.164	0.014	8.41	0.10	0.03	0.01	1.80	0.11	0.004	0.000	0.213	0.018
201.46	24.05	1.734	0.104	0.007	0.010	0.323	0.017	8.60	1.15	0.03	0.05	1.61	0.21	0.004	0.006	0.186	0.015
137.50	1.54	1.070	0.006	bdl		0.221	0.014	7.78	0.10	bdl		1.60	0.12	<0.001		0.207	0.013
87.76	0.98	0.648	0.004	0.247	0.003	0.337	0.019	7.38	0.10	2.82	0.04	3.84	0.13	0.381	0.005	0.520	0.029
143.30	1.25	0.984	0.007	bdl		0.243	0.012	6.87	0.08	bdl		1.70	0.08	<0.001		0.247	0.012
95.53	0.76	0.771	0.006	bdl		0.154	0.008	8.07	0.09	bdl		1.61	0.08	<0.001		0.200	0.010
121.18	1.03	0.958	0.007	bdl		0.193	0.013	7.90	0.09	bdl		1.59	0.11	<0.001		0.201	0.014
101.89	0.61	0.820	0.006	bdl		0.158	0.009	8.05	0.07	bdl		1.55	0.09	<0.001		0.193	0.011
127.96	1.22	1.032	0.005	bdl		0.208	0.012	8.06	0.09	bdl		1.63	0.10	<0.001		0.202	0.012
142.68	2.01	1.044	0.006	bdl		0.231	0.016	7.32	0.11	bdl		1.62	0.12	<0.001		0.221	0.015
270.23	2.08	1.983	0.016	0.007	0.001	0.456	0.019	7.34	0.08	0.03	0.00	1.69	0.03	0.004	0.001	0.230	0.010
243.74	4.06	1.893	0.017	0.004	0.001	0.399	0.018	7.76	0.15	0.01	0.01	1.64	0.08	0.002	0.001	0.211	0.010
74.66	0.84	0.597	0.004	bdl		0.123	0.008	7.99	0.10	bdl		1.65	0.11	<0.001		0.206	0.013
320.40	4.51	2.652	0.017	0.007	0.001	0.547	0.021	8.28	0.13	0.02	0.00	1.71	0.07	0.003	0.000	0.206	0.008
630.18	6.67	5.112	0.029	bdl		1.094	0.042	8.11	0.10	bdl		1.74	0.07	<0.001		0.214	0.008
108.79	0.96	0.906	0.006	bdl		0.174	0.010	8.32	0.09	bdl		1.60	0.10	<0.001		0.192	0.011

Table 4.14: Replicate analyses of undegassed aliquots of hematite sample HM2048 (n=25); bdl = below detection limit.

mass	1σ	U	1σ	Th	1σ	Sm	1σ	U	1σ	Th	1σ	Sm	1σ	Th/U	1σ	Sm/U	1σ
[µg]		[ng]		[ng]		[ng]		[ppm]		[ppm]		[ppm]					
88.57	1.10	0.005	0.000	0.004	0.001	0.002	0.001	0.06	0.00	0.04	0.01	0.03	0.01	0.80	0.20	0.40	0.20
19.38	0.23	0.005	0.000	0.004	0.001	0.001	0.001	0.23	0.01	0.19	0.04	0.04	0.03	0.80	0.20	0.20	0.20
24.50	0.29	0.015	0.000	0.010	0.001	0.032	0.003	0.62	0.02	0.42	0.04	1.31	0.11	0.67	0.07	2.13	0.20
34.88	0.35	0.008	0.000	0.116	0.002	0.004	0.001	0.24	0.01	3.34	0.06	0.11	0.04	14.50	0.25	0.50	0.13
12.24	0.14	bdl		bdl		bdl		bdl		bdl		bdl		bdl		bdl	
17.56	0.22	bdl		bdl		bdl		bdl		bdl		bdl		bdl		bdl	
37.44	0.51	bdl		bdl		bdl		bdl		bdl		bdl		bdl		bdl	
39.79	0.54	bdl		bdl		bdl		bdl		bdl		bdl		bdl		bdl	
27.57	0.41	bdl		bdl		bdl		bdl		bdl		bdl		bdl		bdl	
18.50	0.21	bdl		bdl		bdl		bdl		bdl		bdl		bdl		bdl	
13.14	0.16	bdl		bdl		bdl		bdl		bdl		bdl		bdl		bdl	
58.25	0.61	bdl		bdl		bdl		bdl		bdl		bdl		bdl		bdl	
14.53	0.17	bdl		bdl		bdl		bdl		bdl		bdl		bdl		bdl	
65.37	0.87	bdl		bdl		bdl		bdl		bdl		bdl		bdl		bdl	
13.63	0.17	bdl		bdl		bdl		bdl		bdl		bdl		bdl		bdl	
31.20	0.35	0.008	0.000	bdl		bdl		bdl		bdl		bdl		<0.001		<0.001	
68.65	0.93	0.004	0.000	bdl		bdl		bdl		bdl		bdl		<0.001		<0.001	
79.15	1.11	0.012	0.000	0.048	0.001	0.005	0.001	0.15	0.00	0.61	0.01	0.07	0.01	4.00	0.08	0.42	0.08
42.15	0.58	bdl		bdl		bdl		bdl		bdl		bdl		bdl		bdl	
77.83	1.11	bdl		bdl		bdl		bdl		bdl		bdl		bdl		bdl	
105.56	1.26	bdl		bdl		bdl		bdl		bdl		bdl		bdl		bdl	
35.87	0.40	bdl		bdl		bdl		bdl		bdl		bdl		bdl		bdl	
40.26	0.49	bdl		bdl		bdl		bdl		bdl		bdl		bdl		bdl	
88.68	1.09	0.006	0.000	0.002	0.001	0.002	0.001	0.06	0.00	0.02	0.01	0.02	0.01	0.33	0.17	0.33	0.17
37.83	0.44	bdl		bdl		bdl		bdl		bdl		bdl		bdl		bdl	

Table 4.15: Replicate analyses of undegassed aliquots of hematite sample GC (n=25).

mass	1σ	U	1σ	Th	1σ	Sm	1σ	U	1σ	Th	1σ	Sm	1σ	Th/U	1σ	Sm/U	1σ
[µg]		[ng]		[ng]		[ng]		[ppm]		[ppm]		[ppm]					
74.77	1.14	0.889	0.005	0.454	0.003	0.127	0.006	11.89	0.19	6.08	0.10	1.69	0.09	0.511	0.004	0.143	0.007
32.92	0.40	0.371	0.002	0.216	0.002	0.088	0.006	11.28	0.15	6.56	0.09	2.67	0.17	0.582	0.006	0.237	0.016
37.61	0.58	0.599	0.005	0.297	0.002	0.065	0.003	15.94	0.29	7.89	0.13	1.73	0.09	0.496	0.005	0.109	0.005
21.42	0.24	0.282	0.002	0.180	0.001	0.091	0.005	13.17	0.18	8.39	0.11	4.25	0.23	0.638	0.006	0.323	0.018
16.60	0.18	0.215	0.001	0.121	0.001	0.065	0.004	12.95	0.15	7.31	0.10	3.89	0.22	0.563	0.005	0.302	0.019
28.53	0.34	0.409	0.003	0.242	0.002	0.104	0.006	14.32	0.19	8.49	0.12	3.65	0.21	0.592	0.007	0.254	0.015
42.04	0.43	0.621	0.004	0.372	0.002	0.154	0.008	14.76	0.18	8.84	0.11	3.67	0.18	0.599	0.005	0.248	0.013
42.09	0.45	0.534	0.004	0.299	0.002	0.098	0.004	12.69	0.17	7.11	0.09	2.33	0.11	0.560	0.006	0.184	0.008
48.65	0.62	0.687	0.004	0.279	0.002	0.122	0.005	14.12	0.20	5.74	0.08	2.50	0.11	0.406	0.004	0.178	0.007
10.12	0.12	0.116	0.001	0.042	0.001	0.036	0.003	11.43	0.17	4.14	0.12	3.51	0.34	0.362	0.009	0.310	0.026
10.96	0.11	0.105	0.001	0.179	0.001	0.012	0.001	9.62	0.13	16.35	0.20	1.08	0.12	1.705	0.019	0.114	0.010
42.88	0.39	0.161	0.001	0.336	0.003	0.015	0.002	3.76	0.05	7.84	0.10	0.35	0.05	2.087	0.023	0.093	0.012
39.16	0.38	0.561	0.003	0.318	0.002	0.132	0.006	14.32	0.16	8.13	0.10	3.38	0.17	0.567	0.005	0.235	0.011
19.18	0.18	0.227	0.002	0.107	0.001	0.045	0.002	11.82	0.14	5.59	0.09	2.37	0.13	0.471	0.006	0.198	0.009
42.77	0.50	0.294	0.002	0.550	0.003	0.026	0.002	6.88	0.09	12.85	0.17	0.61	0.04	1.871	0.016	0.088	0.007
20.34	0.19	0.230	0.002	0.103	0.002	0.043	0.003	11.31	0.13	5.08	0.10	2.13	0.14	0.448	0.010	0.187	0.013
11.61	0.10	0.126	0.001	0.063	0.001	0.023	0.002	10.87	0.13	5.43	0.09	1.99	0.18	0.500	0.009	0.183	0.016
46.14	0.41	0.635	0.005	0.338	0.003	0.084	0.005	13.76	0.16	7.32	0.09	1.83	0.12	0.532	0.006	0.132	0.008
36.14	0.32	0.501	0.004	0.277	0.002	0.105	0.005	13.88	0.17	7.68	0.09	2.91	0.13	0.553	0.006	0.210	0.010
17.20	0.17	0.236	0.001	0.133	0.001	0.054	0.003	13.71	0.16	7.74	0.11	3.15	0.19	0.564	0.005	0.229	0.013
20.15	0.17	0.236	0.002	0.141	0.001	0.050	0.003	11.72	0.14	6.98	0.09	2.47	0.14	0.597	0.007	0.212	0.013
30.54	0.28	0.407	0.004	0.212	0.002	0.055	0.004	13.34	0.17	6.96	0.09	1.79	0.12	0.521	0.007	0.135	0.010
37.95	0.39	0.448	0.003	0.264	0.003	0.093	0.005	11.81	0.15	6.96	0.10	2.45	0.13	0.589	0.008	0.208	0.011
35.52	0.37	0.466	0.004	0.264	0.003	0.145	0.008	13.11	0.17	7.43	0.11	4.08	0.22	0.567	0.008	0.311	0.017
26.23	0.31	0.284	0.002	0.140	0.002	0.068	0.004	10.84	0.15	5.32	0.10	2.58	0.17	0.493	0.008	0.239	0.014

Table 4.16: Replicate analyses of undegassed aliquots of goethite sample CIT (n=26); bdl = below detection limit.

mass	1σ	U	1σ	Th	1σ	Sm	1σ	U	1σ	Th	1σ	Sm	1σ	Th/U	1σ	Sm/U	1σ
[µg]		[ng]		[ng]		[ng]		[ppm]		[ppm]		[ppm]		10^{-4}			
223.62	8.73	23.393	0.269	bdl		0.289	0.012	104.61	4.26	0.01	0.01	1.29	0.07	<0.001		0.012	0.001
54.32	1.47	5.747	0.069	bdl		0.270	0.012	105.79	3.13	0.03	0.02	4.98	0.26	<0.001		0.047	0.002
100.84	3.22	9.628	0.095	bdl		0.470	0.020	95.48	3.19	0.01	0.01	4.66	0.24	<0.001		0.049	0.002
40.49	0.98	3.795	0.040	bdl		0.094	0.004	93.72	2.47	0.04	0.03	2.33	0.11	<0.001		0.025	0.001
174.83	5.13	18.400	0.184	bdl		0.301	0.012	105.25	3.26	0.01	0.01	1.72	0.08	<0.001		0.016	0.001
311.29	10.08	27.240	0.273	bdl		0.085	0.005	87.51	2.97	0.01	0.00	0.27	0.02	<0.001		0.003	0.000
315.29	21.56	34.083	0.327	bdl		1.114	0.050	108.10	7.46	0.00	0.00	3.53	0.29	<0.001		0.033	0.002
65.40	1.59	5.937	0.053	bdl		0.066	0.003	90.78	2.35	0.01	0.02	1.01	0.06	<0.001		0.011	0.001
291.24	15.59	14.429	0.263	0.006	0.003	0.072	0.022	49.54	2.80	0.02	0.01	0.25	0.08	4.2	2.1	0.005	0.002
78.86	2.74	7.311	0.082	bdl		0.028	0.002	92.71	3.38	0.01	0.01	0.35	0.03	<0.001		0.004	0.000
162.92	5.20	16.095	0.153	bdl		0.064	0.003	98.79	3.29	0.01	0.01	0.39	0.02	<0.001		0.004	0.000
48.40	1.28	4.716	0.043	bdl		0.133	0.007	97.44	2.73	0.01	0.03	2.75	0.16	<0.001		0.028	0.002
20.99	0.71	2.165	0.021	bdl		0.068	0.004	103.14	3.65	0.06	0.05	3.26	0.23	<0.001		0.031	0.002
51.60	2.42	4.465	0.048	bdl		0.035	0.004	86.53	4.16	0.04	0.02	0.68	0.08	<0.001		0.008	0.001
329.04	15.02	29.475	0.344	bdl		0.080	0.005	89.58	4.22	0.00	0.00	0.24	0.02	<0.001		0.003	0.000
76.96	1.89	7.080	0.074	bdl		0.093	0.005	91.99	2.46	0.01	0.02	1.21	0.08	<0.001		0.013	0.001
42.66	1.36	4.096	0.042	bdl		0.088	0.007	96.03	3.23	0.02	0.03	2.07	0.17	<0.001		0.021	0.002
62.37	2.03	6.413	0.066	bdl		0.215	0.013	102.82	3.51	0.02	0.02	3.44	0.23	<0.001		0.034	0.002
187.14	13.71	10.605	0.200	0.003	0.003	0.050	0.009	56.67	4.29	0.02	0.01	0.27	0.05	2.8	2.8	0.005	0.001
177.98	6.22	18.601	0.224	bdl		0.343	0.018	104.51	3.86	0.01	0.01	1.93	0.12	<0.001		0.018	0.001
160.68	3.59	15.376	0.071	0.007	0.002	0.599	0.023	95.69	2.18	0.04	0.01	3.73	0.17	4.6	1.3	0.039	0.002
31.13	0.52	2.745	0.010	0.008	0.001	0.042	0.004	88.16	1.51	0.25	0.04	1.36	0.12	29.1	3.6	0.015	0.001
160.06	2.83	12.591	0.035	bdl		0.150	0.007	78.67	1.41	0.01	0.01	0.94	0.05	<0.001		0.012	0.001
126.44	2.15	10.109	0.028	bdl		0.121	0.005	79.94	1.38	0.01	0.01	0.95	0.05	<0.001		0.012	0.000
27.68	0.52	2.717	0.011	0.008	0.001	0.101	0.005	98.16	1.90	0.29	0.04	3.64	0.18	29.4	3.7	0.037	0.002
103.27	1.70	9.587	0.024	bdl		0.516	0.017	92.84	1.54	0.00	0.01	4.99	0.18	<0.001		0.054	0.002

Table 4.17: Replicate analyses of undegassed aliquots of goethite sample RH (n=25); bdl = below detection limit.

mass	1σ	U	1σ	Th	1σ	Sm	1σ	U	1σ	Th	1σ	Sm	1σ	Th/U	1σ	Sm/U	1σ
[µg]		[ng]		[ng]		[ng]		[ppm]		[ppm]		[ppm]					
72.91	2.47	0.063	0.001	0.006	0.001	0.179	0.008	0.86	0.03	0.09	0.02	2.46	0.14	0.10	0.02	2.84	0.13
73.53	2.40	0.063	0.001	0.008	0.001	0.248	0.011	0.86	0.03	0.11	0.01	3.37	0.19	0.13	0.02	3.94	0.19
69.16	2.01	0.054	0.001	0.008	0.001	0.069	0.004	0.78	0.02	0.11	0.02	0.99	0.07	0.15	0.02	1.28	0.08
88.67	1.88	0.078	0.001	0.012	0.001	0.237	0.012	0.88	0.02	0.14	0.01	2.67	0.15	0.15	0.01	3.04	0.16
323.39	10.83	0.302	0.004	0.023	0.001	0.761	0.032	0.93	0.03	0.07	0.00	2.35	0.13	0.08	0.00	2.52	0.11
271.36	60.63	0.475	0.049	0.041	0.010	0.963	0.206	1.75	0.43	0.15	0.05	3.55	1.10	0.09	0.02	2.03	0.48
39.52	1.88	0.035	0.001	0.008	0.001	0.092	0.006	0.88	0.04	0.21	0.04	2.32	0.19	0.23	0.03	2.63	0.19
69.10	1.55	0.091	0.001	0.003	0.001	0.205	0.011	1.32	0.04	0.04	0.02	2.97	0.17	0.03	0.01	2.25	0.12
40.21	1.13	0.035	0.001	0.004	0.001	0.103	0.005	0.86	0.03	0.10	0.03	2.57	0.15	0.11	0.03	2.94	0.17
28.93	1.07	0.027	0.000	bdl		0.074	0.004	0.94	0.04	0.08	0.04	2.57	0.18	<0.01		2.74	0.15
30.57	1.15	0.026	0.000	0.003	0.001	0.094	0.006	0.85	0.04	0.11	0.04	3.08	0.21	0.12	0.04	3.62	0.23
180.00	5.63	0.174	0.002	0.004	0.001	0.611	0.031	0.97	0.03	0.02	0.01	3.39	0.20	0.02	0.01	3.51	0.18
252.49	7.18	0.231	0.003	0.007	0.001	1.047	0.051	0.92	0.03	0.03	0.00	4.15	0.24	0.03	0.00	4.53	0.23
46.67	1.68	0.041	0.001	0.006	0.001	0.140	0.009	0.87	0.03	0.12	0.03	2.99	0.22	0.15	0.02	3.41	0.23
84.17	2.55	0.072	0.001	0.004	0.001	0.250	0.013	0.86	0.03	0.05	0.01	2.97	0.18	0.06	0.01	3.47	0.19
79.78	2.46	0.073	0.001	0.030	0.002	0.279	0.015	0.92	0.03	0.37	0.02	3.50	0.22	0.41	0.03	3.82	0.21
41.10	0.99	0.035	0.001	0.007	0.001	0.112	0.006	0.85	0.03	0.18	0.03	2.73	0.17	0.20	0.03	3.20	0.19
126.56	4.84	0.115	0.001	0.015	0.002	0.391	0.019	0.91	0.04	0.12	0.01	3.09	0.19	0.13	0.02	3.40	0.17
40.58	1.47	0.037	0.001	0.003	0.001	0.105	0.005	0.91	0.04	0.08	0.03	2.60	0.16	0.08	0.03	2.84	0.16
140.67	4.56	0.121	0.002	0.011	0.002	0.382	0.019	0.86	0.03	0.08	0.01	2.72	0.16	0.09	0.02	3.16	0.17
272.21	4.70	0.277	0.002	0.010	0.001	0.982	0.034	1.02	0.02	0.04	0.01	3.61	0.14	0.04	0.00	3.55	0.13
26.66	0.46	0.026	0.000	0.005	0.001	0.072	0.004	0.99	0.02	0.21	0.05	2.68	0.14	0.19	0.04	2.77	0.15
120.39	2.03	0.103	0.001	0.006	0.001	0.394	0.014	0.86	0.02	0.05	0.01	3.27	0.13	0.06	0.01	3.83	0.14
160.67	2.65	0.137	0.001	0.027	0.001	0.447	0.015	0.85	0.02	0.17	0.01	2.78	0.10	0.20	0.01	3.26	0.11
110.88	1.95	0.093	0.001	0.005	0.001	0.353	0.016	0.83	0.02	0.05	0.01	3.18	0.15	0.05	0.01	3.80	0.18

Table 4.18: Replicate analyses of undegassed aliquots of goethite sample Lyp (n=10).

mass	1σ	U	1σ	Th	1σ	Sm	1σ	U	1σ	Th	1σ	Sm	1σ	Th/U	1σ	Sm/U	1σ
[µg]		[ng]		[ng]		[ng]		[ppm]		[ppm]		[ppm]					
64.85	0.83	0.269	0.002	0.540	0.004	0.063	0.004	4.15	0.06	8.33	0.13	0.97	0.07	2.007	0.021	0.234	0.015
59.53	0.59	0.213	0.002	0.524	0.005	0.062	0.005	3.58	0.04	8.80	0.13	1.05	0.08	2.460	0.033	0.291	0.024
58.35	0.55	0.166	0.001	0.267	0.003	0.049	0.004	2.84	0.03	4.57	0.07	0.84	0.06	1.608	0.021	0.295	0.024
75.24	0.79	0.247	0.002	0.669	0.004	0.067	0.005	3.28	0.04	8.89	0.11	0.89	0.07	2.709	0.027	0.271	0.020
96.98	1.04	0.335	0.002	0.814	0.006	0.094	0.006	3.46	0.04	8.40	0.11	0.97	0.06	2.430	0.023	0.281	0.018
32.49	0.32	0.135	0.001	0.507	0.003	0.084	0.006	4.15	0.05	15.62	0.17	2.57	0.19	3.756	0.036	0.622	0.045
45.40	0.43	0.163	0.004	0.431	0.005	0.060	0.005	3.58	0.10	9.50	0.15	1.31	0.12	2.644	0.072	0.368	0.032
68.20	0.77	0.199	0.001	0.346	0.003	0.062	0.004	2.92	0.04	5.08	0.07	0.90	0.06	1.739	0.017	0.312	0.020
39.37	0.40	0.144	0.002	0.896	0.006	0.047	0.004	3.66	0.06	22.75	0.27	1.20	0.11	6.222	0.096	0.326	0.028
77.08	0.79	0.281	0.002	0.801	0.004	0.109	0.006	3.64	0.04	10.39	0.12	1.42	0.07	2.851	0.025	0.388	0.022

Table 4.19: Replicate analyses of undegassed aliquots of goethite sample YAN (n=26); bdl = below detection limit.

mass	1σ	U	1σ	Th	1σ	Sm	1σ	U	1σ	Th	1σ	Sm	1σ	Th/U	1σ	Sm/U	1σ
[µg]		[ng]		[ng]		[ng]		[ppm]		[ppm]		[ppm]					
38.58	0.64	0.113	0.001	0.059	0.001	0.075	0.004	2.93	0.06	1.54	0.04	1.95	0.12	0.52	0.01	0.66	0.04
53.59	0.47	0.081	0.001	0.211	0.003	0.052	0.004	1.51	0.03	3.93	0.07	0.97	0.07	2.60	0.05	0.64	0.05
52.34	0.42	0.092	0.001	0.096	0.017	0.061	0.004	1.76	0.02	1.84	0.33	1.16	0.08	1.04	0.19	0.66	0.04
33.10	0.29	0.056	0.001	0.014	0.001	0.042	0.005	1.70	0.03	0.44	0.04	1.26	0.15	0.25	0.02	0.75	0.09
30.18	0.19	0.037	0.001	0.038	0.001	0.023	0.002	1.22	0.02	1.25	0.04	0.75	0.07	1.03	0.04	0.62	0.06
26.73	0.24	0.040	0.001	0.072	0.001	0.032	0.004	1.51	0.03	2.68	0.05	1.19	0.13	1.80	0.05	0.80	0.10
26.25	0.24	0.016	0.000	0.020	0.001	0.012	0.001	0.62	0.02	0.78	0.04	0.47	0.05	1.25	0.06	0.75	0.06
23.77	0.27	0.034	0.000	0.046	0.001	0.022	0.002	1.43	0.02	1.94	0.06	0.92	0.10	1.35	0.03	0.65	0.06
23.26	0.23	0.036	0.000	0.007	0.001	0.013	0.001	1.57	0.02	0.30	0.04	0.57	0.05	0.19	0.03	0.36	0.03
25.80	0.26	0.035	0.001	0.030	0.001	0.034	0.003	1.36	0.03	1.15	0.05	1.30	0.12	0.86	0.04	0.97	0.09
31.32	0.49	0.054	0.001	0.060	0.001	0.034	0.004	1.72	0.03	1.90	0.04	1.09	0.12	1.11	0.03	0.63	0.07
22.84	0.16	0.026	0.000	bdl		0.029	0.002	1.14	0.02	0.06	0.04	1.27	0.10	<0.01		1.12	0.08
53.18	0.68	0.093	0.001	0.180	0.003	0.068	0.004	1.76	0.03	3.39	0.07	1.28	0.08	1.94	0.04	0.73	0.04
19.50	0.16	0.014	0.000	0.003	0.001	0.019	0.003	0.74	0.03	0.13	0.07	0.95	0.14	0.21	0.07	1.36	0.21
42.64	0.42	0.038	0.001	0.005	0.001	0.113	0.005	0.89	0.02	0.11	0.02	2.64	0.12	0.13	0.03	2.97	0.15
23.65	0.22	0.052	0.000	0.066	0.001	0.040	0.003	2.22	0.03	2.78	0.07	1.67	0.14	1.27	0.02	0.77	0.06
18.16	0.14	0.029	0.000	0.048	0.001	0.020	0.003	1.58	0.02	2.66	0.08	1.09	0.17	1.66	0.03	0.69	0.10
24.71	0.26	0.061	0.001	0.083	0.001	0.061	0.004	2.45	0.04	3.36	0.07	2.49	0.15	1.36	0.03	1.00	0.07
17.48	0.15	0.028	0.000	0.056	0.001	0.024	0.002	1.59	0.03	3.21	0.07	1.35	0.12	2.00	0.04	0.86	0.07
84.79	1.17	0.069	0.001	0.041	0.001	0.115	0.008	0.82	0.01	0.48	0.01	1.35	0.09	0.59	0.02	1.67	0.12
36.64	0.29	0.043	0.001	0.042	0.001	0.053	0.004	1.18	0.02	1.15	0.03	1.44	0.12	0.98	0.03	1.23	0.10
23.53	0.24	0.022	0.000	0.026	0.001	0.047	0.002	0.95	0.02	1.08	0.05	1.99	0.09	1.18	0.05	2.14	0.09
36.28	0.38	0.045	0.001	0.046	0.001	0.024	0.004	1.24	0.03	1.26	0.03	0.66	0.10	1.02	0.03	0.53	0.09
36.56	0.35	0.014	0.000	0.042	0.001	0.034	0.002	0.39	0.01	1.16	0.04	0.93	0.07	3.00	0.07	2.43	0.14
26.74	0.19	0.024	0.000	0.004	0.001	0.034	0.003	0.89	0.01	0.14	0.03	1.28	0.11	0.17	0.04	1.42	0.13
46.42	0.38	0.147	0.001	0.091	0.002	0.127	0.007	3.17	0.03	1.95	0.04	2.74	0.15	0.62	0.01	0.86	0.05

Table 4.20: Replicate analyses of undegassed aliquots of goethite sample blade (n=10); bdl = below detection limit.

mass	1σ	U	1σ	Th	1σ	Sm	1σ	U	1σ	Th	1σ	Sm	1σ	Th/U	1σ	Sm/U	1σ
[µg]		[ng]		[ng]		[ng]		[ppm]		[ppm]		[ppm]					
89.07	1.17	0.117	0.001	0.198	0.002	0.678	0.032	1.31	0.02	2.23	0.04	7.61	0.38	1.692	0.022	5.795	0.278
45.20	0.49	0.086	0.001	0.019	0.001	0.036	0.003	1.90	0.04	0.42	0.02	0.79	0.07	0.221	0.012	0.419	0.035
48.57	0.60	0.077	0.001	0.071	0.002	0.216	0.011	1.59	0.02	1.46	0.04	4.46	0.24	0.922	0.029	2.805	0.147
13.64	0.17	0.040	0.000	bdl		0.005	0.002	2.94	0.05	0.09	0.07	0.34	0.13	<0.01		0.125	0.050
40.49	0.44	0.156	0.002	bdl		0.067	0.006	3.85	0.06	0.06	0.02	1.66	0.14	<0.01		0.429	0.039
57.93	0.68	0.436	0.003	0.004	0.001	0.070	0.004	7.53	0.10	0.06	0.02	1.21	0.08	0.009	0.002	0.161	0.009
19.99	0.21	0.005	0.000	bdl		bdl		0.27	0.01	0.01	0.04	0.09	0.10	<0.01		<0.01	
27.73	0.32	0.053	0.000	0.006	0.001	0.020	0.002	1.89	0.03	0.23	0.04	0.73	0.08	0.113	0.019	0.377	0.038
14.69	0.16	0.051	0.001	bdl		0.029	0.003	3.49	0.06	0.16	0.06	1.96	0.21	<0.01		0.569	0.060
34.54	0.45	0.170	0.001	bdl		0.057	0.005	4.92	0.08	0.04	0.02	1.64	0.14	<0.01		0.335	0.029

4.F Data of (U-Th)/He analyses

Given here is the data for all hematite and goethite experiments, in which aliquots of the same sample were heated to different temperatures in vacuum as well as partial oxygen pressures ($p(O_2)$) of 0.2-0.6 torr, 30-60 torr, and 100-130 torr. Results of vacuum heating experiments for Pt and Nb tubes are given separately. Oxygen partial pressures of <2 torr were produced by heating CuO packets, while pressures in excess 20 torr were drawn from an oxygen tank. Some oxygen pressures were measured with a manometer, and others were estimated from the average oxygen pressure produced by CuO packets and from the depletion of the oxygen tank. Average temperature and isothermal holding time of degassing are given for every aliquot. Absolute temperature control was within ~2% (for details see Appendix 4.B).

Some samples have Th below the level of the procedural blank (<0.002 ng). For these samples, we utilized the Sm/U ratio instead of the Th/U ratio to test for U loss. All uncertainties given here are solely analytical uncertainties (1σ), external uncertainties might be larger. Scatter in U, Th, and Sm concentrations as well as Th/U and Sm/U ratios are mainly due to inhomogeneity of the sample material. Grey areas in plots represent the interquartile range of undegassed aliquots, encompassing 50% of the values around the median. Many distributions of trace elements and ratios are skewed towards higher values. Data of undegassed aliquots is given below in this document. The absolute amount of U loss at any specific temperature also varies widely between samples and between aliquots of the same sample. He concentrations and calculated age at any temperature might vary due to differences in heating time.

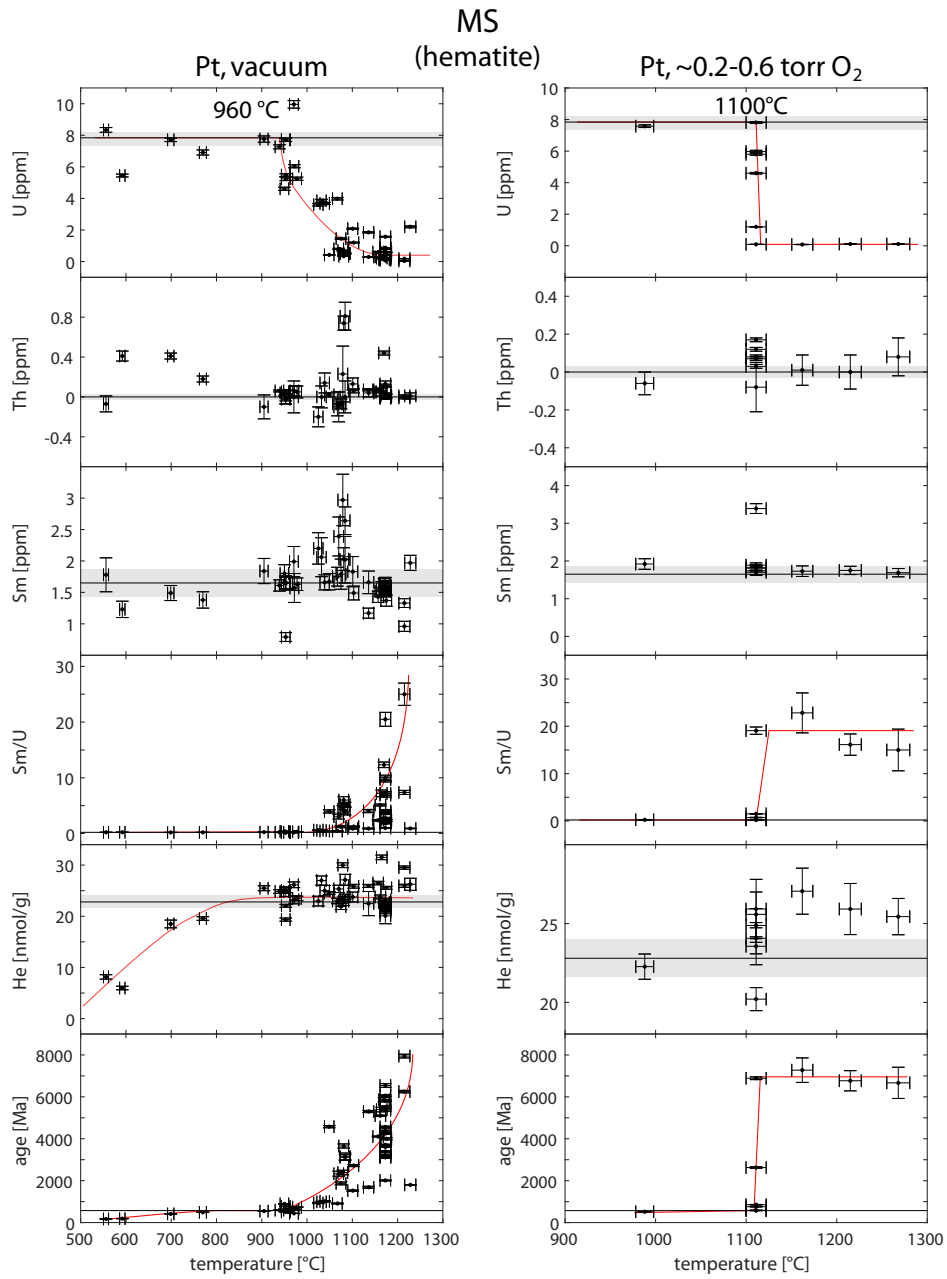

Figure 4.40: Heating experiments of hematite sample MS in vacuum and 0.2-0.6 torr (25-80 Pa) of O_2 in Pt packets. Samples were degassed at between 6 and 90 min. Horizontal line is the median value from undegassed aliquots (U, Th, Sm, Sm/U) or two-aliquot bulk analyses (age, He concentration), grey areas represent the interquartile range of values, and red lines show general trends. Detectable U loss occurs at 960 °C in vacuum and 1100 °C in 0.2-0.6 torr of O_2.

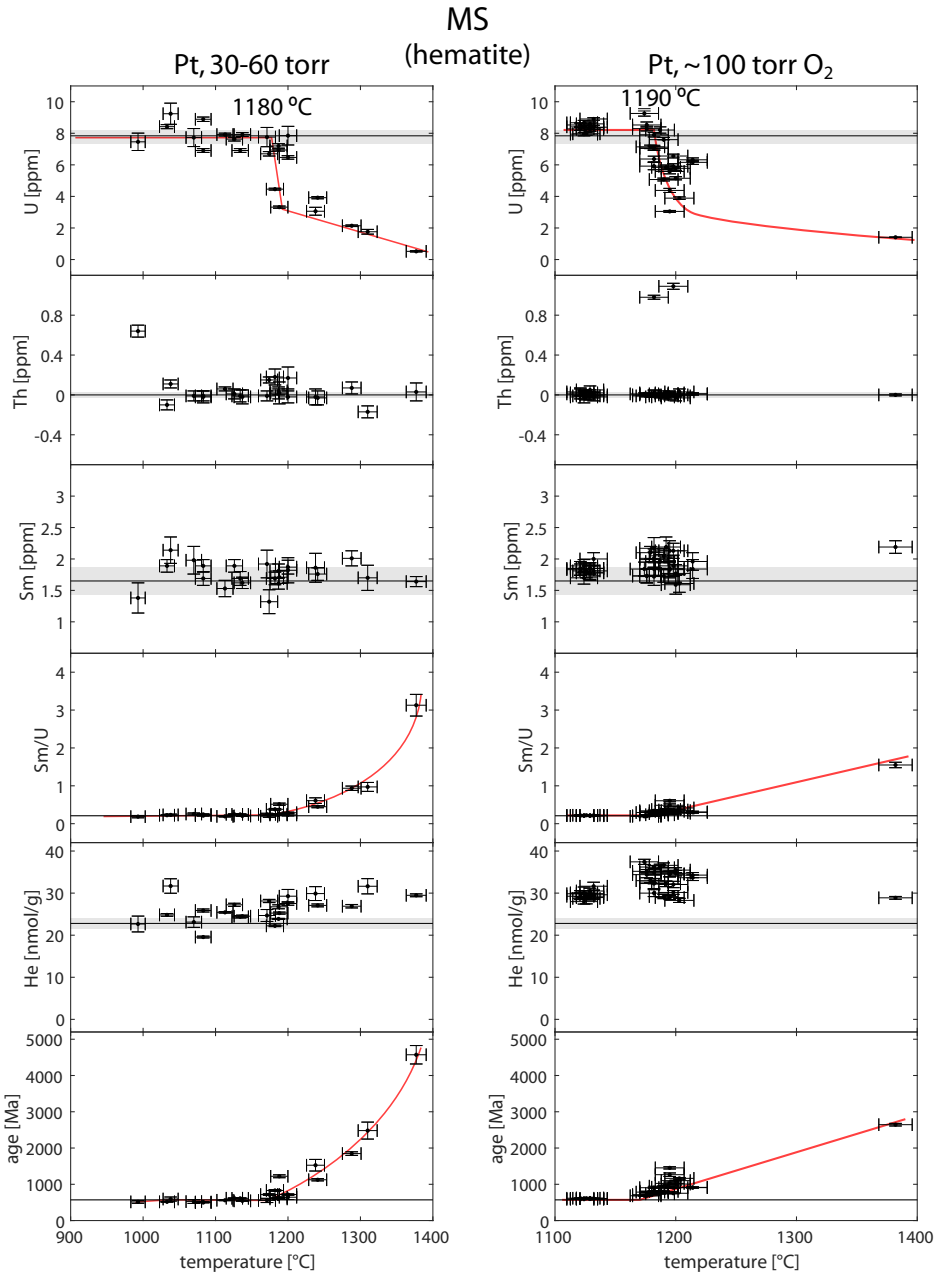

Figure 4.41: Heating experiments of hematite sample MS in 30-60 torr (4-8 kPa) and 100 torr (13 kPa) of O_2 in Pt packets. Samples were degassed at between 6 and 90 min. Horizontal line is the median value from undegassed aliquots (U, Th, Sm, Sm/U) or two-aliquot bulk analyses (age, He concentration), grey areas represent the interquartile range of values, and red lines show general trends. Detectable U loss occurs at 1180 °C in 50 torr and at 1190 °C in 100 torr of O_2.

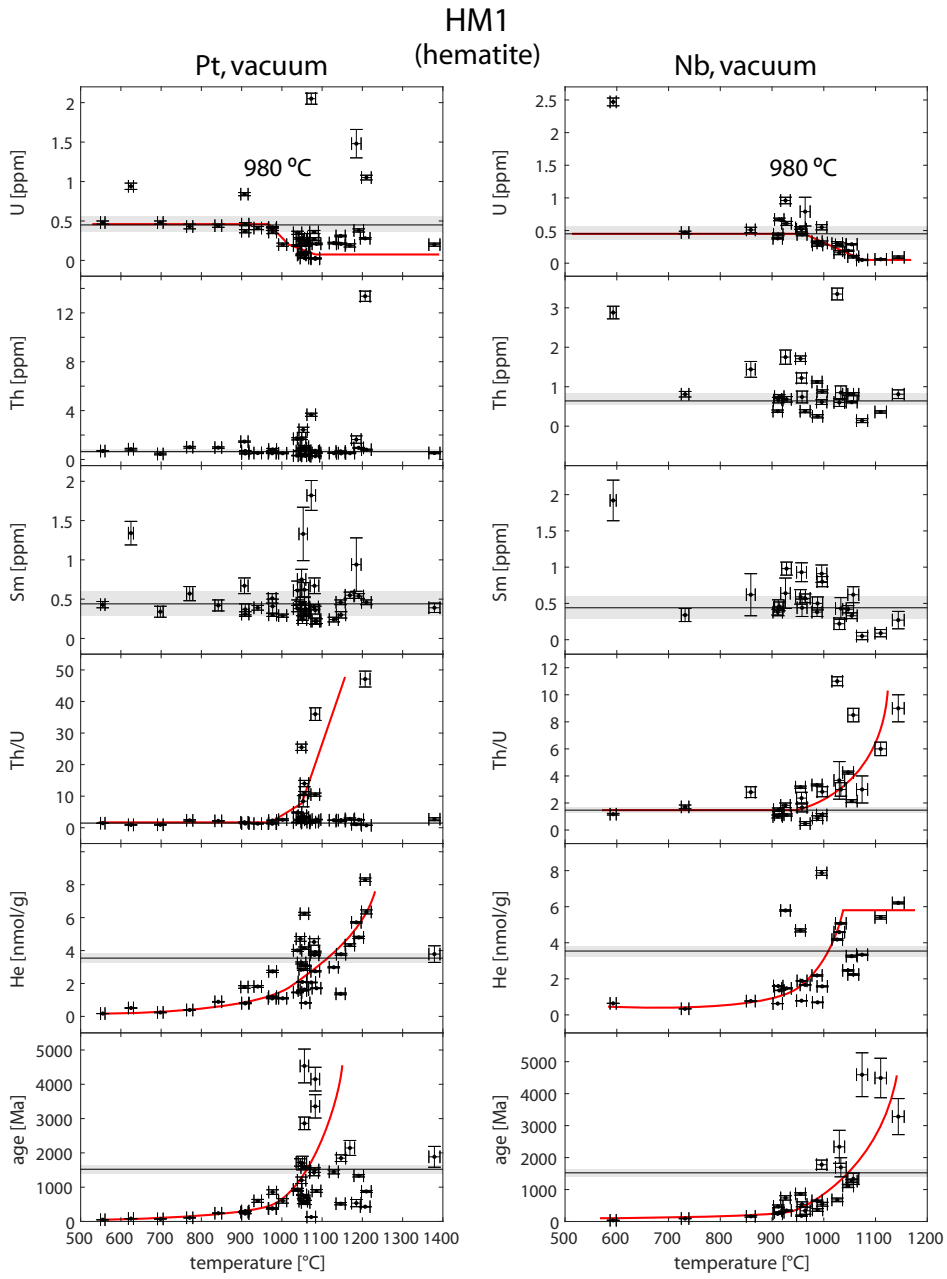

Figure 4.42: Heating experiments of hematite sample HM1 in vacuum using Pt and Nb packets. Samples were degassed at between 6 and 360 min. Horizontal line is the median value from undegassed aliquots (U, Th, Sm, Sm/U) or two-aliquot bulk analyses (age, He concentration), grey areas represent the interquartile range of values, and red lines show general trends. Detectable U loss occurs at ~980 °C for both Pt and Nb packets.

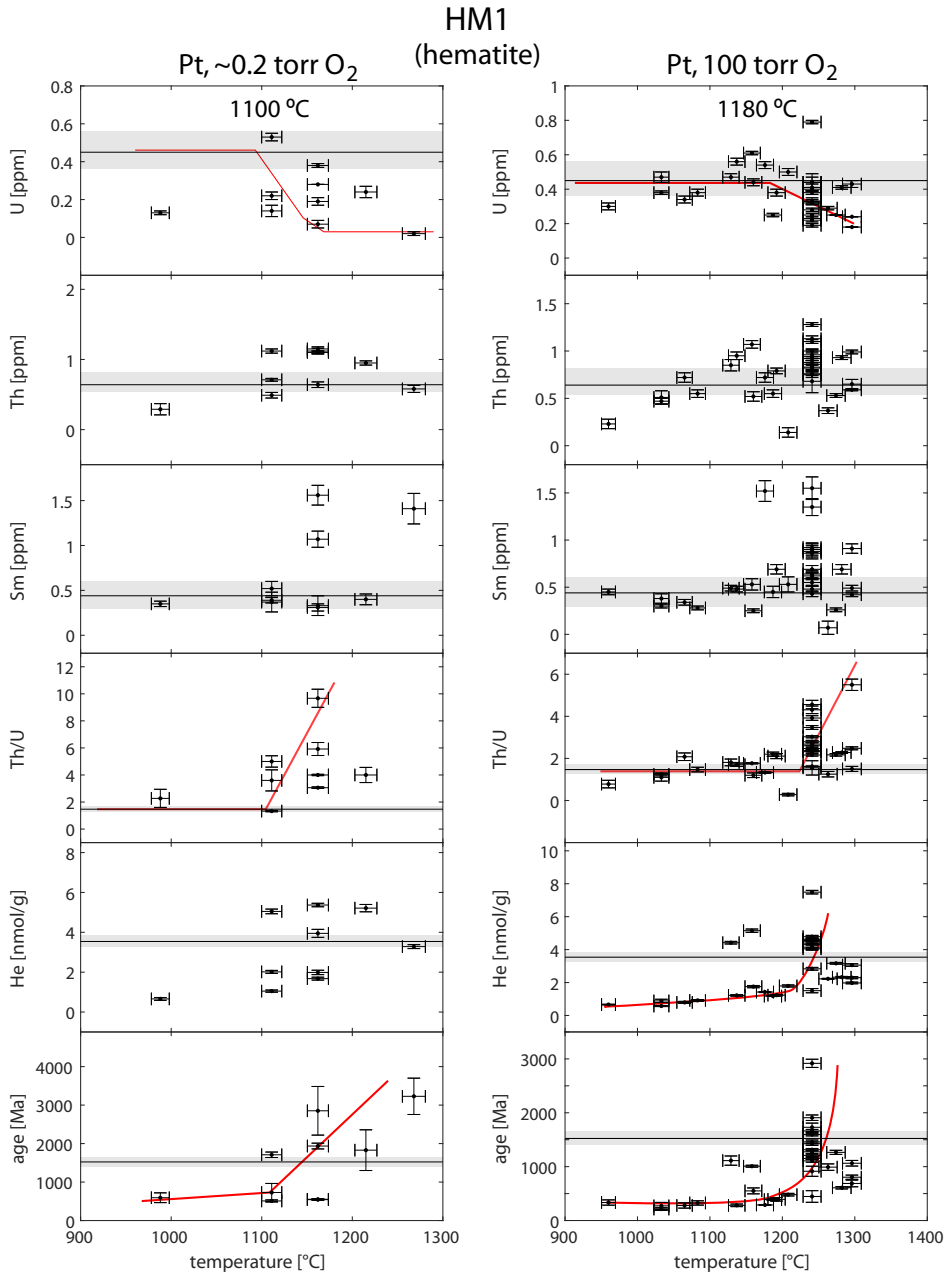

Figure 4.43: Heating experiments of hematite sample HM1 in ~0.2 torr (27 Pa) and ~100 torr (13 kPa) of O_2 in Pt packets. Samples were degassed at between 10 and 130 min. Horizontal line is the median value from undegassed aliquots (U, Th, Sm, Sm/U) or two-aliquot bulk analyses (age, He concentration), grey areas represent the interquartile range of values, and red lines show general trends. Detectable U loss occurs at ~1100 °C in 0.2 torr and at 1180 °C in 100 torr of O_2.

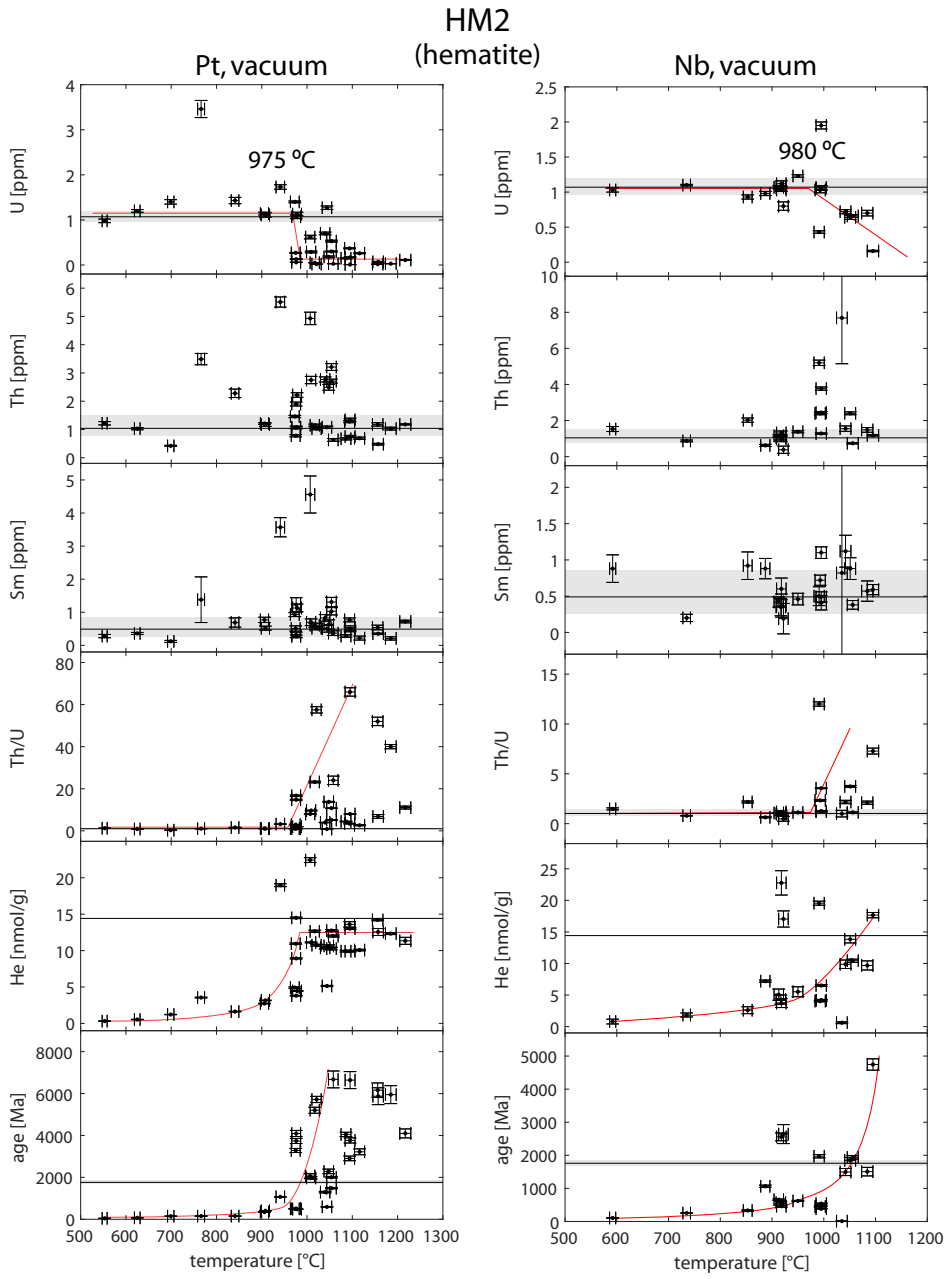

Figure 4.44: Heating experiments of hematite sample HM1 in vacuum using Pt and Nb packets. Samples were degassed at between 6 and 120 min. Horizontal line is the median value from undegassed aliquots (U, Th, Sm, Sm/U) or two-aliquot bulk analyses (age, He concentration), grey areas represent the interquartile range of values, and red lines show general trends. Detectable U loss occurs at ~980 °C for both Pt and Nb packets.

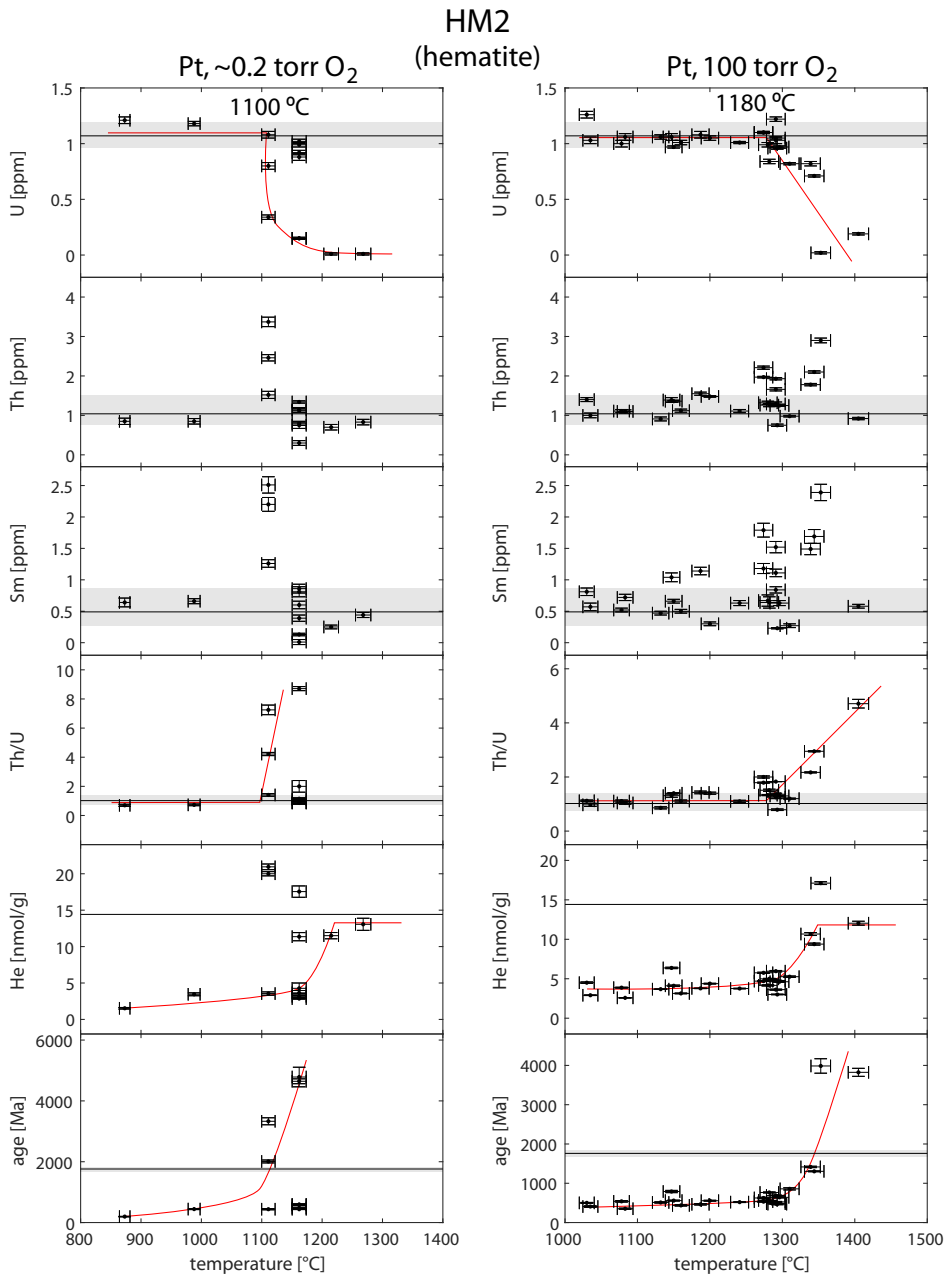

Figure 4.45: Heating experiments of hematite sample HM2 in ~0.2 torr (27 Pa) and ~100 torr (13 kPa) of O_2 in Pt packets. Samples were degassed at between 10 and 110 min. Horizontal line is the median value from undegassed aliquots (U, Th, Sm, Sm/U) or two-aliquot bulk analyses (age, He concentration), grey areas represent the interquartile range of values, and red lines show general trends. Detectable U loss occurs at ~1100 °C in 0.2 torr and at 1180 °C in 100 torr of O_2.

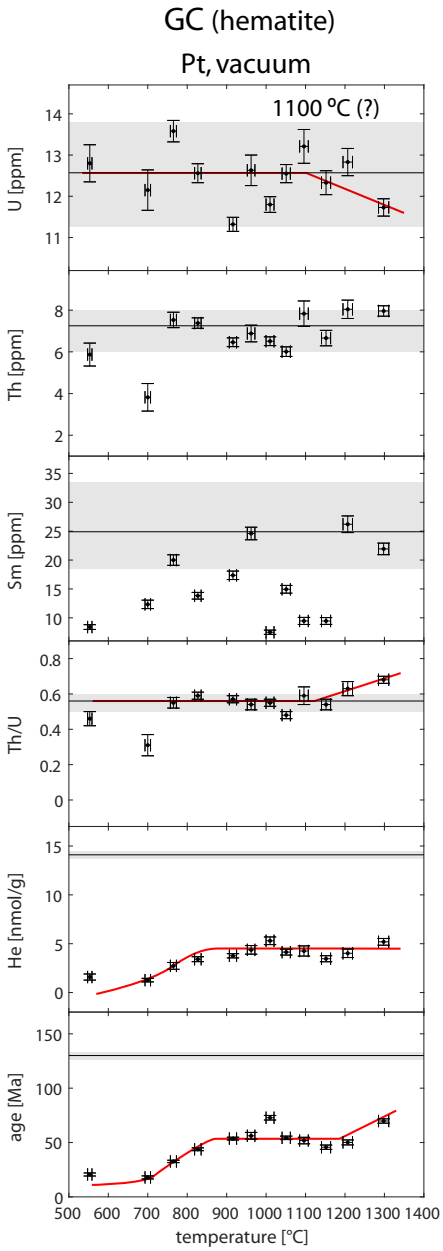

Figure 4.46: Heating experiments of hematite sample GC in vacuum in Pt packets. Samples were degassed for 20 min. Horizontal line is the median value from undegassed aliquots (U, Th, Sm, Sm/U) or two-aliquot bulk analyses (age, He concentration), grey areas represent the interquartile range of values, and red lines show general trends. No major U loss was observed, with minor U loss possible at ~1100 °C. Age and He concentration are only ~50% of the two-aliquot values.

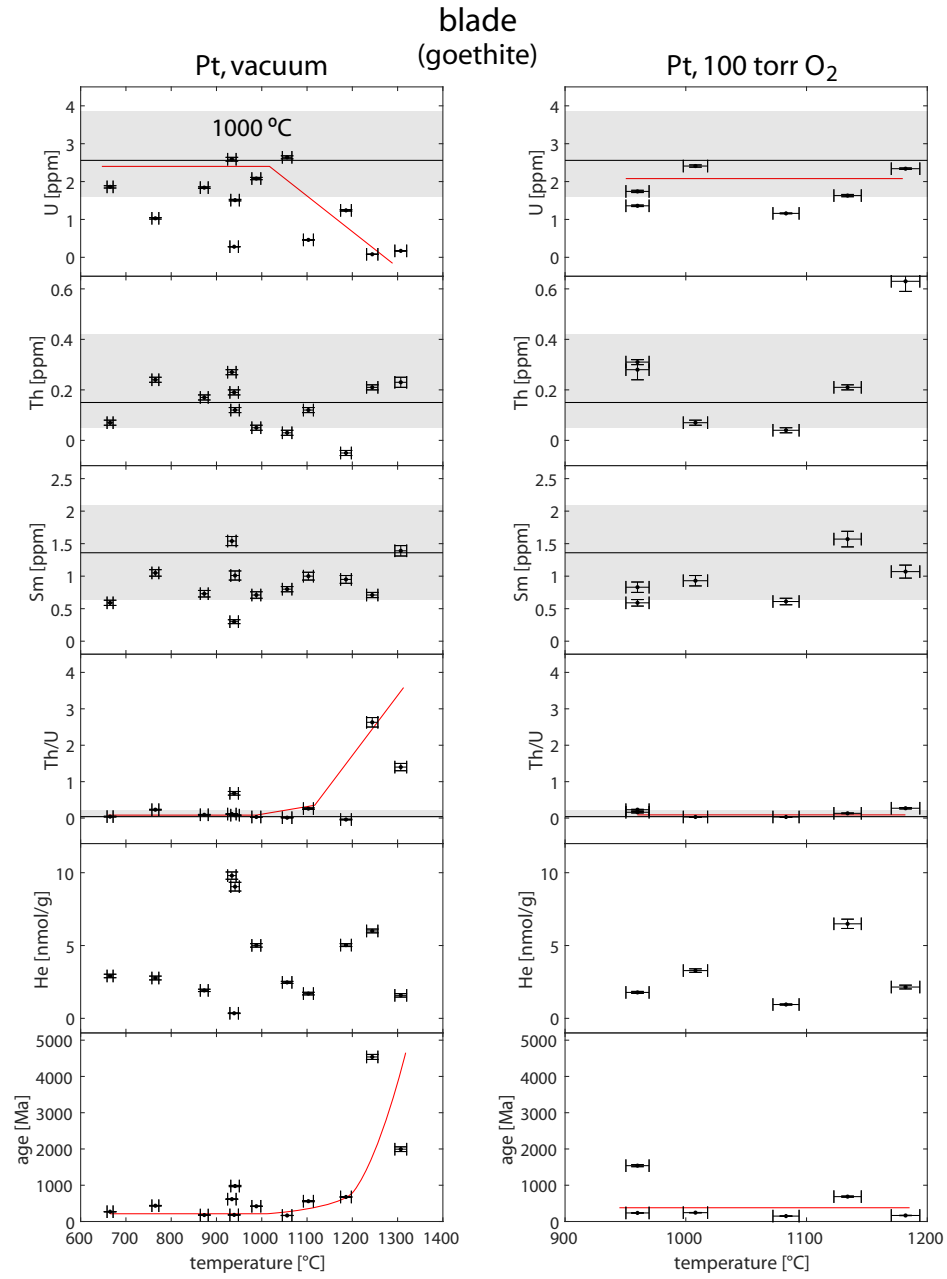

Figure 4.47: Heating experiments of goethite sample blade in vacuum and ~100 torr of O_2 in Pt packets. Samples were degassed between 6 and 20 min. Horizontal line is the median value from undegassed aliquots (U, Th, Sm, Sm/U), grey areas represent the interquartile range of values, and red lines show general trends. The 'true' age of the sample is unknown. U loss occurs at around 1000 °C in vacuum and no major U loss was observed in O_2.

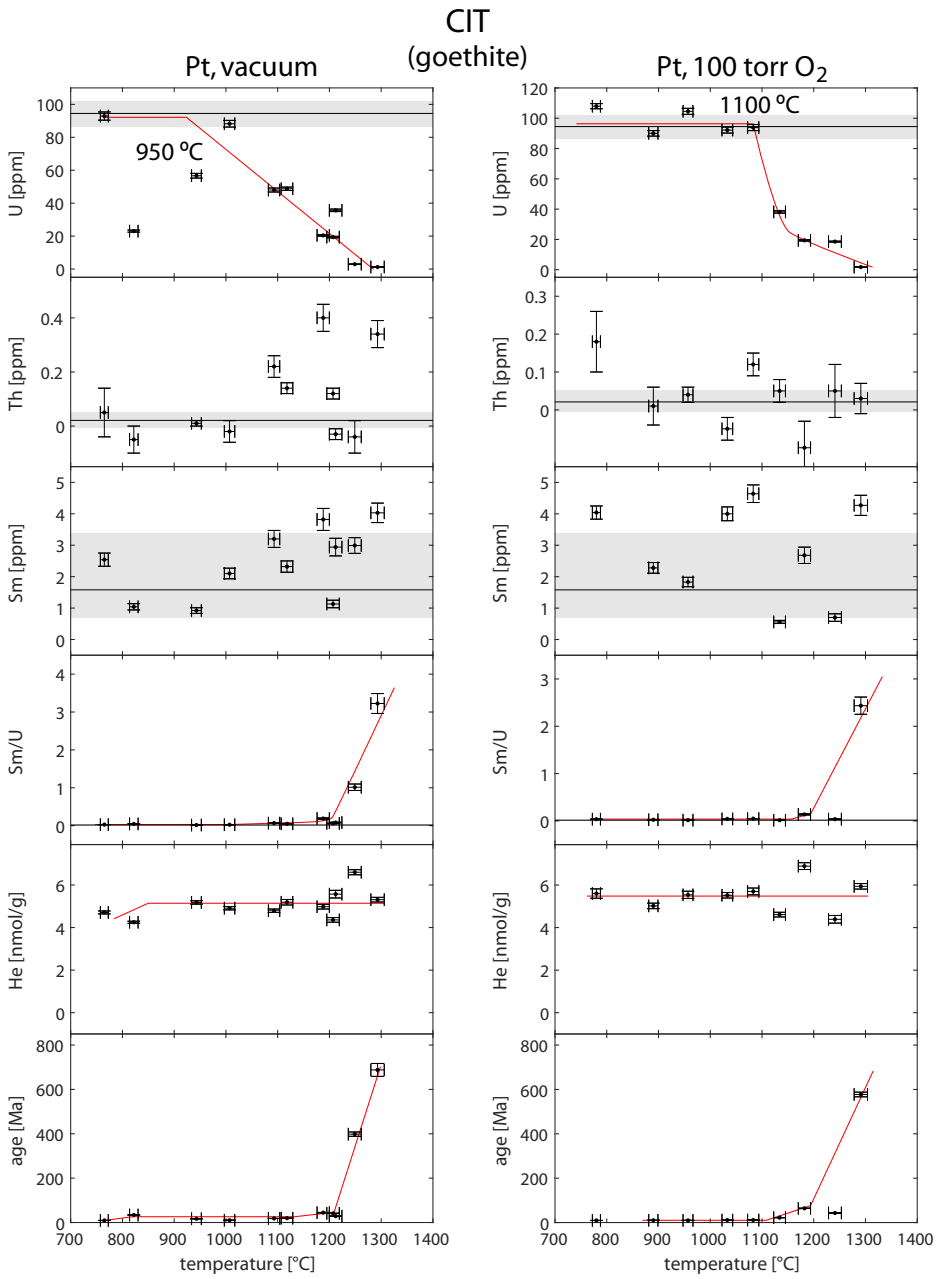

Figure 4.48: Heating experiments of goethite sample CIT in vacuum and ~100 torr of O_2 in Pt packets. Samples were degassed between 6 and 20 min. Horizontal line is the median value from undegassed aliquots (U, Th, Sm, Sm/U), grey areas represent the interquartile range of values, and red lines show general trends. The age of the sample is around 10 Ma. U loss occurs at around 950 °C in vacuum and at about 1100 °C in O_2.

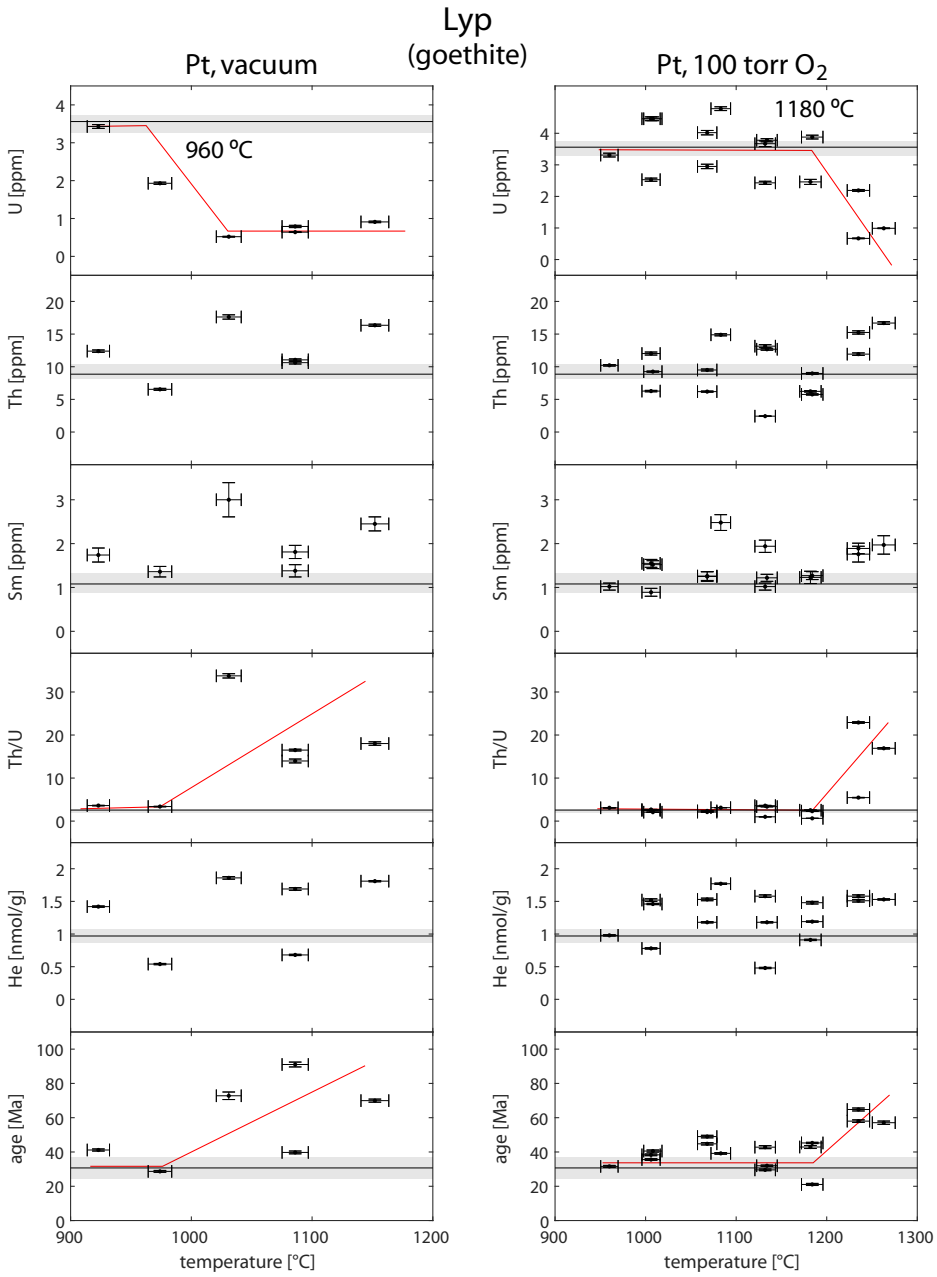

Figure 4.49: Heating experiments of goethite sample Lyp in vacuum and ~100 torr of O_2 in Pt packets. Samples were degassed between 10 and 20 min. Horizontal line is the median value from undegassed aliquots (U, Th, Sm, Sm/U), grey areas represent the interquartile range of values, and red lines show general trends. The 'true' age of the sample is the average of Vasconcelos et al. (2013). Detectable U loss occurs at 960 °C in vacuum and at about 1180 °C in O_2.

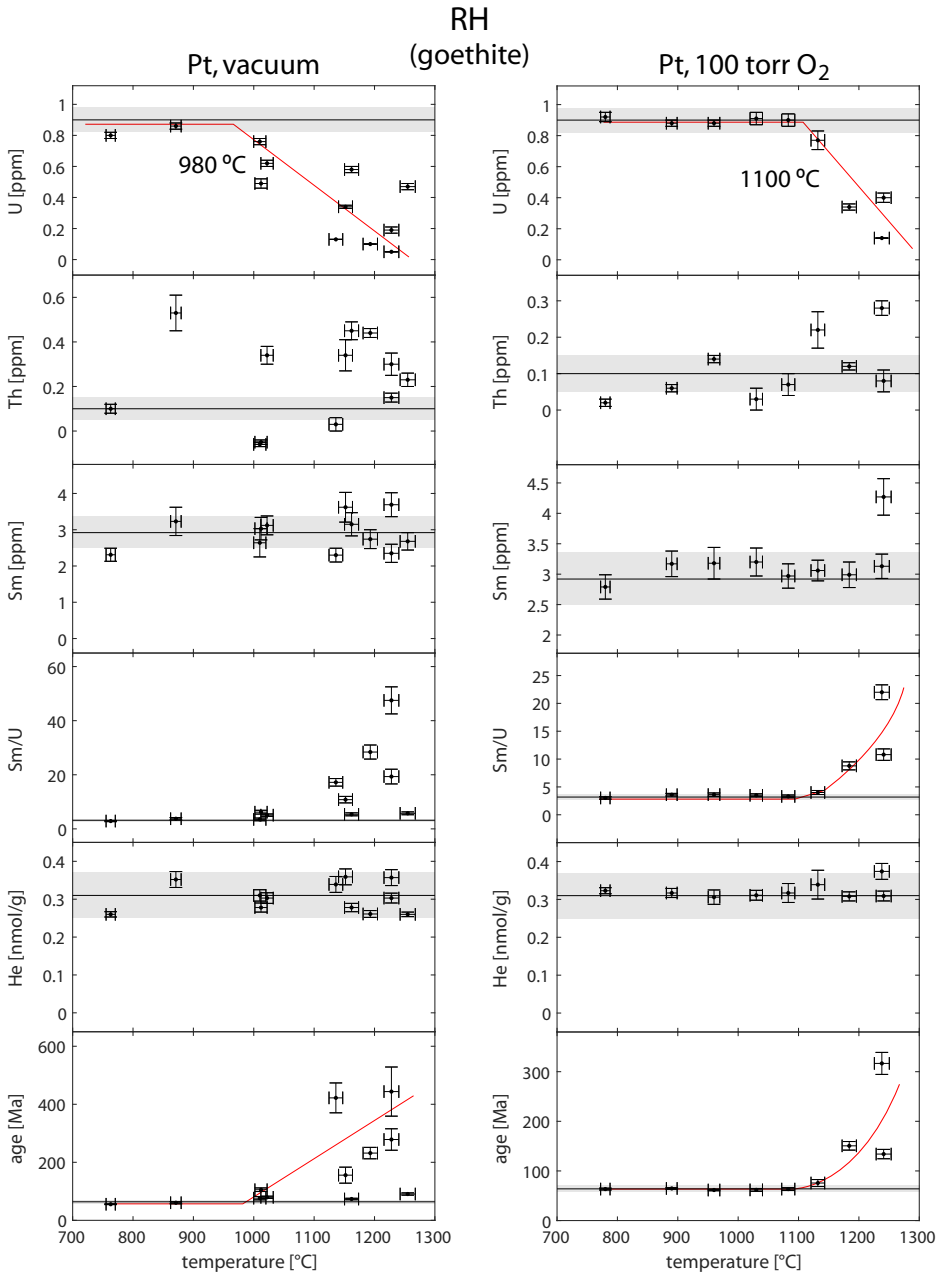

Figure 4.50: Heating experiments of goethite sample CIT in vacuum and ~100 torr of O_2 in Pt packets. Samples were degassed for 20 min. Horizontal line is the median value from undegassed aliquots (U, Th, Sm, Sm/U), grey areas represent the interquartile range of values and red lines are general trends. The 'true' age of the sample is the average of Vasconcelos et al. (2013). Detectable U loss occurs between 900 and 1000 °C in vacuum and at about 1100 °C in O_2.

Table 4.21: Heating experiment data for hematite sample HM1 degassed in vacuum in Pt packets. T = temperature, t = total isothermal heating time, age = calculated (U-Th)/He age, mass = Fe-based sample mass.

T	t	age	1σ	mass	1σ	U	1σ	Th	1σ	Sm	1σ	He	1σ	Th/U	1σ	Sm/U	1σ
[°C]	[min]	[Ma]		[µg]		[ppm]		[ppm]		[ppm]		[nmol/g]					
555	24	50	2	95.7	3.6	0.48	0.02	0.69	0.04	0.43	0.04	0.17	0.01	1.43	0.05	0.89	0.09
625	24	82	3	32.0	1.1	0.94	0.04	0.84	0.07	1.34	0.15	0.51	0.02	0.90	0.07	1.43	0.17
698	24	75	6	35.5	1.1	0.48	0.02	0.45	0.07	0.34	0.07	0.24	0.01	0.94	0.13	0.71	0.12
771	24	107	7	27.9	1.1	0.43	0.03	1.00	0.07	0.57	0.09	0.39	0.01	2.33	0.21	1.33	0.20
842	24	240	9	38.3	1.4	0.44	0.02	0.97	0.06	0.42	0.07	0.89	0.03	2.18	0.06	0.94	0.18
909	24	229	6	66.7	2.2	0.46	0.02	0.69	0.04	0.37	0.07	0.79	0.03	1.48	0.06	0.81	0.13
907	24	272	9	40.4	0.7	0.84	0.02	1.46	0.05	0.67	0.10	1.79	0.03	1.74	0.06	0.79	0.12
909	24	304	7	95.5	4.2	0.37	0.02	0.49	0.04	0.31	0.03	0.81	0.04	1.34	0.06	0.86	0.09
977	24	378	18	56.9	1.1	0.42	0.01	0.62	0.03	0.30	0.02	1.20	0.02	1.46	0.10	0.71	0.05
977	24	857	66	19.5	0.7	0.36	0.02	0.82	0.08	0.41	0.09	2.73	0.09	2.29	0.14	1.14	0.29
976	24	380	15	80.7	3.0	0.40	0.02	0.51	0.03	0.51	0.06	1.09	0.04	1.28	0.05	1.28	0.16
1039	24	925	41	114.2	3.3	0.19	0.01	0.32	0.02	0.38	0.04	1.46	0.04	1.68	0.09	1.95	0.24
1081	24	1499	69	45.0	1.8	0.27	0.02	0.60	0.05	0.67	0.10	3.74	0.15	2.25	0.08	2.50	0.33
1147	24	1846	98	67.7	2.0	0.21	0.01	0.50	0.03	0.30	0.04	3.77	0.11	2.43	0.19	1.43	0.24
1207	18	430	8	67.0	2.0	0.28	0.01	13.36	0.42	60.28	3.14	8.30	0.24	47.11	2.52	212.47	14.49
1039	80	929	31	34.3	1.1	0.35	0.02	1.69	0.09	0.61	0.12	4.01	0.13	4.83	0.17	1.75	0.33
1051	80	773	16	95.8	3.3	0.26	0.01	0.90	0.04	0.26	0.03	2.09	0.07	3.44	0.04	1.00	0.12
1051	80	1703	199	62.8	1.7	0.08	0.01	0.30	0.02	0.24	0.05	1.57	0.04	3.80	0.79	3.00	0.85
1058	80	1576	41	88.4	2.9	0.21	0.01	0.43	0.02	0.34	0.03	3.08	0.10	2.00	0.05	1.58	0.11
1083	60	3357	340	50.4	1.5	0.02	0.00	0.71	0.05	0.36	0.05	3.91	0.12	36.00	2.00	18.00	2.00
1129	80	1446	58	73.5	2.8	0.22	0.01	0.52	0.03	0.24	0.03	2.98	0.11	2.38	0.06	1.13	0.13
1049	60	1201	95	29.5	0.9	0.07	0.01	1.73	0.10	0.75	0.13	3.25	0.10	25.50	1.00	11.00	2.00
1083	80	4151	346	76.8	2.9	0.03	0.00	0.27	0.02	0.22	0.04	2.74	0.10	10.50	0.50	8.50	1.50
1086	80	890	41	58.1	2.0	0.21	0.01	0.53	0.02	0.22	0.03	1.71	0.06	2.58	0.08	1.08	0.17
1073	80	128	2	38.0	1.1	2.05	0.07	3.66	0.13	1.82	0.19	2.06	0.06	1.78	0.03	0.88	0.09
1056	160	722	46	57.8	2.0	0.22	0.02	0.73	0.03	0.45	0.07	1.63	0.06	3.23	0.26	2.00	0.34
1056	240	2861	184	21.1	0.9	0.10	0.01	1.05	0.08	0.62	0.09	6.23	0.26	11.00	0.50	6.50	1.00
1056	360	4535	493	34.8	1.0	0.03	0.00	0.40	0.05	0.32	0.04	4.14	0.11	14.00	1.00	11.00	1.00
1053	120	591	71	17.3	0.7	0.29	0.05	2.43	0.21	1.33	0.34	2.86	0.12	8.40	1.78	4.60	1.51
1002	6	599	65	187.0	2.5	0.20	0.02	0.51	0.04	0.29	0.02	1.10	0.01	2.53	0.27	1.42	0.17
1059	6	555	62	212.4	4.3	0.19	0.01	0.29	0.03	0.38	0.04	0.83	0.02	1.51	0.20	1.98	0.22
1046	6	1720	108	232.2	2.6	0.28	0.01	0.69	0.03	0.45	0.02	4.71	0.05	2.52	0.17	1.63	0.12
1146	6	518	35	194.3	2.6	0.31	0.01	0.66	0.04	0.46	0.03	1.37	0.02	2.10	0.15	1.46	0.12
1210	6	875	29	212.7	5.2	1.05	0.03	0.80	0.04	0.46	0.03	6.35	0.15	0.77	0.03	0.43	0.03
1169	6	2144	218	183.4	3.7	0.19	0.02	0.52	0.04	0.55	0.04	4.33	0.09	2.79	0.32	2.94	0.33
1379	12	1885	304	117.9	1.7	0.20	0.02	0.53	0.06	0.39	0.06	3.78	0.05	2.70	0.47	2.00	0.43
1080	12	1428	95	147.7	1.2	0.36	0.02	0.65	0.04	0.40	0.03	4.52	0.04	1.81	0.15	1.11	0.10
940	12	600	43	148.1	1.8	0.41	0.02	0.53	0.05	0.39	0.03	1.81	0.02	1.30	0.12	0.97	0.07
1185	12	535	105	111.5	5.1	1.48	0.18	1.63	0.3	0.94	0.34	5.71	0.26	1.10	0.24	0.64	0.24
1191	10	1332	34	106.4	3.2	0.38	0.02	0.95	0.04	0.54	0.03	4.80	0.14	2.53	0.10	1.43	0.08

Table 4.22: Heating experiment data for hematite sample HM1 degassed in vacuum in Nb packets. T = temperature, t = total isothermal heating time, age = calculated (U-Th)/He age, mass = Fe-based sample mass.

T	t	age	1σ	mass	1σ	U	1σ	Th	1σ	Sm	1σ	He	1σ	Th/U	1σ	Sm/U	1σ
[°C]	[min]	[Ma]		[µg]		[ppm]		[ppm]		[ppm]		[nmol/g]					
593	6	37	2	7.3	0.0	2.47	0.06	2.88	0.16	1.92	0.28	0.64	0.00	1.17	0.06	0.78	0.11
732	6	93	7	14.7	0.1	0.47	0.02	0.81	0.07	0.34	0.09	0.34	0.00	1.71	0.14	0.71	0.14
859	6	163	25	4.9	0.0	0.51	0.04	1.44	0.20	0.62	0.29	0.77	0.01	2.80	0.40	1.20	0.40
912	6	474	43	18.1	0.1	0.44	0.02	0.66	0.07	0.44	0.11	1.60	0.01	1.50	0.13	1.00	0.25
911	6	239	11	46.9	0.2	0.38	0.01	0.38	0.03	0.38	0.04	0.63	0.00	1.00	0.11	1.00	0.11
914	6	288	13	23.9	0.1	0.67	0.02	0.75	0.05	0.46	0.06	1.36	0.01	1.13	0.06	0.69	0.06
958	6	538	76	6.8	0.0	0.44	0.02	0.74	0.15	0.44	0.12	1.89	0.01	1.67	0.33	1.00	0.33
964	6	336	110	36.5	0.2	0.79	0.22	0.38	0.04	0.57	0.06	1.66	0.01	0.48	0.14	0.72	0.21
957	6	179	22	14.0	0.1	0.52	0.04	1.22	0.13	0.93	0.13	0.78	0.01	2.36	0.43	1.81	0.37
1033	6	1696	299	7.0	0.1	0.28	0.03	0.85	0.17	0.43	0.15	5.07	0.04	3.00	0.50	1.50	0.50
1026	6	676	57	9.9	0.1	0.30	0.03	3.35	0.15	9.04	0.47	4.18	0.05	11.00	0.33	29.67	1.67
1030	6	2337	516	18.5	0.1	0.16	0.03	0.60	0.10	0.22	0.08	4.59	0.02	3.67	1.39	1.33	0.56
1074	6	4592	686	22.2	0.2	0.05	0.01	0.14	0.05	0.05	0.05	3.33	0.03	3.00	1.00	1.00	1.00
1144	6	3282	564	11.1	0.1	0.09	0.02	0.81	0.11	0.27	0.12	6.21	0.05	9.00	1.00	3.00	1.00
926	30	738	68	6.3	0.0	0.96	0.05	1.75	0.18	0.64	0.21	5.79	0.04	1.83	0.17	0.67	0.17
928	6	344	17	29.6	0.6	0.61	0.03	0.68	0.07	0.98	0.09	1.47	0.03	1.11	0.08	1.61	0.19
996	6	1777	145	16.4	0.3	0.55	0.04	0.61	0.06	0.91	0.12	7.87	0.13	1.11	0.11	1.67	0.22
988	6	363	45	28.2	0.6	0.28	0.02	0.25	0.04	0.50	0.09	0.69	0.01	0.88	0.17	1.75	0.43
997	6	540	60	26.1	0.5	0.31	0.03	0.88	0.04	0.80	0.07	1.58	0.03	2.83	0.37	2.58	0.40
955	6	862	37	22.2	0.4	0.54	0.02	1.71	0.07	0.59	0.10	4.68	0.08	3.17	0.08	1.08	0.17
987	6	646	23	44.8	0.8	0.33	0.01	1.12	0.03	0.38	0.06	2.19	0.04	3.33	0.07	1.13	0.20
1047	6	1112	52	49.4	0.8	0.19	0.01	0.81	0.03	0.42	0.05	2.47	0.04	4.25	0.11	2.23	0.32
1054	6	1263	45	73.5	1.2	0.29	0.01	0.61	0.02	0.33	0.04	3.26	0.05	2.14	0.11	1.14	0.15
1057	6	1336	177	20.9	0.4	0.10	0.02	0.81	0.04	0.62	0.11	2.24	0.04	8.50	0.50	6.50	1.00
1110	6	4490	618	33.3	0.6	0.06	0.01	0.36	0.03	0.09	0.05	5.41	0.09	6.00	0.50	1.50	1.00

Table 4.23: Heating experiment data for hematite sample HM1 degassed in oxygen. $p(O_2)$ = oxygen partial pressure, T = temperature, t = total isothermal heating time, age = calculated (U-Th)/He age, mass = Fe-based sample mass.

$p(O_2)$	T	t	age	1σ	mass	1σ	U	1σ	Th	1σ	Sm	1σ	He	1σ	Th/U	1σ	Sm/U	1σ
[torr]	[°C]	[min]	[Ma]		[µg]		[ppm]		[ppm]		[ppm]		[nmol/g]					
~0.2	1111	10	1709	71	53.6	1.1	0.22	0.02	1.12	0.03	0.52	0.08	5.05	0.10	5.00	0.42	2.33	0.39
~0.2	1162	10	1936	73	68.9	1.6	0.19	0.02	1.12	0.04	1.07	0.09	5.37	0.12	5.92	0.48	5.69	0.64
~0.2	1162	10	543	17	47.6	0.7	0.38	0.01	1.15	0.03	0.31	0.04	1.99	0.03	3.06	0.06	0.83	0.11
~0.2	1162	10	553	17	72.4	1.1	0.28	0.00	1.10	0.02	1.56	0.11	1.68	0.03	4.00	0.05	5.65	0.40
~0.2	988	10	593	127	86.2	0.7	0.13	0.01	0.29	0.08	0.35	0.03	0.66	0.01	2.27	0.67	2.73	0.37
~0.2	1111	10	729	230	73.0	1.1	0.14	0.03	0.49	0.04	0.37	0.11	1.05	0.02	3.60	0.78	2.70	0.97
~0.2	1162	10	2852	627	45.6	0.6	0.07	0.02	0.64	0.04	0.33	0.11	3.95	0.05	9.67	0.67	5.00	1.67
~0.2	1215	10	1829	533	92.6	1.1	0.24	0.03	0.95	0.03	0.40	0.06	5.21	0.06	4.00	0.56	1.68	0.36
~0.2	1268	10	3228	518	41.3	0.7	0.02	0.01	0.58	0.05	1.41	0.17	3.28	0.05	24.00	2.00	58.00	7.00
~0.2	1111	25	510	29	131.5	2.0	0.53	0.02	0.71	0.02	0.39	0.03	2.01	0.03	1.33	0.05	0.73	0.06
51.2	1129	10	1112	86	121.0	0.4	0.47	0.02	0.85	0.06	0.49	0.03	4.42	0.08	1.81	0.16	1.04	0.09
35.92	1033	6	213	25	301.7	5.2	0.38	0.01	0.47	0.03	0.30	0.02	0.57	0.03	1.24	0.07	0.80	0.06
34.73	1083	6	326	40	191.9	4.3	0.38	0.02	0.55	0.04	0.28	0.02	0.92	0.05	1.47	0.11	0.75	0.06
34.16	1137	6	282	24	205.1	3.2	0.56	0.02	0.95	0.04	0.48	0.03	1.22	0.05	1.70	0.08	0.86	0.07
33.62	1192	6	393	33	258.6	4.4	0.38	0.02	0.79	0.03	0.69	0.05	1.23	0.04	2.11	0.12	1.84	0.15
33.03	1241	6	914	94	130.1	2.0	0.33	0.02	0.86	0.06	1.35	0.09	2.83	0.08	2.60	0.26	4.07	0.40
32.53	1296	6	688	62	172.0	2.6	0.43	0.02	0.65	0.05	0.49	0.03	2.30	0.06	1.50	0.12	1.14	0.08
45	1065	10	279	49	153.6	3.0	0.34	0.02	0.72	0.05	0.34	0.03	0.79	0.06	2.08	0.18	1.00	0.11
46	1033	10	272	64	89.9	1.5	0.47	0.03	0.51	0.07	0.38	0.05	0.88	0.10	1.10	0.18	0.81	0.11
44	1160	10	550	55	161.9	3.3	0.44	0.02	0.52	0.05	0.25	0.02	1.75	0.07	1.20	0.11	0.56	0.06
~150	960	6	334	49	119.7	1.3	0.30	0.02	0.23	0.05	0.45	0.03	0.66	0.02	0.78	0.18	1.50	0.17
~150	1241	6	446	108	50.0	0.6	0.44	0.05	0.68	0.12	0.86	0.06	1.51	0.13	1.55	0.34	1.95	0.30
~145	1158	40	1008	18	51.2	1.0	0.61	0.01	1.07	0.04	0.53	0.06	5.15	0.10	1.77	0.03	0.87	0.10
~145	1263	40	991	60	27.2	0.4	0.29	0.01	0.37	0.03	0.07	0.07	2.23	0.03	1.25	0.13	0.25	0.25
~145	1208	40	480	24	36.1	1.3	0.50	0.02	0.14	0.05	0.53	0.08	1.79	0.06	0.28	0.06	1.06	0.18
~140	1176	40	289	6	44.2	1.0	0.54	0.02	0.72	0.05	1.52	0.11	1.42	0.03	1.33	0.04	2.79	0.21
~140	1187	40	388	17	39.7	0.8	0.25	0.01	0.55	0.04	0.45	0.06	1.18	0.02	2.20	0.10	1.80	0.20
68.46	1296	90	804	39	192.5	2.1	0.24	0.00	0.59	0.01	0.91	0.05	1.98	0.05	2.48	0.07	3.83	0.21
65.32	1274	120	1265	38	195.2	1.5	0.25	0.00	0.53	0.02	0.26	0.02	3.17	0.05	2.17	0.06	1.04	0.08
64.43	1282	60	608	22	236.3	2.7	0.41	0.01	0.93	0.02	0.69	0.05	2.33	0.05	2.28	0.04	1.69	0.13
60.81	1296	90	1063	52	122.2	1.4	0.18	0.00	0.99	0.02	0.42	0.02	3.06	0.08	5.50	0.27	2.32	0.17
~130	1241	180	1209	21	152.9	9.2	0.41	0.02	0.96	0.06	1.55	0.12	4.56	0.27	2.37	0.05	3.81	0.20
~130	1241	180	1314	23	124.2	1.6	0.38	0.01	0.88	0.02	0.92	0.05	4.63	0.06	2.32	0.07	2.43	0.14
~130	1241	180	2917	76	46.9	0.7	0.4	0.01	1.13	0.03	0.62	0.04	13.64	0.20	2.79	0.05	1.53	0.11
~130	1241	180	1595	24	161.6	5.3	0.25	0.01	0.75	0.03	0.55	0.04	4.15	0.14	3.03	0.05	2.23	0.15
~130	1241	180	1459	35	141.9	2.9	0.28	0.01	0.76	0.02	0.48	0.03	4.05	0.09	2.68	0.08	1.70	0.11
~130	1241	180	1107	25	128.8	7.7	0.44	0.03	0.94	0.06	0.59	0.07	4.30	0.26	2.16	0.05	1.36	0.13
~130	1241	180	1730	78	113.7	1.8	0.22	0.01	1.00	0.02	0.9	0.06	4.79	0.08	4.56	0.20	4.08	0.29
~130	1241	180	1908	51	136.0	3.7	0.19	0.01	0.83	0.03	0.43	0.03	4.52	0.13	4.31	0.18	2.27	0.14
~130	1241	180	1663	28	166.1	2.4	0.23	0.01	0.92	0.02	0.69	0.04	4.59	0.07	3.92	0.11	2.95	0.17
~130	1241	180	1275	30	135.3	2.2	0.32	0.01	1.10	0.02	3.05	0.17	4.40	0.07	3.47	0.09	9.58	0.56
~130	1241	180	1426	32	166.2	6.2	0.33	0.01	0.82	0.03	0.88	0.06	4.53	0.17	2.47	0.06	2.65	0.15
~130	1241	180	1153	19	131.3	1.9	0.79	0.01	1.28	0.02	0.64	0.04	7.49	0.11	1.62	0.02	0.81	0.05

Table 4.24: Heating experiment data for hematite sample HM2 degassed in vacuum in Pt packets. T = temperature, t = total isothermal heating time, age = calculated (U-Th)/He age, mass = Fe-based sample mass.

T	t	age	1σ	mass	1σ	U	1σ	Th	1σ	Sm	1σ	He	1σ	Th/U	1σ	Sm/U	1σ
[°C]	[min]	[Ma]		[µg]		[ppm]		[ppm]		[ppm]		[nmol/g]					
553	24	46	1	56.39	2.15	0.98	0.04	1.22	0.06	0.28	0.05	0.32	0.01	1.25	0.04	0.29	0.04
625	24	69	2	84.40	2.03	1.20	0.03	1.03	0.04	0.36	0.03	0.54	0.02	0.86	0.02	0.30	0.03
699	24	148	2	104.49	3.52	1.40	0.05	0.42	0.02	0.12	0.03	1.22	0.02	0.30	0.01	0.09	0.02
766	24	151	10	34.70	1.36	3.46	0.19	3.49	0.20	1.38	0.69	3.55	0.05	1.01	0.06	0.40	0.20
841	24	152	5	18.90	0.92	1.43	0.07	2.28	0.15	0.69	0.14	1.63	0.03	1.59	0.07	0.48	0.11
906	24	345	6	136.49	3.76	1.14	0.03	1.21	0.03	0.77	0.08	2.73	0.04	1.06	0.02	0.68	0.07
908	24	406	9	109.87	4.95	1.11	0.05	1.17	0.06	0.52	0.06	3.16	0.03	1.06	0.02	0.47	0.06
973	24	498	7	102.08	1.69	1.40	0.02	1.46	0.04	0.93	0.06	4.92	0.11	1.04	0.02	0.66	0.04
978	24	480	13	37.33	1.17	1.13	0.04	2.22	0.08	1.13	0.12	4.45	0.06	1.98	0.07	1.00	0.10
976	24	510	6	97.08	3.58	1.07	0.04	1.06	0.04	0.27	0.04	3.81	0.04	0.99	0.02	0.25	0.04
1044	24	592	15	57.60	1.74	1.27	0.04	1.08	0.04	0.50	0.10	5.14	0.08	0.85	0.02	0.40	0.08
1095	24	3762	123	47.68	1.81	0.17	0.01	1.34	0.06	0.50	0.09	13.01	0.11	8.00	0.13	3.00	0.50
1156	18	6163	349	44.05	1.91	0.02	0.00	1.18	0.06	0.54	0.07	14.21	0.12	52.00	2.00	24.00	3.00
1185	24	5949	430	38.82	1.65	0.03	0.00	1.03	0.05	0.21	0.05	12.33	0.13	40.00	1.00	8.00	2.00
1040	80	1296	36	31.39	0.89	0.70	0.03	2.77	0.09	0.83	0.10	10.38	0.15	3.95	0.09	1.18	0.14
1048	80	2286	114	22.07	0.73	0.18	0.02	2.49	0.10	0.63	0.14	10.64	0.15	13.75	0.25	3.50	0.75
1021	40	5718	148	111.21	3.45	0.02	0.00	1.03	0.04	0.52	0.05	10.74	0.13	57.50	1.50	29.00	2.50
1058	80	6675	413	38.02	1.34	0.03	0.00	0.63	0.05	0.37	0.07	11.99	0.13	24.00	2.00	14.00	3.00
1095	60	6642	393	88.03	3.20	0.01	0.00	0.75	0.04	0.49	0.05	9.91	0.11	66.00	2.00	43.00	4.00
1116	80	3220	137	53.47	1.78	0.26	0.01	0.69	0.04	0.22	0.06	10.07	0.11	2.64	0.24	0.86	0.22
1017	60	5204	142	100.47	2.80	0.05	0.00	1.15	0.04	0.61	0.06	12.65	0.15	23.20	0.40	12.20	1.20
1086	80	4049	98	93.23	4.30	0.15	0.01	0.67	0.04	0.28	0.04	9.92	0.12	4.43	0.14	1.86	0.29
941	80	1070	14	60.80	1.83	1.73	0.05	5.51	0.18	3.57	0.29	18.98	0.20	3.19	0.05	2.07	0.15
976	80	3737	118	31.01	1.00	0.13	0.01	1.90	0.07	1.23	0.21	14.49	0.10	14.75	0.25	9.50	1.50
975	160	3283	104	41.07	1.03	0.27	0.01	0.78	0.04	0.51	0.08	10.94	0.10	2.91	0.09	1.91	0.27
976	240	4095	142	46.43	1.17	0.06	0.00	1.08	0.04	0.32	0.08	8.93	0.08	16.67	0.33	5.00	1.33
1007	180	2065	107	8.11	0.25	0.62	0.04	4.93	0.22	4.56	0.56	22.42	0.33	8.00	0.20	7.40	0.80
1009	360	1974	57	38.51	1.74	0.29	0.02	2.75	0.13	0.70	0.10	11.12	0.06	9.64	0.18	2.45	0.36
1054	360	1483	28	38.04	0.87	0.53	0.02	2.71	0.07	1.03	0.11	10.27	0.18	5.15	0.05	1.95	0.20
1054	120	2006	40	43.55	1.52	0.30	0.01	3.21	0.12	1.31	0.14	12.75	0.13	10.77	0.08	4.38	0.46
1094	12	2905	109	200.69	2.44	0.37	0.01	1.28	0.04	0.77	0.06	13.60	0.37	3.43	0.17	2.07	0.17
1157	12	5874	399	242.66	2.95	0.07	0.01	0.48	0.03	0.35	0.02	12.55	0.48	6.82	0.90	5.06	0.69
1217	10	4099	205	150.2	1.28	0.11	0.01	1.18	0.02	0.72	0.04	11.34	0.48	11.06	0.70	6.75	0.61

Table 4.25: Heating experiment data for hematite sample HM2 degassed in vacuum in Nb packets. T = temperature, t = total isothermal heating time, age = calculated (U-Th)/He age, mass = Fe-based sample mass.

T	t	age	1σ	mass	1σ	U	1σ	Th	1σ	Sm	1σ	He	1σ	Th/U	1σ	Sm/U	1σ
[°C]	[min]	[Ma]		[µg]		[ppm]		[ppm]		[ppm]		[nmol/g]					
592	6	106	7	9.80	0.05	1.03	0.03	1.53	0.14	0.88	0.19	0.80	0.38	1.48	0.10	0.85	0.20
735	6	254	5	29.96	0.19	1.10	0.01	0.87	0.05	0.20	0.05	1.84	0.32	0.79	0.03	0.18	0.03
853	6	332	19	10.87	0.05	0.93	0.03	2.02	0.12	0.92	0.19	2.60	0.55	2.17	0.10	0.99	0.20
918	6	462	31	8.39	0.05	1.12	0.04	1.31	0.11	0.60	0.15	3.73	0.71	1.17	0.11	0.53	0.11
913	6	658	22	19.14	0.09	1.07	0.02	1.15	0.06	0.42	0.07	5.06	0.89	1.07	0.05	0.39	0.05
917	6	572	39	8.47	0.06	1.06	0.03	1.06	0.14	0.35	0.12	4.28	0.72	1.00	0.11	0.33	0.11
950	6	622	17	17.43	0.08	1.23	0.02	1.38	0.06	0.46	0.08	5.52	0.79	1.12	0.05	0.37	0.05
1035	6	12	2	0.39	0.01	7.69	0.44	7.69	2.54	0.82	2.21	0.62	0.15	1.00	0.33	0.11	0.33
1042	6	1495	107	8.38	0.06	0.72	0.03	1.55	0.15	1.12	0.22	9.88	0.67	2.17	0.17	1.57	0.33
1084	6	1507	129	8.81	0.09	0.70	0.04	1.48	0.13	0.57	0.14	9.69	0.72	2.10	0.16	0.81	0.16
918	30	2558	117	8.17	0.05	1.03	0.02	0.98	0.15	0.37	0.16	22.77	1.93	0.95	0.12	0.36	0.12
922	6	2642	287	5.26	0.05	0.80	0.06	0.38	0.20	0.19	0.21	17.05	1.28	0.48	0.24	0.24	0.24
995	6	385	8	24.66	0.49	1.06	0.03	3.77	0.09	0.41	0.10	4.18	0.13	3.55	0.04	0.38	0.08
995	6	460	7	36.95	0.76	1.95	0.05	2.44	0.06	0.49	0.07	6.51	0.15	1.25	0.02	0.25	0.04
995	6	540	18	32.73	0.53	1.06	0.03	1.28	0.04	1.10	0.08	4.17	0.13	1.21	0.05	1.04	0.09
993	6	453	17	29.23	0.59	1.03	0.04	2.39	0.07	0.72	0.07	4.04	0.11	2.33	0.08	0.70	0.07
887	6	1065	35	19.32	0.39	0.98	0.03	0.62	0.06	0.88	0.14	7.20	0.17	0.63	0.05	0.89	0.16
991	6	1973	52	16.14	0.33	0.43	0.02	5.20	0.15	0.50	0.13	19.55	0.32	12.00	0.22	1.14	0.29
1056	6	1938	54	36.64	0.67	0.66	0.02	0.74	0.04	0.38	0.06	10.44	0.25	1.13	0.04	0.58	0.08
1051	6	1846	91	15.82	0.28	0.64	0.03	2.40	0.08	0.88	0.15	13.83	0.57	3.73	0.10	1.37	0.20
1095	6	4745	171	25.40	0.45	0.16	0.01	1.18	0.04	0.59	0.07	17.66	0.42	7.28	0.30	3.64	0.49

Table 4.26: Heating experiment data for hematite sample HM2 degassed in oxygen. $p(O_2)$ = oxygen partial pressure, T = temperature, t = total isothermal heating time, age = calculated (U-Th)/He age, mass = Fe-based sample mass.

$p(O_2)$	T	t	age	1σ	mass	1σ	U	1σ	Th	1σ	Sm	1σ	He	1σ	Th/U	1σ	Sm/U	1σ
[torr]	[°C]	[min]	[Ma]		[µg]		[ppm]		[ppm]		[ppm]		[nmol/g]					
~0.2	1162	10	4645	80	91.24	1.17	0.15	0	1.34	0.03	0.60	0.06	17.55	0.78	8.71	0.14	3.93	0.43
~0.2	873	10	196	8	101.46	0.69	1.21	0.03	0.85	0.08	0.64	0.07	1.53	0.11	0.70	0.07	0.53	0.06
~0.2	988	10	443	17	101.81	0.66	1.18	0.02	0.85	0.07	0.66	0.04	3.45	0.20	0.73	0.06	0.56	0.03
~0.2	1111	10	439	20	94.46	0.67	1.08	0.03	1.52	0.09	1.26	0.06	3.55	0.23	1.41	0.09	1.17	0.07
~0.2	1162	10	4785	322	105.04	0.67	0.15	0.01	0.30	0.06	0.13	0.02	11.36	0.56	2.00	0.40	0.88	0.20
~0.2	1215	10	7188	987	86.72	0.76	0.01	0.01	0.70	0.07	0.25	0.03	11.50	0.43	61.00	6.00	22.00	3.00
~0.2	1268	10	7332	887	96.92	0.78	0.01	0.01	0.83	0.07	0.44	0.04	13.06	0.83	80.00	7.00	43.00	4.00
~0.2	1162	10	477	25	94.06	1.47	0.88	0.03	0.75	0.08	0.01	-0.04	2.86	0.08	0.86	0.09	0.01	0.05
~0.4	1162	10	580	22	133.2	0.75	0.92	0.02	0.80	0.05	0.39	0.05	3.65	0.32	0.87	0.06	0.43	0.05
~0.6	1162	10	596	22	111.43	0.42	0.99	0.02	1.14	0.06	0.86	0.07	4.27	0.73	1.15	0.07	0.87	0.07
~2	1162	10	439	12	149.69	1.32	1.02	0.02	1.12	0.05	0.81	0.08	3.18	0.14	1.10	0.05	0.79	0.07
~0.2	1111	20	2009	48	147.86	4.09	0.80	0.03	3.37	0.12	2.51	0.13	20.00	0.29	4.22	0.11	3.14	0.15
~0.2	1111	65	3330	115	153.38	2.91	0.34	0.02	2.46	0.08	2.20	0.11	20.95	0.39	7.25	0.33	6.50	0.38
50.6	1160	10	437	17	208.19	0.95	1.01	0.02	1.12	0.04	0.50	0.03	3.14	0.05	1.11	0.04	0.49	0.03
49.7	1293	10	470	17	251.94	1.53	0.96	0.01	0.75	0.03	0.23	0.01	3.01	0.04	0.79	0.03	0.24	0.01
33.88	1035	6	408	20	103.7	1.14	1.03	0.03	1.00	0.06	0.57	0.06	2.91	0.04	0.97	0.06	0.55	0.06
32.78	1083	6	352	16	201.86	1.58	1.06	0.03	1.10	0.04	0.72	0.05	2.58	0.02	1.04	0.05	0.68	0.05
31.69	1291	6	525	13	185.62	1.28	1.22	0.02	1.66	0.04	1.11	0.06	4.78	0.03	1.36	0.04	0.91	0.05
30.68	1132	6	512	17	186.3	1.62	1.06	0.02	0.91	0.05	0.47	0.03	3.68	0.03	0.86	0.04	0.45	0.03
29.67	1187	6	465	19	249.14	1.97	1.08	0.03	1.55	0.04	1.14	0.06	3.78	0.03	1.43	0.05	1.06	0.06
28.68	1241	6	520	11	264.54	2.46	1.01	0.01	1.11	0.04	0.63	0.04	3.76	0.04	1.10	0.04	0.62	0.04
26.79	1291	6	481	15	200.58	4.06	1.03	0.03	1.29	0.05	0.84	0.05	3.62	0.07	1.25	0.05	0.82	0.05
25.03	1353	6	3986	184	187.98	1.99	0.02	0.01	2.90	0.06	2.39	0.13	17.12	0.18	181.67	3.33	150.00	8.00
31	1030	6	501	12	345	7.85	1.26	0.03	1.40	0.05	0.81	0.06	4.50	0.10	1.12	0.03	0.64	0.04
30	1078	6	540	20	219.23	3.33	1.00	0.03	1.11	0.04	0.52	0.03	3.87	0.06	1.11	0.04	0.52	0.04
29	1147	6	790	29	143.9	2.13	1.06	0.03	1.39	0.06	1.04	0.07	6.37	0.09	1.31	0.06	0.98	0.07
25.9	1344	100	1304	11	218.2	3.10	0.71	0.01	2.10	0.03	1.69	0.11	9.39	0.13	2.95	0.02	2.38	0.14
38.1	1405	80	3824	102	180.1	3.68	0.19	0.01	0.92	0.03	0.58	0.03	12.04	0.25	4.71	0.16	2.97	0.19
58.8	1274	110	532	13	175.11	1.39	1.10	0.01	1.97	0.02	1.18	0.08	4.70	0.06	1.79	0.02	1.07	0.07
57.9	1310	90	858	28	116.08	1.21	0.82	0.01	0.98	0.02	0.27	0.03	5.26	0.09	1.20	0.02	0.33	0.04
57.4	1296	90	642	15	176.89	1.59	0.97	0.01	1.25	0.02	0.63	0.04	4.62	0.07	1.30	0.01	0.65	0.04
96.8	1339	60	1416	18	162.0	2.81	0.82	0.02	1.78	0.03	1.49	0.09	10.67	0.19	2.17	0.02	1.82	0.11
95.8	1291	40	690	8	194.0	2.65	1.05	0.01	1.93	0.03	1.52	0.09	5.96	0.09	1.83	0.00	1.44	0.08
~100.0	1282	60	766	13	60.95	0.7	0.84	0.02	1.26	0.04	0.64	0.09	4.99	0.06	1.51	0.04	0.76	0.08
~100.0	1280	60	563	10	98.74	2.01	0.99	0.02	1.32	0.04	0.67	0.09	4.16	0.08	1.33	0.02	0.67	0.05
~100.0	1200	40	556	12	39.88	0.48	1.05	0.02	1.48	0.02	0.30	0.03	4.38	0.05	1.40	0.04	0.29	0.07
~100.0	1150	40	559	12	87.38	1.88	0.97	0.01	1.36	0.02	0.66	0.03	4.11	0.09	1.40	0.02	0.68	0.05
~100.0	1274	40	626	19	45.26	0.62	1.10	0.01	2.21	0.04	1.79	0.11	5.75	0.08	2.00	0.04	1.62	0.12
121.4	1132	240	1725	39	112.13	0.85	0.91	0.01	0.95	0.06	0.49	0.02	12.45	0.34	1.05	0.12	0.54	0.04
121.4	1129	240	1732	35	133.09	1.76	0.72	0.01	1.31	0.05	0.82	0.03	11.07	0.15	1.81	0.15	1.14	0.08

Table 4.27: Heating experiment data for hematite sample MS degassed in vacuum in Pt packets. T = temperature, t = total isothermal heating time, age = calculated (U-Th)/He age, mass = Fe-based sample mass, bdl = below detection limit.

T	t	age	1σ	mass	1σ	U	1σ	Th	1σ	Sm	1σ	He	1σ	Th/U	1σ	Sm/U	1σ
[°C]	[min]	[Ma]		[µg]		[ppm]		[ppm]		[ppm]		[nmol/g]					
556	24	172	4	14.03	0.18	8.34	0.15	bdl		1.78	0.27	8.15	0.10	bdl		0.21	0.03
592	24	187	5	17.07	0.16	5.45	0.09	0.41	0.05	1.23	0.13	5.98	0.06	0.08	0.01	0.23	0.02
699	12	413	7	31.52	0.32	7.71	0.11	0.41	0.03	1.49	0.12	18.50	0.19	0.05	0.00	0.19	0.02
770	24	489	7	43.57	0.93	6.91	0.16	0.18	0.03	1.38	0.13	19.56	0.42	0.03	0.00	0.20	0.02
905	24	545	12	9.79	0.23	7.76	0.20	bdl		1.84	0.20	25.48	0.60	bdl		0.24	0.03
978	12	735	15	19.03	0.31	5.25	0.10	0.05	0.06	1.63	0.10	23.50	0.38	0.01	0.01	0.31	0.02
972	24	639	8	17.23	0.25	6.04	0.10	0.06	0.05	1.57	0.23	23.22	0.34	0.01	0.01	0.26	0.04
971	24	439	7	8.03	0.18	9.96	0.24	bdl		1.99	0.24	26.14	0.59	bdl		0.20	0.03
1039	12	1012	27	13.85	0.16	3.68	0.07	0.14	0.10	1.66	0.12	25.00	0.29	0.04	0.02	0.45	0.04
1101	12	1523	35	15.85	0.16	2.08	0.04	0.13	0.06	1.83	0.24	23.76	0.24	0.06	0.03	0.88	0.12
1136	12	1684	48	25.35	0.36	1.85	0.04	bdl		1.66	0.18	22.48	0.32	bdl		0.89	0.09
1025	18	934	28	10.01	0.12	3.60	0.08	bdl		2.20	0.25	22.96	0.28	bdl		0.61	0.06
1032	24	989	24	7.28	0.12	3.85	0.09	bdl		2.06	0.31	26.98	0.44	bdl		0.54	0.07
1079	12	2389	109	4.37	0.17	0.69	0.04	0.23	0.28	2.97	0.41	29.95	1.17	0.33	0.33	4.33	0.67
1070	12	2330	117	6.27	0.15	0.80	0.04	bdl		2.39	0.31	25.34	0.61	bdl		3.00	0.40
1075	12	1871	69	14.49	0.24	1.45	0.05	bdl		1.79	0.24	21.91	0.36	bdl		1.24	0.20
1067	20	910	24	14.83	0.24	3.98	0.08	bdl		1.75	0.15	22.97	0.37	bdl		0.44	0.03
1081	40	3654	99	14.77	0.19	0.34	0.01	0.74	0.07	2.03	0.18	22.98	0.30	2.20	0.20	6.00	0.60
1084	60	3146	172	5.93	0.11	0.51	0.03	bdl		2.02	0.37	27.10	0.50	bdl		4.00	0.67
1084	90	3115	121	9.83	0.20	0.51	0.02	0.81	0.14	2.64	0.22	23.78	0.48	1.60	0.20	5.20	0.40
953	12	505	8	105.35	1.10	7.71	0.10	bdl		1.65	0.11	22.05	0.23	bdl		0.21	0.01
953	12	564	9	105.35	1.10	7.71	0.10	bdl		1.65	0.11	24.81	0.26	bdl		0.21	0.01
1228	10	1799	9	131.66	3.71	2.20	0.06	bdl		1.97	0.12	26.25	0.74	bdl		0.90	0.05
939	10	591	10	125.85	2.06	7.27	0.13	0.06	0.01	1.61	0.09	24.84	0.41	0.01	0.00	0.22	0.01
950	10	891	13	48.36	1.01	4.61	0.10	bdl		1.80	0.14	24.82	0.52	bdl		0.39	0.03
953	10	771	12	51.98	0.68	5.48	0.09	bdl		1.65	0.09	25.07	0.33	bdl		0.30	0.02
1049	10	4576	53	56.74	1.07	0.42	0.01	bdl		1.67	0.13	24.56	0.46	bdl		3.96	0.29
953	10	632	9	93.68	1.74	5.24	0.11	0.05	0.02	0.79	0.07	19.35	0.36	0.01	0.00	0.15	0.01
1103	10	2721	50	52.49	0.98	1.20	0.03	bdl		1.49	0.11	25.87	0.48	bdl		1.24	0.10
1215	10	7945	90	77.80	1.41	0.04	0.00	bdl		0.96	0.08	25.94	0.47	bdl		25.00	2.00
1136	10	5300	53	106.61	2.31	0.29	0.01	0.07	0.01	1.17	0.08	25.93	0.56	0.23	0.03	4.03	0.29
1157	10	4107	25	124.83	2.32	0.60	0.01	bdl		1.43	0.09	26.49	0.49	bdl		2.37	0.15
1215	10	6251	58	105.35	1.91	0.18	0.00	bdl		1.33	0.07	29.51	0.53	bdl		7.37	0.37
1175	10	3999	53	84.07	1.61	0.58	0.01	bdl		1.37	0.09	25.56	0.49	bdl		2.35	0.17
1165	10	5392	110	23.19	0.33	0.22	0.01	0.05	0.04	1.55	0.12	31.52	0.45	0.24	0.20	7.20	0.60
1170	10	5863	97	45.08	1.01	0.13	0.01	0.44	0.02	1.64	0.08	22.66	0.51	3.33	0.17	12.33	0.50
1162	10	5100	30	94.09	1.57	0.30	0.01	bdl		1.52	0.06	23.77	0.40	bdl		5.11	0.18
1173	10	4387	88	73.79	1.31	0.41	0.01	bdl		1.64	0.10	22.48	0.40	bdl		4.03	0.27
1173	10	4252	43	63.93	1.29	0.41	0.01	bdl		1.55	0.09	22.22	0.45	bdl		3.81	0.19
1173	10	6542	87	51.27	0.86	0.08	0.00	bdl		1.60	0.09	21.42	0.36	bdl		20.50	1.25
1173	10	5365	55	110.85	2.31	0.22	0.01	bdl		1.56	0.08	20.78	0.43	bdl		7.21	0.33
1173	10	3392	45	51.95	1.01	0.58	0.01	0.13	0.03	1.60	0.09	21.18	0.41	0.23	0.03	2.77	0.13
1173	10	3608	26	206.00	4.10	0.63	0.01	bdl		1.52	0.08	21.24	0.42	bdl		2.43	0.13
1173	10	3119	47	221.25	4.84	0.87	0.02	bdl		1.60	0.08	22.69	0.50	bdl		1.84	0.09
1173	10	6057	43	190.49	4.58	0.16	0.00	bdl		1.57	0.09	22.80	0.55	bdl		9.97	0.50
1173	10	3714	28	200.78	3.27	0.61	0.01	bdl		1.52	0.07	21.88	0.36	bdl		2.51	0.12
1173	10	4330	50	260.65	5.50	0.43	0.01	bdl		1.53	0.08	21.20	0.45	bdl		3.57	0.17
1173	10	5811	48	176.61	3.71	0.16	0.00	bdl		1.53	0.08	20.09	0.42	bdl		9.68	0.43
1173	10	4565	39	202.49	4.85	0.40	0.01	bdl		1.54	0.11	22.12	0.53	bdl		3.89	0.25
1173	10	5520	50	167.75	3.09	0.23	0.01	bdl		1.56	0.08	23.16	0.43	bdl		6.89	0.36
1173	10	3121	34	235.19	4.76	0.84	0.02	bdl		1.54	0.07	22.09	0.45	bdl		1.83	0.08
1173	10	3219	47	185.16	5.12	0.80	0.02	bdl		1.57	0.10	22.23	0.61	bdl		1.95	0.12
1173	10	3168	45	222.25	5.49	0.81	0.02	bdl		1.57	0.08	21.53	0.53	bdl		1.96	0.10
1173	10	2010	25	196.06	3.35	1.57	0.03	bdl		1.56	0.08	21.71	0.37	bdl		0.99	0.05

Table 4.28: Heating experiment data for hematite sample MS degassed in vacuum in Pt packets at 950 °C for various lengths of time. T = temperature, t = isothermal heating time, age = calculated (U-Th)/He age, mass = Fe-based sample mass.

T	t	age	1σ	mass	1σ	U	1σ	Th	1σ	Sm	1σ	He	1σ	Th/U	1σ	Sm/U	1σ
[°C]	[min]	[Ma]		[µg]		[ppm]		[ppm]		[ppm]		[nmol/g]					
983	5	547	9	139.87	3.86	7.29	0.21	bdl		1.49	0.16	22.91	0.63	bdl		0.20	0.02
986	5	446	8	86.23	2.16	7.10	0.19	bdl		1.54	0.17	18.03	0.41	bdl		0.22	0.02
974	10	542	10	69.95	1.63	7.42	0.19	bdl		1.53	0.19	23.12	0.54	bdl		0.21	0.03
981	10	572	12	187.47	5.66	7.42	0.24	bdl		1.49	0.15	24.38	0.74	bdl		0.20	0.02
986	30	586	10	193.18	4.71	7.61	0.20	bdl		1.48	0.15	25.70	0.63	bdl		0.19	0.02
974	30	601	7	95.97	2.66	6.93	0.20	bdl		1.58	0.18	24.23	0.67	bdl		0.23	0.03
986	60	848	18	83.67	2.36	4.96	0.15	bdl		1.63	0.21	25.22	0.71	bdl		0.33	0.04
986	60	648	17	136.20	3.98	6.17	0.20	bdl		1.58	0.17	23.29	0.68	bdl		0.26	0.03
986	120	591	9	98.55	2.05	6.78	0.15	bdl		1.53	0.17	23.21	0.48	bdl		0.23	0.02
986	120	2307	29	84.75	2.39	1.47	0.04	bdl		1.57	0.20	25.26	0.71	bdl		1.06	0.14
979	240	5122	69	59.58	1.75	0.35	0.01	bdl		1.63	0.17	25.32	0.74	bdl		4.62	0.48
981	240	5992	100	95.65	2.50	0.18	0.01	bdl		1.75	0.23	26.76	0.70	bdl		9.82	1.36

Table 4.29: Heating experiment data for hematite sample MS degassed in oxygen in Pt packets. $p(O_2)$ = oxygen partial pressure, T = temperature, t = total isothermal heating time, age = calculated (U-Th)/He age, mass = Fe-based sample mass.

$p(O_2)$	T	t	age	1σ	mass	1σ	U	1σ	Th	1σ	Sm	1σ	He	1σ	Th/U	1σ	Sm/U	1σ
[torr]	[°C]	[min]	[Ma]		[µg]		[ppm]		[ppm]		[ppm]		[nmol/g]					
~0.2	988	10	516	8	103.24	0.71	7.58	0.08	bdl		1.92	0.14	22.26	0.15	bdl		0.25	0.02
~0.2	1111	10	758	14	47.09	0.36	5.80	0.07	bdl		1.74	0.12	25.58	0.20	bdl		0.30	0.02
~0.2	1162	10	7275	585	79.07	0.55	0.08	0.05	bdl		1.73	0.14	27.05	0.19	bdl		22.83	4.22
~0.2	1215	10	6769	482	73.59	0.60	0.11	0.02	bdl		1.75	0.11	25.92	0.21	bdl		16.13	2.25
~0.2	1268	10	6669	745	62.12	0.50	0.11	0.03	0.08	0.10	1.69	0.11	25.44	0.20	0.71	0.88	15.00	4.40
~.2	1111	40	584	10	144.25	1.28	5.97	0.08	0.12	0.01	1.89	0.06	20.21	0.18	0.02	0.00	0.32	0.01
~0.2	1111	60	6889	66	137.03	1.14	0.09	0.00	0.07	0.01	1.81	0.07	24.89	0.21	0.69	0.08	19.08	0.77
~0.2	1111	80	854	12	143.89	1.04	4.60	0.05	0.17	0.01	3.39	0.13	23.56	0.17	0.04	0.00	0.74	0.03
~0.2	1111	50	575	6	132.21	0.66	7.81	0.06	0.08	0.01	1.70	0.06	25.92	0.13	0.01	0.00	0.22	0.01
~0.2	1111	60	2626	40	142.34	1.32	1.20	0.02	bdl		1.82	0.08	24.07	0.22	bdl		1.51	0.07
57.8	1187	10	598	10	181.72	0.89	6.94	0.07	bdl		1.61	0.09	23.87	0.13	bdl		0.23	0.01
56.8	1182	10	830	23	82.60	0.37	4.46	0.06	0.18	0.08	1.69	0.10	22.22	0.18	0.04	0.02	0.38	0.02
55.8	1113	10	560	13	66.67	0.26	7.92	0.09	bdl		1.53	0.13	25.43	0.18	bdl		0.19	0.02
54.8	1174	10	717	22	78.91	0.99	6.70	0.14	0.15	0.03	1.32	0.19	28.13	0.38	0.02	0.02	0.20	0.03
52.2	993	10	515	39	80.87	5.22	7.46	0.55	0.64	0.06	1.38	0.24	22.66	1.88	0.09	0.01	0.19	0.03
42	1241	10	1125	31	86.44	1.01	3.92	0.07	bdl		1.76	0.10	27.08	0.34	bdl		0.45	0.03
42.5	1038	6	594	56	201.01	10.90	9.24	0.67	0.11	0.04	2.14	0.21	31.69	1.72	0.01	0.00	0.23	0.02
42	1070	6	523	51	137.85	7.43	7.73	0.57	bdl		1.98	0.22	23.11	1.25	bdl		0.26	0.03
41.5	1200	6	644	64	119.05	6.50	7.85	0.59	bdl		1.82	0.20	29.27	1.60	bdl		0.23	0.03
41	1171	6	555	58	139.59	8.03	7.76	0.61	bdl		1.92	0.22	24.68	1.42	bdl		0.25	0.03
40.5	1238	6	1526	160	90.88	5.01	3.06	0.25	bdl		1.86	0.23	29.89	1.65	bdl		0.61	0.07
40	1310	6	2481	234	118.48	6.79	1.76	0.15	bdl		1.70	0.20	31.63	1.81	bdl		0.97	0.12
39.8	1033	10	516	9	126.78	1.60	8.42	0.13	bdl		1.89	0.10	24.82	0.32	bdl		0.22	0.01
39.2	1083	10	510	8	115.11	1.53	8.89	0.14	bdl		1.89	0.10	25.87	0.36	bdl		0.21	0.01
38.6	1126	10	616	9	131.25	1.75	7.63	0.12	bdl		1.89	0.10	27.22	0.37	bdl		0.25	0.01
37.9	1187	10	640	13	116.73	2.00	7.20	0.14	bdl		1.81	0.11	26.75	0.47	bdl		0.25	0.01
37.33	1200	10	718	18	58.72	0.81	6.47	0.11	0.17	0.11	1.87	0.11	27.53	0.41	0.03	0.02	0.29	0.02
36.68	1288	10	1847	49	101.71	1.50	2.14	0.05	0.07	0.06	2.01	0.12	26.89	0.41	0.03	0.03	0.94	0.06
~35	1083	12	498	11	104.48	1.20	6.91	0.12	bdl		1.69	0.11	19.56	0.22	bdl		0.25	0.02
~35	1188	12	1221	40	52.65	0.52	3.32	0.07	bdl		1.71	0.10	25.25	0.25	bdl		0.51	0.03
~35	1377	6	4572	254	74.53	0.87	0.52	0.04	bdl		1.64	0.08	29.48	0.34	bdl		3.13	0.29
~35	1134	6	613	15	104.48	1.20	6.91	0.12	bdl		1.69	0.11	24.37	0.28	bdl		0.25	0.02
~35	1137	6	543	11	90.25	0.91	7.92	0.12	bdl		1.62	0.09	24.52	0.25	bdl		0.20	0.01
97.66	1382	20	2644	36	120.99	1.36	1.41	0.02	bdl		2.19	0.10	28.88	0.33	bdl		1.55	0.07
107.3	1129	10	575	4	177.41	2.72	8.39	0.13	bdl		1.78	0.11	27.69	0.56	bdl		0.21	0.01
107.3	1126	10	590	8	172.09	1.47	8.10	0.09	bdl		1.81	0.11	27.50	1.25	bdl		0.22	0.01
107.3	1124	10	577	5	201.73	2.72	8.08	0.11	bdl		1.70	0.10	26.83	0.56	bdl		0.21	0.01
107.3	1129	10	571	7	210.97	5.63	8.50	0.23	bdl		1.78	0.12	27.88	0.35	bdl		0.21	0.01
107.3	1121	10	563	5	146.67	1.97	8.66	0.12	bdl		1.85	0.11	28.08	0.78	bdl		0.21	0.01

Table 4.30: Heating experiment data for hematite sample MS degassed in oxygen in Pt packets (continued). $p(O_2)$ = oxygen partial pressure, T = temperature, t = total isothermal heating time, age = calculated (U-Th)/He age, mass = Fe-based sample mass.

$p(O_2)$	T	t	age	1σ	mass	1σ	U	1σ	Th	1σ	Sm	1σ	He	1σ	Th/U	1σ	Sm/U	1σ
[torr]	[°C]	[min]	[Ma]		[µg]		[ppm]		[ppm]		[ppm]		[nmol/g]					
107.3	1121	10	590	9	135.30	1.25	8.41	0.10	0.01	0.05	1.83	0.09	28.65	0.70	0.00	0.01	0.22	0.01
107.3	1132	10	583	4	154.43	1.30	9.04	0.08	-0.02	-0.04	2.00	0.10	30.28	0.91	0.00	0.00	0.22	0.01
107.3	1129	10	596	4	153.21	2.23	8.50	0.13	0.05	0.04	1.85	0.09	29.23	0.63	0.01	0.00	0.22	0.01
107.3	1132	10	579	7	191.47	2.43	8.52	0.12	0.00	-0.03	1.81	0.08	28.36	1.03	0.00	0.00	0.21	0.01
107.3	1129	10	570	7	208.80	2.75	8.73	0.13	0.02	0.03	1.85	0.09	28.65	0.69	0.00	0.00	0.21	0.01
107.3	1124	10	586	8	110.62	0.97	8.54	0.09	-0.02	-0.06	1.89	0.10	28.75	1.34	0.00	-0.01	0.22	0.01
107.3	1124	10	566	8	144.50	2.14	8.80	0.15	0.00	-0.04	1.85	0.09	28.55	0.66	0.00	0.00	0.21	0.01
~130	1203	40	1164	24	37.80	0.65	3.89	0.08	0.03	0.03	1.61	0.14	28.27	0.49	0.01	0.01	0.41	0.03
~130	1200	40	1007	27	35.14	0.56	5.78	0.13	-0.03	0.03	1.59	0.15	35.47	0.57	0.00	0.00	0.28	0.02
~130	1214	40	915	14	117.63	2.35	6.16	0.13	0.01	0.01	1.84	0.15	33.66	0.67	0.00	0.00	0.30	0.02
~130	1198	40	753	14	79.78	1.18	6.56	0.12	1.09	0.03	1.89	0.17	30.16	0.45	0.17	0.00	0.29	0.03
~130	1195	40	1265	48	83.65	1.59	4.38	0.13	-0.01	0.04	2.13	0.16	34.56	0.66	0.00	-0.01	0.49	0.04
~130	1195	40	1453	31	51.41	0.86	3.05	0.06	0.02	0.02	1.85	0.09	28.94	0.48	0.01	0.01	0.61	0.03
~130	1192	20	919	24	95.93	2.00	5.84	0.15	-0.02	0.02	2.19	0.16	32.21	0.67	0.00	0.00	0.38	0.03
~130	1190	20	949	11	44.41	0.76	5.07	0.09	0.01	0.03	1.73	0.10	29.18	0.50	0.00	0.00	0.34	0.02
~130	1182	20	777	17	66.17	0.84	7.12	0.12	0.01	0.03	1.72	0.14	32.63	0.41	0.00	0.00	0.24	0.02
~130	1214	20	908	13	81.84	1.45	6.32	0.12	0.01	0.01	1.96	0.14	34.28	0.61	0.00	0.00	0.31	0.02
~130	1200	20	1101	12	96.04	1.81	5.15	0.10	-0.01	0.01	1.77	0.14	34.73	0.65	0.00	0.00	0.34	0.03
~130	1182	20	906	19	51.73	1.94	5.92	0.23	0.02	0.03	2.01	0.15	32.28	1.21	0.00	0.00	0.34	0.02
~130	1195	40	1025	37	151.39	2.94	5.58	0.15	0.01	0.01	1.83	0.13	34.52	0.67	0.00	0.00	0.33	0.02
~130	1198	40	909	21	201.98	4.75	5.91	0.16	0.00	0.01	2.13	0.12	32.05	0.75	0.00	0.00	0.36	0.02
~130	1182	20	800	10	233.90	6.36	6.37	0.18	0.00	0.01	1.99	0.12	30.00	0.82	0.00	0.00	0.31	0.01
~130	1176	20	682	7	132.57	2.83	8.66	0.19	-0.01	0.01	1.73	0.11	34.39	0.73	0.00	0.00	0.20	0.01
~130	1187	20	738	7	189.17	4.49	8.34	0.20	-0.02	0.01	1.96	0.11	36.02	0.85	0.00	0.00	0.24	0.01
~130	1179	20	785	7	149.74	2.16	7.14	0.11	-0.01	0.01	2.10	0.10	32.96	0.48	0.00	0.00	0.29	0.01
~130	1176	20	714	18	124.28	1.57	8.43	0.15	0.00	0.01	1.73	0.11	35.18	0.44	0.00	0.00	0.21	0.01
~130	1182	20	815	8	169.22	3.03	7.04	0.13	0.98	0.02	2.17	0.17	34.93	0.63	0.14	0.00	0.31	0.02
~130	1182	20	767	19	162.98	1.62	8.04	0.14	0.01	0.01	1.84	0.10	36.20	0.36	0.00	0.00	0.23	0.01
~130	1190	20	803	13	204.66	3.26	7.73	0.14	-0.01	0.01	2.05	0.11	36.60	0.58	0.00	0.00	0.26	0.01
~130	1174	20	684	9	152.55	2.49	9.39	0.17	0.01	0.01	1.84	0.11	37.43	0.61	0.00	0.00	0.20	0.01
121.4	1008	5	590	7	156.82	1.61	9.00	0.11	-0.01	-0.04	1.94	0.09	30.35	0.60	0.00	0.01	0.22	0.02
121.4	1006	10	573	7	136.44	1.40	8.72	0.10	-0.02	-0.05	1.96	0.10	28.51	0.71	0.00	0.01	0.22	0.02
121.4	1011	30	562	8	112.70	1.28	8.46	0.11	-0.01	-0.05	1.85	0.08	27.09	0.72	0.00	0.01	0.22	0.02
121.4	1008	90	564	10	173.91	2.30	8.97	0.15	0.01	0.04	2.11	0.10	28.84	0.70	0.00	0.01	0.24	0.02
121.4	1004	120	594	9	154.32	1.65	8.24	0.11	-0.02	-0.04	2.05	0.10	28.02	0.98	0.00	0.01	0.25	0.02
121.4	1000	240	563	8	83.89	0.99	8.47	0.12	0.04	0.07	1.94	0.10	27.24	0.76	0.00	0.02	0.23	0.02

Table 4.31: Heating experiment data for hematite sample GC degassed in vacuum. T = temperature, t = total isothermal heating time, age = calculated (U-Th)/He age, mass = Fe-based sample mass.

T	t	age	1σ	mass	1σ	U	1σ	Th	1σ	Sm	1σ	He	1σ	Th/U	1σ	Sm/U	1σ
[°C]	[min]	[Ma]		[µg]		[ppm]		[ppm]		[ppm]		[nmol/g]					
553	10	20.6	1.4	7.50	0.06	12.80	0.45	5.87	0.55	8.40	0.41	1.59	0.31	0.46	0.04	0.66	0.04
700	10	17.9	1.4	5.76	0.07	12.15	0.49	3.82	0.66	12.33	0.73	1.27	0.18	0.31	0.06	1.01	0.07
765	10	32.6	1.1	10.75	0.08	13.58	0.26	7.53	0.37	20.00	0.91	2.73	0.35	0.55	0.03	1.47	0.07
827	10	43.8	1.3	15.85	0.11	12.56	0.23	7.38	0.25	13.82	0.58	3.41	0.25	0.59	0.02	1.10	0.05
916	10	53.6	1.3	23.67	0.19	11.32	0.17	6.46	0.21	17.36	0.73	3.76	0.22	0.57	0.02	1.53	0.07
962	10	56.2	3.1	10.61	0.07	12.63	0.37	6.88	0.40	24.60	1.09	4.37	0.44	0.54	0.03	1.95	0.10
1010	10	72.8	2.1	18.13	0.12	11.80	0.19	6.51	0.21	7.50	0.37	5.30	0.39	0.55	0.02	0.64	0.03
1051	10	54.3	1.6	20.95	0.17	12.55	0.22	6.01	0.23	14.94	0.67	4.14	0.30	0.48	0.02	1.19	0.06
1096	10	51.8	3.0	6.13	0.05	13.21	0.41	7.83	0.61	9.46	0.61	4.25	0.52	0.59	0.05	0.72	0.05
1152	10	45.7	2.0	11.11	0.08	12.33	0.29	6.66	0.37	9.45	0.59	3.46	0.31	0.54	0.03	0.77	0.05
1207	10	50.1	2.3	9.20	0.07	12.83	0.33	8.04	0.44	26.20	1.44	4.02	0.44	0.63	0.04	2.04	0.12
1298	10	69.8	2.0	22.85	0.19	11.73	0.21	7.96	0.25	21.93	1.00	5.19	0.34	0.68	0.02	1.87	0.09

Table 4.32: Heating experiment data for goethite sample blade degassed in vacuum in Pt packets. T = temperature, t = total isothermal heating time, age = calculated (U-Th)/He age, mass = Fe-based sample mass.

T	t	age	1σ	mass	1σ	U	1σ	Th	1σ	Sm	1σ	He	1σ	Th/U	1σ	Sm/U	1σ
[°C]	[min]	[Ma]		[µg]		[ppm]		[ppm]		[ppm]		[nmol/g]					
665	6	281	5	91.99	1.06	1.86	0.03	0.07	0.01	0.59	0.04	2.91	0.03	0.04	0.01	0.32	0.02
765	6	456	9	157.55	1.37	1.03	0.02	0.24	0.01	1.05	0.05	2.77	0.02	0.23	0.01	1.02	0.05
873	6	188	3	77.19	0.82	1.84	0.02	0.17	0.01	0.73	0.05	1.92	0.02	0.09	0.01	0.39	0.03
934	6	647	10	72.84	1.21	2.59	0.05	0.27	0.01	1.54	0.07	9.80	0.16	0.11	0.01	0.59	0.03
939	6	219	9	79.51	0.92	0.28	0.00	0.19	0.01	0.30	0.03	0.35	0.00	0.68	0.05	1.09	0.09
941	6	996	18	142.81	1.43	1.51	0.02	0.12	0.01	1.01	0.07	9.04	0.09	0.08	0.00	0.67	0.05
988	6	426	5	188.76	2.64	2.08	0.03	0.05	0.01	0.71	0.05	5.01	0.07	0.03	0.00	0.34	0.02
1056	6	170	3	131.86	1.47	2.64	0.04	0.03	0.01	0.80	0.04	2.47	0.03	0.01	0.00	0.30	0.01
1103	6	623	17	147.02	0.98	0.46	0.01	0.12	0.01	1.00	0.06	1.70	0.01	0.26	0.02	2.16	0.14
1186	6	703	13	108.10	1.49	1.24	0.02	-0.05	-0.01	0.95	0.06	5.03	0.07	-0.04	-0.01	0.77	0.05
1244	6	4992	67	102.16	1.56	0.08	0.00	0.21	0.01	0.71	0.04	6.00	0.09	2.63	0.13	9.13	0.50
1307	6	2481	96	60.42	0.60	0.17	0.00	0.23	0.02	1.39	0.08	3.22	0.03	1.40	0.10	8.40	0.50

Table 4.33: Heating experiment data for goethite sample blade degassed in oxygen in Pt packets. $p(O_2)$ = oxygen partial pressure, T = temperature, t = total isothermal heating time, age = calculated (U-Th)/He age, mass = Fe-based sample mass.

$p(O_2)$	T	t	age	1σ	mass	1σ	U	1σ	Th	1σ	Sm	1σ	He	1σ	Th/U	1σ	Sm/U	1σ
[torr]	[°C]	[min]	[Ma]		[µg]		[ppm]		[ppm]		[ppm]		[nmol/g]					
~100	960	20	1540	29	52.78	0.56	1.74	0.03	0.28	0.04	0.83	0.08	17.07	0.18	0.16	0.02	0.48	0.04
~100	1008	20	244	5	76.47	0.72	2.41	0.03	0.07	0.01	0.93	0.08	3.28	0.03	0.03	0.01	0.39	0.03
~100	1083	20	149	3	99.94	0.90	1.16	0.01	0.04	0.01	0.61	0.05	0.95	0.01	0.03	0.01	0.53	0.04
~100	1134	20	686	16	76.27	0.58	1.63	0.03	0.21	0.01	1.57	0.12	6.48	0.05	0.13	0.01	0.97	0.07
~100	1182	20	166	4	52.53	0.27	2.34	0.02	0.63	0.04	1.07	0.10	2.15	0.01	0.27	0.02	0.46	0.04
~100	960	20	236	4	74.44	0.73	1.36	0.02	0.31	0.01	0.59	0.05	1.78	0.02	0.23	0.01	0.44	0.04

Table 4.34: Heating experiment data for goethite sample CIT degassed in vacuum in Pt packets. T = temperature, t = total isothermal heating time, age = calculated (U-Th)/He age, mass = Fe-based sample mass.

T	t	age	1σ	mass	1σ	U	1σ	Th	1σ	Sm	1σ	He	1σ	Th/U	1σ	Sm/U	1σ
[°C]	[min]	[Ma]		[µg]		[ppm]		[ppm]		[ppm]		[nmol/g]					
765	20	9.3	0.2	21.26	0.53	92.90	2.49	0.05	0.09	2.54	0.21	4.71	0.07	0.001	0.001	0.027	0.002
822	20	33.9	0.6	40.26	1.04	23.03	0.63	-0.05	0.05	1.04	0.10	4.25	0.05	-0.002	-0.002	0.045	0.004
1007	20	10.2	0.2	42.78	0.91	88.24	2.03	-0.02	0.04	2.10	0.17	4.91	0.08	0.000	-0.001	0.024	0.002
943	20	16.8	0.4	92.82	2.12	56.66	1.43	0.01	0.01	0.92	0.09	5.18	0.08	0.000	0.000	0.016	0.002
1093	20	18.3	0.3	45.97	1.08	47.99	1.22	0.22	0.04	3.20	0.27	4.79	0.08	0.005	0.001	0.067	0.005
1118	20	19.6	0.4	108.83	2.01	48.75	1.02	0.14	0.02	2.32	0.18	5.19	0.13	0.003	0.000	0.048	0.004
1188	20	44.5	1.0	27.73	0.58	20.45	0.49	0.40	0.05	3.82	0.35	4.98	0.11	0.019	0.002	0.187	0.016
1212	20	28.7	0.7	63.02	1.14	35.66	0.76	-0.03	0.02	2.94	0.28	5.57	0.18	-0.001	0.000	0.082	0.008
1293	20	687.8	29.1	32.01	0.66	1.25	0.04	0.34	0.05	4.03	0.31	5.31	0.11	0.275	0.050	3.225	0.263
1249	20	398.3	9.7	24.39	0.54	2.95	0.08	-0.04	0.06	2.99	0.25	6.60	0.12	-0.014	-0.014	1.014	0.085
1207	20	41.3	0.8	49.76	1.16	19.39	0.48	0.12	0.02	1.13	0.12	4.36	0.11	0.006	0.001	0.058	0.006

Table 4.35: Heating experiment data for goethite sample CIT degassed in oxygen in Pt packets. $p(O_2)$ = oxygen partial pressure, T = temperature, t = total isothermal heating time, age = calculated (U-Th)/He age, mass = Fe-based sample mass.

$p(O_2)$	T	t	age	1σ	mass	1σ	U	1σ	Th	1σ	Sm	1σ	He	1σ	Th/U	1σ	Sm/U	1σ
[torr]	[°C]	[min]	[Ma]		[µg]		[ppm]		[ppm]		[ppm]		[nmol/g]					
~120	780	20	9.5	0.1	38.61	0.56	107.95	1.71	0.18	0.08	4.04	0.21	5.60	0.22	0.002	0.001	0.037	0.002
~120	890	20	10.3	0.1	36.82	0.69	90.03	1.81	0.01	0.05	2.28	0.17	5.02	0.13	0.000	0.001	0.025	0.002
~120	957	20	9.7	0.1	52.57	0.94	104.58	1.99	0.04	0.02	1.83	0.15	5.54	0.17	0.000	0.000	0.017	0.001
~120	1033	20	11.1	0.2	38.52	0.78	92.19	1.97	-0.05	0.03	4.00	0.22	5.52	0.13	-0.001	0.000	0.043	0.002
~120	1083	20	11.2	0.2	40.99	0.81	93.85	2.01	0.12	0.03	4.64	0.28	5.70	0.16	0.001	0.000	0.049	0.003
~120	1134	20	22.2	0.3	40.73	0.82	38.20	0.82	0.05	0.03	0.56	0.05	4.61	0.11	0.001	0.001	0.015	0.001
~120	1182	20	64.2	0.8	20.51	0.46	19.41	0.46	-0.10	0.07	2.68	0.26	6.89	0.16	-0.005	-0.003	0.138	0.013
~120	1241	20	43.2	0.7	21.38	0.33	18.57	0.32	0.05	0.07	0.70	0.12	4.39	0.18	0.003	0.003	0.038	0.005
~120	1291	20	577.3	10.5	35.39	0.67	1.75	0.04	0.03	0.04	4.27	0.32	5.94	0.13	0.016	0.016	2.435	0.182

Table 4.36: Heating experiment data for goethite sample Lyp degassed in vacuum in Pt packets. T = temperature, t = total isothermal heating time, age = calculated (U-Th)/He age, mass = Fe-based sample mass.

T	t	age	1σ	mass	1σ	U	1σ	Th	1σ	Sm	1σ	He	1σ	Th/U	1σ	Sm/U	1σ
[°C]	[min]	[Ma]		[µg]		[ppm]		[ppm]		[ppm]		[nmol/g]					
923	10	41.2	0.6	24.8	0.3	3.43	0.05	12.39	0.18	1.74	0.16	1.42	0.01	3.61	0.06	0.51	0.05
974	10	28.7	0.6	17.6	0.3	1.93	0.03	6.54	0.15	1.36	0.12	0.54	0.01	3.38	0.06	0.71	0.06
1031	10	72.8	2.2	7.7	0.1	0.52	0.01	17.62	0.33	3.00	0.39	1.86	0.02	33.75	0.50	5.75	0.75
1086	10	39.7	0.8	21.8	0.3	0.64	0.01	10.62	0.20	1.38	0.14	0.68	0.01	16.50	0.21	2.14	0.21
1086	10	91.0	1.4	40.4	0.5	0.79	0.03	11.05	0.15	1.81	0.15	1.69	0.02	13.97	0.45	2.28	0.20
1152	10	70.0	0.9	51.8	0.4	0.91	0.02	16.35	0.17	2.45	0.16	1.81	0.01	18.02	0.40	2.70	0.18

Table 4.37: Heating experiment data for goethite sample Lyp degassed in oxygen in Pt packets. $p(O_2)$ = oxygen partial pressure, T = temperature, t = total isothermal heating time, age = calculated (U-Th)/He age, mass = Fe-based sample mass.

$p(O_2)$	T	t	age	1σ	mass	1σ	U	1σ	Th	1σ	Sm	1σ	He	1σ	Th/U	1σ	Sm/U	1σ
[torr]	[°C]	[min]	[Ma]		[µg]		[ppm]		[ppm]		[ppm]		[nmol/g]					
~120	960	20	31.6	0.6	60.1	0.5	3.31	0.06	10.22	0.12	1.02	0.08	0.98	0.01	3.09	0.05	0.31	0.03
~120	1008	20	40.5	0.6	66.4	0.5	4.46	0.06	9.25	0.09	1.52	0.09	1.46	0.01	2.07	0.02	0.34	0.02
~120	1083	20	39.2	0.5	43.5	0.3	4.78	0.06	14.89	0.16	2.48	0.18	1.77	0.01	3.12	0.04	0.52	0.04
~120	1134	20	32.0	0.4	23.8	0.2	3.78	0.05	12.68	0.15	1.22	0.08	1.18	0.01	3.36	0.05	0.32	0.02
~120	1184	20	21.1	0.6	13.4	0.1	8.98	0.18	5.76	0.10	50.79	2.67	1.19	0.01	0.64	0.01	5.66	0.31
~120	1263	30	57.1	1.0	24.3	0.2	0.99	0.01	16.69	0.20	1.97	0.21	1.53	0.01	16.92	0.17	2.00	0.21
~120	1006	10	35.6	0.5	34.8	0.5	2.53	0.05	6.27	0.11	0.89	0.09	0.78	0.01	2.48	0.04	0.35	0.03
~120	1006	10	38.3	0.5	11.7	0.2	4.46	0.06	12.02	0.23	1.55	0.09	1.52	0.02	2.69	0.04	0.35	0.02
~120	1068	10	49.0	0.7	17.6	0.2	2.95	0.07	6.19	0.09	1.25	0.11	1.18	0.01	2.10	0.04	0.42	0.04
~120	1068	10	44.8	0.7	20.6	0.2	4.02	0.07	9.50	0.15	1.26	0.10	1.53	0.02	2.36	0.04	0.31	0.02
~120	1132	10	29.6	0.5	25.6	0.4	2.43	0.05	2.43	0.05	1.02	0.08	0.48	0.01	1.00	0.02	0.42	0.03
~120	1132	10	42.8	0.9	14.5	0.2	3.67	0.09	13.15	0.23	1.94	0.14	1.58	0.02	3.58	0.08	0.53	0.04
~120	1184	10	45.3	0.4	47.4	0.7	3.88	0.06	8.97	0.15	1.27	0.09	1.48	0.02	2.31	0.02	0.33	0.02
~120	1182	10	42.9	0.9	14.6	0.2	2.46	0.08	6.23	0.11	1.23	0.14	0.91	0.01	2.53	0.08	0.50	0.06
~120	1235	10	64.8	0.9	16.5	0.2	0.67	0.01	15.25	0.25	1.76	0.18	1.51	0.02	22.91	0.18	2.64	0.27
~120	1235	10	58.0	0.7	16.9	0.2	2.19	0.03	11.93	0.19	1.89	0.12	1.58	0.02	5.46	0.05	0.86	0.05

Table 4.38: Heating experiment data for goethite sample RH degassed in vacuum in Pt packets. T = temperature, t = total isothermal heating time, age = calculated (U-Th)/He age, mass = Fe-based sample mass.

T	t	age	1σ	mass	1σ	U	1σ	Th	1σ	Sm	1σ	He	1σ	Th/U	1σ	Sm/U	1σ
[°C]	[min]	[Ma]		[µg]		[ppm]		[ppm]		[ppm]		[nmol/g]					
763	20	55.5	1.3	112.7	2.3	0.80	0.02	0.10	0.02	2.31	0.18	0.260	0.007	0.12	0.02	2.89	0.22
871	20	60.6	3.6	13.3	0.4	0.86	0.02	0.53	0.08	3.23	0.39	0.352	0.021	0.61	0.09	3.74	0.43
1136	20	422.1	51.5	37.3	0.8	0.13	0.00	0.03	0.03	2.30	0.19	0.339	0.021	0.20	0.20	17.20	1.40
1228	20	278.6	37.0	47.2	1.2	0.19	0.02	0.15	0.02	3.69	0.33	0.357	0.021	0.78	0.14	19.33	2.72
1022	20	79.4	3.9	47.1	1.0	0.62	0.02	0.34	0.04	3.12	0.26	0.303	0.014	0.55	0.07	5.07	0.45
1012	20	105.5	6.2	36.6	1.0	0.49	0.03	-0.05	0.01	3.03	0.31	0.278	0.012	-0.11	-0.06	6.17	0.70
1152	20	155.7	27.6	14.9	0.3	0.34	0.01	0.34	0.07	3.62	0.41	0.359	0.021	1.00	0.20	10.80	1.20
1193	20	231.8	19.7	51.7	1.3	0.10	0.00	0.44	0.02	2.74	0.26	0.261	0.009	4.60	0.20	28.40	2.60
1228	20	443.8	84.7	40.4	1.0	0.05	0.00	0.30	0.05	2.35	0.25	0.303	0.013	6.00	1.00	47.50	5.00
1162	20	73.5	2.6	58.1	1.2	0.58	0.02	0.45	0.04	3.15	0.32	0.278	0.011	0.76	0.06	5.38	0.55
1255	20	90.7	4.0	68.7	1.9	0.47	0.02	0.23	0.03	2.68	0.24	0.260	0.006	0.50	0.06	5.75	0.53
1010	20	76.4	5.8	15.9	0.5	0.76	0.02	-0.06	0.01	2.64	0.39	0.310	0.015	-0.08	-0.08	3.50	0.50

Table 4.39: Heating experiment data for goethite sample RH degassed in oxygen in Pt packets. $p(O_2)$ = oxygen partial pressure, T = temperature, t = total isothermal heating time, age = calculated (U-Th)/He age, mass = Fe-based sample mass.

$p(O_2)$	T	t	age	1σ	mass	1σ	U	1σ	Th	1σ	Sm	1σ	He	1σ	Th/U	1σ	Sm/U	1σ
[torr]	[°C]	[min]	[Ma]		[µg]		[ppm]		[ppm]		[ppm]		[nmol/g]					
~120	780	20	63.5	1.9	100.6	2.7	0.92	0.03	0.02	0.01	2.79	0.20	0.323	0.008	0.02	0.01	3.02	0.21
~120	890	20	64.7	1.6	88.7	1.7	0.88	0.02	0.06	0.01	3.17	0.21	0.317	0.012	0.06	0.01	3.60	0.24
~120	960	20	61.6	1.5	74.0	1.2	0.88	0.02	0.14	0.01	3.18	0.26	0.306	0.019	0.15	0.02	3.62	0.30
~120	1030	20	61.8	2.9	37.2	1.0	0.91	0.04	0.03	0.03	3.20	0.23	0.311	0.013	0.03	0.03	3.50	0.26
~120	1083	20	63.4	2.8	30.0	0.4	0.90	0.04	0.07	0.03	2.97	0.20	0.317	0.025	0.07	0.04	3.30	0.25
~120	1132	20	75.7	7.0	18.3	0.3	0.77	0.06	0.22	0.05	3.06	0.17	0.339	0.038	0.29	0.07	4.00	0.36
~120	1184	20	150.6	8.7	67.5	1.3	0.34	0.02	0.12	0.01	2.99	0.21	0.308	0.012	0.35	0.05	8.78	0.72
~120	1238	20	316.7	22.2	42.2	0.6	0.14	0.00	0.28	0.02	3.13	0.20	0.374	0.021	2.00	0.17	22.00	1.33
~120	1241	20	134.0	9.4	37.9	0.8	0.40	0.03	0.08	0.03	4.27	0.30	0.309	0.013	0.20	0.07	10.80	1.03

References

Gualtieri, A. F. and P. Venturelli (1999) “In situ study of the goethite-hematite phase transformation by real time synchrotron powder diffraction” in: *American Mineralogist* 84.5-6, pp. 895–904.

Houk, R. S. (1986) “Mass spectrometry of inductively coupled plasmas” in: *Analytical Chemistry* 58.1, 97A–105A.

Ketteler, G., W. Weiss, W. Ranke, and R. Schlögl (2001) “Bulk and surface phases of iron oxides in an oxygen and water atmosphere at low pressure” in: *Physical Chemistry Chemical Physics* 3.6, pp. 1114–1122.

Lafuente, B., R. T. Downs, H. Yang, and N. Stone (2016) “The power of databases: the RRUFF project” in: *Highlights in mineralogical crystallography* Walter de Gruyter GmbH, pp. 1–29.

May, T. and R. Wiedmeyer (1998) “A Table of Polyatomic Interferences in ICP-MS” in: *Atomic Spectroscopy* 19.5.

Prasad, P., K. S. Prasad, V. K. Chaitanya, E. Babu, B. Sreedhar, and S. R. Murthy (2006) “In situ FTIR study on the dehydration of natural goethite” in: *Journal of Asian Earth Sciences* 27.4, pp. 503–511.

Ruan, H., R. Frost, and J. Kloprogge (2001) “The behavior of hydroxyl units of synthetic goethite and its dehydroxylated product hematite” in: *Spectrochimica Acta Part A: Molecular and Biomolecular Spectroscopy* 57.13, pp. 2575–2586.

Wolska, E. (1981) “The structure of hydrohematite” in: *Zeitschrift für Kristallographie – Crystalline Materials* 154.1-4, pp. 69–76.

Chapter 5

THE POTENTIAL OF FINE-GRAINED PEDOGENIC IRON-OXIDE FOR COSMOGENIC ^{3}HE DATING: A CASE STUDY OF A RELICT SOIL AT WHITEWATER HILL, CALIFORNIA

with Devin McPhillips[1], Dylan Rood[2], Katherine Kendrick[1], and Kenneth A Farley[3]

Abstract

We test whether pedogenic iron-oxides can be used a geochronological tool to constrain the formation ages of soils. Based on the diffusion parameters of hematite as well as the size and morphology of pedogenic iron-oxides, we estimate that hematite particles as small as 10 nm might quantitatively retain helium at earth-surface conditions for up to 1 Ma. Since these particles are much smaller than the ejection distance of ^{3}He, all of the helium in a particle was implanted from the matrix. We sampled a remnant soil developed on a fanglomerate terrace offset by the San Andreas fault at Whitewater Hill, California, on a depth profile from the surface to 1.75 m depth. Concentrations of ^{10}Be and ^{26}Al in quartz define an exponential depth profile with an in-situ cosmogenic exposure age of 52.4±2.2 ka, assuming no erosion. A depth profile of cosmogenic ^{3}He in pedogenic iron-oxides deviates from an exponential profile, with higher than expected concentrations between 40 cm and 100 cm depth. We interpret this deviation as evidence for vertical movement of pedogenic iron-oxide particles. Based on ^{3}He concentrations in pedogenic iron-

[1]USGS Pasadena, 525 South Wilson Ave., Pasadena, CA 91106-3212

[2]Department of Earth Science and Engineering, Imperial College London, South Kensington Campus, London SW7 2AZ, UK

[3]California Institute of Technology, 1200 E California Blvd, Pasadena, CA 91125, United States

oxides, we calculate a model exposure age of 208±44 ka, which yields a slip rate of of the Banning strand of the San Andreas fault of $10.1^{+6.2}_{-2.5}$ mm/a.

5.1 Introduction

Soils are of critical importance to constrain landscape development and to establish tectonic rates. They are often the only deposits that can be used to date fault offset markers on the 10-100 ka timescale. Obtaining reliable dates for these deposits is required to calculate accurate fault slip rates. In many cases, the formation of soils and surfaces is constrained by dating the deposition of the substratum. Frequently employed dating methods utilizing the cosmogenic nuclides ^{10}Be and ^{26}Al in detrital quartz are expensive, require time-consuming sample preparation, and often have issues with inheritance. We investigate possibilities to develop a new tool for cosmogenic dating using fine-grained iron-oxides, which are ubiquitous in most soils.

A first indication that fine-grained pedogenic iron-oxides might retain helium came from Hofmann et al. (2017), who found ^{3}He concentrations in clayey soil material of a paleosol, which matched those of highly retentive goethite pisoliths when normalized by the iron-oxide content of the soil. They interpreted this as evidence that ^{3}He is being retained in the iron-oxides, but not by the clay minerals that make up the bulk of the paleosol material. Farley (2018) recently measured the fundamental diffusion parameters D and E_a on a single-crystal hematite sample, which enables a prediction of the retention of helium in hematite at a given diffusional domain size. Diffusional modeling showed that hematite crystallites of 20 nm diameter quantitatively retain helium at 25 °C for 100 Ma (Farley, 2018). Even at the highest temperatures expected in hot desert localities, crystallites of 20 nm would retain most of the ingrown radiogenic and cosmogenic helium at geologic timescales (Farley, 2018). No comparable studies on the diffusion parameters of goethite are

available, since the grain size of goethite is usually very small and no single crystal large enough to perform the same type of experiment has been identified.

Iron-oxide particles in soils generally range from a few to several hundred nanometers (Cornell and Schwertmann, 2003). This suggests that most pedogenic hematite particles retain all or most of the helium accumulated since the formation of the particle. We investigate whether helium retained in pedogenic iron-oxides can be used as a geochronological tool.

This technique would have the advantage of dating minerals created during soil formation, which is in general not possible using other methods, mostly focusing on detrital quartz. That is, ^{3}He has the potential to measure soil formation ages, as opposed to simple surface exposure ages. This distinction offers the potential of improved precision by limiting the possibility of contamination by inheritance as well as new insights into the processes of soil formation. In order to assess whether this might be used as a reliable dating tool, we compare ^{3}He concentrations in pedogenic iron-oxides to cosmogenic ^{26}Al and ^{10}Be concentrations in quartz, in a simple setting where we expect both methods to yield identical surface exposure ages. We have selected Whitewater Canyon on the San Gorgonio Pass as a site for this case study. A large fanglomerate terrace shows a well-developed red soil, which is rich in both iron-oxides and quartz sand, providing a suitable situation for this study.

5.2 Theoretical considerations

There are several aspects that make pedogenic iron-oxides different from other phases used for geochronologic and cosmogenic nuclide analyses, mostly related to their diminutive size.

Morphology and species of pedogenic iron-oxides

Iron-oxides in soils are produced primarily by weathering of mafic minerals, and they are typically present as goethite, hematite, lepidocrocite, and ferrihydrite (Cornell and Schwertmann, 2003). Hematite and goethite are by far the dominant pedogenic iron-oxide minerals (Schwertmann et al., 2004; Singh and Gilkes, 1992) and they embue soils with a reddish or yellowish color. Lepidocrocite occurs in some temperate to subtropic hydromorphic soils in association with goethite, but it is only locally concentrated and not dispersed throughout the soil (Schwertmann, 1988a). Pedogenic hematite and goethite are possibly formed through a ferrihydrite precursor (Cornell and Schwertmann, 2003; Schwertmann, 1988a), with pH and temperature being the main controls on speciation (Schwertmann et al., 2004). Hematite is favored in warm environments around neutral pH, whereas goethite is preferentially formed in colder environments with both high and low pH (Schwertmann et al., 2004). The formation of goethite is also favored by high water excess and humidity, whereas hematite occurs preferentially in dry environments. The formation of goethite relative to hematite is also influenced by the availability of Al (Taylor and Schwertmann, 1978) and the organic matter content of the soil (Schwertmann, 1988a). The bulk hematite/(hematite+goethite) fraction in soil can span the full range from 0 to 1 (Schwertmann, 1988a; Singh and Gilkes, 1992), depending on the environmental conditions. Once formed, pedogenic hematite and goethite in modern soils remain unchanged for long periods of time due to their thermodynamic stability (Schwertmann, 1988a). Isomorphous Al-substitution for Fe influences physical behavior and thermodynamic stability of iron-oxide particles, including dehydroxylation temperature (Schulze and Schwertmann, 1984; Schwertmann, 1984, 1988b). Dissolution of goethite is inhibited by Al-substitution, which makes Al-substituted goethites more stable (Schwertmann, 1984). Further post-formation movement in the soil is mostly mechanical, and is often mediated by

larger solid constituents of the soil (Cornell and Schwertmann, 2003).

Iron-oxide particles have small crystal sizes of 10-100 nm, with hematites often developed as hexagonal plates and goethites as needles or laths (Schwertmann, 1988b). Goethites needles are shorter and thicker with increasing amounts of Al-substitution (Schulze and Schwertmann, 1984). The size of goethite crystals is larger for greater formation temperatures (Schwertmann and Kämpf, 1985). Soil goethites were found to be of relatively low acicularity and almost equant (Schwertmann, 1988b).

Accumulation of helium

There are two basic applications of helium contained in iron-oxides: ^{4}He produced by radioactive decay of U, Th, and Sm is used for (U-Th)/He dating (Farley, 2002), whereas ^{3}He produced by cosmic rays is utilized for cosmogenic surface exposure dating (Shuster et al., 2012). Since iron-oxide particles in soils are much smaller than the α-stopping distance of 4-20 μm (Ketcham et al., 2011) in hematite or goethite, none of the ^{4}He produced from U, Th, or Sm contained in the particle is retained. The stopping distances of cosmogenic ^{3}He and ^{3}H, which decays to ^{3}He, are 50 μm and 200 μm, respectively (Farley et al., 2006). All of the helium found in the crystal today was therefore implanted, while all of the helium originating from the inside of the crystal was ejected. This is in contrast to typically much larger crystals used for (U-Th)/He dating and studies of ^{3}He produced by cosmic-ray exposure, in which most of the ^{3}He and ^{4}He contained in the sample actually originated inside of the crystal. For these phases, corrections for α-ejection and α-implantation are applied based on the shape and size of the crystal (Farley, 2002).

Alpha-producing elements (U, Th, Sm) in rocks are generally concentrated in only a few phases, such as apatite and zircon. They are incompatible in the most common rock-forming minerals, such as quartz (Vandenberghe et al., 2008) and feldspar (Smedley and Pearce, 2016), and usually present only in the sub-ppm range. Alpha-

implantation into fine-grained iron-oxide in a soil would occur only from the minerals immediately surrounding the particles. Due to the inhomogeneity in U, Th, and Sm concentrations between the different minerals contained in soil material, it is difficult to determine the rate of α-implantation. (U-Th)/He dating of fine-grained iron-oxides might only be feasible in geological materials, in which the α-implanting phase surrounding the iron-oxide particles is homogeneously distributed throughout, as might be the case in red limestones.

While production of ^{4}He is very dependent on the localization of α-producing elements, ^{3}He produced by cosmic rays is, to first order, independent of chemistry and therefore constant at any depth below the surface. The production rate of ^{3}He is dependent on mineral composition (e.g. Kober et al., 2005). It can be produced on any element, except hydrogen. Since the production rate in minerals is usually dominated by production from O, it varies only slightly between different minerals. The large stopping distances of ^{3}He and ^{3}H add to the homogenization of ^{3}He production throughout soil material. The external variables for utilizing cosmogenic ^{3}He in pedogenic iron-oxides are therefore easier to control than the equivalent variables for (U-Th)/He dating. This study focuses on measuring ^{3}He concentrations in pedogenic iron-oxides as a way to date the formation of soils.

Production of ^{3}He

Due to their size, all of the cosmogenic ^{3}He produced by spallation inside the iron-oxide particles is ejected, and all cosmogenic ^{3}He found in the particle must be implanted. Therefore, the cosmogenic production rate of ^{3}He in pedogenic iron-oxides depends on the average composition of the constituent phases of the soil, each of which has its own production rate. The clay fraction used for concentrating iron-oxides is aggregated from several kilograms of soil material, which represents millions of individual sand-sized clasts. This averages variations of production rate

between the different mineral phases constituting the soil. We therefore propose to approximate cosmogenic production rate in pedogenic iron-oxides as an average of that of the major constituent minerals, weighted by their relative abundance:

$$P_{c,pio} = \sum_{m=1}^{n} P_m \cdot X_m \tag{5.1}$$

where $P_{c,pio}$ is the cosmogenic production rate of ^{3}He in pedogenic iron-oxides, P_m is the production rate in mineral phase m, X_m is the mass fraction of mineral m in the soil, and n is the number of different mineral phases. If the bulk composition of the soil changes with depth, production rate might have to be calculated for every depth increment.

Cosmogenic production rates are poorly calibrated for phases, such as quartz (Brook and Kurz, 1993) and feldspar (Margerison et al., 2005), which constitute the bulk of many crustal rocks, but are not sufficiently helium-retentive (Tremblay et al., 2014b) to be a frequent target for cosmogenic nuclide dating. The ^{3}He production rates in silicates are generally very similar at around 110-120 at g^{-1} a^{-1} (e.g. Goehring et al., 2010; Licciardi et al., 1999). Modern production rate of ^{3}He in quartz was calibrated to 107.6±6.6 at g^{-1} a^{-1} (Vermeesch et al., 2009). Goehring et al. (2010) found no significant difference in cosmogenic ^{3}He production between olivine and pyroxene, with a sea level high latitude (SLHL) production rate of 120±9 at g^{-1} a^{-1}. Amidon and Farley (2012) found a SLHL production rate of 120±18 at g^{-1} a^{-1} in hornblende. This suggests that soils developed on an igneous substratum have production rates close to this value.

Besides the cosmogenic component, ^{3}He can also be produced by other processes. Contributions from muogenic production at shallow depths are likely negligible (Farley et al., 2006). Production by the ^{6}Li(n,α)^{3}H(β)^{3}He thermal neutron capture reaction is a possible source of ^{3}He (e.g. Farley et al., 2006). Li concentrations in

soils are highly dependent on the composition of the substratum and are typically tens of ppm or below (e.g. Davey and Wheeler, 1980; Gough et al., 1988; Pistiner and Henderson, 2003; Shacklette and Boerngen, 1984). Li has been found to be concentrated in the surface soil relative to the subsoil (Davey and Wheeler, 1980). Contributions to the production of ^{3}He from thermal neutron capture come from cosmogenic thermal neutrons (CTN) and from radiogenic neutrons produced by α-decay, usually termed 'nucleogenic'. The stopping distance of ^{3}H produced from the ^{6}Li reaction is about 30 μm in common minerals (Farley et al., 2006), leading to homogenization similar to that of cosmogenically produced ^{3}He.

Another possible source of ^{3}He is from spontaneous ternary fission of ^{238}U, but the production rates for even U-rich material are negligible (Farley et al., 2006). The total accumulated concentration of ^{3}He due to these different sources is:

$$^{3}He_{total} = P_{c,pio} \cdot t_c + P_n \cdot t_r + P_{CTN} \cdot t_r \tag{5.2}$$

where $P_{c,pio}$ is the weighted average cosmogenic production rate of the soil, P_n is the nucleogenic production rate based on U concentration of the soil, P_{CTN} is the production rate from cosmogenic thermal neutrons, t_c is the cosmogenic exposure duration, and t_r is the relevant timescale for nucleogenic and CTN production.

Since pedogenic iron-oxides are formed in situ and start accumulating helium from any source after their transformation to goethite or hematite, the timescales of cosmogenic, nucleogenic, and CTN production of ^{3}He are the same ($t_c = t_r$) and equal to the exposure age (t_{exp}). The exposure age of the of the sample can therefore be calculated as:

$$t_{exp} = \frac{^{3}He_{measured}}{P_{c,pio} + P_n + P_{CTN}} \tag{5.3}$$

where $^{3}He_{measured}$ is the concentration of ^{3}He in the sample.

Retention of helium

Goethite and hematite are both helium-retentive phases (Farley, 2018; Hofmann et al., 2017). The main contributing factor to diffusive loss of helium is the diminutive physical size of pedogenic iron-oxide particles, and therefore their small diffusional domain size. Since hematite predominately forms hexagonal plates, the thickness of the plate is the relevant dimension for diffusion of helium. Schwertmann and Kämpf (1985) found average plate thicknesses of Brazilian Ultisols and Oxisols at 10-20 nm, with plate widths of 20-60 nm. Mean particle diameters of iron-oxide particles in Greek soils have been reported as averaging 13 nm (Gangas et al., 1973) and Janot et al. (1973) found diameters of >8 nm for pedogenic hematite in French soils. For synthetic hematites, Schwertmann and Murad (1983) report sizes of 22±4 nm. Pedogenic goethite crystals are elongated in one dimension (c-axis), with the two other dimensions (a, b) being approximately equal in natural samples (Schwertmann, 1988b). The relevant diffusional domain size is therefore perpendicular to the c-axis. Goethite crystal sizes are generally larger than those of hematite (Schwertmann, 1988a,b), with needles being reported as 50-150 nm in length and 15-50 nm in width (Schwertmann and Murad, 1983).

We use the diffusion parameters for hematite of Farley (2018) and the computational approach of Fechtig and Kalbitzer (1966) for a plate geometry to predict fractional helium loss for isothermal holding at temperatures between 20 °C and 35 °C (Fig. 5.1). These curves show that even at the highest expected effective diffusion temperatures of 35 °C, which corresponds to surface conditions in Death Valley (Farley, 2018; Wolf et al., 1998), >95% of all helium is quantitatively retained in hematite over 10 Ma down to a plate thickness of about 20 nm. On timescales of 1 Ma, >95% of all helium is retained down to a plate thickness of 10 nm. At even shorter timescales, quantitative retention is possible for even smaller particles.

We utilize the effective diffusion temperature (EDT), which is the temperature corre-

sponding to the mean diffusivity over the time of exposure (Tremblay et al., 2014a). The diffusivity changes as a result of the diurnal, seasonal, and long-term climatic variations in temperature. EDT integrates this signal over the time of exposure. Due to the logarithmic nature of diffusivity, diurnal peaks in summer months cause the EDT to be higher than the average temperature. However, EDT is also lower than the maximum temperatures reached. EDT also changes with depth below the surface, since diurnal and seasonal temperature variations only propagate tens of centimeters to meters into the subsurface and are attenuated at greater depths.

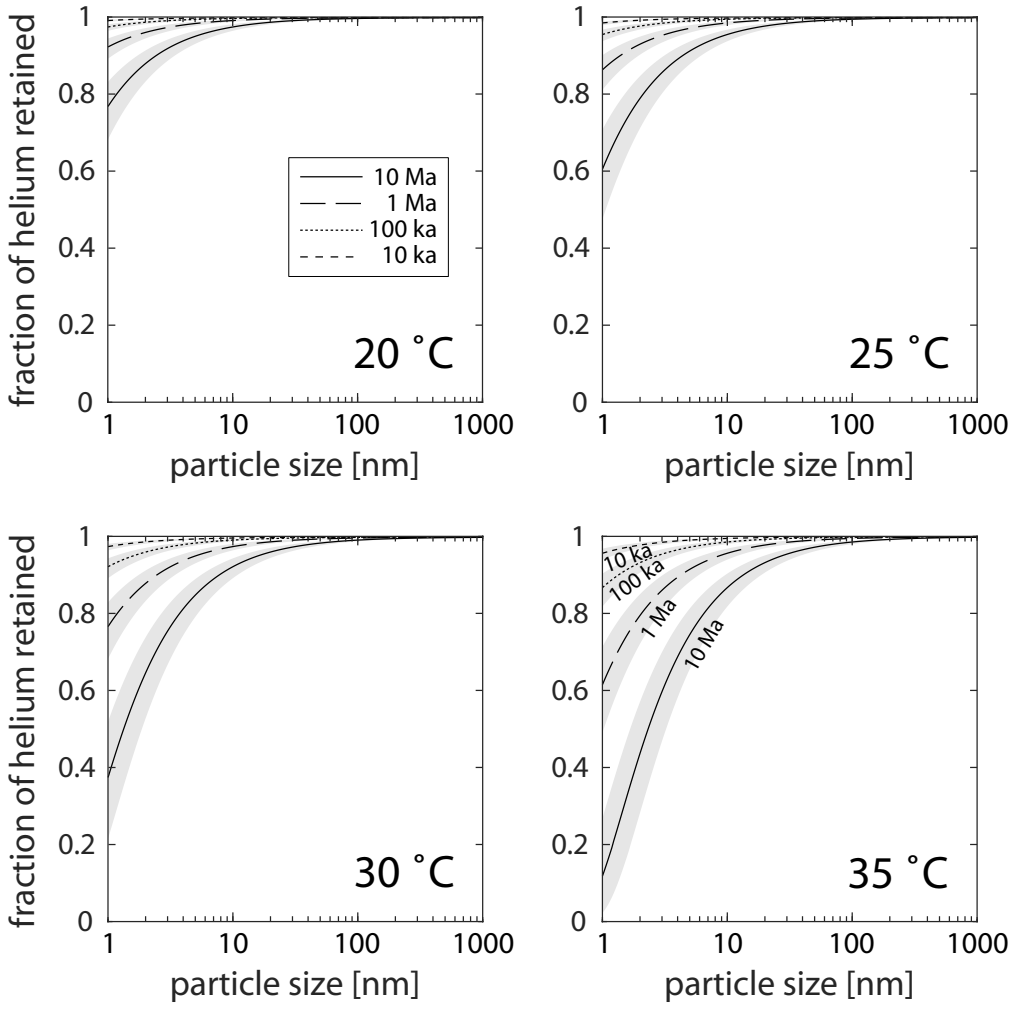

Figure 5.1: Models for helium retention in pedogenic hematite particles at different effective diffusion temperatures. Crystal size is thickness of a plate with thickness:length ratio of 1:3. Four curves in each plot describe helium-retention as a function of crystal size for isothermal holding for 10 ka, 100 ka, 1 Ma, and 10 Ma.

Change in iron-oxide concentrations with soil age

The content of iron-oxides in soils varies widely, from ppm to several percent of total mass (Cornell and Schwertmann, 2003). At the beginning of soil formation, no pedogenic iron-oxides are present. The iron-oxide content of a soil increases over time with the progressive break-down of Fe-bearing minerals (McFadden and Hendricks, 1985). In long-lived soils, only the most stable Fe-bearing minerals derived from the substrate, such as ilmenite, are left (Cornell and Schwertmann, 2003) and the soil attains the final iron-oxide concentration. This implies that pedogenic iron-oxides present today have formed after the initiation of soil formation and any age determined on them is lower than the true age of the soil. The rate at which iron-oxides form in soils is therefore an important factor in calculating an exposure age.

McFadden and Hendricks (1985) studied pedogenic iron-oxides in chronosequences of desert soils in Southern California, similar to the one at Whitewater sampled here. They focused on the relative amounts of oxalate-extractable (mostly amorphous) and dithionide-extractable (mostly well-crystalline) iron-oxide and found that the fraction of dithionide-extractable iron-oxides, most likely hematite and goethite, increases over time (Fig. 5.2). Steady-state in regard to these parameters is not reached until about 500 ka (McFadden and Hendricks, 1985).

We use data from McFadden and Hendricks (1985) to calibrate the iron-oxide content in terms of a fraction of the total amount present in the long-term limit (Fig. 5.2). The iron-oxide fraction increases rapidly after the formation of the soil and asymptotes to unity for old soils. About 50% of the final iron-oxide concentration is present at 10 ka and 90% at 100 ka. The study of McFadden and Hendricks (1985) did not have robust age control on the soils in the chronosequences. Therefore, the uncertainties of this calibration are large. However, this illustrates a general trend of iron-oxide accumulation rates in soils.

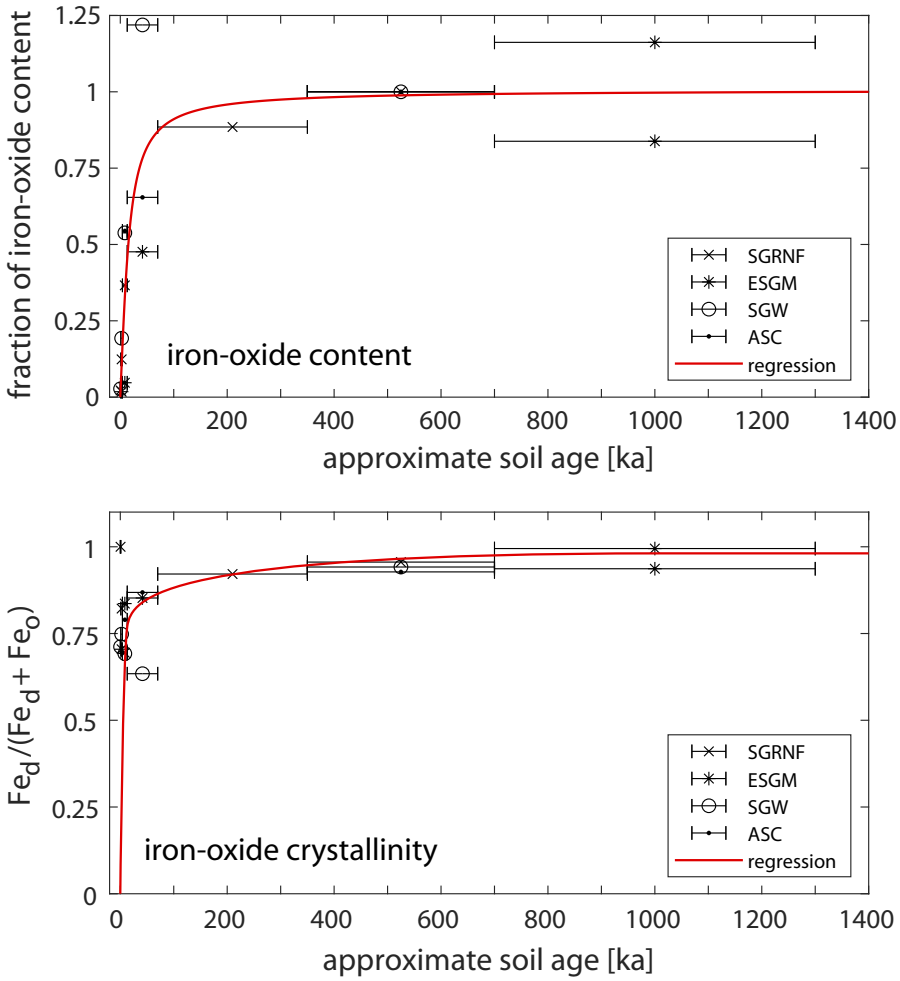

Figure 5.2: The accumulation of pedogenic iron-oxides (top) and their crystallinity (bottom) compiled from data of McFadden and Hendricks (1985). Crystallinity is defined as the ratio between dithionite-extractable (highly crystalline) Fe and the total amount of dithionite- and oxalate-extractable Fe. Data shown here is from chronosequences in Southern California that contain at least one soil >100 ka: SGRNF - San Gabriel River North Fork, ESGM - Eastern San Gabriel Mountains, SGW - San Gorgonio Wash, ASC = Arroyo Seco Canyon.

Since none of the iron-oxide particles were present in the beginning and they increased over time, the overall cosmogenic ^{3}He concentration in pedogenic iron-oxides will be below what would be expected if all of the iron-oxide particles had been present at the time of soil formation. Exposure ages calculated from this are subsequently lower than the true age of the soil. Fig. 5.3 shows the fraction between helium actually recorded in pedogenic iron-oxides and the amount expected

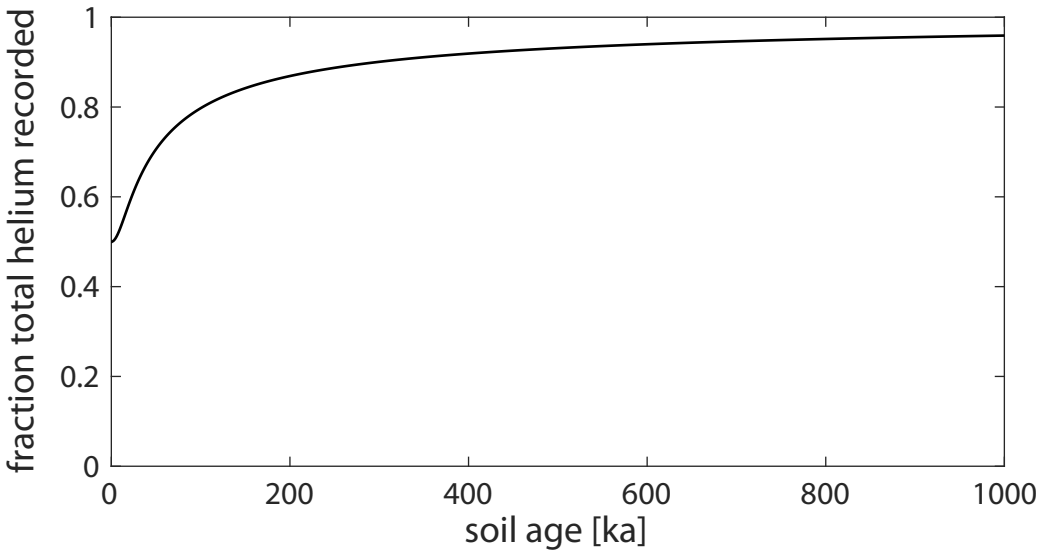

Figure 5.3: Helium recorded in pedogenic iron-oxides as a fraction of total helium that would have been present if all present iron-oxide particles had existed from the beginning of soil formation. This factor can be used to correct ^{3}He concentrations.

if they had been present as a function of soil age. This factor might be used to correct measured ^{3}He concentration in order to obtain a more accurate exposure age. This correction matters greatly for cosmogenic dating of young soils. However, the amount of time required to form most of the iron-oxides in the soil is small compared to the age of long-lived soils of hundreds of thousands to millions of years. This technique might therefore be utilized with greater certainty for long-lived soils.

Soils cannot be accurately dated using iron-oxide accumulation or crystallinity when they approach steady-state, because the rate of change of these parameters slows down considerably. Even small uncertainties would lead to significant change in resulting age. However, ^{3}He cosmogenic dating of pedogenic iron-oxides has its greatest potential for these very long-lived soils, since the relative uncertainty from the accumulation rates of iron-oxides decreases with increasing age.

5.3 Whitewater Hill

To test whether cosmogenic ^{3}He in pedogenic iron-oxides can be used as geochronological tool, we selected a relict soil at Whitewater Hill on San Gorgonio Pass, Riverside County, California (Fig. 5.4).

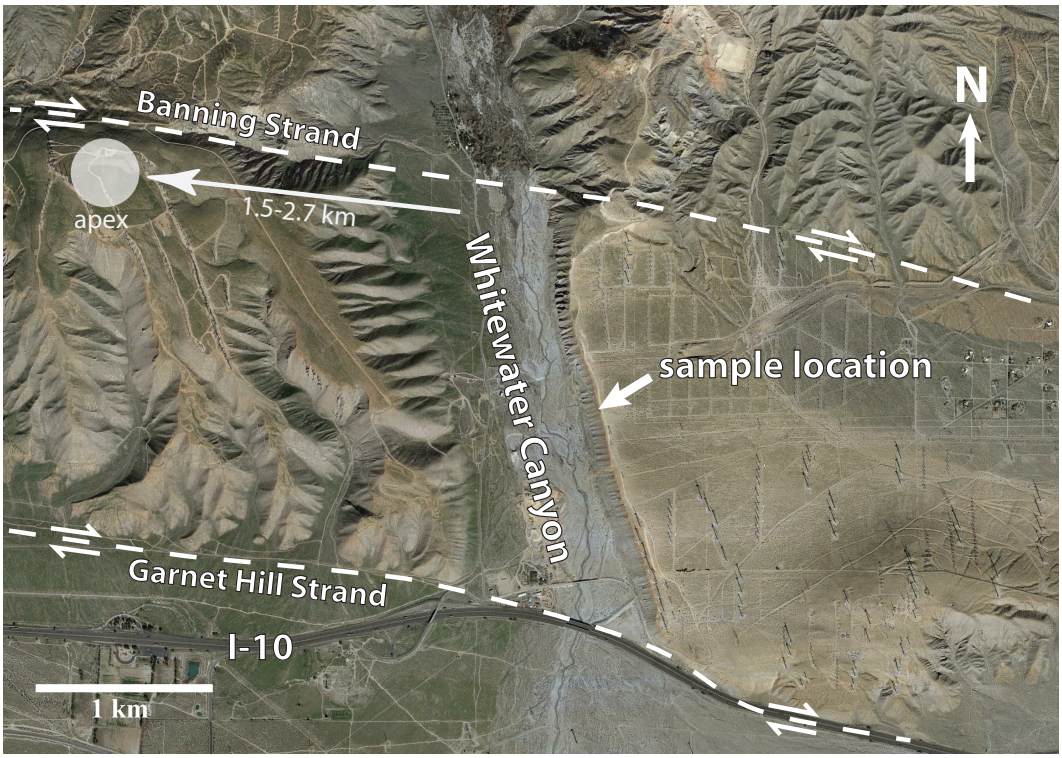

Figure 5.4: Study area on San Gorgonio Pass, California. An offset and uplifted alluvial fan surface between the Banning Strand and the Garnet Hill Strand of the San Andreas Fault shows a well-developed red soil. Samples of the relict soil on the fluvial terrace were taken at the indicated location. Aerial imagery from Google Earth, fault traces after Kendrick et al. (2015), location of apex and offset estimate from Huerta (2017).

Geology

This location is an important place for calculating offset rates of the San Andreas Fault in the last 500 ka (Kendrick et al., 2015). An alluvial fan was offset from its source in Whitewater Canyon by the Banning Strand of the San Andreas fault (see Fig. 5.4). The alluvial terrace is being actively anticlinally folded by dextral oblique thrust on the Banning and Garnet Hill Strands (Owen et al., 2014; Yule and Sieh,

2003). The dextral offset of the apex of the alluvial fan serves as a strain marker to constrain the slip rate of the Banning Strand. The total offset of the apex of the fan is 1.5-2.7 km (Huerta, 2017). A reliable date for the surface of the allvial fan can therefore yield an average slip rate of the Banning Strand.

Based on the stage of soil development, the relict soil has been assigned an age of >100 ka (Kendrick et al., 2015; Yule and Sieh, 2003). Recently, the surface of the terrace has been cosmogenically dated by Owen et al., 2014. They measured ^{10}Be in boulders and found surface concentrations corresponding to 39.7-87.3 ka of exposure, with an average of about 57 ka. A depth profile yielded an age of 53.9±15 ka. This average age leads to a slip rate of 22-77 mm/a. This offset rate of the Banning Strand of the San Andreas Fault would far exceed previous estimates for other faults in the same time frame in this area (e.g. Kendrick et al., 2015) and also the Holocene slip rate of the Banning Strand of 2-6 mm/yr (Gold et al., 2015; Scharer et al., 2015).

We chose the red soil on this alluvial fan surface for this study, because it is well-developed, has an abundance of iron-oxides, and is composed of cobbles and boulders of mainly granitoid composition, which contain quartz necessary for ^{10}Be and ^{26}Al analysis. The grain-supported texture of the soil, with clasts of up to 1 m in diameter, prevents major soil convection, which could obscure in-situ exposure, as was observed by Hofmann et al. (2017). An underlying paleosol exposed in the eastern cliff of Whitewater Canyon (see Fig. 5.5) has been dated to 330-510 ka (unpublished data mentioned in Huerta, 2017) and provides an upper age limit for the overlying relict soil.

Sampling

We sampled the relict soil developed on the alluvial terrace at Eastern Whitewater Hill just below Rock Mine Road at latitude 33.93407 °N, longitude -116.63471 °W,

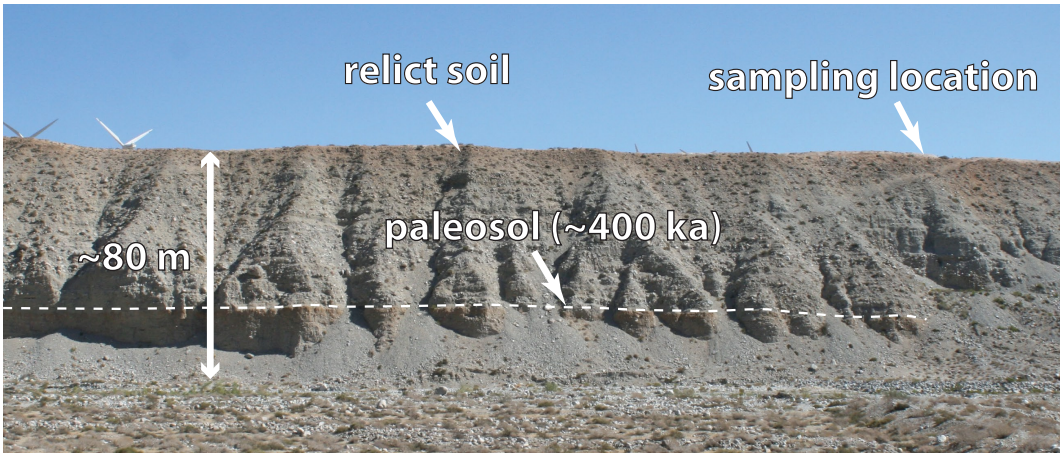

Figure 5.5: Side view of the E cut of the fluvial terrace in Whitewater Canyon. The 80 m tall cut shows a well-developed relict soil at the surface as well as a paleosol in the lower part of the terrace (top is marked by dashed line). We sampled the relict soil at the indicated location.

elevation 515 m (see position in Fig. 5.4 and side view in Fig. 5.5). We cut a trench of about 50 cm width and removed approximately 1 m of material from the cliff face to reduce the influence of lateral cosmic-ray exposure since the incision of the canyon. We took samples on a depth profile from the surface down to 177 cm (Fig. 5.6). About 3 kg of material was scraped off at every sample depth. All samples except the surface sample had a thickness of 2 cm in the vertical direction. In addition, we collected samples of gravel-sized clasts from the fanglomerate at ~7.5 m and ~15 m depth below the surface.

Expected helium retention in pedogenic iron-oxides

We calculated the effective diffusion temperature for the site at Whitewater Hill using records of daily minimum and maximum temperature between 1983 and 2019 (Fig. 5.7) from the PRISM model (PRISM Climate Group, 2019). The average temperature at Whitewater Hill for this period is ~22 °C. Diurnal variations in temperature were approximated using a cubic spline interpolation between the daily minimum and maximum values. This was used as input for the model of EDT of Tremblay et al. (2014a) using the hematite diffusion parameters of Farley (2018).

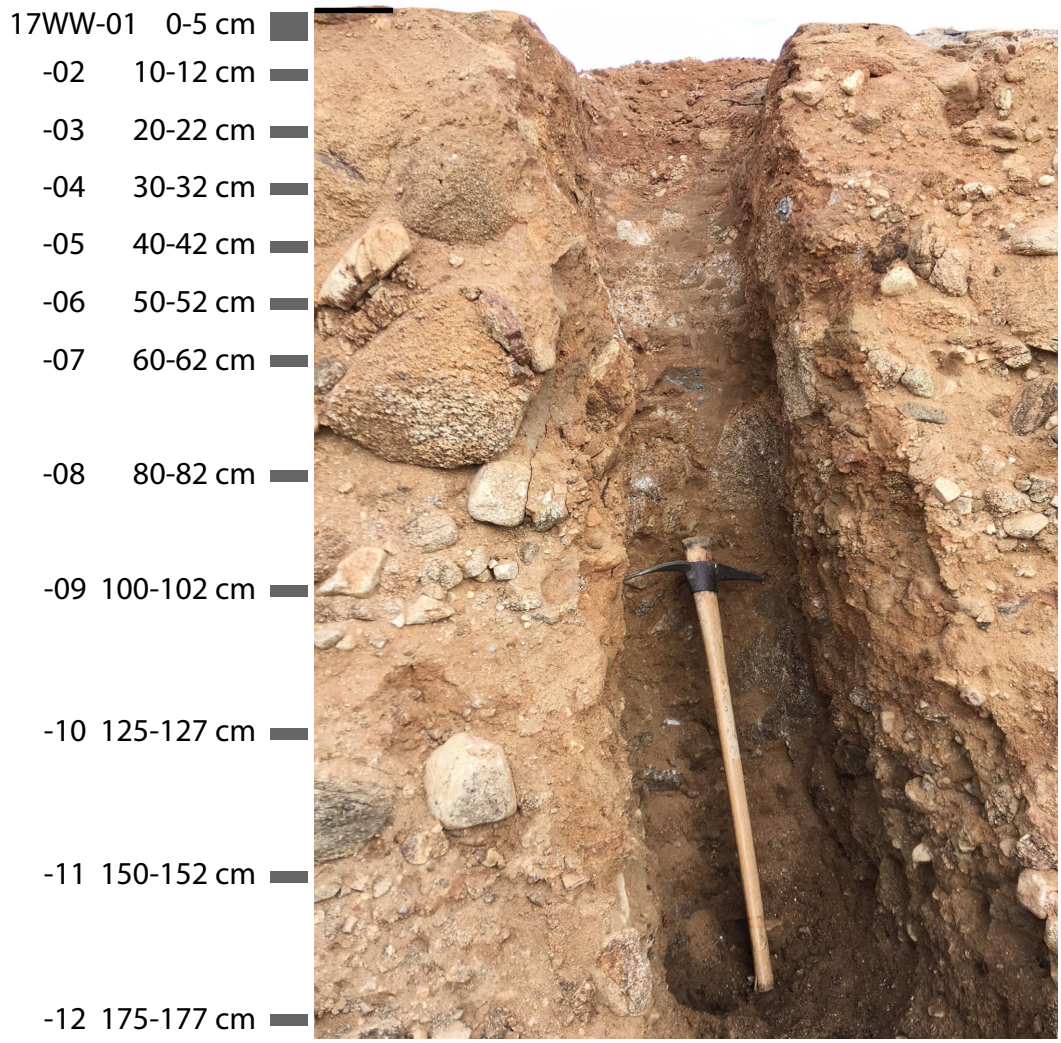

Figure 5.6: Trench cut for sampling at Whitewater Hill. Samples were taken at the indicated positions between the surface (0 cm) and 175 cm depth. Grey boxes indicate the thickness of samples.

The effective diffusion temperature for hematite at the surface of the soil over the period 1981-2019 is 29.9 °C (see Fig. 5.7). For this temperature, >95% of helium is expected to be retained for 1 Ma down to hematite plate thicknesses of ~8 nm (Fig. 5.1). Over 90% of helium is retained for particles of 5 nm over the same period of time. Reported hematite particle sizes are typically 8-20 nm (see Section 5.2). We therefore expect close to quantitative retention in all hematite particles in the soil at Whitewater Hill. The Munsell color of the soil is 2.5YR 5/5-5/6. This implies

almost equal amounts of hematite and goethite as well as a bulk hematite content of about 1% (Torrent et al., 1980).

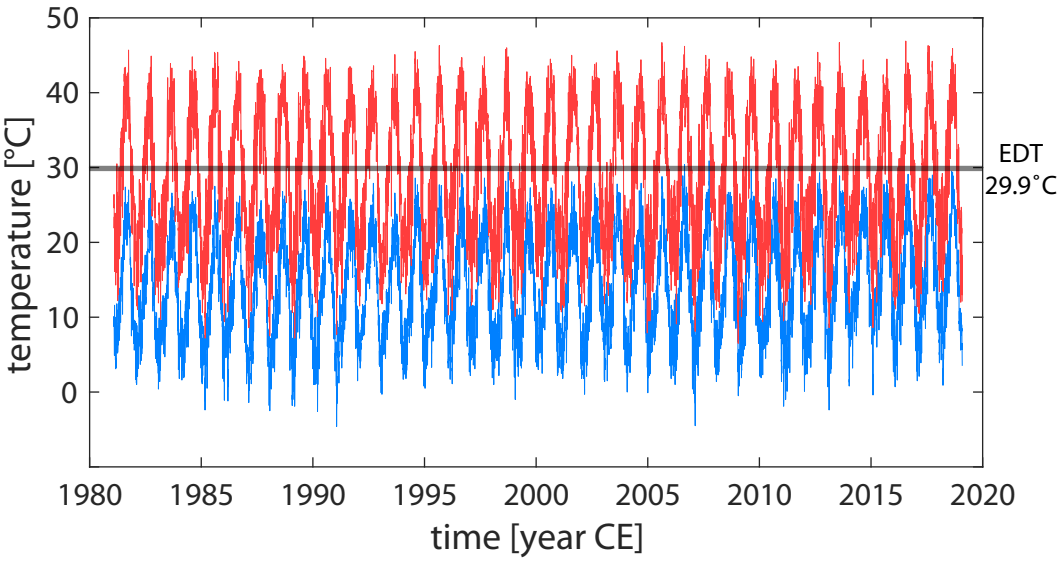

Figure 5.7: Daily minimum (blue) and maximum (red) temperatures for the period 1981-2019 from the PRISM model. EDT is effective diffusion temperature calculated for this data set.

Higher effective diffusion temperatures might be reached on the surface and the uppermost several centimeters of the subsurface due to direct solar heating (Wolf et al., 1998). This might reset some iron-oxide particles at the surface. However, these extreme diurnal temperature peaks do not propagate further than about ~10 cm into the soil. Some of the material found at surface today might have been slowly exhumed by surface erosion and might not have experienced these high temperatures for the full period of time since the formation of the soil.

Production rate of ^{3}He

We calculated ^{3}He production rates based on the scheme outlined above by combining the mineral composition of the soil with individual production rates of minerals. Fosdick and Blisniuk (2018) determined the modal clast compositional data from Whitewater Creek not far from our sample site. They found mostly clasts of grani-

toid rocks, such as granite, granodiorite, and monzonite, (58.5%), and biotite gneiss (35.8%), with some marble (1.9%). We take this as the basis for the modal composition of the soil. Based on typical modal compositions of these rock types, we estimate that the soil at Whitewater is composed of 19.7% quartz, 67.6% feldspar, 7.7% biotite, 0.6% pyroxene, 2.5% amphibole, and 1.9% calcite.

We assumed SLHL production rates of 107.6±6.6 at g^{-1} a^{-1} in quartz (Vermeesch et al., 2009), 133±10 at g^{-1} a^{-1} in biotite and 120±18 at g^{-1} a^{-1} in amphibole (Amidon and Farley, 2012), 120±9 at g^{-1} a^{-1} in pyroxene (Goehring et al., 2010), and 133±13 at g^{-1} a^{-1} in calcite (Amidon et al., 2015). Since feldspars are not retentive to helium, the production rate has not been calibrated. Feldspars are weathered and might be present mostly as clay minerals. In the absence of a calibration, we assume a SLHL production rate of 120±10 at g^{-1} a^{-1}, which is the range generally observed for other silicate minerals (e.g. Goehring et al., 2010).

Combining the production rates of these different minerals with their respective modal fraction yields a combined ^{3}He SLHL production rate of 119±29 at g^{-1} a^{-1} for pedogenic iron-oxides. We scaled this value to a latitude of 33.9°and an elevation of 521 m using the scheme of Lal (1991), which yielded a local cosmogenic ^{3}He surface production rate of 163±39 at g^{-1} a^{-1}.

Nucleogenic production by capture of radiogenic neutrons for a Li concentration of 65 ppm and U and Th concentrations of 4 ppm and 30 ppm contributes about 0.82 at g^{-1} a^{-1} SLHL (1.1 at g^{-1} a^{-1} scaled to Whitewater Hill), according to the approach of Farley et al. (2006). We calculated the cosmogenic thermal neutron contribution to ^{3}He production on Li according to Dunai et al. (2007), taking into account that neutron production rates in clays are lower then in dry granite (Lal, 1987). This contribution is considerable at 17.9 at g^{-1} a^{-1} SLHL (24.2 at g^{-1} a^{-1} scaled Whitewater Hill). Combining these sources, as described above, yields a total scaled ^{3}He surface production rate of 189±45 at g^{-1} a^{-1}.

5.4 Sample processing and measurement procedures

Soil processing

The main object of soil processing was to concentration of pedogenic iron-oxides and to remove any other phases that might retain helium. We followed established protocols for soil processing (Mikutta et al., 2005). However, in order to prevent the loss of helium from iron-oxide particles, we altered protocols so that samples were not heated above room temperature.

About 1 kg of bulk soil samples was soaked in 3 l of distilled water and 50 ml of H_2O_2 was added. Treatment with H_2O_2 destroys organic matter (Mikutta et al., 2005) and helps loosen clay films on clasts. Fe can be complexed by organic matter (Goodman, 1988), which should therefore be removed before iron-oxide separation. This soil slurry was kept at room temperature for several days and occasionally stirred, until visible frothing had subsided.

Samples are then wet-sieved to several grain size ranges. The size fraction >200 μm was used for further processing to high-grade quartz for ^{10}Be and ^{26}Al analysis. The soil slurry of particles <20 μm was used to concentrate iron-oxides. Regular treatment protocols usually involve heating the soil slurry to between 60 °C and 90 °C to accelerate the reaction and to decompose H_2O_2 (Mikutta et al., 2005, and references therein). We omitted this step and instead magnetically stirred the slurry for 24 h, which helps the decomposition of H_2O_2. Any highly magnetic material (mostly magnetite) stuck to the stir bar, and was removed from the slurry.

We explored the use of traditional separation techniques, such as froth flotation, density separation using heavy liquids, and grain size sorting by settling/centrifugation to increase the concentration of iron-oxides in the samples and remove other phases that may be (partially) retentive to helium. However, these techniques did not yield a significant increase in iron-oxides. This is likely a result of the contrast in grain size between iron-oxide particles (<1 μm) and other mineral grains (<20 μm).

The use of 5 M to 1 M NaOH to dissolve clay minerals and disperse iron-oxide particles lead to decreased ^{3}He concentrations. The same was found for heating samples to or drying samples at temperatures over 50 °C. Since extraction and complete purification of iron-oxides from soil samples was not successful, we accepted impure separates for ^{3}He measurements. We measure iron-oxide concentrations of samples and assume that contributions of non-Fe phases can be measured by selectively dissolving iron-oxides in bulk samples.

Li measurement

Li was measured on bulk soil samples to constrain the possible production of ^{3}He from neutron capture reactions on ^{6}Li. Analysis followed the isotope dilution approach of Amidon et al. (2008). About 2 mg of sample material was dissolved by refluxing for 24 h in concentrated HCl and HF, spiked with a solution enriched in ^{6}Li, dried on a hotplate, and brought back into solution in concentrated HNO_3. The ^{7}Li/^{6}Li ratio was measured on an Agilent 8800 ICP-MS, which was used to calculate absolute amounts of Li. This amount was divided by the weighed sample mass to yield concentrations of ppm (μg/g).

Iron-oxide concentrations in soil

Measurements of Fe concentrations in soils by ICP-MS can be challenging, because of the variable nature of soil. Matrix-effects influence the sensitivity of Fe measurement and the exact matrix is hard to predict. We therefore chose to measure Fe by using Ru as an elemental spike. The Ru-spike has been shown to yield accurate and reproducible results for Fe-based mass in pure hematite and goethite samples in Chapter IV. We chose Ru as an elemental spike, because it is present only in trace amounts in soils. We found background concentrations of Ru in soil material in the ppb range. In addition to Fe, we also measured U, Th, and Sm. Trace elements were normalized by the weighed mass of the dissolved sample.

We separated the <20 μm fraction of bulk soil samples by wet sieving. This fraction was dried at room temperature and ground with mortar and pestle. Between 100 mg and 170 mg of this material was weighed on a microbalance and transferred to a Teflon vial. This material was dissolved and spiked with 1 ml concentrated HCl and 1000 μl of calibrated 1000 ppm Ru solution. This was refluxed on a hotplate at 175 °C for 12 hours. After complete dissolution of the iron-oxides and bleaching of the soil material, 50 μl of the solution was extracted and dried on a hotplate at 95 °C. The resulting salts were brought into solution with 500 μl of concentrated HNO_3 and diluted with 9.5 ml of MilliQ H_2O. The $^{58}Fe/^{101}Ru$ ratio was measured on an Agilent 8800 triple quadrupole mass spectrometer, as described in detail in Section 4.C. The absolute amount of iron in the dissolved material was calculated relative to spiked standards with 5 mg, 10 mg, and 15 mg of Fe. For each aliquot, we calculated the amounts of goethite and hematite assuming perfect stoichiometry. We then divided the amount of goethite/hematite by the weighed mass to obtain the iron-oxide percentage. We did not measure the hematite/goethite ratio of the soil, and therefore the actual iron-oxide percentage is between the estimates for goethite and hematite.

Measurement of ^{3}He concentrations

Aliquots of concentrated iron-oxides were analyzed for ^{3}He by total fusion at 1300 °C and with a re-extract at 1350 °C in a vacuum furnace and sector-field mass spectrometry of the resulting gas, following the procedure outlined in Section 2.B. The measured amounts of ^{3}He are normalized by the iron-oxide concentrations.

Measuring ^{10}Be and ^{26}Al concentrations

We enriched quartz in bulk soil material from each sample by removing the <20 μm fraction, which was used for iron-oxide analyses, and by removing the magnetic fraction. The material was rinsed, dried in an oven at 100 °C for 12 h, and ground

with a disk pulverizer to about 500 µm. The material was then dry-sieved and the 250-600 µm fraction was used for further processing. We also aggregated about 100 gravel-sized clasts each for samples taken at 7.5 m and 15 m depth. The gravel-sized clasts were individually crushed with a Chipmunk Jaw Crusher, ground to 500 µm, and sieved to 250-600 µm.

Quartz purification, wet chemistry, and Be/Al isolation was performed at Imperial College London following the methodology of Kohl and Nishiizumi (1992). $^{10}Be/^{9}Be$ and $^{26}Al/^{27}Al$ ratios were measured by accelerator mass spectrometry (AMS) using the 6 MV Sirius tandem accelerator at the Australian Nuclear Science and Technology Organisation (ANSTO) laboratory (Wilcken et al., 2019). Measured $^{10}Be/^{9}Be$ ratios were normalized to the KN-5-2 standard with an assumed ratio of $8.558 \cdot 10^{-12}$ ($t_{1/2}$=1.36 Ma, Nishiizumi et al., 2007). The average of secondary standards KN-5-4 (nominal value $2.851 \cdot 10^{-12}$) and KN-6-2 (nominal value $5.349 \cdot 10^{-13}$) was $2.853 \cdot 10^{-12}$ (±0.56%, n=8) and $5.349 \cdot 10^{-13}$ (±0.78%, n=6), respectively. The $^{26}Al/^{27}Al$ ratio was normalized to the KN-4-2 standard with defined ratio of $3.096 \cdot 10^{-11}$. The average of secondary standards KN-4-3 (nominal value $1.065 \cdot 10^{-11}$) and KN-5-2 (nominal value $1.818 \cdot 10^{-12}$) was $1.070 \cdot 10^{-11}$ (±0.85%, n=7) and $1.81 \cdot 10^{-12}$ (±2.4%, n=6), respectively. Measured sample ratios were converted to concentrations and blank-corrected for procedural blank measurements ($2.005 \pm 0.744 \cdot 10^{-15}$ for $^{10}Be/^{9}Be$ and $3.6 \pm 3.6 \cdot 10^{-16}$ for $^{26}Al/^{27}Al$).

5.5 Results

Concentrations of iron-oxides and trace elements

Bulk iron-oxide concentrations in the Whitewater soil, measured using the Ru-spike, are between 7% and ~12% (Fig. 5.8). They are constant at around 8% in the uppermost 50 cm and they are present at relatively higher concentrations of 8-10% between 60 cm and 160 cm depth. The results vary slightly, depending on whether

it is assumed that all measured Fe is goethite or hematite (see Fig. 5.8). Based on the Munsell color value of the bulk soil material, the goethite/hematite ratio is expected to be close to unity. We therefore used the average of the goethite and hematite values. The increased iron-oxide concentrations at depth are an indication for the process of lessivage, the mechanical movement of small particles down through the soil column from the A to the B horizon (see Blume, 1988).

Bulk trace element concentrations in the soils (Fig. 5.9) show that U, Th, and Sm are present at 3-5 ppm, 20-50 ppm, and 5-15 ppm, respectively. Highly soluble U is enriched in the upper 50 cm, whereas Sm and Th are present at higher concentrations at depths >50 cm. This is reflected in increased Th/U and Sm/U ratios below 50 cm depth. The Li content of bulk soil material is around 65±5 ppm.

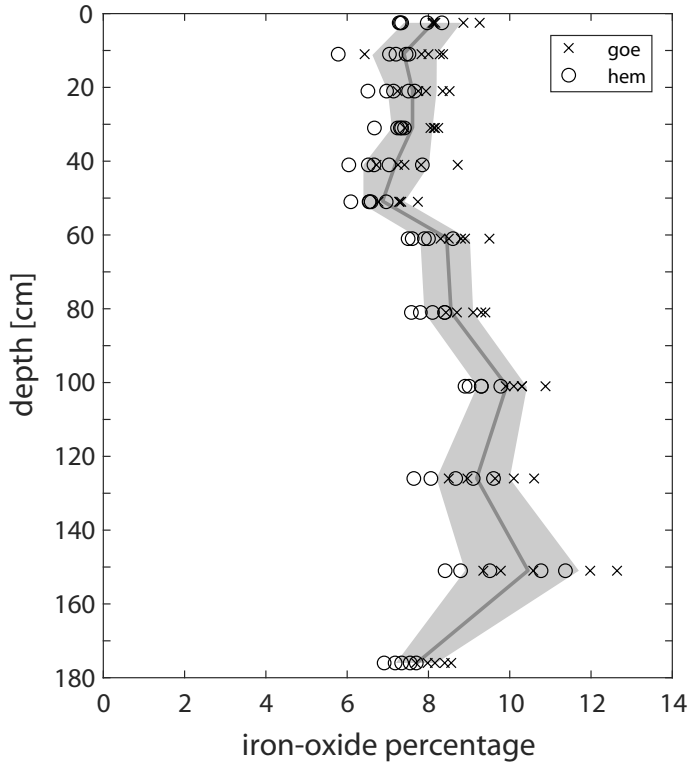

Figure 5.8: Depth profile of percentage of iron-oxides in <20 μm fraction of the soil at Whitewater Canyon measured by ICP-MS. Iron-oxide percentage was calculated assuming that they are completely composed of goethite (goe) or hematite (hem). The iron-oxide content is 7-8% near the surface and 8-10% at 60-160 cm depth. The gray envelope is the 1σ deviation from the mean.

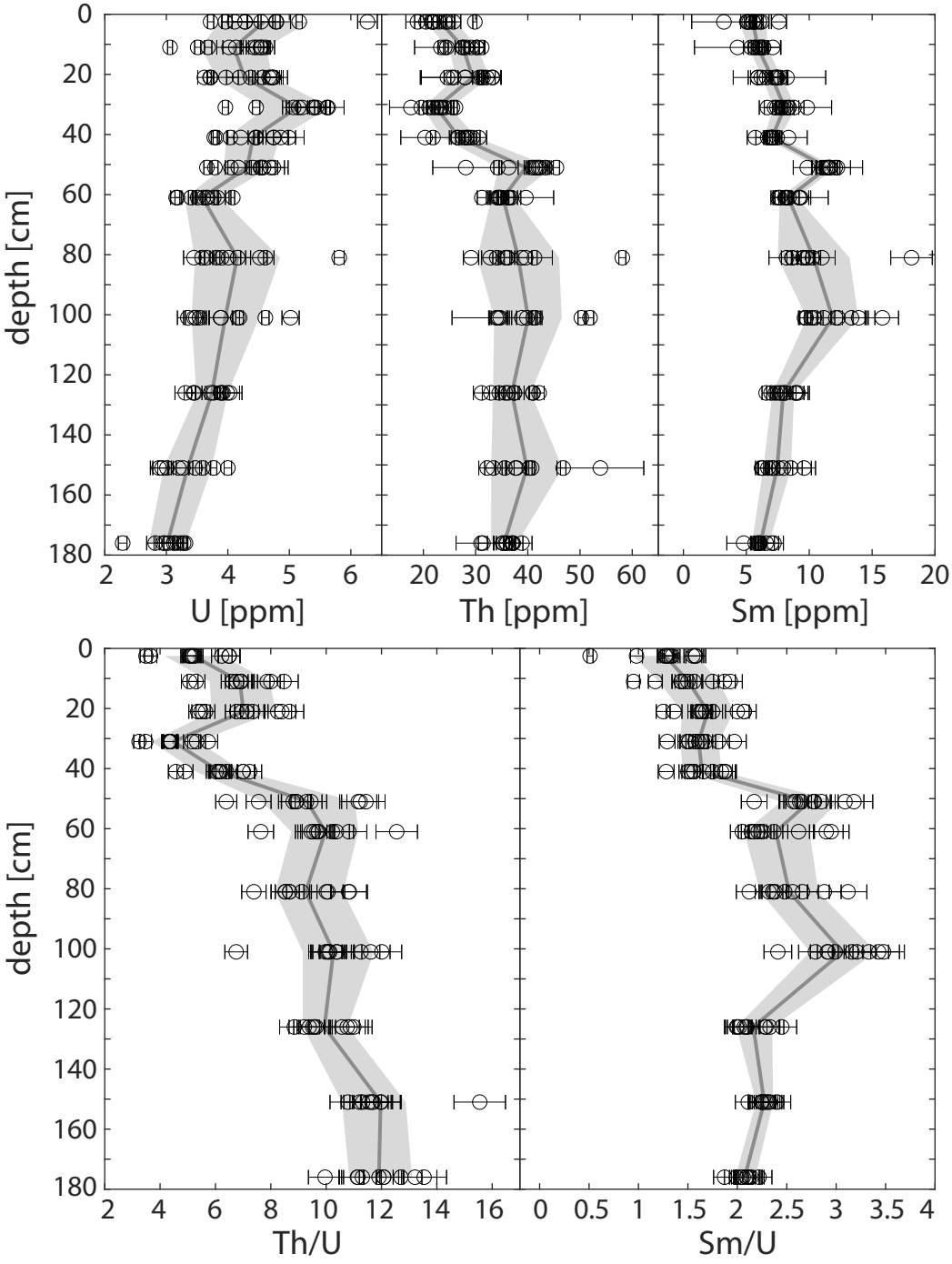

Figure 5.9: Depth profiles of bulk U, Th, and Sm concentrations and Th/U and Sm/U ratios (n=120) in the relict soil at Whitewater measured by ICP-MS. Grey line is depth-averaged value with a 1σ uncertainty envelope. U is enriched relative to less soluble trace elements in the uppermost 0.5 m.

Table 5.1: Iron-oxide concentrations in soil material. Mass/percentage is computed assuming all iron is in the form of either hematite (hem) or goethite (goe). Mass of aliquot was determined with a microbalance.

sample	aliquot	sample mass [mg]	Fe [mg]	goethite [mg]	hematite [mg]	goethite [%]	hematite [%]
17WW-01	a	123.3	6.3	10.1	9.1	8.2%	7.3%
	b	144.4	7.4	11.7	10.6	8.1%	7.3%
	c	148.8	8.7	13.8	12.4	9.3%	8.3%
	d	166.2	9.3	14.7	13.2	8.9%	8.0%
	e	139.0	7.1	11.3	10.1	8.1%	7.3%
17WW-02	a	128.8	6.8	10.8	9.7	8.4%	7.5%
	b	122.3	4.9	7.9	7.1	6.4%	5.8%
	c	156.6	8.2	13.0	11.7	8.3%	7.4%
	d	121.4	6.1	9.7	8.7	8.0%	7.2%
	e	164.6	8.1	12.9	11.6	7.8%	7.0%
17WW-03	a	132.1	6.0	9.6	8.6	7.2%	6.5%
	b	106.9	5.6	8.9	8.0	8.4%	7.5%
	c	138.7	7.4	11.8	10.6	8.5%	7.7%
	d	143.6	7.2	11.4	10.3	7.9%	7.1%
	e	124.0	6.0	9.6	8.6	7.7%	7.0%
17WW-04	a	107.8	5.5	8.8	7.9	8.1%	7.3%
	b	122.7	6.3	10.0	9.0	8.2%	7.3%
	c	130.0	6.7	10.7	9.6	8.2%	7.4%
	d	122.3	5.7	9.1	8.2	7.4%	6.7%
	e	111.1	5.6	8.9	8.0	8.1%	7.2%
17WW-05	a	137.7	5.8	9.3	8.3	6.7%	6.0%
	b	109.8	5.4	8.6	7.7	7.8%	7.0%
	c	161.3	8.9	14.1	12.7	8.7%	7.8%
	d	134.7	6.3	10.0	9.0	7.4%	6.7%
	e	116.3	5.3	8.4	7.6	7.3%	6.5%
17WW-06	a	114.2	5.2	8.3	7.5	7.3%	6.6%
	b	112.1	4.8	7.6	6.8	6.8%	6.1%
	c	119.4	5.5	8.7	7.8	7.3%	6.5%
	d	123.4	6.0	9.6	8.6	7.7%	7.0%
	e	114.0	5.3	8.4	7.5	7.3%	6.6%
17WW-07	a	122.6	6.5	10.4	9.4	8.5%	7.6%
	b	125.8	7.0	11.1	10.0	8.9%	8.0%
	c	142.9	8.6	13.6	12.2	9.5%	8.6%
	d	128.9	7.1	11.4	10.2	8.8%	7.9%
	e	115.6	6.1	9.6	8.7	8.3%	7.5%
17WW-08	a	102.3	5.4	8.6	7.8	8.4%	7.6%
	b	154.8	9.1	14.4	13.0	9.3%	8.4%
	c	112.0	6.4	10.1	9.1	9.1%	8.1%
	d	102.2	6.0	9.6	8.6	9.4%	8.4%
	e	103.7	5.7	9.0	8.1	8.7%	7.8%
17WW-09	a	113.0	7.0	11.2	10.1	9.9%	8.9%
	b	132.2	8.6	13.6	12.3	10.3%	9.3%
	c	125.1	8.6	13.6	12.2	10.9%	9.8%
	d	131.4	8.5	13.6	12.2	10.3%	9.3%
	e	130.1	8.2	13.1	11.8	10.1%	9.0%
17WW-10	a	116.9	7.8	12.4	11.2	10.6%	9.6%
	b	108.6	6.1	9.7	8.8	9.0%	8.1%
	c	114.1	7.2	11.5	10.4	10.1%	9.1%
	d	120.7	7.3	11.6	10.5	9.6%	8.7%
	e	118.0	6.3	10.0	9.0	8.5%	7.6%
17WW-11	a	119.5	8.0	12.6	11.4	10.6%	9.5%
	b	110.1	6.8	10.8	9.7	9.8%	8.8%
	c	133.2	10.0	16.0	14.3	12.0%	10.8%
	d	129.7	10.3	16.4	14.7	12.6%	11.4%
	e	114.8	6.8	10.7	9.7	9.4%	8.4%
17WW-12	a	146.4	7.3	11.7	10.5	8.0%	7.2%
	b	112.6	5.8	9.2	8.3	8.2%	7.3%
	c	128.5	6.2	9.9	8.9	7.7%	6.9%
	d	173.1	9.3	14.8	13.3	8.6%	7.7%
	e	111.9	5.9	9.4	8.5	8.4%	7.6%

Table 5.2: Bulk trace element concentrations in Whitewater soil. Amounts of trace elements were normalized by mass of aliquot measured on a microbalance.

Sample Name	depth [cm]	mass [mg]	U [ppm]	std	Th [ppm]	std	Sm [ppm]	std	Th/U	std	Sm/U	std
17WW-Ru-01a	0-5	123.30	4.28	0.21	21.97	1.10	5.52	0.28	5.19	0.31	1.34	0.08
17WW-Ru-01b	0-5	144.40	4.11	0.21	20.51	1.03	5.11	0.26	5.05	0.30	1.30	0.08
17WW-Ru-01c	0-5	148.80	4.28	0.21	21.56	1.08	5.23	0.26	5.10	0.31	1.27	0.08
17WW-Ru-01d	0-5	166.20	4.54	0.23	23.04	1.15	5.56	0.28	5.14	0.31	1.28	0.08
17WW-Ru-01e	0-5	139.00	4.78	0.24	24.72	1.24	6.04	0.30	5.24	0.31	1.32	0.08
17WW01	0-5	553.86	6.27	0.16	21.91	5.26	3.22	2.56	3.49	0.21	0.51	0.03
17WW01a	0-5	1.47	4.79	0.06	29.86	0.39	7.59	0.60	6.23	0.37	1.58	0.10
17WW01b	0-5	5.30	3.72	0.05	24.14	0.35	5.76	0.46	6.49	0.39	1.55	0.09
17WW01c	0-5	2.59	3.96	0.05	25.76	0.31	6.22	0.58	6.50	0.39	1.57	0.09
17WW01ds2	0-5	390.00	5.16	0.05	18.88	0.55	5.04	0.49	3.66	0.22	0.98	0.06
17WW02	10-12	400.52	4.55	0.12	24.10	5.78	4.30	3.42	5.30	0.32	0.95	0.06
17WW02a	10-12	2.58	3.06	0.04	24.48	0.30	5.71	0.54	8.00	0.48	1.87	0.11
17WW02b	10-12	1.60	3.51	0.05	27.63	0.39	6.15	0.62	7.87	0.47	1.75	0.11
17WW02c	10-12	3.66	3.68	0.06	31.17	0.44	7.10	0.65	8.48	0.51	1.93	0.12
17WW02ds2	10-12	407.30	4.61	0.03	23.36	0.52	5.38	0.61	5.07	0.30	1.17	0.07
17WW-Ru-02a	10-12	128.80	4.02	0.20	27.43	1.37	6.00	0.30	6.90	0.41	1.56	0.09
17WW-Ru-02b	10-12	122.30	4.47	0.22	29.21	1.46	6.13	0.31	6.61	0.40	1.43	0.09
17WW-Ru-02c	10-12	156.60	4.13	0.21	28.20	1.41	5.67	0.28	6.91	0.41	1.43	0.09
17WW-Ru-02d	10-12	121.40	4.53	0.23	30.29	1.51	6.35	0.32	6.77	0.41	1.46	0.09
17WW-Ru-02e	10-12	164.60	4.42	0.22	30.25	1.51	6.37	0.32	6.93	0.42	1.50	0.09
17WW03	20-22	527.72	4.71	0.13	25.82	6.19	8.23	3.08	5.48	0.33	1.75	0.10
17WW03a	20-22	9.26	3.62	0.11	31.42	0.90	7.50	0.70	8.67	0.52	2.07	0.12
17WW03b	20-22	3.28	3.72	0.05	30.70	0.44	7.43	0.80	8.25	0.50	2.00	0.12
17WW03c	20-22	3.59	3.71	0.05	31.12	0.41	7.69	0.62	8.40	0.50	2.07	0.12
17WW03ds3	20-22	426.00	4.37	0.03	24.61	0.65	5.92	0.58	5.64	0.34	1.36	0.08
17WW03rw2	20-22	759.70	4.74	0.13	25.40	5.99	5.91	1.95	5.36	0.32	1.25	0.07
17WW-Ru-03a	20-22	132.10	4.73	0.24	33.28	1.66	7.43	0.37	7.13	0.43	1.64	0.10
17WW-Ru-03b	20-22	106.90	4.19	0.21	28.03	1.40	6.61	0.33	6.77	0.41	1.65	0.10
17WW-Ru-03c	20-22	138.70	3.97	0.20	28.00	1.40	6.19	0.31	7.13	0.43	1.63	0.10
17WW-Ru-03d	20-22	143.60	4.67	0.23	32.14	1.61	7.17	0.36	6.96	0.42	1.60	0.10
17WW-Ru-03e	20-22	124.00	4.57	0.23	33.16	1.66	7.37	0.37	7.35	0.44	1.68	0.10
17WW04	30-32	588.94	5.44	0.14	17.62	4.09	9.84	1.94	3.24	0.19	1.81	0.11
17WW04a	30-32	4.35	3.96	0.05	21.10	0.50	6.68	0.65	5.32	0.32	1.68	0.10
17WW04b	30-32	1.40	5.07	0.07	26.14	0.37	8.39	0.78	5.16	0.31	1.65	0.10
17WW04ds2	30-32	3.12	4.46	0.06	25.57	0.30	8.79	0.79	5.74	0.34	1.97	0.12
17WW04ds2	30-32	436.60	5.63	0.03	19.61	0.42	7.25	0.82	3.48	0.21	1.29	0.08
17WW-Ru-04a	30-32	107.80	5.21	0.26	22.62	1.13	7.84	0.39	4.39	0.26	1.57	0.09
17WW-Ru-04b	30-32	122.70	5.39	0.27	23.17	1.16	7.71	0.39	4.35	0.26	1.49	0.09
17WW-Ru-04c	30-32	130.00	5.15	0.26	21.92	1.10	7.44	0.37	4.31	0.26	1.51	0.09
17WW-Ru-04d	30-32	122.30	5.61	0.28	24.05	1.20	8.10	0.41	4.34	0.26	1.51	0.09
17WW-Ru-04e	30-32	111.10	5.40	0.27	23.43	1.17	8.36	0.42	4.39	0.26	1.61	0.10
17WW05	40-42	563.66	4.45	0.12	20.33	4.65	8.35	1.49	4.57	0.27	1.88	0.11
17WW05a	40-42	1.41	4.04	0.06	28.25	0.41	6.70	0.94	6.99	0.42	1.66	0.10
17WW05b	40-42	2.21	3.78	0.05	26.50	0.32	6.97	0.54	7.01	0.42	1.84	0.11
17WW05c	40-42	4.17	3.81	0.05	27.59	0.36	7.11	0.57	7.24	0.43	1.87	0.11
17WW05ds2	40-42	414.10	4.46	0.03	21.85	0.48	5.72	0.65	4.90	0.29	1.28	0.08
17WW-Ru-05a	40-42	137.70	4.74	0.24	28.77	1.44	7.07	0.35	6.15	0.37	1.56	0.09
17WW-Ru-05b	40-42	109.80	4.75	0.24	28.31	1.42	6.96	0.35	6.03	0.36	1.53	0.09
17WW-Ru-05c	40-42	161.30	4.86	0.24	29.39	1.47	7.00	0.35	6.12	0.37	1.50	0.09
17WW-Ru-05d	40-42	134.70	4.99	0.25	30.59	1.53	7.45	0.37	6.20	0.37	1.56	0.09
17WW-Ru-05e	40-42	116.30	4.21	0.21	26.66	1.33	7.07	0.35	6.40	0.38	1.75	0.10
17WW06	50-52	571.84	4.40	0.12	28.13	6.33	12.24	2.00	6.39	0.38	2.78	0.17
17WW06a	50-52	2.75	3.79	0.05	43.35	0.53	12.06	1.22	11.44	0.69	3.18	0.19
17WW06b	50-52	2.59	3.66	0.05	40.89	0.58	11.31	1.13	11.16	0.67	3.09	0.19
17WW06c	50-52	2.60	4.05	0.05	45.48	0.59	11.52	0.90	11.23	0.67	2.85	0.17
17WW06ds2	50-52	398.10	4.53	0.03	34.24	0.75	9.85	1.12	7.56	0.45	2.17	0.13
17WW-Ru-06a	50-52	114.20	4.58	0.23	42.05	2.10	11.63	0.58	9.29	0.56	2.65	0.16
17WW-Ru-06b	50-52	112.10	4.69	0.23	41.37	2.07	11.64	0.58	8.93	0.54	2.59	0.16
17WW-Ru-06c	50-52	119.40	4.74	0.24	41.72	2.09	11.66	0.58	8.91	0.53	2.57	0.15
17WW-Ru-06d	50-52	123.40	4.54	0.23	42.35	2.12	11.45	0.57	9.45	0.57	2.63	0.16
17WW-Ru-06e	50-52	114.00	4.17	0.21	36.33	1.82	11.07	0.55	8.81	0.53	2.77	0.17

Table 5.3: Bulk trace element concentrations in Whitewater soil, continued.

Sample Name	depth [cm]	mass [mg]	U [ppm]	std	Th [ppm]	std	Sm [ppm]	std	Th/U	std	Sm/U	std
17WW07	60-62	546.00	3.16	0.09	39.64	5.31	9.32	2.19	12.55	0.75	2.95	0.18
17WW07a	60-62	1.32	3.18	0.04	34.44	0.42	9.22	0.90	10.82	0.65	2.90	0.17
17WW07b	60-62	2.52	3.40	0.04	34.83	0.48	8.08	1.12	10.23	0.61	2.37	0.14
17WW07c	60-62	2.85	3.51	0.08	36.42	0.89	9.19	0.77	10.37	0.62	2.62	0.16
17WW07ds2	60-62	411.30	4.08	0.03	31.20	0.87	8.38	0.80	7.64	0.46	2.05	0.12
17WW-Ru-07a	60-62	122.60	3.83	0.19	36.82	1.84	8.22	0.41	9.72	0.58	2.24	0.13
17WW-Ru-07b	60-62	125.80	3.60	0.18	34.37	1.72	7.65	0.38	9.66	0.58	2.21	0.13
17WW-Ru-07c	60-62	142.90	3.65	0.18	34.11	1.71	7.51	0.38	9.46	0.57	2.14	0.13
17WW-Ru-07d	60-62	128.90	3.67	0.18	34.65	1.73	7.65	0.38	9.55	0.57	2.17	0.13
17WW-Ru-07e	60-62	115.60	3.77	0.19	36.21	1.81	8.16	0.41	9.72	0.58	2.26	0.14
17WW08	80-82	649.95	3.65	0.10	39.59	5.11	8.62	1.82	10.84	0.65	2.36	0.14
17WW08a	80-82	7.77	3.82	0.05	41.28	0.50	11.01	1.05	10.81	0.65	2.88	0.17
17WW08b	80-82	0.75	5.81	0.08	58.10	0.67	18.13	1.65	10.01	0.60	3.12	0.19
17WW08c	80-82	2.96	3.58	0.04	36.04	0.53	9.51	0.93	10.07	0.60	2.66	0.16
17WW08ds2	80-82	413.20	4.61	0.03	34.06	0.76	9.79	1.12	7.39	0.44	2.12	0.13
17WW-Ru-08a	80-82	102.30	4.52	0.23	38.82	1.94	10.26	0.51	8.68	0.52	2.36	0.14
17WW-Ru-08b	80-82	154.80	3.90	0.19	32.80	1.64	8.66	0.43	8.52	0.51	2.32	0.14
17WW-Ru-08c	80-82	112.00	3.45	0.17	29.12	1.46	8.20	0.41	8.53	0.51	2.48	0.15
17WW-Ru-08d	80-82	102.20	4.16	0.21	35.70	1.79	9.51	0.48	8.68	0.52	2.38	0.14
17WW-Ru-08e	80-82	103.70	4.01	0.20	36.15	1.81	9.85	0.49	9.12	0.55	2.56	0.15
17WW09	100-102	637.38	5.02	0.14	33.94	8.45	12.11	2.32	6.75	0.41	2.41	0.14
17WW09a	100-102	1.39	3.54	0.05	41.05	0.43	12.29	1.19	11.61	0.70	3.48	0.21
17WW09b	100-102	1.67	4.61	0.06	51.91	0.69	15.82	1.28	11.26	0.68	3.43	0.21
17WW09c	100-102	3.79	4.19	0.06	50.26	0.64	13.93	1.29	12.01	0.72	3.33	0.20
17WW09ds2	100-102	400.60	4.16	0.03	41.49	1.22	13.36	1.33	9.97	0.60	3.21	0.19
17WW-Ru-09a	100-102	113.00	3.89	0.19	39.83	1.99	11.17	0.56	10.37	0.62	2.99	0.18
17WW-Ru-09b	100-102	132.20	3.45	0.17	34.21	1.71	9.63	0.48	10.04	0.60	2.91	0.17
17WW-Ru-09c	100-102	125.10	3.88	0.19	38.85	1.94	10.40	0.52	10.13	0.61	2.79	0.17
17WW-Ru-09d	100-102	131.40	3.48	0.17	34.72	1.74	9.75	0.49	10.09	0.61	2.92	0.18
17WW-Ru-09e	100-102	130.10	3.35	0.17	34.43	1.72	10.15	0.51	10.40	0.62	3.16	0.19
17WW10a	125-127	2.26	3.92	0.05	42.16	0.97	8.95	0.94	10.76	0.65	2.28	0.14
17WW10b	125-127	2.07	3.88	0.05	41.03	0.84	8.88	0.70	10.57	0.63	2.29	0.14
17WW10c	125-127	1.12	3.72	0.06	40.95	0.60	9.11	0.90	11.00	0.66	2.45	0.15
17WW10ds2	125-127	397.70	3.90	0.03	34.54	0.74	7.81	0.89	8.85	0.53	2.00	0.12
17WW10ds2	125-127	410.00	3.44	0.03	37.42	0.95	8.03	0.92	10.87	0.65	2.33	0.14
17WW-Ru-10a	125-127	116.90	3.46	0.17	32.94	1.65	6.97	0.35	9.64	0.58	2.10	0.13
17WW-Ru-10b	125-127	108.60	3.99	0.20	36.28	1.81	7.62	0.38	9.21	0.55	1.99	0.12
17WW-Ru-10c	125-127	114.10	3.31	0.17	31.13	1.56	6.58	0.33	9.52	0.57	2.07	0.12
17WW-Ru-10d	125-127	120.70	3.77	0.19	35.70	1.78	7.32	0.37	9.58	0.57	2.02	0.12
17WW-Ru-10e	125-127	118.00	4.03	0.20	37.42	1.87	8.08	0.40	9.39	0.56	2.09	0.13
17WW11	150-152	518.07	3.47	0.10	53.90	8.31	7.95	2.22	15.55	0.93	2.29	0.14
17WW11a	150-152	1.83	3.77	0.05	40.74	0.55	8.55	0.89	10.79	0.65	2.27	0.14
17WW11b	150-152	2.13	4.00	0.06	46.78	0.51	9.59	0.91	11.70	0.70	2.40	0.14
17WW11c	150-152	3.05	3.59	0.05	40.26	0.57	7.57	0.72	11.21	0.67	2.11	0.13
17WW-Ru-11a	150-152	119.50	3.01	0.15	35.60	1.78	6.72	0.34	11.99	0.72	2.33	0.14
17WW-Ru-11b	150-152	110.10	3.27	0.16	37.63	1.88	7.06	0.35	11.65	0.70	2.25	0.14
17WW-Ru-11c	150-152	133.20	2.88	0.14	32.22	1.61	6.21	0.31	11.32	0.68	2.25	0.13
17WW-Ru-11d	150-152	129.70	2.93	0.15	33.41	1.67	6.29	0.31	11.55	0.69	2.24	0.13
17WW-Ru-11e	150-152	114.80	3.20	0.16	37.85	1.89	7.11	0.36	11.96	0.72	2.31	0.14
17WW12	175-177	607.02	2.29	0.07	31.05	4.79	4.79	1.34	13.54	0.81	2.09	0.13
17WW12a	175-177	2.98	3.23	0.04	35.98	0.50	7.19	0.76	11.13	0.67	2.22	0.13
17WW12b	175-177	5.30	3.28	0.05	37.07	0.59	7.01	0.56	11.31	0.68	2.14	0.13
17WW12c	175-177	5.21	3.31	0.04	36.91	0.56	6.58	0.65	11.15	0.67	1.99	0.12
17WW12ds2	175-177	798.70	3.15	0.03	31.40	0.86	5.90	0.57	9.96	0.60	1.87	0.11
17WW-Ru-12a	175-177	146.40	2.98	0.15	38.87	1.94	6.05	0.30	13.21	0.79	2.12	0.13
17WW-Ru-12b	175-177	112.60	3.12	0.16	37.20	1.86	6.11	0.31	12.08	0.72	2.04	0.12
17WW-Ru-12c	175-177	128.50	3.04	0.15	35.77	1.79	6.01	0.30	11.91	0.71	2.06	0.12
17WW-Ru-12d	175-177	173.10	2.82	0.14	35.32	1.77	5.71	0.29	12.70	0.76	2.12	0.13
17WW-Ru-12e	175-177	111.90	2.95	0.15	35.18	1.76	5.93	0.30	12.08	0.72	2.10	0.13

^{10}Be and ^{26}Al concentration profiles

Blank-corrected ^{10}Be and ^{26}Al concentrations show an exponential decrease with depth from the surface to 175 cm (Fig. 5.10). Relative uncertainty of ^{10}Be and ^{26}Al concentrations are 1.9-4.5% and 3.2-5.8% for samples between the surface and 175 cm depth (Tab. 5.4). Reproducibility of concentrations for two separately prepared replicates of 17WW-06 was 0.7% for ^{10}Be and 5.4% for ^{26}Al. Both sets of concentrations are within uncertainty of each other. Bulk density of the soil (ρ) was determined by regression on the ^{10}Be profile to be (1.9±0.1) g cm^{-3}, assuming an attenuation length Λ of 153±5 g cm^{-2}. This value is comparable to bulk densities of grusified igneous rocks, in which most of the feldspars have been transformed to clay minerals by chemical weathering (e.g. weathering classes 6 and 7 according to the scheme of Clayton et al., 1979). The same bulk density and attentuation length was used to find best-fit regressions for both the ^{10}Be and ^{26}Al concentration profiles.

Surface concentrations of ^{10}Be and ^{26}Al determined by regression analysis are 0.298±0.11 Mat/g and 2.018±0.098 Mat/g, respectively. We used the online CRONUS calculator (Version 2.0, Marrero et al., 2016) to calculate ages for extrapolated surface concentrations and for every sample using depth information. We used a Lal/Stone time-dependent model to scale production rates to the location and elevation of the outcrop at Whitewater Hill. The surface ages derived from ^{10}Be and ^{26}Al are indistinguishable at 53.7±4.6 ka and 53.4±5.6 ka. The average age of samples at all depths is 52.4±2.2 ka. These ages were calculated assuming no erosion and they are therefore minimum ages. The ^{26}Al/^{10}Be ratios of samples within 125 cm of the surface (Fig. 5.10, Tab. 5.4) are within error of the accepted spallogenic production ratio of 6.75 (Balco et al., 2008; Granger and Siame, 2006). This is an indication that there was no major burial of the soil since the beginning of in-situ cosmic-ray exposure.

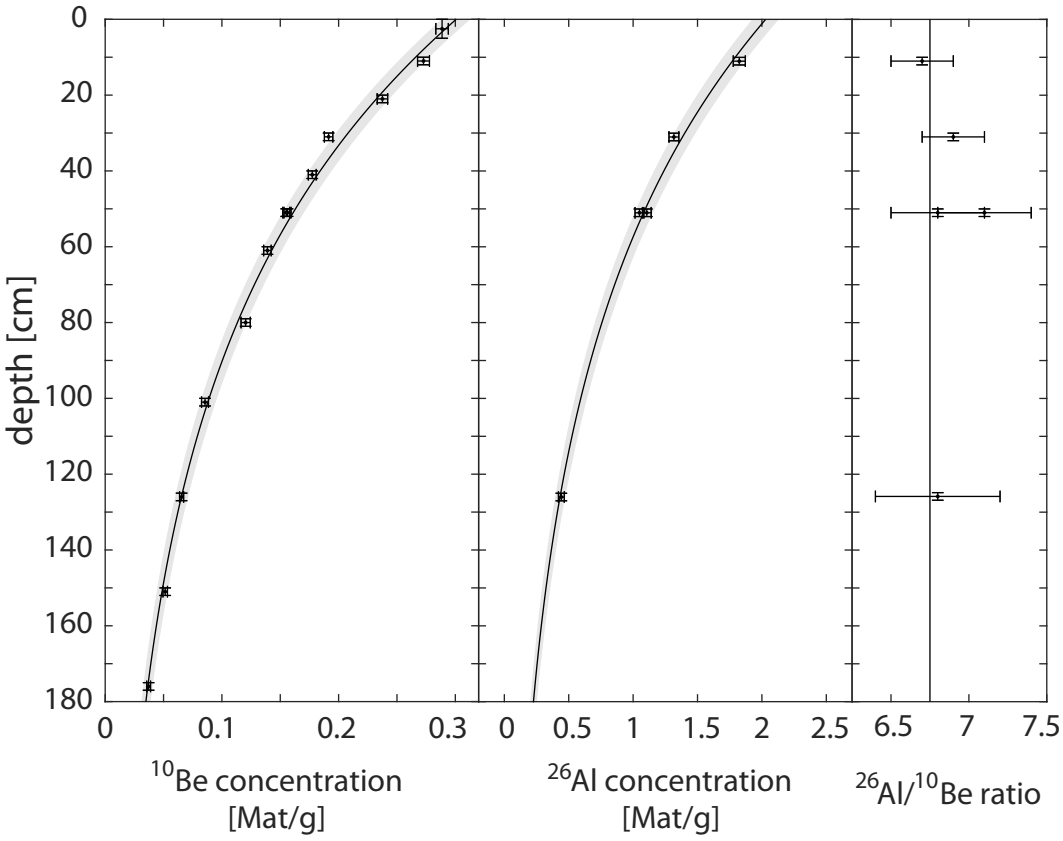

Figure 5.10: Depth profile of ^{10}Be and ^{26}Al concentration and ^{26}Al/^{10}Be ratios. Concentration profiles were regressed with ρ = (1.9±0.1) g cm^{-3} and Λ = 153±5 g cm^{-2}. The ^{26}Al/^{10}Be ratios are within error of the spallogenic ratio of 6.75.

Two samples aggregated from gravel-sized clasts collected at depths of ~7.5 m (17WW-B1) and ~15 m (17WW-B2) below the modern surface, yielded ^{10}Be and ^{26}Al concentrations that were only slighly above blank level. These concentrations were interpreted as inherited concentrations and subtracted from all other samples for the purposes of calculating an age. Burial ages calculated from these deep samples are 65-175 ka (Tab. 5.4). While the concentrations at great depths were not high enough to yield a robust age estimate, this data gives an indication that the true age of the soil is much greater than the ~50 ka determined from in-situ exposure. Longer true exposure duration is possible if there was net erosion of the soil profile.

Table 5.4: AMS measurements of ^{10}Be and ^{26}Al concentrations. Age were calculated assuming no erosion.

Sample	Depth [cm]	Quartz [g]	Be [µg]	^{10}Be [Mat/g]	1σ	age [ka]	1σ	Al [µg]	^{26}Al [Mat/g]	1σ	age [ka]	1σ	^{26}Al/^{10}Be	1σ
17WW-01	0-5	25.007	253.3	0.2886	0.0054	53.7	4.6							
17WW-02	10-12	22.037	255.6	0.2727	0.0051	55.3	4.6	2635	1.8239	0.0469	53.4	5.6	6.69	0.21
17WW-03	20-22	18.759	255.3	0.2375	0.0045	54.4	4.6							
17WW-04	30-32	22.935	252.9	0.1914	0.0036	49.2	4.2	3015	1.3160	0.0382	48.8	5.1	6.87	0.24
17WW-05	40-42	19.733	252.9	0.1774	0.0034	51.6	4.5							
17WW-06	50-52	16.803	254.9	0.1551	0.0030	51.0	4.5	2776	1.0486	0.0344	49.5	5.3	6.76	0.26
17WW-06r	50-52	21.430	255.9	0.1562	0.0030	51.3	4.5	2752	1.1056	0.0340	52.5	5.6	7.08	0.26
17WW-07	60-62	13.846	253.9	0.1390	0.0032	51.5	4.6							
17WW-08	80-82	17.726	255.0	0.0655	0.0018	56.3	5.1	2684	0.4421	0.0228			6.75	0.39
17WW-09	100-102	12.963	254.6	0.0855	0.0030	51.0	5.0							
17WW-10	125-126	20.467	255.2	0.1203	0.0039	52.8	5.2				50.8	6.2		
17WW-11	150-152	12.364	255.3	0.0514	0.0019	55.7	5.7							
17WW-12	175-177	14.310	256.0	0.0372	0.0017	54.0	6.0							
17WW-B1	750	12.156	256.1	0.0035	0.0013	112	43	2677	0.0468	0.0085	176	35	13.43	5.55
17WW-B2	1500	11.016	255.2	0.0026	0.0013	155	81	2582	0.0096	0.0053	65	37	3.74	2.79

^{3}He concentrations in pedogenic iron-oxides

Since soil material <20 µm can contain mineral phases other than iron-oxides that fully or partially retain helium, a bulk analysis will contain helium from all sources. Attempts to high-grade iron-oxide in soil material with traditional approaches without the application of heat was unsuccessful. Therefore, we leached aliquots in HCl to dissolve iron-oxides and compared helium concentrations measured on these aliquots to those of unleached aliquots. We assert that the difference between the unleached and leached aliquots is the fraction of total helium contained in pedogenic iron-oxides.

Bulk concentrations of ^{3}He are consistently lower in leached aliquots than they are in unleached aliquots (Fig. 5.11), supporting the assumption that a significant amount of helium is contained in the HCl-extractable fraction, i.e. in the inferred pedogenic iron-oxides. The bulk concentrations derived from subtracting the ^{3}He concentrations of leached aliquots from those of unleached aliquots are 2-2.5 Mat/g in the upper part and <1 Mat/g in the lower part of the soil profile. Iron-oxide concentrations were measured for every aliquot and ^{3}He concentrations were normalized by the iron-oxides fraction of the bulk mass. This yielded the ^{3}He concentration in the pedogenic iron-oxides. The profile is not close to an exponential, rather ^{3}He

concentrations are highest at 50-100 cm depth (Fig. 5.11). This is not consistent with in-situ cosmic-ray exposure, and implies vertical movement of iron-oxides in the soil column.

Concentrations of ^{4}He show no clear trend with depth (Fig. 5.11). The bulk ^{4}He concentration by difference and the iron-oxide ^{4}He concentration are essentially constant with depth. There are two high outliers of bulk ^{4}He concentrations measured at 30 cm and 50 cm depth. One of them occurs in a leached sample and one in an unleached sample. The result is a much higher and strongly negative ^{4}He bulk concentration by difference. There is no corresponding increase in ^{3}He concentration in these samples. This implies that the excess ^{4}He is contained in a small, helium-retentive phase with high effective uranium concentration, which is not dissolved in concentrated HCl. We interpret this as the contribution of detrital zircons, which can be present in this grain size range (e.g. Larsen and Poldervaart, 1957; Taboada et al., 2006), or similarly insoluble, U-rich detrital phases in individual aliquots.

Step-heating of soil material

We step-heated a bulk soil sample and a sample leached with HCl in order to study differences in retention between the pedogenic iron-oxides and the rest of the bulk soil material as well as whether there is contribution of adsorbed helium from air to the total helium concentration. As for the depth profile analyses above, we assume that HCl completely dissolves pedogenic iron-oxides while leaving all other detrital phases, such as quartz, clay minerals, and mafic minerals, contained in the soil material. These phases are potentially partially retentive to helium and might contribute to the bulk concentration, which needs to be corrected to yield helium concentrations in pedogenic iron-oxides.

Two aliquots of 2.02 g of homogenized bulk soil material with a grain size of <20

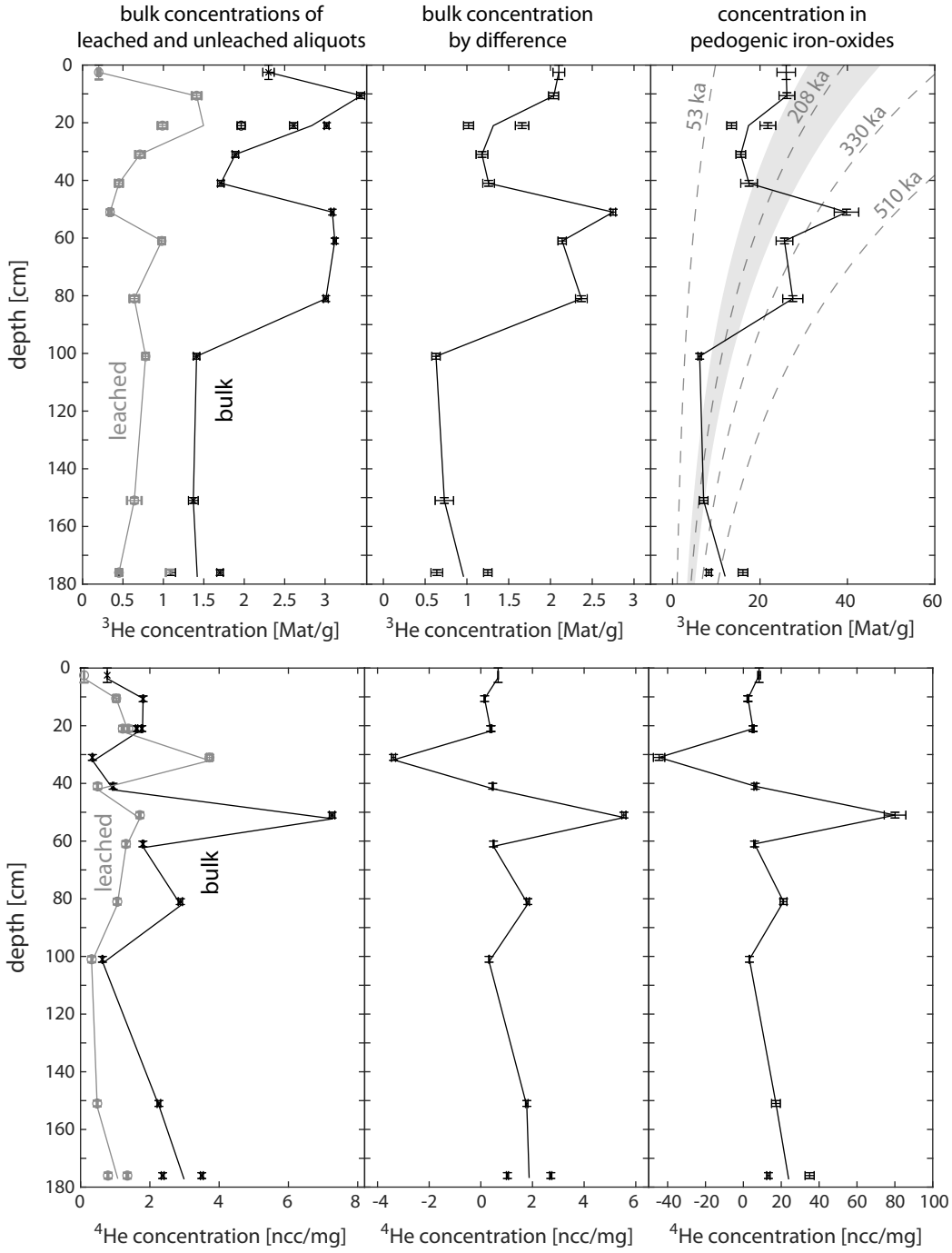

Figure 5.11: Depth profiles of ^{3}He (top) and ^{4}He concentrations (bottom) measured in leached and bulk aliquots (left), difference between bulk and leached aliquots (middle), and difference normalized by iron-oxide content (right). Shown are age constraints of the in-situ exposure age from the ^{10}Be and ^{26}Al depth profiles (53 ka) and the burial age of the underlying paleosol of 330-510 ka. Our preferred age, determined from ^{3}He in pedogenic iron-oxides is 208±44 ka. Concentrations of ^{4}He in pedogenic iron-oxides are small and variable with several outliers.

Table 5.5: Measurements of ^{3}He and ^{4}He in bulk soil material of Whitewater Hill in the <20 µm fraction. Subscript 'bulk' denotes amounts of ^{3}He and ^{4}He normalized by bulk mass of aliquot. Samples were measured in aliquots leached in HCl to dissolve iron-oxides as well as in unleached aliquots. Concentrations of ^{3}He and ^{4}He are determined by difference and normalized by the iron-oxide concentrations of the soil material. Values of sample 17WW-02 are sums of all steps of the step-heating experiment.

					^{3}He										
		unleached aliquot					leached aliquot					by difference			
Sample	depth [cm]	mass [mg]	^{3}He [pcc]	std	$^3He_{bulk}$ [Mat/g]	std	mass [mg]	^{3}He [pcc]	std	$^3He_{bulk}$ [Mat/g]	std	$^3He_{bulk}$ [Mat/g]	std	$^3He_{Feox}$ [Mat/g]	std
17WW-01	0-5	380	0.0325	0.0010	2.30	0.07	553.86	0.0032	0.0003	0.20	0.02	2.10	0.07	26.0	2.1
17WW-02	10-12	2020.00	0.2556	0.0116	3.40	0.15	2020.00	0.1005	0.0072	1.34	0.10	2.06	0.13	27.9	1.7
17WW-03	20-22	496.17	0.0557	0.0014	3.02	0.03	460.15	0.0341	0.0009	1.99	0.05	1.02	0.06	13.5	1.1
17WW-03r	20-22	259.6	0.0253	0.0011	2.61	0.05	219.20	0.0078	0.0005	0.96	0.06	1.66	0.08	21.8	1.8
17WW-04	30-32	267.7	0.0188	0.0007	1.89	0.04	237.14	0.0063	0.0005	0.71	0.06	1.18	0.07	15.6	1.1
17WW-05	40-42	243.05	0.0154	0.0007	1.71	0.04	217.21	0.0036	0.0004	0.45	0.05	1.26	0.07	17.5	1.9
17WW-06	50-52	459.12	0.0528	0.0013	3.09	0.02	525.79	0.0067	0.0004	0.34	0.02	2.75	0.03	39.8	2.8
17WW-07	60-62	433.24	0.0503	0.0013	3.12	0.02	520.36	0.0190	0.0008	0.98	0.04	2.14	0.05	25.6	1.9
17WW-08	80-82	242.28	0.0271	0.0009	3.01	0.03	281.42	0.0067	0.0006	0.64	0.06	2.37	0.07	27.5	2.3
17WW-09	100-102	450.14	0.0236	0.0010	1.41	0.04	558.52	0.0162	0.0007	0.78	0.04	0.63	0.05	6.2	0.4
17WW-11	150-152	241.58	0.0123	0.0007	1.37	0.06	300.48	0.0071	0.0010	0.64	0.09	0.73	0.11	7.1	1.0
17WW-12	175-177	453.3	0.0287	0.0012	1.70	0.04	544.16	0.0091	0.0005	0.45	0.02	1.25	0.05	16.1	1.1
17WW-12r	175-177	305.8	0.0124	0.0007	1.09	0.06	407.51	0.0069	0.0007	0.45	0.04	0.64	0.07	8.3	0.6

					^{4}He										
		unleached aliquot					leached aliquot					by difference			
Sample	depth [cm]	mass [mg]	^{4}He [ncc]	std	$^4He_{bulk}$ [ncc/mg]	std	mass [mg]	^{4}He [ncc]	std	$^4He_{bulk}$ [ncc/mg]	std	$^4He_{bulk}$ [ncc/mg]	std	$^4He_{Feox}$ [ncc/mg]	std
17WW-01	0-5	380	291.69	0.04	0.77	0.01	553.86	56.08	0.05	0.10	0.00	0.67	0.01	8.3	0.7
17WW-02	10-12	2020.00	2411.38	0.39	1.19	0.01	2020.00	2071.91	0.42	1.03	0.01	0.17	0.01	2.3	0.7
17WW-03	20-22	496.17	876.99	0.10	1.77	0.02	460.15	635.17	0.10	1.38	0.02	0.39	0.02	5.1	0.4
17WW-03r	20-22	259.6	420.13	0.15	1.62	0.03	219.20	268.35	0.09	1.22	0.03	0.39	0.04	5.2	0.4
17WW-04	30-32	267.7	91.76	0.02	0.34	0.01	237.14	882.85	0.17	3.72	0.08	-3.38	0.08	-44.5	-3.0
17WW-05	40-42	243.05	229.50	0.07	0.94	0.02	217.21	106.16	0.07	0.49	0.01	0.46	0.02	6.3	0.7
17WW-06	50-52	459.12	3330.93	0.35	7.26	0.08	525.79	901.53	0.16	1.71	0.02	5.54	0.08	80.1	5.7
17WW-07	60-62	433.24	780.60	0.13	1.80	0.02	520.36	682.31	0.10	1.31	0.01	0.49	0.02	5.9	0.4
17WW-08	80-82	242.28	698.77	0.18	2.88	0.06	281.42	299.03	0.13	1.06	0.02	1.82	0.06	21.2	1.8
17WW-09	100-102	450.14	285.13	0.05	0.63	0.01	558.52	176.01	0.04	0.32	0.00	0.32	0.01	3.2	0.2
17WW-11	150-152	241.58	545.48	0.13	2.26	0.05	300.48	144.33	0.03	0.48	0.01	1.78	0.05	17.2	2.3
17WW-12	175-177	453.3	1585.77	0.30	3.50	0.04	544.16	429.30	0.08	0.79	0.01	2.71	0.04	35.0	2.4
17WW-12r	175-177	305.8	725.51	0.16	2.37	0.04	407.51	548.71	0.14	1.35	0.02	1.03	0.04	13.2	0.9

μm were prepared. One was directly used for analysis, while the other was leached with HCl at room temperature for 24 h, with the acid being decanted and discarded every 8 h. Samples were loaded into five small foil balls, which were dropped into a double-vacuum resistance furnace at once. We calibrated the temperatures reached in the furnace at different power inputs with a K-type thermocouple prior to the measurement. The same heating schedule with temperature steps between 200 °C and 1400 °C for 20 min each was applied to both aliquots.

The resulting amounts of ^{3}He and ^{4}He for each temperature step were normalized by the bulk (pre-leaching) mass (Fig. 5.12). The amount of ^{3}He in the bulk material is much larger than in the leached material, suggesting that most ^{3}He is contained in the pedogenic iron-oxides. The ^{4}He concentration curves of the bulk and leached aliquots are almost identical (Fig. 5.12), which suggests that most of the ^{4}He is being contained in the insoluble fraction. This is expected, since the detrital silicates are partially or fully retentive to helium at earth-surface conditions and are derived from mostly Cretaceous-Precambrian rocks (Fosdick and Blisniuk, 2018), thereby allowing several orders of magnitude more time to accumulate ^{4}He than the pedogenic iron-oxides, which have developed in the last ~200 ka. The total amounts of ^{3}He and ^{4}He in pedogenic iron-oxides in this sample, normalized by an iron-oxide percentage of 7.4±0.8%, are 27.9±1.7 Mat/g and 2.27±0.74 ncc/mg.

Both ^{3}He and ^{4}He are released in the same temperature range, indicating that they are equally strongly bound in the crystal, which is consistent with uniform distributions of ^{3}He and ^{4}He. The ^{3}He/^{4}He ratio of helium contained in pedogenic iron-oxides is approximately constant at a value of ~0.7 RA (Fig. 5.12) for all temperature steps. Since helium derived from air with a ^{3}He/^{4}He ratio of 1 RA would be released preferentially at lower temperatures steps, we interpret this as evidence that this material does not contain significant amounts of adsorbed helium from air.

Table 5.6: Measurements of ^{3}He and ^{4}He from step-heating of bulk and leached aliquots of a soil sample from Whitewater Hill taken at 10-12 cm depth. Concentrations in pedogenic iron-oxides was calculated by difference. bdl = below detection limit

bulk aliquot										
T [°C]	^{3}He [pcc]	1σ	^{3}He [Mat/g]	std	^{4}He [ncc]	std	^{4}He [ncc/g]	1σ	^{3}He/^{4}He [RA]	1σ
266	0.0208	0.0035	0.28	0.05	182.028	0.070	90.113	0.035	0.16	0.03
300	0.0135	0.0026	0.18	0.03	205.328	0.067	101.648	0.033	0.09	0.02
350	0.0226	0.0038	0.30	0.05	487.922	0.175	241.545	0.086	0.06	0.01
400	0.0236	0.0037	0.31	0.05	359.391	0.195	177.916	0.097	0.09	0.01
450	0.0195	0.0030	0.26	0.04	295.408	0.161	146.242	0.080	0.09	0.01
500	0.0250	0.0032	0.33	0.04	343.560	0.144	170.079	0.071	0.10	0.01
550	0.0215	0.0030	0.29	0.04	189.236	0.090	93.681	0.045	0.16	0.02
600	0.0132	0.0026	0.18	0.03	78.970	0.056	39.094	0.028	0.23	0.05
650	0.0253	0.0041	0.34	0.05	99.969	0.058	49.490	0.029	0.35	0.06
700	0.0249	0.0036	0.33	0.05	54.241	0.079	26.852	0.039	0.63	0.09
750	0.0215	0.0036	0.29	0.05	35.143	0.046	17.398	0.023	0.85	0.14
800	0.0154	0.0028	0.21	0.04	29.868	0.031	14.786	0.015	0.71	0.13
850	0.0086	0.0019	0.11	0.03	25.037	0.024	12.394	0.012	0.47	0.11
900	bdl		bdl		11.279	0.014	5.584	0.007	bdl	
950	bdl		bdl		5.453	0.011	2.699	0.005	bdl	
1000	bdl		bdl		6.043	0.014	2.992	0.007	bdl	
1100	bdl		bdl		2.415	0.008	1.196	0.004	bdl	
1200	bdl		bdl		0.091	0.002	0.045	0.001	bdl	
1300	bdl		bdl		bdl		bdl		bdl	
1350	bdl		bdl		bdl		bdl		bdl	
total	0.2556	0.0116	3.40	0.15	2411.382	0.387	1193.754	0.192		

aliquot leached in HCl										
T [°C]	^{3}He [pcc]	1σ	^{3}He [Mat/g]	std	^{4}He [ncc]	std	^{4}He [ncc/g]	1σ	^{3}He/^{4}He [RA]	1σ
266	0.0142	0.0029	0.19	0.04	177.514	0.060	87.878	0.030	0.11	0.02
300	0.0097	0.0023	0.13	0.03	190.185	0.069	94.151	0.034	0.07	0.02
350	0.0167	0.0026	0.22	0.03	478.805	0.210	237.032	0.104	0.05	0.01
400	0.0056	0.0016	0.07	0.02	338.118	0.172	167.385	0.085	0.02	0.01
450	0.0044	0.0014	0.06	0.02	262.498	0.113	129.950	0.056	0.02	0.01
500	0.0060	0.0017	0.08	0.02	304.878	0.267	150.930	0.132	0.03	0.01
550	0.0051	0.0018	0.07	0.02	153.551	0.035	76.015	0.017	0.05	0.02
600	0.0044	0.0013	0.06	0.02	52.239	0.077	25.861	0.038	0.12	0.04
650	0.0081	0.0019	0.11	0.03	51.075	0.060	25.285	0.030	0.22	0.05
700	0.0085	0.0022	0.11	0.03	25.070	0.029	12.411	0.014	0.47	0.12
750	0.0065	0.0019	0.09	0.02	12.677	0.017	6.276	0.009	0.71	0.20
800	0.0064	0.0019	0.09	0.03	10.729	0.019	5.311	0.010	0.82	0.25
850	0.0049	0.0015	0.06	0.02	7.854	0.013	3.888	0.007	0.86	0.27
900	bdl		bdl		3.545	0.008	1.755	0.004	bdl	
950	bdl		bdl		1.671	0.008	0.827	0.004	bdl	
1000	bdl		bdl		0.945	0.006	0.468	0.003	bdl	
1100	bdl		bdl		0.507	0.005	0.251	0.002	bdl	
1200	bdl		bdl		0.047	0.002	0.023	0.001	bdl	
1300	bdl		bdl		bdl		bdl		bdl	
1350	bdl		bdl		bdl		bdl		bdl	
total	0.1005	0.0072	1.34	0.10	2071.906	0.422	1025.696	0.209		

difference (in pedogenic iron-oxides)										
T [°C]	^{3}He [pcc]	1σ	^{3}He [Mat/g]	std	^{4}He [ncc]	std	^{4}He [ncc/g]	1σ	^{3}He/^{4}He [RA]	1σ
266	0.0067	0.0045	0.09	0.04	4.514	0.092	2.235	0.046	2.04	0.98
300	0.0038	0.0035	0.05	0.03	15.143	0.096	7.497	0.048	0.35	0.22
350	0.0059	0.0046	0.08	0.04	9.117	0.273	4.513	0.135	0.89	0.49
400	0.0181	0.0040	0.24	0.04	21.273	0.260	10.531	0.129	1.17	0.19
450	0.0150	0.0033	0.20	0.03	32.910	0.197	16.292	0.098	0.63	0.10
500	0.0190	0.0037	0.25	0.03	38.682	0.303	19.149	0.150	0.68	0.09
550	0.0164	0.0035	0.22	0.03	35.685	0.097	17.666	0.048	0.63	0.10
600	0.0089	0.0029	0.12	0.03	26.731	0.095	13.233	0.047	0.46	0.11
650	0.0171	0.0045	0.23	0.04	48.894	0.084	24.205	0.041	0.48	0.09
700	0.0164	0.0042	0.22	0.04	29.172	0.084	14.441	0.042	0.78	0.14
750	0.0151	0.0041	0.20	0.04	22.466	0.049	11.122	0.024	0.92	0.18
800	0.0090	0.0034	0.12	0.03	19.140	0.037	9.475	0.018	0.65	0.17
850	0.0037	0.0025	0.05	0.02	17.183	0.028	8.507	0.014	0.30	0.14
900	bdl		bdl		7.735	0.016	3.829	0.008	bdl	
950	bdl		bdl		3.782	0.013	1.872	0.007	bdl	
1000	bdl		bdl		5.098	0.015	2.524	0.007	bdl	
1100	bdl		bdl		1.908	0.009	0.944	0.005	bdl	
1200	bdl		bdl		0.043	0.003	0.021	0.001	bdl	
1300	bdl		bdl		bdl		bdl		bdl	
1350	bdl		bdl		bdl		bdl		bdl	
total	0.1551	0.0137	2.06	0.13	339.476	0.572	168.058	0.284		

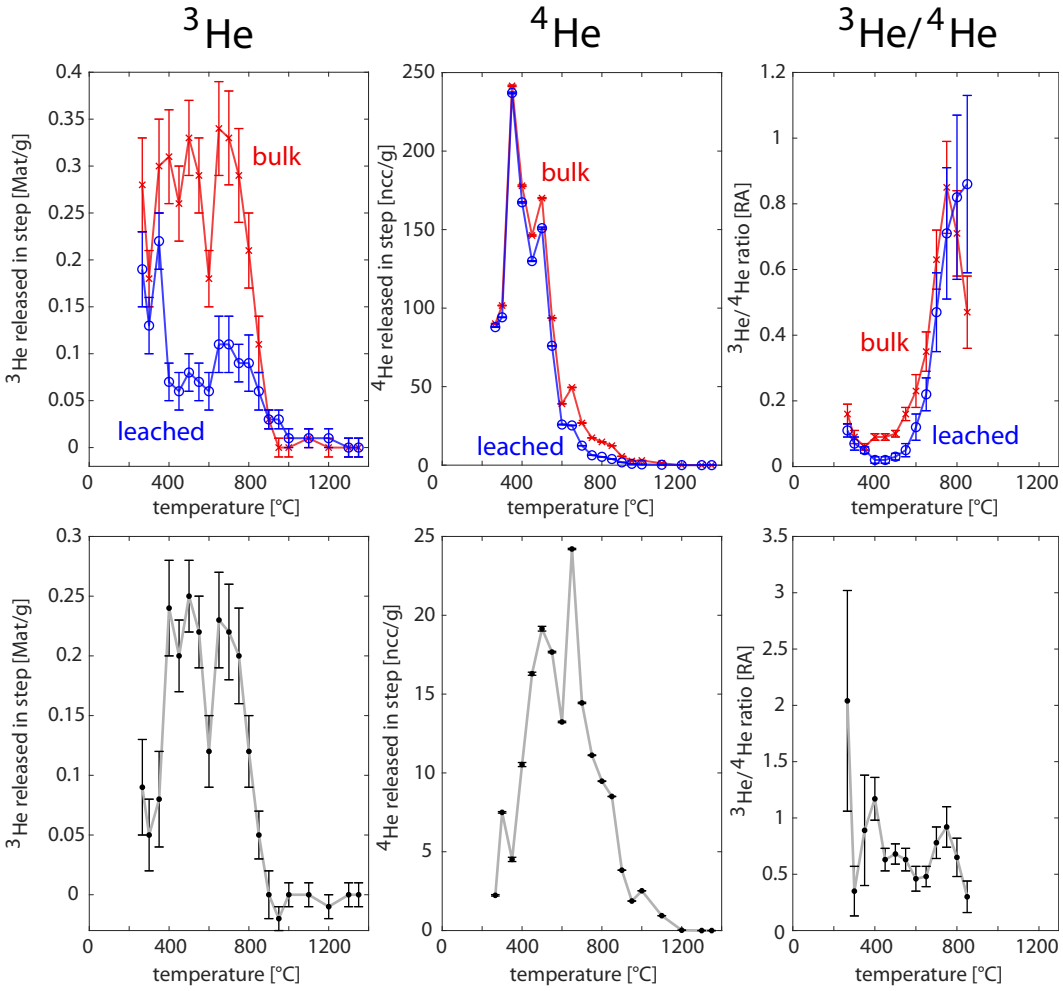

Figure 5.12: Step-heating experiments of soil samples from Whitewater taken at 10-12 cm depth. A bulk aliquot and an aliquot leached in HCl to dissolve iron-oxides were heated to temperatures between 200 °C and 1400 °C for 20 min each step. Both ^{3}He and ^{4}He are extracted between 200 °C and 800 °C. Most ^{3}He is contained in the dissolved fraction, while almost all of the ^{4}He is contained in the insoluble fraction. We assume that the difference between the leached and bulk aliquots is the amount of He contained in pedogenic iron-oxides (bottom row). This data was normalized by the bulk mass and was not corrected for the fraction of iron-oxides.

5.6 Discussion

Helium-retention in pedogenic iron-oxides

Iron-oxides in soils are predominately goethite and hematite (Cornell and Schwertmann, 2003; Schwertmann, 1988a; Schwertmann et al., 2004; Singh and Gilkes, 1992). The diffusion parameters of hematite have been established (Farley, 2018),

which permits the prediction of helium-retentivity by grain size. We show through diffusion modeling that the typical grain sizes and grain shapes of pedogenic hematite particles are expected to retain helium at near-quantitative levels. Equivalent absolute diffusion parameters have not been measured for goethite. However, pedogenic goethite particles are usually larger than hematite particles (Schwertmann, 1988a,b) and aggregates of fine-grained, polycrystalline goethite particles have been shown to be retentive to helium (e.g. Hofmann et al., 2017). This suggests that pedogenic goethite particles might retain helium to fractions similar to those of hematite particles at the same environmental conditions.

Besides goethite and hematite, there are other iron-oxide phases that might contribute to the total iron-content of the soil. Ferrihydrite is poorly crystalline and exists as extremely small particles of a few nanometers in diameter (Schwertmann, 1988a). Even hematite at this particle size is not retentive to helium (Farley, 2018). This suggests that ferrihydrite does not retain helium. The accumulation of helium in pedogenic iron-oxides would therefore only initiate with re-crystallization of ferrihydrite to goethite or hematite.

Age of the Whitewater soil

Since the measured ^{3}He concentration profile of pedogenic iron-oxides at Whitewater deviates from an exponential (Fig. 5.11), which we interpret as downward migration of iron-oxide particles during exposure, it cannot be used directly to calculate an exposure age. We propose the assumption that the depth-integrated ^{3}He concentration of a profile that has experienced downward migration of iron-oxides is equal to that of an undisturbed, exponential profile. The integrated ^{3}He profile of the Whitewater soil corresponds to an exposure age of 208±44 ka (1σ) using a scaled cosmogenic ^{3}He production rate of 189±45 at g^{-1} a^{-1}. This value satisfies previous age constraints: it is lower than the burial age of the underlying paleo-surface of

330-510 ka (unpublished data quoted in Huerta, 2017), and it is over 100 ka, which is the minimum age estimate from soil analyses (Kendrick et al., 2015; Yule and Sieh, 2003).

Since the ^{3}He concentrations were measured as the difference between the concentrations of bulk samples and samples leached in concentrated HCl, this age might be higher than the true age if any helium-retentive phase was present in the HCl-extractable fraction. Possible phases include apatite, which is a frequently found detrital phase and quantitatively retains helium, and calcite, which might be formed in soils and is at least partially retentive to helium (Amidon et al., 2015).

An apparent exposure age calculated from pedogenic iron-oxides higher than that obtained from the ^{10}Be and ^{26}Al in-situ profiles is allowable, because downward migration of iron-oxides particles has been going on since the formation of the soil. Additionally, the in-situ exposure age was calculated assuming no erosion since deposition. This assumption is most likely invalid for this location, which is experiences deflation, and the in-situ exposure age therefore represents a minimum age estimate. Due to downward migration of iron-oxide particles, they were preferentially protected from surface erosion and therefore record a greater fraction of the true cosmogenic exposure than larger detrital phases, which are stationary. More efficient separation techniques, such as high-gradient magnetic separation (e.g. Schulze and Dixon, 1979), could yield higher purity pedogenic iron-oxides for analysis, which might lead to improvements in accuracy and precision of this method.

Implications for Banning Strand slip rate

Using the total offset of the apex of the alluvial fan, determined by Huerta (2017) to be 1.5-2.7 km (see Fig. 5.4), and the age estimate from cosmogenic ^{3}He in pedogenic iron-oxides of 208±44 ka, we calculate an average slip rate of the Banning Strand of

the San Andreas fault of 10.1 mm/a, with a total range of uncertainty of 5.1 mm/a to 22.5 mm/a. This range overlaps with the slip rates of 7.0-23 mm/a calculated by Huerta (2017) based on their preferred age of 120-230 ka for this surface. Previous ^{10}Be boulder ages of 39.7-87.3 ka reported by Owen et al. (2014), yield a slip rate of 17.2-68.0 mm/a, which is much larger than previous estimates (e.g. Kendrick et al., 2015). A depth profile of ^{10}Be and ^{26}Al concentrations in this study replicated the surface exposure age of Owen et al. (2014) to within uncertainty. Since this age was calculated assuming no erosion, it represents a minimum estimate. The slip rate is likely to be <68.0 mm/a, a condition which is satisfied by our slip rate estimate. We therefore prefer a slip rate of $10.1^{+6.2}_{-2.5}$ mm/a, based on our cosmogenic exposure age estimate from pedogenic iron-oxides.

Possible uses of ^{3}He in pedogenic iron-oxides

We interpret the shape of the cosmogenic ^{3}He depth profile as evidence for vertical movement of iron-oxide particles in the Whitewater soil over the period of cosmic-ray exposure. This is most likely due to lessivage, which is the mechanical migration of clay particles from the A to the B horizon of soils (Blume, 1988). Pedogenic iron-oxides often adsorb to the surface of clay-sized particles, and they are transported downwards with them (Schwertmann, 1988a). This leads to accumulations of ^{3}He in pedogenic iron-oxides at depth that are in excess of those expected from in-situ exposure. Lessivage has been recognized as a major soil-forming process (Bockheim and Gennadiyev, 2000) in many types of soils. For soils that exhibit lessivage, ^{3}He can be used as a tool to study the vertical migration of pedogenic iron-oxides, and its uses for geochronology might be secondary.

However, not all types of soils show pronounced lessivage (Blume, 1988). Other disturbances to the exponential depth-profile of cosmogenic ^{3}He in pedogenic iron-oxide might come from bulk soil convection, which we have previously observed

in paleosols (Hofmann et al., 2017). In this process, material is moved up and down the soil column in the A and B horizon due to burrowing organisms. An indication of this process can be found in vertical profiles which exhibit a constant ^{3}He concentration with depth. This shows that ^{3}He concentrations in pedogenic iron-oxides can be used to make inferences about their formation and migration. Knowledge of time-scales of these processes can also lead to an improved age estimate.

5.7 Conclusions

Pedogenic iron-oxides are much smaller than ejection distances of radiogenic α-particles or cosmogenic ^{3}He. Therefore, all of the helium produced in the particle is ejected and all of the helium in the particles is implanted. This makes helium accumulation rates in pedogenic iron-oxides dependent on the matrix. Due to the large ejection distances and nearly phase-independent production, cosmogenic ^{3}He accumulation rates in pedogenic iron-oxides are easier to constrain than those of radiogenic ^{4}He. Based on established diffusion parameters, hematite particles are of a size and shape that they are expected to retain most of the implanted helium. There are no similar constraints on goethite diffusion parameters, but based on previous studies of helium-retentivity in goethite and their generally larger grain size, we expect it to retain helium at similar levels as hematite.

Since pedogenic iron-oxides tend to migrate downwards through the soil, they are preferentially protected from surface erosion. Therefore, they could potentially record longer periods of surface exposure than minerals in situ. Pedogenic iron-oxides can yield constraints that can be used in conjunction with other cosmogenic dating methods. If soil processes, such as lessivage, can be constrained, pedogenic iron-oxides themselves might yield a reliable exposure age. Conversely, if the age of a soil is known from independent constraints, cosmic-ray produced ^{3}He concentra-

tions measured on pedogenic goethite and hematite can be used to make inferences about the rate of iron-oxide formation in the soil. Deviations from an exponential depth-profile are likely due to movement of iron-oxide particles after formation, related to lessivage of iron-oxides (Bockheim and Gennadiyev, 2000) or bulk soil convection. ^{3}He concentrations in pedogenic iron-oxides can be used to constrain the rates of these processes.

Pedogenic iron-oxides are a new phase for geochronology of soils, which can yield both age constraints and insight into soil-forming processes. More effective techniques for iron-oxide separation could eliminate potential interferences from other helium-retentive phases and improve the accuracy of this method.

References

Amidon, W. H. and K. A. Farley (2012) "Cosmogenic ^{3}He and ^{21}Ne dating of biotite and hornblende" in: *Earth and Planetary Science Letters* 313, pp. 86–94.

Amidon, W. H., K. A. Farley, D. W. Burbank, and B. Pratt-Sitaula (2008) "Anomalous cosmogenic ^{3}He production and elevation scaling in the high Himalaya" in: *Earth and Planetary Science Letters* 265.1-2, pp. 287–301.

Amidon, W. H., D. Hobbs, and S. A. Hynek (2015) "Retention of cosmogenic ^{3}He in calcite" in: *Quaternary Geochronology* 27, pp. 172–184.

Balco, G., J. O. Stone, N. A. Lifton, and T. J. Dunai (2008) "A complete and easily accessible means of calculating surface exposure ages or erosion rates from ^{10}Be and ^{26}Al measurements" in: *Quaternary geochronology* 3.3, pp. 174–195.

Blume, H.-P. (1988) "The fate of iron during soil formation in humid-temperate environments" in: *Iron in soils and clay minerals* Springer, pp. 749–777.

Bockheim, J. and A. Gennadiyev (2000) "The role of soil-forming processes in the definition of taxa in Soil Taxonomy and the World Soil Reference Base" in: *Geoderma* 95.1-2, pp. 53–72.

Brook, E. J. and M. D. Kurz (1993) "Surface-exposure chronology using in situ cosmogenic ^{3}He in Antarctic quartz sandstone boulders" in: *Quaternary Research* 39.1, pp. 1–10.

Clayton, J. L., W. F. Megahan, and D. Hampton (1979) "Soil and bedrock properties: Weathering and alteration products and processes in the Idaho Batholith" in: *Department of Agriculture, Forest Service, Intermountain Forest and Range Experiment Station, USDA Forest Service Research Paper INT-237*.

Cornell, R. M. and U. Schwertmann (2003) *The iron oxides: structure, properties, reactions, occurrences and uses* John Wiley & Sons.

Davey, B. and R. Wheeler (1980) "Some aspects of the chemistry of lithium in soils" in: *Plant and Soil* 57.1, pp. 49–60.

Dunai, T. J., F. M. Stuart, R. Pik, P. Burnard, and E. Gayer (2007) "Production of ^{3}He in crustal rocks by cosmogenic thermal neutrons" in: *Earth and Planetary Science Letters* 258.1-2, pp. 228–236.

Farley, K. (2018) "Helium diffusion parameters of hematite from a single-diffusion-domain crystal" in: *Geochimica et Cosmochimica Acta* 231, pp. 117–129.

Farley, K., J. Libarkin, S. Mukhopadhyay, and W. Amidon (2006) "Cosmogenic and nucleogenic ^{3}He in apatite, titanite, and zircon" in: *Earth and Planetary Science Letters* 248.1-2, pp. 451–461.

Farley, K. A. (2002) "(U-Th)/He Dating: Techniques, Calibrations, and Applications" in: *Reviews in Mineralogy and Geochemistry* 47.1, pp. 819–844 DOI: 10.2138/rmg.2002.47.18.

Fechtig, H. and S. Kalbitzer (1966) "The diffusion of argon in potassium-bearing solids" in: *Potassium argon dating* Springer, pp. 68–107.

Fosdick, J. C. and K. Blisniuk (2018) "Sedimentary signals of recent faulting along an old strand of the San Andreas Fault, USA" in: *Scientific reports* 8.1, p. 12132.

Gangas, N., A. Simopoulos, A. Kostikas, N. Yassoglou, and S. Filippakis (1973) "Mössbauer studies of small particles of iron oxides in soil" in: *Clays and Clay Minerals* 21.3, pp. 151–160.

Goehring, B. M., M. D. Kurz, G. Balco, J. M. Schaefer, J. Licciardi, and N. Lifton (2010) "A reevaluation of in situ cosmogenic ^{3}He production rates" in: *Quaternary Geochronology* 5.4, pp. 410–418.

Gold, P. O., W. M. Behr, D. Rood, W. D. Sharp, T. K. Rockwell, K. Kendrick, and A. Salin (2015) "Holocene geologic slip rate for the Banning strand of the southern San Andreas Fault, southern California" in: *Journal of Geophysical Research: Solid Earth* 120.8, pp. 5639–5663.

Goodman, B. (1988) "The characterization of iron complexes with soil organic matter" in: *Iron in soils and clay minerals* ed. by J. Stucki, B. Goodman, and U. Schwertmann Springer, pp. 677–687.

Gough, L. P., R. Severson, and H. T. Shacklette (1988) *Element concentrations in soils and other surficial materials of Alaska* U.S. Geological Survey Professional Paper 1458, US Government Printing Office Washington, DC.

Granger, D. E. and L. Siame (2006) "A review of burial dating methods using ^{26}Al and ^{10}Be" in: *Special Papers-Geological Society of America* 415, p. 1.

Hofmann, F., B. Reichenbacher, and K. A. Farley (2017) "Evidence for >5 Ma paleoexposure of an Eocene–Miocene paleosol of the Bohnerz Formation, Switzerland" in: *Earth and Planetary Science Letters* 465, pp. 168–175.

Huerta, B. (2017) "Structure and Geomorphology of West Whitewater Hill, a Compressive Stepover between the Banning and Garnet Hill Strands of the San Andreas Fault, Whitewater, CA" MA thesis California State University, Northridge.

Janot, C., H. Gibert, and C. Tobias (1973) "Caractérisation des kaolinites ferrifères par spectrométrie Mössbauer" in: *Bulletin de la Societé Française de Minéralogie et de Cristallographie* 96, pp. 281–291.

Kendrick, K. J., J. Matti, and S. Mahan (2015) "Late Quaternary slip history of the Mill Creek strand of the San Andreas fault in San Gorgonio Pass, southern California: The role of a subsidiary left-lateral fault in strand switching" in: *Bulletin* 127.5-6, pp. 825–849.

Ketcham, R. A., C. Gautheron, and L. Tassan-Got (2011) "Accounting for long alpha-particle stopping distances in (U–Th–Sm)/He geochronology: Refinement of the baseline case" in: *Geochimica et Cosmochimica Acta* 75.24, pp. 7779–7791.

Kober, F., S. Ivy-Ochs, I. Leya, H. Baur, T. Magna, R. Wieler, and P. Kubik (2005) "In situ cosmogenic ^{10}Be and ^{21}Ne in sanidine and in situ cosmogenic ^{3}He in Fe–Ti-oxide minerals" in: *Earth and Planetary Science Letters* 236.1-2, pp. 404–418.

Kohl, C. and K. Nishiizumi (1992) "Chemical isolation of quartz for measurement of in-situ-produced cosmogenic nuclides" in: *Geochimica et Cosmochimica Acta* 56.9, pp. 3583–3587.

Lal, D. (1987) "Production of ^{3}He in terrestrial rocks" in: *Chemical Geology: Isotope Geoscience Section* 66.1-2, pp. 89–98.

– (1991) "Cosmic ray labeling of erosion surfaces: in situ nuclide production rates and erosion models" in: *Earth and Planetary Science Letters* 104.2-4, pp. 424–439.

Larsen, L. H. and A. Poldervaart (1957) "Measurement and distribution of zircons in some granitic rocks of magmatic origin" in: *Mineralogical Magazine and Journal of the Mineralogical Society* 31.238, pp. 544–564.

Licciardi, J., M. Kurz, P. Clark, and E. Brook (1999) "Calibration of cosmogenic ^{3}He production rates from Holocene lava flows in Oregon, USA, and effects of the Earth's magnetic field" in: *Earth and Planetary Science Letters* 172.3-4, pp. 261–271.

Margerison, H., W. Phillips, F. Stuart, and D. Sugden (2005) "Cosmogenic ^{3}He concentrations in ancient flood deposits from the Coombs Hills, northern Dry Valleys, East Antarctica: interpreting exposure ages and erosion rates" in: *Earth and Planetary Science Letters* 230.1-2, pp. 163–175.

Marrero, S. M., F. M. Phillips, B. Borchers, N. Lifton, R. Aumer, and G. Balco (2016) "Cosmogenic nuclide systematics and the CRONUScalc program" in: *Quaternary Geochronology* 31, pp. 160–187.

McFadden, L. D. and D. M. Hendricks (1985) "Changes in the content and composition of pedogenic iron oxyhydroxides in a chronosequence of soils in southern California" in: *Quaternary Research* 23.2, pp. 189–204.

Mikutta, R., M. Kleber, K. Kaiser, and R. Jahn (2005) "Organic matter removal from soils using hydrogen peroxide, sodium hypochlorite, and disodium peroxodisulfate" in: *Soil Science Society of America Journal* 69.1, pp. 120–135.

Nishiizumi, K., M. Imamura, M. W. Caffee, J. R. Southon, R. C. Finkel, and J. McAninch (2007) "Absolute calibration of ^{10}Be AMS standards" in: *Nuclear Instruments and Methods in Physics Research Section B: Beam Interactions with Materials and Atoms* 258.2, pp. 403–413.

Owen, L. A., S. J. Clemmens, R. C. Finkel, and H. Gray (2014) "Late Quaternary alluvial fans at the eastern end of the San Bernardino Mountains, Southern California" in: *Quaternary Science Reviews* 87, pp. 114–134.

Pistiner, J. S. and G. M. Henderson (2003) "Lithium-isotope fractionation during continental weathering processes" in: *Earth and Planetary Science Letters* 214.1-2, pp. 327–339.

PRISM Climate Group (2019) *Oregon State University* URL: `http://prism.oregonstate.edu`, (visited on 01/05/2019).

Scharer, K., K. Blisniuk, W. Sharp, and S. Mudd (2015) "Slip transfer and the growth of the Indio and Edom Hills, southern San Andreas fault" in: *American Geophysical Union, Fall Meeting 2015, abstract ID T51H-07*.

Schulze, D. and J. Dixon (1979) "High Gradient Magnetic Separation of Iron Oxides and other Magnetic Minerals from Soil Clays" in: *Soil Science Society of America Journal* 43.4, pp. 793–799.

Schulze, D. and U. Schwertmann (1984) "The influence of aluminium on iron oxides: X. Properties of Al-substituted goethites" in: *Clay Minerals* 19.4, pp. 521–539.

Schwertmann, U. (1984) "The influence of aluminium on iron oxides: IX. Dissolution of Al-goethites in 6 M HCl" in: *Clay Minerals* 19.1, pp. 9–19.

– (1988a) "Occurrence and formation of iron oxides in various pedoenvironments" in: *Iron in soils and clay minerals* Springer, pp. 267–308.

– (1988b) "Some properties of soil and synthetic iron oxides" in: *Iron in soils and clay minerals* ed. by J. Stucki, B. Goodman, and U. Schwertmann Springer chap. 9, pp. 203–250.

Schwertmann, U. and N. Kämpf (1985) "Properties of goethite and hematite in kaolinitic soils of southern and central Brazil" in: *Soil Science* 139.4, pp. 344–350.

Schwertmann, U. and E. Murad (1983) "Effect of pH on the formation of goethite and hematite from ferrihydrite" in: *Clays and Clay Minerals* 31.4, pp. 277–284.

Schwertmann, U., H. Stanjek, and H.-H. Becher (2004) "Long-term in vitro transformation of 2-line ferrihydrite to goethite/hematite at 4, 10, 15 and 25 °C" in: *Clay Minerals* 39.4, pp. 433–438.

Shacklette, H. T. and J. G. Boerngen (1984) "Element concentrations in soils and other surficial materials of the conterminous United States" in:

Shuster, D. L., K. A. Farley, P. M. Vasconcelos, G. Balco, H. S. Monteiro, K. Waltenberg, and J. O. Stone (2012) "Cosmogenic ^{3}He in hematite and goethite from Brazilian "canga" duricrust demonstrates the extreme stability of these surfaces" in: *Earth and Planetary Science Letters* 329, pp. 41–50.

Singh, B. and R. Gilkes (1992) "Properties and distribution of iron oxides and their association with minor elements in the soils of south-western Australia" in: *Journal of soil Science* 43.1, pp. 77–98.

Smedley, R. and N. Pearce (2016) “Internal U, Th and Rb concentrations of alkali-feldspar grains: Implications for luminescence dating” in: *Quaternary Geochronology* 35, pp. 16–25.

Taboada, T., A. M. Cortizas, C. García, and E. García-Rodeja (2006) “Particle-size fractionation of titanium and zirconium during weathering and pedogenesis of granitic rocks in NW Spain” in: *Geoderma* 131.1-2, pp. 218–236.

Taylor, R. and U. Schwertmann (1978) “The influence of aluminum on iron oxides. Part I. The influence of Al on Fe oxide formation from the Fe (II) system” in: *Clays and Clay Minerals* 26.6, pp. 373–383.

Torrent, J., U. Schwertmann, and D. Schulze (1980) “Iron oxide mineralogy of some soils of two river terrace sequences in Spain” in: *Geoderma* 23.3, pp. 191–208.

Tremblay, M. M., D. L. Shuster, and G. Balco (2014a) “Cosmogenic noble gas paleothermometry” in: *Earth and Planetary Science Letters* 400, pp. 195–205.

– (2014b) “Diffusion kinetics of ^{3}He and ^{21}Ne in quartz and implications for cosmogenic noble gas paleothermometry” in: *Geochimica et Cosmochimica Acta* 142, pp. 186–204.

Vandenberghe, D., F. De Corte, J.-P. Buylaert, J. Kučera, et al. (2008) “On the internal radioactivity in quartz” in: *Radiation Measurements* 43.2-6, pp. 771–775.

Vermeesch, P., H. Baur, V. S. Heber, F. Kober, P. Oberholzer, J. M. Schaefer, C. Schlüchter, S. Strasky, and R. Wieler (2009) “Cosmogenic ^{3}He and ^{21}Ne measured in quartz targets after one year of exposure in the Swiss Alps” in: *Earth and Planetary Science Letters* 284.3-4, pp. 417–425.

Wilcken, K., T. Fujioka, D. Fink, R. Fülöp, A. Codilean, K. Simon, C. Mifsud, and S. Kotevski (2019) “SIRIUS Performance: ^{10}Be, ^{26}Al and ^{36}Cl measurements at ANSTO” in: *Nuclear Instruments and Methods in Physics Research Section B: Beam Interactions with Materials and Atoms*.

Wolf, R., K. Farley, and D. Kass (1998) “Modeling of the temperature sensitivity of the apatite (U–Th)/He thermochronometer” in: *Chemical Geology* 148.1-2, pp. 105–114.

Yule, D. and K. Sieh (2003) “Complexities of the San Andreas fault near San Gorgonio Pass: Implications for large earthquakes” in: *Journal of Geophysical Research: Solid Earth* 108.B11.

INDEX

Symbols

^{3}H, 274, 275

^{3}He, 1, 21
- atmospheric, 37
- concentration, 2, 3, 12, 15, 16, 18, 20–23, 25, 31, 39–42, 271, 275, 277, 281, 282, 290, 300–303, 307–311
- cosmogenic, 2, 8, 11, 12, 21, 54, 272, 274, 275, 277, 282, 302, 303, 309, 310
- cosmogenic production, 20–22, 42, 275
- cosmogenic production rate
  - in amphibole, 288
  - in biotite, 288
  - in calcite, 288
  - in goethite, 15
  - in pedogenic iron-oxides, 275, 276, 287, 288, 307
  - in pyroxene, 276, 288
  - in silicates, 276
- depth profile, 16, 18, 23, 302, 307, 310
- detection limit, 38
- ejection, 275
- fissiogenic, 277
- implantation, 275
- in pedogenic iron-oxides, 18, 41, 271, 272, 274–279, 285–288, 300–311
- measurement, 14, 291
- muogenic production, 20, 21
- neutron capture, 290
- nucleogenic production, 20, 277, 288
- paleo-exposure, 9, 20–23, 25, 57, 75, 76, 78
- production rate, 20, 275
- radiogenic production, 20, 277, 288
- spike, 64
- stopping distance, 275
- thermal neutron capture, 277

^{4}He, 21, 54
- concentration, 302
- depth profile, 302
- detection limit, 38
- measurement, 15
- production, 12, 21
- retention, 14, 15
- standard, 43

^{4}He/^{3}He method, 14, 31, 32, 50–52, 65
- proton irradiation, 31, 32

^{10}Be, 3, 8, 271, 272, 284, 289, 291, 292, 298–300
- concentration, 300
- depth profile, 3, 298, 299
- exposure age, 3, 298, 299
- measurement, 291, 292
- sample preparation, 284, 291
- sample processing, 289

^{21}Ne, 21, 147

^{26}Al, 3, 8, 271, 272, 284, 289, 291, 292, 298–300
- concentration, 3, 300
- depth profile, 298, 299

exposure age, 3, 298, 299
measurement, 291, 292
sample preparation, 284, 291
sample processing, 289
$^{26}Al/^{10}Be$, 298–300
(U-Th)/He dating, 14, 17, 275
analytical procedure, 14, 15, 43, 64–66, 148, 150, 151
formation age, 11, 12, 15–20, 23, 25, 44–49
measurement, 14, 15, 64–66, 148, 150, 151
Nb packets, 144, 155, 157, 176, 189, 198, 245, 248, 250
Pt packets, 43, 64, 144, 148, 150, 151, 155, 157, 160, 166, 175–177, 180, 181, 186, 188–190, 196, 198–200, 202–206, 208, 217, 245–257, 260, 263–268
rejection criteria, 66
(U-Th)/Ne dating, 147

A

adsorption
helium, 14, 20, 21, 176, 197
oxygen, 170, 187, 191, 196
adsorption
helium, xliv
ÄJC, 12
Ältere Juranagelfluh conglomerate (ÄJC), 12
amphibole, 288
apatite, 144, 145, 274, 308
ATR-FTIR, 151, 152, 217–236
Aufberg, 60, 74, 75, 77, 110, 112

B

Balsthal Erzmatt, 61, 74, 76, 110, 123
Balsthal Holzfluh, 60, 74, 112
bauxite, 19
biotite, 288
Bohnerz, 10
Bohnerz Formation, 9–11, 19, 21, 24, 25, 55, 67, 68

C

Ca-spike, 43, 209, 211
calcite, 218, 219, 222, 288, 308
calcrete, 12, 16
cement, 19
Cerithium beds, 71
chemistry
dissolution of samples, 14, 15, 41, 43, 64, 65, 72
spike, 64
Cholplatz, 60, 74, 76, 79, 82, 83, 113
cortex, xliv, 10, 13, 14, 17–20, 23, 32, 34–37, 63, 66
cosmic-ray exposure
exposure duration, 22–24
modern exposure, 21
paleo-exposure, 2, 8, 9, 20–23, 25, 57, 75, 76, 78
cosmogenic nuclides
production rate, 15
scaling, 15, 42, 75
crushate, 16, 20, 38
cryostat, 64
crystallites, 21

D

diffusion experiment, 31
dissolution-precipitation, 8, 82

duricrust, 19, 23

E

effective diffusion temperature, 285
Erpfingen, 59, 74
exposure duration, 22–24

F

fanglomerate, 285
feldspar, 274, 276, 288, 298
ferrihydrite, 273, 307
fissure, 9
fissure filling, 9, 10, 20, 54, 56–61, 67–69, 71–75, 77, 78, 81, 82, 84–86, 111, 112, 186
formation age, 11, 12, 15–20, 23, 25, 44–49
Franconian Alb, 9, 10, 20, 54, 58, 68–72, 75, 79, 81, 82, 86

G

Gelberde, *see* Rossemaison Formation
Germany, Southern, 20
goethite, 1, 2, 8–12, 14, 15, 17, 19, 24, 25, 37, 38, 41, 44–51, 57, 62, 63, 65, 66, 72, 74, 75, 79, 82–84, 86, 143–151, 155–159, 162, 165–167, 169, 171, 173, 174, 180, 181, 201, 209–211, 216, 218, 228–236, 242–245, 253–256, 266–268, 271–274, 277, 278, 280, 287, 290, 291, 293, 295, 306, 307, 310, 311
  Al-substitution, 72, 172, 273, 274
  dehydroxylation, 273
  pedogenic, 50, 51, 273, 274, 278, 295, 306, 307, 310, 311
  precipitation, 19
  synthetic, 159, 218
Grand Canyon, 147

H

Hauptrogenstein Formation, 71
helium
  cryogenic trapping of, 38, 64
  extraction, 21
  extraction by laser-heating, 64
  retention in goethite, 12, 14, 16, 19, 32
  retention in iron-oxides, 54
  retention in kaolinite, 18
  retention in pedogenic iron-oxides, 3, 25, 271
hematite, 1–4, 8, 50, 51, 143, 145–152, 154, 155, 157–169, 171–175, 177–181, 189, 209–211, 215, 218–222, 236, 272, 273, 277, 278, 280, 291, 293, 295, 306, 307, 311
  botryoidal, 147
  hydrothermal, 147
  pedogenic, 3, 50, 51, 272–274, 279, 295, 306, 307, 311
  synthetic, 159, 219, 221
Huppersand, 56

I

inductively coupled plasma mass spectrometry (ICP-MS), 15, 18, 41, 43, 65
iron-oxides
  lepidocrocite, 273

mineral species, 273
pedogenic, 3, 4, 12, 20, 23, 25, 271–278, 280–283, 288, 289, 300, 306, 308, 311
precipitation, 23, 24
isotope dilution, 43, 65

J

Jura Mountains, 9, 58, 68–71, 74, 78–80, 82

K

kaolinite, 10, 12, 14, 18, 24, 41, 50, 51, 62, 63
karst, 15
fissure, 9
fissure filling, 9, 10, 20, 54, 56–61, 67–69, 71–75, 77, 78, 81, 82, 84–86, 111, 112, 186
karstic weathering, 55, 85
Kraichgau, 69, 71, 78

L

laterite, 19, 24
lateritic soil, 19
lepidocrocite, 273
lessivage, 293, 309–311
Li, 20, 276, 277, 288, 290, 293
limestone, 10–12
dissolution, 11
Jurassic, 13
residues, 11
Lohn am Randen, 10, 11, 13, 16, 24, 44, 49, 56, 62, 72–74, 76, 78, 79, 82, 95, 96, 123–125
Luvisols, 19

M

Malsenhof, 61, 74–77, 110, 125
mass spectrometry
inductively coupled plasma mass spectrometry (ICP-MS), 65
quadrupole mass spectrometer, 43, 64
sector field mass spectrometry, 15, 38, 291
mass spetrometry
inductively coupled plasma mass spectrometry (ICP-MS), 15, 18, 41, 43
Mervelier, 62, 74, 125
Minas Gerais, 147
minerals
amphibole, 288
apatite, 144, 145, 274, 308
biotite, 288
calcite, 218, 219, 222, 288, 308
detrital, 301, 308
feldspar, 274, 276, 288, 298
ferrihydrite, 273, 307
goethite, 1, 2, 8–12, 14, 15, 17, 19, 24, 25, 37, 38, 41, 44–51, 57, 62, 63, 65, 66, 72, 74, 75, 79, 82–84, 86, 143–151, 155–159, 162, 165–167, 169, 171, 173, 174, 180, 181, 201, 209–211, 216, 218, 228–236, 242–245, 253–256, 266–268, 271–274, 277, 278, 280, 287, 290, 291, 293, 295, 306, 307, 310, 311
hematite, 1–4, 8, 50, 51, 143, 145–152, 154, 155, 157–169, 171–175, 177–181, 189,

209–211, 215, 218–222, 236, 272, 273, 277, 278, 280, 291, 293, 295, 306, 307, 311
kaolinite, 10, 12, 14, 18, 24, 41, 50, 51, 62, 63
lepidocrocite, 273
portlandite, 218, 219, 222
pyroxene, 276, 288
quartz, 9, 14, 56, 59, 83, 84, 148, 218, 219, 271, 272, 274, 276, 284, 288, 289, 291, 292, 301
titanite, 144, 145
zircon, 144, 145, 274, 301
minerals
quartz, xlv
Molasse alsacienne, 60
Munsell color, 11, 286, 293
muogenic production of ^{3}He, 20
Muschelkalk, 71

N

Nb packets, 144, 155, 157, 176, 189, 198, 245, 248, 250
Niederhorn Formation, 71
normal solution, 64
nucleogenic production, 20
nucleus, xlv, 10, 13, 14, 17, 35, 36, 63

O

Oberbuchsiten, 99
Oberdorf, 62, 74, 97, 125
Obere Brackwassermolasse (OBM, Upper Brackish Molasse), 12
Obere Meeresmolasse (OMM), Upper Marine Molasse, 12
OBM, 12
Öhrli Formation, 69
OMM, 12
outcrops
Aufberg, 60, 74, 75, 77, 110, 112
Balsthal Erzmatt, 61, 74, 76, 110, 123
Balsthal Holzfluh, 60, 74, 112
Cholplatz, 60, 74, 76, 79, 82, 83, 113
Erpfingen, 59, 74
Lohn am Randen, 10, 11, 13, 16, 24, 44, 49, 56, 62, 72–74, 76, 78, 79, 82, 95, 96, 123–125
Malsenhof, 61, 74–77, 110, 125
Mervelier, 62, 74, 125
Oberbuchsiten, 99
Oberdorf, 62, 74, 97, 125
Petersbuch, 56, 58, 59, 72, 75, 77, 78, 94, 110, 118
Rothenstein, 58, 59, 72, 75, 78, 96, 98, 110, 119
Weißenburg, 75, 93, 121
Weißenburg, 58, 59, 72, 78, 85, 110
Whitewater Hill, 283–286
Willmandingen, 60, 74, 75, 77, 79, 110, 121
Oxisols, 8, 278

P

paleo-elevation, 22
paleo-exposure, 2, 8, 9, 20–23, 25, 57, 75, 76, 78
paleosol, 8, 9, 11–13, 15, 18–25, 39, 41, 42, 44, 55–58, 61, 68, 72, 75–78, 81, 82, 84–86, 271, 284, 285, 310
burial, 21

pedogenic iron-oxides, 308
Petersbuch, 56, 58, 59, 72, 75, 77, 78, 94, 110, 118
pisolith, 13–21, 23, 25, 37, 44, 49, 55, 57–68, 71, 72, 74–83, 85, 86, 110, 127, 144, 271
  cortex, 10, 13, 14, 17–20, 23, 32, 34–37, 63, 66
  nucleus, 10, 13, 14, 17, 35, 36, 63
  radial age profile, 17
pisolith
  nucleus, xlv
pisolith
  cortex, xliv
portlandite, 218, 219, 222
projector-lamp heating, 31
proton irradiation, 31, 32
Pt packets, 43, 64, 144, 148, 150, 151, 155, 157, 160, 166, 175–177, 180, 181, 186, 188–190, 196, 198–200, 202–206, 208, 217, 245–257, 260, 263–268
pyrometer, 148, 164, 175, 180, 187–189, 198–208, 217
pyroxene, 276, 288

Q

quadrupole mass spectrometer, 43, 64
quartz, xlv, 9, 14, 56, 59, 83, 84, 148, 218, 219, 271, 272, 274, 276, 284, 288, 289, 291, 292, 301
  ATR-FTIR spectrum, 219

R

Rüssingen Formation, 71
Randen fault, 11, 13, 15
re-extract, 38, 43, 64
Redwall Limestone, 147
relict soil, 283–285, 294
Reuchenette Formation, 61, 62
Rheingraben, 24, 69, 71, 78
Rossemaison Formation, 67, 71
Rothenstein, 58, 59, 72, 75, 78, 96, 98, 110, 119
Ru-spike, 64, 151, 209–216, 290, 292

S

Salmendingen, 60
sample preparation
  for (U-Th)/He dating, 14, 64
  for measuring ^{3}He, 20, 66, 300, 301
samples
  dissolution of, 14, 15, 41, 43, 64, 65, 72
  preparation, 64
  projector-lamp heating, 31
  proton irradiation of, 31, 32
sampling
  paleosol, 12
sampling locations
  Aufberg, 60, 74, 75, 77, 110, 112
  Balsthal Erzmatt, 61, 74, 76, 110, 123
  Balsthal Holzfluh, 60, 74, 112
  Cholplatz, 60, 74, 76, 79, 82, 83, 113
  Erpfingen, 59, 74
  Lohn am Randen, 10, 11, 13, 16, 24, 44, 49, 56, 62, 72–74, 76, 78, 79, 82, 95, 96, 123–125
  Malsenhof, 61, 74–77, 110, 125
  Mervelier, 62, 74, 125
  Oberbuchsiten, 99

Oberdorf, 62, 74, 97, 125
Petersbuch, 56, 58, 59, 72, 75, 77, 78, 94, 110, 118
Rothenstein, 58, 59, 72, 75, 78, 96, 98, 110, 119
Weißenburg, 75, 93, 121
Weißenburg, 58, 59, 72, 78, 85, 110
Whitewater Hill, 283–286
Willmandingen, 60, 74, 75, 77, 79, 110, 121
San Andreas fault, 283
Banning Strand, 283, 284
Garnet Hill Strand, 283
San Gorgonio Pass, 283
Sanetsch Formation, 71, 79
saprolite, 8
Scanning Electron Microscope (SEM), 14, 18
Seewen Formation, 69
Siderolithic (Siderolithikum), 9, 55, 56, 60–62, 67, 69, 79
small mammal fossils, 25
soil convection, 22
model, 22, 25, 42
soils, 25
clay soils, 18, 23, 24
development, 7, 11, 19, 20, 23, 25
lateritic, 24
lessivage, 309–311
long-term stability, 24, 25
Luvisols, 19
modern, 7, 23, 24
Oxisols, 8, 278
oxisols, 7
relict soil, 283–285, 294
residence time, 7, 24, 25
Ultisols, 8, 19, 278
ultisols, 7
spallation, 21, 275
spike, 41, 43, 64
Ca-spike, 43, 209, 211
Ru-spike, 64, 151, 209–216, 290, 292
standard solution, 64
Swabian Alb, 9, 10, 20, 54, 55, 58, 68–71, 74
Switzerland, 11

T

terra rossa, 19, 25
Terrain sidérolithique, 9, 55, 56, 60–62, 67, 69, 79
terre jaune, *see* Rossemaison Formation
Th concentration, 16
Th/U ratio, 16
titanite, 144, 145
tropical weathering, 19, 20, 25

U

U concentration, 16
Ultisol, 8
Ultisols, 19, 278
unconformity, 54
Upper Brackish Molasse (OBM), German: Obere Brackwassermolasse, 12
Upper Marine Molasse (OMM), 12

V

Vallorbe Formation, 69

W

weathering, 7, 23
    dissolution-precipitation, 8, 82
    limestone dissolution, 11
    rate, 7
Weißenburg, 75, 93, 121
Weißenburg, 58, 59, 72, 78, 85, 110
Whitewater Hill, 283–286
Willmandingen, 60, 74, 75, 77, 79, 110, 121

Z

zircon, 144, 145, 274, 301